This document was too large to scan as a single document. It has been divided into smaller sections.

Section 3 of 4

Document Information			
Document #	**RPP-10098**	**Revision**	**1**
Title	FIELD INVESTIGATION REPORT FOR WASTE MGMT AREA B-BX-BY [VOL 2 APPENEDICES D-I]		
Date	**1/6/2003**		
Originator	**KNEPP AJ**	**Originator Co.**	**CH2M**
Recipient		**Recipient Co.**	
References	**EDT-630527**		
Keywords			
Projects	**TFARM**		
Other Information			

59677 3/4

FIELD INVESTIGATION REPORT FOR WASTE MANAGEMENT AREA B-BX-BY

VOLUME 2, APPENDICES D - I

December 13, 2002

Prepared for
CH2M HILL Hanford Group, Inc.
Richland, Washington

Prepared by
Jacobs Engineering Group, Inc.
Richland, Washington

FIELD INVESTIGATION REPORT FOR WASTE MANAGEMENT AREA B-BX-BY

VOLUME 2, APPENDICES D - I

December 13, 2002

Author
Anthony J. Knepp

Prepared for
CH2M HILL Hanford Group, Inc.
Richland, Washington

Prepared by
Jacobs Engineering Group, Inc.
Richland, Washington

This page intentionally left blank.

RPP-10098
Revision 0
Volume 2

FIELD INVESTIGATION REPORT FOR WASTE MANAGEMENT AREA B-BX-BY

VOLUME 2, Appendices D-I

Prepared for the U.S. Department of Energy
Assistant Secretary for Environmental Management

CH2MHILL
Hanford Group, Inc.
Richland, Washington

Contractor for the U.S. Department of Energy
Office of River Protection under Contract DE-AC27-99RL14047

Approved for Public Release
(Upon receipt of Clearance approval)
Further Dissemination Unlimited

RPP-10098
Revision 0
Volume 2

FIELD INVESTIGATION REPORT FOR WASTE MANAGEMENT AREA B-BX-BY

VOLUME 2, Appendices D-I

A. J. Knepp, CH2M HILL Hanford Group, Inc.

December 2002

Prepared for the U.S. Department of Energy
Assistant Secretary for Environmental Management

CH2MHILL
Hanford Group, Inc.
Richland, Washington

Contractor for the U.S. Department of Energy
Office of River Protection under Contract DE-AC27-99RL14047

JAN 06 2003
DATE:
STA: 15
HANFORD RELEASE
ID: 22

Chris Gillingham 1/6/03
Clearance Approval Date

Release Approval (stamp)

Approved for Public Release
(Upon receipt of Clearance approval)
Further Dissemination Unlimited

RPP-10098
Revision 0
Volume 2

For use with Technical Documents (when appropriate)	
EDC-	FMP-
EDT- 630527	ECN-
Project No.:	Division:
Document Type: ENV	Page Count: ~~1084~~ 626

For use with Speeches, Articles, or Presentations (when appropriate)							
Abstract		Summary		Full Paper		Visual Aid	
Conference Name:							
Conference Date:							
Conference Location:							
Conference Sponsor:							
Published in:							
Publication Date:							

TRADEMARK DISCLAIMER

Reference herein to any specific commercial product, process, or service by trade name, trademark, manufacturer, or otherwise, does not necessarily constitute or imply its endorsement, recommendation, or favoring by the United States Government or any agency thereof or its contractors or subcontractors.

Scientific or technical information is available to U.S. Government and U.S. Government contractor personnel through the Office of Scientific and Technical Information (OSTI). It is available to others through the National Technical Information Service (NTIS).

This report has been reproduced from the best available copy.

Printed in the United States of America

APPENDIX D

DIGEST OF SCIENCE AND TECHNOLOGY PROJECT EVALUATIONS

This page intentionally left blank.

CONTENTS

D.1.0 OVERVIEW AND SUMMARY D-1
D.1.1 KEY FINDINGS D-2
D.1.1.1 Strontium Adsorption, Desorption, and Transport in Pristine and Contaminated Sediment D-2
D.1.1.2 Uranium Speciation and Dissolution from BX-102 Sediments D-3
D.1.1.3 Fluid Migration in the BX Tank Farm (Preliminary Findings) D-5
D.1.1.4 Isotope Tracking of the Fate and Transport of Radionuclides in Waste Management Area B-BX-BY Sediments D-5

D.2.0 STRONTIUM ADSORPTION, DESORPTION, AND TRANSPORT IN PRISTINE AND CONTAMINATED SEDIMENT D-7
D.2.1 STRONTIUM IN THE B-BX-BY TANK FARMS D-9
D.2.1.1 References D-11
D.2.2 ION EXCHANGE STUDIES D-13
D.2.2.1 Introduction D-13
D.2.2.2 Experimental Methods D-14
D.2.2.3 Results and Discussion D-19
D.2.2.4 Conclusions D-30
D.2.2.5 References D-31
D.2.3 MODELING BATCH REACTOR ION EXCHANGE EXPERIMENTS OF STRONTIUM-CALCIUM-MAGNESIUM-POTASSIUM-SODIUM ON HANFORD SEDIMENTS D-33
D.2.3.1 Introduction D-33
D.2.3.2 Model Formulation D-34
D.2.3.3 Model Results D-35
D.2.3.4 Discussion D-48
D.2.3.5 Conclusions D-48
D.2.3.6 References D-49
D.2.4 DESORPTION AND MINERALOGIC RESIDENCE OF STRONTIUM-90 IN B-110 SEDIMENT D-50
D.2.4.1 Introduction D-50
D.2.4.2 Experimental Methods D-50
D.2.4.3 Results and Discussion D-52
D.2.4.4 Conclusions D-67
D.2.4.5 References D-68
D.2.5 STRONTIUM MIGRATION IN HANFORD SEDIMENT FROM THE B, BX, AND BY TANK FARMS: A CATION EXCHANGE MODEL BASED ON LABORATORY TRANSPORT EXPERIMENTS. D-69
D.2.5.1 Introduction D-69
D.2.5.2 Experimental Procedures D-69
D.2.5.3 Modeling Procedures D-71
D.2.5.4 Results and Discussion D-72
D.2.5.5 Conclusions D-81

D.2.5.6 References D-82
D.2.6 ONE-DIMENSIONAL REACTIVE FLOW AND TRANSPORT MODEL OF STRONTIUM MIGRATION AT TANK B-110 ..... D-83
D.2.6.1 Introduction D-83
D.2.6.2 Model Formulation D-84
D.2.6.3 Model Calibration D-87
D.2.6.4 Model Results D-98
D.2.6.5 Discussion D-101
D.2.6.6 Conclusion D-102
D.2.6.7 References D-102

D.3.0 URANIUM SPECIATION AND DISSOLUTION FROM BX-102 SEDIMENTS D-103
D.3.1 SIMULATED B, BX, AND BY TANK FARMS SUPERNATE COMPOSITIONS D-107
D.3.1.1 Introduction D-107
D.3.1.2 Results D-107
D.3.1.3 Observations and Qualifiers D-119
D.3.1.4 Conclusions D-120
D.3.1.5 References D-121
D.3.2 THE IDENTIFICATION OF URANIUM-BEARING PHASES BY X-RAY MICROPROBE, ELECTRON MICROPROBE, AND SCANNING ELECTRON MICROSCOPY D-122
D.3.2.1 Introduction D-122
D.3.2.2 Experimental Methods D-123
D.3.2.3 Results and Discussion D-125
D.3.2.4 Conclusions D-138
D.3.2.5 References D-138
D.3.3 X-RAY SPECTROSCOPIC INVESTIGATION OF THE DISTRIBUTION AND SPECIATION OF URANIUM IN SAMPLES FROM THE BX-102 BOREHOLE D-140
D.3.3.1 Introduction D-140
D.3.3.2 Methods D-142
D.3.3.3 Results D-144
D.3.3.4 Conclusions D-153
D.3.3.5 References D-154
D.3.4 FLUORESCENCE SPECTROSCOPIC STUDIES OF URANIUM-BEARING VADOSE ZONE SEDIMENTS D-161
D.3.4.1 Introduction D-161
D.3.4.2 Experimental Procedures D-162
D.3.4.3 Results D-167
D.3.4.4 Conclusions and Implications D-184
D.3.4.5 References D-185
D.3.5 THERMODYNAMICS AND DISSOLUTION KINETICS OF URANYL MINERALS IN HANFORD BX-102 SEDIMENTS D-188
D.3.5.1 Introduction D-188
D.3.5.2 Background D-188

D.3.5.3 Thermodynamic Properties of Potential Relevant Uranium(VI) Phases D-190
D.3.5.4 Thermodynamic Analysis of Porewater D-193
D.3.5.5 Dissolution Experiments D-196
D.3.5.6 Physical Model of Uranyl Leaching D-203
D.3.5.7 Thermodynamic and Kinetic Analysis of Uranyl Dissolution D-206
D.3.5.8 Implications of Solubility Behavior to Kd D-212
D.3.5.9 Conclusions D-214
D.3.5.10 References D-217

D.4.0 FLUID MIGRATION AND TRANSPORT D-221
D.4.1 HYDROLOGIC TESTS OF LATERAL FLOW AND TRANSPORT IN THE HANFORD VADOSE ZONE D-223
D.4.1.1 Introduction D-223
D.4.1.2 The Vadose Zone Transport Field Study Site D-226
D.4.1.3 Implications of Studies at the Vadose Zone Transport Field Study Site for the BX Tank Farm D-231
D.4.1.4 References D-232
D.4.2 MODELING STUDIES OF FLUID FLOW AND SOLUTE TRANSPORT AT TANK BX-102 IN THE HANFORD VADOSE ZONE D-234
D.4.2.1 Introduction D-234
D.4.2.2 Definition of Test Case D-239
D.4.2.3 Modeling Approach D-244
D.4.2.4 Two-Dimensional R-Z Model D-245
D.4.2.5 Two-Dimensional Vertical Section D-249
D.4.2.6 Space Discretization Issues D-261
D.4.2.7 Three-Dimensional Model D-263
D.4.2.8 Conclusions D-272
D.4.2.9 References D-273
D.4.3 CESIUM-137 REACTIVE TRANSPORT MODELING AT TANK BX-102 ..... D-276
D.4.3.1 Introduction D-276
D.4.3.2 Experiment Descriptions D-277
D.4.3.3 Experimental Results D-278
D.4.3.4 Modeling Cesium Adsorption Experiments D-282
D.4.3.5 Application to Tank BX-102 ..... D-285
D.4.3.6 Tank BX-102 Modeling D-287
D.4.3.7 Conclusions D-289
D.4.3.8 References D-290

D.5.0 ISOTOPE TRACKING OF THE FATE AND TRANSPORT OF RADIONUCLIDES IN B, BX, AND BY TANK FARMS SEDIMENTS D-292
D.5.1 THE ISOTOPIC COMPOSITIONS OF WATER LABILE URANIUM FROM 299-E33-45 AND 299-E33-46 CORE SAMPLES: IMPLICATIONS FOR THE SOURCE AND HISTORY OF GROUNDWATER CONTAMINATION IN THE WMA B-BX-BY AREA D-293

D.5.1.1 Introduction D-293
D.5.1.2 Analytical Methods D-293
D.5.1.3 Results D-295
D.5.1.4 Discussion D-299
D.5.1.5 Conclusions D-301
D.5.1.6 References D-301
D.5.2 STRONTIUM ISOTOPE EVIDENCE FOR INTERACTION BETWEEN WASTE FLUIDS AND SEDIMENTS IN THE WMA B-BX-BY VADOSE ZONE D-302
D.5.2.1 Introduction D-302
D.5.2.2 Results D-302
D.5.2.3 Discussion D-304
D.5.2.4 Conclusions D-305
D.5.2.5 Reference D-305

FIGURES

D.1. The Depth Distribution of Strontium-90 in Borehole 299-E33-46 (Near Tank 241-B-110) D-10
D.2. Porewater Concentrations of Major Cations and Anions in Borehole 299-E33-46 Shown in Reference to the Depth Distribution of Strontium-90 ..... D-11
D.3. Strontium Sorption on Na-OAc Extracted Hanford Fine Sand Composite in Sodium Nitrate Electrolyte. Depicted are K_d Functions (a) and Isotherms(b) D-19
D.4. Strontium Sorption on Na-OAc Extracted Fine Sand Composite in Calcium-Nitrate Electrolyte. Depicted are K_d Functions (a) and Isotherms (b) D-20
D.5. Relationship of Sr-K_d to Electrolyte Concentration in Sodium and Calcium Electrolyte D-22
D.6. Strontium Sorption on Selected Hanford Sediments in Sodium Nitrate and Sodium Bicarbonate Electrolyte D-23
D.7. Strontium Sorption on the Upper and Lower B Tank Farm Composite Sediments in Mixed Sodium and Calcium Electrolyte (each at 0.001 mole/L) D-25
D.8. Strontium Sorption on B Tank Farm Composite Sediments in Sodium Nitrate or Sodium Biocarbonate Electrolyte with NTA (nitrilo-triacetic acid) D-26
D.9. K_d Functions and Adsorption Isotherms for Strontium on the Na-OA_c Treated Hanford Fine Sand Composite D-30
D.10. Fitted Sr^{2+} Isotherm Compared with Experimental Data for Type 2 Experiments D-38
D.11. Fitted Ca^{2+} Isotherm Compared with Experimental Data for Type 2 Experiments D-39
D.12. Fitted Mg^{2+} Isotherm Compared with Experimental Data for Type 2 Experiments D-39
D.13. Fitted K^+ Isotherm Compared with Experimental Data D-40
D.14. Predicted Na^+ Isotherm Compared with Experimental Data D-41
D.15. Calculated pH Plotted as a Function of Total Aqueous Sr^{2+} Concentration D-41
D.16. Prediction of Experiments 57488-45, 60, 63, 69 using a CEC of 50.2. μeq/g D-43
D.17. Predicted Simulations of Experiments 57488-66, 72, and 77 Using a CEC of 50.2 μeq/g and Fitted Selectivity Coefficients Listed in (Table D.4) D-44
D.18. Prediction of Experiments 57869 for a CEC of 50.2 μeq/g D-45
D.19. Prediction of Experiments 57869 for a CEC of 50.2 μeq/g D-45
D.20. Prediction of Experiments 57869 Involving H_3NTA with a CEC of 50.2 μeq/g D-47
D.21. Concentrations of Water and Acid Extractable Strontium, Calcium, and Strontium-90 in the B-110 Borehole D-52
D.22. Time-Dependent Desorption of Strontium-90 from B-110 Sediment (26A) in Various Electrolytes D-53
D.23. Concentrations of Strontium-90 and Stable Strontium Isotopes Desorbed from 26A D-55
D.24. Desorbed/Dissolved Concentrations of Calcium (Ca^{2+}) from 26A in Different Electrolytes D-56
D.25. Desorbed/Dissolved Concentrations of Magnesium (Mg^{2+}) from 26A in Different Electrolytes D-56
D.26. Desorbed/Dissolved Concentrations of Strontium (Sr^{2+}) from 26A in Different Electrolytes D-57
D.27. Desorbed/Dissolved Concentrations of Potassium (K^{2+}) from 26A in Different Electrolytes D-57

D.28. Model Predictions for Calcium, Strontium, and Magnesium from the Desorption Experiments D-60
D.29. Photograph of Segregated Positive and Negative Particles D-62
D.30. Comparative Coarse-Scale Images of Sample 26A, Diameter 1.25 cm D-64
D.31. SEM Photomicrograph of Radioactive Basalt Fragment #1 Figure D.30 That Shows Collonade Texture D-65
D.32. SEM Photmicrograph of Radioactive Basalt Fragment #2 in Figure D.30 that Shows Entabulature Texture D-65
D.33. SEM Photomicrograph of Radioactive Basalt Fragment #3 in Figure D.30 that Shows Collonade Texture D-66
D.34. SEM Photomicrograph of the Right Side of the Large Radioactive Basalt Fragment #4 in Figure D.30 that Shows Collonade Texture D-66
D.35. Breakthrough of ^{22}Na and Iodide (a tracer) in Flow-Through Column Experiment D-74
D.36. Iodide (tracer) Breakthrough in Experiment 1 is Matched with a Dispersivity of 3.5 Centimeters D-74
D.37. Strontium Breakthrough and Subsequent Desorption in Experiments 1 through 4 (0.01, 0.1, 1, and 5 M $NaNO_3$, respectively in the sorption stage and 0.01, 0.1, 1, and 1 M KNO_3, respectively in the desorption stage). D-77
D.38. Strontium breakthrough and subsequent desorption in Experiments 1 through 4 (0.01, 0.1, 1, and 5 M $NaNO_3$ respectively in the sorption stage and 0.01, 0.1, 1, and 1 M KNO_3 respectively in the desorption stage) D-79
D.39. Strontium breakthrough and subsequent desorption in Experiment 5, 1 M $NaNO_3$ and 1 M KNO_3 with an injection concentration of 10^{-6} M strontium D-80
D.40. Dependence of the Sodium-Strontium and Potassium-Strontium Selectivity Coefficients Based on Column Experiments D-80
D.41. Vertical Profiles for Ca^{2+}, K^+, HPO_4^{2-}, and F^- Comparing Field Observations with FLOTRAN (FT) After an Elapsed Time of 35 Years D-99
D.42. Vertical Profiles for Ca^{2+}, K^+, HPO_4^{2-}, and F^- Comparing Field Observations with FLOTRAN (FT) After an Elapsed Time of 35 Years D-99
D.43. Depth Profiles for Minerals Fluorite and Whitlockite After an Elapsed Time of 35 Years D-100
D.44. Strontium Sorption Profile After an Elapsed Time of 35 Years D-100
D.45. Time Evolution of Sorbed Strontium Plotted as a Function of Depth for Times of 25, 50, and 100 Years D-101
D.46. Distribution of Uranium(U) in Borehole 299-E33-45 (near Tank 241-BX-102) D-105
D.47. The Predicted Solubility of Clarkeite in a $NaOH$-$NaNO_3$-$NaHCO_3$ Solution Using the Pitzer Activity Coefficient Model D-117
D.48. Backscattered-Electron SEM Image of Sample 61AB at Right, Left, and with XMP Overlay of False-Color Uranium Abundance D-125
D.49. EXAFS Plots Of Bulk Measurements of BX Samples (Left, Top), and for a Single Uranium-Rich Grain Compared to Rutherfordine (Bottom), a Uranyl Carbonate [Uranium(VI)O_2CO_3] D-126
D.50. Backscattered-Electron EMP Image of the Region from Figure D.48 that Lies Between the Upper Edge of the Imaged Mica and the Adjacent Silicate D-128

D.51. Composite Backscattered Electron Images of Uranium Silicates Associated with a Single Silicate Clast D-129
D.52. Backscattered-Electron SEM Images of the Mica and Silicate Grains in Figure D.48 and Figure D.50 ..... D-130
D.53. Plots of Uranium, Iron, and Strontium Abundance, and of Overall X-Ray Absorption (4 pages) D-134
D.54. Model Compound Uranium L_{III}-EXAFS Library Used in Linear Combination Fitting of Sample EXAFS Data D-144
D.55. Uranium L_{α} Fluorescence (top) and X-ray Transmission (bottom) Maps of a Thin Section from Sample 61AB D-145
D.56. Uranium L_{α} Fluorescence (left) and X-ray Transmission (right) Maps of the Areas Around (a) Hotspot 1, (b) Hotspot 2, (c) Hotspot 3, and (d) Hotpot D-146
D.57. Uranium Lα Fluorescence (top) and X-ray Transmission (bottom) Maps of the Area Around Hotspot 5 ..... D-147
D.58. XANES Spectra of the Four BX-102 Borehole Sample, as Well as Those of Schoepite, a Uranium(VI) Standard, and Uraninite, a Uranium(IV) Standard D-148
D.59. Uranium L_{III} μ-XANES Spectra of Five Hotpots from the Sample 61A Thin Section D-149
D.60. Uranium L_{III}-EXAFS (right) and Corresponding Fourier Transforms (left) Data (black) and Structural Model Fits (red dashed) for the Four BX-102 Core Samples D-151
D.61. Comparison of Uranium-Uranium Distances Derived from the Fits to the Uranium L_{III}-EXAFS Spectra of the Four BX-102 Samples to Crystallographic Distances in Uranium Minerals D-152
D.62. Linear Combination Least Squares Fit of the Uranium L_{III}-EXAFS Spectra of Borehole BX-102 Samples Using One Component (Uranophane) D-153
D.63. Aqueous Speciation of Uranium(VI) (Partial Pressure of $CO_2 = 10^{-3.5}$ atm; Total Uranium(VI) = 1×10^{-6} M; I = 0.1 M $NaClO_4$) D-165
D.64. Uranyl Fluorescence Emission Spectra at Different Temperature D-168
D.65. Fluorescence Spectra of Standard Uranyl Minerals. λ_{ex} = 415 nm. D-169
D.66. Fluorescence Spectra of Standard Uranyl Minerals (Continued). λ_{ex} = 415 nm. D-170
D.67. Time-Resolved Fluorescence Emission Spectra of a Mixture of Soddyite and Curite; λ_{ex} = 415 nm. D-172
D.68. Time-Resolved Fluorescence Emission Spectra of Saleeite ($Mg[(UO_2)(PO_4)]_2 \cdot (H_2O)_{10}$). λ_{ex} = 415 nm. D-173
D.69. Fluorescence Emission Spectra of Hanford Vadose Sediments Under Tank BX-102 at 5.5 K. λ_{ex} = 415 nm. D-174
D.70. Time-Resolved Fluorescence Emission Spectra of Hanford Vadose Zone Sediments S01014-61AB (upper panel) and S01014-67AB (lower panel) Under Tank BX-102 at 5.5 K. λ_{ex} = 415 nm. D-175
D.71. Fluorescence Emission Spectra at 5.2K of Hanford Vadose Sediments -61AB (upper panel) and -67AB (lower panel) Under Tank BX-102 Before and After Leaching with Electrolyte Solutions Na-1 and Na-2 ..... D-177
D.72. Fluorescence Emission Spectra at 5.2 K of Hanford Vadose Sediments -61AB (upper panel) and -67AB (lower panel) Under Tank BX-102 Before and After Leaching with Ca^{2+}-Saturated Electrolyte Solutions, Ca-1 and Ca-2. ..... D-178

D.73. Fluorescence Emission Spectra of Uranyl from Hanford Vadose Sediments -61AB (upper panel) and -67AB (lower panel) Leached into the Electrolyte Solutions Na-1 and Na-2. ..... D-179
D.74. Fluorescence Emission Spectra at 5.2 K of Uranyl from the Sediment -61AB (upper panel) and -67AB (lower panel) Leached into the Ca^{2+}-Saturated Electrolyte Solutions, Ca-1 and Ca-2. ..... D-180
D.75. Fluorescence Emission Spectra of Uranyl Carbonate Solutions at Different pH at 5.5 K. I = 0.1 M; $[Na_2CO_3] = 8 \times 10^{-3}$ M; $[UO_2^{2+}] = 2 \times 10^{-5}$ M; $\lambda_{ex} = 415$ nm. D-182
D.76. Fluorescence Emission Spectra at 5.2 K of Hanford Vadose Zone Porewaters Under Tank BX-102. $\lambda_{ex} = 415$ nm. D-183
D.77. Uranyl Solubility in Sodium or Sodium-Calcium Electrolyte Suspensions D-199
D.78. Uranium(VI) Time-Dependent Dissolution from BX-102 Sediments in Sodium-Nitrate Electrolye D-200
D.79. Uranium(VI) Time-Dependent Dissolution from BX-102 Sediments in Sodium-Calcium Electrolyte D-201
D.80. X-ray Microscopic Image of BX-102 Sample 61 ..... D-204
D.81. X-ray Microscopic Image of BX-102 Sample 67 ..... D-205
D.82. Measured and Calculated Uranyl Solubility of Samples 61AB and 67AB in $NaNO_3$ (0.05M) Electrolyte D-206
D.83. Measured and Calculated Uranyl Solubility of Samples 61AB and 67AB in Sodium-Calcium (0.05M) Electrolyte D-207
D.84. Distribution Coefficients (K_d) for Uranium in Kinetic Desorption/Dissolution Experiments in Sodium-Electrolyte D-213
D.85. Lateral Spreading of Water in Hanford Formation Sediments D-223
D.86. Moisture and Dye Distributions at the Army Loop Road Clastic Dike Site at the Hanford Site D-224
D.87. Schematic of Well Placement at the Sisson and Lu Experimental Site D-227
D.88. Stratigraphic Column at the Sisson and Pre-Injection Moisture Contents Profile Measured for Samples from the S1 Core Lu Experimental Site D-227
D.89. Comparison of the (a) Observed and (b) Predicted Soil Water Contents at the H-Section of the Injection Experiment using Parameters Derived from a Combination of Parameter Scaling and Inverse Modeling D-230
D.90. Comparison of the Predicted and Observed Soil Water Contents at the H Section of the Injection Experiment Described in Sisson and Lu (1984) D-230
D.91. Observed Water Content Distribution Following the Sisson and Lu Injection Experiment along a North-South Transect (from Rockhold et al. 1999) D-238
D.92. Alternative Conceptual Models for Lateral Moisture Migration in a Layered Medium D-239
D.93. Hydraulic Conductivity Functions for Different Stratigraphic Units from the WMA B-BX-BY Data Package (Khaleel et al. 2001) D-242
D.94. Hydraulic Conductivities for 15 Samples from the Sisson and Lu Site D-243
D.95. Hydraulic Conductivity Functions Selected for Base Case D-243
D.96. Simulated Water Flow Rates Across Different Horizons for the Model with Homogeneous Properties for the Sand D-247
D.97. Simulated Water Flow Rates Across Different Horizons for the COMA Model that Includes Silt Layers Amounting to 10% of Vertical Thickness in the Sand D-247

D.98. Simulated Flow Rates of Spilled Fluid Across Different Horizons for the Model with a Homogeneous Sand and for the COMA Model D-248
D.99. Mass Fractions of Spilled Fluid after 50 Years for the Model with a Homogeneous Sand (a) and for the COMA Model (b) D-248
D.100. Gridding used for 2-Dimensional Tilted Section D-250
D.101. Schematic of 2-Dimensional Section, Tilted by an Angle α Against the Horizontal Direction D-250
D.102. Simulated Moisture Content in a Model with Layers Sloping at an Angle of 3° Slope D-252
D.103. Simulated Mass Fractions of Spilled Fluid after 50 years in the Model with 3° Slope D-252
D.104. Simulated Moisture Content in a Model with Layers Sloping at an Angle of 10°Slope D-253
D.105. Simulated Mass Fractions of Spilled Fluid after 50 years in the Model with 10° Slope D-253
D.106. Horizontal-to-Vertical Conductivity Anisotropy Required for Moisture Migration to Occur at a 45° Angle with Respect to the Vertical, as a Function of Layer Slope D-255
D.107. Moisture Plume for Anisotropy a = 20 at 38.26 Days after Start of Injection D-256
D.108. Simulated Mass Fractions of Spilled Fluid after 38.3 Days for Anistotropy a = 20 . D-257
D.109. Moisture Plume for Anisotropy a = 20 at 8.65 yr after Start of Injection D-257
D.110. Simulated Mass Fractions of Spilled Fluid after 8.65 yr for Anistotropy a = 20 ..... D-258
D.111. Simulated Mass Fractions of Spilled Fluid after 50 yr for Anistotropy a = 20 ..... D-258
D.112. Simulated Mass Fractions of Spilled Fluid after 8.65 yr for a System with Horizontal Layers and an Anistotropy a = 20 ..... D-259
D.113. Simulated Mass Fractions of Spilled Fluid after 50 yr for a System with Horizontal Layers and an Anistotropy a = 20 ..... D-260
D.114. Mass Fractions of Spilled Fluid for a System with Horizontal Layers and an Anistotropy a = 20 ..... D-261
D.115. Definition Domain of the Three-Dimensional Model D-264
D.116. Water Flow Rate Across Three Horizons at 6, 22, and 50 m depth, respectively, shown on logarithmic time scale (top) and linear time scale (bottom) D-265
D.117. Moisture Distribution in the Vertical Plane X = 1.25 m after 38.26 days D-266
D.118. Moisture Distribution in the Vertical Plane X = 1.25 m after 1 year D-266
D.119. Gravity-Driven Seepage in an Anisotropic Medium D-267
D.120. Solute Distribution in the Vertical Plane X = 1.25 m after 38.26 days D-268
D.121. Solute Distribution in the Vertical Plane X = 1.25 m after 1 year D-269
D.122. Solute Ddistribution in the (sub-)horizontal Plane Z' = -13.0 m after 1 year D-269
D.123. Solute Distribution in the Vertical Plane X = 1.25 m after 8.65 years D-270
D.124. Solute Distribution in the (sub-)horizontal Plane Z' = -27.0 m after 8.65 years D-270
D.125. Solute Distribution in the Vertical Plane X = 1.25 m after 50 years D-271
D.126. Tracer Breakthrough Curves at Different Depths, on Logarithmic Time Scale (top) and Linear Time Scale (bottom) D-271
D.127. Cesium-137 Concentrations in Borehole 21-02-04 Measured with High Rate Logging System (DOE-GJO 2000) D-277

D.128. Cesium Sorption on B Tank Farm Upper and Lower Composite Sediments in 1 M $NaNO_3$ Electrolyte (top) and 1 M $NaHCO_3$ (bottom) D-281
D.129. Comparison of Model Predictions of Cesium Sorption for the Upper B Tank FarmComposite Sediment Batch Experiments D-284
D.130. Comparison of Model Predictions of Cesium Sorption for the Lower B Tank Farm Composite Sediment Batch Experiments D-285
D.131. Predicted Spatial Distribution of Total Cesium on Exchange Sites After 21 Days (left) and 50 Years (right) D-289
D.132. $^{238}U/^{235}U$ versus $^{236}U/^{238}U$ D-296
D.133. $^{234}U/^{238}U$ versus $^{236}U/^{238}U$ D-297
D.134. Depth versus ^{238}U Concentration (ppb) in Porewater for the Borehole 299-E33-46 core Near Tank B-110 ..... D-299
D.135. Concentrations and $^{87}Sr/^{86}Sr$ Ratios of Sr in De-Ionized Water Leaches and Acid-Extractable 90Sr in the Sediments Plotted versus Depth in Borehole 299-E33-46 ..... D-305

TABLES

D.1. Ion Composition of the Hanford Ion Exchange Phases as Determined by Rapid NH4Cl Extraction D-21
D.2. Added Sodium and Strontium Concentrations, and Subsequent Equilibrium Distribution of Calcium, Potassium, Magnesium, Strontium and Sodium in Strontium: Sodium Exchange on Sodium-Acetate Treated Hanford Fine Sand Composite D-27
D.3. Aqueous Complexes with Log K Values at 25°C used in the Model Calculations D-37
D.4. Fitted Selectivity Coefficients Relative to Na^+ Assuming a CEC of 50.2 μeq/g D-37
D.5. Experimental Parameters for System $NaNO_3$ + $Sr(NO_3)_2$ Using <2mm, NaOAc Extracted Hanford Fine Sand Composite Sediment D-43
D.6. Experimental Parameters for System $Ca(NO_3)_2$ + $Sr(NO_3)_2$ Using <2mm, NaOAc Extracted Hanford Fine Sand Composite Sediment D-44
D.7. Experimental Parameters for System $NaHCO_3$, $NaNO_3$, $Ca(NO_3)_2$ + $Sr(NO_3)_2$ Using Hanford Fine Sand, Upper, and Lower Composite Sediment D-46
D.8. NTA Species Included in the Calculations with Log K Values at 25 °C D-47
D.9. Experimental Parameters for System $NaHCO_3$, $NaNO_3$, H_3NTA + $Sr(NO_3)_2$ using Upper and Lower Composite Sediment D-48
D.10. K_d – Strontium-90 Values Suggest the Presence of a Residual Solid Phase with Strontium-90 ..... D-53
D.11. Base Saturation of the Exchange Complex in Sediment Sample 26 Determined from the Desorption Data and Direct Extraction D-54
D.12. Isotopic Distribution of Strontium Released into the Different Desorption Electrolytes D-55
D.13. Total Concentration of Sorbed, Soluble, and Electrolyte Ions Used to Initialize the Desorption Model Calculations D-59
D.14. Reactions, Equations, and Thermodynamic Data Used in Desorption Modeling D-61
D.15. Calculated Equilibrium Cation Desorption (Minteqa2) and Final Carbonate Concentration (All values in mmol/L) D-62
D.16. Summary of Strontium Transport Experiments Using Composite Sediment from WMA B-BX-BY D-70
D.17. CEC Determinations on Composite Sediment from WMA B-BX-BY D-73
D.18. Selectivity Coefficients and Exchanger Activity Corrections Based on Batch Exchange Experiments (Zachara et al., Section D.2.2) D-76
D.19. Strontium Retardation in Reactive Transport Experiments D-76
D.20. Selectivity Coefficients Based on Individual Column Experiments D-78
D.21. Aqueous Complexes Included in the Model Calculations. D-90
D.22. List of Material Properties and van-Genuchten Parameters Used in the Model Simulations D-90
D.23. Fitted Selectivity Coefficients Relative to Na^+ for Batch Experiments with Hanford Sediment Assuming a CEC of 50.2 μeq/g taken from Section D.2.3 ..... D-91
D.24. Initial and Infiltrating Fluid Composition D-92
D.25. Source Composition for the Tank B-110 Leak D-94
D.26. Source Composition for the Transfer Line Leak D-96

D.27. List of Tanks in the B-BX-BY Tank Farms for Which Inventories were Provided by Jones et al. (2001) D-108
D.28. Initial Tank Waste Inventory for Total Liquid and Solid Contributions Used as Starting Solution in Reaction Path Calculations D-108
D.29. Calculated Supernatant Composition for Tank B-110 without EDTA D-109
D.30. Calculated Supernatant Composition for Tank B-110 with EDTA D-111
D.31. Calculated Supernatant Composition for Tank BX-101 ..... D-113
D.32. Calculated Supernatant Composition for Tank BX-102 ..... D-115
D.33. Tank Supernatant Concentrations [mol/L], pH and Eh for Representative Tanks in the B-BX-BY Tank Farms Derived from Reaction Path Calculations Using FLOTRAN (Lichtner 2001) with the Pitzer Activity Coefficient Model. D-119
D.34. Composition and Stoichiometry of SEM Compositional Standards D-124
D.35. Compositional Analysis Results for BX-102-61AB D-132
D.36. Uranium Silicate Minerals for Comparison to Analytical Results D-133
D.37. Description of the Four BX-102 Borehole Samples Analyzed by XAFS Spectroscopy D-142
D.38. Uranium L_{III}-EXAFS Fitting Result for the Four BX-102 Core Samples Compared to the XRD-Derived Values for Uranophane, a Potential Phase Occurring in the Hanford Subsurface D-150
D.39. List of Natural Standard Minerals and Corresponding Formulas D-163
D.40. Summary of X-Ray-Diffraction Analysis of the Natural Minerals D-164
D.41. Chemical Composition (mmol/L) of Porewater from BX-102 Core Samples D-166
D.42. Fluorescence Spectral Characteristics of Standard Natural Minerals. $\lambda_{ex} = 415$ nm D-171
D.43. Fluorescence Spectral Characteristics of Hanford Vadose Zone Sediments. $\lambda_{ex} = 415$ nm D-176
D.44. Fluorescence Spectral Characteristics of U(VI) in Sodium Carbonated Solutions at Different pH D-181
D.45. Fluorescence Spectral Characteristics of U(VI) in Porewaters of Hanford Sediments. $\lambda_{ex} = 415$ nm. D-182
D.46. Uranyl Speciation (mol/L) of Porewater Extracted from Selected BX-102 (Borehole 299-E33-45) Core Samples D-184
D.47. Thermodynamic Properties of Potential Relevant Uranyl Minerals that May Form in Hanford Sediment D-191
D.48. Molar Contribution of Structural Components to ΔG_0^f of Uranyl Minerals.[a] D-192
D.49. Free Energy of Auxiliary Components for Calculating Stability Constant of Uranyl Minerals[a] D-192
D.50. Stability Constants for Potentially Relevant Minerals at Hanford Site D-194
D.51. Chemical Composition (mmol/L) of Porewater from BX-102 ..... D-195
D.52. Uranyl Speciation (mol/L) of Porewater from BX-102 ..... D-195
D.53. Saturation Index of Porewater in BX-102 Sediments with Respect to Potential Relevant U (VI) Minerals D-196
D.54. Sediment Characterization D-196
D.55. Electrolyte pH and Composition D-197
D.56. Calculated Solutes (μmol/L) in the Solid Suspensions Contributing from Sediment Porewater D-202

D.57. Selected Solutes Measured in the Aqueous Phase of the Sodium-Electrolyte Solubility Experiment (Figure D.77) D-208
D.58. Selected Solutes Measured in the Aqueous Phase of the Sodium-Calcium-Electrolyte Solubility Experiment (Figure D.78) D-209
D.59. Calculated Solubility of Uranyl Minerals in the Solid Suspensions of Sodium-Electrolyte D-215
D.60. Calculated Solubility of Uranyl Minerals in the Solid Suspensions of Sodium-Calcium-Electrolyte D-216
D.61. Stratigraphic Sequence at B, BX, and BY Tank Farms D-240
D.62. Anisotropy at a Conductivity of 0.1 m/yr (3.17×10^{-9} m/s), Calculated with a COMA Model from Data Provided by Khaleel et al. (2001) for Different Stratigraphic Units D-241
D.63. Formation Parameters for R-Z Model[a] D-243
D.64. Simulated Moisture Content for 10 cm/yr Net Infiltration D-246
D.65. Matrix of Adsorption Measurements D-277
D.66. Distribution of Cesium on B Tank Farm Upper Composite Sediment in 1 M $NaNO_3$ Electrolyte D-279
D.67. Distribution of Cesium on B Tank Farm Lower Composite Sediment in 1 M $NaNO_3$ Electrolyte D-279
D.68. Distribution of Cesium on B Tank Farm Upper Composite Sediment in 1 M $NaHCO_3$ Electrolyte D-280
D.69. Distribution of Cesium on B Tank Farm Lower Composite Sediment in 1 M $NaHCO_3$ Electrolyte D-280
D.70. Distribution of Exchange Sites for SX Tank Farm Sediments (Steefel et al. 2002) D-282
D.71. Equilibrium Constants for SX Tank Farm Sediments (Steefel et al. 2002) D-282
D.72. Concentrations of Porewater and Waste Source D-287
D.73. Uranium Isotopic Data Core 299-E33-45 (Near Tank BX-102) D-294
D.74. Uranium Isotopic Data Core 299-E33-46 (Near Tank B-110) D-294
D.75. Strontium Isotopic Data Core 299-E33-45 (Near Tank BX-102) D-303
D.76. Strontium Isotopic Data Core 299-E33-46 (Near Tank B-110) D-303

LIST OF TERMS

AMNH	American Museum of Natural History
APS	Advanced Photon Source
bgs	below ground surface
BSE	backscattered-electron
CB	charge balance
CEC	cation exchange capacity
CLIFS	cryogenic laser-induced fluorescence spetroscopy
COMA	composite medium approximation
DOE	Department of Energy
EDS	energy dispersive spectroscopy
EDTA	ethylene-dinitrilo-tetraacetic acid
EMP	electron microprobe
EMSP	Environmental Management Science Program
ERT	electrical resistance tomography
EXAFS	X-ray absorption fine structure
FWHM	full-width half-maximum
HFSC	Hanford fine sand composite
HRR	high resolution resistivity
ICP	inductively coupled plasma
ICP-OES	inductively coupled plasma – optical emission spectroscopy
K_d	distribution coefficient
KPA	Kinetic Phosphorescence Analyzer
LIFS	laser induced fluorescence spectroscopy
NTA	nitrilo-triacetic acid
PCA	principal component analysis
PEST	Parameter Estimation Inc.
PNC-CAT	Pacific Northwest Consortium – Collaborative Access Team
PNNL	Pacific Northwest National Laboratory
PVC	polyvinyl chloride
rcf	relative centrifugal force)
RCRA	*Resource Conservation and Recovery Act*
RPP	River Protection Project
R-Z model	2-dimensional radial model
S&T	Science and Technology
S&T Project	Hanford Science and Technology Project
SEM	scanning electron microscope
SI	Smithsonian Institution
SSRL	Stanford Synchrotron Radiation Laboratory
STOMP	Subsurface Transport Over Multiple Phases
TFVZ	Tank Farms Vadose Zone
TRLFS	Time-Resolved Laser-Induced Fluorescence Spectroscopy
UCODE	universal inverse modeling code
WDS	wavelength-dispersive spectrometers
WMA	Waste Management Area

XAFS	X-ray absorption fine structure
XANES	X-ray absorption near-edge structure
XAS	X-ray absorption spectroscopy
XBR	cross borehole radar
XMP	X-ray microprobe
XRD	X-ray diffraction
ZAF	atomic number, absorption, and fluorescence

This page intentionally left blank.

D.1.0 OVERVIEW AND SUMMARY

The Hanford Science and Technology (S&T) Project was initiated in 1998 as part of the Groundwater/Vadose Zone Integration Project with the goal of coordinating and performing mission-oriented scientific research in support of decision making for environmental cleanup at Hanford. The S&T Project is now part of the Groundwater Protection Program at the Hanford Site. The S&T scope, as well as the major site milestones that it supports, has been described in the Science and Technology Roadmap for the Hanford Site (DOE 1999, 2000). The S&T Project consists of focused, site-specific investigations funded by DOE-Richland Operations through the Groundwater Protection Program, and the Environmental Management Science Program (EMSP) projects funded in fiscal year 1999 vadose zone and fiscal year 2002 subsurface science calls.

The S&T Project has used the process of roadmapping, where problem holders (e.g., the U.S. Department of Energy (DOE), Tribal Nations, regulators, stakeholders, and remediation contractors) come together with problem solvers (e.g., scientists and engineers from universities and the DOE national laboratories) to define the problems and establish a path to solution. The scope and outcomes of S&T activities, linkages of outcomes to the Groundwater Protection Program or other Hanford Site projects, and the schedule, budget, and priorities for these activities are documented in the S&T roadmap, which was issued and revised (DOE 1999, 2000).

This appendix contains research performed by three elements of the Hanford S&T Project: Representative Sites Research, Reactive Transport Modeling, and Vadose Zone Field Experiments. This scientific input to the waste management area (WMA) B-BX-BY field investigation peport represents a specific milestone in the S&T roadmap. The research has addressed important scientific issues associated with the chemical speciation of bismuth-phosphate metal waste; the retardation, chemical speciation, desorbability, and migration of strontium and uranium in the vadose zone; and hydrogeologic/soil physical features and processes controlling lateral waste migration. These studies were performed to provide insights on water and chemical distribution, the future migration of the BX-102 and B-110 vadose zone plumes, and additional contaminant fluxes to groundwater.

This appendix summarizes key results of the S&T Project research that have important implications to: 1) conceptual and numeric models of water and waste migration in the vadose zone of the B, BX, and BY tank farm complex and 2) the potential for future migration as it may influence contaminant fluxes to groundwater, need for corrective actions, and management activities and strategies for the in-ground contaminant inventory. The research is organized around four theme areas in the summary that follows immediately and in the body of Appendix D: 1) strontium geochemistry and transport at B-110, 2) uranium speciation and dissolution from BX-102 sediments, 3) fluid flow and transport in the B, BX, and BY tank farm, and 4) isotope tracking of the fate and transport of radionuclides. The research summaries in Appendix D represent status reports on the individual scientific activities. The research activities in this appendix have been underway for less than one year, and some for less than six months at the time of reporting. Most are not yet complete, but first order conclusions are evident and may be stated with confidence. In the interest of brevity, many details and supporting experimental, theoretical, and computational information has not been included in the scientific summaries that follow. Readers desiring full disclosure of methods and results are best directed to the peer-reviewed publications that are resulting from this work.

D.1.1 KEY FINDINGS

D.1.1.1 Strontium Adsorption, Desorption, and Transport in Pristine and Contaminated Sediment

1. The primary attenuation mechanism for strontium-90 in Hanford sediments is isotopic exchange with the labile, indigenous, stable isotopic pool. Most of the labile strontium repository exists on the cation exchange complex in the sediment. The cation exchange complex exhibits a concentration range of 20 to 60 μeq/g on B tank farm sediments. Indigenous strontium typically occupies 5 to 10% of the exchange complex.

2. Distribution ratios measured for strontium on a variety of Hanford sediments (including two from the B tank farm) in sodium and calcium electrolytes varied from 1000 ml/g to 0 in sodium electrolyte (0.001 to 5 mol/L sodium) and 58.9 ml/g to 0.68 ml/g in calcium electrolyte (0.0005 to 0.05 mol/L), attesting to the strong electrolyte ion effect on Sr^{2+} adsorption.

3. The ion exchange adsorption of Sr^{2+} was enhanced in HCO_3 electrolyte (the dominant anion in the B-110 strontium plume), presumably by formation of adsorbing $SrHCO_3^+$ complexes. NTA (nitrilo-triacetic acid, a possible complexant present in the B-110 strontium recovery waste stream) had no effect on Sr^{2+} ion exchange adsorption in HCO_3 electrolyte when its concentration was 1.5 mmol/L, but reduced Sr^{2+} ion exchange adsorption by a factor of approximately 18 when NTA was present at 15 mmol/L. More specifically, the presence of NTA at 15 mmol/L reduced the Sr^{2+}-K_d in B tank farm composite sediment in 0.015 mol/L $NaHCO_3$ electrolyte from approximately 56 ml/g to 3.16 ml/g.

4. A multicomponent (Na^+, K^+, Ca^{2+}, Mg^{2+}, Sr^{2+}) cation exchange model was developed to describe the distribution of both stable strontium and strontium-90 between porewater/wastewater and sediment. Calcium is the most important competitive ion, and accurate calculations with the model require specification of the total, labile calcium concentration in the sediment; the distribution of calcium between water and the exchange complex; and the sediment exchange capacity. Sodium becomes an important competitive ion when its aqueous concentration exceeds approximately 0.1 mol/L.

5. Approximately 75% of the sorbed strontium-90 in sample 26A was present in an ion exchangeable state and 25% was precipitated in a high magnesium-calcite. Many of the ion exchange sites exist within zones of smectite in the interparticle domain of basalt lithic fragments. Smectite is a weathering product of glass. The isotopic ratios of strontium in these ion exchangeable and carbonate-precipitated strontium pools were different indicating that they were not in isotopic equilibrium.

6. The ion exchangeable strontium-90 was fully and rapidly exchangeable under the necessary ionic conditions. The desorption extent and its dependence on electrolyte composition was well described with the multicomponent exchange model. The ionic compositions and concentrations required to induce significant desorption

(e.g., 1 to 5 mol/L sodium and 0.05 mol/L calcium) were much higher than those currently existing in the B-110 plume.

7. The use of a deionized water extraction to characterize the porewater concentration of strontium-90 probably underestimated its true in situ concentration through the dilution of the porewater electrolyte ions. The most accurate assessment of porewater strontium-90 concentration would be obtained by sediment extraction using $NaHCO_3$ at the approximate in situ concentration (e.g., 0.1 mol/L). The best estimate of the ^{90}Sr-K_d for the ion exchangeable pool under the existing in situ geochemical condition is 5.62 ml/g. The effective in situ retardation factor would be quite high because the low volumetric moisture content. Additional measurements and calculations underway will further refine this value.

8. Approximately 25% of the sorbed strontium-90 pool appears to be incorporated into a precipitated carbonate phase. This precipitated strontium-90 is not desorbable in sodium or calcium electrolyte, and is essentially fixed unless subsurface pH changes to more acidic values. The precipitated strontium-90 appears to exchange very slowly with other indigenous stable strontium pools.

9. The vadose zone strontium-90 plume currently appears stable and immobile. Infiltration of dilute meteoric waters could further increase retardation by the dilution of porewater Na^+. An increase in porewater Ca^{2+} could mobilize a portion of the adsorbed strontium-90.

10. A transport analysis using the ion exchange model developed above is needed to ascertain whether the current in-ground distribution of Na^+ and strontium-90 is consistent with multicomponent ion exchange, or whether the mobilizing effect of a complexant such as NTA need be evoked. Such calculations are planned during fiscal year 2003.

D.1.1.2 Uranium Speciation and Dissolution from BX-102 Sediments

1. Uranium exists in all three BX-102 samples studied as uranium(VI). The uranium(VI) exists primarily as a precipitated phase. The uranium(VI) precipitates are found as discontinuous grain coatings, filamentous intergrain deposits, and as micron size crystallites within mineral microfractures.

2. The spectroscopic signature of the precipitated uranium(VI) as measured by X-ray absorption spectroscopy (XAS) and laser induced fluorescence spectroscopy (LIFS) is the same in all BX-102 samples studied.

3. Various independent lines of evidence suggest that the precipitated phase is a 1:1 uranium sheet silicate falling in the uranophane $[Ca(H_3O)_2(UO_2)_2(SiO_4)_2 \bullet 2H_2O]$ – boltwoodite $[(Na_{0.7}K_{0.3})(H_3O)(UO_2)(SiO_4) \bullet H_2O]$ mineralogic series. Ongoing studies will seek a definitive identification of the uranium(VI) phase. All lines of evidence also suggest that there is only one dominant precipitated uranium(VI) phase.

4. The geochemical evolution of carbonate complexed uranium(VI) in the metal waste stream into precipitated uranium(VI)-silicate is not fully understood and will remain

under study. The precipitation of metal waste bicarbonate in solid carbonate phases through sediment reaction, and sediment drainage leaving uranium(VI)-enriched capillary water films on silicate surfaces and within microfractures has probably played a major role.

5. The precipitated uranium(VI) can dissolve from the sediments if water is added and the pH is above 8.5. The precipitated phase exhibits solubility behavior like that of uranophane/boltwoodite, although mass transfer of uranium(VI) from particle interiors is a limiting factor. In a system that is open to the atmosphere, the solubility of these phases increases from approximately 10^{-6} mol/L at pH 8, to 10^{-4} mol/L and above at pH values in excess of 9.0. From 40 to 85% of the precipitated uranium(VI) will dissolve at pH 9.5 <u>in excess water</u>, given sufficient time.

6. The amount of the precipitated uranium(VI) pool that will dissolve appears predictable (with additional analyses), and is most dependent on pH, HCO_3/CO_3 concentration, and water content. Dissolved silicon is also an important factor, but its concentration is nominally fixed by equilibrium with poorly crystalline sediment silica. The dissolution of the precipitated uranium(VI) phase exhibits strong kinetic behavior, requiring over 100 d to reach equilibrium in a well-mixed system. Much longer periods for equilibrium may be expected in the vadose zone with low moisture content.

7. Because of the psuedo-solubility behavior of the sediment uranium(VI) in the BX-102 samples, there is no uniform K_d. K_d varies from 450 ml/g to 0.25 ml/g depending on the total uranium(VI) concentration, the pH, the carbonate concentration, and water content (or the rock-water ratio). The complex relationships between these factors are understood to large degree. K_d also varies with water contact or residence time, as the uranium(VI) silicate slowly dissolves to the equilibrium state.

8. At the present time, most of the uranium(VI) inventory in the BX-102 samples studied is associated with the solid phase and is effectively immobile. However, the precipitated uranium(VI) phases do maintain appreciable solubility and, for that reason, the porewater concentrations of uranium(VI) are quite high. Spectroscopic measurements of the porewater indicate that the soluble pool exists as uranium(VI)-carbonato complexes. This soluble uranium(VI) pool will continue to migrate, albeit slowly, because of the low water content.

9. The precipitated uranium(VI) phases in the BX-102 sediments are sufficiently soluble and reactive to function as long term source terms to infiltrating waters if allowed. However, the slow dissolution kinetics of the precipitated phases indicates that non-equilibrium behavior is likely to prevail. Water management will be key to limiting further contamination because the total solubility of the precipitated uranium(VI) phases are a strong function of water content or water:rock ratio.

10. Direct spectroscopic measurements (by cryogenic laser-induced fluorescence spectroscopy) of uranium in porewater from borehole 299-E-33-45 indicate that the residual mobile aqueous uranium species resulting from the metal waste spill are $UO_2(CO_3)_2^{2-}$ and $UO_2(CO_3)_3^{4-}$ complexes. Using thermodynamic models with the best

available database, the $UO_2(CO_3)_3^{4-}$ complex was computed and determined to be the dominant uranyl species in BX-102 metal waste supernate. This species has persisted in porewater since the time of the metal waste spillage in 1951.

D.1.1.3 Fluid Migration in the BX Tank Farm (Preliminary Findings)

1. Cores from the contemporary boreholes 299-E33-45, 299-E3-46, and 299-E33-338 and logs from nearby *Resource Conservation and Recovery Act* (RCRA) wells indicate the presence of continuous, small scale, silty fine sand layers at about 75 ft, 100 ft, and 120 ft. The migration direction of the plumes proximate to tank BX-102 is generally consistent with the ~3% slope of these layers, which dip to the northeast. These layers alone, however, cannot explain the current distribution of contaminants to the east and northeast of tank BX-102.

2. Injection experiments performed at the S&T Vadose Zone Transport Field Study test site in the 200 East Area provide insights on the lateral migration process as it may have occurred in the BX tank farm. The S&T field experiments have documented cases of lateral unsaturated fluid migration promoted by discontinuous, low permeability laminations/lenses in the H2 (Hanford formation). These observations support a conceptual model of moisture-dependent anisotropy, whereby fluids (metal waste in the case of the BX-102 spill) migrate horizontally along a conductive fine-textured lamination until it terminates, or its air entry potential is sufficient to allow breakthrough. The waste fluid migrates vertically after breakthrough, until encountering another wetter, conductive lamination that, again, promotes lateral migration. Lateral migration of tens of meters from the point of origin is possible with this anisotropy mechanism. It appears that the mechanism of anisotropic flow could have contributed to the lateral migration of uranium in a northeasterly direction from tank BX-101 to the west of tank BX-102.

3. Large horizontal to vertical permeability ratios are necessary to model the observed lateral migration in the field. The apparent anisotropy is greater than observed in small field samples.

4. Enhanced lateral flow cannot be attributed to strong flow diversion at a few major layers, but is caused by strong anisotropy throughout the formation due to pervasive multi-scale layering of the sediments.

D.1.1.4 Isotope Tracking of the Fate and Transport of Radionuclides in Waste Management Area B-BX-BY Sediments

1. The uranium isotopic composition of the deionized water rinses of sediment samples from the uranium plume encountered in borehole 299-E33-45 are uniform and probably represent the uranium isotopic composition of the 1951 tank BX-102 spill event. The uranium isotope ratios of groundwater samples from the uranium plume in the WMA B-BX-BY area (Dresel et al. 2002) lie along mixing lines between the composition of the 299-E33-45 samples and natural background uranium, suggesting that the groundwater plume is primarily derived from the same source.

2. The uranium isotopic composition of the deionized water rinses from borehole 299-E33-45 samples are not consistent with the presumed isotopic composition of the 1970 to 1971 tank B-110 leak (Jones et al. 2001), suggesting that the contamination in those sediments was derived from a different source. The isotopic ratios are compatible with derivation from earlier fuel types (i.e., circa 1950).

3. The stable strontium isotope ratios (i.e., strontium-87/strontium-86) of deionized water rinses from the borehole 299-E33-45 (tank B-110) plume have been shifted towards the isotopic ratio of the sediments, indicating rapid exchange through dissolution of the silicate minerals in the sediments by reaction with the waste solutions.

D.2.0 STRONTIUM ADSORPTION, DESORPTION, AND TRANSPORT IN PRISTINE AND CONTAMINATED SEDIMENT

Strontium-90 was a major fission product generated in high yield at the Hanford Site. Exhibiting a half-life ($t_{1/2}$) of 28.1 years, its overall activity in the irradiated uranium fuel was second only to cesium as an intermediate half-life contaminant. Strontium-90 has been disposed to many cribs, retention basins, and other soil sites in the 200 Areas where it has migrated to varying degrees depending on the waste and sediment composition, and the volume of liquid discharge. Its retardation in Hanford sediment is considered moderate. To large degree, strontium-90 has been held up in the sediment column through sorption processes (DOE-RL 1993). Sizeable in-ground inventories of strontium-90 exist in numerous sites on the 200 Area plateau (Waite et al. 1991; DOE-RL 1997; Todd 2000). One major strontium-90 groundwater plume exists near the 100-N Area as a result of cooling water discharge to the 1325-N liquid waste disposal facility (Alexander and Johnson 1993). This sizeable groundwater plume, that discharges strontium-90 to the Columbia River, has been the subject of a pump-and-treat remedial action that has not been especially effective because of strontium sorption to the sediments.

Both strontium-90 and the natural, stable strontium isotopes [e.g., ^{84}Sr (0.55%), ^{86}Sr (9.75%), strontium-87 (6.96%), and strontium-88 (82.74 %)] exist in the environment as Sr^{2+} exhibiting qualitative geochemical behavior comparable to the other alkaline earth cations (e.g., Mg^{2+}, Ca^{2+}, and Ba^{2+}). Strontium exhibits no redox behavior in the Hanford environment. Hanford sediments contain appreciable concentrations of indigenous strontium existing as stable isotopes in primary aluminosilicates, in detrital and authigenic carbonates, and as an exchangeable ion on smectites and vermiculites in the silt and clay sized fraction of the sediment. The nominal concentrations of water and acid extractable strontium in Hanford sediments are typically 10^{3} μmol/g and 1 μmol/g, respectively. Contaminant strontium concentrations are invariably much smaller than the indigenous concentrations of stable isotope strontium (e.g., by factors of 10^3 to 10^4 times), with the consequence that the primary retardation mechanism of strontium-90 is isotopic exchange with the cold strontium pool. The primary implication of the isotopic exchange reaction is that the K_d for strontium-90 will initially tend toward the K_d of the labile, or exchangeable cold strontium pool, such as may exist on fixed charge sites on clays, or possibly amphoteric sites on weathered feldspars or other like phases. The strontium K_d may further increase with time as strontium-90 diffuses into precipitated strontium phases (such as strontium substituted $CaCO_{3(s)}$) in pursuit of isotopic equilibrium. Thus, it is necessary to understand the geochemical reactions controlling the distribution of the much larger strontium-86 and strontium-87 pool in order to understand and forecast the sorption/desorption behavior of strontium.

Adsorption and precipitation reactions are generally responsible for the geochemical retardation of Sr^{2+} migration. Ion exchange to phyllosilicates such as smectite and vermiculite and surface complexation to iron and aluminum oxides (Jackson and Inch 1983, 1989) are the most commonly implicated adsorption mechanisms. Strontium may also precipitate as carbonate, phosphate, and sulfate solids and substitute as a minor component via coprecipitation in other mineral phases such as calcite [$CaCO_{3(s)}$]. There have been several Hanford-specific studies of strontium sorption by various Hanford sediment types with emphasis on the measurement of K_d and the quantification of factors affecting it (Routson et al. 1978, 1981; Serne and LeGore 1996). While the identification of adsorption mechanism was generally not a focus of this work, a

strong apparent dependence of K_d on sediment CEC, and electrolyte concentration and valence (Routson et al. 1981) points strongly to an ion exchange sorption process involving the phyllosilicate fraction of Hanford sediment. The mass action expression for cation exchange may be generalized as follows:

$$vAX_u + uB^{v+} = uBX_v + vA^{u+}$$

where X^- denotes one equivalent of the exchange complex, and A^{u+} and B^{v+} are two cations exchanging on X^-. Ion exchange in the pristine and contaminated Hanford subsurface environment is a complex, mulitcomponent problem involving Sr^{2+}, Ca^{2+}, Mg^{2+}, and Na^+. While empirical relationships have been developed to estimate strontium-K_d (Routson et al. 1981), they do not incorporate all the important factors and, consequently, are not accurate. The details of the strontium-ion/isotopic exchange process on Hanford sediment require investigation to formulate more accurate transport models.

D.2.1 STRONTIUM IN THE B-BX-BY TANK FARMS

In fiscal year 2001, the River Protection Project (RPP) placed borehole 299-E33-46 near tank B-110 to investigate a potential strontium-90 plume implied by spectral gamma monitoring of drywells proximate to tanks B-107, B-108, B-110, and B-111. Tank B-110 is a 530,000 gal tank that was suspected to have leaked approximately 25,000 gal between 1971 and 1972 (Jones 2001). Characterization of the borehole samples confirmed the presence of strontium-90 between the depths of approximately 50 and 90 ft (Figure D.1), with a maximum concentration of 11,000 pCi/g of sediment. The strontium-90 plume was also associated with a plume of sodium-HCO_3-F at a concentration of sodium-HCO_3 of 100 to 150 mmol/L (Figure D.2). No other contaminants in appreciable concentration were observed in this plume. The noted contaminant distribution in borehole 299-E33-46 was anomalous and not expected given the waste inventory records for tank B-110 (Jones 2001 and Section 3.2.2.4). The observed waste constituents are now postulated to result from the leakage of PUREX strontium-recovery waste from a transfer line (Section 3.2.2.4). The strontium-recovery waste was believed to contain NTA (nitrilo-triacetic acid) and other organic complexants, but chemical analysis of the borehole sediments did not detect their presence.

The S&T project has focused on the development of information to interpret the migration of strontium-90 in borehole 299-E33-46 and at other sites at Hanford. Two primary research activities were initiated on strontium geochemistry that are planned to be completed in October 2002. The scientific and analytical issues involved in these have been found to be far more complex than originally anticipated. Status reports on these activities are given in the sections that follow. The remaining research is expected to be completed in the first quarter of fiscal year 2003. In the first activity, pristine sediments from various locations in the 200 East and 200 West Areas, including two composite sediments from different depth intervals in the B tank farm, have been used in experiments to define a multicomponent ion exchange model for strontium in sodium-HCO_3 and sodium-NO_3 electrolytes. For the second activity, contaminated sediments from the B-110 strontium plume were studied to identify: 1) the mineral phases hosting sorbed strontium-90, and 2) the desorbability of strontium-90 as a measure of the potential for future migration. Although these activities are incomplete, important insights are provided on the geochemical behavior in the B-110 borehole.

Figure D.1. The Depth Distribution of Strontium-90 in Borehole 299-E33-46 (Near Tank 241-B-110) Data and Figure from Serne et al. (2002b)

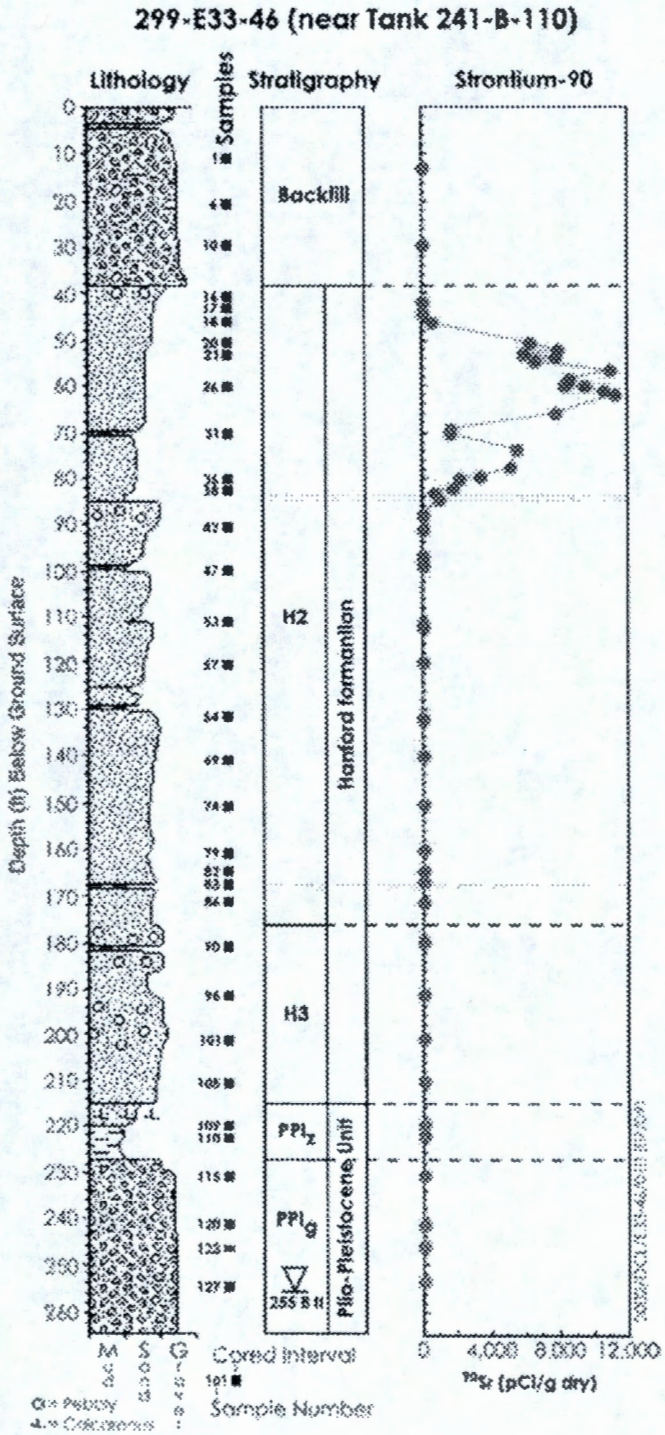

Figure D.2. Porewater Concentrations of Major Cations and Anions in Borehole 299-E33-46 Shown in Reference to the Depth Distribution of Strontium-90 Data from Serne et al. (2002).

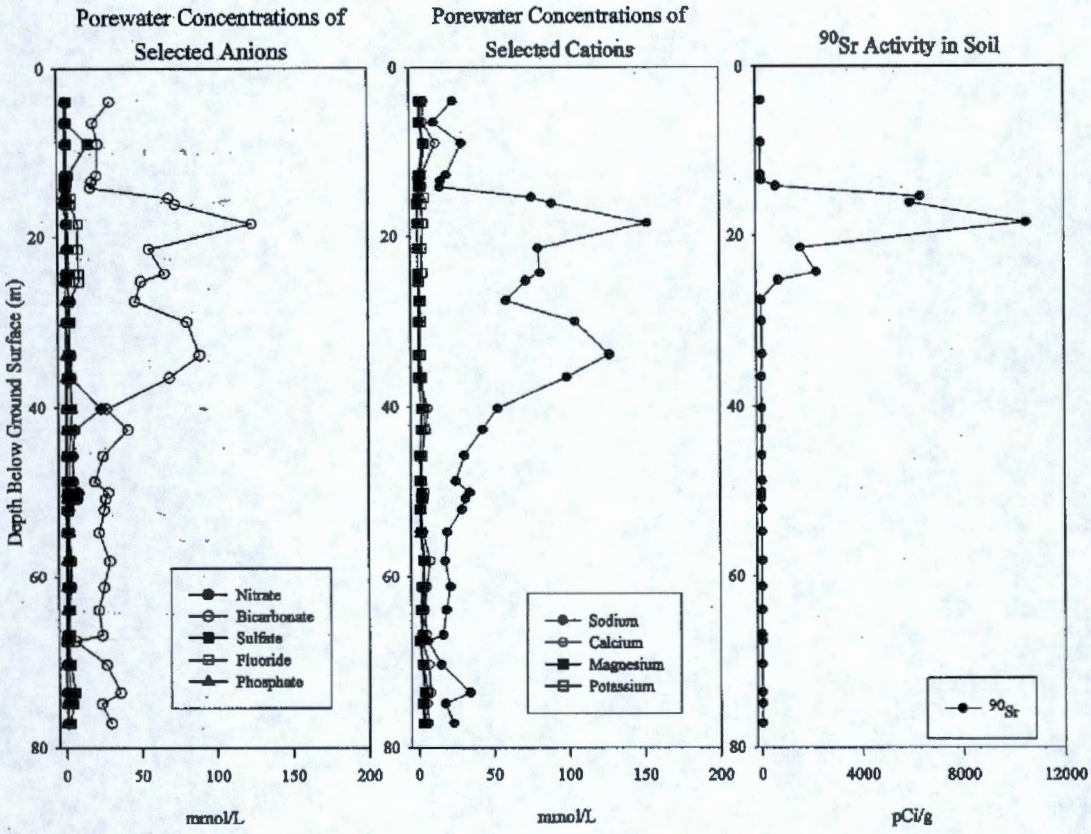

D.2.1.1 References

Alexander, D. J., and V. G. Johnson, 1993, *Groundwater Impact Assessment Report for the 1325-N Liquid Waste Disposal Facility*, WHC-EP-0675, U.S. Department of Energy, Office of Environmental Restoration and Waste Management, Richland, Washington.

DOE-RL, 1993, *Phase I Remedial Investigation Report for 200-BP-1 Operable Unit, Vols. 1 and 2*, DOE/RL-92-70, Rev. 0, U.S. Department of Energy, Richland Operations Office, Richland, Washington.

DOE-RL, 1997, *Waste Site Grouping for 200 Areas Soil Investigations*, DOE/RL-96-81, *Rev. 0*, U.S. Department of Energy, Richland Operations Office, Richland, Washington.

Jackson, R. E., and K. J. Inch, 1983, "Partitioning of Strontium-90 Among Aqueous and Mineral Species in a Contaminated Aquifer," *Environmental Science and Technology*, Vol. 17:231-237.

Jackson, R. E., and K. J. Inch, 1989, "The In-Situ Adsorption of ^{90}Sr in a Sand Aquifer at the Chalk River Nuclear Laboratories," *Journal of Contaminant Hydrology*, Vol. 4:27-50.

Jones, T. E., B. C. Simpson, M. I. Wood, and R. A. Corbin, 2001, *Preliminary Inventory Estimates for Single-Shell Tank Leaks in B, BX, and BY Tank Farms*, RPP-7389, CH2M HILL Hanford Group, Inc., Richland, Washington.

Routson, R. C., G. S. Barney, and R. O. Seil, 1978, *Measurement of Fission Product Sorption Parameters for Hanford 200 Area Sediment Types*, RHO-LD-73, U.S. Department of Energy, Rockwell Hanford Operations, Richland, Washington.

Routson, R. C., G. S. Barney, R. M. Smith, C. H. Delegard, and L. Jensen, 1981, *Fission Product Sorption Parameters for Hanford 200 Area Sediment Types*, RHO-ST-35, U.S. Department of Energy, Rockwell Hanford Operations, Richland, Washington.

Serne, R. J., and V. L. LeGore, 1996, *Strontium-90 Adsorption-Desorption Properties and Sediment Characterization at the 100 N-Area*, PNL-10899, Pacific Northwest National Laboratory, Richland, Washington.

Todd, M. E., 2000, *Data Quality Objectives Summary Report for the 200-TW-1 Scavenged Waste Group and 200-TW-2 Tank Waste Group Operable Units*, BHI-01356, CH2M HILL Hanford Group, Inc., Richland, Washington.

Waite, J. L., 1991, *Tank Wastes Discharged Directly to the Soil at the Hanford Site*, WHC-MR-0227, U.S. Department of Energy, Office of Environmental Restoration and Waste Management, Richland, Washington.

D.2.2 ION EXCHANGE STUDIES

John M. Zachara[1], Steven C. Smith[1], and Chongxuan Liu[1]

[1]Pacific Northwest National Laboratory, Richland, Washington 99352

D.2.2.1 Introduction

As noted in Section D.2.0, ion exchange appears to be the primary retardation mechanism for Sr^{2+} and strontium-90 in Hanford sediments. The ion exchange of Sr^{2+} may be depicted generally as:

$$vAX_u + Sr^{2+} = SrX_2 + vA^{u+} \quad \text{(E.1)}$$

where X^- is one equivalent of fixed charge on the exchange complex and A^{u+} is one of several different types of exchangeable cations at the mineral surface that are compensating for fixed negative charge. The adsorption mechanism of strontium-90, in turn, may be viewed as an isotopic exchange process with stable strontium isotopes on the exchange complex:

$$SrX_2 + {}^{90}Sr^{2+}_{(aq)} = {}^{90}SrX_2 + Sr^{2+}_{(aq)} \quad \text{(E.2)}$$

There is no change in the total aqueous concentration of Sr^{2+} with isotopic exchange, but there is a major redistribution in counts (Serne and LeGore 1996). The degree of partitioning of strontium-90 is controlled by the concentration distribution ratio (e.g., K_d) of stable strontium isotopes between the aqueous and solid phase.

Hanford sediments are generally coarse-textured and contain a small silt and clay sized fraction. Their measured cation exchange capacity (CEC) is typically low (CEC = $X^-_{total} \approx$ 20-80 μeq/g) compared to surface soil, but is sufficient to strongly retard the migration of mono and divalent radioactive cations (e.g., strontium-90, cesium-137) released to the Hanford vadose zone in high radioactive (e.g., > 10^7 pCi/L), but low molar concentrations (e.g., < 10^{-8} mol/L). The low CEC of the Hanford sediment actually translates to a significant molar concentration (≈0.233 mol X^-/L) when referenced to porewater in water saturated sediment. This solid-phase ion repository greatly exceeds the total ion composition of typical Hanford porewater and groundwater (0.001-0.01 mol/L). The exchange complex in Hanford sediment is saturated with Ca^{2+}, Mg^{2+}, Na^+, K^+, and Sr^{2+} cations (in that approximate concentration order from left to right with Ca^{2+} being the highest), but the functional relationships between surface and aqueous cation distributions have not been quantitatively established.

Key to the development of a predictive relationship for strontium-90 sorption is the parameterization of a multicomponent ion exchange model for Sr^{2+} that allows for the calculation of [Sr^{2+}] and [SrX_2], and hence K_d-Sr, as a function of the controlling system parameters: CEC and the total concentrations (aqueous plus adsorbed) of the primary competitive cations. In this section, results are presented of experiments to characterize the ion exchange process in a variety of Hanford subsurface sediments, including two composite materials from the B tank farm. The experimental objective was to parameterize a general multicomponent exchange model for Sr^{2+}on Hanford sediment, like one that was developed for Cs^+ (Zachara et al. 2002) that would allow tank farm-specific calculations when site-specific

values of CEC, Ca_{total}, Sr_{total}, and others were used. Additionally, an evaluation was made of the effects of HCO_3 electrolyte and NTA (nitrilo-triacetic acid) as a complexant on Sr^{2+} ion exchange to provide basis for the interpretation of strontium-90 migration in the B-110 plume. Experimental data is provided in this section in the form of adsorption isotherms and distribution ratios (K_d) (Section D.2.1) and the numeric multicomponent ion exchange model is developed in Section D.2.3.

D.2.2.2 Experimental Methods

D.2.2.2.1 Conceptual Model. The multicomponent model may be described in the most general sense by the following mass action and material balance relationships:

Mass action

$$2NaX + Sr^{2+}_{(aq)} = SrX_2 + 2Na^{+}_{(aq)} \qquad K_{vNa\text{-}Sr} \qquad (E.3)$$

$$CaX_2 + Sr^{2+}_{(aq)} = SrX_2 + Ca^{2+}_{(aq)} \qquad K_{vCa\text{-}Sr} \qquad (E.4)$$

$$CaX_2 + Mg^{2+}_{(aq)} = MgX_2 + Ca^{2+}_{(aq)} \qquad K_{vCa\text{-}Mg} \qquad E.5)$$

$$CaX_2 + K^{+}_{(aq)} = KX + Ca^{2+}_{(aq)} \qquad K_{vCa\text{-}K} \qquad (E.6)$$

$$K_{vNa\text{-}Sr} = N(SrX_2)\{Na^{+}\}^2/N(NaX)^2\{Sr^{2+}\} \qquad (E.7)$$

(and similarly for $K_{vCa\text{-}Sr}$, $K_{vCa\text{-}Mg}$,, and $K_{vCa\text{-}K}$) where N( )= mole fraction of the noted exchange complex and {} thermodynamic activity. Other concentration terms may be used for the adsorbed species such as equivalent fraction.

Material balance

$$CEC = X_T = \Sigma\, NaX + KX + 2CaX_2 + 2MgX_2 + 2SrX_2 \qquad (E.8)$$

$$Ca_{total} = Ca^{2+}_{(aq)} + CaX_2 \qquad (E.9)$$

(and similarly for Na_{total}, Mg_{total}, Sr_{total}, and K_{total})

and all concentrations other than N are in mol/L. See Sposito (1981a, b) and Sposito (1989) for additional details on ion exchange formulations. Similarly, algebraic relationships can be defined relating concentration terms (e.g., $[Sr^{2+}]$ and $[SrX_2]$, and Na^+ and [NaX]) and reaction constants above (e.g., $K_{vNa\text{-}Sr}$) to K_d in binary, ternary, and multicomponent systems (e.g., Liu et al. 2002).

D.2.2.2.2 K_d Relationships. The distribution ratio [K_d (ml/g) = adsorbed concentration (mmol/L)/aqueous concentration (mmol/mL)] is a commonly used measure of sorption affinity in Hanford soil and for transport models generally. The K_d is explicitly related to the ion exchange equilibria depicted in Section D.2.2.2.1 through algebraic relationships shown below. The relationship is straightforward for homovalent, calcium-strontium exchange, but more complex for heterovalent, ternary sodium-calcium-strontium exchange. In both cases, K_d is a

function of three controlling factors: 1) the cation exchange capacity (CEC), 2) concentrations of competing cations, and 3) ion selectivity for the exchanger phase quantified by K_c or K_v.

Binary reaction in binary system

$$CaX_2 + Sr^{2+} = SrX_2 + Ca^{2+} \qquad K_v \text{ or } K_c$$

$$K_d(L/g) = \frac{CEC}{2}\frac{K_v \gamma_{Sr^{2+}}}{\{Ca^{2+}\} + K_v\{Sr^{2+}\}} \text{ or } K_d = \frac{CEC}{2}\frac{K_c}{[Ca^{2+}] + K_c[Sr^{2+}]}$$

where γ is the activity coefficient, K_c is the conditional exchange coefficient, and K_v is the Vanselow exchange coefficient, {} is the activity, [] is the concentration (μmol/L), and CEC is cation exchange capacity (μequivalent /g).

Binary reactions in ternary system

Note that for a ternary system, the selectivity coefficient must be expressed using equivalent fraction (E) as the surface concentration term in order to have an explicit expression for Kd. Either a conditional equilibrium constant (K_c) or the Gaines – Thomas selectivity coefficient (K_{GT}) may be used.

$$CaX_2 + Sr^{2+} = SrX_2 + Ca^{2+} \qquad K_{GT}(Ca\text{-}Sr) \text{ or } K_c(Ca\text{-}Sr)$$

$$2NaX + Sr^{2+} = SrX_2 + 2Na^{+} \qquad K_{GT}(Na\text{-}Sr) \text{ or } K_c(Na\text{-}Sr)$$

$$K_d = \frac{CEC}{2}\frac{\gamma_{Sr^{2+}} K_{GT}(Na-Sr)}{\{Na^{2+}\}^2}\left(\frac{\sqrt{1+4a}-1}{2a}\right)^2$$

$$\text{where } a = \frac{\{Sr^{2+}\}}{\{Na^{2+}\}^2}K_{GT}(Na\text{-}Sr) + \frac{K_{GT}(Na\text{-}Sr)}{K_{GT}(Ca\text{-}Sr)}\frac{\{Ca^{2+}\}}{\{Na^{2+}\}^2}$$

or

$$K_d = \frac{CEC}{2}\frac{K_c(Na-Sr)}{[Na^{2+}]^2}\left(\frac{\sqrt{1+4a}-1}{2a}\right)^2$$

$$\text{where } a = \frac{[Sr^{2+}]}{[Na^{2+}]^2}K_c(Na\text{-}Sr) + \frac{K_c(Na\text{-}Sr)}{K_c(Ca\text{-}Sr)}\frac{[Ca^{2+}]}{[Na^{2+}]^2}$$

D.2.2.2.3 Materials Origin and Preparation. The Hanford fine sand composite (HFSC) was made by the mixing of subsamples from borehole B8814 (well 299-W22-50 on the east side of the S-SX tank farm) over the depth interval of 62.5 to 96.0 ft below ground surface (bgs).

The B tank farm sediments came from the placement of RCRA monitoring well 299-E33-337. The upper composite was made by mixing samples from the depth interval of 36 to 70 ft bgs, and the lower composite was made by mixing samples from depths of 75 to 120 ft bgs. In practice, the two B tank farm composite sediments were found to be virtually identical.

The three composite sediments were air dried and sieved to <2mm. All were characterized in terms of particle size distribution, mineralogy, cation exchange capacity, and exchangeable bases.

Type I Experiments

D.2.2.2.4 Sodium Acetate Extraction. A portion of the Hanford fine sand composite was treated to dissolve carbonate minerals and soluble salts by extraction with sodium acetate (Na-OAc). On day one, five 200-g aliquots of Hanford fine sand composite were transferred to separate 60 cm lengths of SpectraPor 7® (1000 molecular weight cutoff) cellulose dialysis tubing and combined with 200 mL of 1 mol/L sodium acetate solution, pH 5.0 with glacial acetic acid. The dialysis tubes were placed in a plastic container with excess sodium acetate solution. On day four, the lysate was replaced with 3 L of fresh sodium acetate solution. On day six, the lysate was replaced with deionized water. The treated soil was dialyzed for five additional days against deionized water to remove dissolved cations. On days eleven and fourteen, the lysate was replaced with 0.001 mol/L $NaHCO_3$, pH adjusted to 7.5 with HNO_3. On day fifteen, the lysate was replaced with deionized water and was frequently changed to further remove dissolved cations. The final rinsing step with deionized water required approximately two to three weeks and was stopped when the lysate solution was < 5 μS/cm after overnight contact. The suspensions were carefully removed from the dialysis tubing, combined in a plastic jar, and placed in an oven at 30 °C to hasten evaporation of water. When nearly all the water was evaporated, the sediment was removed from the oven and allowed to air-dry to constant mass.

D.2.2.2.5 Preparation of Strontium-85 Spike Solutions. A stock 1 mol/L strontium solution was prepared by dissolving $Sr(NO_3)_2$ in deionized water. Subsequent dilutions were made with deionized water to prepare strontium solutions of desired concentrations. Strontium-85, as $SrCl_2$ in 0.5 mol/L HCl, obtained from PerkinElmer™ Life Science, was included in the spike solutions to track strontium behavior.

D.2.2.2.6 Preparation of Strontium-85-NTA Spike Solutions. Stock solutions of 1 mol/L strontium were prepared by dissolving $Sr(NO_3)_2$ in either 0.15 or 0.015 mol/L Na_3NTA. Subsequent dilutions of these stocks were made using the respective Na_3NTA solution to prepare solutions of desired strontium concentrations. Strontium-85, as $SrCl_2$ in 0.5 mol/L HCl, obtained from PerkinElmer™ Life Science, was included in the spike solutions to track strontium behavior.

D.2.2.2.7 Strontium Sorption in $NaNO_3$ or $NaHCO_3$ Electrolytes. Four $NaNO_3$ electrolytes were used: 1, 0.1, 0.01, and 0.001 mol/L. The stock electrolyte solutions were prepared at a concentration 1.11 times the final target concentrations listed. A desired mass of sodium acetate treated Hanford fine sand composite was placed in a plastic reaction vessel; either 50 mL polycarbonate Oakridge® centrifuge tube or 250 mL polypropylene centrifuge bottle. The solid:solution ratios used for the sorption experiments were: 600 g/L (3.6 g/6 mL) in 1 mol/L Na,

100 g/L (0.6 g/6 mL) in 0.1 mol/L Na, 30 g/L (0.3 g/10 mL) in 0.01 mol/L Na, and 3 g/L (0.3 g/100 mL) in 0.001 mol/L Na. An appropriate volume (90% of the target total final volume) of stock electrolyte solution was added to the soil followed by an appropriate volume of ^{85}Sr-labeled spike solution (10% of the target total final volume).

Strontium sorption on the untreated Hanford fine sand composite and on the B tank farm upper and lower sediment composites in 0.015 mol/L $NaNO_3$ or 0.015 mol/L $NaHCO_3$ was also investigated. The solid:solution ratio used with the Hanford fine sand composite was 30 g/L (0.3 g/10 mL) and 100 g/L (1.0 g/10 mL) with the B tank farm composites. These experiments were similarly conducted except the sediments were washed three times with electrolyte prior to addition of strontium-85-labeled spike solution. As previously described, the volume of sodium electrolyte with the sediment prior to addition of strontium was 90% of the target total final volume. The intent of washing the soil with electrolyte prior to addition of strontium was to rinse the soil of water soluble and readily exchangeable cations.

D.2.2.2.8 Strontium-NTA Sorption in $NaNO_3$ or $NaHCO_3$ Electrolytes. The sorption of strontium-NTA on the B tank farm upper and lower sediment composites in 0.015 mol/L $NaNO_3$ or 0.015 mol/L $NaHCO_3$ was measured. The stock electrolyte solutions were prepared as previously described. The solid:solution ratio was 100 g/L (1.0 g/10 mL). The sediments were washed three times with electrolyte prior to addition of strontium 85-labeled strontium-NTA spike solution. As previously described, the volume of sodium electrolyte with the sediment prior to addition of strontium was 90% of the target total final volume. The initial solution NTA concentration was either 0.015 or 0.0015 mol/L.

D.2.2.2.9 Strontium Sorption in $Ca(NO_3)_2$ Electrolytes. Three $Ca(NO_3)_2$ electrolytes were used: 0.05, 0.005, and 0.0005 mol/L. The stock electrolyte solutions were prepared as previously described. The solid:solution ratios used for the sorption experiments were; 300 g/L (1.8 g/6 mL) in 0.05 mol/L Ca, 60 g/L (0.6 g/10 mL) in 0.05 mol/L Ca, and 10 g/L (0.3 g/30 mL) in 0.0005 mol/L Ca. The sediment was washed three times with the electrolyte solution prior to addition of strontium-85-labeled spike solution.

D.2.2.2.10 Strontium Sorption in Mixed $NaNO_3$ and $Ca(CO_3)_2$ Electrolytes. Strontium sorption to the B tank farm upper or lower sediment composites in combined 0.001 mol/L $NaNO_3$ and 0.001 mol/L $Ca(NO_3)_2$ electrolyte was investigated. The stock electrolyte solutions were prepared as previously described. The solid:solution ratio used for these experiments was 50 g/L (1.0 g/20 mL). The sediment was washed three times with the electrolyte solution prior to addition of strontium-85-labeled spike solution.

D.2.2.2.11 Equilibration. The suspensions were equilibrated overnight (~16 h) in an incubator shaker at 25 °C and 80 revolutions per minute.

D.2.2.2.12 Sampling Scheme. Following equilibration, the suspensions were centrifuged for 30 min at 5000 rcf (relative centrifugal force). The supernatant was sampled for strontium-85 activity and pH. In select experiments, the concentrations of calcium, sodium, magnesium, and strontium in the supernatant were determined by ICP analysis.

Type II Experiments

This experimental design originated from the classic work of Jensen and Babcock (1973).

D.2.2.2.13 Preparation of Strontium:Sodium Spike Solutions. A series of $Sr(NO_3)_2$ and $NaNO_3$ solutions were prepared to yield Sr:(Sr+Na) ratios of 1.000, 0.800, 0.600, 0.400, 0.200, 0.100, 0.050, 0.010, 0.005, 0.001, and 0 with total normality of 0.1, 0.01, or 0.001 eq/L. The solutions were split into two equal volumes and one set was radio labeled with ^{85}Sr (as $SrCl_2$ in 0.5 mol/L HCl; PerkinElmer™, Boston, Massachusetts) and the other set was radio labeled with ^{22}Na (as NaCl in water; PerkinElmer™, Boston, Massachusetts). Solutions without strontium received no strontium-85 spike and solutions without sodium received no sodium-22 spike.

D.2.2.2.14 Sediment Washing. Two grams of sodium acetate treated Hanford fine sand composite were weighed into tared 50 mL polycarbonate Oakridge® centrifuge tubes and the tubes re-weighed. One set of thirty tubes received 10 mL of the strontium-85 labeled spike solutions and another set of thirty tubes received 10 mL of the sodium-22-labeled solutions. The suspensions were gently mixed overnight (~16 h) in an incubator shaker at 25 °C and 50 rpm. The suspensions were centrifuged at 5000 rcf for 20 min and 8 mL of the clear supernatant were carefully removed and discarded. Eight mL of the same strontium-85 or sodium-22-labeled solution were re-added to each tube and the suspensions were re-equilibrated overnight under identical conditions. The suspensions were centrifuged as described previously and 8 mL of the clear supernatant were carefully removed and discarded. The discarded supernatant was replaced with 8 mL of the same strontium-85 or sodium-22-labeled solution as before and the tubes re-weighed to determine the solid:solution ratio.

D.2.2.2.15 Sampling of Equilibrium Suspension. Following the third overnight equilibration of sediment with the strontium-85 or sodium-22-labeled solution, the suspensions were centrifuged for 30 min at 5000 rcf. One mL of supernatant was transferred to a gamma count tube to determine the activity of radiolabel in solution. The gamma samples were counted for a period of time so that the count error was < 1%. After completion of gamma counting, the pH of the sample was measured using a Microelectrodes® combination pH electrode. Seven mL of supernatant were transferred to a plastic syringe fitted with a 0.2 μm filter. The first 1 mL of filtrate was discarded and the remaining collected in a plastic vial for ICP analysis of select cations (e.g., sodium, calcium, potassium, magnesium, and strontium).

D.2.2.2.16 Ammonium Acetate Extraction. Immediately following sampling of the supernatant, the tubes with sediment and ~2 mL of supernatant were weighed to determine the mass of entrained solution. Eight mL of 1.25 mol/L ammonium acetate (NH_4OAc) solution (pH 6.8 with acetic acid) were added to each tube and re-weighed to determine the mass of NH_4OAc solution added. The suspensions were equilibrated overnight (~16 hours) as described previously. Following equilibration, the tubes were centrifuged at 5000 rcf for 1 hour. One mL of supernatant was transferred to a gamma count tube and counted for either sodium-22 or strontium-85 activity. Seven mL of supernatant were filtered and analyzed by ICP as described previously. A three-step sequential extraction of sediment by 1.0 mol/L NH_4OAc in 4 tubes indicated that over 98% of the sorbed strontium-85 radio label was desorbed in the first extraction.

D.2.2.3 Results and Discussion

D.2.2.3.1 Type I Ion Exchange Experiments. Known masses of pretreated or untreated Hanford sediments were placed into electrolytes of variable, but known, electrolyte concentration. Total electrolyte normality varied within an experiment by as much as 100% in the dilute electrolyte experiments. Strontium exchange adsorption was measured by monitoring strontium-85 counts in the aqueous phase. Sediment mass was adjusted to obtain optimal statistics for adsorption measurements based on aqueous phase analyses. Counts lost from solution were assumed to be adsorbed to the mineral surface. Adsorption density and the surface equivalent fractions of exchangeable ions were calculated from solution mass loss and the CEC.

D.2.2.3.1.1 Electrolyte Concentration Effects with the HFSC. The ion exchange adsorption of Sr^{2+} was a strong function of electrolyte concentration in both $NaNO_3$ and $Ca(NO_3)_2$ electrolyte (Figure D.3 and Figure D.4). Adsorption isotherms were the basic data measurement (e.g., Figure D.3b and Figure D.4b) and these were recalculated as K_ds in Figure D.3a and Figure D.4a to allow ready comparison to past measurements of strontium-90 sorption on Hanford sediment that are typically reported in these units. Not shown are comparable measurements made of Sr^{2+} sorption in 5 mol/L $NaNO_3$ where no statistically measurable sorption was defined (e.g., $K_d = 0$). Trace Sr^{2+} contamination in $NaNO_3$, that was determined by XRF analyses of the solid salt, was accounted for in all results presented herein. This level of electrolyte contamination provided a lower limit on the Sr^{2+} concentration that could be achieved at high $NaNO_3$ concentration.

Figure D.3. Strontium Sorption on Na-OAc Extracted Hanford Fine Sand Composite in Sodium Nitrate Electrolyte. Depicted are K_d Functions (a) and Isotherms(b)

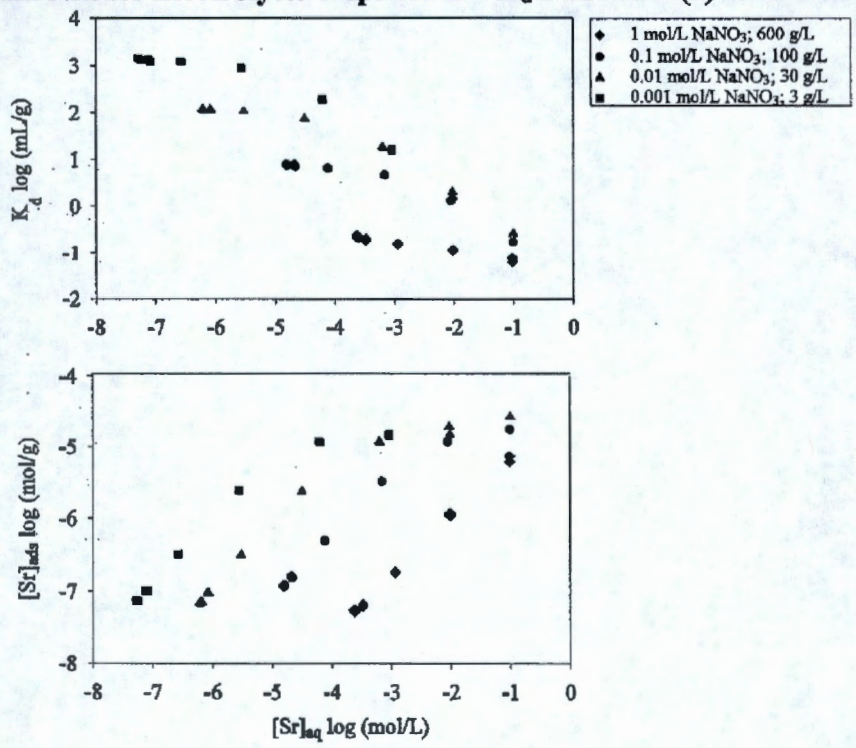

The K_d functions showed some constancy at lower Sr^{2+} concentrations, with a constant Kd observed over a larger concentration interval in calcium electrolyte. The noted Kd behavior characterized by a constant value at low concentration, and decreasing value at higher concentrations where [Sr] ≈ [Na] or [Ca] is fully consistent with an ion exchange reaction.

At equal solution normality, Ca^{2+} was a much stronger competitor with Sr^{2+} than was Na^{+}. The assymtotic K_ds (the value at the lowest concentration of measurement; calcium:sodium in mL/g) compared as follows for electrolyte normalities of 0.001, 0.01, and 0.1 eq/L: 58.8:1318, 6.60:114, 0.69:7.41. While the K_ds in Ca electrolyte were qualitatively similar in magnitude and trend to those reported for N-trench sediment, they were not well predicted by their regression relationship [e.g., log K_d = -0.89 log (Ca+Mg) – 1.06]. Differences may be attributed to the different CEC of the sediments and the presence of other competitive cations (e.g., Na^{+}, K^{+}) in the aqueous phase and on the exchange complex that were not explicitly considered. The Sr-K_ds in Ca electrolyte defined an excellent relationship with electrolyte Ca concentration (Figure D.5a). In contrast to the strontium-calcium system, a slight curvilinear relationship existed between log Sr-K_d and log sodium concentration (Figure D.5b), with proportionally higher decreases in K_d noted at higher Na concentration. The strong correlation between Sr-K_d and log [Ca] or [Na] (Figure D.5) suggested that predictive ion exchange relationships could be developed to describe and forecast strontium and strontium-90 adsorption.

Figure D.4. Strontium Sorption on Na-OAc Extracted Fine Sand Composite in Calcium-Nitrate Electrolyte. Depicted are K_d Functions (a) and Isotherms (b).

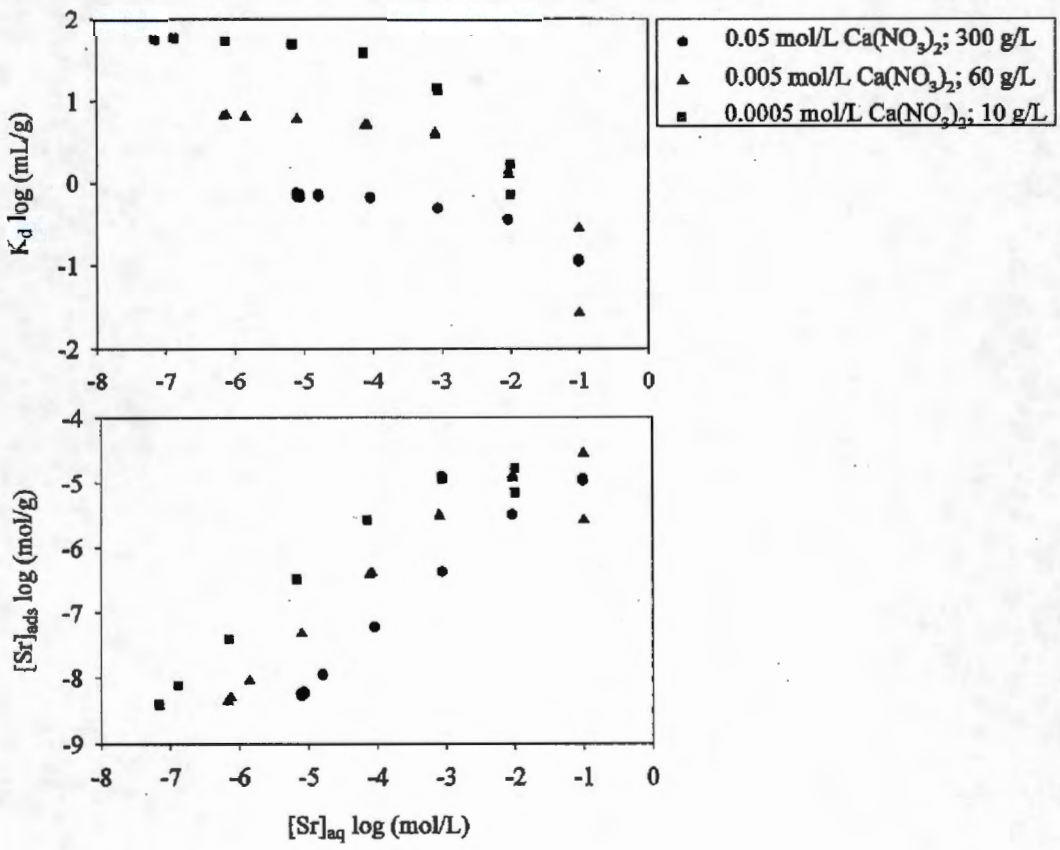

After the experiments in Figure D.3 were completed, it was found that the Na-OAc extracted sediment was not sodium-saturated as believed. The "Na-saturated sediment" contained appreciable exchangeable calcium (Table D.1). This was not expected, as all the calcium carbonates had been dissolved by the NaOAc treatment, and repeated washings with 1.0 mol/L sodium should have been sufficient to saturate the exchange complex with sodium. It is currently surmised that calcium may have been released by dissolution from ubiquitous calcium-feldspars during the two-week dialysis that followed carbonate dissolution. The important implication of this observation was that the experiment shown in Figure D.3 and Figure D.5b (and all others using the NaOAc-Na saturated sediment) was a ternary (sodium-calcium-strontium), rather than a binary (sodium-strontium) experiment. The ternary character of sodium-strontium experiment contributed to the curvilinear behavior of log Sr-K_d in Figure D.5b. The observations with the "sodium-saturated sediment" underscore an important characteristic of the Hanford sediment exchanger phase: it desires saturation with divalent cations, and calcium specifically. This has been a repeated observation in the ion exchange experiments.

Table D.1. Ion Composition of the Hanford Ion Exchange Phases as Determined by Rapid NH4Cl Extraction

Sediment	Net Ammonium Extractable						
	Net Na Extrctd (μeq/g)	Net Ca Extrctd (μeq/g)	Net K Extrctd (μeq/g)	Net Mg Extrctd (μeq/g)	Net Sr Extrctd (μeq/g)	Total NH4 (μeq/g)	Avg (μeq/g)
B Tank Upper Comp.[a]	1.67	71.98	1.98	7.55	0.121	83.30	79.3
	1.71	64.28	1.78	6.78	0.106	74.64	
	1.70	68.47	1.88	7.64	0.119	79.81	
B Tank Lower Comp.[a]	1.52	63.88	1.04	5.48	0.087	72.81	73.1
	1.65	64.41	1.01	5.52	0.090	72.69	
	1.53	65.92	1.18	5.91	0.093	74.64	
NaOAc-trtd HFSC	1.64	35.76	0.98	8.07	0.032	46.47	46.6
	1.66	36.33	0.99	8.11	0.031	47.12	
	1.50	35.75	1.00	7.90	0.030	46.18	

[a] Ca^{2+} values high from $CaCO_3$ dissolution.

Figure D.5. Relationship of Sr-K_d to Electrolyte Concentration in Sodium and Calcium Electrolyte
The K_ds are Asymptote Values at Low $[Sr]_{aq}$ Concentration

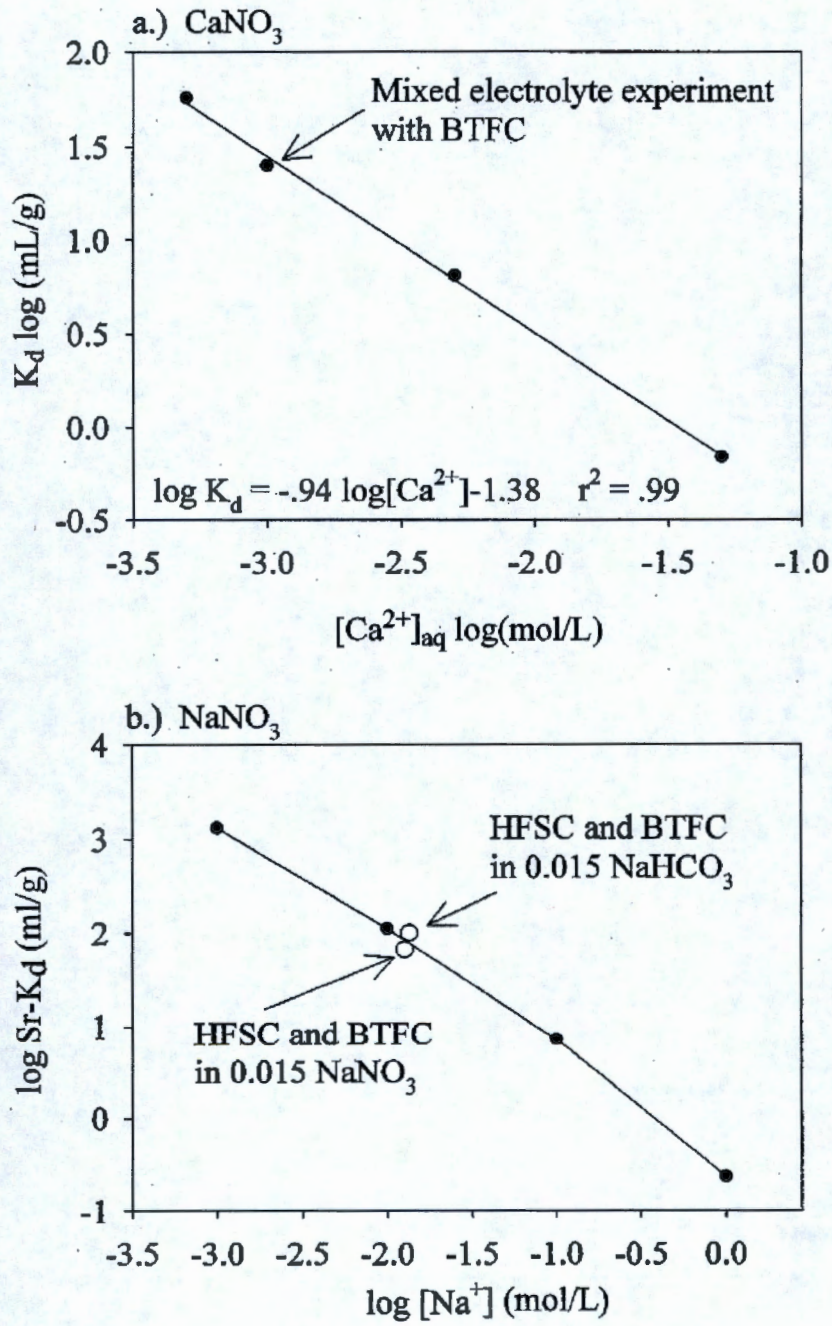

D.2.2.3.1.2 Electrolyte and Sediment Origin Effects. The electrolyte concentration study described in the preceding section was performed with the HFSC that originated from near the S-SX tank farm at the 200 West Area. Given the focus of this field investigation report on WMA B-BX-BY, a series of experiments were performed with the HFSC and the two B tank farm sediments under identical electrolyte conditions to assess their comparative sorption behavior. Two electrolytes were used: 0.015 mol/L $NaNO_3$ and 0.015 mol/L $NaHCO_3$ (Figure D.6). As it turned out, all three of these sediments had comparable base saturation at initiation of the experiment (Table D.1) with 96% of the exchange complex occupied by calcium and magnesium at an equivalent ratio (magnesium/calcium) of 0.23. Accordingly, the ion exchange behavior shown in Figure D.6 was again ternary. The bicarbonate electrolyte was used to provide insights on strontium ion exchange under the electrolyte conditions noted in the B-110 strontium plume. However, the sodium-bicarbonate concentration used (0.015 mol/L) was one decade below that found in B-110 porewater to avoid carbonate precipitation.

Figure D.6. Strontium Sorption on Selected Hanford Sediments in Sodium Nitrate and Sodium Bicarbonate Electrolyte

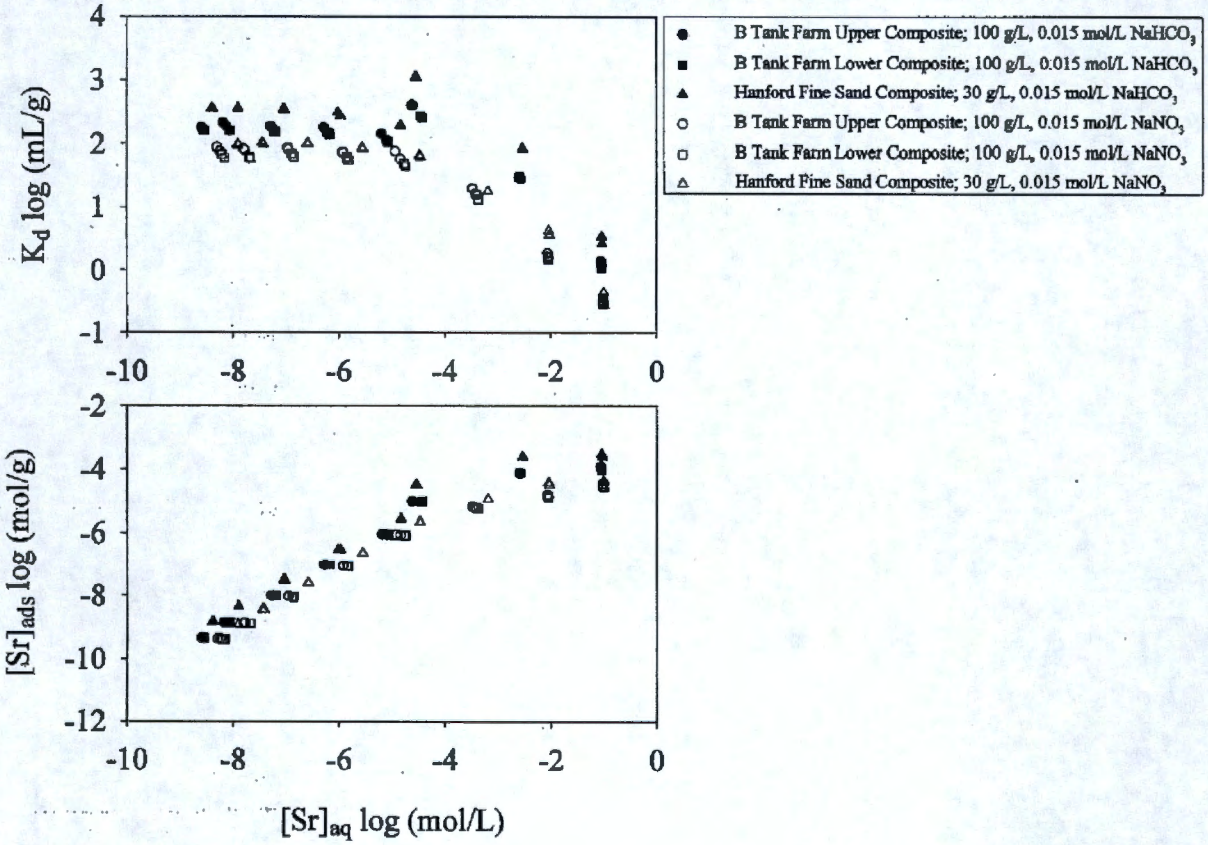

The HFSC and the two B tank farm composites exhibited similar strontium adsorption behavior (Figure D.6), displaying a nearly constant K_d below a $Sr^{2+} = 10^{-5}$ mol/L. The HFSC gave slightly higher strontium adsorption than either of the B tank farm composites, consistent with its incrementally higher CEC. The Sr-K_ds for these predominantly calcium-saturated sediments in sodium electrolyte were consistent with those measured in Figure D.3 and plotted in Figure D.5.

Strontium ion exchange adsorption was observed to be a bit higher from bicarbonate electrolyte in all sediments studied. The Sr-K_ds were about two times higher (0.3 log units) in bicarbonate electrolyte. The reasons for this increase will be explored in the next section but could result from the ion exchange of $SrHCO_3^+$, or the withdrawal Ca^{2+} from the exchange complex by aqueous carbonate complexation ($CaHCO_3^+$, $CaCO_3^\circ$). The increase in Sr^{2+} sorption that occurred in bicarbonate electrolyte at approximately 10^{-5} mol/L and above resulted from the precipitation of strontianite ($SrCO_3$) with some admixed calcite ($CaCO_3$). Strontianite precipitation was, in part, self-inhibiting as it generated acid:

$$Sr^{2+} + HCO_3^- = SrCO_3 + H^+$$

For this reason, the Sr-K_ds did not continue to increase at Sr^{2+} concentrations above the precipitation threshold.

Strontium adsorption was also measured on the two B tank farm composite sediments from a mixed sodium-calcium electrolyte (each at 0.001 mol/L) with composition similar to that observed in dilute vadose zone water and groundwater. Ammonium chloride extraction of the sediment after 24 hours equilibration in the electrolyte showed that greater than 95% of the exchange complex was saturated with calcium and magnesium (calcium primarily). The two different composite sediments showed virtually identical sorption behavior (Figure D.7), yielding a log Sr-K_d value of 1.3 (19.95 ml/L) at low concentration. This value compared favorably with those measured for the HFSC in variable concentration Ca electrolyte (Figure D.5a). Thus, the mixed electrolyte behaved primarily as a calcium-strontium binary system. These results demonstrate that sodium is a weak competitor for exchange sites in the Hanford sediment, and that high sodium and low calcium concentrations are needed for sodium to be the primary ionic competitor. Also clear is that the Hanford sediments from the 200 East (B, BX, and BY tank farms) and the 200 West (S and SX tank farms) Areas exhibit almost identical ion exchange behavior for Sr^{2+} with small differences in CEC being the primary factor causing variation.

D.2.2.3.1.3 Complexant Effects. Ion exchange isotherms were measured on the B tank farm composites with two concentrations of NTA (nitrilo-triacetic acid) in both NaNO3 and NaHCO3 electrolytes to assess whether the presence of this complexant could expedite strontium migration in the B tank farm. It is important to note that the influence of complexants on contaminant mobility cannot be easily forecast, a-priori. In some cases, mobility may be enhanced if the complex is non-adsorbing and remains intact in the subsurface. In other cases, mobility may be unaffected if the ligand itself is strongly adsorbed by mineral surfaces and the complex dissociates. Still again, mobility may actually be reduced if the metal-ligand complex is more strongly adsorbed than the primary contaminant. Examples of these complex behaviors exist for strontium in Oak Ridge sediment and cobalt in Hanford sediment (Jardine et al. 1993; Zachara et al. 1995a, b; Szecsody et al. 1998).

Figure D.7. Strontium Sorption on the Upper and Lower B Tank Farm Composite Sediments in Mixed Sodium and Calcium Electrolyte (each at 0.001 mole/L)

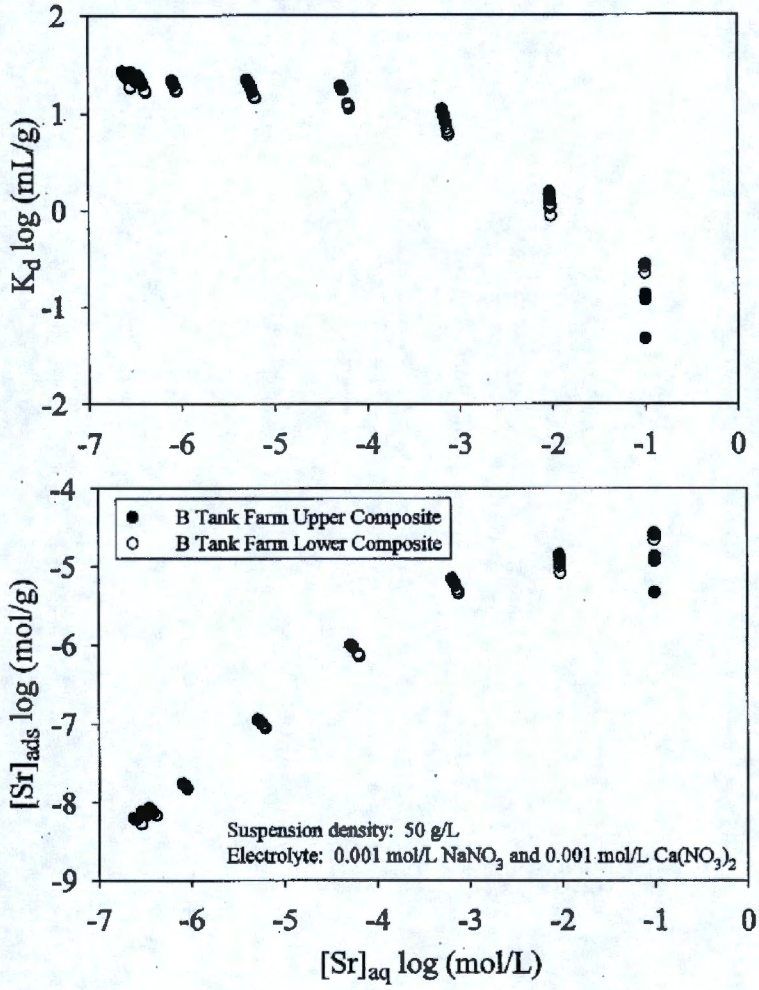

NTA did not affect the ion exchange behavior of Sr^{2+} at 1.5 mmol/L, but had a major effect at 15 mmol/L (Figure D.8). The effects were comparable in both nitrate and bicarbonate electrolyte. At the higher concentration, NTA reduced strontium adsorption by approximately 1.5 orders of magnitude. The effect of NTA was more pronounced at lower strontium concentration, where the log Sr-K_d was reduced from 1.9 (79.4 ml/g) to 0.5 (3.16 ml/g). A tentative explanation is that the reaction of strontium with NTA has led to the formation of non-adsorbing $SrNTA^-$ complexes. The situation, however, is actually complicated in that NTA may also form aqueous complexes with Ca^{2+}, which dominates the exchangeable ion pool in concentration. Therefore, the chemical system involves both competitive ion exchange and competitive aqueous complexation. Modeling calculations in Section D.2.2 will seek to illuminate these multicomponent effects. Regardless of mechanism, the results show that NTA can potentially enhance strontium-90 migration by increasing stable isotope strontium in the aqueous phase.

Figure D.8. Strontium Sorption on B Tank Farm Composite Sediments in Sodium Nitrate or Sodium Biocarbonate Electrolyte with NTA (nitrilo-triacetic acid)

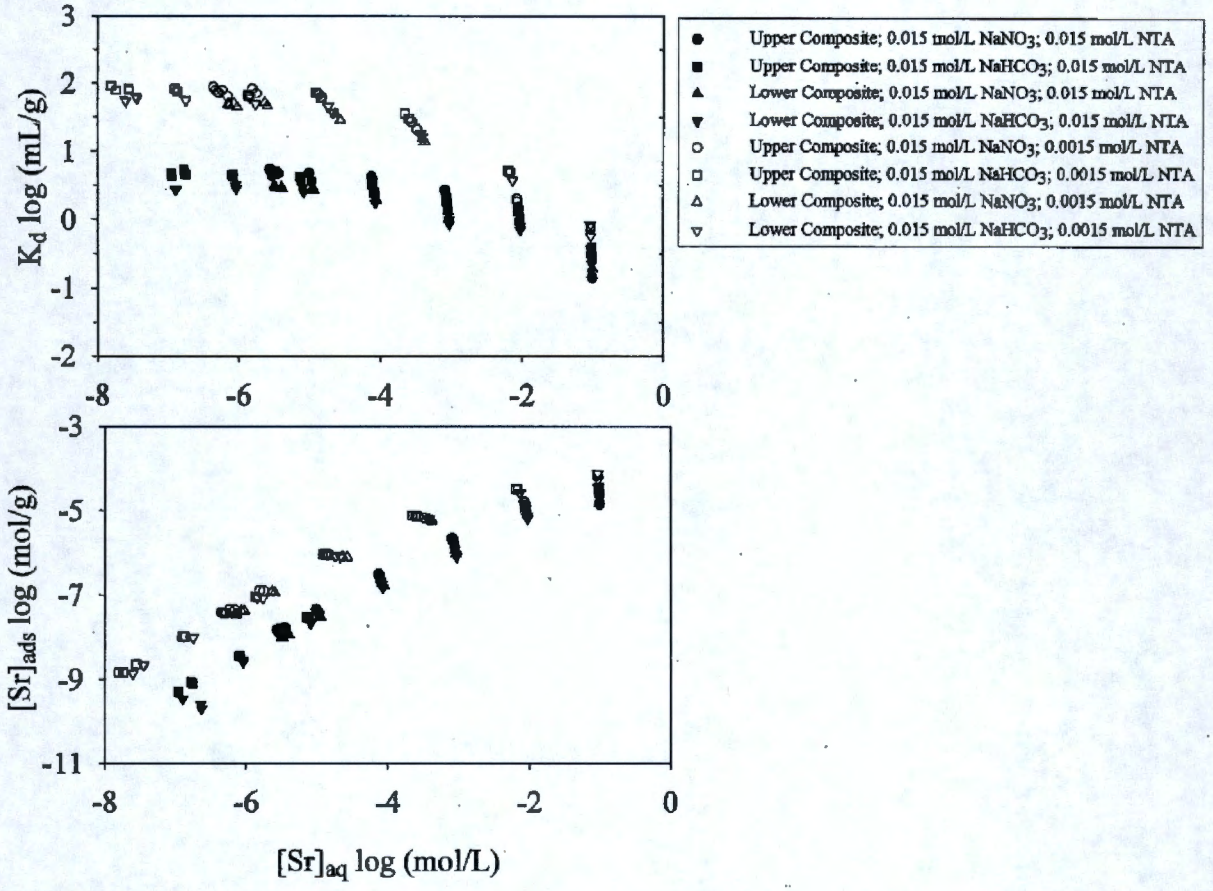

D.2.2.3.2 Type II Ion Exchange Experiments. This experiment differed greatly from the Type I Ion Exchange experiment. Here, the Na-OAc treated HFSC was brought to equilibrium with three different sets of solutions of fixed normality (i.e., 0.1, 0.01, 0.001) and variable strontium:sodium ratio. Equilibrium was achieved by washing the sediment three times with the noted solutions. Approximately 94% of the exchange complex was calcium/magnesium saturated before the initiation of the experiment. The initial two wash solutions desorbed a portion of the exchangeable Ca^{2+}, with greater desorption occurring at the highest solution normality. After equilibrium was achieved, the aqueous phase was sampled and analyzed, and the exchange complex was displaced by ammonium chloride to yield a full differentiation of the adsorbed cation charge.

The results from this complex experiment are summarized in Table D.2. Many of the analyses of the equilibrium solution and the ammonium extract are still underway, and only a partial summary of analytical results is reportable. The results demonstrate that even experiments performed with pre-equilibrated sediments and binary electrolytes can evolve to complicated multicomponent systems. This multicomponent behavior has complicated past attempts to develop predictive relationships for strontium adsorption in Hanford sediment.

Table D.2. Added Sodium and Strontium Concentrations, and Subsequent Equilibrium Distribution of Calcium, Potassium, Magnesium, Strontium and Sodium in Strontium: Sodium Exchange on Sodium-Acetate Treated Hanford Fine Sand Composite (2 pages)

		Initial Solution		Equilibrium Solution					Ammonium Extractable					
	Target	Initial [Sr]	Initial [Na]	$[Ca]_{aq}$ [a]	$[K]_{aq}$ [a]	$[Mg]_{aq}$ [a]	$[Sr]_{aq}$ [b]	$[Na]_{aq}$ [b]	$[Ca]_{ads}$ [a]	$[K]_{ads}$ [a]	$[Mg]_{ads}$ [a]	$[Sr]_{ads}$ [b]	$[Na]_{ads}$ [b]	Sum
	Total Normality	(mol/L)	(mol/L)	(mol/L)	(mol/L)	(mol/L)	(mol/L)	(mol/L)	(μeq/g)	(μeq/g)	(μeq/g)	(μeq/g)	(μeq/g)	(μeq/g)
Solution	(Na+Sr)			(ICP)	(ICP)	(ICP)	(Sr-85)	(Na-22)	(ICP)	(ICP)	(ICP)	(Sr-85)	(Na-22)	
A1	0.1	4.972E-02					4.972E-02					40.19		
A2	0.1	3.941E-02	1.982E-02	1.912E-04	1.423E-04	4.870E-05	3.941E-02	1.98E-02	3.14	0.54	1.18	40.77	1.84	47.5
A3	0.1	2.952E-02	3.983E-02				2.952E-02	3.97E-02				39.57	4.25	
A4	0.1	1.970E-02	5.994E-02				1.959E-02	5.97E-02				35.65	8.59	
A5	0.1	9.866E-03	7.997E-02				9.686E-03	7.87E-02				29.26	12.44	
A6	0.1	4.934E-03	8.988E-02	4.503E-04	1.654E-04	8.972E-05	4.633E-03	8.90E-02	5.40	0.59	1.77	23.27	25.82	56.8
A7	0.1	2.466E-03	9.494E-02				2.080E-03	9.40E-02				16.28	22.45	
A8	0.1	5.048E-04	9.898E-02				3.438E-04	9.67E-02				4.80	32.11	
A9	0.1	2.524E-04	9.988E-02				1.643E-04	9.99E-02				2.56	31.26	
A10	0.1	5.186E-05	9.999E-02	5.052E-04	1.621E-04	1.099E-04	3.059E-05	9.93E-02	10.53	0.75	2.67	0.57	33.09	47.6
A11	0.1		1.001E-01					9.77E-02					35.05	
B1	0.01	5.033E-03					4.447E-03					37.66		
B2	0.01	3.971E-03	1.987E-03	6.446E-04	5.829E-05	1.379E-04	3.248E-03	1.97E-03	9.57	0.60	2.43	34.64	0.82	48.1
B3	0.01	2.974E-03	3.985E-03				2.270E-03	3.98E-03				31.55	1.53	
B4	0.01	1.985E-03	5.999E-03				1.294E-03	6.00E-03				26.19	2.38	
B5	0.01	9.925E-04	8.006E-03				4.556E-04	8.01E-03				16.87	4.14	
B6	0.01	4.952E-04	8.991E-03	3.722E-04	4.969E-05	9.977E-05	1.518E-04	8.85E-03	27.39	0.66	6.11	9.75	6.00	49.9
B7	0.01	2.491E-04	9.484E-03				5.380E-05	9.24E-03				5.23	7.80	
B8	0.01	5.063E-05	9.892E-03				7.503E-06	9.61E-03				1.13	9.16	
B9	0.01	2.523E-05	9.972E-03				3.492E-06	9.53E-03				0.57	9.67	
B10	0.01	5.205E-06	1.000E-02	1.991E-04	4.272E-05	6.014E-05	6.495E-07	9.62E-03	31.44	0.81	7.24	0.12	9.94	49.6
B11	0.01		9.993E-03					9.74E-03					10.10	
C1	0.001	5.010E-04					1.270E-04					10.84		

Table D.2. Added Sodium and Strontium Concentrations, and Subsequent Equilibrium Distribution of Calcium, Potassium, Magnesium, Strontium and Sodium in Strontium: Sodium Exchange on Sodium-Acetate Treated Hanford Fine Sand Composite (2 pages)

		Initial Solution		Equilibrium Solution					Ammonium Extractable					
	Target	Initial [Sr]	Initial [Na]	$[Ca]_{eq}$ [a]	$[K]_{eq}$ [a]	$[Mg]_{eq}$ [a]	$[Sr]_{eq}$ [b]	$[Na]_{eq}$ [b]	$[Ca]_{ads}$ [a]	$[K]_{ads}$ [a]	$[Mg]_{ads}$ [a]	$[Sr]_{ads}$ [b]	$[Na]_{ads}$ [b]	Sum
	Total Normality	(mol/L)	(mol/L)	(mol/L)	(mol/L)	(mol/L)	(mol/L)	(mol/L)	(μeq/g)	(μeq/g)	(μeq/g)	(μeq/g)	(μeq/g)	(μeq/g)
Solution	(Na+Sr)			(ICP)	(ICP)	(ICP)	(Sr-85)	(Na-22)	(ICP)	(ICP)	(ICP)	(Sr-85)	(Na-22)	
C2	0.001	4.005E-04	2.003E-04	2.893E-04	2.437E-05	8.398E-05	8.187E-05	1.74E-04	33.30	1.00	7.52	8.83	0.48	51.1
C3	0.001	3.001E-04	4.015E-04				4.884E-05	3.82E-04				6.79	0.62	
C4	0.001	2.003E-04	6.036E-04				2.527E-05	5.75E-04				4.63	0.95	
C5	0.001	1.002E-04	8.066E-04				8.060E-06	7.53E-04				2.42	1.33	
C6	0.001	5.012E-05	9.065E-04	9.354E-05	2.096E-05	2.962E-05	2.780E-06	8.38E-04	38.25	0.95	9.18	1.20	1.65	51.2
C7	0.001	2.505E-05	9.563E-04				1.131E-06	8.84E-04				0.61	1.80	
C8	0.001	5.053E-06	9.957E-04				1.899E-07	9.03E-04				0.12	1.96	
C9	0.001	2.525E-06	1.006E-03				8.945E-08	9.45E-04				0.061	2.06	
C10	0.001	5.304E-07	1.006E-03	6.911E-05	1.954E-05	2.448E-05	1.945E-08	9.22E-04	38.23	0.94	9.18	0.013	1.98	50.4
C11	0.001		1.009E-03					9.05E-04					2.00	
													Mean =	50.2

[a] = Average of two samples.
[b] = Single sample.

Sizeable concentrations of calcium, magnesium, and potassium existed in the equilibrium solution and on the exchange complex. Adsorbed (e.g., ammonium extractable) calcium and magnesium generally increased with decreasing solution normality (e.g., to 0.001) in response to lower aqueous concentrations of strontium and sodium in the initial solutions. In turn, sodium dominated the exchange complex only at the highest solution normality (0.1 eq/L) when its aqueous concentration was high (e.g., $\approx 10^{-1}$ mol/L) and that of the other divalent cations (e.g., strontium and calcium) was considerably lower (e.g., $< 10^{-3.5}$ mol/L). The sum of the adsorbed cation charge defined a rather uniform CEC (50.2 μeq/g) that significantly exceeded that measured by isotopic dilution with calcium-45 (34.7 μeq/g).

The adsorption isotherms and Sr-K_d functions (Figure D.9) derived from the data in Table D.2 were consistent with those reported in Figure D.3, given the differences in experimental design and total Ca^{2+} of the system at equilibrium. The adsorption isotherms moved to the left with decreasing total normality (and sodium concentration). The Sr^{2+} concentration regions over which a constant K_d was observed were much abbreviated in this latter experiment, but the same approximate range of values was observed (e.g., assymtotic values ranged from log $K_d = 1$ to log $K_d = 2.6$). Differences in K_d between this experiment and that in Figure D.3 result from differences in the total Ca^{2+} concentration of the system. The prewashing steps in this experiment removed a significant portion of adsorbed Ca^{2+} at the highest solution normality (0.1 eq/L). These data demonstrated that a constant Sr-K_d is unlikely if the overall exchange process is a multicomponent one. In fact, the data in Table D.2 is difficult to interpret without a multicomponent ion exchange model. Such modeling forms the basis for the following section of the report (Section D.2.3).

The experimental results in Table D.2 indicated that it is quite difficult to achieve a fully Na^{+}-saturated Hanford sediment that remains so during storage. A continuous source of Ca^{2+} resupply, even in the absence of carbonates, and the higher affinity of the exchanger phase for divalent cations promotes partial Ca saturation of the exchange complex even at high Na^{+} concentration. In contrast, it is relatively easy to create a stable, Ca^{2+}-saturated Hanford sediment. As a result, the Table D.2 experiment is currently being replicated using Ca^{2+}-saturated HFSC and calcium-sodium, calcium-strontium, and calcium-magnesium electrolytes to quantitatively characterize the binary exchange behavior of the noted cation pairs. These results will totally define the ion exchange behavior of Hanford sediment.

Figure D.9. K_d Functions and Adsorption Isotherms for Strontium on the Na-OA_c Treated Hanford Fine Sand Composite Data Derived from Table D.2

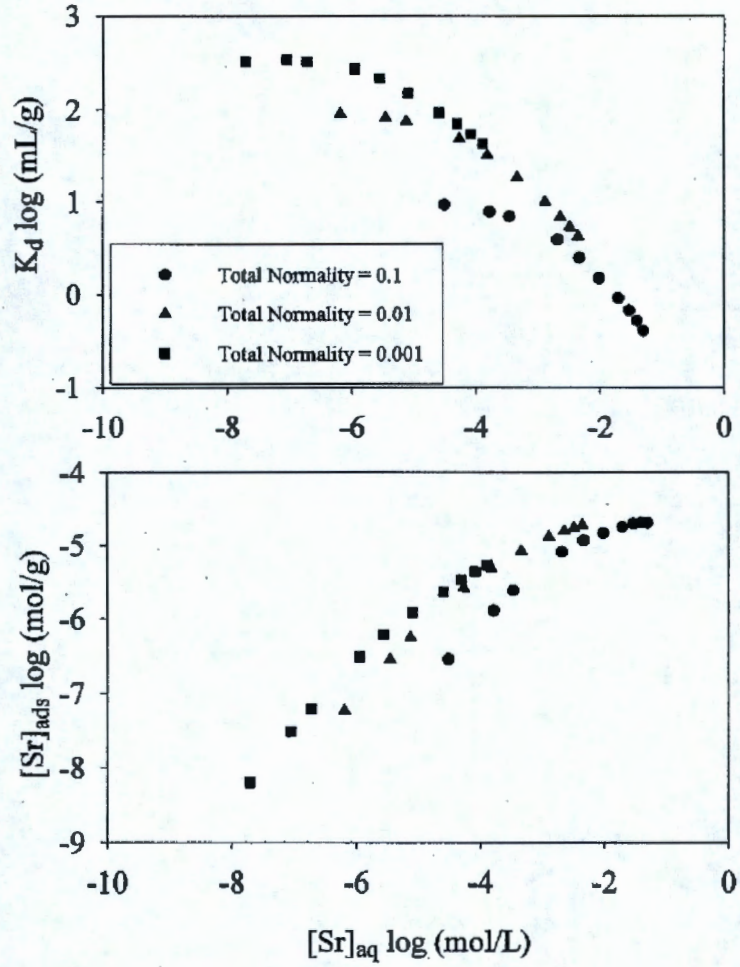

D.2.2.4 Conclusions

A variety of strontium adsorption experiments were performed with sediments from the 200 East Area (upper and lower B tank farm composites) and the 200 West Area (Hanford fine sand composite) in sodium and calcium electrolytes to characterize the ion exchange process of Sr^{2+}. All of the sediments used showed comparable adsorption behavior for Sr^{2+}, with slight variations noted consistent with their different cation exchange capacities. Qualitative conclusions regarding the ion exchange process were made by evaluating the variation in K_d and the exchangeable ion distribution as influenced by electrolyte cation valence and concentration. Ion-exchange modeling to quantify sediment cation selectivity coefficients is reported in Section D.2.3. The following are primary conclusions of this work:

1. The primary attenuation mechanism for strontium-90 in Hanford sediments is isotopic exchange with the labile, indigenous, stable isotopic pool. Most of the labile repository of stable isotope strontium exists on the cation exchange complex in the sediment. The cation exchange complex demonstrates an approximate concentration range of 20 to

60 μeq/g on B tank farm sediments. Indigenous strontium typically occupies 5 to 10% of the exchange complex.

2. Even though the ion exchange complex exists in sediment at relatively low concentration, it exhibits a concentration of approximately 0.233 mol/L (assuming a CEC of 50 μeq/g) when referenced to water-saturated pore volume. Its ability to influence and control the ion distribution of porewater is therefore significant.

3. The ion exchanger phase in the Hanford sediments prefers divalent cations (e.g., calcium, magnesium, and strontium) over monovalent cations (e.g., sodium, potassium). Ninety-six percent of the ion exchange complex of pristine sediments from the S-SX and B, BX, and BY tank farms was calcium and magnesium saturated with a magnesium/calcium mole ratio of 0.23. This repository of sorbed cations has a major influence on the exchange behavior of Sr^{2+} and strontium-90. Relatively large aqueous Na^+ concentrations (>0.1 mol/L) are needed to change the ion distribution of the exchange complex.

4. Distribution ratios (Sr-K_d) measured for strontium on predominantly calcium-saturated Hanford sediments (including two from the B tank farm) in sodium and calcium electrolytes varied from 1000 ml/g to 0 in sodium electrolyte (0.001 to 5 mol/L Na) and 58.9 ml/g to 0.68 ml/g in calcium electrolyte (0.0005 to 0.05 mol/L), attesting to the strong electrolyte ion effect on Sr^{2+} adsorption. Log Sr-K_d showed linear dependence on log [Ca^{2+}] and slight curvilinear dependence on log [Na^+] indicating that the development of predictive ion exchange relationships was possible.

5. The ion exchange adsorption of Sr^{2+} was slightly enhanced in HCO_3 electrolyte (the dominant anion in the B-110 strontium plume), presumably by formation of adsorbing $SrHCO_3^+$ complexes. NTA (nitrilo-triacetic acid, a possible complexant present in the B-110 strontium recovery waste stream) had no effect on Sr^{2+} ion exchange adsorption in HCO_3 electrolyte when its concentration was 1.5 mmol/L, but reduced Sr^{2+} ion exchange adsorption by a factor of approximately 18 when NTA was present at 15 mmol/L. More specifically, the presence of NTA at 15 mmol/L reduced the Sr^{2+}-K_d in B tank farm composite sediment in 0.015 mol/L $NaHCO_3$ electrolyte from approximately 56 ml/g to 3.16 ml/g.

6. The best estimate of the K_d for strontium in the core of the strontium-90 plume at B-110 promoted by ion exchange is 3.54 ml/g. This value is reduced by a factor of 18 to 0.20 ml/g in presence of 15 mmol NTA.

D.2.2.5 References

Jardine, P. M., G. K. Jacobs, and J. D. O'Dell, 1993, "Unsaturated Transport Processes in Undisturbed Heterogeneous Porous Media: II. Co-Contaminants," *Soil Science Society of America Journal*, Vol. 57:954-962.

Jensen, H. E., and K. L. Babcock, 1973, "Cation-Exchange Equilibria on a Yolo Loam," *Hilgardia*, Vol. 41:475-488.

Liu, C., J. M. Zachara, and S. C. Smith, 2002, "A Cation Exchange Model to Describe Cs Sorption at High Ionic Strength in Subsurface Sediments at Hanford Site, USA," *Journal of Contaminant Hydrology* (submitted).

Serne, R. J., and V. L. LeGore, 1996, *Strontium-90 Adsorption-Desorption Properties and Sediment Characterization at the 100 N-Area*, PNL-10899, Pacific Northwest National Laboratory, Richland, Washington.

Sposito, G., 1981a, "Cation Exchange in Soils: An Historical and Theoretical Perspective," In *The Thermodynamics of Soil Solutions*, G. Sposito, ed., American Society of Agronomy, Soil Science Society of America, Madison, Wisconsin, pp. 13-30.

Sposito, G., 1981b, "*The Thermodynamics of Soil Solutions*," G. Sposito, ed., Oxford University Press, Oxford, pp. 223.

Szecsody, J. E., A. Chilakapati, J. M. Zachara, and A. L. Garvin, 1998, "Influence of Iron Oxide Inclusion Shape on $Co^{II/III}$EDTA Reactive Transport Through Spatially Heterogeneous Sediment," *Water Resources Research*, Vol. 34:2501-2514.

Zachara, J. M., S. C. Smith, and L. S. Kuzel, 1995a, "Adsorption and Dissociation of Co-EDTA Complexes in Iron Oxide – Containing Subsurface Sands," *Geochimica et Cosmochimica Acta*, Vol. 59:4825-4844.

Zachara, J. M., P. L. Gassman, S. C. Smith, and D. Taylor, 1995b, "Oxidation and Adsorption of Co(II)$EDTA^{2-}$ Complexes in Subsurface Materials with Iron and Manganese Oxide Grain Coatings," *Geochimica et Cosmochimica Acta*, Vol. 59:4449-4463.

Zachara, J. M., S. C. Smith, C. Liu, J. P. McKinley, R. J. Serne, and P. L. Gassman, 2002, "Sorption of Cs^+ to Micaceous Subsurface Sediments from the Hanford Site, USA," *Geochimica et Cosmochimica Acta*, Vol. 66:193-211.

D.2.3 MODELING BATCH REACTOR ION EXCHANGE EXPERIMENTS OF STRONTIUM-CALCIUM-MAGNESIUM-POTASSIUM-SODIUM ON HANFORD SEDIMENTS

Peter C. Lichtner[1] and John M. Zachara[2]

[1]Los Alamos National Laboratory, Los Alamos, New Mexico 87545
[2]Pacific Northwest National Laboratory, Richland, Washington 99352

D.2.3.1 Introduction

A common, albeit often unjustified, approach is to use a constant distribution coefficient, or K_D (defined as the ratio of sorbed to aqueous concentration), to represent retardation of contaminants. This approach, however, is generally valid only if the K_D remains constant over the entire flow domain. Because the K_D of a contaminant species varies with the composition of the background electrolyte solution, it is necessary to measure its value over a range of compositions corresponding to each particular system under consideration. For the situation at the Hanford tank farm where highly concentrated fluids (Lichtner and Felmy 2002) have leaked from underground tanks or ancillary pipelines resulting in a pulse release of contaminants, the K_D is inherently variable, possibly over many orders of magnitude (Lichtner et al. 2002). These effects are most pronounced shortly after the tank waste leak event when tank fluid chemistry dominates the local geochemical environment and minimal buffering reactions have occurred between tank waste, soil, and porewater. In such cases, use of a constant K_D approach to describe migration of contaminants is highly questionable. As shown in Section D.2.2, the K_D for strontium is highly variable showing dependence on strontium concentration, aqueous electrolyte composition and concentration, and surface saturating ions.

In circumstances where it cannot be assured that a constant K_D provides an accurate description, a mechanistic approach is called for. Use of a mechanistic model for sorption has a number of advantages over a phenomenological K_D approach. First of all, a mechanistic approach enables the K_D to be parameterized with only a few parameters, referred to as selectivity coefficients, as compared to the entire groundwater composition that is needed in the phenomenological approach. More importantly, the mechanistic approach can easily handle variable electrolyte compositions such as is characteristic of pulse releases from the Hanford tanks, and the mixing of vadose zone porewater or wastewaters with groundwater.

Perhaps the simplest means of constructing a mechanistic sorption model is through the use of batch-type experiments carried out over a range of solution compositions. Another, more complicated approach, is to use column experiments involving flow of fluids and measurement of contaminant breakthrough curves. The work presented in this report illustrates the use of batch experiments to derive a mechanistic sorption model for retardation of strontium in the Hanford sediments. It must be stated at the outset, however, that the results presented in this report are preliminary and that additional experiments are currently underway to refine the multicomponent ion exchange model. The ultimate goal of this work is to provide a mechanistic sorption model for strontium that can be used in reactive transport models involving variable composition fluids to predict the behavior of strontium in the B-110 plume, at the 1325-N liquid waste disposal facility, and other locations in the Hanford vadose zone and aquifer system.

This contribution reports the results of model fitting and predictions of batch experiments involving ion exchange of strontium on Hanford sediments performed by Smith and Zachara at Pacific Northwest National Laboratory (PNNL) (Section D.2.2). The experiments performed to date consisted of different electrolyte solutions made up of $NaNO_3$, $NaHCO_3$, $Ca(NO_3)_2$, and H_3NTA combined with $Sr(NO_3)_2$, and reacted with different Hanford sediment types from the B, BX, and BY tank farms.

D.2.3.2 Model Formulation

Experiments were preformed in a batch reactor consisting of a well-stirred aqueous solution reacting with Hanford sediments with a fixed rock/fluid ratio. In the experiments, the aqueous solution was allowed to equilibrate with the suspended solid. A multicomponent exchange process took place in the experiments involving cations Na^+, K^+, Ca^{2+}, Mg^{2+}, and Sr^{2+}. The general form of the reaction for the exchange of cations $A_j^{z_j+}$ and $A_i^{z_i+}$ with valencies z_i and z_j, may be expressed as:

$$\frac{1}{z_j}A_j^{z_j+}+\frac{1}{z_i}X_{z_i}A_i \Leftrightarrow \frac{1}{z_j}X_{z_j}A_j+\frac{1}{z_i}A_i^{z_i+}.$$

Here, the exchange site is denoted by X^-, with sorbed species $X_{z_i}A_i$ and $X_{z_j}A_j$. The mass action equation corresponding to the exchange reaction has the form

$$\mathrm{K}_{ji}=\left(\frac{\lambda_j X_j}{a_j}\right)^{1/z_j}\left(\frac{a_i}{\lambda_i X_i}\right)^{1/z_i},$$

with selectivity coefficient K_{ji}, X_j denoting the sorbed fraction with activity coefficient correction λ_j, and a_j the aqueous activity of the jth exchange cation. Different conventions are used to relate the sorbed fraction X_j to the sorbed concentration S_j, or sorption isotherm. There are $N-1$ independent coefficients for N exchangeable cations. For example, for exchange of cations strontium, calcium, magnesium, potassium, and sodium, N = 5, giving 4 independent selectivity coefficients. The sorbed fraction X_j is obtained as a function of solution composition by combining the mass action equations with the normalization condition

$$\sum_j X_j = 1,$$

to yield a single nonlinear equation for any one of the X_j. From this result, the remaining X_i can be obtained directly from the mass action equations. For multivalent exchanges, these equations must be solved numerically.

For the batch reactor with rock/fluid ratio r, the exchange site concentration ω is related to the cation exchange capacity CEC of the sediment by the expression

$$\omega=\frac{N_{\text{sites}}}{\mathrm{V}}=\frac{N_{\text{sites}}}{M_s}\frac{M_s}{V_s}\frac{V_s}{V}=\rho_s\phi_s\mathrm{CEC}=\frac{r\rho_s}{r+\rho_s}\mathrm{CEC},$$

or

$$\omega = \phi r \mathrm{CEC},$$

where N_{sites} denotes the number of exchange sites within a control volume V, ϕ denotes the ratio of aqueous fluid to total volume of the system calculated from the equation

$$\phi = \frac{V_l}{V} = \frac{\rho_s}{r+\rho_s},$$

where ρ_s refers to the sediment grain density, and the sediment fraction ϕ_s is given by

$$\phi_s = \frac{V_s}{V} = 1-\phi = \frac{r}{r+\rho_s}.$$

and ρ_s refers to the sediment grain density. The concentration of sorption sites is conserved by exchange reactions satisfying the relation

$$\omega = \sum_j z_j S_j .$$

The sorption isotherm $S_j(c)$ for a batch reactor is obtained by solving a system of nonlinear algebraic equations for the aqueous concentration of the form

$$\phi \Psi_j(c) + S_j(c) = \phi t_j,$$

where Ψ_j denotes the total aqueous concentration and t_j represents the total initial concentration of the jth primary species, and $c=(c_1,\cdots,c_N)$ represents the solution concentration for N independent primary species. For nonsorbing species, the corresponding sorbed concentration S_j vanishes. Charge balance may be used to determine the solution pH if it is not provided directly from the experiment. As written, these equations apply to a single sorption site, but may be easily extended to multiple sites by summing the sorbed concentration over the distinct sites.

The batch reactor equations are solved using FLOTRAN (Lichtner 2001, 2002). A Newton-Raphson scheme was used to solve the resulting nonlinear algebraic equations. This approach converged in several iterations. The Debye-Hückel activity coefficient algorithm was found to be adequate for all but possibly the experiments involving a 1M $NaNO_3$ solution.

The sorption isotherm $S_j(c)$ is fit to experimental data using the selectivity coefficients as fit parameters. To fit the experimental data, the parameter estimation code PEST (Parameter Estimation Inc.) (Doherty et al. 1994) is used which provides a versatile interface to FLOTRAN. The PEST code uses the Gauss-Marquardt-Levenberg algorithm to fit nonlinear model parameters to a data set provided by the user.

D.2.3.3 Model Results

Two distinct types of experiments were used in the modeling exercises, referred to as Type 1 and Type 2 experiments. These are described in detail in Section D.2.2. Type 1 experiments, which were performed first, involved variable solution normality in which the background electrolyte

solution was fixed, for example, with a specified amount of $NaNO_3$, $NaHCO_3$, or $Ca(NO_3)_2$ to which was added a variable amount of $Sr(NO_3)_2$. Only a limited analysis of the exchangeable cation concentrations, both for the aqueous and exchanger phases, was performed for the Type 1 experiments. By contrast, Type 2 experiments were performed with fixed solution normalities using three different values of 0.1, 0.01, and 0.001 N. The Type 2 experiments included a complete analysis of all relevant cations in both aqueous and exchanger phases. However, the number of analyses for each ionic strength solution was limited to three.

The data from the Type 2 experiments, because they involved a complete analysis of the relevant cation concentrations and also provided an average value for the Hanford sediment cation exchange capacity (CEC), were used for fitting exchange model parameters. The experimentally measured exchange isotherms were fit using the computer code FLOTRAN (Lichtner 2001) combined with the parameter estimation code PEST (Doherty et al. 1994). The fitted parameters consisted of the four independent selectivity coefficients for exchange reactions involving cations strontium, calcium, magnesium, potassium, and sodium. The sediment CEC was derived from the average value of total adsorbed cation charge obtained from the Type 2 experiments. Precipitation of strontianite, although found to be supersaturated in several of the experiments analyzed, was not included in the present work.

Exchange isotherms experimentally derived from the Type 1 experiments were used to test the predictive capability of the fitted selectivity coefficients obtained from the Type 2 experiments. To carry this out, it was necessary to make some assumption regarding the initially sorbed concentrations of cations calcium, magnesium, and potassium. While these were measured by NH_4Cl extraction of the whole sediment, they were not explicity analyzed in the Type 1 experiments. Two different approaches were followed as described below. It is clear, however, that additional experiments will be necessary before a truly predictive modeling capability is achieved.

D.2.3.3.1 Fitted Type 2 Experiments. The Type 2 ion exchange experiments involved cations Na^+, K^+, Sr^+, Ca^{2+}, and Mg^{2+}. The experiments were carried out at 25 °C by reacting sediment with a $NaNO_3$+$Sr(NO_3)_2$ solution in which the sodium:strontium ratio was varied while maintaining a constant ionic strength. Three sets of experiments corresponding to ionic strengths of 0.1, 0.01, and 0.001 mol/L were performed. The rock/fluid ratio used in the experiments was fixed at 0.2 g/cm^3. It was found that significant amounts of calcium, magnesium, and potassium were desorbed from the sediment during the experiment. Three measurements of the aqueous and sorbed cation concentrations were obtained for different sodium:strontium ratios at each ionic strength (Table D.2). The experimental data for equilibrated aqueous and sorbed concentrations for species Sr^{2+}, Ca^{2+}, Mg^{2+}, and K^+ were fit using FLOTRAN combined with the parameter estimation code PEST for the four independent selectivity coefficients $K_{Na/Sr}$, $K_{Na/Ca}$, $K_{Na/Mg}$, and $K_{Na/K}$. The sediment CEC was fixed at 50.2 μeq/g the average adsorbed cation charge from 12 explicit measurements. The calculations were performed by inputting total aqueous concentrations for species Na^+, Sr^{2+}, Ca^{2+}, Mg^{2+}, and K^+, corresponding to the measured equilibrated concentrations. The total NO_3^- concentration was fixed at 0.1, 0.01, or 0.001 M, corresponding to the three different ionic strength solutions used in the experiment. The pH was determined by charge balance and $\log P_{CO_2} = -3.5$, as determined by equilibrium with the atmosphere. Aqueous complexing reactions included in the calculations are listed in Table D.3

along with their log K values at 25 °C corresponding to the primary cations: {Na^+, Sr^{2+}, Ca^{2+}, Mg^{2+}, K^+, H^+, HCO_3^-, NO_3^-}.

Table D.3. Aqueous Complexes with Log K Values at 25°C used in the Model Calculations

Species	log K [25 °C]
OH^-	13.990
CO_3^{2-}	10.320
CO2(aq)	6.341
NaNO3(aq)	1.044
CaOH+	12.850
$CaHCO_3^+$	1.043
CaCO3(aq)	7.009
$CaNO_3^+$	0.700
MgOH+	11.790
$MgHCO_3^+$	1.164
MgCO3(aq)	7.356
SrCO3(aq)	7.470
$SrHCO_3^+$	-1.180

A simultaneous fit to the measured sorbed concentrations (converted from μeq/g to mol/dm^3 assuming a solid grain density of 2.85 g/cm^3) for species Sr^{2+}, Ca^{2+}, Mg^{2+}, and K^+ was obtained using the four independent selectivity coefficients as fit parameters. Experimental data for the Na^+ isotherm was not used in the fitting process, but was predicted by the model. The pH was not provided from the experiment and was also predicted by the model. The fitted values for the selectivity coefficients listed in Table D.4 were obtained.

Table D.4. Fitted Selectivity Coefficients Relative to Na^+ Assuming a CEC of 50.2 μeq/g

$K_{Na/Sr}$	9.508
$K_{Na/Ca}$	8.759
$K_{Na/Mg}$	6.072
$K_{Na/K}$	21.010

The resulting fit is shown in Figure D.10 through Figure D.13 for species Sr^{2+}, Ca^{2+}, Mg^{2+}, and K^{+}, respectively. Plotted in the figures is the sorbed concentration versus aqueous concentration of each of the four species. For strontium, there is more data as compared to the other cations for which only three data points are available. This limited the number of points that could be used in the computations also to three. Additional analyses will allow a more robust fit of these parameters. In the figures, symbols denote experimental data points. Straight-line segments represent the model results with computed values lying at the endpoints of the line segments. It is important to note that the line segments drawn between the computed points do not represent actual computed values. It should also be noted that in these plots, the concentrations of all cations, including Na^{+}, are varying from point to point. Thus, the plots do not represent a strict isotherm in which all but the species plotted along the abscissa are held constant. For this reason, it was not possible to compute a continuous curve for the model results because the precise solution composition at the intermediate points was unknown.

Figure D.10. Fitted Sr^{2+} Isotherm Compared with Experimental Data for Type 2 Experiments

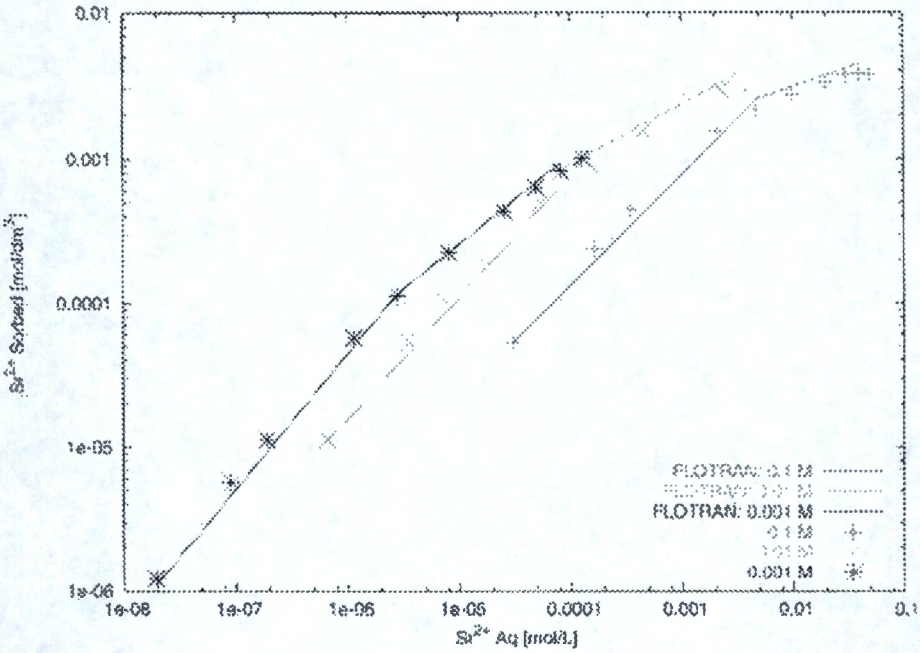

Figure D.11. Fitted Ca^{2+} Isotherm Compared with Experimental Data for Type 2 Experiments

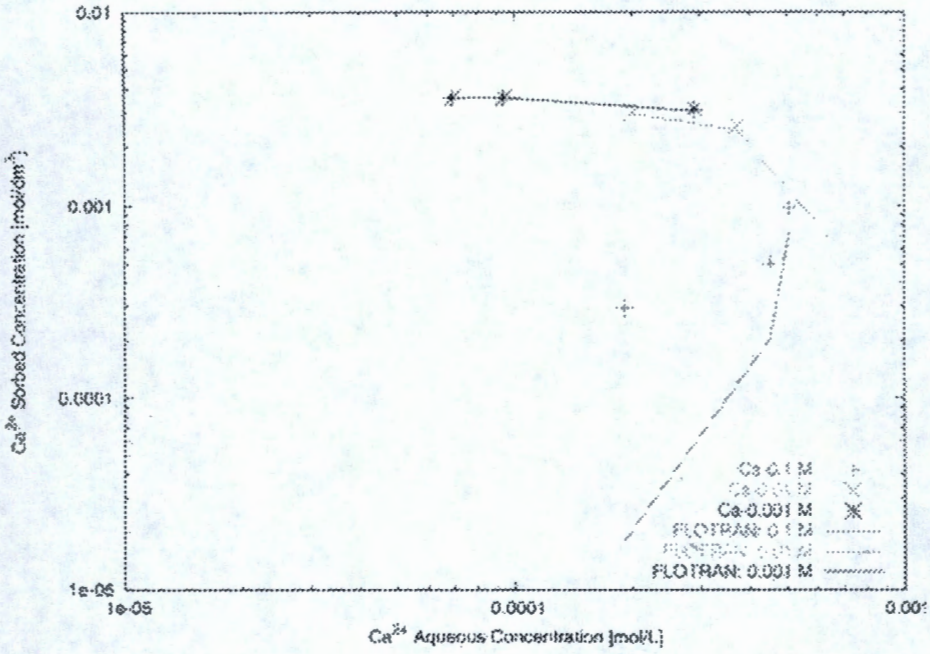

Figure D.12. Fitted Mg^{2+} Isotherm Compared with Experimental Data for Type 2 Experiments

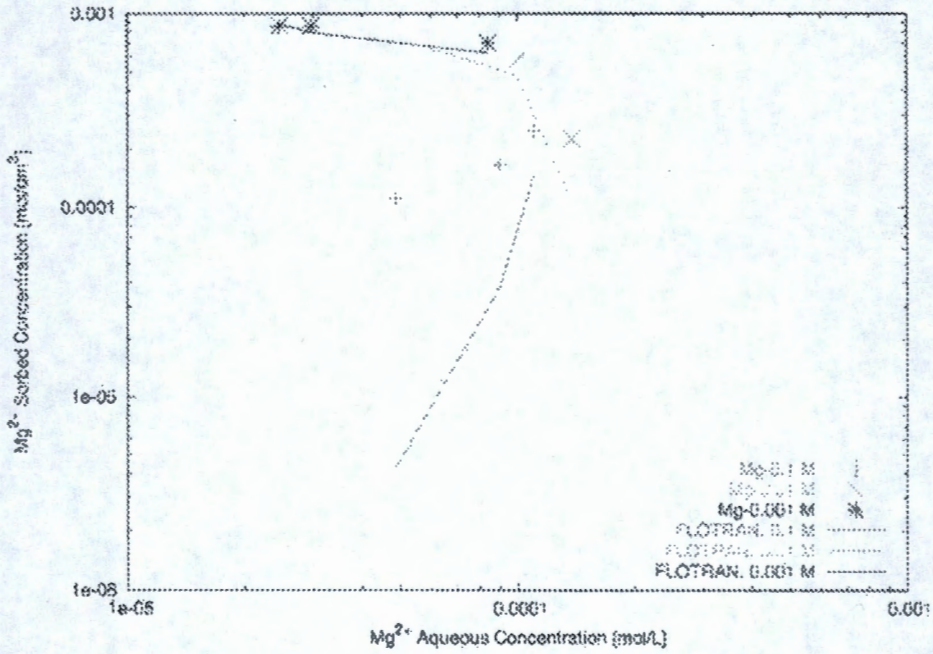

Figure D.13. Fitted K^+ Isotherm Compared with Experimental Data

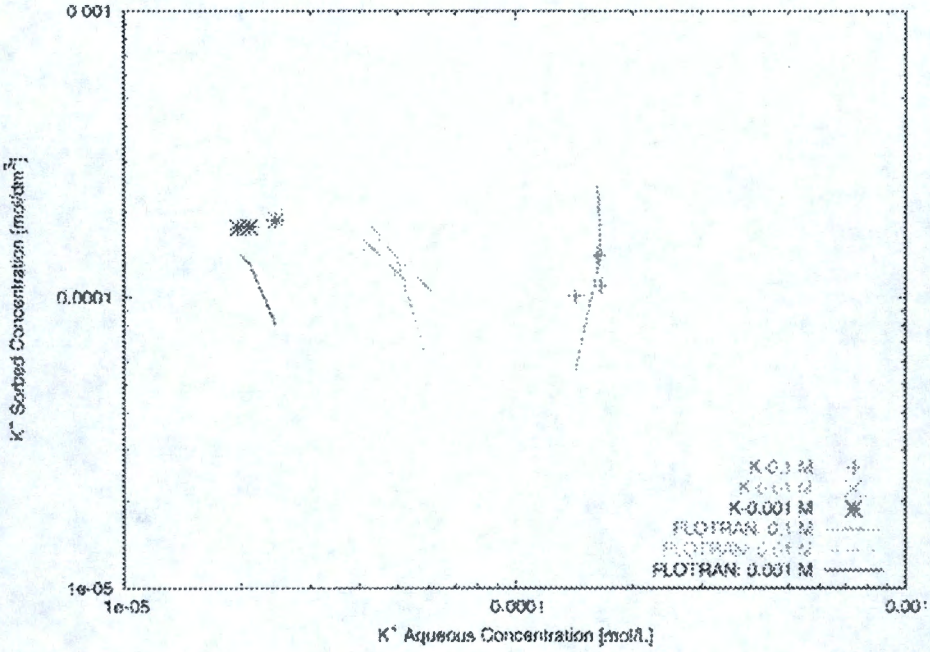

Excellent fits are obtained to the Sr^{2+} isotherm for all three values of the ionic strength. The fit to the Ca^{2+} and Mg^{2+} isotherms are also excellent for the 0.01 and 0.001 N experiments, but not for the 0.1 N experiment. The fit to the K^+ isotherm is good for the 0.1 and 0.01 N experiments, but lies below the sorbed value for the 0.001 N experiment.

The predicted Na^+ isotherm is shown in Figure D.14. The predicted sorbed concentration of Na^+ agrees remarkably well with the 0.1 and 0.01 N experiments, and for the high end of the aqueous Na^+ concentration for the 0.001 N experiment. For lower Na+ concentrations, the predicted isotherm is low compared to the data for the 0.001 M experiment, but otherwise gives reasonable agreement. The predicted pH is shown in Figure D.15. The calculated pH lies around 7.5 with two low values of approximately 3.5 for the 0.1 M experiment. pH measurements are underway to confirm these values, but it is unlikely the pH reached such low values because of the buffering capacity of the sediment.

Figure D.14. Predicted Na^+ Isotherm Compared with Experimental Data

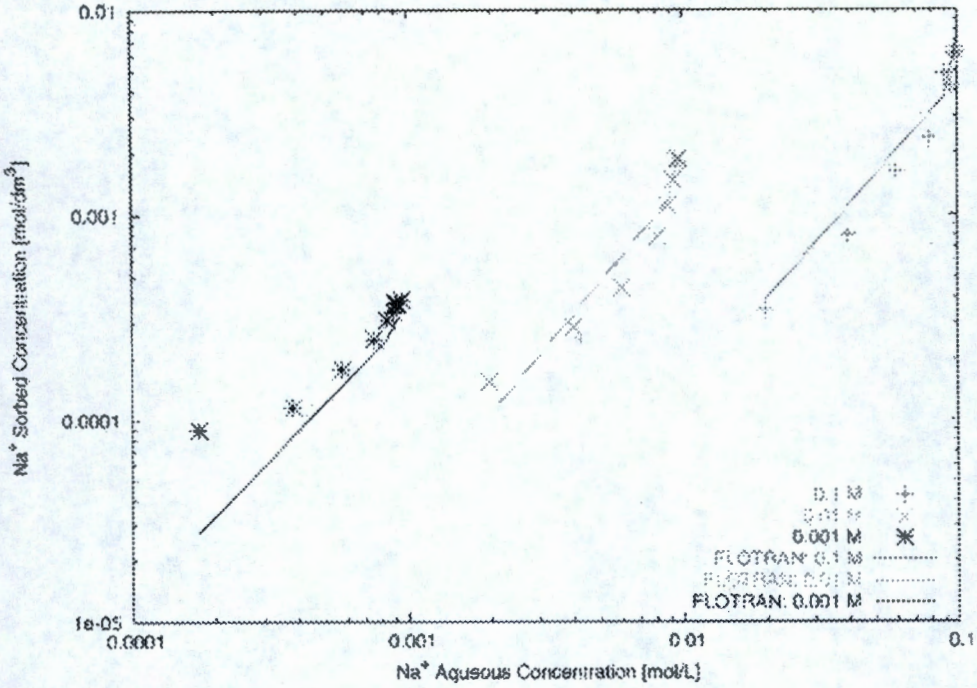

Figure D.15. Calculated pH Plotted as a Function of Total Aqueous Sr^{2+} Concentration

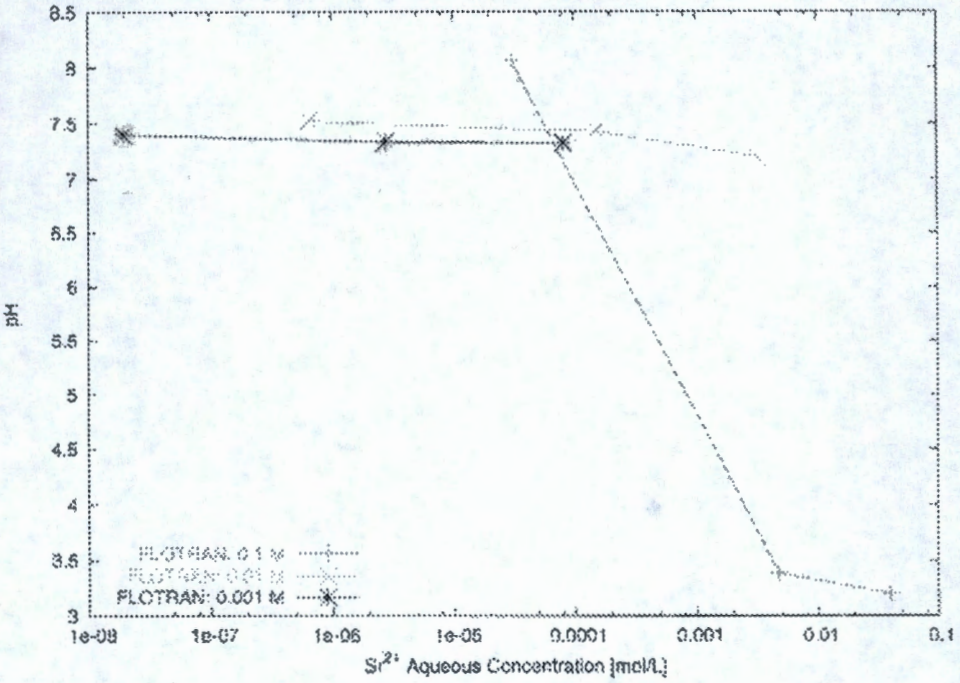

D.2.3.3.2 Discussion. The CEC value used in the simulations was taken as the average over all experiments. The measured CEC ranged in value from 47.5 to 56.8 mol/g with the latter value much higher than the others. This range of values was not accounted for in the model fit. Several of the analyses leading to the CEC calculation are being repeated to reduce analytical variance and improve the accuracy of the CEC estimate.

The NH_4Cl used for the surface cation displacements in the experiments contained many impurities that contributed uncertainty to both the CEC and adsorbed cation charge. New experiments will use specially ordered ultra-pure NH_4Cl yielding more accurate values of CEC and adsorbed cation charge.

D.2.3.3.3 Prediction of Type 1 Experiments. The selectivity coefficients obtained from fitting the Type 2 experiments and the same value for the CEC of 50.2 μeq/g, were used to predict the sorption isotherms measured in Type 1 experiments. The Type 1 experiments involved sodium-strontium, calcium-strontium, sodium-calcium-strontium, and, in addition, H_3NTA solution compositions. Similar to the Type 2 experiments, they also involved residual strontium, calcium, magnesium, sodium, and potassium on the exchange sediment at the beginning of the experiment. To model the Type 1 experiments, the following initial sorbed concentrations were used for these cations: E_{Ca} = 35.88 μeq/g, E_{Na} = 1.54 μeq/g, E_K = 1.05 μeq/g, E_{Mg} = 8.25 μeq/g, and E_{Sr} = 0.031 μeq/g, giving a total CEC of 46.75 μeq/g. These values, adjusted by the rock-water ratio, define the total calcium, magnesium, sodium, and potassium concentrations in all of the Type 1 experiments with sodium and the sodium-saturated, NaOAc-extracted Hanford fine sand composite (HFSC). The residual value for strontium was not included in the model calculations and would have been too small to affect all but the lowest strontium concentrations used in the experiments. It should be noted that the sum of the residual values is somewhat less than the 50.2 μeq/g used for the CEC.

The B tank farm composite samples were not NaOAc extracted and required a slightly different approach for determining the residual initially sorbed concentrations. For these experiments, it was assumed that the sediment was 96% saturated with calcium and magnesium with a magnesium/calcium ratio of 0.23. The remaining 4% was attributed to potassium. This distribution of exchangeable ions was determined by a rapid NH_4Cl extraction of the sediments.

D.2.3.3.4 $NaNO_3$ + $Sr(NO_3)_2$ Experiments. For the set of experiments labeled 57488-45, 57488-60, 57488-63,and 57488-69, four different $NaNO_3$ concentrations were used with <2mm NaOAc-extracted Hanford fine sand composite sediment as listed in Table D.5 and Figure D.3. Also listed in Table D.5 is the rock/fluid ratio r and aqueous fluid fraction ϕ. The results of the model predictions are plotted in Figure D.16. The predicted values are in reasonable agreement with the experimental measurements, although differences are apparent. Use of the Pitzer model for the 1M $NaNO_3$ experiment yields values lower than the experiment, in contrast to the Debye-Hückel model, which is much closer to the experiment.

Figure D.16. Prediction of Experiments 57488-45, 60, 63, 69 using a CEC of 50.2. μeq/g

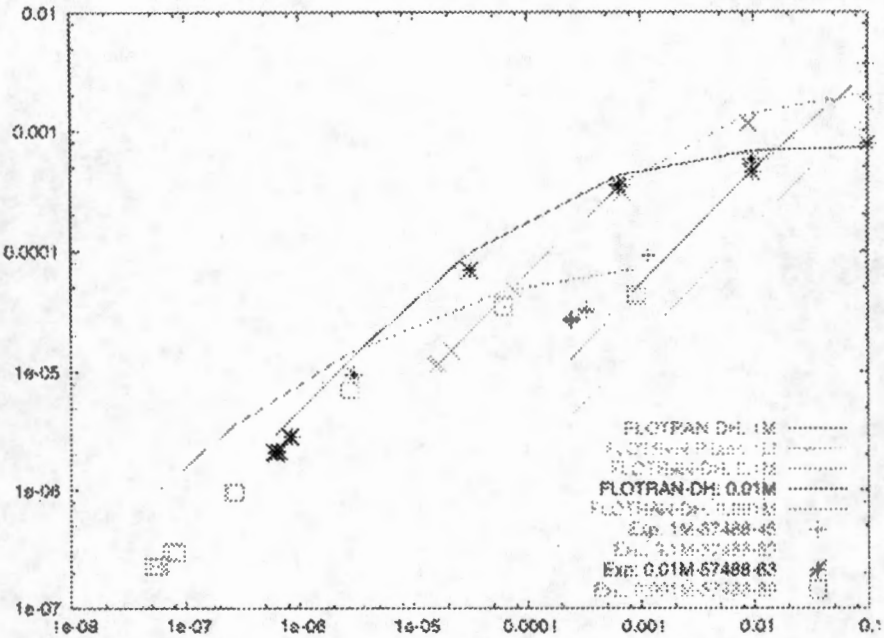

Table D.5. Experimental Parameters for System $NaNO_3$ + $Sr(NO_3)_2$ Using <2mm, NaOAc Extracted Hanford Fine Sand Composite Sediment

Experiment	m_{NaNO_3} |M|	r |g/L|	ϕ
57488-45	1	600	0.8261
57488-60	0.1	100	0.9661
57488-63	0.01	30	0.9896
57488-69	0.001	3	0.9990

D.2.3.3.5 $Ca(NO_3)_2$ + $Sr(NO_3)_2$ Experiments. In this set of experiments (labeled 57488-66, 57488-72, and 57488-77), $Ca(NO_3)_2$ was used in place of $NaNO_3$. The experimental parameters are listed in Table D.6. The results are shown in Figure D.17. As can be seen from the figure, the predicted results are in excellent agreement with the experiments.

Figure D.17. Predicted Simulations of Experiments 57488-66, 72, and 77 Using a CEC of 50.2 μeq/g and Fitted Selectivity Coefficients Listed in (Table D.4) Derived from the Type 2 Experiments

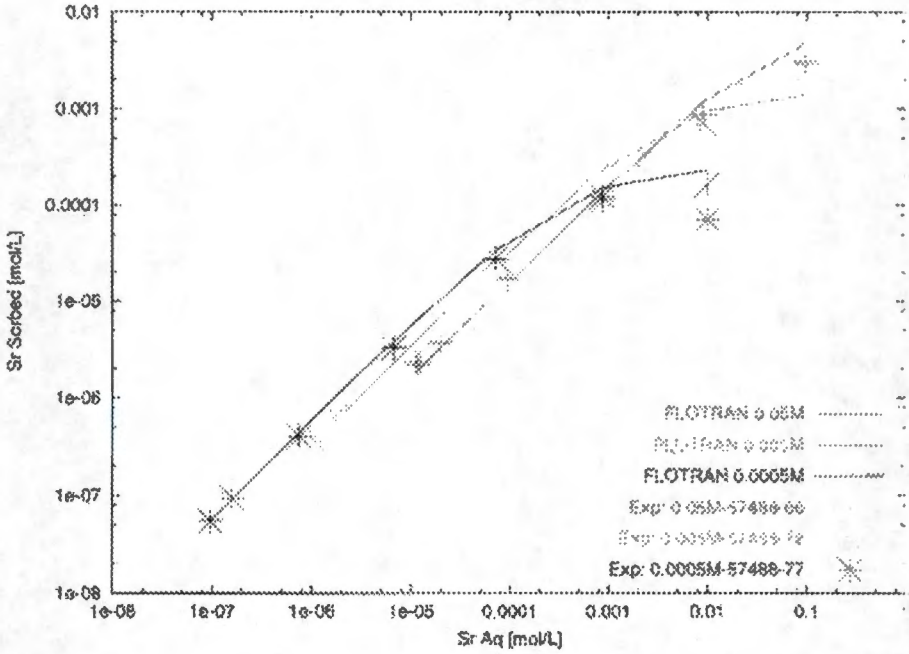

Table D.6. Experimental Parameters for System $Ca(NO_3)_2 + Sr(NO_3)_2$ Using <2mm, NaOAc Extracted Hanford Fine Sand Composite Sediment

Experiment	$m_{Ca(NO_3)_2}$ [M]	r [g/L]	ϕ
57488-66	0.05	300	0.8261
57488-72	0.005	60	0.9661
57488-77	0.0005	10	0.9965

D.2.3.3.6 [$NaHCO_3$, $NaNO_3$, $Ca(NO_3)_2$] + $Sr(NO_3)_2$ Experiments. The experiment suite labeled 57869 involved $NaHCO_3$ and $Ca(NO_3)_2$ with B tank farm upper and lower composite and Hanford fine sand sediments as listed in Table D.7. FLOTRAN simulations were carried out for 100 and 30 g/L rock/fluid ratios with the $NaHCO_3$ electrolyte, and for the mixed electrolyte solution involving calcium with $r = 50$ g/L. The results of the predicted simulation are presented in Figure D.18 and Figure D.19. As is apparent from the figure, significant differences exist for the sorption isotherm depending on whether $NaNO_3$ or $NaHCO_3$ is used as the electrolyte solution. At strontium concentrations above approximately 2×10^{-5} M, a slight rise in the sorbed strontium concentration occurs for experiments labeled 57869-40, 57869-43, and 57869-48, involving $NaHCO_3$, which is not captured by the model simulations.

Figure D.18. Prediction of Experiments 57869 for a CEC of 50.2 μeq/g

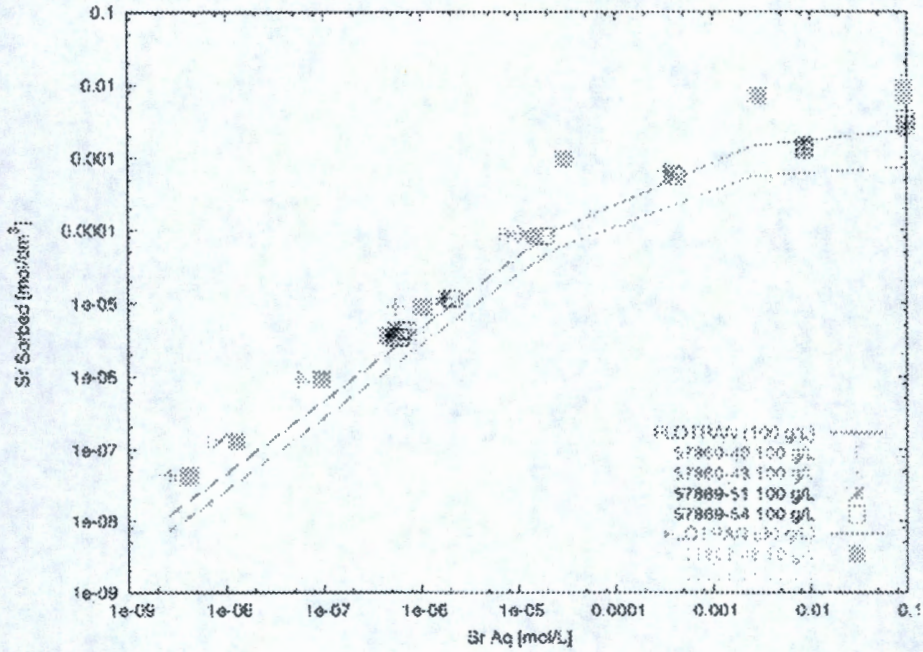

Figure D.19. Prediction of Experiments 57869 for a CEC of 50.2 μeq/g

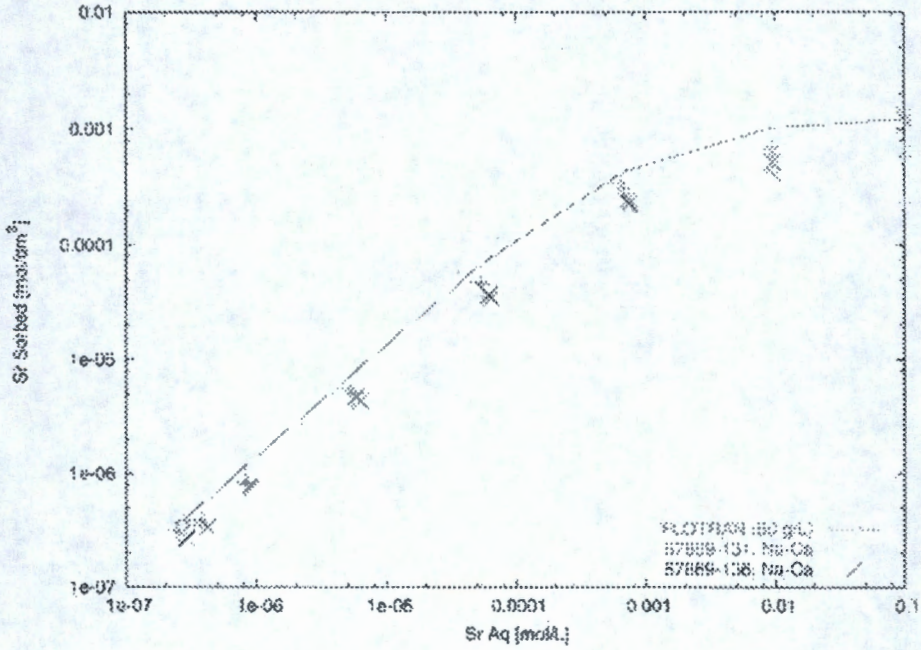

Table D.7. Experimental Parameters for System $NaHCO_3$, $NaNO_3$, $Ca(NO_3)_2$ + $Sr(NO_3)_2$ Using Hanford Fine Sand, Upper, and Lower Composite Sediment

Experiment	m_{NaHCO_3} [M]	m_{NaNO_3} [M]	$m_{Ca(NO_3)_2}$ [M]	r [g/L]	ϕ	Sediment
57869-40	0.015	0	0	100	0.9661	upper composite
57869-51	0	0.015	0	100	0.9661	upper composite
57869-43	0.015	0	0	100	0.9661	lower composite
57869-54	0	0.015	0	100	0.9661	lower composite
57869-48	0.015	0	0	30	0.9990	fine sand composite
57869-57	0	0.015	0	30	0.9990	fine sand composite
57869-131	0	0.001	0.001	50	0.9828	upper composite
57869-136	0	0.001	0.001	50	0.9828	lower composite

D.2.3.3.7 H_3NTA + ($NaNO_3$, $NaHCO_3$) + $Sr(NO_3)_2$ Experiments. Experiments with H_3NTA involving $NaNO_3$ or $NaHCO_3$ were predicted using the log K values for species involving NTA listed in Table D.8. The experimental properties are listed in Table D.9. Two different sediments were used in the experiments consisting of upper and lower B-tank composites. The experiments were carried out with two different H_3NTA concentrations of 0.015 and 0.0015 M. Experiments with the same H_3NTA concentration gave similar results with the larger H_3NTA concentration giving lower sorbed strontium concentrations, regardless of the electrolyte ($NaNO_3$ or $NaHCO_3$) used. This is caused by the formation of the complex SrNTA. In addition, it was found that the complex CaNTA competes strongly with SrNTA and both complexes are required to obtain the fit shown in the figure. The FLOTRAN simulations were carried out for the two different H_3NTA concentrations using $NaNO_3$ as the background electrolyte. The results of the prediction are shown in Figure D.20. Excellent agreement was obtained for both values of H_3NTA used in the experiments.

Figure D.20. Prediction of Experiments 57869 Involving H_3NTA with a CEC of 50.2 μeq/g

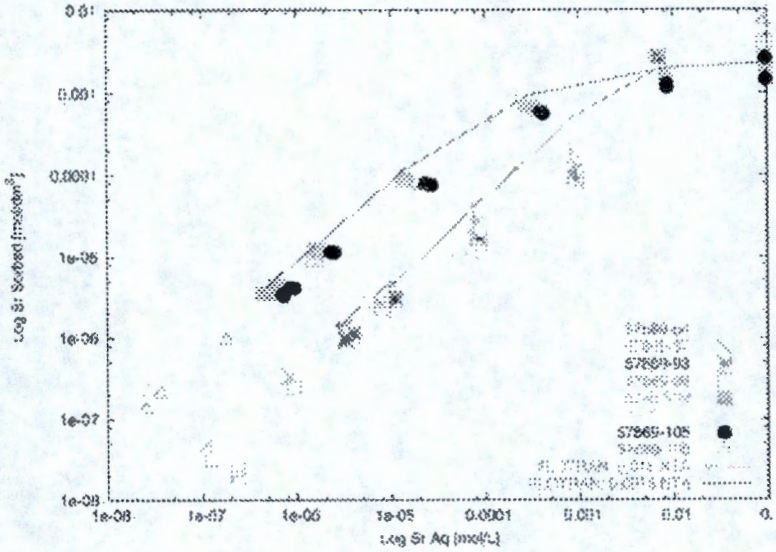

Table D.8. NTA Species Included in the Calculations with Log K Values at 25 °C Species NTA^{3-} is used as Primary Species. No other Species Involving NTA Complexes were Available in the Current Database.

Species	log *K* [25 °C]
$H_3NTA_{(aq)}$	−14.90
H_2NTA^-	−13.30
$HNTA^{2-}$	−10.30
$SrNTA^-$	−6.31
$CaNTA^-$	−7.67

Table D.9. Experimental Parameters for System $NaHCO_3$, $NaNO_3$, H_3NTA + $Sr(NO_3)_2$ using Upper and Lower Composite Sediment

Experiment	m_{NaNO_3} [M]	m_{NaHCO_3} [M]	H_3NTA [M]	r [g/L]	ϕ	Sediment
57869-84	0.015	0	0.015	100	0.9661	upper composite
57869-87	0	0.015	0.015	100	0.9661	upper composite
57869-93	0.015	0	0.015	100	0.9661	lower composite
57869-96	0	0.015	0.015	100	0.9661	lower composite
57869-99	0.015	0	0.0015	100	0.9661	upper composite
57869-102	0	0.015	0.0015	100	0.9661	upper composite
57869-105	0.015	0	0.0015	100	0.9661	lower composite
57869-108	0	0.015	0.0015	100	0.9661	lower composite

D.2.3.4 Discussion

Several points derived from the modeling exercise are noted:

- In several of the experiments with high CO_2 and Sr^{2+} concentrations, strontianite was found to be supersaturated in the model simulations. The experimental data implied the occurrence of precipitation in some cases (Figure D.6). However, precipitation of strontianite was not included in the present simulations.

- The aqueous complex $SrHCO_3^+$ was found to be present in insignificant concentrations for all of the experiments, including those with elevated CO_2 concentrations, indicating that it was not a significant factor in the ion exchange adsorption process.

- Although not allowed to participate in exchange reactions, the species $CaNO_3^+$ was present in sufficiently high concentrations that it could potentially have a significant influence on sorption.

D.2.3.5 Conclusions

A multicomponent ion exchange model involving Sr^{2+}, Ca^{2+}, Mg^{2+}, Na^+, and K^+ was derived from the Type 2 experimental ion exchange data presented in Section D.2.2. The derived multicomponent model was used to predict Sr^{2+} ion exchange adsorption (Type 1 experiments) from different electrolytes on three different Hanford sediments. The following are key results:

1. Strontium adsorption to Hanford sediment can be quantitatively described as a multicomponent ion exchange process.

2. The sorption properties of different Hanford sediments for Sr^{2+} were found to be identical when normalized to sediment CEC.

3. The full suite of exchangeable cations, and their chemical interactions, must be considered to model the adsorption/exchange process. Failure to do so may result in what appear to be excellent fits to the data, but which violate model assumptions such as the approximate constancy of the selectivity coefficients across ionic strength.

4. Ion selectivities for the Hanford exchanger phase follow the selectivity trend $K^{+} >> Sr^{2+} \geq Ca^{2+} > Mg^{2+} > Na^{+}$.

5. The ion exchange process of Sr^{2+} in bicarbonate electrolyte is still not sufficiently well understood to allow prediction in that electrolyte.

6. The developed ion exchange model is general to the Hanford Site and currently allows semi-quantitative prediction of Sr^{2+} adsorption by ion exchange given knowledge of the total, labile concentrations (aqueous plus exchangeable) of Ca^{2+}, Mg^{2+}, Na^{+}, and K^{+}. New experiments underway will allow robust calibration of the model and quantitative predictive capability.

D.2.3.6 References

Appelo, C. A. J., and D. Postma, 1996, *Geochemistry, Groundwater and Pollution*, A. A. Balkema, Rotterdam, pp. 536.

Doherty, J., B. Lindsay, and P. Whyte, 1994, *PEST: Model Independent Parameter Estimation*, Watermark Computing, Brisbane, Australia.

Lichtner, P. C., 2002a, *FLOTRAN User Guide*, LA-UR-01-xxxx, Los Alamos National Laboratory, Los Alamos, New Mexico, (in preparation).

Lichtner, P. C., 2002b, *Simulated B-BX-BY Hanford Tank Farm Supernate Compositions, B-BX-BY FIR*, (in preparation).

Lichtner, P. C., and A. Felmy, 2002, "Estimation of Hanford SX Tank Waste Compositions from Historically Derived Inventories," *Computers & Geosciences*, (in press).

Lichtner, P. C., S. Yabusaki, K. Pruess, and C. I. Steefel, 2002, "Cesium Migration in the SX Tank Farm", 2002, *Field Investigation Report for Waste Management Area S-SX*, RPP-7884, Rev. 0, CH2M HILL Hanford Group, Inc., Richland, Washington.

Lichtner, P. C., 2001, *FLOTRAN User Manual*, LA-UR-01-2349, Los Alamos National Laboratory, Los Alamos, New Mexico.

D.2.4 DESORPTION AND MINERALOGIC RESIDENCE OF STRONTIUM-90 IN B-110 SEDIMENT

John M. Zachara[1], James P. McKinley[1], Chongxuan Liu[1], and Steven C. Smith[1]

[1]Pacific Northwest National Laboratory, Richland, Washington 99352

D.2.4.1 Introduction

The future mobility of strontium-90 in the B-110 vadose zone plume will be determined by the amount and ion composition of infiltrating waters and the desorbability of the sediment-bound strontium pool. Desorption is the reverse of the sorption process. Desorption may involve the release of an ion localized at the mineral surface in the form of an exchange or surface coordination complex, or the dissolution of a solid phase. If a sorbed ion is desorbable by, or exchangeable with, other ions in the aqueous phase, it may be remobilized and migrate in the future. Alternatively, if an ion is not desorbable, it will not migrate further even if the geochemical conditions promote mobility. Desorption may be caused by a concentration shift in the aqueous concentrations of competing ions (e.g., magnesium, calcium, or sodium), or a change in the solid-liquid distribution of the stable strontium isotope pool. These effects are often interrelated. A lack of desorption may result from the formation of a kinetically inert surface complex, diffusion into particle interiors, or incorporation into a solid phase with sparing solubility.

Sorbed strontium-90 has generally been found to be desorbable, to large degree, even after long in-ground contact times. Serne and LeGore (1996) found that strontium-90 that was bound to Hanford aquifer sediments beneath the N-trench for over 27 y was desorbable in dilute groundwater, and concluded that its adsorption/desorption behavior conformed to an equilibrium distribution model. Jackson and Inch (1983) investigated strontium-90 partitioning in a contaminated aquifer in Ontario, finding that approximately 80% of the adsorbed strontium-90 was exchangeable. Characterized strontium-90 adsorption-desorption behavior in contaminated stream sediments, observing that 80 to 90% of the sorbed pool was exchangeable. Only in the case of Sr precipitation, which mainly occurs as a carbonate phase (e.g., $SrCO_3$, $Ca_{1-x}Sr_xCO_3$) in calcareous sediment (e.g., Lefevre et al. 1993), does desorption appear to be appreciably limited.

Here, the desorption behavior and mineralogic residence of strontium-90 in sample 26 A from the B-110 borehole (299-E33-46) was investigated. This sample contained the highest sorbed concentration of strontium-90 and was located at the center of mass of the strontium-90 plume (Figure D.1). Additional studies are planned in late fiscal year 2002 using other high strontium-90 samples from different locations in the B-110 strontium-90 plume to confirm the generality of the results noted in the results that follow. Only preliminary results will be presented on the mineralogic residence of strontium-90 because time and funding constraints prevented significant progress on this task.

D.2.4.2 Experimental Methods

D.2.4.2.1 Strontium-90 Desorption. Approximately 2.0 g of air-dry sediment from the B-110 borehole 299-E33-46 (sample 26A) were weighed into polycarbonate centrifuge tubes and 4.0 mL of solution were added to each tube. Seven desorption electrolytes were used: deionized

water, 0.01 mol/L $NaNO_3$, 0.05 mol/L $Ca(NO_3)_2$, 1 mol/L $NaNO_3$, 1 mol/L Na acetate at pH 5.0, 5.0 mol/L $NaNO_3$, and 0.5 mol/L HCl. Some of these electrolytes were the same as those used in the ion exchange isotherm studies (Section D.2.2). The tubes were placed in a horizontal position in an incubator shaker set at 60 rpm and 25 °C for continuous mixing through 7 days. After seven days, the suspensions were mixed by hand daily. Single tubes of each solution were sampled at 30 min, 2 hours, 4 hours, 8 hours, 24 hours, 2 days, 4 days, 7 days, 14 days, 21 days, and 28 days. The solution sample was obtained by centrifuging the tubes for 15 min and 5000 rcf (relative centrifugal force). One mL of the clear supernatant was transferred to a polycarbonate tube containing 9 mL deionized water. The diluted sample was filtered using a 10 mL plastic syringe fitted with a 0.2 µm filter. The first 1 mL of filtrate was discarded and the remaining collected in a polystyrene tube. At every other sampling event (i.e., 0.5 hours, 4 hours, 24 hours, 4 days, 14 days, and 28 days) a portion of the filtrate was collected in a 4-mL glass, septum-capped vial for determination of dissolved inorganic carbon and a separate portion was analyzed by inductively coupled plasma – optical emission spectroscopy (ICP-OES) for barium, calcium, chromium, potassium, magnesium, strontium, and sodium. Additionally, at every other sampling event, the suspension pH was determined using a Microelectrodes® combination pH electrode calibrated with an Orion® pH meter.

At each sampling event, the strontium-90/yttrium-90 activity in the solution phase was determined using liquid scintillation counting and a count window of 0 to 2000 keV. Since these two isotopes co-exist in equilibrium after 28 days due to the relatively short half-life of yttrium-90, the strontium-90/yttrium-90 activity was counted 28 days after sampling. The strontium-90/yttrium-90 activity was converted to disintegrations per minute (dpm) by use of a quench curve and divided by 2 to yield the true strontium-90 activity.

D.2.4.2.2 Phosphor Imaging and Scanning Electron Microscopy Analyses. A combination of digital autoradiography and scanning electron microscopy (SEM) was used to identify and examine sediment particles containing radioactive strontium-90. The autoradiography system was a Molecular Dynamics Storm laser scanning device with an optical resolution of 50 µm, and a detection limit of approximately 0.05 Bq, as tested against low level gamma counting for cesium-137 contaminated micas (McKinley et al. 2001). Sediment particles identified as radioactive using digital autoradiography were examined using a JEOL 6340 field emission scanning electron microscope.

Sediments were prepared in two ways for autoradiographical examination. Dry sediments were dispersed onto glass slides and fixed using collodion. The slides were exposed to the autoradiography plate for approximately 48 hours, and the resultant radioactivity image was used to map and identify radioactive particles on the slides. Approximately twenty radioactive (positive) and twenty non-radioactive (negative) particles were removed from each slide and segregated onto a new glass slide, and re-analyzed. The new slides, on which positive and negative particles were known, were used to determine the mineralogic identity of the strontium-90-bearing particles. In addition, sediments were imbedded in epoxy, and the epoxy mounts were wafered and polished on glass slides. The thin sections were then exposed to the autoradiography plate, and images of the distribution of radioactivity were used to identify strontium-90-bearing particles for examination via SEM.

D.2.4.3 Results and Discussion

D.2.4.3.1 Field Context. Sample 26A was obtained from the center of mass of the strontium-90 plume from a region that was high Na-HCO_3 (Figure D.2, Section D.2.1). All of the core materials obtained from the B-110 borehole were remarkably similar in their acid-extractable concentrations of calcium and strontium with depth (Figure D.21; data from Serne et al. 2002). Generally, acid-extractable calcium exceeded that of strontium by 2.25 orders of magnitude. Water-extractable calcium and strontium were close to 2.25 orders of magnitude lower than the acid extractable concentrations. The lowered concentrations of water extractable calcium and strontium in the plume region (e.g., 15 to 40 m) were suggestive of carbonate precipitation induced by sodium-HCO_3 intrusion (e.g., Na^+ induced displacement of Ca^{2+}, Mg^{2+}, and Sr^{2+} from the exchange complex and precipitation of waste-derived HCO_3/CO_3). Unfortunately, sufficiently accurate pH measurements could not be obtained on these sediments because of their low water content to assess whether the porewater was or was not saturated with $CaCO_3$ or $SrCO_3$ by solubility calculation. The indigenous pool of stable isotopic strontium (e.g., acid extractable) exceeded the total concentration of strontium-90 by close to 6 orders of magnitude, indicating that isotopic exchange was a plausible sorption mechanism.

Figure D.21. Concentrations of Water and Acid Extractable Strontium, Calcium, and Strontium-90 in the B-110 Borehole

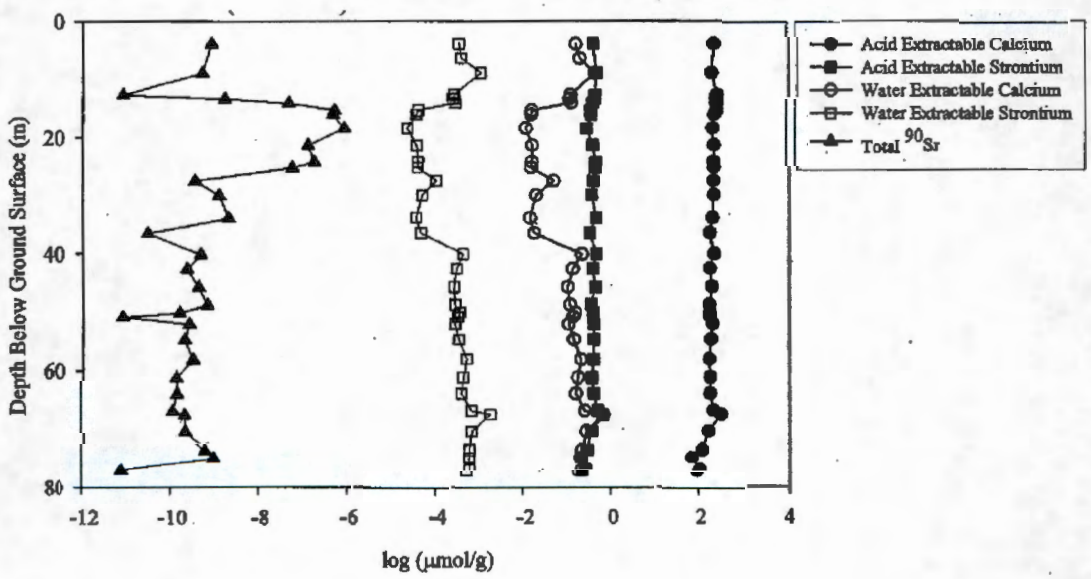

D.2.4.3.2 Desorption Behavior. The extent of strontium-90 desorption was strongly dependent on the nature of the contacting electrolyte solution (Figure D.22). Consistent with the water extraction data of Serne et al. (2002), virtually no strontium-90 was released into deionized H_2O or 0.01 mol/L $NaNO_3$. Approximately 50% was released in 1 mol/L $NaNO_3$ and 0.05 mol/L $Ca(NO_3)_2$, and 75% was released in 5 mol/L $NaNO_3$. All of the strontium-90 was released in 0.5 mol/L HCl and 1 mol/L NaOAc at pH 5. The desorption of strontium-90 showed some kinetic behavior, but was relatively rapid. A majority of the strontium-90 release occurred within 7 days or less.

Figure D.22. Time-Dependent Desorption of Strontium-90 from B-110 Sediment (26A) in Various Electrolytes (*model prediction from Section D.2.4.3.3)

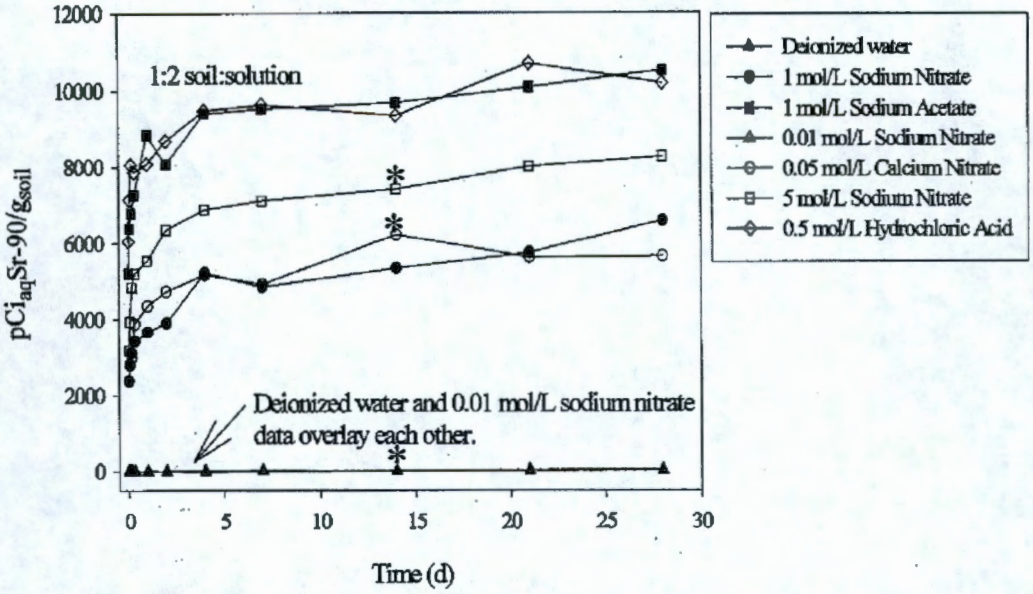

The results were consistent with the residence of strontium-90 in an ion exchangeable and carbonate-precipitated pool. The strontium-90 isotherm measurements in 0.01 and 1 mol/L $NaNO_3$ on pristine sediment (Section D.2.2) yielded K_ds of 112 and 0.25 ml/g, respectively, at strontium concentrations well below surface saturation (Figure D.3 and Table D.10). Strontium adsorption (e.g., ion exchange) was below detection in comparable experiments in 5 mol/L $NaNO_3$ (e.g., $K_d = 0$ Table D.10; isotherm data not shown) because of electrolyte competitive mass action. The 5 mol/L $NaNO_3$ was therefore used as a desorption electrolyte that would fully displace adsorbed ions on the exchange complex. The measured K_d at the end of the 5 mol/L $NaNO_3$ experiment was 0.88 ml/g, a higher value than could be justified by ion exchange. Indeed, the measured K_ds for the $NaNO_3$ and $Ca(NO_3)_2$ desorption experiments after 14 days were also higher than measured in the isotherm experiments (Table D.10). It was surmised that the residual sorbed strontium-90 after 14 days equilibration in 5 mol/L $NaNO_3$ (3279 pCi/g) existed in precipitated state, and recalculated the desorption K_d ($K_{d\text{-recalc}}$) after removal of the hypothesized precipitated mass. The recalculated desorption K_d values were quite similar to those measured on pristine sediment in these same electrolytes (with the exception of 0.01 $NaNO_3$) affirming the likely presence of precipitated strontium-90. The desorption K_d values measured in 0.01 $NaNO_3$ had a high degree of uncertainty because of the small amount of strontium-90 released to the fluid phase (<20 pCi/g).

Table D.10. K_d – Strontium-90 Values Suggest the Presence of a Residual Solid Phase with Strontium-90

0.01 mol/L $NaNO_3$			0.05 mol/L $CaCO_3$			1 mol/L $NaNO_3$			5 mol/L $NaNO_3$		
14d	14d-adj K_d-(ml/g)	ISO[a]	14d	14d-adj K_d-(ml/g)	ISO[1]	14d	14d-adj K_d-(ml/g)	ISO	14d	14d-adj K_d-(ml/g)	ISO[a]
509	370	112	1.81	0.63	0.71	2.00	0.67	0.25	0.88	0.67	0.0

[a]K_d values measured from isotherms in Section D.2.2.

The presence of precipitated strontium-90 was also implied by the high fractional desorption (almost 100%) measured in both acidified ammonium acetate and 0.5 mol/L HCl. The ammonium acetate reagent is typically used to dissolve carbonates from soils (Kunze and Dixon 1986). Dilute HCl will dissolve carbonates and phosphates, poorly crystalline Al and Fe oxides, and other phases as well. Both of the reagents displace the exchangeable ion pool through the mass action effects of H^+ and Na^+, and the release of Ca^{2+}, Mg^{2+}, and other cations, from solid-phase dissolution. The comparable effects of both these reagents on strontium-90 desorption (Figure D.22) strongly implied that the residual strontium-90 after 5 mol/L $NaNO_3$ extraction was associated with a carbonate precipitate.

Table D.11. Base Saturation of the Exchange Complex in Sediment Sample 26 Determined from the Desorption Data and Direct Extraction

	Extractant		
	1 mol/L $NaNO_3$ and 0.05 mol/L $Ca(NO_3)_2$[a]	5 mol/L $NaNO_3$ and 0.05 mol/L $Ca(NO_3)_2$[a]	1 mol/L NH_4Cl[b]
Total μeq/g[c]	22.5	27.5	52.8
E(Na)	0.472	0.386	0.343
E(K)	0.228	0.337	0.088
E(Ca)	0.248	0.237	0.569
E(Mg)	0.051	0.039	ND
E(Sr)	0.0013	0.0015	0.00084

[a] 14 day extraction
[b] 2 h extraction with water followed by 2 h extraction with NH_4Cl
[c] Sum of extractable Na, K, Ca, Mg, and Sr minus water soluble

The cold ion fluxes measured in the different desorption electrolytes (Figure D.23 to Figure D.27) lended further support to the concept of ion-exchangeable and precipitated strontium-90 pools. The ion displacement trends in both sodium and calcium electrolyte collectively indicated that the exchange complex was dominated by Na^+, Ca^{2+}, and K^+ (Table D.11). The base saturation of the exchange complex on 26A was further evaluated by repeated 1 mol/L NH_4Cl extraction, which yielded comparable, albeit slightly different values (Table D.11). Calcium, magnesium, and strontium increased by factors of 71, 44, and 10, respectively, in the sodium-acetate and HCl extractions over the 5 mol/L $NaNO_3$ extract, implying dissolution of a strontium-substituted, high magnesium (8.9%) calcite. The extraction values indicated that the calcite was present in the contaminated sediment at relatively low concentration, 170.6 μmol/g, or 1.71 mass percent. Potassium does not easily substitute within the calcite lattice, and the relatively constant concentration of K^+ that was displaced in 1.0 and 5.0 mole/L $NaNO_3$, and in 5.0 mol/L HCl and pH 4.5 NaOAc (Figure D.22) indicated that all four of these electrolytes were equally effective in displacing ions from the exchange complex.

The desorption/dissolution kinetics of the strontium-90 and the stable strontium isotopes were generally similar, and tracked one another in each of the different electrolytes (Figure D.23). This observation confirmed the co-association of strontium-90 with the stable isotopes, as anticipated for an isotopic exchange attenuation mechanism. However, the concentration ratio of strontium-90 to the stable strontium isotopes (strontium-90/strontium) was much higher on the exchange complex (≈ 0.330 - 0.38 Ci/mol) than it was within the hypothetical magnesium-calcite (0.066 – 0.068 Ci/mol) (Table D.12), indicating that the two sorbed strontium pools were not at global isotopic equilibrium. Isotopic fractionation of strontium is not expected in the abiotic precipitation of calcite, and does not occur during ion exchange. Implied, possibly, was the presence of two calcite pools, one that was detrital with low strontium-90, and another resulting from waste-sediment reaction with strontium-90/strontium values comparable to the exchange complex. Alternatively, detrital calcite may have functioned as a precipitation template for a second stage of carbonate precipitation resulting from waste-sediment reaction. Further studies are seeking to resolve the reasons for this apparent lack of isotopic equilibrium between the exchanger phase and the precipitated strontium-90.

Table D.12. Isotopic Distribution of Strontium Released into the Different Desorption Electrolytes

Extractant	$^{90}Sr/Sr_{Total}$ (Ci/mol)
Deionized water	0.008
0.01 mol/L $NaNO_3$	0.025
0.5 mol/L HCl	0.066
1 mol/L Sodium acetate; pH 5.0	0.068
1 mol/L $NaNO_3$	0.330
5 mol/L $NaNO_3$	0.336
0.05 mol/L $Ca(NO_3)_2$	0.378

$Sr_{Total} = \Sigma[^{90}Sr] + [^{84}Sr] + [^{86}Sr] + [^{87}Sr] + [^{88}Sr]$

Figure D.23. Concentrations of Strontium-90 and Stable Strontium Isotopes Desorbed from 26A

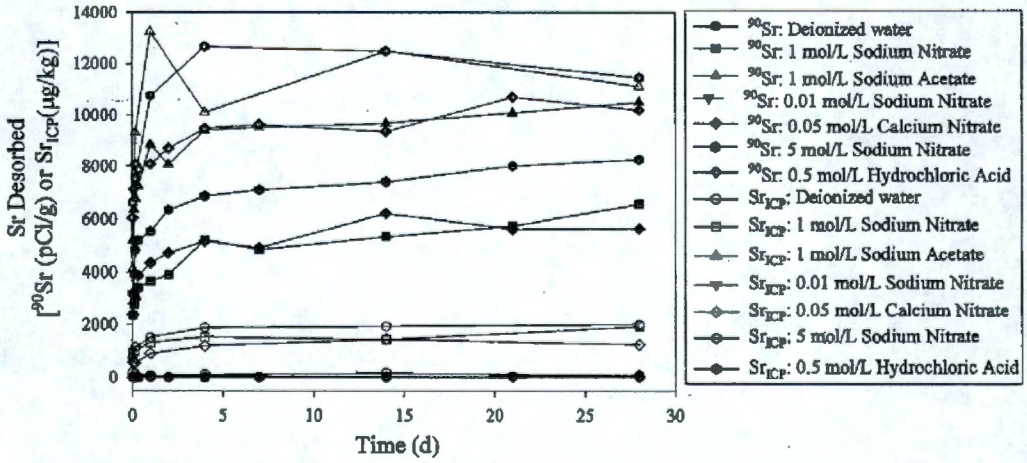

Figure D.24. Desorbed/Dissolved Concentrations of Calcium (Ca^{2+}) from 26A in Different Electrolytes

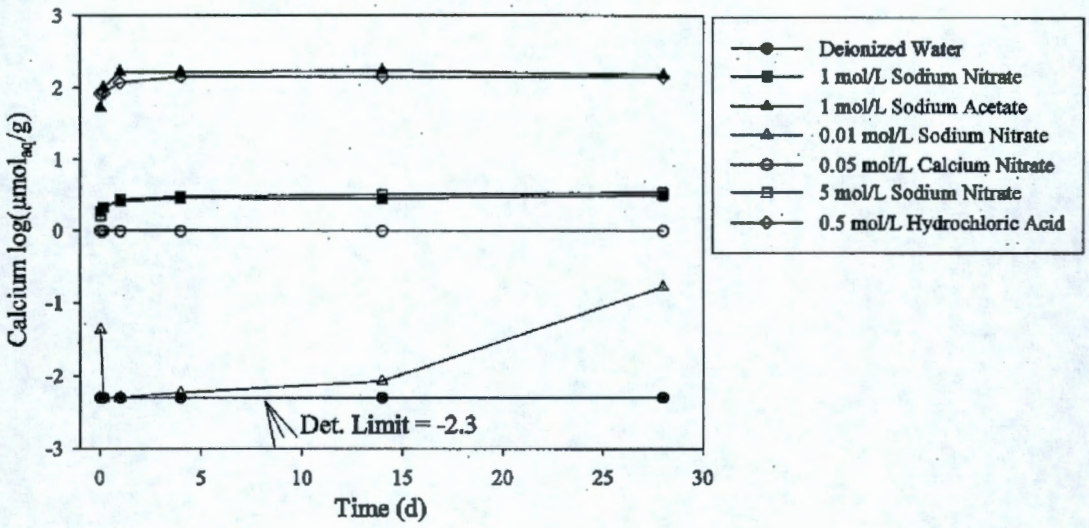

Figure D.25. Desorbed/Dissolved Concentrations of Magnesium (Mg^{2+}) from 26A in Different Electrolytes

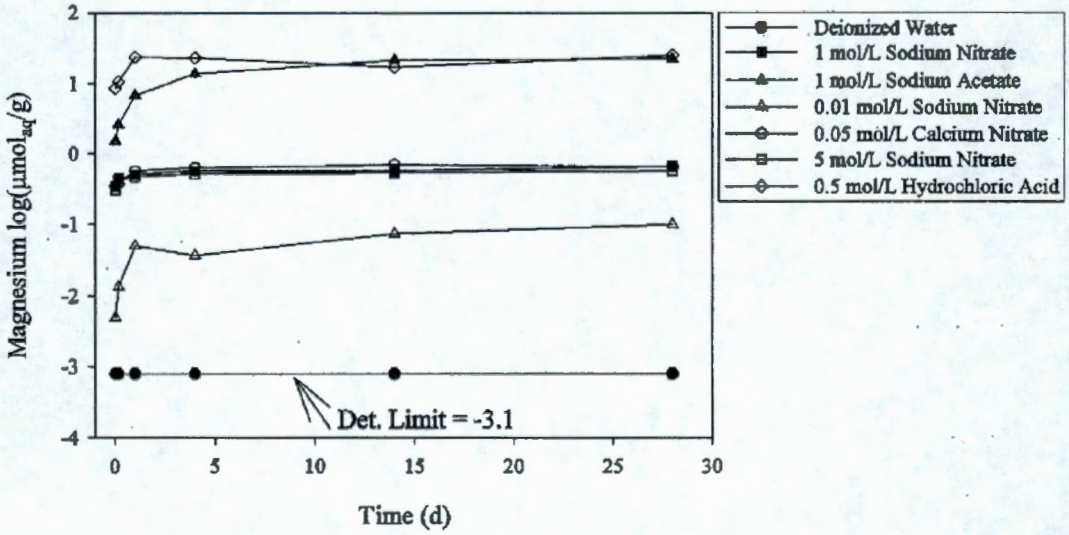

Figure D.26. Desorbed/Dissolved Concentrations of Strontium (Sr^{2+}) from 26A in Different Electrolytes

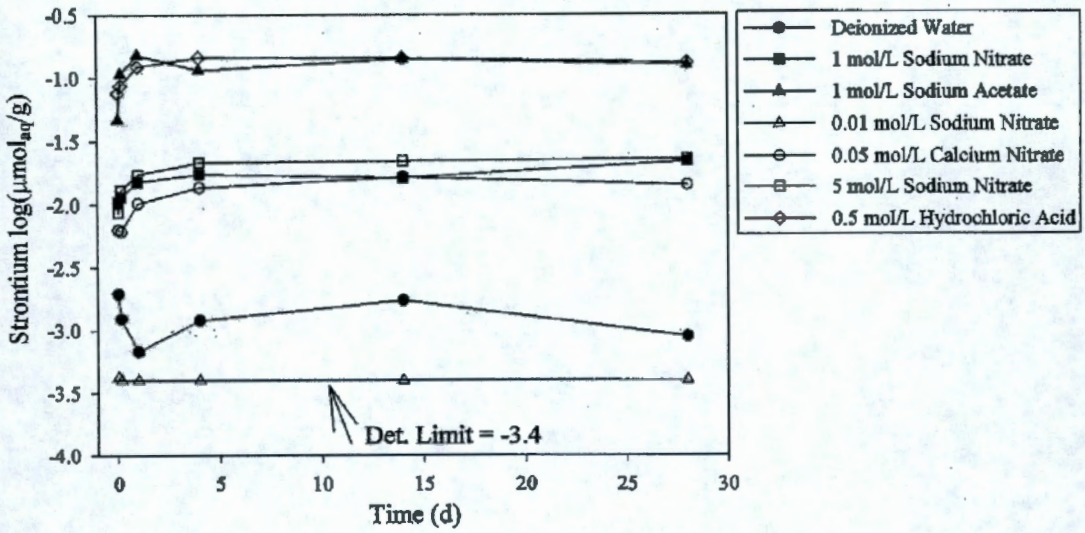

Figure D.27. Desorbed/Dissolved Concentrations of Potassium (K^{2+}) from 26A in Different Electrolytes

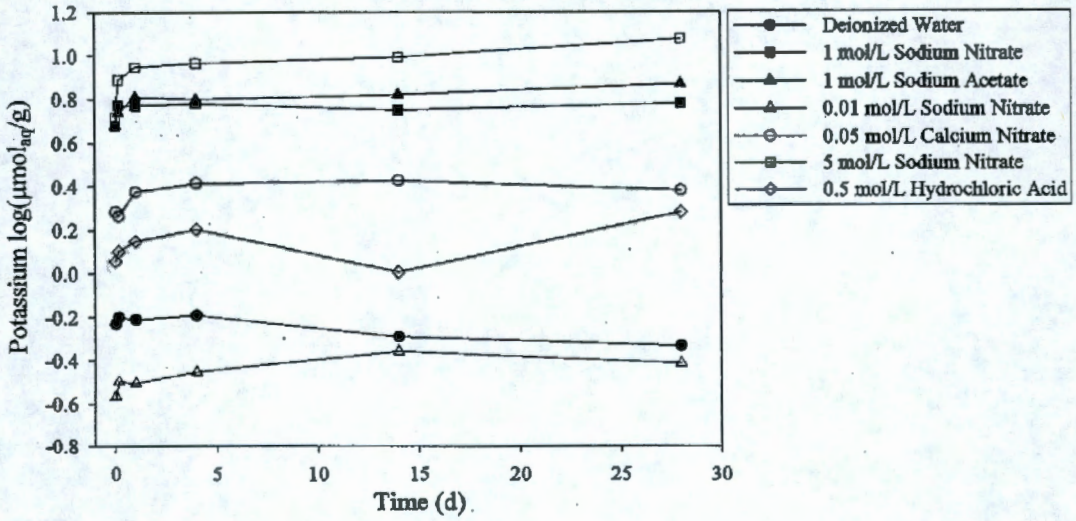

D.2.4.3.3 Modeling Desorption Extent. Predicting the future migration of the strontium-90 plume near B-110 (e.g., Figure D.1) requires a model that includes the primary geochemical reactions that control the solid liquid-distribution of strontium-90 as function of pertinent mineralogic and aqueous chemical variables. The desorption of approximately 70 percent of the sorbed strontium-90 from sediment 26A in 0.01, 1.0, and 5.0 mol/L $NaNO_3$ and 0.05 mol/L $Ca(NO_3)_2$ (e.g., Figure D.22) appeared to be controlled by ion exchange. Here, we apply the ion exchange model developed for Sr^{2+}, Ca^{2+}, Mg^{2+}, and Na^+ in Sections D2.2 and D2.3 to predict the equilibrium desorption of Sr^{2+}, Ca^{2+}, and Mg^{2+} from the B-110 sediments controlled by mass action displacement of the exchange complex with the added electrolyte cations.

The model calculations were driven by the total concentrations of cations, hydrogen ion (pH), and carbon dioxide/bicarbonate (TCO2) in the 26A sample (Table D.13). The sorbed cation concentrations on the 26A sediment were obtained by ammonium chloride extraction [water soluble cation concentrations (described below) were subtracted from these to give the true cation concentrations displaced by ammonium chloride]; the sum of these cation concentrations (in equivalents per gram) defined the sediment exchange capacity (CEC). Similarly, water-soluble components (e.g., solutes present in concentrations above those needed for surface charge compensation) were determined by deionized water extraction of the sediments. The critical water-soluble components were Na^+ and HCO_3^-. The total concentrations recorded for the desorption experiments in Table D.13 representated materials added in the electrolyte solution. It was assumed that the measured sorbed and water soluble ions existed in each sample at the time of electrolyte addition. The pH and TCO_2 for the desorption electrolytes were steady state values measured after 14 days of desorption. Hydrogen ion activity (pH) and total inorganic carbon were measured in the desorption experiments at the same frequency as were the cations (Figure D.23 through Figure D.27). The noted decrease in the equilibrium pH and TCO_2 with increasing electrolyte normality (Table D.13) was consistent with the precipitation of calcium carbonate in the desorption experiments:

$$CaX_{2(s)} + Na^+ = 2NaX_{(s)} + Ca^{2+} \quad (1)$$

$$Ca^{2+} + HCO_3^- = CaCO_{3(s)} + H^+ \quad (2)$$

The precipitation of $CaCO_3$ occurred as sorbed Ca^{2+} was displaced from the exchange complex ($CaX_{2(s)}$) in the desorption experiment and reacted with residual HCO_3 from the waste solution. Also, calcite precipitation occurred in the 0.05 mol/L $CaNO_3$ electrolyte as electrolyte Ca^{2+} reacted with residual bicarbonate in the sediment.

The geochemical modeling included four ion exchange reactions, calcite precipitation, and a number of aqueous species (Table D.14). The Davies convention was used for activity coefficients. The Davies equation is not valid for the 5 mol/L ionic strength and the calculations reported for this electrolyte need be viewed with caution. The Pitzer model, which is valid to high ionic strength (above 5 mol/L) when appropriately parameterized, has been applied to this same experiment with comparable results to those summarized here. Pitzer model results will be described in a later journal publication on this experiment. The equilibrium pH was fixed for the calculation at the measured 14-day value (Table D.13), and equilibrium constants for the exchange reactions were taken from Section D.2.3. The modeling represented a prediction of the data as no parameters were adjusted to maximize fit to the data. The calculation was an equilibrium one and no attempt was made to describe the kinetic phase of desorption that occurred between 0 to 5 days. The modeling was an attempt to simulate the steady-state or equilibrium concentrations that were achieved after 7 days of desorption (Figure D.23 through Figure D.27).

The geochemical modeling semi-quantitatively matched the measured TCO_2 concentrations through the precipitation of calcite (e.g., ≈ 4 mmol/L; Table D.15). The desorbed concentrations of both Mg^{2+} and Sr^{2+} were also well described (Figure D.28b, c). For Sr^{2+}, the total desorbed concentration in 1 and 5 mol/L (0.02 mmol/kg) was identical to sorbed concentration estimated by ammonium chloride extraction (Table D.13). This same value was well predicted by the

quaternary exchange model (Figure D.28b). The Mg^{2+} concentrations where slightly overpredicted by the model. The model predicted that over 95% of the sorbed Mg^{2+} (e.g., ≈ 0.8 mmol/kg) would be displaced in 1 to 5 mol/L $NaNO_3$. The lower observed experimental values (e.g., 0.55 to 0.70 mmol/kg; Figure D.28) may result from Mg^{2+} coprecipitation within calcite (a well known phenomenon). Calcites from the Hanford vadose zone are invariably Mg-substituted. The greatest discrepancy between model and data was in the Ca^{2+} concentrations (Figure D.28a). The modeled results for Ca^{2+} are far more sensitive to the experimental input data (e.g., pH, TCO_2, sorbed concentration) and the thermodynamic model (activity coefficient or ion association model) than those for the other ions because of the calcite precipitation reaction. Ongoing research will refine and improve upon these parameters. The model correctly predicted that the total desorbed Ca^{2+} concentration would be similar in both 1 and 5 mol/L $NaNO_3$, and that its value, unlike that for Mg^{2+} and Sr^{2+}, would be significantly less than its initial adsorbed concentration (e.g., 15.05 mmol/kg; Table D.13). The lower concentration results from the precipitation of desorbed Ca^{2+} as calcite and its continued association with the solid phase in the form of this precipitate.

The experimental data in Figure D.22 and Figure D.23 showed that the isotopic ratio of $^{90}Sr/Sr_{Total}$ ranged between 0.33 to 0.38 Ci/mol for ion exchangeable Sr (Table D.12). Applying this ratio to the model calculations in Figure D.28b allowed us to predict the desorbable concentration of ^{90}Sr from the exchange complex in sediment 26A. These predicted concentrations (marked with ⊗ in Figure D.22) were remarkably close to the observed values. The accurary of this prediction reinforces the generality of the cation exchange model that was developed in Section D.2.3, and parameterized on a different Hanford sediment (the Hanford fine sand composite). Embodied in this prediction is the assumption that 29% of the sorbed ^{90}Sr was existed in precipitated state, possibly in association with calcium carbonate.

Table D.13. Total Concentration of Sorbed, Soluble, and Electrolyte Ions Used to Initialize the Desorption Model Calculations

	Na	Ca	K	Mg	Sr	pH	T_{CO2}
Sorbed on Soil (mmol/kg)	18.13	15.05	4.62	0.88	0.022		
Water-Soluble (mmol/kg)	8.13	0.28	0.00	0.00	0.000		8.70
M $NaNO_3$ (mmol/L)	10.00	0.00	0.00	0.00	0.000	9.39	2.69
0.05 M $CaNO_3$ (mmol/L)	0.00	50.00	0.00	0.00	0.000	7.67	0.19
1 M $NaNO_3$ (mmol/L)	1000.00	0.00	0.30	0.00	0.000	8.42	0.87
5 M $NaNO_3$ (mmol/L)	5000.00	0.00	1.50	0.00	0.000	8.04	1.15

Figure D.28. Model Predictions for Calcium, Strontium, and Magnesium from the Desorption Experiments

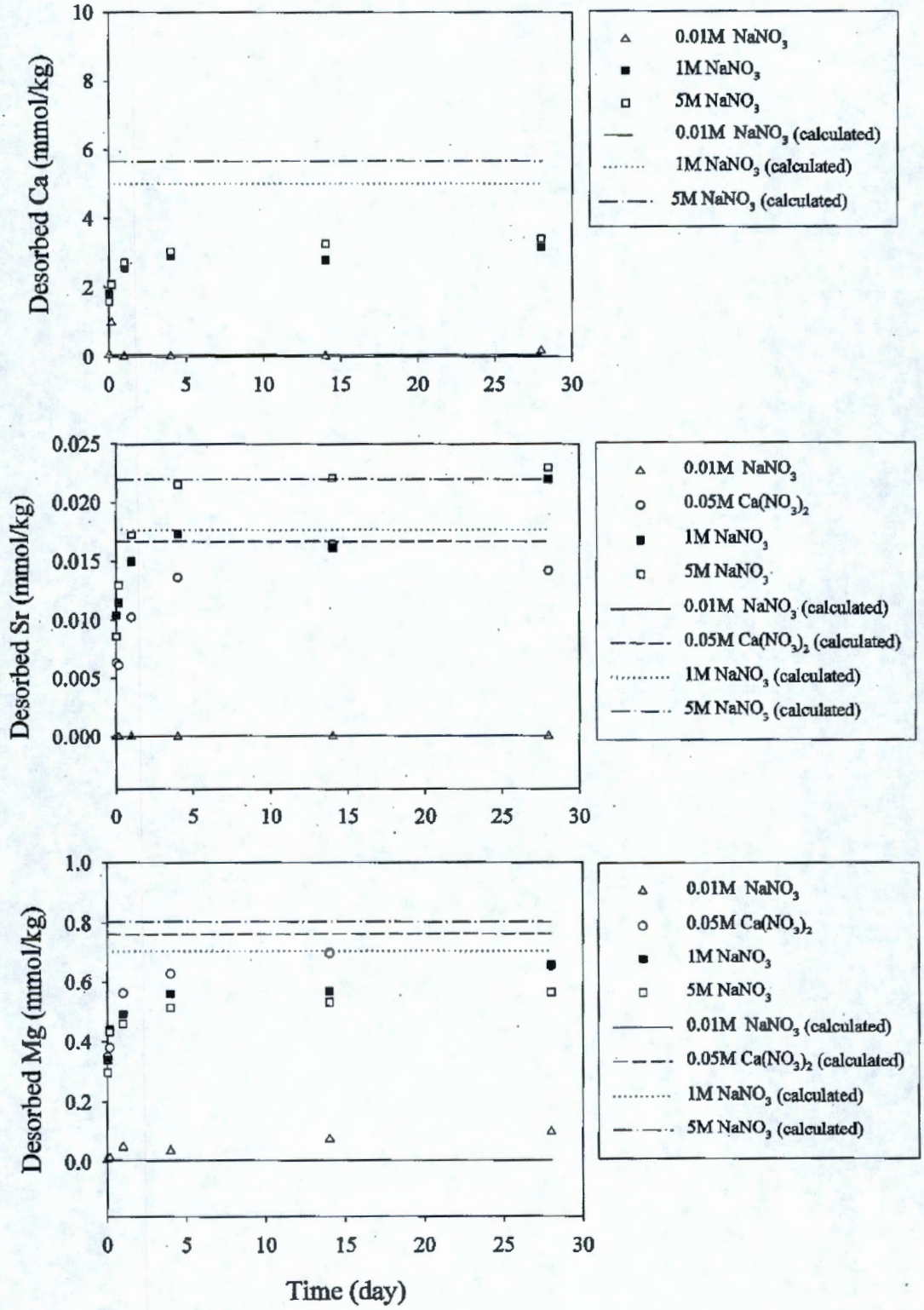

Table D.14. Reactions, Equations, and Thermodynamic Data Used in Desorption Modeling

Binary exchange constants for Minteqa2:

$$uBX_v + vA^{u+} = vAX_u + uB^{v+}$$

$$K_g = \frac{\{B^{v+}\}^u}{\{A^{u+}\}^v}\frac{[AX_u]^v}{[BX_v]^u} = \frac{\{B^{v+}\}^u}{\{A^{u+}\}^v}\frac{[un_{AX_u}]^v}{[vn_{BX_v}]^u}[r_s CEC]^{u-v}$$

$$= K_r\left(\frac{u^v}{v^u}[r_s CEC]^{u-v}\right)$$

where r_s is the ratio of solid to liquid (kg/L); n_i (mol/L) is the solid phase concentration of cation i in the solution. For r_s = 0.5 kg/L, CEC = 54.7 meq/kg, the K_r could be calculated from K_g as follows:

	K_g	log K_r
$2NaX + Sr^{2+} = SrX_2 + 2Na^+$	90.402	3.218
$2NaX + Ca^{2+} = CaX_2 + 2Na^+$	76.720	3.147
$2NaX + Mg^{2+} = MgX_2 + 2Na^+$	36.869	2.829
$NaX + K^+ = KX + Na^+$	21.010	1.322

Species considered in the model and their stability constants:

Species	Reaction	log K	Source
$SrOH^+$	$Sr^{2+} + H_2O - H^+ = SrOH^+$	-13.177	NIST
$SrCO_3(aq)$	$Sr^{2+} + CO_3^{2-} = SrCO_3(aq)$	2.81	NIST
$SrHCO_3^+$	$Sr^{2+} + CO_3^{2-} + H^+ = SrHCO_3^+$	11.539	NIST
$SrNO_3^+$	$Sr^{2+} + NO_3^+ = SrNO_3^+$	0.6	NIST
$NaNO_3$	$Na^+ + NO_3^- = NaNO_3$	-1.044	GMIN
$NaCO_3^-$	$Na^+ + CO_3^{2-} = NaCO_3^-$	1.27	NIST
$NaHCO_3$	$Na^+ + CO_3^{2-} + H^+ = NaHCO_3(aq)$	10.079	NIST
$CaOH^+$	$Ca^{2+} + H_2O - H^+ = CaOH^+$	-12.697	NIST
$CaCO_3(aq)$	$Ca^{2+} + CO_3^{2-} = CaCO_3(aq)$	3.20	NIST
$CaHCO_3^+$	$Ca^{2+} + CO_3^{2-} + H^+ = CaHCO_3^+$	11.599	NIST
$MgOH^+$	$Mg^{2+} + H_2O - H^+ = MgOH^+$	-11.397	NIST
$MgCO_3(aq)$	$Mg^{2+} + CO_3^{2-} = MgCO_3(aq)$	2.92	NIST
$MgHCO_3^+$	$Mg^{2+} + CO_3^{2-} + H^+ = MgHCO_3^+$	11.339	NIST
Calcite	$Ca^{2+} + CO_3^{2-} = CaCO_3$	8.48	NIST

Table D.15. Calculated Equilibrium Cation Desorption (Minteqa2) and Final Carbonate Concentration (All values in mmol/L)

	Na	Ca	K	Mg	Sr	T_{CO2}	T_{CaCO3}
0.01M $NaNO_3$	1.272×10^{1}	2.168×10^{-2}	1.561×10^{-1}	2.433×10^{-3}	2.485×10^{-5}	4.29	0.056
0.05M $CaNO_3$	1.286×10^{1}	4.036×10^{1}	1.625×10^{0}	3.819×10^{-1}	8.344×10^{-3}	0.18	4.166
1M $NaNO_3$	9.885×10^{2}	2.509×10^{0}	1.661×10^{0}	3.511×10^{-1}	8.845×10^{-3}	0.54	3.812
5M $NaNO_3$	4.986×10^{3}	2.837×10^{0}	3.320×10^{0}	4.018×10^{-2}	1.098×10^{-2}	0.08	4.270

D.2.4.3.4 Autoradiography. Beta-emitting, strontium-90-containing particles were readily isolated from the 26A sediment by autoradiography and particle manipulation (Figure D.29). The negative (non-radioactive) particles were generally monomineralic silicate minerals including quartz and feldspar. The positive (radioactive) particles were lithic fragments.

Figure D.29. Photograph of Segregated Positive and Negative Particles

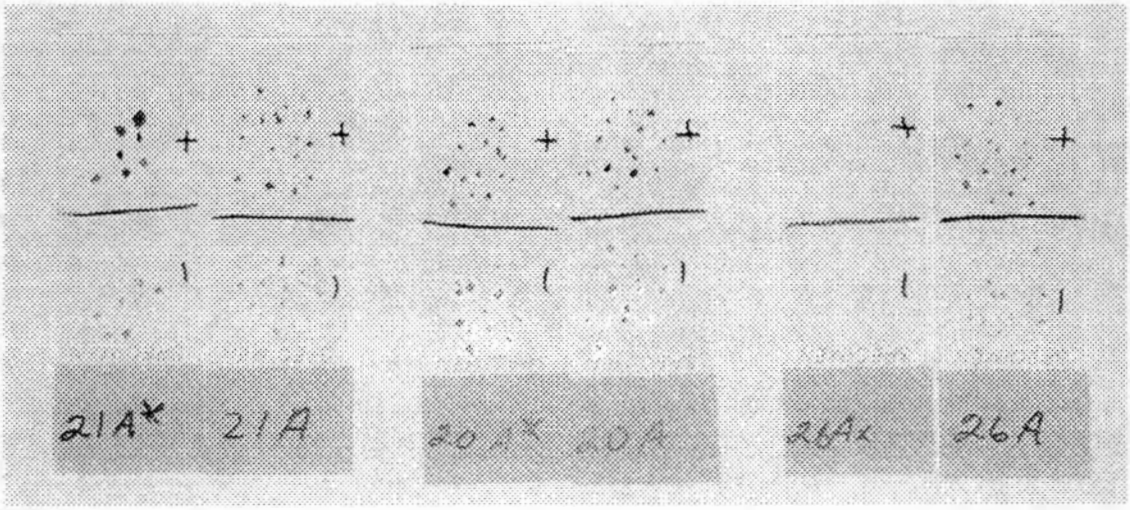

The autoradiography results for the thin sections (Figure D.30) showed that ^{90}Sr was highly enriched in selected particles. When the autoradiography results were superimposed upon backscattered electron (bse) images collected by scanning electron microscopy (SEM), radioactive grains were observed to be basaltic lithic fragments. The bse image, which records the average atomic number, or density, of the sample, was inverted to show high-atomic-number (high-z) phases as darker shades of gray (Figure D.30, top). A similarly inverted, partially transparent, autoradiography plot was superimposed on the bse image (Figure D.30, center). Comparison of the bse and autoradiography images facilitated the identification of lithic fragments containing sorbed strontium-90. The four radioactive particles labeled in the upper Figure D.30 were basaltic. The Hanford formation, underlying much of the Hanford site, was deposited by catastrophic flooding during the Pleistocene, which traversed and scoured the regional Columbia River Flood basalts. Basaltic lithic fragments from these rocks thus comprise a significant petrographic fraction of the Hanford formation (Bjornstad 1990). Not all basaltic lithic fragments were radioactive; the large, dark speckled lithic fragment below and slightly left of Fragment 1 (Fragment 5, Figure D.30) was basaltic but non-radioactive. Lithic fragments and

mineral clasts can be observed in overall dimensions in the bottom panel of Figure D.30, an optical photomicrograph of the petrographic section of 26A. Monomineralic silicates are colorless or clear, and lithic fragments are mottled, brown if basaltic.

The Columbia River Basalts are composed of primary phases that would not be expected to significantly adsorb Sr^{2+}, and have textures that include little void space within which Sr-bearing solids could precipitate. Mineralogically, the basalts consist of varying proportions of augite, plagioclase, titanomagnetite, and glass (Allen and Strope 1985; Long and Wood 1986). Olivine also occurs in basalts. The petrographic textures vary according to cooling history. Collonade basalts (massive columnar outcrops) include compositionally homogeneous glass; entablature basalts (massive non-columnar outcrops) include glass that separated into immiscible phases prior to solidifying. Petrographically intact lithic fragments would therefore not be expected to provide an environment favorable to strontium-90 sorption (adsorption or precipitation). Detailed inspection of basalt Fragments 1 to 4 in Figure D.30 by scanning electron microscopy (Figure D.31 through Figure D.34), however, suggest that weathering reactions may have induced the formation of phyllosilicate clay (e.g., smectite) within these particles. Phyllosilicate regions were definitively identified as a weathering product of glass by: 1) their morphology including dessication cracks, 2) compositional zonation, and 3) texture. Smectites exhibit isomorphic structural cation substitution that leads to an internal positive charge deficit and a cation exchange capacity. Smectite therefore functions as an exchanger phase capable of adsorbing strontium-90.

Petrographically, lithic Fragments 1, 3, and 4 had collonade textures (Figure D.31, Figure D.33, and Figure D.34). Fragment 2 had an entablature texture with the development of Fe-rich and Fe-poor glass phases (Figure D.32, note spotty appearance of glass regions). Each of the fragments had areas where smectite had formed as a weathering product of glass, marked 'C' in Figure D.31 through Figure D.34. The textural relationships of the primary and secondary phases was more apparent in the SEM micrographs recorded at higher enlargement (Figure D.31 through Figure D.34). The areas of each lithic fragment examined are indicated by arrows on Figure D.30. As indicated, the clasts included primary augite (A), plagioclase (P), titanomagnetite (T), olivine (O), and glass (G), and secondary smectite (i.e., a fine-grained silicate including Al and varying proportions of Na, Ca, K, Fe, and Mg). The smectite has replaced areas of glass that had cemented primary mineral grains. This noted smectite formation is consistent with past observations of fracture mineralization in basalt aquifers (McKinley et al. 1986). Basaltic glass in the groundwater environment was found to be most susceptible mineral phase to weathering, followed by augite. Fractures were coated with compositionally banded smectite, and pockets of banded smectite developed in basalt adjacent to fractures. The banded clay in 26A, particularly apparent in lithic Fragment 4, was identical in appearance and composition to the clay formed in weathered basalts.

The detailed analysis of B-110 sediment 26A using autoradiography and SEM suggested that sand-sized, weathered basalt fragments in Hanford formation sediments were responsible for sorbing strontium-90. The interparticle secondary smectite, which may have developed after deposition, or may have been developed in basalt flow surfaces prior to scour and transport to the Hanford Site, provided exchange sites to adsorb strontium-90. These observations were unexpected, as most of the cation exchange capacity of Hanford sediment is generally believed to be associated with detrital phyllosilicates and weathered micas in the silt and clay sized

fraction. At this point, the relative importance of interparticle smectite and fine-grained smectite as strontium-90 sorbents remains undocumented. Sediment 26A, however, was a coarse sand that was almost bereft of a fine fraction. Therefore, the exchange capacity of the weathered basalt fragments may represent a significant fraction of the overall sediment cation exchange capacity (CEC).

The experiments shown in Figure D.22 and Figure D.23 indicate strontium-90 that is adsorbed to interparticle smectite undergoes relatively rapid ion exchange with electrolyte Na and Ca. Ongoing experiments are trying to resolve the mineralogic residence of the electrolyte-resistent, sorbed strontium-90 pool. These experiments will identify the locations of sorbed strontium-90 that remain after extraction with 1 and 5 mol/L $NaNO_3$, confirming whether the immobilized fraction of strontium-90 is or is not associated with carbonate precipitates.

Figure D.30. Comparative Coarse-Scale Images of Sample 26A, Diameter 1.25 cm

Top: Inverted base photomosaic; high-z phases are dark. Mottled multi-phase clasts are basaltic lithic fragments. Numbered clasts are keyed to finer-scaled images in Figure D.31 to Figure D.34. Center: Autoradiography map of activity overlain on base photomosaic. Areas (clasts) with relatively high activity are dark. Arrows designate areas detailed in Figure D.31 to Figure D.34for each clast. Bottom: Optical photomicrograph in transmitted light. Dark, mottled clasts are lithic fragments, predominantly basaltic in origin; the large, central, banded, non-radioactive lithic fragment was not basaltic, and some basaltic clasts were also not radioactive.

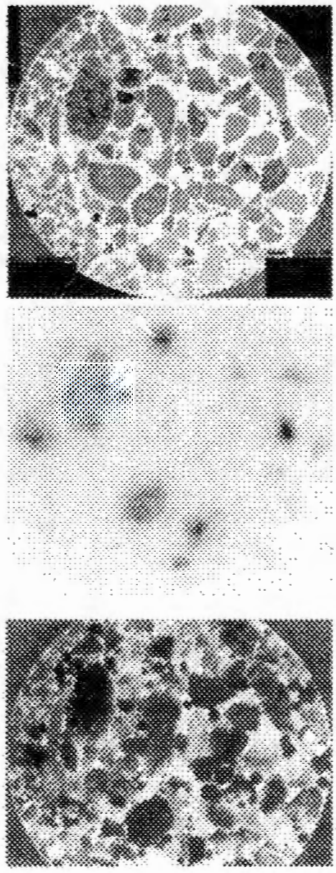

Figure D.31. SEM Photomicrograph of Radioactive Basalt Fragment #1 Figure D.30 That Shows Collonade Texture
A = Augite, P = Plagioclase, T = Titanomagnetite, G = Glass, and C = Smectite Clay. Clay was Observed as Altered Regions with Glass and Along Fractures

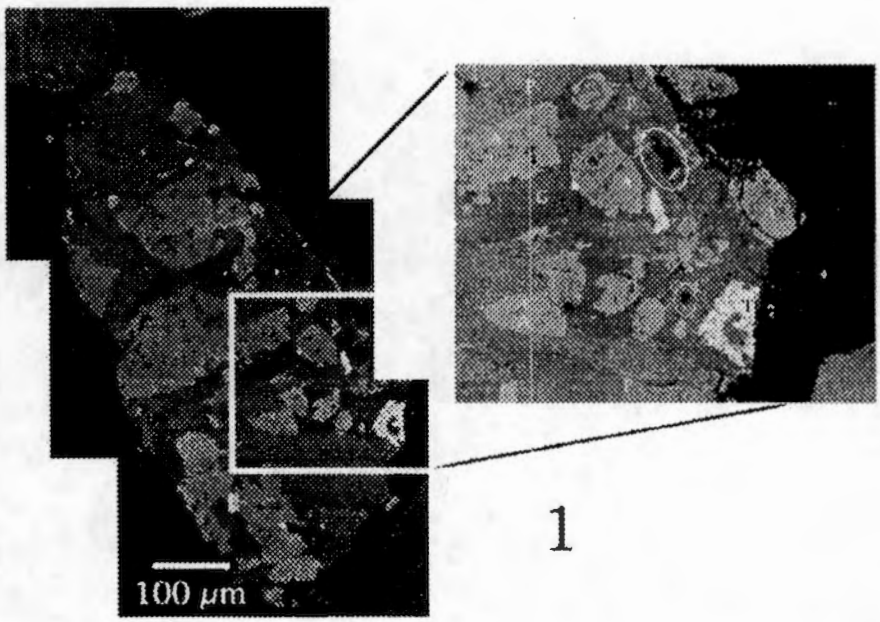

Figure D.32. SEM Photmicrograph of Radioactive Basalt Fragment #2 in Figure D.30 that Shows Entabulature Texture
T = Titanomagnetite, P = Plagioclase, A = Augite, C/G = Glass Clay Association. Primary Areas of Clay (C) Formation were Observed in Inter-Glass Channels

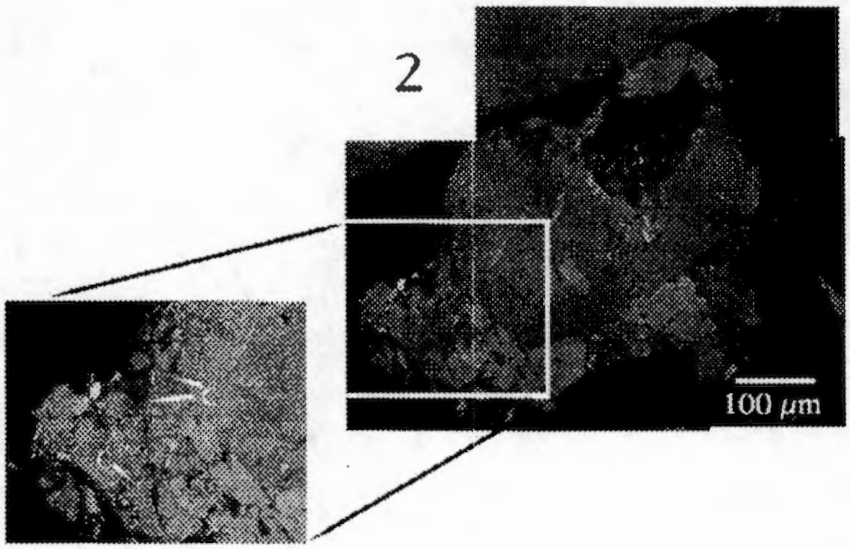

Figure D.33. SEM Photomicrograph of Radioactive Basalt Fragment #3 in Figure D.30 that Shows Collonade Texture
A = Augite, T = Titanomagnetite, O = Orthoclase, P = Plagioclase, and C = Smectite Clay. Clay was Observed in Distinctive, Inter-Grain Domains

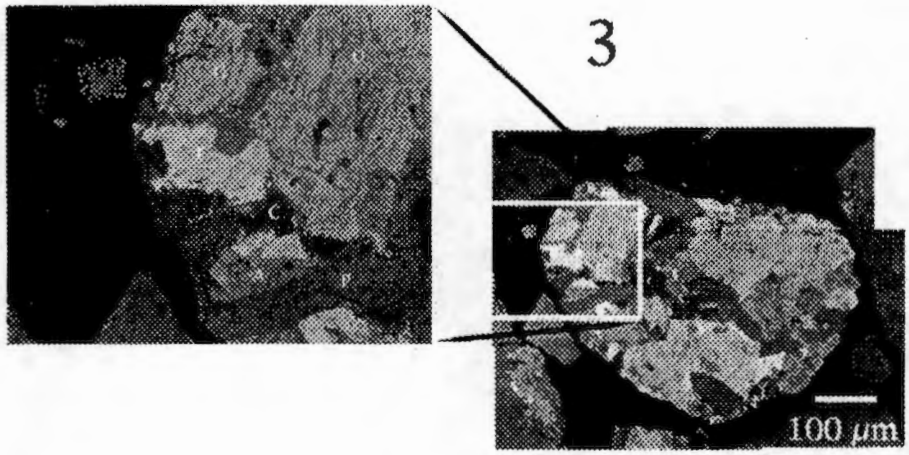

Figure D.34. SEM Photomicrograph of the Right Side of the Large Radioactive Basalt Fragment #4 in Figure D.30 that Shows Collonade Texture
A = Augite, P = Plagioclase, G = Glass, and C = Smectite Clay. Clay was Observed in Large Spatial Regions and Showed Desiccation Cracks and Compositional Zonation

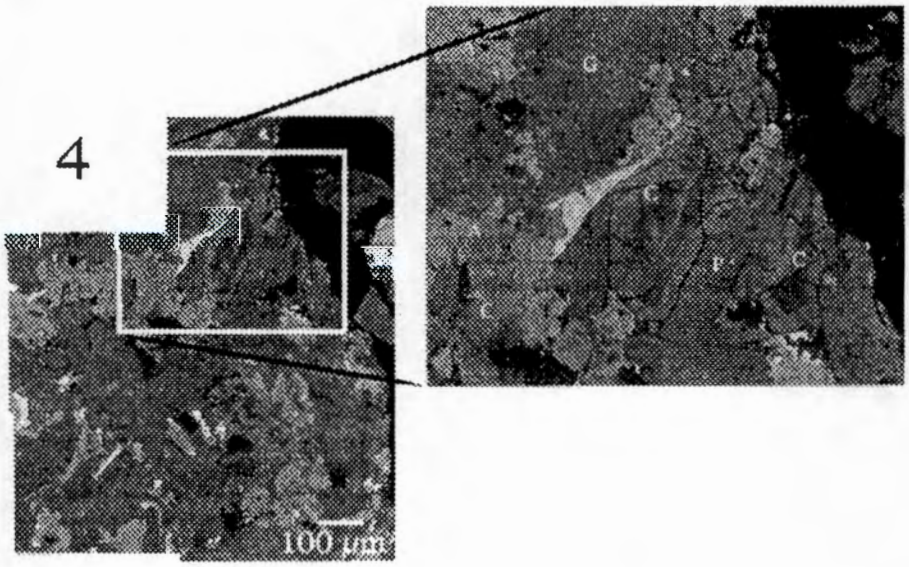

D.2.4.4 Conclusions

Sediments from B-110 core sample 26A have been examined to determine: 1) factors controlling strontium-90 is desorbability, and 2) the chemical or mineralogic residence of sorbed strontium-90. The following are primary conclusions from this work:

1. Approximately 75% of the sorbed strontium-90 in sample 26A was present in an ion exchangeable state and 25% appeared to be precipitated in a high magnesium-calcite. The isotopic ratios of strontium in these two strontium-90-containing geochemical pools were different indicating that they were not in isotopic equilibrium.

2. The ion exchangeable strontium-90 was fully and rapidly exchangeable under the necessary ionic conditions. The desorption extent and its dependence on electrolyte composition was well described with the multicomponent exchange model developed in Section D.2.3. The ion compositions required to induce significant desorption (e.g., 1 to 5 mol/L Na and 0.05 mol/L Ca) were much different from the current in situ ion regime. The existing ion regime in the B-110 plume is unlikely to induce additional mobility to sorbed strontium-90.

3. The use of a deionized water extraction to characterize the porewater concentration of strontium-90 probably underestimated its true in situ concentration through the dilution of the porewater electrolyte ions. The most accurate assessment of porewater strontium-90 concentration would be obtained by sediment extraction using $NaHCO_3$ at the approximate in situ concentration (e.g., 0.1 mol/L). The best estimate of the ^{90}Sr-K_d (adsorption and descorption) for the ion exchangeable pool under the existing in situ geochemical condition is 5.62 ml/g. The effective in situ retardation factor would be quite high because the low volumetric moisture content. Additional measurements and calculations underway will further refine this value.

4. Approximately 25% of the sorbed strontium-90 pool appears to be incorporated into a precipitated carbonate phase. This precipitated strontium-90 is not desorbable in sodium or calcium electrolyte, and is essentially fixed unless subsurface pH changes to more acidic values. The precipitated strontium-90 appears to exchange very slowly with other indigenous stable strontium pools.

5. Radioactive mineral particles were isolated from B-110 sediment. A significant fraction of the ion-exchangeable strontium-90 appeared to be absorbed to phyllosilicate minerals located along the margins and within the intersticies of sand sized basalt fragments. The phyllosilicates were alteration products of basaltic glass.

6. The vadose zone strontium-90 plume currently appears stable and virtually immobile. Infiltration of dilute meteoric waters could further increase retardation by the dilution of porewater Na^+. Any geochemical change to this particular system that would increase porewater Ca^{2+} would decrease the ^{90}Sr-K_d below the value estimated above.

D.2.4.5 References

Allen, C. C., R. G. Johnston, and M. B. Strope, 1985, *Characterization of Reference Umtanum and Cohassett Basalt,* SD-BWI-DP-053, Rockwell Hanford Operations, Richland, Washington.

Bjornstad, B. N., 1990, *Geohydrology of the 218-W-5 Burial Ground, 200-West Area, Hanford Site*, PNL-7336, Pacific Northwest Laboratory, Richland, Washington.

Jackson, R. E., and K. J. Inch, 1983, "Partitioning of Strontium-90 Among Aqueous and Mineral Species in a Contaminated Aquifer," *Environmental Science and Technology*, Vol. 17:231-237.

Kunze, G. W., and J. B. Dixon, 1986, "Pretreatment for Mineralogical Analysis," In *Methods of Soil Analysis – Part 1 Physical and Mineralogical Methods Second Edition*, A. Klute, ed., American Society of Agronomy, Inc., Madison, Wisconsin, pp. 91-100.

Lefevre, F., M. Sardin, and D. Schweich, 1993, "Migration of Strontium in Clayey and Calcareous Sandy Soil: Precipitation and Ion Exchange," *Journal of Contaminant Hydrology*, Vol. 13:215-229.

Long, P. E., and B. Wood, 1986, "Structures, textures, and cooling histories of Columbia River basalt flows", *Geol. Soc. Amer. Bull*, 97:1144-1155.

McKinley, J. P., S. A. Rawson, and D. G. Horton, 1986, "Form and composition of secondary mineralization in fractures in Columbia River Basalts," in A. D. Romig, Jr., and W. F. Chambers, eds, *Microbeam Analysis, 1986*, San Francisco Press. pp. 127-130.

McKinley, J. P., C. J. Zeissler, J. M. Zachara, R. J. Serne, R. M. Lindstrom, H. T. Schaef, and R. D. Orr, 2001, "Distribution and Retention of ^{137}Cs in Sediments at the Hanford Site, Washington," *Environmental Science and Technology*, Vol. 35:3433-3441.

Serne, R. J., and V. L. LeGore, 1996, *Strontium-90 Adsorption-Desorption Properties and Sediment Characterization at the 100 N-Area*, PNL-10899, Pacific Northwest National Laboratory, Richland, Washington.

Serne, R. J., B. N. Bjornstad, G. W. Gee, H. T. Schaef, D. C. Lanigan, C. W. Lindenmeier, R. D. Orr, V. L. LeGore, R. E. Clayton, M. J. Lindberg, I. V. Kutnyakov, S. R. Baum, K. N. Geiszler, M. M. Valenta, T. S. Vickerman, and L. J. Royack, 2002, *Characterization of Vadose Zone Sediment: Borehole 299-E33-46 Near Tank B-110 in the B-BX-BY Waste Management Area*, PNNL-14119, Pacific Northwest National Laboratory, Richland, Washington.

D.2.5 STRONTIUM MIGRATION IN HANFORD SEDIMENT FROM THE B, BX, AND BY TANK FARMS: A CATION EXCHANGE MODEL BASED ON LABORATORY TRANSPORT EXPERIMENTS.

Carl I. Steefel[1], Susan Carroll[1], and Sarah Roberts[1]

[1]Lawrence Livermore National Laboratory, Livermore, California 94550

D.2.5.1 Introduction

This report presents preliminary results of strontium transport experiments using flow-through columns packed with a composite of Hanford formation sediment from the B, BX, and BY tank farms. One of the specific objectives of the study was to test the ability of a multicomponent cation exchange model derived from batch experiments to predict strontium transport in column experiments. This validated model, in turn, will be used to simulate both the emplacement and future migration of the strontium-90 plume defined by borehole 299-E33-46 (Section D.2.1). Unlike earlier studies on cesium transport at the SX tank farm where migration takes place primarily in a binary system, the column experiments in this report have been designed to evaluate the effect on strontium migration of multiple competing cations, including Na^+, K^+, Ca^{++}, and Mg^{++}. The column experiments were also used to provide a direct test of the reversibility of exchange by following the strontium injection with flushing of the column with concentrated KNO_3.

The strontium column experiments completed to date evaluate the dependence of strontium retardation on sodium nitrate concentrations ranging from 0.01 to 5 M. The competition of potassium and strontium was also addressed using desorption experiments, with KNO_3 concentrations ranging from 0.01 to 1 M. Most experiments were carried out with a concentration of strontium in the injection fluid of 10^{-5} M. Duplicate experiments at a strontium concentration of 10^{-6} and 10^{-7} M were used to determine whether the strontium concentration affected its retardation. Cation exchange capacities (CEC) were determined by measuring the equivalent sum of calcium, magnesium, and potassium eluted from the columns in 1 and 5 M $NaNO_3$ solutions prior to strontium injection and in one experiment from the sum of strontium, calcium, magnesium, and sodium eluted by 1 M KNO_3 after strontium injection. The sediment CEC was also determined by a separate isotopic equilibrium exchange column experiment using ^{22}Na.

D.2.5.2 Experimental Procedures

A total of six one-dimensional column experiments using uncontaminated Hanford sediments were carried out at 25 °C to investigate the mobility of strontium (Table D.16). A Hanford formation composite sample from borehole B8814 at the B, BX, and BY tank farms was used as the experimental medium. The sediment was lightly crushed to pass through a 2 mm sieve, air-dried, and mixed thoroughly. In addition, the sediment was repeatedly washed with a sodium-acetate solution to remove any carbonate phases present. The sediments were loaded into a reactor column (1 cm x 15 cm) filled with distilled and deionized water. Sediment density was determined to be 2.75 g cm^{-3} by volume displacement. The elution experiments consisted of three phases. In the pretreatment phase, the background $NaNO_3$ electrolyte was passed through

the column to replace potassium, calcium, and magnesium with sodium on the sediment exchange sites. At lower concentrations of $NaNO_3$ (0.01 to 0.1 M), complete desorption of calcium, magnesium, and potassium was not achieved after as much as 15 pore volumes had been flushed through the column. The pretreatment phase was followed by a stage in which 10, 1, and 0.1 μM (10^{-5}, 10^{-6}, and 10^{-7} M) $SrNO_3$ and 1 mM $Ca(NO_3)_2$ and $Mg(NO_3)_2$ along with $NaNO_3$ at concentrations ranging from 0.01 to 5 M were passed through the sediment column to measure strontium retardation from the breakthrough curve. The final phase was a strontium desorption experiment using KNO_3 ranging in concentration from 0.01 to 1 M. Iodide behaved as a non-reactive tracer and was used to obtain the dispersivity of the columns.

Table D.16. Summary of Strontium Transport Experiments Using Composite Sediment from WMA B-BX-BY

Experiment	Sorption Stage Solution	Desorption Stage Solution	Flow Rate (ml min^{-1})	Darcy Flux (cm min^{-1})	Sediment-Solution Ratio (g/L)	Porosity %
1	0.01 M $NaNO_3$ 10^{-5} M Sr 0.001M Ca, Mg	0.01 M KNO_3	0.2	0.260	3187	46.3
2	0.1 M $NaNO_3$ 10^{-5} M Sr 0.001M Ca, Mg	0.1 M KNO_3	0.1	0.130	3789	42.1
3	1 M $NaNO_3$ 10^{-5} M Sr 0.001M Ca, Mg	1 M KNO_3	0.1	0.130	3294	45.5
4	5 M $NaNO_3$ 10^{-5} M Sr 0.001M Ca, Mg	1 M KNO_3	0.1	0.130	3673	42.8
5	1 M $NaNO_3$ 10^{-6} M Sr 0.001 Ca, Mg	1 M KNO_3	0.1	0.130	3362	45.0
6	1 M $NaNO_3$ 10^{-7} M Sr 0.001M Ca, Mg	1 M KNO_3	0.1	0.130	4014	40.7

The CEC of the composite sediment was measured in several ways. The cation exchange capacity was determined from the equivalent sum of calcium, magnesium, and potassium eluted with a 0.1, 1, and 5 M $NaNO_3$ flush of the sediments in the pre-treatment phase of the experiments. In addition, one CEC determination was made by summing the equivalents of strontium, sodium, calcium, and magnesium eluted by a 0.1 M KNO3 solution during the desorption stage. The CEC was also determined by ^{22}Na isotopic equilibrium in a flow-through column using 1 and 5 M $NaNO_3$. In this experiment, several pore volumes of $NaNO_3$ solution were flushed through the column to saturate the sediment column with Na prior to injection of a ^{22}Na spiked solution of a 1 or 5 M $NaNO_3$. The mass of ^{22}Na on exchange sites was determined by integrating the ^{22}Na elution curve and subtracting this from the integrated iodide elution curve which behaves as a non-reactive tracer. With the assumption of isotopic equilibrium between the

^{22}Na and the bulk sodium on exchange sites, the total CEC can be calculated by assuming that the accessible exchange sites are occupied by sodium.

D.2.5.3 Modeling Procedures

Distribution of species calculations and the simulations of multicomponent ion exchange and transport in the column experiments were carried out with the general purpose reactive transport code CRUNCH (Steefel in preparation), a combined and updated FORTRAN 90 version of the codes GIMRT and OS3D (Steefel and Yabusaki 1996; Steefel 2001; Steefel et al. 2002).

A single exchange site concentration (CEC) was used in all simulations (Sections D.2.2 and D.2.3). Selectivity coefficients for strontium, sodium, potassium, calcium, and magnesium were determined in two ways. First, a global fit of the batch data from Zachara et al. (Section D.2.2) was carried out. This fit relied primarily on nine multicomponent batch experiments in which strontium and sodium were varied systematically so as to sum up to 0.001, 0.01, and 0.1 equivalents per liter. Both aqueous and solid phase strontium, sodium, calcium, potassium, and magnesium were measured. Lacking any data at higher sodium concentrations, it was necessary to augment the nine multicomponent experiments with an earlier set of batch experiments carried out at 1 M $NaNO_3$ and a variety of strontium concentrations (Zachara et al., Section D.2.2). These experiments were intended to be binary, but later experiments showed that measureable amounts of calcium, magnesium, and potassium were also present in the solution and on the exchangers, although these amounts could not be quantified. As a first order correction, calcium, magnesium, and potassium concentrations in these 1 M $NaNO_3$ experiments were assumed to be the highest values obtained in the multicomponent experiments in which all cations were measured. Added to the nine multicomponent batch experiments and the sodium-strontium binary experiments was data from a set of calcium-strontium binary experiments (Zachara et al., Section D.2.2). All of these data were then used to fit a set of "batch" selectivity coefficients using the nonlinear optimization program PEST (Parameter Estimation Inc.) combined with distirbution of species calculations carried out with CRUNCH. The resulting parameter set is then fully compatible with the reactive transport simulations of strontium migration in the column experiments.

Multicomponent cation exchange was formulated using the Vanselow activity convention, which assumes a reaction stoichiometry of the following form (Appelo and Postma 1993):

$$Cs^{+} + \tfrac{1}{m} MX(i)_m \leftrightarrow CsX(i) + \tfrac{1}{m} M^{m+}, \qquad (1)$$

where M is the competing cation (Na^+, K^+, Ca^{++}, Mg^{++}), m is its charge, and $X(i)$ refers to the ith type of exchange site. In the Vanselow convention, each exchange site, $X(i)$, has a charge of -1. The activities of adsorbed species in the Vanselow convention correspond to the mole fractions, $\beta(i)_M$,

$$\beta(i)_M = \frac{q(i)_M}{\sum_M q(i)_M} = [X(i)_M], \qquad (2)$$

where $q(i)_M$ is the concentration of adsorbed cation M in exchange site i (moles/g), and the square brackets denote activities. The exchange reactions can then be used to write a mass action equation for binary Sr-M exchange:

$$K_{M/Cs} = \frac{\beta(i)_M^{1/m}[Cs^+]}{\beta(i)_{Cs}[M^{m+}]^{1/m}} = \frac{[X(i)_M]^{1/m}[Cs^+]}{[X(i)_{Cs}][M^{m+}]^{1/m}} \tag{3}$$

In a single-site ion exchange model, the CEC is equal to the sum of the charge equivalent concentrations of the adsorbed cations:

$$CEC = \sum_M z_M q_M , \tag{4}$$

while in a multi-site model, the CEC is the charge summed over all of the cation exchange sites (Voegelin et al. 2000)

$$CEC = \sum_i \sum_M z_M q(i)_M , \tag{5}$$

A Debye-Huckel formulation was used to calculate activity coefficients. This approach was augmented with fitting parameters for ion pair formation to describe cation and anion activities accurately. Free cation activities were calculated by adjusting the log Ks for the ion pairs $SrNO_3^+$, $CaNO_3^+$, $MgNO_3^+$, KNO_3, and $NaNO_3$ (aq) to match ion activities (not activity coefficients) determined with the Pitzer approach as implemented in the code GMIN (Felmy 1995). Ion pair formation, therefore, is described with effective equilibrium constants that incorporate the effects of ion interaction parameters in the Pitzer approach. The cation activities calculated by GMIN were used as "observations" to be matched by adjusting the effective equilibrium constants for the ion pair reactions in the global fitting procedure. While this method cannot be recommended as a general substitute for the full Pitzer approach, it captures the change in major cation activities over the concentration range of interest in the column experiments.

It was also necessary to include an empirical activity coefficient, γ, to capture the strong ionic strength dependence of selectivity coefficients, particularly those reactions involving a monovalent and divalent cation. This took the form of a "bdot" correction affecting only the activity of the exchange species:

$$\ln \gamma_X = BI$$

where I is the ionic strength of the solution and B is a fitted constant parameter.

Transport processes treated in the simulation of the experiments include advection and dispersion. All of the simulations used 100 equally spaced grid cells to discretize the one-dimensional columns (typically 15 cm in length).

D.2.5.4 Results and Discussion

D.2.5.4.1 Determination of Cation Exchange Capacity. Elution of calcium, magnesium, and potassium from sediment exchangers using various concentrations of $NaNO_3$ was used in the

pre-strontium injection phase of the column experiments to determine a sediment CEC. Results for flushes with $NaNO_3$ concentrations of 0.01, 0.1, 1, and 5 M (corresponding to Experiments 1 through 4, respectively) are given in Table D.17. These determinations of the CEC should be minimum values, since they neglect the sodium on the exchange sites. Since the sediment was pre-washed with a sodium acetate solution to leach carbonates, the sodium concentration could be significant. The CEC values determined using this method show a strong dependence on the concentration of the $NaNO_3$ flush, with the CEC increasing from a minimum of 30.2 μeq/g at 0.01 M $NaNO_3$ to as much as 64.6 μeq/g at 5 M $NaNO_3$. Also listed in Table D.17 is a CEC value of 45 μeq/g determined using a 0.1 M KNO_3 flush after an extended period of strontium and sodium nitrate injection in Experiment 2. Two separate ^{22}Na isotopic equilibrium experiments were conducted, although only the experiment using 1 M $NaNO_3$ is considered reliable. The high ^{22}Na concentrations in the 5 M $NaNO_3$ experiment resulted in a very small separation of the non-reactive tracer breakthrough and the ^{22}Na breakthrough, thus magnifying any errors in the calculation of the CEC. This would appear to explain the anomalously high value of 127 μeq/g determined using this approach. The value of 65 μeq/g determined in the 1 M $NaNO_3$ ^{22}Na experiment is within the range of values determined with the other methods and is based on a easily measureable separation of the exchangeable ^{22}Na and the non-reactive iodide (Figure D.35).

Table D.17. CEC Determinations on Composite Sediment from WMA B-BX-BY

Method	Experimental Conditions	CEC (μeq/g)	Reference
Cation Elution	0.01 M $NaNO_3$	30.2	This Study
Cation Elution	0.1 M $NaNO_3$	31.4	This Study
Cation Elution	1 M $NaNO_3$	54.1	This Study
Cation Elution	5 M $NaNO_3$	64.6	This Study
Cation Elution	0.1 M KNO_3	45.0	This Study
^{22}Na Isotopic Dilution	1 M $NaNO_3$	65	This Study
^{22}Na Isotopic Dilution	5 M $NaNO_3$	127	This Study
Batch Exchange	Various	50.2	Zachara et al. (Section D.2.2)

D.2.5.4.2 Determination of Column Dispersivity. Iodide was used as a non-reactive tracer to determine the dispersivity of the column. Figure D.36 shows a breakthrough curve for iodide from Experiment 1 carried out at a flow rate of 0.2 ml/minute, plotted as a function of pore volumes. While there is some scatter in the data, the iodide curve is matched well using a dispersivity of 3.5 cm. This value for the dispersivity was used in all of the simulations presented here.

Figure D.35. Breakthrough of ^{22}Na and Iodide (a tracer) in Flow-Through Column Experiment
The Difference in the Integrated Masses of ^{22}Na and Iodide eluted can be used to Calculate the Total CEC After the Sediment Exchange Sites have been Saturated with Sodium. Results are for 1 M $NaNO_3$ experiment.

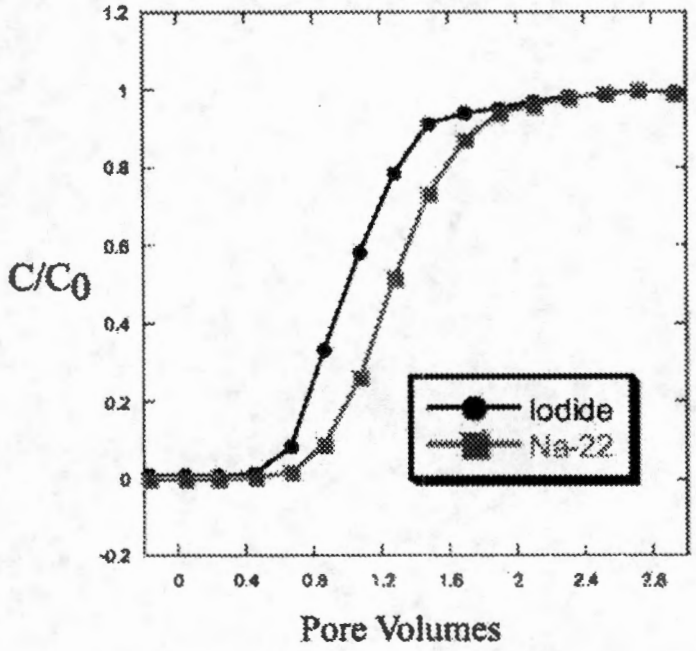

Figure D.36. Iodide (tracer) Breakthrough in Experiment 1 is Matched with a Dispersivity of 3.5 Centimeters

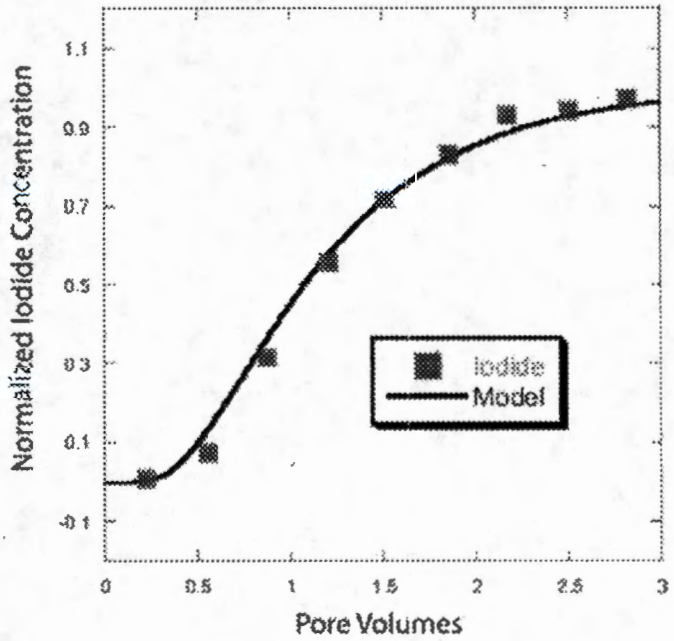

D.2.5.4.3 Multi-Component Strontium Exchange Model: Fitting Batch-Derived Data. As discussed above, batch data from Zachara et al. (Section D.2.2) were used to determine selectivity coefficients for strontium, calcium, magnesium, and sodium. The batch data consisted of a set of nine multicomponent experiments in which the concentrations of all relevant cations (strontium, calcium, sodium, potassium, and magnesium) were measured in both the aqueous phase and on the exchangers. Since these experiments only went up to 0.1 M $NaNO_3$, an earlier set of batch experiments conducted at 1 M $NaNO_3$ were also included in the fitting procedure, despite the fact that other cations (calcium, potassium, and magnesium) were not measured. To minimize this effect, calcium, potassium, and magnesium concentrations were assumed to be the highest values for those elements obtained in the nine multicomponent exchange experiments. A set of calcium-strontium binary exchange experiments were also included in the optimization (Zachara et al., Section D.2.2). As discussed above, only a single exchanger site with a concentration of 50.2 μeq/g was considered. In all, 54 exchange experiments were considered in the global fit of the selectivity coefficients. Since none of the batch experiments included much variation in the concentrations of potassium and magnesium, the results cannot be expected to be robust with respect to these cations.

Table D.18 summarizes the results of the global optimization of the selectivity coefficients and exchanger activity corrections. Note that in order to fit the 1 M $NaNO_3$ data, it was necessary to include a large activity correction as a function of ionic strength for the divalent ions. This correction has the effect of increasing the preference for the divalent cation relative to the monovalent cation over and above what would be predicted with a mass action equation based on classical ion exchange theory. While there is some uncertainty as to the correct value here because of the lack of measurements of calcium, potassium, and magnesium in the sodium-strontium exchange experiments carried out at 1 M $NaNO_3$, the effect appears to be far too large to be attributed to the relatively low concentrations of these cations. Moreover, as discussed below, the effect is even more pronounced in the reactive transport experiments, where any residual calcium, magnesium, and potassium on the exchangers will tend to be flushed out of the column. The apparent increase in preference for the divalent cation (strontium, calcium, or magnesium) with increasing concentration of the low-charge ion (sodium or potassium) is well documented in the literature (McBride 1980, 1989). While the explanation for the effect is not completely clear, it has been suggested that it is linked to the change in the structure of the clay minerals as the ionic strength increases, with the largest change occurring between about 0.1 and 1 M (McBride 1989). At higher concentrations, the divalent cations tend to occupy internal exchange sites, while the lower charged ions favor the external surfaces of the clay.

Table D.18. Selectivity Coefficients and Exchanger Activity Corrections Based on Batch Exchange Experiments (Zachara et al., Section D.2.2)
Exchange activity corrections correspond to the "Bdot" term in Equation 6.

Exchange Reaction	Batch Parameters Log K
$0.5SrX_2 + Na^+ = 0.5\ Sr^{2+} + NaX$	0.238
$0.5SrX_2 + K^+ = 0.5\ Sr^{2+} + KX$	0.00
$SrX_2 + Ca^{2+} = Sr^{2+} + CaX_2$	0.094
$SrX_2 + Mg^{2+} = Sr^{2+} + MgX_2$	0.006
Exchanger Activity Corrections	**Bdot**
$Sr\text{-}X_2$	0.989
$Ca\text{-}X_2$	0.989
$Mg\text{-}X_2$	0.989
Na-X	0.000
K-X	0.000

Table D.19. Strontium Retardation in Reactive Transport Experiments
Calculated retardations are based on fit of batch data as summarized in Table D.18.

Experiment	Sorption Stage Solution	Observed Retardation	Calculated Retardation
1	0.01 M $NaNO_3$ 10^{-5} M Sr 0.001M Ca, Mg	27	34.5
2	0.1 M $NaNO_3$ 10^{-5} M Sr 0.001M Ca, Mg	20	26
3	1 M $NaNO_3$ 10^{-5} M Sr 0.001M Ca, Mg	3.5	1.4
4	5 M $NaNO_3$ 10^{-5} M Sr 0.001M Ca, Mg	1.7	3.9
5	1 M $NaNO_3$ 10^{-6} M Sr	9.5	1.5

Figure D.37. Strontium Breakthrough and Subsequent Desorption in Experiments 1 through 4 (0.01, 0.1, 1, and 5 M $NaNO_3$, respectively in the sorption stage and 0.01, 0.1, 1, and 1 M KNO_3, respectively in the desorption stage).

The concentration of strontium in the injection solution is 10^{-5} M. Calculations are based on fits of batch data.

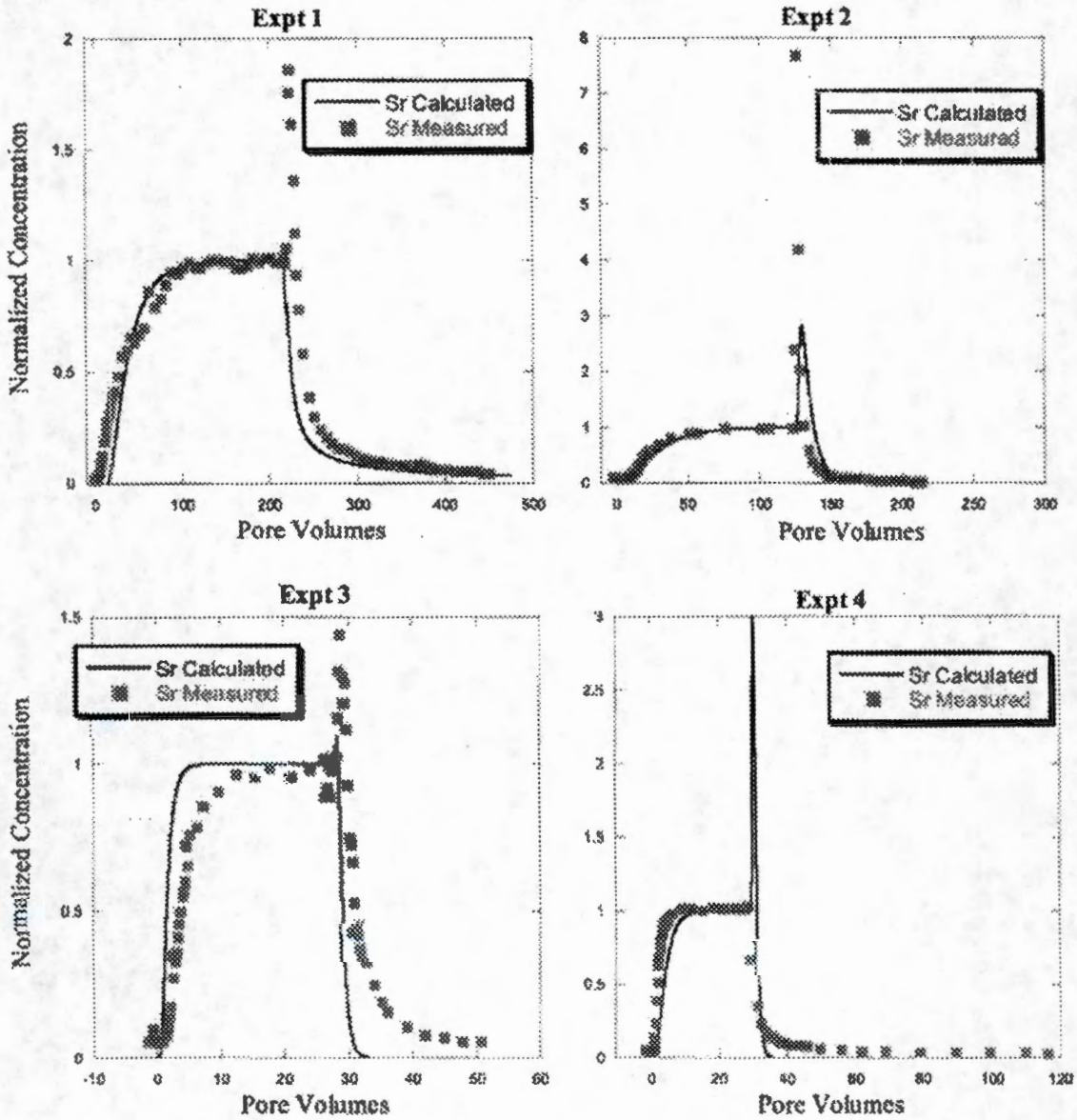

D.2.5.4.4 Simulation of Reactive Transport Experiments using Batch Experiment-Fitted Selectivity Coefficients. With the inclusion of a strong dependence of the divalent-monovalent cation selectivity coefficients on ionic strength based on the batch experimental results, it is possible to simulate many of the observed features of the reactive transport experiments. At 0.01 M $NaNO_3$ (Experiment 1), the match of the strontium sorption breakthrough curve is relatively close (Figure D.37). The shape of the strontium desorption limb resulting from the KNO_3 flush is also captured, except that the height of the peak when the eluent is switched from sodium to potassium is underestimated. This pronounced peak, present in most of the experiments, is the result of the stronger affinity of the exchanger for potassium than sodium at equal concentrations of the two cations. The match with the 0.1 M $NaNO_3$ experiment is also good (Figure D.37 and Table D.19). More serious discrepancies arise as the $NaNO_3$ concentration is increased to 1 M, however, despite the inclusion of an ionic strength dependence in the batch fits which increases the preference of the exchanger for the divalent strontium relative to sodium (Figure D.37). The column experiments, therefore, present even stronger evidence of the pronounced ionic strength dependence of the divalent-monovalent cation selectivity coefficients than do the batch experiments. As noted above, these effects occur despite the flushing out of the system of other potentially competing cations like calcium, magnesium, and potassium. At 5 M $NaNO_3$ (Experiment 4), the ionic strength dependence (Figure D.37 and Table D.19) actually improves the fit relative to the 1 M $NaNO_3$ experiment. The selectivity of the exchanger for potassium relative to strontium, however, is greatly overestimated, as indicated by the overly large peak when the eluent is switched and by the rapid desorption of the strontium that is not observed in the experiment.

D.2.5.4.5 Estimation of Sodium-Strontium and Potassium-Strontium Selectivity Coefficients Based on Column Experiments. An attempt was made to fit all of the column experiments with a single value of the "Bdot" parameter. While a larger value for the parameter (approximately 1.75) allowed for fitting of the 0.01, 0.1, and 1 M $NaNO_3$ experiments, the 5 M $NaNO_3$ experiment could not be fit with this procedure. It appears, therefore, that the dependence of the selectivity coefficients on ionic strength is not linear. We took the approach of fitting each of the column experiments separately. Results of the fits are shown in Figure D.38 and Figure D.39. Values for the sodium-strontium and potassium-strontium selectivity coefficients needed to obtain these fits are given in Table D.20. These results are also presented in graphical form in Figure D.40. Note that the non-constancy of the selectivity coefficients is an expression of the deviation from classical "mass action" behavior. These results are also qualitatively similar to those obtained by McBride (1989) for the cadmium-sodium exchange in a nitrate electrolyte.

Table D.20. Selectivity Coefficients Based on Individual Column Experiments

Experiment	$K_{Na\text{-}Sr}$	$K_{K\text{-}Sr}$
1	0.12	-0.50
2	0.22	-0.25
3	1.00	0.87
4	1.50	1.25
5	1.22	1.10

Some of the apparent ionic strength dependence (e.g., increase in $K_{Na\text{-}Sr}$ and $K_{K\text{-}Sr}$) may be the result of ion pair formation in the nitrate system. Pitzer-type calculations for this system using GMIN indicating strong interaction between strontium and nitrate. Whether this interaction is manifested as a discrete strontium-nitrate ion pair, however, is less clear. If the ion pair does form, it is also not evident from the data what the actual concentration of the complex is. This is an issue because strontium nitrate forms a monovalent complex (like calcium nitrate), which may be capable of exchanging with the sediment. In contrast, a $NaNO_3$ ion pair is neutral and will therefore migrate through the sediment without exchanging at all. Since exchange of the strontium nitrate ion pair is neglected in the simulations, this may explain part of the "ionic strength" effect. With a better knowledge of the actual ion pair concentration, it would be possible to quantify this effect.

Figure D.38. Strontium breakthrough and subsequent desorption in Experiments 1 through 4 (0.01, 0.1, 1, and 5 M $NaNO_3$ respectively in the sorption stage and 0.01, 0.1, 1, and 1 M KNO_3 respectively in the desorption stage)

The concentration of strontium in the injection solution is 10^{-5} M. Fits are based on column experiments, with selectivity coefficients summarized in Table D.17

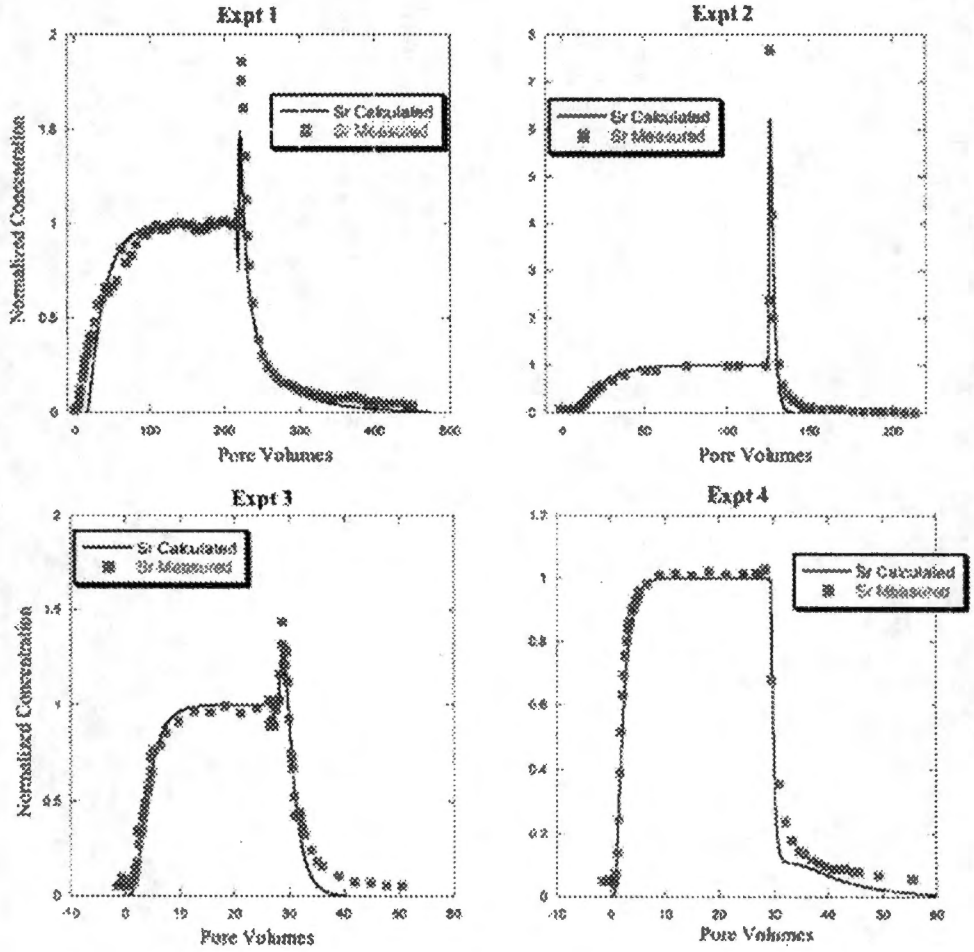

Figure D.39. Strontium breakthrough and subsequent desorption in Experiment 5, 1 M $NaNO_3$ and 1 M KNO_3 with an injection concentration of 10^{-6} M strontium

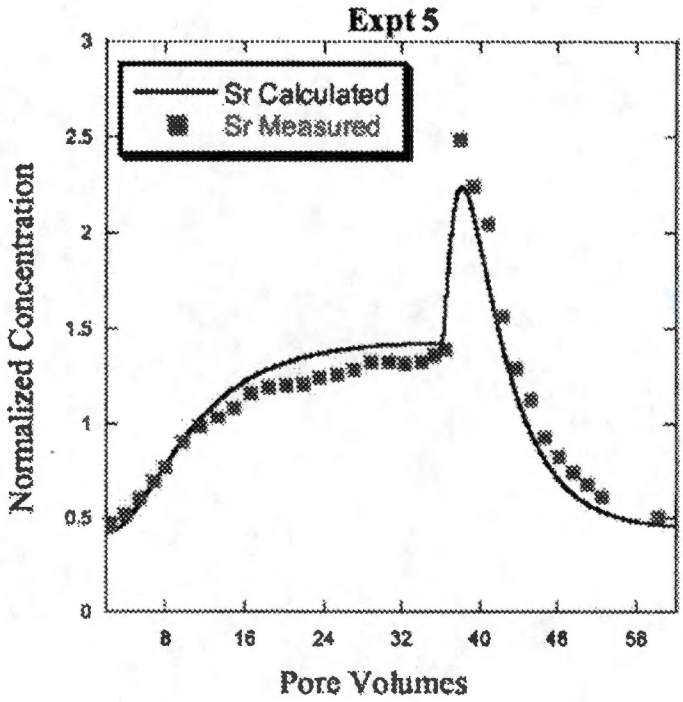

Figure D.40. Dependence of the Sodium-Strontium and Potassium-Strontium Selectivity Coefficients Based on Column Experiments

Deviations from "mass action" behavior appear as non-constant selectivity coefficients.

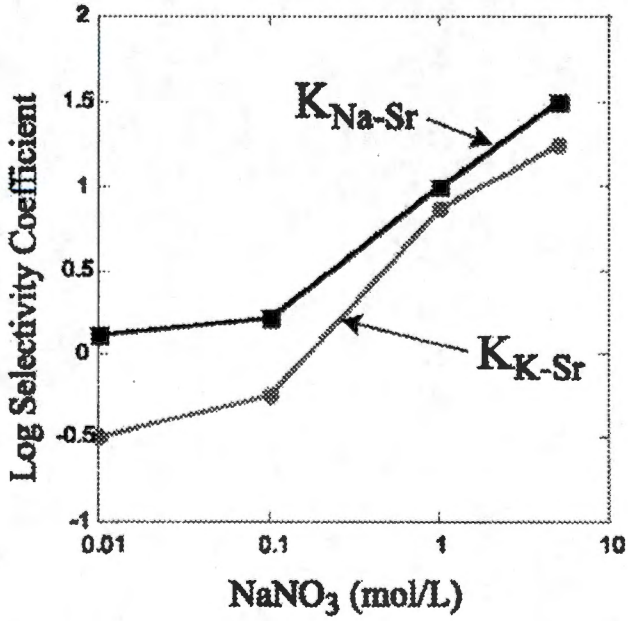

D.2.5.5 Conclusions

This section summarizes the results of a series of one-dimensional, reactive transport experiments designed to test a multicomponent ion exchange model for strontium transport. Column experiments have been used to assess the effect of competing $NaNO_3$ and KNO_3 concentrations on strontium sorption and desorption respectively. These experiments were also carried out with sorption injection solutions containing 0.001 M calcium and magnesium, and 10^{-5} M strontium. CEC values for the composite sediment were estimated based on the equivalent sum of cations desorbed by 0.01, 0.1, 1, and 5 M $NaNO_3$ and by 0.1 M KNO_3. The estimates of the CEC range from as low as 30 μeq/g when the sediment is eluted with 0.01 M $NaNO_3$ to a high of 65 meq/g when 5 M $NaNO_3$ is used. A ^{22}Na isotopic dilution experiment also indicated a CEC of 65 μeq/g. A value of 50.2 μeq/g determined by Zachara et al. (Section D.2.2) fell in the middle of this range and therefore was used in all of the calculations presented in this report. The preliminary conclusions from these studies are as follows:

1. The reactive transport behavior of strontium in nitrate electrolyte through composite Hanford formation sediment from WMA B-BX-BY can be simulated with a transport model that includes modified multicomponent ion exchange as the only geochemical retardation process. Selectivity coefficients for the ion exchange of strontium with sodium, calcium, and magnesium were fitted from the batch experimental data in Section D.2.2. The modeling captured both the strontium breakthrough and desorption reasonably well at $NaNO_3$ and KNO_3 concentrations of 0.01 and 0.1 mol/L. The modeling, however, underpredicts the retardation of strontium at 1 mol/L $NaNO_3$, even when a strong dependence of the divalent-monovalent cation selectivity coefficient on ionic strength is included. The batch data also fails to capture the slow release of strontium during the desorption step using 1 M KNO_3, although this is partly due to the lack of batch data on strontium-potassium exchange.

2. The column experiments provide even stronger evidence for a dependence of the divalent-monovalent cation on ionic strength than do the batch experiments. The dependence has the effect of making the higher charged cation more strongly favored than the monovalent cation (either sodium or potassium) as either the $NaNO_3$ or the KNO_3 concentration is increased. This preference is expressed as a deviation from the classical "mass action" behavior expected for ion exchange.

3. While a classical cation exchange model may not be easily applicable over the entire range of ionic strengths possible in the B, BX, and BY tank farms, the ion exchange model still captures much of the dependence of strontium retardation on competing cation concentration, particularly at lower salt concentrations. It is expected that the cation exchange model can be substantially improved by considering new batch and column experiments at higher salt concentrations. It is noteworthy that even at 5 M $NaNO_3$, there is still a measurable retardation of strontium (about 1.7).

D.2.5.6 References

Appelo, C. A. J., and D. Postma, 1993, *Geochemistry, Groundwater, and Pollution*, A. A. Balkema, Rotterdam.

Felmy, A. R., 1995, "GMIN, A Computerized Chemical Equilibrium Program Using a Constrained Minimization of the Gibbs Free Energy: Summary Report," In *Chemical Equilibrium and Reaction Models*, Soil Science Society of America, Madison, Wisconsin.

McBride, M. B., 1980, "Interpretation of the variability of selectivity coefficients for exchange between ions of unequal charge on smectites", *Clays Clay Miner*, Vol.28, 255-261.

McBride, M. B., 1989, "Surface chemistry of soil minerals", In *Minerals in Soil Environments* J. B. Dixon nd S. B. Weed, eds., Soil Science Society of America, pp. 35-88.

Steefel, C. I., 2001, *GIMRT, Version 1.2: Software for Modeling Multicomponent, Multidimensional Reactive Transport, User's Guide*, UCRL-MA-143182, Lawrence Livermore National Laboratory, Livermore, California.

Steefel, C. I., in preparation, *CRUNCH, Software for Multicomponent Reactive Transport, User's Guide*, Lawrence Livermore National Laboratory, Livermore, California.

Steefel, C. I., and K. T. B. MacQuarrie, 1996, "Approaches to Modeling Reactive Transport in Porous Media," In *Reactive Transport in Porous Media*, P. C. Lichtner, C. I. Steefel, and E. H. Oelkers, Eds, Reviews in Mineralogy, Vol. 34:83-125.

Steefel, C. I., and S. B. Yabusaki, 1996, *OS3D/GIMRT, Software for Multicomponent-Multidimensional Reactive Transport: User's Manual and Programmer's Guide*, PNL-11166, Pacific Northwest National Laboratory, Richland, Washington.

Steefel, C. I., and S. B. Yabusaki, 2001, *Evaluation of the Field Exchange Capacity of Hanford Sediments with Implications for ^{137}Cs Migration*, PNNL-2001-7, Pacific Northwest National Laboratory, Richland, Washington.

Steefel, C. I., S. Carroll, P. Zhao, and S. Roberts, 2002, "Cesium Migration in Hanford Sediment: A Multi-Site Cation Exchange Model Based on Laboratory Transport Experiments," *Journal of Contaminant Hydrology*.

Voegelin, A., V. M. Vulava, F. Kuhnen, and R. Kretschmar, 2000, "Multicomponent Transport of Major Cations Predicted from Binary Adsorption Experiments," *Journal of Contaminant Hydrology*, Vol. 46:319-338.

D.2.6 ONE-DIMENSIONAL REACTIVE FLOW AND TRANSPORT MODEL OF STRONTIUM MIGRATION AT TANK B-110

Peter C. Lichtner[1] and R. Jeffrey Serne[2]

[1] Los Alamos National Laboratory, Los Alamos, New Mexico 87545
[2] Pacific Northwest National Laboratory, Richland, Washington 99352

D.2.6.1 Introduction

A one-dimensional reactive flow and transport model is presented in an attempt to understand major features of the strontium plume in the vadose zone at tank B-110 located at the Hanford B tank farm. It must be emphasized that the results presented here are preliminary and will undoubtedly change as more accurate representations of sorption processes in the vadose zone, and in particular the Hanford formation sediment, become available. The one-dimensional simulations performed are expected to give a qualitative description of the processes involved. However, a full three-dimensional simulation is essential for a quantitative analysis, which is planned for future work. By first modeling the one-dimensional case, it is possible to quickly and efficiently scope out the essential processes that will need to be incorporated into a three-dimensional simulation, the latter requiring a significantly greater computational cost.

There does not exist a clearly identified leak date for tank B-110. The best estimate appears to be 1968 when a high strontium-90 waste stream was transferred into tank B-110, and the tank was left with greater than the 530,000 gal fill limit for about a year. Drywells in the vicinity of tank B-110 were drilled in 1973 and encountered contamination during drilling. There is no evidence of additional leaks after the drywells were put in place. During 1969 and 1970, tank B-110 received cesium-137 recovery waste (and was maintained near the 530,000 gal fill limit). In the fall of 1971, the supernatant was pumped out of tank B-110 leaving about 280,000 gal of sludge. The first indication of a suspected leak was in the first quarter of 1973. It is believed that the strontium-90 plume originated from leakage of PUREX strontium-recovery waste from a transfer line between tanks B-110 and B-111 (Section 3.2.2.4) in 1968.

The numerical model used in the simulations involves coupled flow and transport under partially saturated conditions. A mechanistic description of multivalent ion exchange is used in the model, rather than a constant K_D approach. The K_D approach is not expected to be valid because of the continuously changing solute concentrations during and following a leak event. As a consequence of the spatially and temporally varying groundwater composition, the K_D can be a strong function of time and depth, possibly ranging over many orders of magnitude. A mechanistic approach does not suffer from the limitation of a constant K_D and can handle easily variable electrolyte compositions such as is characteristic of a pulse release associated with a tank leak event.

For the simulations presented here, two sources are postulated for contaminant release to the vadose zone. One is from the base of tank B-110 at a depth of 16.5 m, and the other is assumed to be a transfer line leak between tanks B-110 and B-111 at a depth of 6 m. Both leaks are assumed to occur simultaneously for a duration of two weeks, but with slightly different compositions in order to fit the observed field data. Superimposed on the leak events is steady infiltration from the ground surface. The model calculations are calibrated against field data

collected by Serne et al. (2002) at borehole 299-E33-46. A 35-year time span is assumed from the leak events to the time field observations were conducted.

The ultimate goal of this work is to provide insight into processes affecting strontium migration at tank B-110, and to be able to predict with sufficient accuracy the long-term behavior of strontium in the Hanford vadose zone. This task is made more difficult, however, because of the large uncertainties inherent in characterization of the source term, including source composition, timing and duration. As a result, it is likely that different conceptual models for the source term may also lead to equally good fits to field observations. However, it is only by studying and comparing the different modeling approaches based on different conceptual formulations that the possible system behavior can be narrowed. This work presents one such model.

D.2.6.2 Model Formulation

The migration of contaminants released from the tank and transfer line leaks to the Hanford sediments lying in the vadose zone is a complicated interaction of hydrologic and chemical processes. A one-dimensional, sequentially coupled, reactive flow and transport model is used to approximately simulate the strontium plume behavior in the vicinity of tank B-110. For this purpose, the computer code FLOTRAN (Lichtner 2001) is used. FLOTRAN is a multi-component, multi-phase flow and transport code incorporating chemical processes involving aqueous, gaseous, and mineral species applicable to nonisothermal, variably saturated systems in one, two, or three spatial dimensions. In what follows, a brief summary of the processes included in the model simulations is presented.

D.2.6.2.1 Chemical Reactions. Chemical reactions included in the simulations involve local equilibrium reactions consisting of homogeneous complexing reactions in the aqueous phase and heterogeneous reactions involving gaseous species and ion exchange. Kinetic rate laws are used to describe reactions with minerals. Reactions are expressed in terms of a set of primary or basis species A_j belonging to the aqueous phase. These reactions may be written in the general form for homogeneous reactions involving aqueous species as

$$\sum_j \nu^l_{jl} A_j \Leftrightarrow A^l_l,$$

for aqueous secondary species A^l_l with stoichiometric reaction coefficients ν^l_{jl}. Heterogeneous reactions between aqueous species and gaseous species A^g_l have the form

$$\sum_j \nu^g_{jl} A_j \Leftrightarrow A^g_l,$$

and heterogeneous reactions between aqueous species and minerals M_m are described by

$$\sum_j \nu_{jm} A_j \Leftrightarrow M_m,$$

with stoichiometric coefficients ν^g_{jl} and ν_{jm}. Multivalent ion exchange reactions have the form

$$\frac{1}{z_k} A_k^{z_k+} + \frac{1}{z_l} X_{z_l} A_l \Leftrightarrow \frac{1}{z_k} X_{z_k} A_k + \frac{1}{z_l} A_l^{z_l+},$$

describing the exchange of cations $A_k^{z_k+}$ and $A_l^{z_l+}$ with valences z_i and z_j, respectively. The exchange site is denoted by X^-, with sorbed species $X_{z_l}A_l$ and $X_{z_k}A_k$.

D.2.6.2.2 Mass Conservation Equations. The time evolution of the vadose zone fluid-rock system following a tank leak event is described by mass conservation equations for each of the primary species and minerals in the system. A coupled system of nonlinear partial differential equations are solved for liquid saturation and mole fraction of water determined by the flow equations for water and air

$$\frac{\partial}{\partial t}\left[\phi\left(s_l n_l X_i^l + s_g n_g X_i^g\right)\right] + \nabla \bullet \left(F_i^l + F_i^g\right) = Q_i^l, \quad (i = water,\ air).$$

These equations are coupled through saturation and velocity fields to the multi-component reactive solute transport equations for each primary species

$$\frac{\partial}{\partial t}\left[\phi\left(s_l \Psi_j^l + s_g \Psi_j^g + \Gamma_j\right)\right] + \nabla \bullet \left(\Omega_j^l + \Omega_j^g\right) = Q_{water}^l \Psi_j^{0l} - \sum_m \nu_{jm} I_m.$$

These equations, in turn, are coupled to the mineral mass transfer equations

$$\frac{\partial \phi_m}{\partial t} = \overline{V}_m I_m.$$

In these equations, ϕ denotes the porosity of the sediment, s_l, s_g=1-s_l, liquid and gas saturations, n_l, n_g liquid and gas molar densities, X_i^l, X_i^g mole fractions of components water and air in liquid and gas phases ($\sum_i X_i^\pi = 1$), Q_i^l the source/sink term representing the tank leak, and F_i^l, F_i^g the liquid and gas Darcy fluxes consisting of advective and diffusive contributions defined by

$$F_i^\pi = q_\pi X_i^\pi - \phi s_\pi D_\pi n_\pi \nabla X_i^\pi,$$

where D_π denotes the diffusion coefficient corresponding to phase π, and q_π the Darcy velocity

$$q_\pi = -\frac{k_\pi k_\pi^r}{\mu_\pi}\left(\nabla p_\pi - \rho_\pi g z\right),$$

with pressure p_π of phase π, saturated permeability k_π, relative permeability k_π^r, acceleration of gravity g, z coordinate, fluid viscosity μ_π and density ρ_π. The total solute concentration is denoted by Ψ_j^l, Ψ_j^g in liquid and gas phases defined by

$$\Psi_j^\pi = \delta_{\pi l} c_j^\pi + \sum_i \nu_{ji}^\pi c_i^\pi,$$

with individual solute concentrations denoted by c_j^π for primary species and c_i^π for secondary species. Concentration of secondary species A_i^l appearing in homogeneous reactions and gaseous species A_i^g are determined from the mass action relations

$$c_i^\pi = \left(\gamma_i^\pi\right)^{-1} K_i^\pi \Pi\left(\gamma_j^l c_j^l\right)^{\nu_{ji}^\pi},$$

with equilibrium constant K_i^π and activity coefficients $\gamma_{i,j}^\pi$. The quantity Ψ_j^{0l} denotes the leak concentration associated with the source term. The quantity Γ_j denotes the total sorbed concentration involving both primary and secondary cations

$$\Gamma_j = S_j + \sum_i \nu_{ji}^I S_i,$$

where S_j, S_i refer to the sorption isotherms for primary and secondary cations, respectively. The quantities Ω_j^l, Ω_j^g refer to the total solute fluxes in liquid and gas phases defined by

$$\Omega_j^\pi = \delta_{\pi l} J_j^\pi + \sum_i \nu_{ji}^\pi J_i^\pi,$$

and J_j^π, J_i^π refers to the individual solute flux in liquid and gas phases defined by

$$J_k^\pi = q_\pi c_k^\pi - \phi s_\pi D_\pi \nabla c_k^\pi,$$

with species independent diffusion coefficients D_π. Mineral reaction rates are represented by the quantity I_m, derived from transition state theory, for the mth mineral with volume fraction ϕ_m and molar volume $\overline{V}_m$. The kinetic rate law has the form

$$I_m = -k_m a_m \frac{1 - K_m Q_m}{1 + \frac{1}{f_m} K_m Q_m},$$

for $\phi_m > 0$, or $K_m Q_m > 1$, and zero otherwise, where k_m refers to the kinetic rate constant, a_m the specific surface area, K_m the equilibrium constant, and Q_m the ion activity product defined by

$$Q_m = \Pi\left(\gamma_j^l c_j^l\right)^{\nu_{jm}},$$

with activity coefficients γ_j^l. The quantity f_m provides a cutoff value of the precipitation rate for cases where the factor $K_m Q_m$ becomes too large and would lead to an unacceptably large rate of reaction. A value of unity is used for f_m. Additional constitutive relations are needed to represent capillarity affects, including relative permeability and saturation as functions of capillary pressure $p_c = p_g - p_l$. These are provided through the van Genuchten relations, which are not discussed further (see e.g., Lichtner 1996).

Sorption processes involving ion exchange are incorporated in the model through a bulk cation exchange capacity (CEC) associated with the sediment as a whole, and not with individual minerals. The exchange site concentration ω is related to the CEC of the bulk sediment by the expression

$$\omega = \frac{N_{\text{sites}}}{\text{V}} = \frac{N_{\text{sites}}}{M_s} \frac{M_s}{V_s} \frac{V_s}{V} = \rho_s (1-\phi)\text{CEC},$$

where N_{sites} denotes the number of exchange sites within a control volume and ρ_s refers to the sediment grain density. The concentration of sorption sites is conserved by exchange reactions satisfying the relation

$$\omega = \sum_j z_j S_j.$$

For nonsorbing species, the corresponding sorbed concentration S_j vanishes. As written, these equations apply to a single sorption site, but may be easily extended to multiple sites by summing the sorbed concentration over the distinct sites.

Mass action equations corresponding to exchange reactions have the form

$$K_{ji} = \left(\frac{\lambda_j X_j}{a_j}\right)^{1/z_j} \left(\frac{a_i}{\lambda_i X_i}\right)^{1/z_i},$$

with selectivity coefficients K_{ji}, X_j denoting the sorbed fraction with activity coefficient correction λ_j, and a_j the aqueous activity of the jth exchange cation. Values for the exchange selectivity coefficients were derived from experiments performed in a batch reactor consisting of a well-stirred aqueous solution reacting with Hanford sediments with a fixed rock/fluid ratio (Lichtner and Zachara, Section D.2.3). In the experiments, the aqueous solution was allowed to equilibrate with the suspended solid. The experiments involved multi-component exchange with cations Na^+, K^+, Ca^{2+}, Mg^{2+}, and Sr^{2+}.

The model formulation presented above reduces to the constant K_D approximation for the situation where the local distribution coefficient, defined in dimensionless units as

$$K_j^D = \frac{\Gamma_j}{\phi s_l \Psi_j^l},$$

is equal to a constant. The distribution coefficient is inversely proportional to the porosity, saturation, and total solute concentration, and directly proportional to the sorbed concentration. In the case of constant K_j^D, the retardation can be calculated from the relation

$$R_j = 1 + K_j^D.$$

For a pulse release of concentrated fluid from a tank leak, K_j^D clearly cannot be constant over the entire flow path, but generally will vary strongly in the vicinity of the leak.

The mass conservation equations for flow and transport are solved sequentially using a fully implicit finite volume formulation. First, the flow equations are solved to provide an initial steady state saturation profile and liquid and gas velocity fields. The time evolution of the system is then calculated by first solving the flow equations over a single time step to provide transient liquid and gas phase velocities and saturation to the transport equations. Next, the transport equations are solved, generally with a smaller time step than was used to solve the flow equations. The liquid and gas velocities and saturation are linearly interpolated at intermediate times. After the transport equations have been solved over a time step, the mineral mass transfer equations are solved using an explicit finite difference scheme with the same time step as the transport equations. By controlling the maximum time step size allowed, a mass conserving scheme is obtained to solve the coupled flow and transport equations.

D.2.6.3 Model Calibration

The input data required to model contaminant migration in the vadose zone is fairly extensive and may be divided into three categories: sediment physical and chemical properties, source

term properties, and various supporting data including thermodynamic and kinetic data to represent chemical reactions among aqueous and gaseous species and minerals.

The source term presents one of the largest uncertainties in the model. Detailed knowledge of the composition, timing, and duration of the sources is generally unknown; however, some constraining information is available based on the work of Jones et al. (2001) using historical records of tank inventories combined with tank supernate speciation calculations (Lichtner, Section D.3.1). The lack of knowledge for the source term requires fitting the source term parameters in the model simulation to available field data. As a result, the number of fit parameters in the model is increased, thereby increasing the likelihood of obtaining a better fit to the field data. On the other hand, this offers the possibility of enabling certain properties of the source term to be deduced from the field data through inverse modeling. In addition to properties of the source term, the average infiltration rate is also unknown and is used as a fit parameter. To obtain values for these parameters, the model is calibrated against data for total species concentrations obtained from borehole 299-E33-46. The origin of this data is discussed next.

D.2.6.3.1 Field Data. The numerical model is calibrated against characterization of vadose sediment cores obtained from borehole 299-E33-46 over the past two years (Serne et al. 2002). The borehole is located approximately 15 ft (5 m) from the northeast edge of single-shell tank 241-B-110. Total depth of the borehole was 264.4 ft bgs; the groundwater table was encountered at 255.8 ft bgs. During drilling, a total of 33 two-ft long, 4-inch diameter splitspoon core samples were collected between 10 and 254 ft bgs which is an average of every 7.5 ft. The splitspoon samples were taken ahead of the casing by driving a splitspoon sampler into the undisturbed formations below the casing. Grab samples were collected between these core sample intervals to yield near continuous samples to a depth of 78.3 m (257 ft). Geologic logging occurred after each core segment was emptied into an open plastic container, followed by photographing and sub-sampling for physical and chemical characterization. In addition, 54 out of a total of 120 composite grab samples were opened, sub-sampled, logged, and photographed.

Immediately upon extracting material from each core liner or grab sample container, moisture samples were collected. An attempt was made to sample the finer grained and/or wetter materials as well as distinct hydrogeologic units, while at the same time trying to avoid slough and/or other unrepresentative portions of the sediment profile. The remaining portions of the samples were then used for a brief visual geologic evaluation and for chemical and mineralogical characterization.

Following geologic examination, the core and selected grab samples were sub-sampled for moisture content, gamma-emission radiocounting, tritium and strontium-90 determinations, total carbon and inorganic carbon content, and 8 M nitric acid extracts (which provide a measure of the total leachable sediment content of contaminants) and one-to-one sediment to water extracts (which provide soil pH, electrical conductivity, cation, and anion data and water soluble contaminant data). The remaining sediment from each sleeve was then sealed and placed in cold storage. Later, additional aliquots of selected sleeves or grab samples were removed to measure particle size distribution and mineralogy and to squeeze porewater. Details on characterization methodologies and results are found in Serne et al. (2002).

It must be emphasized that it is not generally possible to distinguish directly between aqueous, solid, and sorbed concentrations in the vadose zone sediments obtained from the borehole. Dilution corrected, 1:1 sediment to water extracts were used to estimate the aqueous composition of the vadose zone porewater. It would also be possible to determine the total mass that was ion exchangeable using some other fluid such as 1 M ammonium acetate to estimate the sorbed concentrations; however, this has not been done to date.

D.2.6.3.2 Calibration Approach. The chemical system is modeled using 12 primary species: Ca^{2+}, Mg^{2+}, Sr^{2+}, K^+, Na^+, H^+, NO_3^-, Cl^-, F^-, HCO_3^-, HPO_4^{2-}, and $EDTA^{4-}$. This represents only a subset of the complete set of species in the tank waste and, as a result, no attempt is made to charge balance the waste composition leaked from the tank and transfer line. Because of the high total carbonate concentration assumed for the source terms of 0.4 mol/L, a greater cation concentration would be needed to balance the solution. Alternatively, it is possible that a portion of the total measured carbonate could be attributed to solids such as calcium carbonate leading to a lower aqueous concentration. For simplicity, the system is assumed to be isothermal with a constant temperature of 25 °C. Aqueous complexes, gaseous species, and minerals included in the calculations are listed in Table D.21. For simplicity, identical material properties are used for the backfill region surrounding the tank and the Hanford formation H2 as listed in Table D.22. Data for sorption selectivity coefficients are taken from Lichtner and Zachara (Section D.2.3).

To fit the field data from borehole 299-E33-46, a number of parameters in the model were varied to obtain as reasonable a representation as possible to the data. The parameters that were "optimally fit" were the leak rate, infiltration rate, leak composition, infiltrating fluid composition, cation exchange capacity, and kinetic rate constants for minerals calcite ($CaCO_3$), fluorite (CaF_2) and whitlockite [$Ca_3(PO_4)_2$], which were included in the simulations. Ion exchange selectivity coefficients for cations Ca^{2+}, Mg^{2+}, Sr^{2+}, K^+, and Na^+, were not adjusted, but taken directly from fits to batch experiments with Hanford sediments (Lichtner and Zachara, Section D.2.3) with the values listed in Table D.23.

Two source terms were used in the model. Evidence exists from borehole 299-E33-46 for more than a single source of contaminants. A clear bimodal distribution is present in field measurements for the concentrations of species sodium, bicarbonate, and fluoride, and pH, and less so for phosphate and potassium (Serne et al. 2002). Nitrate shows a large single peak associated with the deeper sodium peak, and a much smaller peak associated with the upper sodium peak. There are several possibilities to account for this bimodal distribution in species concentrations. One is to assume that more than one leak event took place from the same source location. However, historical evidence suggests that the most probable time for the leak was in 1968 associated with the cascade line piping that drained liquids from tank B-110 into tank B-111. Another possibility is to assume that two leaks took place simultaneously from different sources located at different depths. Evidence exists for this possibility with one leak occurring from the transfer line between tanks B-110 and B-111, and the other from overfilling tank B-110 at the same time. A third possibility is that flow in the highly heterogeneous sediments was both lateral and vertical due to the presence of capillary barriers in the vadose zone, providing different fluid pathways from a single leak event. The second possibility, allowing for two simultaneous leaks from two different depths, is explored further in this report. The two source terms correspond to the transfer line leak and a leak directly from the base of tank B-110.

Table D.21. Aqueous Complexes Included in the Model Calculations. The corresponding species log K values are listed in Table D.24 for the initial fluid distribution of species results.

Aqueous Complexes

EDTAH---	CaOH+	KOH(aq)	NaNO3(aq)
EDTAH2--	CaP2O7--	KP2O7---	NaOH(aq)
EDTAH3-	CaPO4-	Mg4(OH)4++++	NaP2O7---
EDTAH4(aq)	H2F2(aq)	MgCO3(aq)	OH-
EDTAH5+	H2P2O7--	MgCl+	P2O7----
KEDTA---	H2PO3F(aq)	MgF+	PO3F--
MgEDTA--	H2PO4-	MgH2PO4+	PO4---
MgEDTAH-	H3P2O7-	MgHCO3+	SrCO3(aq)
CO2(aq)	H3PO4(aq)	MgHPO4(aq)	SrHCO3+
CO3--	H4P2O7(aq)	MgP2O7--	SrCl+
CaCO3(aq)	HCl(aq)	MgPO4-	SrEDTA--
CaCl+	HF(aq)	Na2P2O7--	SrF+
CaCl2(aq)	HF2-	NaCO3-	SrH2PO4+
CaF+	HNO3(aq)	NaCl(aq)	SrHPO4(aq)
CaH2PO4+	HP2O7---	NaF(aq)	SrNO3+
CaHCO3+	HPO3F-	NaHCO3(aq)	SrOH+
CaHPO4(aq)	KCl(aq)	NaHP2O7--	SrP2O7--
CaNO3+	KHPO4-	NaHPO4-	

Gaseous Species

CO2(g)

Minerals

Calcite	Magnesite	Fluorapatite	Fluorite
Strontianite	Whitlockite		

Table D.22. List of Material Properties and van-Genuchten Parameters Used in the Model Simulations

Material Properties		
Rock Density	ρ_r	2800 kg/m^3
Tortuosity	$\frac{}{\tau}$	0.5
Gas Diffusivity	D_g	2.13 10^{-5} cm^2/s
Porosity	ϕ	0.33
Saturated Permeability	k_{sat}	5.5 10^{-12} m^2
Van-Genuchten Parameters		
Residual Saturation	s_r	0.095
Lambda	λ	0.429
Alpha	α	2.55 10^{-4} Pa^{-1}

Table D.23. Fitted Selectivity Coefficients Relative to Na^+ for Batch Experiments with Hanford Sediment Assuming a CEC of 50.2 μeq/g taken from Section D.2.3

$K_{Na/Sr}$	9.508
$K_{Na/Ca}$	8.759
$K_{Na/Mg}$	6.072
$K_{Na/K}$	21.010

A two-stage approach was used to fit the data. First, the position, peak concentration, and peak width for the species NO_3^- was fit by adjusting the infiltration rate, leak rate, and leak concentrations of NO_3^- in the two source terms. This species acts as a nonreactive tracer and is unaffected by sorption and mineral reactions. Concentrations for NO_3^- of 0.062 and 0.02 mol/L were determined as best fit values for the tank and transfer line leaks, respectively. A single leak rate of 0.0002 kg/s and an infiltration rate of 0.04 m/yr were chosen as best fits to the field data. The leak duration was fixed at two weeks for both sources. It must be emphasized that because the calculation was being done in a single spatial dimension, the fitted leak rate had little bearing on the actual leak rate.

Next, the sodium leak concentrations were adjusted to give a fit to the peak sodium concentrations measured in the field. Values of 0.65 and 0.5 mol/L were obtained for the tank and transfer line leaks, respectively. To match the pH, it was found necessary to include calcite in the reacting sediment. The high carbonate concentration in the source terms was found essential in order to cause precipitation of calcite, which in turn enabled a more reasonable fit to the calcium concentration (which otherwise was predicted to be much too high). However, it was found necessary to use a rather small effective kinetic rate constant for calcite of 10^{-17} mol/cm^3/s, because otherwise, the calcium concentration was predicted to be much too low governed by the solubility of calcite at pH 9.

The values obtained for sodium and nitrate concentrations in the source terms are considerably less than the projected leak concentration estimated by Jones et al. (2001). This discrepancy could be related to the one-dimensional nature of the simulations. A three-dimensional simulation would be expected to give greater dilution and thus lead to higher source term concentrations.

The initial and infiltrating fluid composition are taken to be identical with the composition listed in Table D.24 with the exception of strontium for which a lower value was used in the infiltrating fluid to represent rainwater. A pH of 7.5 is assumed, and the fluid is taken to be in equilibrium with calcite, fluorapatite, and fluorite. The leak composition is listed in Table D.25 for the tank leak and in Table D.26 for the transfer line leak. A pH of 10 and a fixed total carbonate concentration of 0.1 M are used in both cases. The source term fluid compositions were constrained to be in equilibrium with calcite and magnesite. Strontianite was saturated in the line leak, but undersaturated in the tank leak fluid. Fluorapatite was not allowed to react although it was supersaturated in both source term fluids.

Table D.24. Initial and Infiltrating Fluid Composition

temperature = 2.5000E+01 [C] pressure = 1.0000E+00 [bars]
iter = 13 ionic strength = 3.9554E-02
solution density = 1.0013 [g/cm^3]
pH = 7.5000

species	molality	tot	act. coef.	act. ratio/H+	constraint
Ca++	8.9945E-03	9.0651E-03	5.1219E-01	1.2829E+01	3 Calcite
Mg++	9.8282E-07	1.0000E-06	5.4265E-01	8.8677E+00	1 total
K+	2.4984E-03	2.5000E-03	8.2527E-01	4.8353E+00	1 total
Na+	9.9604E-03	1.0000E-02	8.3368E-01	5.4359E+00	1 total
H+	3.6509E-08	2.5152E-05	8.6615E-01	0.0000E+00	8 pH
NO3-	9.7702E-05	1.0000E-04	8.2527E-01	-1.1448E+01	1 total
Cl-	2.9681E-02	2.9744E-02	8.2527E-01	-8.9651E+00	-1 chrg
HCO3-	5.8862E-04	6.6705E-04	8.3368E-01	-1.0668E+01	4 CO2(g)
HPO4--	4.7568E-11	1.2651E-10	4.7768E-01	-2.5198E+01	3 Fluorapatite
EDTA----	3.5220E-20	1.0000E-16	5.1486E-02	-4.9204E+01	1 total
F-	1.7212E-04	1.7600E-04	8.2958E-01	-1.1202E+01	3 Fluorite
Sr++	1.4815E-05	1.5000E-05	4.9549E-01	1.0046E+01	1 total

complex	molality	act. coef.	act/H+	log K
CO2(aq)	3.40620E-05	1.0000	-4.4677	6.3414
NaCl(aq)	3.35901E-05	1.0000	-4.4738	-0.78213
CaHCO3+	2.99305E-05	0.83368	2.9137	1.0429
CaCl+	2.69824E-05	0.83368	2.8687	-0.70039
CaCO3(aq)	7.00620E-06	1.0000	-5.1545	-7.0088
NaHCO3(aq)	5.83230E-06	1.0000	-5.2342	0.15573
CaF+	3.75354E-06	0.83368	2.0120	0.67736
CaNO3+	2.23308E-06	0.83368	1.7865	0.70000
KCl(aq)	1.59570E-06	1.0000	-5.7970	-1.5004
CO3--	1.50897E-06	0.48673	-20.697	-10.325
CaCl2(aq)	6.13881E-07	1.0000	-6.2119	-0.65346
OH-	3.89082E-07	0.82958	-13.848	-13.991
SrCl+	1.20370E-07	0.83368	0.51811	-0.25328
NaF(aq)	1.17905E-07	1.0000	-6.9285	-1.0024
NaNO3(aq)	6.04970E-08	1.0000	-7.2183	-1.0440
SrHCO3+	5.45218E-08	1.0000	-7.2634	1.1800
CaOH+	2.46835E-08	0.83368	-0.17000	-12.850
NaCO3-	2.36331E-08	0.83368	-15.064	-9.8156
MgCl+	1.13871E-08	0.83368	-0.50599	-0.13865
HF(aq)	6.58409E-09	1.0000	-8.1815	3.1638
SrNO3+	4.47950E-09	0.83368	-0.91118	0.80000
HCl(aq)	3.88149E-09	1.0000	-8.4110	0.69993
SrCO3(aq)	3.85744E-09	1.0000	-8.4137	-7.4703
MgHCO3+	3.38620E-09	0.83368	-1.0327	1.0329
MgF+	2.03826E-09	0.83368	-1.2531	1.3486
SrF+	1.71528E-09	0.83368	-1.3281	0.13493
NaOH(aq)	4.17490E-10	1.0000	-9.3794	-14.799
MgCO3(aq)	3.64440E-10	1.0000	-9.4384	-7.3562
KOH(aq)	2.26077E-10	1.0000	-9.6457	-14.460
CaHPO4(aq)	5.75261E-11	1.0000	-10.240	2.7400
SrOH+	1.42802E-11	0.83368	-3.4077	-13.290
H2PO4-	1.36997E-11	0.83368	-18.301	7.2013
CaPO4-	5.45838E-12	0.83368	-18.701	-5.8618
NaHPO4-	1.88249E-12	0.83368	-19.163	0.92000
KHPO4-	3.38619E-13	0.83368	-19.908	0.78000
HF2-	2.71907E-13	0.83368	-20.003	2.5461
HNO3(aq)	1.25418E-13	1.0000	-12.902	-1.3081
SrHPO4(aq)	1.91510E-14	1.0000	-13.718	2.0600
MgHPO4(aq)	9.85035E-15	1.0000	-14.007	2.9100
PO3F--	3.39855E-15	0.47768	-29.344	7.1993
PO4---	1.82778E-15	0.18881	-37.051	-12.318

MgPO4-	8.50454E-16	0.83368	-22.508	-5.7328
H2F2(aq)	1.19496E-16	1.0000	-15.923	6.7680
MgEDTA--	8.39400E-17	0.45868	-30.951	10.600
H3PO4(aq)	5.27239E-17	1.0000	-16.278	9.3656
SrEDTA--	1.31432E-17	0.55656	-31.756	8.7400
EDTAH---	2.76980E-18	0.18881	-39.870	9.9600
HPO3F-	7.74339E-19	0.83368	-25.549	11.299
CaH2PO4+	9.97387E-20	0.83368	-11.564	1.4000
EDTAH2--	6.41171E-20	0.45868	-34.068	16.210
MgEDTAH-	4.66536E-20	0.82527	-26.769	15.100
CaP2O7--	5.63485E-21	0.47768	-35.124	3.0537
KEDTA---	9.92439E-22	0.18881	-43.316	1.7000
SrH2PO4+	3.39773E-23	0.83368	-15.031	0.73000
HP2O7---	2.27363E-23	0.18881	-44.956	5.4198
MgH2PO4+	2.10112E-23	0.83368	-15.240	1.6600
NaHP2O7--	2.00840E-24	0.47768	-38.572	6.8498
P2O7----	1.70647E-24	5.14862E-02	-53.518	-3.7691
MgP2O7--	1.64503E-24	0.47768	-38.659	3.4554
H2P2O7--	1.24914E-24	0.47768	-38.779	12.063
NaP2O7---	7.94062E-25	0.18881	-46.413	-1.4563
EDTAH3-	5.03373E-25	0.82527	-31.736	18.860
SrP2O7--	3.57444E-25	0.47768	-39.322	1.6537
Na2P2O7--	2.07027E-25	0.47768	-39.559	0.44370
KP2O7---	1.99262E-25	0.18881	-47.013	-1.4517
H2PO3F(aq)	1.30567E-25	1.0000	-24.884	12.105
H3P2O7-	4.95892E-30	0.83368	-36.742	14.403
EDTAH4(aq)	1.54342E-30	1.0000	-29.812	20.930
Mg4(OH)4++++	2.25544E-34	6.37896E-02	-3.8964	-39.750
EDTAH5+	2.02251E-35	0.82527	-27.257	23.464
H4P2O7(aq)	4.34919E-36	1.0000	-35.362	15.925

mineral saturation indices

mineral	SI (Log KQ)	log K
Calcite	-5.12724E-09	-1.85424E+00
Fluorite	-7.45723E-09	1.00272E+01
Fluorapatite	-3.88225E-08	2.49589E+01
Strontianite	-6.34979E-01	3.08450E-01
Dolomite	-2.75194E+00	-2.52402E+00
Exch-Solid	-3.08072E+00	-1.00000E+00
Magnesite	-4.38065E+00	-2.29848E+00
Halite	-5.28192E+00	-1.59027E+00
Nesquehonite	-7.22080E+00	-5.13863E+00
NaNO3(s)	-7.26479E+00	-1.09056E+00
Whitlockite	-9.09160E+00	4.20526E+00
Gaylussite	-9.28047E+00	-1.11641E+01
Portlandite	-9.89284E+00	-2.25562E+01

gas	log partial pressure	pressure [bars]	log K
CO2(g)	-3.000	1.0000E-03	7.8092

Table D.25. Source Composition for the Tank B-110 Leak

temperature = 2.5000E+01 [C] pressure = 1.0000E+00 [bars]
iter = 15 ionic strength = 8.0591E-01
solution density = 1.0444 [g/cm^3]
pH = 10.000

species	molality	tot	act. coef.	act. ratio/H+	constraint
Ca++	4.2341E-07	9.4253E-06	2.3460E-01	1.3442E+01	3 Calcite
Mg++	9.0078E-07	1.6961E-05	3.0671E-01	1.3770E+01	3 Magnesite
K+	1.4926E-02	1.5000E-02	6.1597E-01	8.0814E+00	1 total
Na+	5.4677E-01	6.5000E-01	6.6453E-01	9.6453E+00	1 total
H+	1.2374E-10	2.5472E-01	8.0814E-01	0.0000E+00	8 pH
NO3-	6.0771E-02	6.2000E-02	6.1597E-01	-1.1124E+01	1 total
Cl-	5.3030E-03	5.5000E-03	6.1597E-01	-1.2183E+01	1 total
HCO3-	1.0830E-01	4.0000E-01	6.6453E-01	-1.0873E+01	1 total
HPO4--	5.6307E-03	1.0000E-02	1.5521E-01	-2.2064E+01	1 total
EDTA----	2.2031E-18	1.0000E-16	4.6195E-04	-5.7287E+01	1 total
F-	9.7733E-03	1.0000E-02	6.4155E-01	-1.1917E+01	1 total
Sr++	1.6469E-17	1.0000E-16	1.9558E-01	3.0316E+00	1 total

complex	molality	act. coef.	act/H+	log K
CO3--	0.19407	0.17551	-20.527	-10.325
NaCO3-	6.01669E-02	0.66453	-11.128	-9.8156
NaHCO3(aq)	3.74274E-02	1.0000	-1.4268	0.15573
NaHPO4-	3.97462E-03	0.66453	-12.308	0.92000
NaNO3(aq)	1.22894E-03	1.0000	-2.9105	-1.0440
PO4---	3.05285E-04	1.37496E-02	-33.238	-12.318
NaF(aq)	2.26555E-04	1.0000	-3.6448	-1.0024
NaCl(aq)	1.96005E-04	1.0000	-3.7077	-0.78213
OH-	1.59098E-04	0.64155	-13.706	-13.991
KHPO4-	7.28573E-05	0.66453	-14.045	0.78000
CO2(aq)	1.57971E-05	1.0000	-4.8014	6.3414
MgCO3(aq)	8.75545E-06	1.0000	-5.0577	-7.3562
CaCO3(aq)	7.00620E-06	1.0000	-5.1545	-7.0088
MgPO4-	6.72229E-06	0.66453	-15.080	-5.7328
NaOH(aq)	5.77680E-06	1.0000	-5.2383	-14.799
H2PO4-	2.09041E-06	0.66453	-15.587	7.2013
Na2P2O7--	1.80464E-06	0.15521	-25.559	0.44370
CaPO4-	1.79588E-06	0.66453	-15.653	-5.8618
KCl(aq)	9.48868E-07	1.0000	-6.0228	-1.5004
NaP2O7---	7.05850E-07	1.37496E-02	-35.874	-1.4563
MgHCO3+	3.22740E-07	0.66453	3.4163	1.0329
KOH(aq)	3.18783E-07	1.0000	-6.4965	-14.460
P2O7----	2.81364E-07	4.61947E-04	-46.181	-3.7691
MgHPO4(aq)	1.96260E-07	1.0000	-6.7072	2.9100
CaHCO3+	1.18741E-07	0.66453	2.9821	1.0429
MgF+	5.81686E-08	0.66453	2.6722	1.3486
PO3F--	5.58645E-08	0.15521	-27.068	7.1993
CaHPO4(aq)	4.77080E-08	1.0000	-7.3214	2.7400
CaNO3+	2.80439E-08	0.66453	2.3553	0.70000
KP2O7---	1.80501E-08	1.37496E-02	-37.466	-1.4517
CaF+	4.45880E-09	0.66453	1.5567	0.67736
MgP2O7--	3.87970E-09	0.15521	-28.226	3.4554
HP2O7---	1.46062E-09	1.37496E-02	-38.558	5.4198
NaHP2O7--	1.26524E-09	0.15521	-28.713	6.8498
MgCl+	9.86870E-10	0.66453	0.90175	-0.13865
HF(aq)	9.14310E-10	1.0000	-9.0389	3.1638
CaP2O7--	5.53163E-10	0.15521	-29.072	3.0537
CaOH+	2.11147E-10	0.66453	0.23207	-12.850
CaCl+	9.73359E-11	0.66453	-0.10424	-0.70039
HF2-	2.08019E-12	0.66453	-21.589	2.5461
HCl(aq)	1.63686E-12	1.0000	-11.786	0.69993
CaCl2(aq)	2.35399E-13	1.0000	-12.628	-0.65346

HNO3(aq)	1.84127E-13	1.0000	-12.735	-1.3081
H2P2O7--	5.68709E-14	0.15521	-33.060	12.063
H3PO4(aq)	2.02788E-14	1.0000	-13.693	9.3656
HPO3F-	1.64078E-14	0.66453	-23.692	11.299
MgEDTA--	9.76952E-17	0.11458	-35.825	10.600
SrCO3(aq)	7.85005E-17	1.0000	-16.105	-7.4703
SrHCO3+	3.50868E-18	1.0000	-17.455	1.1800
H2F2(aq)	2.30435E-18	1.0000	-17.637	6.7680
MgH2PO4+	1.66080E-18	0.66453	-7.8722	1.6600
SrNO3+	1.14482E-18	0.66453	-8.0338	0.80000
CaH2PO4+	3.28154E-19	0.66453	-8.5764	1.4000
SrHPO4(aq)	3.23215E-19	1.0000	-18.491	2.0600
EDTAH---	6.75063E-20	1.37496E-02	-48.893	9.9600
SrF+	4.14654E-20	0.66453	-9.4748	0.13493
KEDTA---	3.41067E-20	1.37496E-02	-49.190	1.7000
SrCl+	8.83662E-21	0.66453	-10.146	-0.25328
SrOH+	2.48591E-21	0.66453	-10.697	-13.290
SrP2O7--	7.14090E-22	0.15521	-40.961	1.6537
H3P2O7-	2.91034E-22	0.66453	-31.444	14.403
MgEDTAH-	5.74667E-23	0.61597	-32.148	15.100
H2PO3F(aq)	6.97373E-24	1.0000	-23.157	12.105
Mg4(OH)4++++	6.05726E-24	1.71034E-03	16.412	-39.750
EDTAH2--	1.44057E-24	0.11458	-43.656	16.210
SrEDTA--	5.30650E-30	0.33949	-49.090	8.7400
SrH2PO4+	2.27498E-30	0.66453	-19.736	0.73000
H4P2O7(aq)	6.43396E-31	1.0000	-30.192	15.925
EDTAH3-	1.19695E-32	0.61597	-41.829	18.860
EDTAH4(aq)	8.66229E-41	1.0000	-40.062	20.930
EDTAH5+	4.80924E-48	0.61597	-37.410	23.464

mineral saturation indices

mineral	SI (Log KQ)	log K
Fluorapatite	8.56616E+00	2.49589E+01
Dolomite	1.62871E+00	-2.52402E+00
Calcite	0.00000E+00	-1.85424E+00
Magnesite	0.00000E+00	-2.29848E+00
Gaylussite	-1.33207E+00	-1.11641E+01
Fluorite	-1.38111E+00	1.00272E+01
Exch-Solid	-1.43968E+00	-1.00000E+00
Nesquehonite	-2.84014E+00	-5.13863E+00
Whitlockite	-2.92046E+00	4.20526E+00
NaNO3(s)	-2.95699E+00	-1.09056E+00
Halite	-4.51587E+00	-1.59027E+00
Strontianite	-8.32641E+00	3.08450E-01
Portlandite	-9.55915E+00	-2.25562E+01

gas	log partial pressure	pressure [bars]	log K
CO2(g)	-3.334	4.6378E-04	7.8092

SrHPO4(aq)	7.22957E-11	1.0000	-10.141	2.0600
CaCl2(aq)	2.25092E-11	1.0000	-10.648	-0.65346
SrCl+	1.76375E-11	0.66611	-0.84700	-0.25328
HCl(aq)	1.65879E-11	1.0000	-10.780	0.69993
SrF+	8.23902E-12	0.66611	-1.1776	0.13493
HF2-	2.11209E-12	0.66611	-21.582	2.5461
SrOH+	4.89617E-13	0.66611	-2.4036	-13.290
SrP2O7--	1.76774E-13	0.15889	-32.566	1.6537
H2P2O7--	7.13107E-14	0.15889	-32.960	12.063
HNO3(aq)	5.99569E-14	1.0000	-13.222	-1.3081
H3PO4(aq)	2.29754E-14	1.0000	-13.639	9.3656
HPO3F-	1.87095E-14	0.66611	-23.634	11.299
MgEDTA--	9.77283E-17	0.11840	-35.823	10.600
H2F2(aq)	2.34523E-18	1.0000	-17.630	6.7680
MgH2PO4+	1.74785E-18	0.66611	-7.8509	1.6600
CaH2PO4+	3.45354E-19	0.66611	-8.5552	1.4000
EDTAH---	7.06853E-20	1.45786E-02	-48.870	9.9600
KEDTA---	3.58374E-21	1.45786E-02	-50.165	1.7000
SrEDTA--	1.15685E-21	0.34132	-40.750	8.7400
SrH2PO4+	5.07656E-22	0.66611	-11.388	0.73000
H3P2O7-	3.72698E-22	0.66611	-31.335	14.403
MgEDTAH-	5.91253E-23	0.61888	-32.135	15.100
H2PO3F(aq)	7.97087E-24	1.0000	-23.098	12.105
Mg4(OH)4++++	4.23134E-24	1.84018E-03	16.253	-39.750
EDTAH2--	1.54770E-24	0.11840	-43.623	16.210
H4P2O7(aq)	8.25887E-31	1.0000	-30.083	15.925
EDTAH3-	1.32263E-32	0.61888	-41.785	18.860
EDTAH4(aq)	9.61712E-41	1.0000	-40.017	20.930
EDTAH5+	5.31421E-48	0.61888	-37.368	23.464

mineral saturation indices

mineral	SI (Log KQ)	log K
Fluorapatite	8.57762E+00	2.49589E+01
Dolomite	1.62871E+00	-2.52402E+00
Calcite	0.00000E+00	-1.85424E+00
Magnesite	0.00000E+00	-2.29848E+00
Strontianite	0.00000E+00	3.08450E-01
Fluorite	-1.40448E+00	1.00272E+01
Gaylussite	-1.53860E+00	-1.11641E+01
Exch-Solid	-1.55845E+00	-1.00000E+00
Nesquehonite	-2.84014E+00	-5.13863E+00
Whitlockite	-2.90503E+00	4.20526E+00
NaNO3(s)	-3.56303E+00	-1.09056E+00
Halite	-3.62885E+00	-1.59027E+00
Portlandite	-9.59015E+00	-2.25562E+01

gas	log partial pressure	pressure [bars]	log K
CO2(g)	-3.303	4.9810E-04	7.8092

D.2.6.4 Model Results

The resulting fit to the field data is shown in Figure D.41 and Figure D.42. As can be seen from Figure D.41, non-radioactive strontium above the tank remains essentially in place. This is to be expected because of its strong retardation of strontium in dilute solutions. In the vicinity of the leaks, strontium is displaced by the high sodium concentration in the leak fluid. The displaced naturally occurring strontium reaches a depth of approximately 35 m. The calculated aqueous strontium concentration profile appears to be shifted upwards somewhat compared to the field data but otherwise has a similar shape suggesting that strontium retarded too stongly. Although not attempted, it is possible that through slight adjustment in the exchange selectivity coefficients, a better fit could have been obtained. It should be noted that because of the rather high ambient strontium concentration and very low strontium-90 concentration, strontium-90 released from the transfer line leak has very little influence on the calculated strontium profile. The model simulations do not distinguish between stable and radioactive strontium. The sodium peak is slightly retarded compared to the unretarded advance of nitrate, but less so in the simulation compared to the field. The double peaks observed in the "field" for sodium, carbonate, fluoride, and pH are reproduced in the simulation.

As is apparent from the figures, phosphate and fluoride are slightly retarded compared to the nitrate peaks. The concentration of solid precipitates for fluorite and whitlockite are shown in Figure D.43. Three peaks in the solid concentrations are discernable. Note that in the figure, the concentration scale for whitlockite is reduced by a factor of 0.05 compared to fluorite. The upper two peaks coincide with the position of the source terms at 6 m and 16.5 m.

The sorbed concentration profile for strontium is shown in Figure D.44. The top peak results from desorption at the surface of the initially sorbed strontium in the sediment profile. The second peak at a depth of approximately 20 m is produced by the transfer line leak at a depth of 6 m, resulting in desorption of natural strontium and displacement of sorbed strontium from the sediment. The third peak is from the tank leak at the 16.5 m depth, which displaces additional natural strontium from the sediment. The calculated middle peak in sorbed strontium at 20 m corresponds nicely to the position of strontium-90 observed in borehole 299-E33-46. It should be recalled that the position of the strontium peak is not a fitted value, but is predicted by the model through fitting the source terms to the sodium and nitrate profiles. Had a different depth been used to represent the transfer line leak, the second strontium peak would have occurred at a different depth. The good agreement with the observed strontium-90 profile is consistent with the basic conceptual model of superimposed leaks from two different sources at different depths.

To investigate the implications of the model calculations on the long-term behavior of strontium in the vadose zone, the time evolution of the sorbed strontium concentration is shown in Figure D.45 plotted at three different times indicated in the figure. As can be seen from the figure, very little downward migration occurs over the 100 years of the simulation.

Figure D.41. Vertical Profiles for Ca^{2+}, K^+, HPO_4^{2-}, and F^- Comparing Field Observations with FLOTRAN (FT) After an Elapsed Time of 35 Years

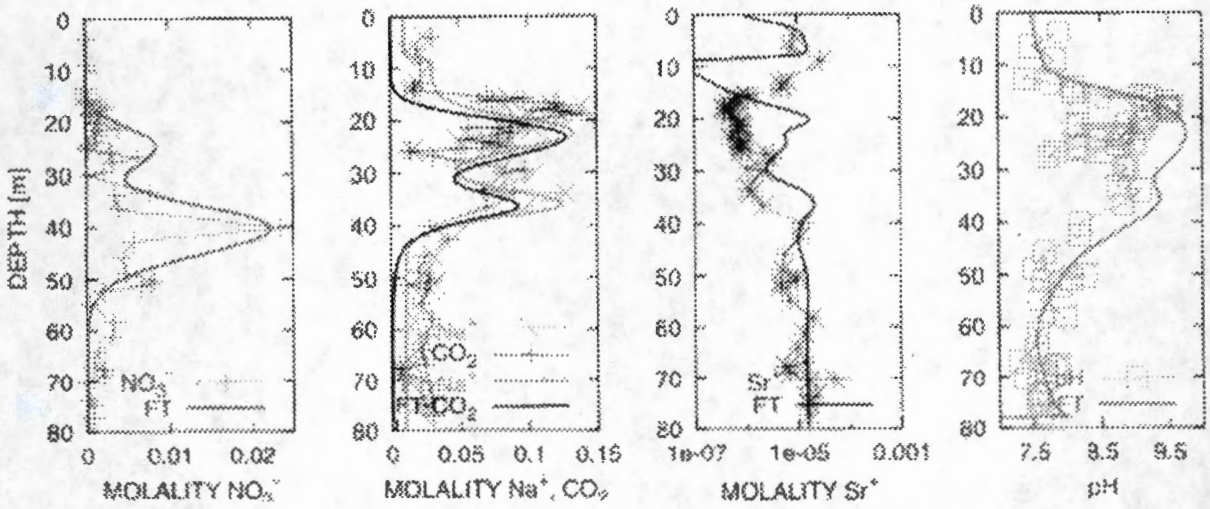

Figure D.42. Vertical Profiles for Ca^{2+}, K^+, HPO_4^{2-}, and F^- Comparing Field Observations with FLOTRAN (FT) After an Elapsed Time of 35 Years

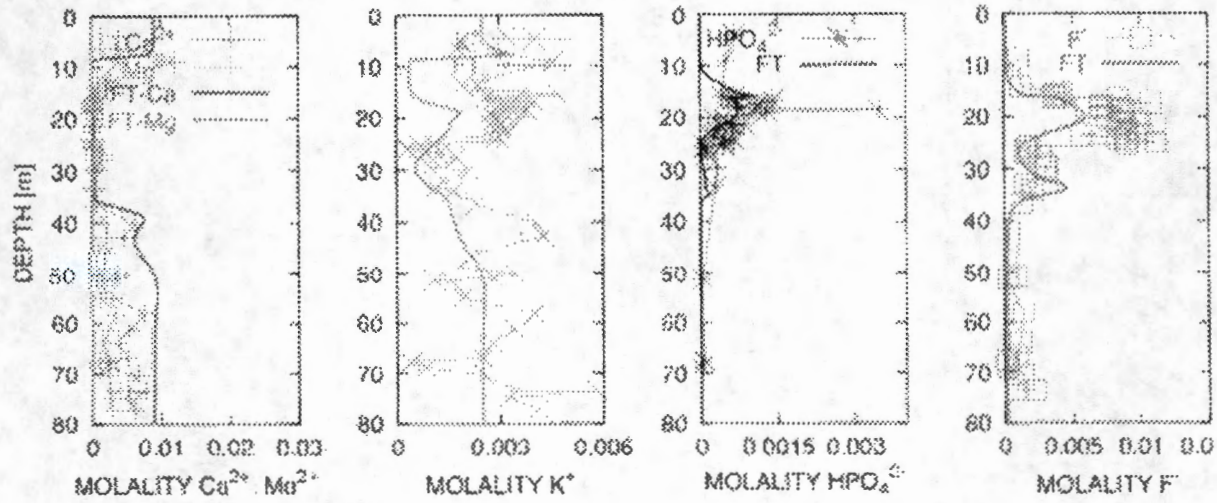

Figure D.43. Depth Profiles for Minerals Fluorite and Whitlockite After an Elapsed Time of 35 Years

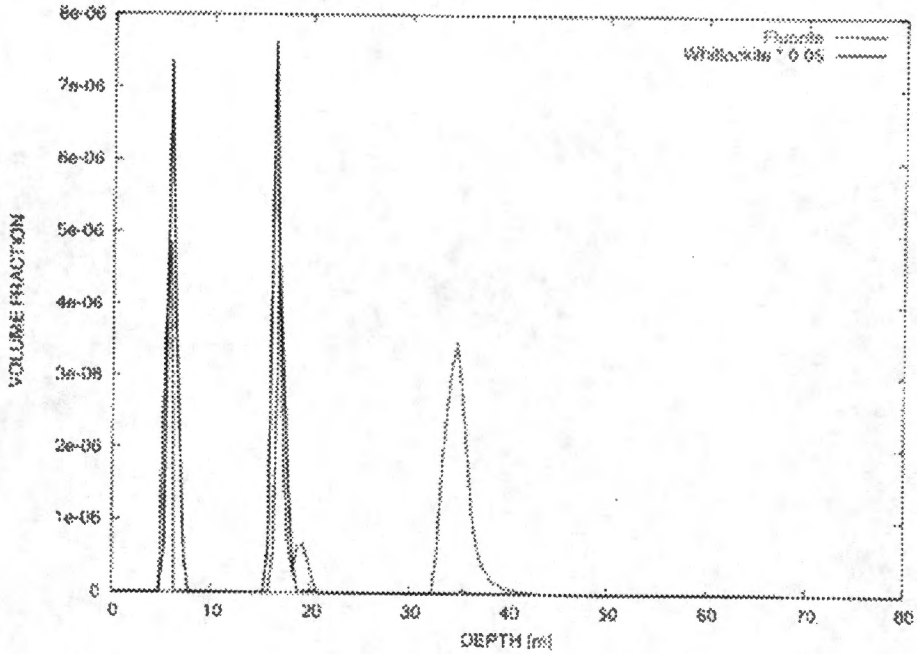

Figure D.44. Strontium Sorption Profile After an Elapsed Time of 35 Years

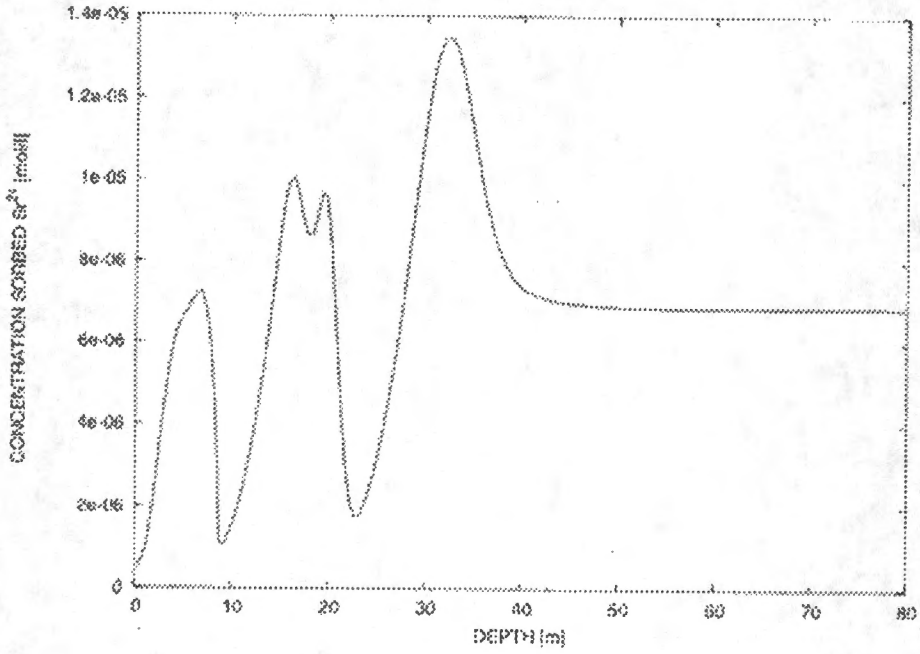

Figure D.45. Time Evolution of Sorbed Strontium Plotted as a Function of Depth for Times of 25, 50, and 100 Years

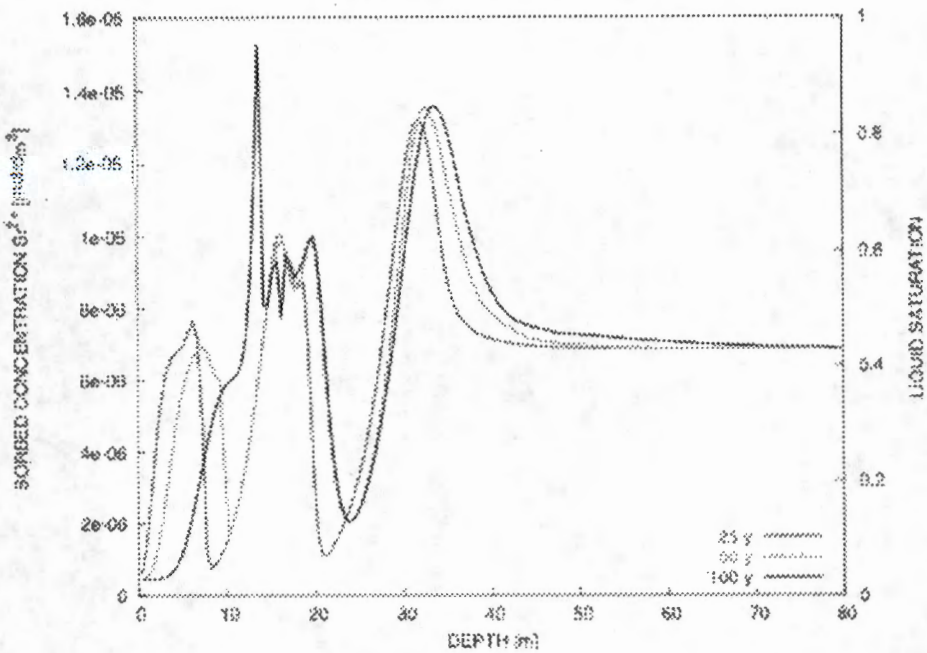

D.2.6.5 Discussion

Several points are noted regarding the modeling exercise:

- The fitted tank leak concentrations for nitrate and sodium are substantially less than that estimated from historical records obtained from performing a speciation calculation for the tank supernate (Lichtner, Section D.3.1).

- The one-dimensional model does not allow for lateral spreading which would be expected to lead to faster mixing with the ambient groundwater, which in turn would lead to more dilute solutions and greater retardation.

- The leak fluid composition used in the simulation is highly sensitive to the leak rate. A slower leak rate, keeping the leak duration fixed, requires a higher leak concentration to fit the data because of the greater mixing effect with the dilute infiltrating fluid.

- It should be noted that the field measurements really determine the total concentration of any particular species including aqueous, solid phase, and sorbed concentrations, and not necessarily just the concentration in the aqueous solution.

- It was not possible to charge balance the leak composition with the subset of species used in the simulations because of the high carbonate concentration of 0.4 mol/L needed to fit the field data. One possibility is that part of the measured carbonate concentration comes from solid carbonate minerals that are dissolved during treatment of the sediment, in which case a lower concentration may be applicable.

D.2.6.6 Conclusion

The model simulations appear to be in qualitative agreement with field observations. The model fits the general picture of the tank leak fluid containing high sodium concentrations displacing the initial strontium sorbed on the sediment in addition to calcium and potassium. The position of the sorbed strontium peak resulting from the transfer line leak was not fit, but is predicted from the fit to nitrate and sodium profiles. This peak is in excellent agreement with the strontium-90 peak observed in the field and provides strong support for the conceptual model of two leak events occurring at different depths. This appears to be at least one plausible way to obtain a bimodal distribution of tank contaminants. The calculated aqueous strontium profile was displaced upward from the field measurements, suggesting that strontium was too strongly retarded. This could be a result of incorrect selectivity coefficients used in the simulation. More work is currently underway to refine the sorption model used in the simulation.

Future work will address three-dimensional issues and consider simulations over longer time periods to determine how fast the strontium plume is advancing. In addition, it would be useful to model separately the stable and radioactive strontium field data. Finally, the issue of charge balancing the source term needs to be addressed.

D.2.6.7 References

Jones, T. E., B. C. Simpson, M. I. Wood, and R. A. Corbin, 2001, *Preliminary Inventory Estimates for Single-Shell Tank Leaks in B, BX, and BY Tank Farms*, RPP-7389, Rev. 0, CH2M HILL Hanford Group, Inc., Richland, Washington.

Lichtner, P.C., 2001, *FLOTRAN User's Manual*, LA-UR-01-2349, Los Alamos National Laboratory, Los Alamos, New Mexico.

Lichtner, P.C., 1996, "Continuum formulation of reactive transport," MSA, Vol. 34, Eds P. C. Lichtner, C. I. Steefel, and E. H. Oelkers, *Reactive Transport in Porous Media.*

Serne, R. J., B. N. Bjornstad, G. W. Gee, H. T. Schaef, D. C. Lanigan, C. W. Lindenmeier, R. D. Orr, V. L. LeGore, R. E. Clayton, M. J. Lindberg, I. V. Kutnyakov, S. R. Baum, K. N. Geiszler, M. M. Valenta, T. S. Vickerman, and L. J. Royack, 2002, *Characterization of Vadose Zone Sediment: Borehole 299-E33-46 Near B-110 in the B-BX-BY Waste Management Area.* PNNL-14119, Pacific Northwest National Laboratory, Richland, Washington.

D.3.0 URANIUM SPECIATION AND DISSOLUTION FROM BX-102 SEDIMENTS

Uranium is a common subsurface contaminant at the Hanford Site. Uranium exhibits two primary oxidation states in the environment: uranium(IV) and uranium(VI). The chemistry of each of the oxidation states is complex and varied. The dominant uranium(IV) form is the uranous cation (U^{4+}), while that for uranium(VI) is the uranyl cation (UO_2^{2+}). Each forms an extensive series of solid phases and aqueous complexes (Langmuir 1978; Grenthe 1992). The standard half-cell potential (E^o) for the valence conversion of uranium(VI) to uranium(IV) is dependent upon the aqueous/solid phase speciation of the two valence states.

Tetravalent uranium is the valence form used in nuclear fuel, but the uranyl cation [uranium(VI)] is the dominant uranium valence state under oxidizing conditions that characterize the Hanford vadose zone and the unconfined aquifer the underlies the 200 Area plateau. The redox reaction may be stated as follows for the tris-carbonato uranium(VI) complex that thermodynamic calculations project as a dominant aqueous species in some Hanford vadose zone waters:

$$0.5UO_2(CO_3)_3^{4-} + 1.5H^+ + e- = 0.5UO_{2(s)} + 1.5HCO_3^- \; E^o = 0.687 \text{ V} \qquad (1)$$

The reduction of uranium(VI) to uranium(IV) occurs readily under reducing conditions, and may be anticipated when aqueous iron(II)$_{aq}$ concentrations become detectable. The thermodynamic database for uranium is relatively extensive (e.g., Grenthe 1992) allowing for defensible calculations of the valence distribution of uranium as a function of pH, and the redox potential as defined by indicator redox couples.

Plumes of uranium(VI) exist in Hanford groundwater and their number is growing as residuals from various types of waste stream discharges to cribs, retention basins, and tank leaks move through the vadose zone. Sizeable groundwater plumes under interim regulatory status are present in the 200 and 300 Areas, and single-shell, high level waste tanks in the B and T tank farms have discharged up to 7 to 8 metric tons of uranium(VI) in the form of bismuth-phosphate metal wastes to the vadose zone (Section 3.2.1.4). There is only small apparent retardation of uranium(VI) mobility in these plumes, which is believed to be expedited by carbonate complexation as shown in Equation (1).

While the thermodynamics and geochemistry of uranium(VI) have been extensively studied (e.g., Grenthe 1992; Burns and Finch 1999), there is limited understanding of the geochemical retardation mechanisms that may slow uranium(VI) migration in the Hanford subsurface. These retardation mechanisms include adsorption and precipitation reactions. Most literature attention has focused on the sorption behavior of uranium(VI) to iron(III) oxides and iron(II) oxide containing subsurface materials at circumneutral pH and below because iron(III) oxides have strong surface affinity for uranium(VI). Credible uranium(VI) adsorption models have been developed for these conditions (Payne and Waite 1991; Waite et al. 1994, 2000). In contrast, sediments that host uranium(VI) vadose zone and groundwater plumes at Hanford are relatively unweathered and are virtually devoid of iron(III) oxides (Zachara et al. 2002). Aqueous chemistry in the vadose zone and groundwater is mildly calcareous with pH values ranging between 7.5 and 9.5. Most of the reactive surface area is contributed by phyllosilicates. The identity of uranium(VI) sorbing phases, responsible surface chemical reactions, the nature of trace uranium(VI) precipitates, and the magnitude of forward and reverse kinetic behavior in

Hanford subsurface sediments are all unknown. Unknown also is whether adsorption or precipitation dominates the retardation mechanism, and/or the conditions promoting one or the other. Distribution coefficients (K_d) measured on Hanford sediments have been low (as a result of carbonate complexation) but highly variable (0.1 to >25 ml/g) as a result of the physical and chemical heterogeneity of the Hanford sediments and the contributions of different types of geochemical reaction.

Uranium in the B, BX, and BY Tank Farms

An estimated 91,600 gal of $BiPO_4$ metal waste solution containing approximately 7 to 8 metric tons of uranium(VI) was discharged to the vadose zone in the BX tank farm as a result of the overfilling of tank BX-102 (Section 3.2.1.4). This "aqueous solution" contained nominal concentrations of 0.5 mol/L uranium(VI), 2.5 to 5.0 mol/L (sodium)$_2CO_3$, 0.36 mol/L PO_4, and virtually all fission products except plutonium with pH of approximately 10 (Jones et al. 2001) (Table D.27 and Table D.28). Characterization studies of the vadose zone near BX-102 have defined an extensive plume containing cesium, uranium, and other contaminants (Womack and Larkin 1971) resulting from the 1951 leak event, whose character was apparently modified by the later leakage of waste solutions of different composition from tanks BX-102 and BX-101 (Jones 2001).

Borehole 299-E33-45 was drilled through the metal waste plume proximate to tank BX-102 by the River Protection Project in 2001 to provide information on the depth distribution and inventory of uranium and technetium resulting from the 1951 metal waste overfill of tank BX-102. Samples from this borehole were characterized by the RPP and these results have defined the presence of several zones of enriched uranium concentrations at depths between 70 and 170 ft bgs (Figure D.46). The S&T Project selected three high-uranium samples from borehole 299-E33-45 (i.e., samples 53, 61, and 67) for study to provide information on the chemical speciation, mineral association, and leachability of uranium in and from the contaminated sediments. The scientific goals of this work were to identify: 1) post-release waste-sediment reactions that impacted uranium(VI) mobility, 2) retardation extent and mechanism, and 3) potential for future uranium(VI) migration and controlling factors. The science performed in support of these goals is presented in five sections that follow: Section 3.1, speciation of calculations of tank waste; Section 3.2, spatial distribution and mineral association of uranium; Sections 3.3 and 3.4, spectroscopic characterization of uranium phases, and Section 3.5, uranium desorption/dissolution rate and extent from contaminated sediment.

Figure D.46. Distribution of Uranium(U) in Borehole 299-E33-45 (near Tank 241-BX-102) S&T Research to Date has Focused on Samples, 53, 61, and 67 from the Uranium-Plume at 210-145'. Data and Figure from Serne et al. (2002).

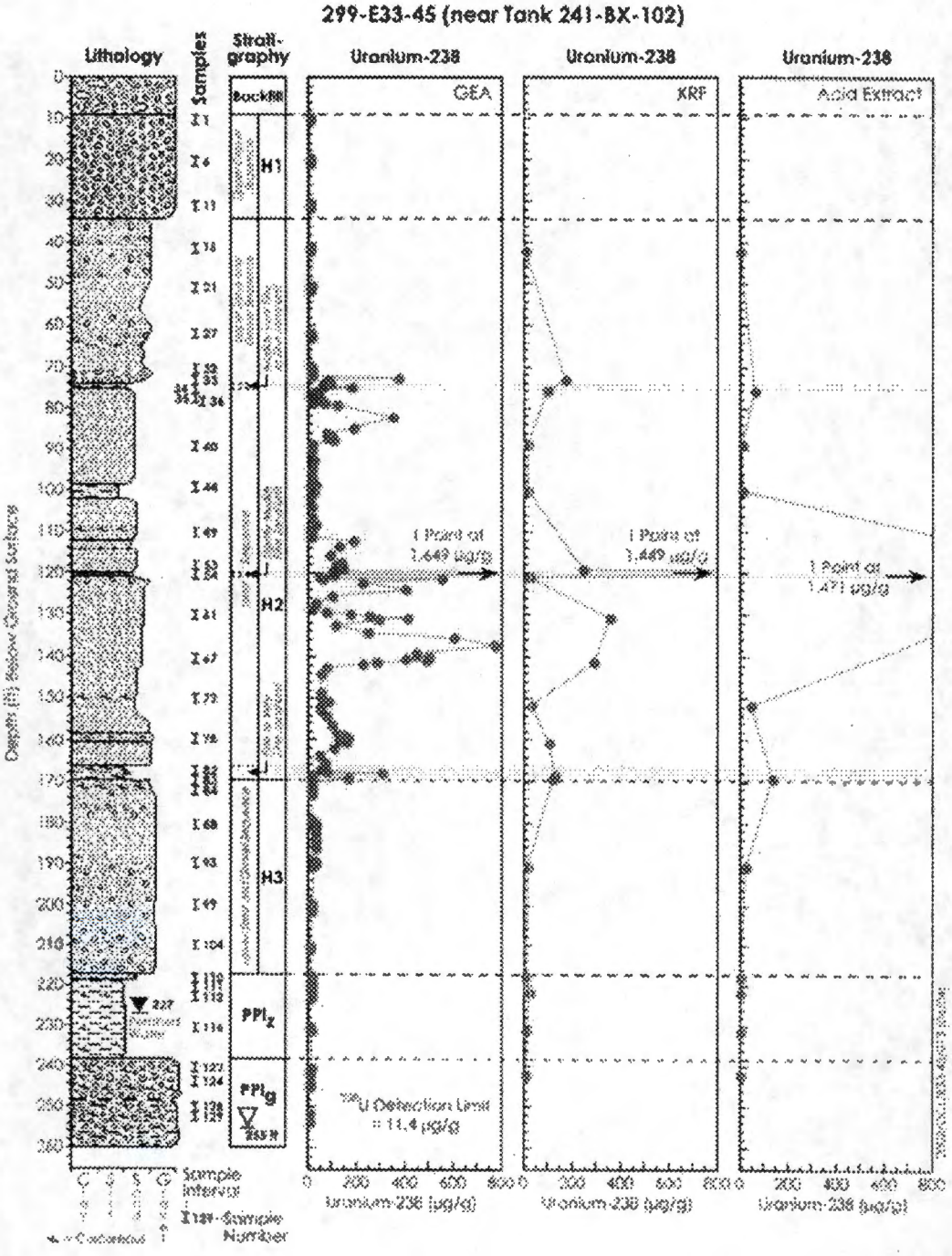

References

Burns, P. C., and R. Finch, 1999, "*Uranium: Mineralogy, Geochemistry and the Environment*," P. H. Ribbe, ed., Mineralogical Society of America, Washington, D. C.

Grenthe, I., 1992, *Chemical Thermodynamics of Uranium*, Vol. 1, North-Holland Elsevier Science Publishers B.V., Amsterdam, The Netherlands.

Jones, T. E., B. C. Simpson, M. I. Wood, and R. A. Corbin, 2001, *Preliminary Inventory Estimates for Single-Shell Tank Leaks in B, BX, and BY Tank Farms*, RPP-7389, CH2M HILL Hanford Group, Inc., Richland, Washington.

Langmuir, D., 1978, "Uranium Solution-Mineral Equilibria at Low Temperatures with Applications to Sedimentary Ore Deposits," *Geochimica et Cosmochimica Acta*, 42:547-569.

Payne, T. E., and T. D. Waite, 1991, "Surface Complexation Modeling of Uranium Sorption Data Obtained by Isotope Exchange Techniques," *Radiochimica Acta*, Vol. 52/53:487-493.

Serne, R. J., B. N. Bjornstad, G. W. Gee, H. T. Schaef, D. C. Lanigan, C. W. Lindenmeier, R. D. Orr, V. L. LeGore, R. E. Clayton, M. J. Lindberg, I. V. Kutnyakov, S. R. Baum, K. N. Geiszler, M. M. Valenta, T. S. Vickerman, and L. J. Royack, 2002, *Characterization of Vadose Zone Sediment: Borehole 299-E33-46 Near Tank B-110 in the B-BX-BY Waste Management Area*, PNNL-14119, Pacific Northwest National Laboratory, Richland, Washington.

Waite, T. D., J. A. Davis, T. E. Payne, G. A. Waychunas, and N. Xu, 1994, "Uranium(VI) Adsorption to Ferrihydrite: Application of a Surface Complexation Model," *Geochimica et Cosmochimica Acta*, Vol. 54:5465-5478.

Waite, T. D., J. A. Davis, B. R. Fenton, and T. E. Payne, 2000, "Approaches to Modeling Uranium(VI) Adsorption on Natural Mineral Assemblages," *Radiochimica Acta*, Vol. 88:687-693.

Womack, J. C., and D. J. Larkin, 1971, *Investigation and Evaluation of 102-BX Tank Leak*, ARH-2035, Atlantic Richfield Hanford Company, Richland, Washington.

Zachara, J. M., S. C. Smith, C. Liu, J. P. McKinley, R. J. Serne, and P. L. Gassman, 2002, "Sorption of Cs^+ to Micaceous Subsurface Sediments from the Hanford Site, USA," *Geochimica et Cosmochimica Acta*, Vol. 66:193-211.

D.3.1 SIMULATED B, BX, AND BY TANK FARMS SUPERNATE COMPOSITIONS

Peter C. Lichtner[1]

[1]Los Alamos National Laboratory, Los Alamos, New Mexico 87545

D.3.1.1 Introduction

This contribution presents simulated supernate compositions for the B, BX, and BY tank farms based on tank inventories developed by Jones et al. (2001). The B tank farm is one of the oldest tank farms at the Hanford Site constructed in 1943 to 1944. The BX and BY tank farms were constructed in 1946 to 1947 and 1948 to 1949, respectively. With the exception of tank BX-102, there is very little direct information about leaks from these tanks and the only sources of leak volumes are derived from historical waste transfer records and the Hanlon (2002) report which tabulates estimated leak volumes from tanks known or suspected to have leaked. A summary of the B, BX, and BY tank farms inventories and estimates of their associated leaks and timings is given by Jones et al. (2001).

The same methodology is used as that presented for the SX tank farm (Lichtner and Felmy 2002) based on a reaction path approach. The computer code FLOTRAN, modified to include the Pitzer model adapted from the GMIN code developed by Felmy (1995), is used to calculate tank supernate concentrations.

D.3.1.2 Results

Calculations for the supernatant concentrations for the B, BX, and BY tank farms are performed at 60 °C based on the derived tank inventories summarized in Table D.27 for major species as presented in Jones et al. (2001). Tank BX-102 contains the highest uranium inventory. Detailed results of the simulations are presented for tanks B-110, BX-101, and BX-102. The tank inventories used in the calculations are taken from Jones et al. (2001) and are listed in Table D.28. The results of the calculations are presented in Table D.29 through Table D.32 for tanks B-110 in the absence of and with ethylene-dinitrilo-tetraacetic acid (EDTA), BX-101, and BX-102, respectively.

Table D.27. List of Tanks in the B-BX-BY Tank Farms for Which Inventories were Provided by Jones et al. (2001) Shown are Major Ion Concentrations, and Total Uranium Concentration Associated with each Tank in mol/L.

Tank	Na	NO_3	NO_2	CO_2	PO_4	SO_4	UO_2
B-101	3.42	0.836	0.053	0.27	0.01	0.044	8.74e-5
B-105	4.98	2.85	0.403	0.207	0.153	0.221	4.08e-3
B-107	1.87	0.777	0.371	0.022	0.01	0.029	3.66e-3
B-110	3.78	1.33	0.774	0.108	0.019	0.108	4.58e-3
B-201	2.70	2.50	0.003	0.016	0.065	0.005	6.57e-4
B-203	13.00	1.20	0.024	0.079	0.313	0.027	3.16e-3
B-204	0.177	0.143	0.02	0.002	0.0003	0.003	2.63e-6
BX-101	3.90	1.02	0.357	0.259	0.011	0.07	1.23e-3
BX-102	2.92	0.53	0.046	0.643	0.36	0.23	1.14e-1
BX-111	1.81	0.801	0.319	0.016	0.009	0.019	3.94e-3

Table D.28. Initial Tank Waste Inventory for Total Liquid and Solid Contributions Used as Starting Solution in Reaction Path Calculations

Tank Species	B-110	BX-101	BX-102
	Total Concentration (mol/L)		
Al(OH)4-	0.579	0.319	5.68e-4
Fe(OH)4-	4.31e-3	3.03e-3	7.62e-3
Ca++	1.31e-2	9.1e-3	1.33e-2
Ni++	2.47e-3	1.82e-3	1.62e-3
Mn++	1.58e-3	1.13e-3	0.
K+	1.47e-2	1.67e-2	2.73e-3
Na+	3.78	3.9	2.92
OH-	0.1	0.1	0.1
NO3-	1.33	1.02	0.53
NO2-	0.774	0.357	0.0461
Cl-	5.53e-2	6.9e-2	1.25e-2
F-	1.87e-2	1.56e-3	0.
HCO3-	0.108	0.259	0.643
HPO4--	0.0192	0.0112	0.36
SO4--	0.108	0.0696	0.23
CrO4--	2.72e-2	1.63e-2	1.6e-3
SiO2(aq)	2.85e-2	3.44e-2	4.05e-3
Cs+	5.706e-5	3.916e-6	3.44e-6
Sr++	1.34e-5	1.45e-5	2.775e-6
UO2++	4.58e-3	1.23e-3	0.114
TcO4-	8.692e-5	4.334e-5	5.608e-6

Table D.29. Calculated Supernatant Composition for Tank B-110 without EDTA (2 pages)

```
H2O mole fraction    =  8.9123E-01, weight fraction =  7.9757E-01
 activity of water    =  8.8360E-01
 osmotic coefficient =  1.0140E+00
 ionic strength       =  3.5613E+00
 solution density     =  1.2637      [g/cm^3]
 pH =  12.927      pe = -0.2707      Eh = -1.7897E-02 [V]
```

primary species	molarity	tot [mol/L]	act. coef.
Al(OH)4-	8.9554E-02	8.9554E-02	5.7464E-01
Fe(OH)4-	1.3460E-07	1.3460E-07	5.1954E-01
Ca++	4.6622E-08	7.5876E-08	1.8937E-02
Ni++	6.1563E-14	6.1563E-14	3.0609E-02
Mn++	1.2728E-10	1.2728E-10	5.1696E-03
K+	1.4747E-02	1.4747E-02	4.5653E-01
Na+	3.2641E+00	3.7522E+00	6.9319E-01
OH-	9.7091E-01	1.1010E+00	7.1943E-01
NO3-	9.1066E-01	1.3300E+00	7.2036E-01
NO2-	7.0517E-01	7.7400E-01	5.9220E-01
Cl-	5.5300E-02	5.5300E-02	6.0765E-01
F-	1.6080E-02	1.6080E-02	6.4834E-01
HCO3-	2.6460E-05	1.0799E-01	4.0783E-01
HPO4--	3.0208E-05	1.1340E-02	2.0740E-02
SO4--	1.0800E-01	1.0800E-01	3.1008E-02
CrO4--	2.7200E-02	2.7200E-02	3.1425E-02
SiO2(aq)	3.0960E-08	5.4786E-03	1.0000E+00
Cs+	5.7000E-05	5.7000E-05	3.9397E-01
Sr++	2.8142E-07	3.2556E-07	1.2518E-02
UO2++	8.5048E-28	4.7085E-10	5.5314E-03
TcO++	3.6808E-29	1.2523E-10	5.1696E-03

complex	molarity	act. coef.	log K
NaNO3(aq)	0.41934	1.0000	-0.54895
CO3--	0.10796	0.62328E-01	2.8970
NaNO2(aq)	6.88279E-02	0.99437	-1.1401
PO4---	1.13098E-02	3.47958E-04	0.90014
H2SiO4--	5.33310E-03	5.04247E-02	4.2505
H3SiO4-	1.45449E-04	0.46944	3.5531
SrCO3(aq)	4.41319E-08	1.0000	6.1669
CaCO3(aq)	2.87032E-08	1.0000	6.5810
CaSO4(aq)	5.50280E-10	1.0000	2.2698
UO2(CO3)3----	4.70846E-10	3.98223E-06	29.808
TcO4-	1.12245E-10	0.29148	20.328
TcO(OH)2(aq)	1.29855E-11	1.0000	20.146
H2PO4-	3.94473E-12	0.29148	-5.8384
CO2(aq)	2.68866E-12	1.0000	-6.7594
H+	2.20132E-13	0.53767	-13.029
HSO4-	2.01344E-13	0.54003	-10.591
UO2(CO3)2--	3.09137E-15	1.97324E-02	23.251
NH3(aq)	9.88192E-16	1.0000	-14.086
UO2OH+	4.32824E-21	0.30723	8.6071
UO2CO3(aq)	2.33301E-22	1.0000	12.764
Fe++	7.47160E-25	5.16964E-03	-19.654
O2(aq)	3.22843E-27	1.0000	-26.883
Al+++	6.74956E-28	9.18650E-07	-32.542
Fe+++	5.81414E-34	9.18650E-07	-32.740

Table D.29. Calculated Supernatant Composition for Tank B-110 without EDTA (2 pages)

mineral	volume fraction	concentration [mol/Lb]	rate [mol/dm^3/s]
Boehmite	9.1149E-03	4.6659E-01	4.4409E-23
Nepheline	1.2554E-03	2.3180E-02	1.3323E-22
Goethite	8.9731E-05	4.3099E-03	2.6645E-26
Ni(OH)2	5.5180E-05	2.4700E-03	3.1086E-22
Na2U2O7	2.1833E-04	2.2900E-03	4.6629E-24
Mn(OH)2(am)	3.5329E-05	1.5800E-03	-1.1102E-23
Fluorapatite	1.3100E-03	2.6200E-03	1.3767E-21
Strontianite	5.1003E-07	1.3074E-05	-2.4425E-22
TcO2.2H2O(am)	4.3458E-05	8.6916E-05	-3.3307E-22

mineral saturation indices

mineral	SI (Log KQ)	log K
Cancrinite	1.18173E+01	6.17029E+01
Trevorite	4.10676E+00	3.29273E+01
Ni2SiO4	2.73878E+00	4.02135E+01
Diaspore	3.49043E-01	1.42798E+00
Goethite	0.00000E+00	6.94577E+00
Ni(OH)2	0.00000E+00	1.50365E+01
TcO2.2H2O(am)	0.00000E+00	3.10860E+01
Boehmite	0.00000E+00	1.07894E+00
Na2U2O7	0.00000E+00	5.87195E+01
Nepheline	0.00000E+00	8.33561E+00
Fluorapatite	0.00000E+00	6.61678E+01
Strontianite	0.00000E+00	1.35221E+01
Mn(OH)2(am)	0.00000E+00	1.24935E+01
CaUO4	-3.07229E-01	3.85902E+01
Gibbsite	-4.17406E-01	7.15274E-01
NaNO3(s)	-1.28805E+00	-1.45956E+00
Thenardite	-1.32349E+00	4.42396E-01
Analcime	-1.97151E+00	1.41944E+01
NaNO2(s)	-1.97324E+00	-1.94861E+00
Dawsonite	-2.09955E+00	3.59169E+00
Rhodonite	-2.36113E+00	1.75878E+01
Calcite	-2.42463E+00	1.16985E+01
Halite	-2.73450E+00	-1.61549E+00
Jadeite	-2.95665E+00	1.28882E+01
Fluorite	-3.10683E+00	9.91108E+00
Portlandite	-3.50357E+00	5.86219E+00
Rhodochrosite	-3.59666E+00	1.36541E+01
Quartz	-4.04155E+00	3.46765E+00
Muscovite	-4.23367E+00	2.38046E+01
Nahcolite	-4.78322E+00	-1.70910E-01
SiO2(am)	-5.10825E+00	2.40095E+00
Hydroxylapatite	-5.25680E+00	5.90849E+01
K-Feldspar	-5.36388E+00	2.05166E+01
Gypsum	-7.02327E+00	4.61341E+00
Whitlockite	-7.09903E+00	3.26736E+01
Kaolinite	-8.00053E+00	9.22948E+00

gas	log partial pressure	pressure [bars]	log K
CO2(g)	-9.785	1.6398E-10	-4.9741
O2(g)	-23.43	3.7337E-24	-23.820

Table D.30. Calculated Supernatant Composition for Tank B-110 with EDTA (2 pages)

```
H2O mole fraction    =  8.9514E-01, weight fraction =  7.8555E-01
activity of water    =  8.9099E-01
osmotic coefficient  =  9.8529E-01
ionic strength       =  4.1863E+00
solution density     =  1.2836      [g/cm^3]
pH =  12.565      pe =  8.9454E-02 Eh =  5.9130E-03 [V]
```

primary species	molarity	tot [mol/L]	act. coef.
Al(OH)4-	5.6709E-02	5.6709E-02	4.0140E-01
Fe(OH)4-	8.5083E-08	8.5083E-08	3.6354E-01
Ca++	7.4802E-08	9.9485E-08	1.7561E-02
Ni++	4.0581E-13	4.0581E-13	2.4132E-02
Mn++	7.9467E-10	7.9467E-10	4.3030E-03
K+	1.4721E-02	1.4721E-02	3.7214E-01
Na+	3.2919E+00	3.7496E+00	9.0476E-01
OH-	6.0667E-01	7.3125E-01	5.0505E-01
NO3-	9.3801E-01	1.3300E+00	4.9663E-01
NO2-	7.0832E-01	7.7400E-01	4.2117E-01
Cl-	5.5300E-02	5.5300E-02	4.4606E-01
F-	1.6080E-02	1.6080E-02	4.4094E-01
HCO3-	4.7864E-05	1.0800E-01	2.9331E-01
HPO4--	6.7757E-05	1.1340E-02	1.2464E-02
SO4--	1.0800E-01	1.0800E-01	1.9474E-02
CrO4--	2.7200E-02	2.7200E-02	1.9005E-02
SiO2(aq)	5.4065E-08	2.7546E-03	1.0000E+00
EDTA----	9.9987E-02	1.0000E-01	6.5557E-06
Sr++	3.6554E-08	1.3400E-05	9.0357E-03
Cs+	5.7000E-05	5.7000E-05	3.2286E-01
UO2++	9.3385E-27	1.0071E-09	4.5909E-03

complex	molarity	act. coef.	log K
NaNO3(aq)	0.39199	1.0000	-0.54895
CO3--	0.10795	0.35275E-01	2.8970
NaNO2(aq)	6.56767E-02	0.97994	-1.1401
PO4---	1.12723E-02	2.04726E-04	0.90014
H2SiO4--	2.59529E-03	3.48177E-02	4.2505
H3SiO4-	1.59246E-04	0.33119	3.5531
SrEDTA--	1.33634E-05	8.90312E-03	8.7400
CaCO3(aq)	2.41687E-08	1.0000	6.5810
UO2(CO3)3----	1.00712E-09	3.07523E-06	29.808
CaSO4(aq)	5.14203E-10	1.0000	2.2698
H2PO4-	1.69698E-11	0.20996	-5.8384
CO2(aq)	7.97380E-12	1.0000	-6.7594
H+	5.34593E-13	0.50894	-13.029
HSO4-	4.18356E-13	0.37522	-10.591
UO2(CO3)2--	1.68383E-14	1.05737E-02	23.251
NH3(aq)	1.66582E-15	1.0000	-14.086
UO2OH+	1.82898E-20	0.29065	8.6071
UO2CO3(aq)	1.20324E-21	1.0000	12.764
Fe++	4.69847E-24	4.30300E-03	-19.654
Al+++	1.05488E-26	7.02210E-07	-32.542
O2(aq)	3.19020E-27	1.0000	-26.883
Fe+++	9.08685E-33	7.02210E-07	-32.740

Table D.30. Calculated Supernatant Composition for Tank B-110 with EDTA (2 pages)

mineral	volume fraction	concentration [mol/Lb]	rate [mol/dm^3/s]
Boehmite	9.7053E-03	4.9682E-01	-3.3307E-23
Nepheline	1.3979E-03	2.5810E-02	-2.2204E-22
Goethite	8.9732E-05	4.3099E-03	-8.8818E-27
Ni(OH)2	5.5180E-05	2.4700E-03	-3.8858E-22
Na2U2O7	2.1833E-04	2.2900E-03	4.6629E-24
Mn(OH)2(am)	3.5329E-05	1.5800E-03	3.5527E-22
Fluorapatite	1.3100E-03	2.6200E-03	1.3767E-21

mineral saturation indices

mineral	SI (Log KQ)	log K
Cancrinite	1.17732E+01	6.17029E+01
Trevorite	4.09953E+00	3.29273E+01
Ni2SiO4	2.97366E+00	4.02135E+01
Diaspore	3.49043E-01	1.42798E+00
Goethite	0.00000E+00	6.94577E+00
Ni(OH)2	0.00000E+00	1.50365E+01
Boehmite	0.00000E+00	1.07894E+00
Na2U2O7	0.00000E+00	5.87195E+01
Nepheline	0.00000E+00	8.33561E+00
Fluorapatite	0.00000E+00	6.61678E+01
Mn(OH)2(am)	0.00000E+00	1.24935E+01
Gibbsite	-4.13790E-01	7.15274E-01
CaUO4	-6.13728E-01	3.85902E+01
Strontianite	-1.27523E+00	1.35221E+01
Thenardite	-1.28675E+00	4.42396E-01
NaNO3(s)	-1.31734E+00	-1.45956E+00
Analcime	-1.70640E+00	1.41944E+01
Dawsonite	-1.86593E+00	3.59169E+00
NaNO2(s)	-1.99994E+00	-1.94861E+00
Rhodonite	-2.12263E+00	1.75878E+01
Calcite	-2.49930E+00	1.16985E+01
Jadeite	-2.71453E+00	1.28882E+01
Halite	-2.74939E+00	-1.61549E+00
Rhodochrosite	-3.12815E+00	1.36541E+01
Fluorite	-3.26911E+00	9.91108E+00
Quartz	-3.79944E+00	3.46765E+00
Muscovite	-3.95836E+00	2.38046E+01
Portlandite	-4.04676E+00	5.86219E+00
Na2UO4(alpha)	-4.11976E+00	2.52547E+01
Nahcolite	-4.54959E+00	-1.70910E-01
Paragonite	-4.57913E+00	2.04485E+01
Na2CrO4	-4.84910E+00	-2.51051E+00
SiO2(am)	-4.86614E+00	2.40095E+00
K-Feldspar	-5.08857E+00	2.05166E+01
Hydroxylapatite	-5.44726E+00	5.90849E+01
Eskolaite	-6.93238E+00	-1.73317E+00
Whitlockite	-7.04493E+00	3.26736E+01
Gypsum	-7.04549E+00	4.61341E+00
Kaolinite	-7.51268E+00	9.22948E+00

gas	log partial pressure	pressure [bars]	log K
CO2(g)	-9.313	4.8632E-10	-4.9741
O2(g)	-23.43	3.6895E-24	-23.820

Table D.31. Calculated Supernatant Composition for Tank BX-101 (2 pages)

```
H2O mole fraction    =  8.8754E-01, weight fraction =  8.0746E-01
activity of water    =  8.7751E-01
osmotic coefficient  =  1.0312E+00
ionic strength       =  3.8783E+00
solution density     =  1.2451      [g/cm^3]
pH =  13.149     pe = -0.3916     Eh = -2.5884E-02 [V]
```

primary species	molarity	tot [mol/L]	act. coef.
Al(OH)4-	1.5274E-01	1.5274E-01	5.5414E-01
Fe(OH)4-	2.2575E-07	2.2575E-07	5.0945E-01
Ca++	1.9043E-06	2.8924E-06	7.6768E-03
Ni++	5.2342E-14	5.2342E-14	1.3126E-02
Mn++	1.1300E-03	1.1300E-03	4.5314E-03
K+	1.6700E-02	1.6700E-02	5.8685E-01
Na+	3.4885E+00	3.8721E+00	7.1520E-01
OH-	1.5700E+00	1.8501E+00	7.3682E-01
NO3-	6.7062E-01	1.0200E+00	7.3911E-01
NO2-	3.2273E-01	3.5700E-01	6.1332E-01
Cl-	6.9000E-02	6.9000E-02	5.6231E-01
F-	1.4540E-07	1.4540E-07	6.5738E-01
HCO3-	3.3740E-05	2.5900E-01	3.9681E-01
HPO4--	8.9072E-06	5.7417E-03	1.8736E-02
SO4--	6.9600E-02	6.9600E-02	2.5599E-02
CrO4--	1.6300E-02	1.6300E-02	2.9426E-02
SiO2(aq)	1.6837E-08	7.7688E-03	1.0000E+00
Cs+	3.9160E-06	3.9160E-06	4.8553E-01
Sr++	1.3929E-07	1.3929E-07	1.2224E-02
UO2++	1.8894E-28	9.3128E-10	4.9199E-03
TcO++	9.6456E-29	2.5535E-09	4.5314E-03

complex	molarity	act. coef.	log K
NaNO3(aq)	0.34938	1.0000	-0.54895
CO3--	0.25896	0.53760E-01	2.8970
NaNO2(aq)	3.42663E-02	1.0439	-1.1401
H2SiO4--	7.63625E-03	5.25260E-02	4.2505
PO4---	5.73283E-03	3.04929E-04	0.90014
H3SiO4-	1.32533E-04	0.46080	3.5531
CaCO3(aq)	9.83265E-07	1.0000	6.5810
CaSO4(aq)	4.84745E-09	1.0000	2.2698
TcO4-	2.47170E-09	0.28085	20.328
UO2(CO3)3----	9.31275E-10	3.52328E-06	29.808
TcO(OH)2(aq)	8.18071E-11	1.0000	20.146
CO2(aq)	2.01421E-12	1.0000	-6.7594
H2PO4-	6.53955E-13	0.28085	-5.8384
H+	1.44975E-13	0.48957	-13.029
HSO4-	6.53666E-14	0.53070	-10.591
UO2(CO3)2--	3.08085E-15	1.67468E-02	23.251
NH3(aq)	6.88598E-17	1.0000	-14.086
UO2OH+	1.45698E-21	0.29866	8.6071
UO2CO3(aq)	9.53761E-23	1.0000	12.764
Fe++	2.45306E-25	4.53136E-03	-19.654
O2(aq)	8.20391E-27	1.0000	-26.883
Al+++	2.09742E-28	6.46354E-07	-32.542
Fe+++	1.80674E-34	6.46354E-07	-32.740

Table D.31. Calculated Supernatant Composition for Tank BX-101 (2 pages)

mineral	volume fraction	concentration [mol/Lb]	rate [mol/dm^3/s]
Boehmite	2.7277E-03	1.3963E-01	-3.3307E-23
Nepheline	1.4423E-03	2.6631E-02	1.3323E-22
Goethite	6.3080E-05	3.0298E-03	8.8818E-27
Ni(OH)2	4.0659E-05	1.8200E-03	-3.8858E-22
Na2U2O7	5.8634E-05	6.1500E-04	4.6629E-24
Fluorapatite	7.7993E-04	1.5599E-03	1.3767E-21
Hydroxylapatite	1.2978E-04	2.5957E-04	-7.1054E-22
Strontianite	1.0282E-07	2.6357E-06	-2.4425E-22
TcO2.2H2O(am)	1.9569E-06	3.9138E-06	-7.7716E-23

mineral saturation indices

mineral	SI (Log KQ)	log K
Cancrinite	1.16468E+01	6.17029E+01
Trevorite	4.11277E+00	3.29273E+01
Ni2SiO4	2.48024E+00	4.02135E+01
CaUO4	1.08990E+00	3.85902E+01
Diaspore	3.49043E-01	1.42798E+00
Goethite	0.00000E+00	6.94577E+00
Ni(OH)2	0.00000E+00	1.50365E+01
Boehmite	0.00000E+00	1.07894E+00
Na2U2O7	0.00000E+00	5.87195E+01
Nepheline	0.00000E+00	8.33561E+00
Fluorapatite	0.00000E+00	6.61678E+01
Hydroxylapatite	0.00000E+00	5.90849E+01
Strontianite	0.00000E+00	1.35221E+01
TcO2.2H2O(am)	0.00000E+00	3.02897E+01
Gibbsite	-4.20409E-01	7.15274E-01
Calcite	-8.89886E-01	1.16985E+01
NaNO3(s)	-1.36732E+00	-1.45956E+00
Thenardite	-1.51264E+00	4.42396E-01
Portlandite	-1.84640E+00	5.86219E+00
Dawsonite	-1.96344E+00	3.59169E+00
NaNO2(s)	-2.25502E+00	-1.94861E+00
Analcime	-2.26022E+00	1.41944E+01
Jadeite	-3.22119E+00	1.28882E+01
Whitlockite	-4.14688E+00	3.26736E+01
Quartz	-4.30610E+00	3.46765E+00
Muscovite	-4.64215E+00	2.38046E+01
Nahcolite	-4.64711E+00	-1.70910E-01
Na2CrO4	-5.03546E+00	-2.51051E+00
SiO2(am)	-5.37280E+00	2.40095E+00
Paragonite	-5.59246E+00	2.04485E+01
K-Feldspar	-5.77236E+00	2.05166E+01
Gypsum	-6.08435E+00	4.61341E+00
Kaolinite	-8.53263E+00	9.22948E+00
Fluorite	-1.19633E+01	9.91108E+00

gas	log partial pressure	pressure [bars]	log K
CO2(g)	-9.911	1.2285E-10	-4.9741
O2(g)	-23.02	9.4879E-24	-23.820

Table D.32. Calculated Supernatant Composition for Tank BX-102 (2 pages)

```
H2O mole fraction    =  9.2619E-01, weight fraction =  8.1627E-01
activity of water    =  9.4213E-01
osmotic coefficient  =  7.4814E-01
ionic strength       =  4.5183E+00
solution density     =  1.2367      [g/cm^3]
pH =  10.008      pe =   3.078      Eh =  2.0345E-01 [V]
```

primary species	molarity	tot [mol/L]	act. coef.
Al(OH)4-	7.9780E-08	7.9780E-08	2.8431E-01
Fe(OH)4-	3.5077E-10	3.5077E-10	2.7301E-01
Ca++	6.7965E-06	8.7201E-06	1.0045E-02
Ni++	1.7454E-07	1.7454E-07	6.5448E-03
K+	2.7301E-03	2.7301E-03	3.4284E-01
Na+	2.8055E+00	2.9088E+00	7.6441E-01
OH-	2.3928E-03	7.2020E-01	3.7493E-01
NO3-	4.2896E-01	5.3000E-01	3.8877E-01
NO2-	4.3811E-02	4.6100E-02	3.3535E-01
Cl-	1.2500E-02	1.2500E-02	3.4895E-01
HCO3-	3.3698E-02	6.4299E-01	2.2524E-01
HPO4--	2.4643E-01	3.5114E-01	1.1001E-02
SO4--	2.3000E-01	2.3000E-01	1.4777E-02
CrO4--	1.6000E-03	1.6000E-03	1.5603E-02
SiO2(aq)	2.9628E-04	4.0069E-03	1.0000E+00
Sr++	5.2644E-07	5.2644E-07	7.8982E-03
Cs+	3.4400E-06	3.4400E-06	2.6084E-01
UO2++	6.3117E-19	1.0285E-01	4.0865E-03
TcO++	1.6805E-22	1.0145E-10	4.0279E-03

complex	molarity	act. coef.	log K
CO3--	0.30075	0.18956E-01	2.8970
PO4---	0.10468	0.19595E-03	0.90014
UO2(CO3)3----	0.10284	0.60792E-05	29.808
NaNO3(aq)	0.10104	1.0000	-0.54895
H3SiO4-	3.55561E-03	0.25166	3.5531
NaNO2(aq)	2.28869E-03	0.99719	-1.1401
H2SiO4--	1.54962E-04	2.73950E-02	4.2505
H2PO4-	2.39796E-05	0.17225	-5.8384
UO2(CO3)2--	2.65206E-06	9.05223E-03	23.251
CaCO3(aq)	1.88041E-06	1.0000	6.5810
CO2(aq)	1.47240E-06	1.0000	-6.7594
CaSO4(aq)	4.31853E-08	1.0000	2.2698
HSO4-	3.30093E-10	0.27754	-10.591
H+	2.43145E-10	0.40411	-13.029
TcO(OH)2(aq)	7.61964E-11	1.0000	20.146
TcO4-	2.52533E-11	0.17225	20.328
UO2CO3(aq)	1.08373E-13	1.0000	12.764
UO2OH+	3.35566E-15	0.27905	8.6071
NH3(aq)	8.15737E-17	1.0000	-14.086
Fe++	2.23311E-19	4.02791E-03	-19.654
Al+++	1.16690E-22	8.60703E-07	-32.542
(UO2)2(OH)2++	1.49495E-24	4.08927E-03	21.058
Fe+++	3.12306E-25	8.60703E-07	-32.740
O2(aq)	1.68558E-25	1.0000	-26.883

Table D.32. Calculated Supernatant Composition for Tank BX-102 (2 pages)

mineral	volume fraction	concentration [mol/Lb]	rate [mol/dm^3/s]
Analcime	2.0617E-06	2.1299E-05	-7.1054E-22
Goethite	1.5865E-04	7.6200E-03	-8.8818E-27
Ni(OH)2	3.6187E-05	1.6198E-03	3.1086E-22
Whitlockite	4.3252E-04	4.4306E-03	1.1102E-28
Na2U2O7	5.3176E-04	5.5775E-03	4.6629E-24
Strontianite	5.4509E-07	1.3973E-05	1.1102E-22
TcO2.2H2O(am)	1.7217E-06	3.4434E-06	-7.7716E-23

mineral saturation indices

mineral	SI (Log KQ)	log K
Ni2SiO4	6.66397E+00	4.02135E+01
Trevorite	4.05105E+00	3.29273E+01
Goethite	0.00000E+00	6.94577E+00
Ni(OH)2	0.00000E+00	1.50365E+01
Na2U2O7	0.00000E+00	5.87195E+01
Analcime	0.00000E+00	1.41944E+01
Whitlockite	0.00000E+00	3.26736E+01
Strontianite	0.00000E+00	1.35221E+01
TcO2.2H2O(am)	0.00000E+00	3.02897E+01
Quartz	-6.06525E-02	3.46765E+00
Calcite	-6.08304E-01	1.16985E+01
K-Feldspar	-6.89591E-01	2.05166E+01
Haiweeite	-9.97561E-01	8.68497E+01
SiO2(am)	-1.12735E+00	2.40095E+00
CaUO4	-1.30088E+00	3.85902E+01
Thenardite	-1.36360E+00	4.42396E-01
Jadeite	-1.42962E+00	1.28882E+01
NaNO3(s)	-1.90612E+00	-1.45956E+00
Nahcolite	-1.95932E+00	-1.70910E-01
Eskolaite	-1.96675E+00	-1.73317E+00
Nepheline	-2.45388E+00	8.33561E+00
Dawsonite	-2.76799E+00	3.59169E+00
Diaspore	-3.14329E+00	1.42798E+00
NaNO2(s)	-3.45019E+00	-1.94861E+00
Boehmite	-3.49234E+00	1.07894E+00
Halite	-3.64448E+00	-1.61549E+00
Gibbsite	-3.88189E+00	7.15274E-01
Cancrinite	-4.03067E+00	6.17029E+01
Gypsum	-5.07281E+00	4.61341E+00
Paragonite	-6.54011E+00	2.04485E+01
Muscovite	-6.54405E+00	2.38046E+01
Kaolinite	-6.99555E+00	9.22948E+00
Portlandite	-7.39788E+00	5.86219E+00

gas	log partial pressure	pressure [bars]	log K
CO2(g)	-4.047	8.9801E-05	-4.9741
O2(g)	-21.71	1.9494E-22	-23.820

D.3.1.2.1 Tank B-110. The simulated supernatant for tank B-110 in the absence of EDTA is in equilibrium with minerals boehmite (AlO_2H), nepheline ($NaAlSiO_4$), goethite (FeOOH), $Ni(OH)_2$, clarkeite ($Na_2U_2O_7$), $Mn(OH)_{2(am)}$, fluorapatite [$Ca_5(PO_4)_3F$], strontianite ($SrCO_3$), and $TeO_2 \cdot 2H_2O_{(am)}$. The calculated pH = 12.93 and Eh = -10.79 mV. The concentration of uranium is extremely low and limited by the solubility of clarkeite, in spite of the high carbonate concentration of 0.11 mol/L in the form of CO_3^{2-}. Clarkeite has a much higher solubility at lower pH as shown in Figure D.47. Likewise, nickel has an extremely low concentration limited by the solubility of $Ni(OH)_2$. The concentration of strontium is limited by the solubility of strontianite. Finally, technetium is limited by the solubility of $TeO_2 \cdot 2H_2O_{(am)}$. However, thermodynamic data for this latter phase only exists at 25 °C, and therefore equilibrium with this phase at 60 °C may not be reliable.

Figure D.47. The Predicted Solubility of Clarkeite in a $NaOH$-$NaNO_3$-$NaHCO_3$ Solution Using the Pitzer Activity Coefficient Model

The Concentration of NO_3 was Calculated by Charge Balance for a Solution with Fixed pH, CO_2, and Total Sodium Concentrations in Equilibrium with Clarkeite.

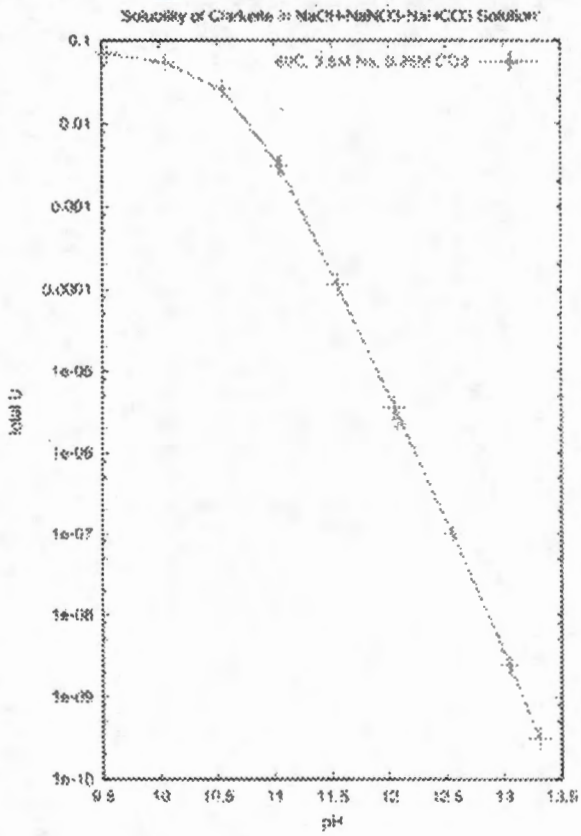

Jones et al. (2001) included organic compounds such as EDTA, HEDTA, or NTA in their inventory estimates. For the B-110 supernate calculation with EDTA, an assumed concentration of 0.1 mol/L was used. Only the complex $SrEDTA^{2-}$ was included in the calculation. However, thermodynamic data for the log K for this species was only available at 25 °C and so the results are only approximate. In this case, strontianite became undersaturated and the total strontium

concentration was several orders of magnitude higher, equal to its initial inventory value, compared to the case without EDTA.

D.3.1.2.2 Tank BX-101. For tank BX-101, minerals boehmite, nepheline, goethite, $Ni(OH)_2$, clarkeite, fluorapatite, hydroxylapatite [$Ca_5(OH)(PO_4)_3$], strontianite, and $TcO_2 \cdot 2H_2O_{(am)}$ are in equilibrium. The tank pH = 13.15 is very high and thus the concentration of uranium is extremely low limited by the solubility of clarkeite.

D.3.1.2.3 Tank BX-102. Calculations predict that tank BX-102 should have the highest uranium concentration of 0.1 mol/L, equal to its initial inventory, for the B, BX, and BY tank farms. This is because of its relatively low pH = 10 and high carbonate concentration. Minerals analcime ($Na_{96}Al_{96}Si_{2.04}O_6 \cdot H_2O$), goethite, $Ni(OH)_2$, whitlockite [$Ca_3(PO_4)_2$], clarkeite, strontianite, and $TcO_2 \cdot 2H_2O_{(am)}$ are in equilibrium.

The speciation results are summarized in Table D.33. Noteworthy is that only two tanks of the ten tanks analyzed, tanks BX-102 and B-201, exhibit high uranium concentrations. This is because of their lower pH (10 to 11) compared to the other tanks with pH values ranging from 12 to ~13. Tank BX-102 is in equilibrium, and tank B-201 is undersaturated with respect to clarkeite. For all the other tanks considered, the uranium concentration is extremely low, limited by the solubility of clarkeite at high pH (12 to 13). For the high pH cases, the mineral $CaUO_4$ was found to be supersaturated, which would have resulted in even lower uranium concentrations had it been included in the simulations. The results obtained for the different tank supernatants are similar to the values derived by Jones et al. (2001). Jones et al. (2001) did not give the uranium concentration for speciation of tank B-107, presumably because it was too low, which is consistent with the results obtained in this study.

Table D.33. Tank Supernatant Concentrations [mol/L], pH and Eh for Representative Tanks in the B-BX-BY Tank Farms Derived from Reaction Path Calculations Using FLOTRAN (Lichtner 2001) with the Pitzer Activity Coefficient Model.

A Fixed Temperature of 60 °C is Used for all Simulations. Calculations are Based on Tank Inventory Estimates Presented by Jones et al. (2000, 2001). With the Exception of Tank B-201, in all other Cases, Total UO_2 Coincides with the Carbonate Species $UO_2(CO_3)_3^{4-}$

Tank	pH	Na	HCO_3	HPO_4^{2-}	UO_2	Eh [V]	Clarkeite
B-101	13.123	3.13	0.261	0.01	9.691e10	-8	sat
B-105	12.3	4.95	0.207	0.147	1.109e7	-43	sat
B-107	12.54	1.86	0.022	0.004	6.23e11	-26	sat
B-110	12.87	3.75	0.108	0.01	6.66e10	-0.014	sat
B-201	6.92	2.70	0.009	0.055	6.57e4	-545	unsat
B-203	13.671	12.997	0.061	0.313	9.64e10	-75	sat
B-204	10.170	0.177	1.5e-5	4.03e-9	6.19e14	-186	sat
BX-101	13.109	3.868	0.25	0.0112	1.04e9	-23	sat
BX-102	10.	2.91	0.643	0.351	0.103	0.203	sat
BX-111	12.556	1.81	0.016	0.0028	2.204e11	0.0137	sat

D.3.1.3 Observations and Qualifiers

The pH is determined by charge balance and as a consequence, is significantly influenced by total sodium and NO_3 tank inventories.

The Eh of the supernatant is determined by the $NO_3^-NO_2$ redox couple. If this redox couple is not at equilibrium, then the calculated Eh is not correct, assuming correct concentrations of NO_3 and NO_2.

For tanks B-110, BX-101, and BX-102, the concentration of technetium was limited to low concentrations by the solubility of the phase $TcO_2 \cdot 2H_2O_{(am)}$. However, as already noted, thermodynamic data was available for this phase only at 25 °C.

Jones et al. (2001) did not provide inventory data for the BY tank farm or for the other tanks not listed in Table D.27.

Because of the bismuth-phosphate process used in the extraction of uranium, a number of the tanks contain high phosphate concentrations that would be expected to complex with uranium. However, thermodynamic data for these species is absent from the database for the Pitzer model, and only available at 25 °C for the Debye-Huckel model. The mineral whitlockite [$Ca_3(PO_4)_2$] was predicted to be saturated in the high phosphate solutions.

Bismuth was not included in the calculations because of lack of data in the Pitzer model database. However, its omission is not expected to greatly affect the supernatant simulation results.

Organic species were not included in the calculations because of lack of data in the Pitzer model database.

Clarkeite was saturated for all tank compositions except B-201.

There is very sparse thermodynamic data for aqueous uranium species above 25 °C.

Eskolaite (Cr_2O_3) precipitated out in tank B-201.

Cancrinite was found to be supersaturated in many of the tank fluids. Because thermodynamic data is not available at 60 °C, but only for approximately 89 °C (Bickmore et al. 2002), it was not included in the simulations.

D.3.1.4 Conclusions

Thermodynamic speciation calculations were performed on selected tanks for WMA B-BX-BY with inventory estimated by Jones et al. (2001). The objectives of these calculations were to estimate aqueous concentrations for the tank supernatant and identify plausible chemical species present that may have been released to the ground through transfer line leakage or other routes.

1. The main conclusion to be drawn from this study is that for most of the tanks in the B, BX, and BY tank farms, the concentration of uranium in the supernatant is extremely low, and limited by the solubility of clarkeite at high pH (12 to 13). This is in spite of the high carbonate inventories derived by Jones et al. (2001) for most of the tanks. The only exceptions found for the tanks studied were BX-102 and B-201, for which essentially all uranium was in solution. These tanks have relatively low pH values ranging from 10 to 11. The results of the simulations are consistent with observations of elevated uranium concentrations near tank BX-102 presumably resulting from a 1951 overfill event (Jones et al. 2001).

2. A surprise finding of these results is that most of the tanks in the B, BX, and BY tank farms have extremely high pH values similar to the S and SX tank farms (Jones et al. 2000a), the notable exceptions being BX-102 and B-201. The calculated pH is based on charge balance involving primarily sodium and NO_3 concentrations, and as a consequence, is sensitive to the inventories predicted for these species.

3. Of all the tanks considered, tank BX-102 had by far the highest uranium inventory, followed by tank B-110 with a lower total uranium inventory by a factor 400. Nevertheless, the supernatant concentration of uranium for these two tanks was calculated to differ by over 10 orders of magnitude with tank BX-102 having the highest concentration. This illustrates the extreme differences in supernate compositions that can result from subtle differences in tank inventories.

4. Because of the lack of thermodynamic data at elevated temperatures, calculations incorporating EDTA for simulations involving the tank B-110 are of limited value. Much more work needs to be done to obtain the necessary data for EDTA complexes involving strontium and other species. In addition, only limited data was available for describing complexes with fluoride.

5. Finally, the calculations suggest that the concentration of technetium in the supernatant may be limited to low values by the solubility of the phase $TcO_2 \cdot 2H_2O_{(am)}$. This result is consistent with lack of observed technetium in the Hanford sediments at the BX tank farm. Additional thermodynamic data is needed, however, to test this hypothesis at the elevated temperatures of the tanks.

D.3.1.5 References

Bickmore, B. R., K. L. Nagy, J. S. Young, and J. W. Drexler, 2001, "Nitrate-Cancrinite Precipitation on Quartz Sand in Simulated Hanford Tank Solutions," *Environmental Science and Technology*, Vol. 35:4481-4486.

Felmy, A. R., 1995, "GMIN, A Computerized Chemical Equilibrium Program Using a Constrained Minimization of the Gibbs Free Energy: Summary Report," *Soil Science Society of America*, Special Publication Vol. 42:377-407.

Hanlon, B. M., 2000, *Waste Tank Summary Report for Month Ending July 31, 2000*, HNF-EP-0182-148, CH2M HILL Hanford Group, Inc., Richland, Washington.

Jones, T. E., R. A. Watrous, and G. T. Maclean, 2000, *Inventory Estimates for Single-Shell Tank Leaks in S and SX Tank Farms*, RPP-6285, CH2M HILL Hanford Group, Inc., Richland, Washington.

Jones, T. E., B. C. Simpson, M. I. Wood, and R. A. Corbin, 2001, *Preliminary Inventory Estimates for Single-Shell Tank Leaks in B, BX, and BY Tank Farms*, RPP-7389, CH2M HILL Hanford Group, Inc., Richland, Washington.

Lichtner, P. C., 2001, *FLOTRAN: User's Manual*, LA-UR-02-2349, Los Alamos National Laboratory, Los Alamos, New Mexico.

Lichtner, P. C., and A. R. Felmy, 2002, "Estimation of Hanford SX Tank Waste Compositions from Historically Derived Inventories," *Computers & Geosciences*, (in press).

D.3.2 THE IDENTIFICATION OF URANIUM-BEARING PHASES BY X-RAY MICROPROBE, ELECTRON MICROPROBE, AND SCANNING ELECTRON MICROSCOPY

James P. McKinley[1], Steven M. Heald[1,2], John M. Zachara[1], and Charles T. Resch[1]

[1]Pacific Northwest National Laboratory, Richland, Washington 99352
[2]Argonne National Laboratory, Argonne, Illinois 60439

D.3.2.1 Introduction

The chemical environment, composition, valence, mineralogy, and habit of uranium in the BX tank farm sediments have direct bearing on its mobility, transport, and fate for these contaminated sediments. Adsorbed uranium may be readily desorbed and mobilized by solutions moving into and through the vadose zone. Uranium(IV) forms essentially insoluble oxides and would require oxidation prior to solubilization. If the uranium is in the form of uranyl solids, such as schoepite [$UO_2(OH)_2$], the solubility of the solid phase could control the aqueous concentration of uranyl. Finally, the habit of the solid phase (including its relationship to other minerals) could control the kinetics of uranyl release to the aqueous environment.

The form and valence of the contaminant uranium in the BX sediments was investigated using x-ray spectroscopic and microprobe methods at the U.S. Department of Energy Advanced Photon Source (APS) at Argonne National Laboratory, as well as electron microprobe and scanning electron microscope methods at Pacific Northwest National Laboratory. Petrographic thin sections of contaminated sediments were examined first by x-ray microprobe (XMP) and x-ray absorption fine structure (XAFS) or x-ray absorption near-edge structure (XANES) measurements. These methods allow valence determinations and the construction of elemental abundance maps for a limited number of elements, at an optical resolution of a few microns. To compare the results of these measurements to measurements and observations using electron microprobe (EMP) and scanning electron microscope (SEM) methods at much higher optical resolutions, an optical, low-resolution video image was collected for registration. This approach allowed the close comparison and integration of the relatively high-resolution, broad-spectrum electron-beam methods with the relatively low-resolution, low-detection-limit, and valence-sensitive methods available at the APS. These methods were used in combination to determine the form and composition of uranium within the BX tank farm sediments.

This combination of methodologies provides a precise and powerful tool for examining the chemistry and chemical relationships in natural samples. The XMP relies on a focused high-intensity beam of x-rays to produce images of the distribution of selected elements. Characteristic x-rays are detected using solid-state or wavelength-dispersive spectrometers, and the high flux of primary x-rays yields a very low analytical detection limit. In addition, by purposefully varying the wavelength of the beam impinging on the sample, the relative x-ray fluorescence can be measured to determine the position of the x-ray absorption edge for elements of interest. The edge position provides information on the valence of the absorbing element. The SEM and EMP make use of an excited and focused beam of electrons, electronically scanned over the sample surface. In the EMP, induced x-ray signals are screened for characteristic x-rays using wavelength-dispersive spectrometers. The instrument is designed to

provide a quantitative analysis of solid substances and can be used also to provide elemental distribution maps at much higher optical resolution but with a higher detection limit. The SEM employs a very finely focused and controlled electron beam to produce images of very high resolution, but detects secondary x-rays using a solid-state detector that has poor energy resolution compared to that of the EMP. The SEM cannot provide compositional data of precision and accuracy comparable to the EMP. The three techniques thus have a combination of strengths and weaknesses that can be exploited to provide unique and useful information about the chemistry and chemical relationships within solid samples of interest.

D.3.2.2 Experimental Methods

Samples 57AB, 61AB, and 67AB from borehole 299-E33-45 were selected for detailed study using a combination of EMP, SEM, and XMP.

It was anticipated that secondary uranium precipitates would occur predominantly as surface precipitates on mineral grains in the impacted sediments. It was also understood, however, that the precipitation of uranium solids could take place within mineral particles or as components of mineral aggregates, and that the valence of uranium in these solids could have been reduced by oxidation-reduction reactions with the associated solid phases. To examine uranium precipitates in cross-section and within the primary sediment clasts, thin section mounts of the contaminated sediments were prepared. A short section of 1 cm inside-diameter tubing was placed in a holding jig, a premixed aliquot of low-viscosity epoxy was added, and then a few grams of sediment were poured into the epoxy. The slurry was incubated in an evacuated chamber to exsolve gas and to prevent the formation of bubbles. After hardening, the imbedded sediment was wafered on a diamond saw, fixed with epoxy to a fused quartz slide, and polished and carbon-coated for examination in the electron and x-ray facilities.

The EMP analysis used wavelength-dispersive spectrometers (WDS) with 30-eV resolution that were tuned to wavelengths for uranium, phosphorous, iron, calcium, and potassium X-alpha radiation and left fixed during image acquisition. The samples were examined using an accelerating potential of 20 keV and a beam current of 20 nA, with the electron beam focused to approximately 50 to 100 nm on the sample surface. The beam position was digitally controlled, and a digital compositional image of the sample was acquired by rastering the beam over the sample surface in a 1024- by 1024-pixel grid at, typically, 50-nm steps with a beam dwell time that would allow image collection in 8 to 12 hours.

The x-ray microprobe measurements were performed at the Pacific Northwest Consortium – Collaborative Access Team (PNC-CAT) insertion device beamline (Heald et al. 1999) at Argonne National Laboratory APS. The beam was focused using Kirkpatick-Baez mirrors (Eng et al. 1998). The entrance slits were set at 0.6 x 0.6 mm, and the beam focused to 5 μm horizontally x 6 μm vertically. Typical flux was about 2×10^{11} photons/sec. The sample was rotated 30 degrees from normal incidence, giving an effective horizontal spot of about 6 μm. The beam energy was selected with a silicon (111) double crystal monochromator with an energy resolution of $\Delta E/E = 1.4 \times 10^{-4}$. The fluorescence from the sample was detected using either a 13-element solid-state detector, with typical energy resolution of about 300 eV, or a WDS tuned to the uranium L_α fluorescence. The WDS was either a log-spiral bent silicon Laue detector (Zhong et al. 1999) combined with a proportional counter or a Microspec WDX detector with

LiF 220 analyzer crystal. The log-spiral detector provided better sensitivity with about 90-eV energy resolution, while the WDX gave better energy resolution (30 eV). Both detectors had sufficient resolution to isolate the uranium L_α line from nearby rubidium and strontium fluorescence, and could detect about 2 to 5×10^9 uranium atoms in the beam spot. Energy windows on the 13-element detector were set to also record the fluorescence signals from iron, rubidium, and strontium as the sample was rastered under the x-ray beam. For imaging, the incident energy was set to 17,200 eV. The presence and abundance of uranium were imaged using an arbitrary violet-to-red false color spectrum, lowest-to-highest abundance, respectively, for each area examined; abundances were not comparable image-to-image.

SEM images were collected at 250X magnification and used to construct relatively small-scale mosaics of sample surfaces for comparison with XMP images. In addition, quantitative analysis was conducted using the SEM for uranium-containing grains whose surface expression was one to several microns across. The grain size presented potential problems for compositional analysis. The diameter of the electron beam on the sample surface in an EMP is approximately 150 nm using a tungsten filament, depending upon the accelerating potential and beam current, whereas, the equivalent beam diameter in the SEM used (a JEOL 6340 with a field emission) was 10 to 20 nm (Goldstein et al. 1992). Also, because the SEM is used primarily for imaging whereas the EMP is used for compositional analysis, the SEM provided a superior determination of the location of the electron beam on the sample surface. Use of the SEM thus provided better control of analyte location and volume on the sample surface. A data reduction procedure accounting for inter-element x-ray interactions from differences in atomic number, absorption, and fluorescence (ZAF), identical to the reduction procedure used in EMP analysis, was used for SEM data. The method of detection for these X-rays was a solid-state, energy-dispersive detector, similar to that used at the APS. As noted above, this detector had higher detection limits and lower resolution than the WDS.

The standards against which analyses were measured are given in Table D.34. To confirm the accuracy of standardization, each standard was analyzed as an unknown prior to the analysis of samples. Because a beam current monitor is not used in SEM analyses, the compositional data were collected under operating conditions nominally identical to the standards collections, and the results were reported as normalized values (totaling 100 wt%).

Table D.34. Composition and Stoichiometry of SEM Compositional Standards

Element	Standard	Element	Standard
C	C	O	UO_2
Na	NaCl	Mg	MgO
Al	Al_2O_3	Si	SiO_2
P	$CaPO_4$	S	FeS_2
K	KCl	Ca	$CaPO_4$
Ti	TiO_2	Mn	Mn
Fe	FeS_2	U	UO_2

D.3.2.3 Results and Discussion

The superimposition of XMP data for uranium onto a backscattered-electron SEM photomosaic of the data collection region (Figure D.48) shows the uneven distribution of uranium. Most uranium was concentrated on mineral grain surfaces, but some uranium occurred also in grain interiors. Within the quartz grain to the upper right of the false color overlay, the uranium map defined several curvilinear accumulations. In general, the distribution of relatively concentrated forms of uranium was independent of other elements, and uranium did not appear to associate preferentially with any mineral. Bulk and microscopic extended x-ray absorption fine structure (EXAFS) measurements (Figure D.49) showed that all of the uranium associated with these samples was hexavalent. The absorption edges overlay one another perfectly for bulk sample analyses and for microscopic XANES analyses. The peak position and post-maximum shoulder were characteristic of uranium(VI).

Figure D.48. Backscattered-Electron SEM Image of Sample 61AB at Right, Left, and with XMP Overlay of False-Color Uranium Abundance

Uranium is Concentrated at Grain Boundaries and Within Mineral Grains. A Set of Elemental Abundance Maps at Finer Scale was Collected by EMP Where Indicated by the Circle (Figure D.50), and Detailed SEM Images of Areas Near A and B are Presented in Figure D.52. Scale Bar = 200 μm

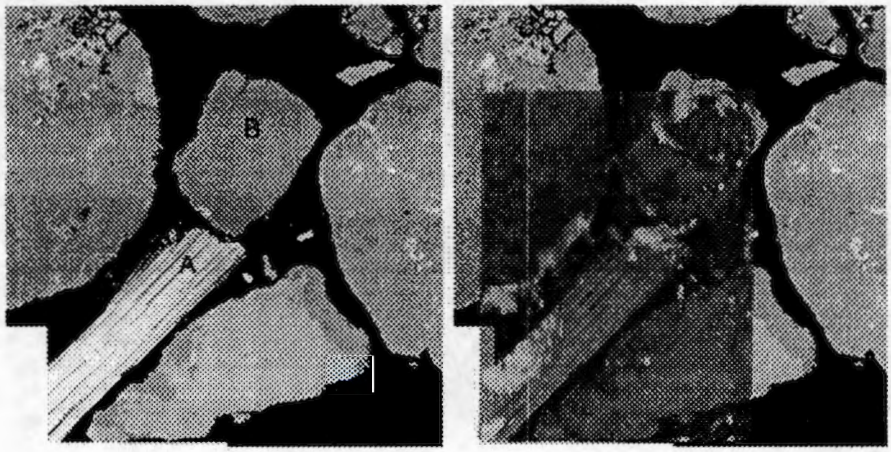

Figure D.49. EXAFS Plots Of Bulk Measurements of BX Samples (Left, Top), and for a Single Uranium-Rich Grain Compared to Rutherfordine (Bottom), a Uranyl Carbonate [Uranium(VI)O_2CO_3]

The Uranium Valence for all Samples is Essentially Uniform and Conforms to the Reference Spectrum for Uranium(VI) (Top Right). Note the Arbitrary Scale Offset in the Sample Data; the Peak and Post-Edge Shoulder Conform to the Reference Positions, with the Maxima at Approximately 17,180eV.

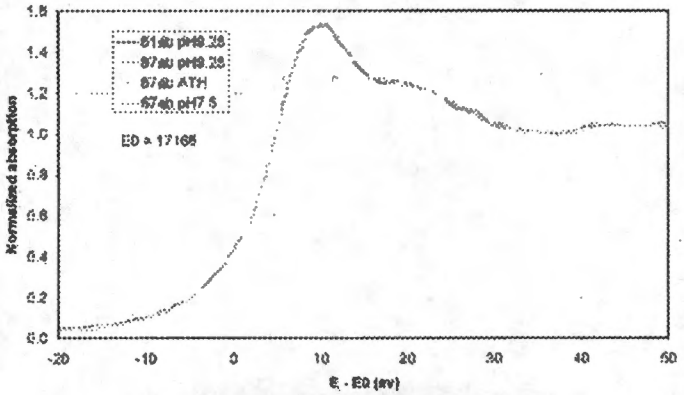

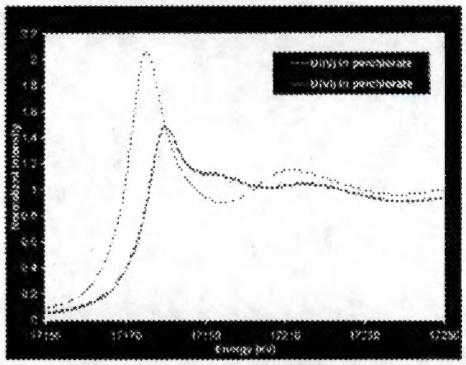

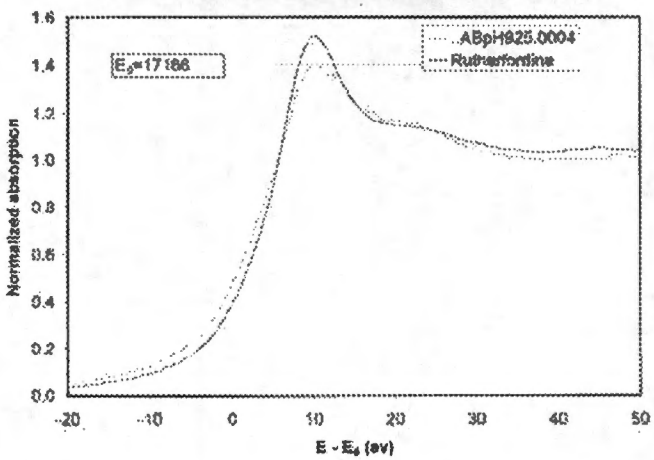

The sample-surface spot size for the XMP was approximately 6 to 7 µm square, and energetic X-radiation from uranium could originate from within a larger volume within the sample and be included in the elemental map. The low detection limit for this method could also show the presence of uranium that was adsorbed, obscuring the occurrence of discrete uranium solids. To detect potential uranium solids, an area that included the edges of the biotite flake and adjacent quartz grain from Figure D.48 was examined using the EMP at much finer scale. The spatial resolution if this method was approximately 100 to 200 nm, and the detection limit was approximately 0.05 wt%; the comparative values for XMP were 6 to 7 µm and 0.0001 wt%, respectively. The EMP thus had the advantage in detecting and imaging discrete granules of uranium-rich materials. The distribution of uranium shown in Figure D.50 indicated the presence of discrete uranium-bearing solids and of uranium that may have been disseminated. In the backscattered-electron (BSE) image, bright (high-Z) grains were readily identified as uranium solids by comparison with the uranium distribution map (bracketed area). Note however, that the bright uranium-rich grains were also associated with uranium that appeared not to be included in dense solids; some of the detected uranyl may have been adsorbed or precipitated in nm-scale solids too small to image. A comparison with abundance maps for phosphorous and iron showed that the abundance of uranium was not correlated with the abundances of phosphorous or iron. Phosphorous was present within a precipitated solid on the surface of the silicate grain but was not associated with uranium. Careful examination of the iron-rich mica showed that while uranium was associated with this iron-rich mineral, it was not associated with iron per se; the bright, uranium-rich solids observed in BSE and uranium images were in voids depleted or free of iron (Figure D.52). Some minute uranium solids were present on the silicate grain surface.

The surfaces of the mica and silicate grains shown in Figure D.48 were examined using a SEM to more carefully and definitively identify the uranium-bearing solids on and within sediment clasts. A small area of the mica grain near the mark **A** in Figure D.48 and a small area of the silicate grain near the mark **B** in the same figure were imaged in the backscattered-electron mode (Figure D.52). The uranium minerals associated with the biotite and silicate were found to be composed predominantly of uranium, silicon, and oxygen by energy dispersive spectroscopy (EDS). They were of relatively uniform size, generally 1 to 3 µm across, but some much smaller grains were observed also. Several dozen individual grains were surveyed using EDS analysis. Although uranium-bearing solids were observed abundantly on mineral grain surfaces, as with the association with biotite and on the surface of the adjacent silicate grain, they were also abundant within microfractures in silicate minerals.

Figure D.50. Backscattered-Electron EMP Image of the Region from Figure D.48 that Lies Between the Upper Edge of the Imaged Mica and the Adjacent Silicate

Also Shown are Gray-Scale Elemental Distribution Maps for Phosphorous, Iron, and Uranium. The Bracketed Area is at the High-Uranium Area Shown Near A in Figure D.48. Note the Association of Uranium with Discrete Grains, as well as its Disseminated Distribution Around Those Grains.

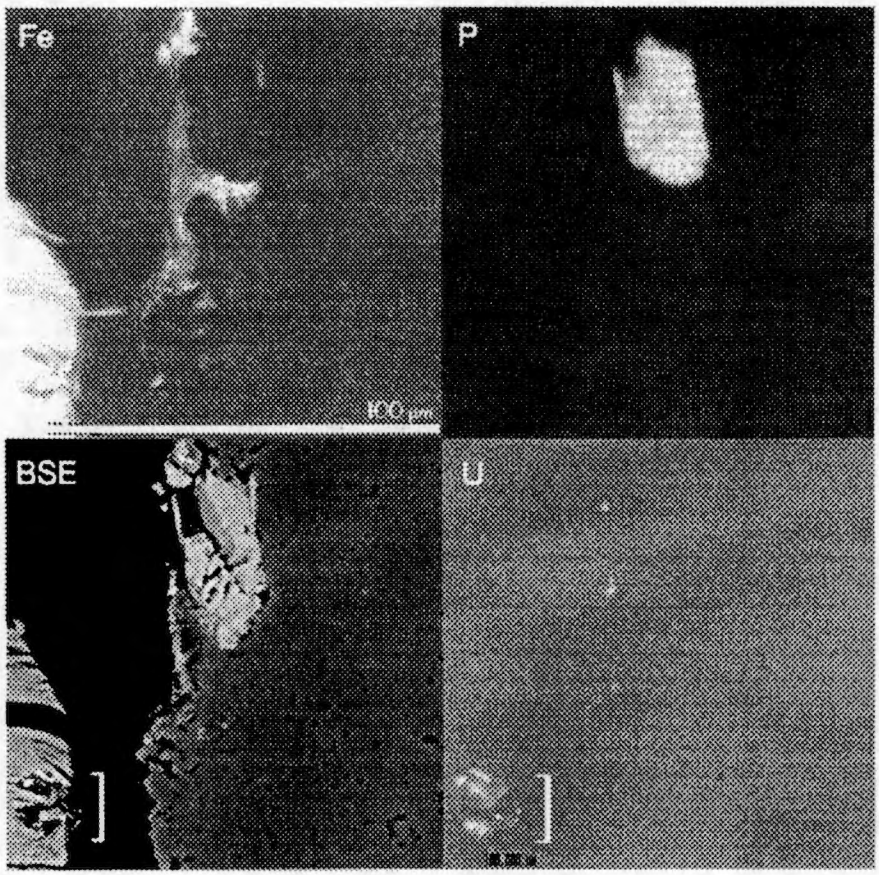

Careful examination of the distribution of uranium solids showed the abundant presence of uranium microcrystallites within fractures in silicate sediment clasts (Figure D.51, a composite of backscattered electron images). The single mm-size rounded grain (Figure D.51A) was composed of intergrown potassium feldspar (lighter and labeled K) and plagioclase feldspar (darker and labeled P); a single titanomagnetite grain adhered to the clast surface (T). The clast was interpenetrated by abundant microfractures occupied by fine 1 to 3 µm crystals of uranium precipitate, presumed at this point to be uranium silicate. (All of the bright, tiny objects shown occupying the fractures were uranium solids.) While uranium minerals occured near the surface of the silicate grain (Figure D.51B), they were predominantly within near-surface fractures. The most abundant occurrence of uranium silicates was within fractures internal to the silicate grain (Figure D.51C and D), where they form radiating crystal clusters and linear vein-filling masses.

Figure D.51. Composite Backscattered Electron Images of Uranium Silicates Associated with a Single Silicate Clast.

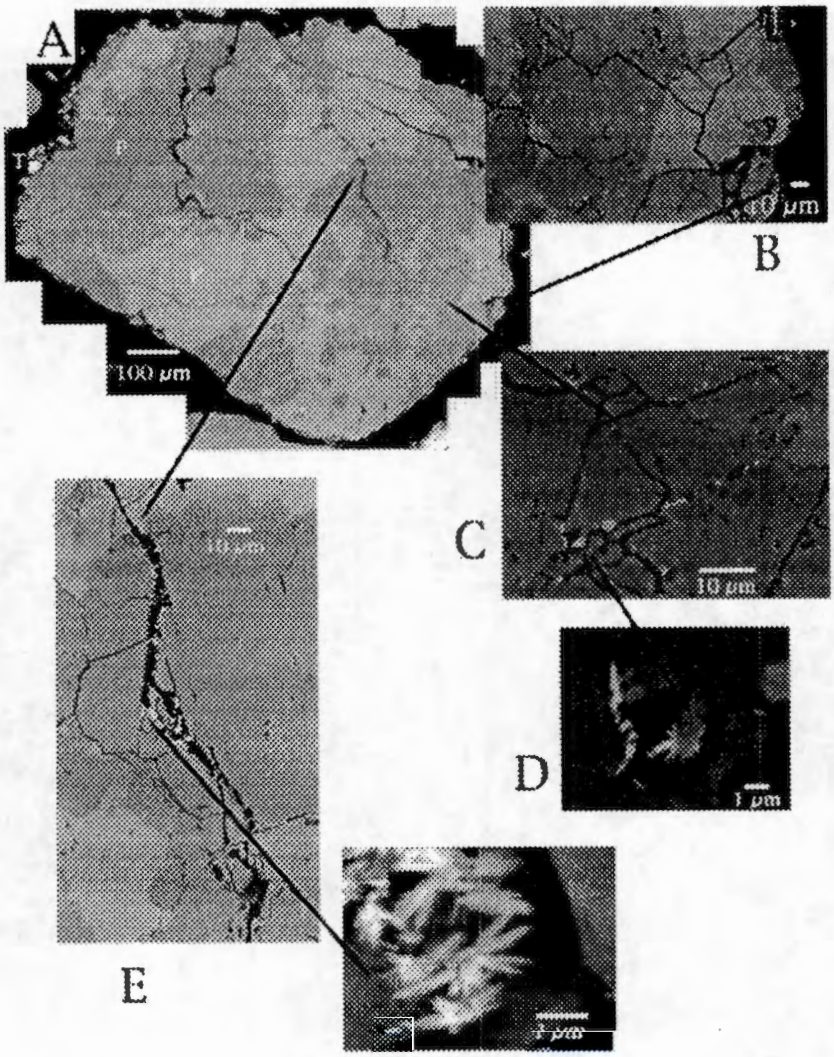

Figure D.52. Backscattered-Electron SEM Images of the Mica and Silicate Grains in Figure D.48 and Figure D.50.

On the Mica Grain (Left) are Shown Several Discrete Uranium Silicate Grains, one of which has a Radiating, Acicular Habit. On the right is shown a Microfracture Enclosing Uranium Silicate Grains. All of the Imaged Uranium Minerals are 1 to 3 µm across. The Aligned Uranium Bearing Grains at Right Define the Brightest Area (Area of Highest Abundance) shown in Figure D.48. Scale bar: 10 µm.

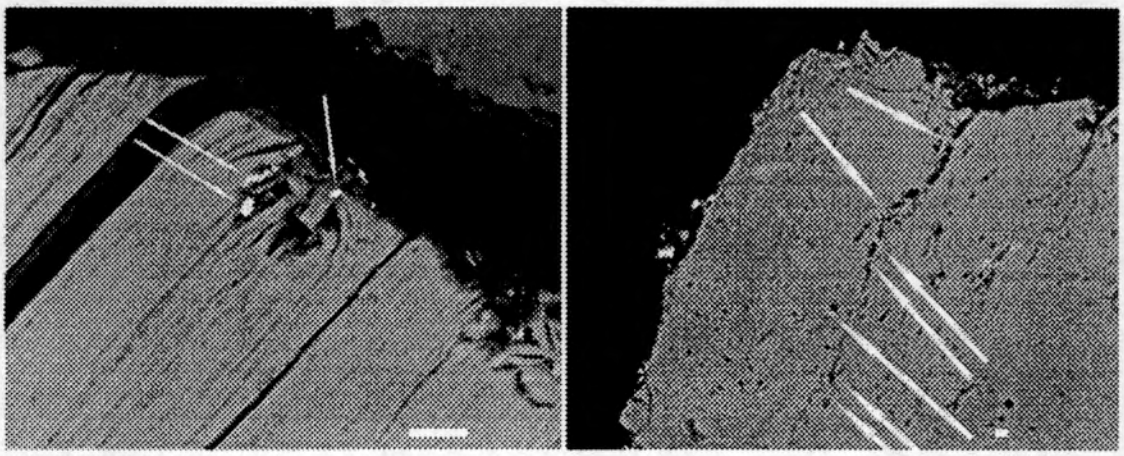

Compositional analysis was attempted on grains that were more than 2 µm across. The analysis of small particles is complicated by the unknown geometry of the analyte solid (Goldstein et al. 1992). For thin and irregular bodies, electrons can penetrate across the boundary between the target material and into underlying materials. The resultant x-rays can have unpredictable effects on x-ray yield and inter-element x-ray interactions. The potential analyte volume for these particles was estimated using an electron flight simulation method (Chernov 2000). Using a hypothetical solid composition of $USiO_5$ and an accelerating potential of 15 keV for the electron beam, the x-ray generating volume was approximately 0.8 µm on the sample surface, to a depth of approximately 0.6 µm. The x-ray emission from this volume was a function of depth, with the detectible x-ray intensity dropping from its maximum near the sample surface to approximately 10% of that maximum at a depth of 0.5 µm. It was likely that the enclosing mineral grains contributed significant compositional information during the analysis of micron-scale particles.

EDS spectra were collected and processed in combinations of four possible standards sets:

1. The standards table was used as given in Table D.34.
2. Al_2O_3 was used as the standard for oxygen.
3. Carbon was omitted from each of these alternative oxygen-standard tables (i.e., two carbon-free standards sets were produced).

Because the oxygen x-ray intensity is small for UO_2, it was considered prudent to try an oxygen-rich standard. Carbon was both included and excluded because it could have a dramatic effect on compositional determinations through inter-element correction calculations. Carbon was not found after many initial analyses, so it was eliminated from the standards table. In addition, it was found that the use of Al_2O_3 as an oxygen standard caused a large negative

charge imbalance (as opposed to a lower positive charge imbalance when using UO_2), so UO_2 was used as the oxygen standard for reported compositions. Before compiling results, obviously erroneous analyses were discarded, i.e., analyses for which uranium was found to be too low to represent a uranium silicate or oxide.

The remaining normalized compositional data are presented in Table D.35. Included in the analyzed minerals were several elements other than uranium, silicon, and oxygen; variable amounts of sodium, magnesium, aluminum, phosphorous, calcium, manganese, and iron also were observed. It was difficult to judge which of these could be a component of the analyte and which were the result of extraparticle x-ray emission. As an ad hoc screen, the mean and standard deviation of compositional results for each measured element were calculated, and elements whose 1-sigma standard deviation was greater than 0.5 of the mean were considered to result from outside the uranium mineral analyte. In addition, all compositions were reduced to hypothetical stoichiometries where uranium was set to 1 relative to other elements (Table D.35). The compositional analysis and calculated stoichiometry for the uranium and oxygen standard, UO_2, were calculated as a method reference: the composition and stoichiometry for this mineral match known values. The calculated stoichiometries were compared to a set of potential mineral formulae (Table D.36; Finch and Murakami 1999) to determine whether the compositional analysis could identify the uranium mineral observed in the samples.

The charge balance (number of cations:number of anions) for each analysis was positive, i.e., cations were overestimated. This could be due to the absorption of extraparticle oxygen x-rays by uranium or from some other cause. No mineral stoichiometry was matched by the analyses produced. Silicon was overestimated in all cases. The uranium:silicon ratio in uranium silicates is generally 1 or 0.5, but in the compositions obtained it was greater than 2. Also, the minerals analyzed had a relatively consistent and significant aluminum content. The uranium precipitate analyses apparently included significant extraparticle components. These results could nevertheless be used to restrict the possible mineral species occurring in the sub-tank sediments. The analyses indicated that the following elements were not present in the secondary uranium minerals: magnesium, phosphorous, sulfur, calcium, manganese, and iron. No reported uranium silicates include aluminum (Finch and Murakami 1999). The remaining elements are uranium, silicon, oxygen, sodium, and potassium. With reference to Table D.36, the possibilities for the secondary uranium mineral in these sediments are boltwoodite $[K(H_3O)(UO_2)(SiO_4)(H_2O)]$, sodium-boltwoodite $[(Na,K)(UO_2)(SiO_3OH)(H_2O)_{1.5}]$, and weeksite $[K_{1-x}Na_x(UO_2)_2(Si_5O_{13})(H_2O)_4]$.

Table D.35. Compositional Analysis Results for BX-102-61AB

As Described in the Text, Uranium-Bearing Solids were Found to Significantly Contain only Oxygen, Sodium, Aluminum, Silicon, Potassium, and Uranium (bold). Elemental Abundances, Reduced to a Stoichiometry Based on one Uranium, did not Conform to Known Minerals. C.B. = Charge Balance.

***Normalized* Wt. %**

Analysis	O	Na	Mg	Al	Si	P	S	K	Ca	Mn	Fe	U
Uraninite, UO_2	11.59	0.38	0.51	0	0.26	0	0	0.11	0	0	0	87.16
1	20.03	1.44	0.45	5.68	19.49	0.63	0	1.37	0.00	0.27	0.56	50.09
2	11.38	2.34	7.62	4.16	25.90	0.47	0	0.38	0.82	0.42	9.42	37.09
3	10.19	1.92	3.63	6.97	20.69	0.68	0	1.24	0.93	0.40	14.53	38.82
4	16.80	2.14	2.63	6.39	23.01	0	0	1.54	0.13	0	5.21	42.16
5	14.00	1.24	1.70	7.47	22.64	0.98	0	0.61	1.61	0	3.05	46.69
6	19.76	1.76	0.37	5.28	15.72	2.00	0	0.98	3.95	0.41	0.32	49.46
7	18.78	0.52	0.79	4.50	9.88	5.10	0	1.72	4.00	0.57	3.05	51.10
8	24.95	1.65	4.93	7.03	19.62	0.29	0	0.99	1.13	0.08	4.88	34.47
Mean	**16.99**	**1.62**	2.77	**5.94**	**19.62**	1.27	0	**1.10**	1.57	0.27	5.13	**43.73**
S.D.	4.93	0.57	2.54	1.23	4.95	1.66	0	0.46	1.57	0.22	4.77	6.47
S.D./Mean	0.29	0.35	**0.92**	0.21	0.25	**1.31**		0.41	**1.00**	**0.81**	**0.93**	0.15

***Elemental Abundance* U=1**

Analysis	O	Na	Mg	Al	Si	P	S	K	Ca	Mn	Fe	U	C.B.
Uraninite, UO_2	1.98	0.05	0.06	0	0.02	0	0	0.01	0	0	0	1.00	0.10
1	5.95	0.30	0.09	1.00	3.30	0.10	0	0.17	0.00	0.02	0.05	1.00	0.80
2	4.56	0.65	2.01	0.99	5.91	0.10	0	0.06	0.13	0.05	1.08	1.00	1.83
3	3.90	0.51	0.92	1.58	4.51	0.13	0	0.19	0.14	0.04	1.60	1.00	1.88
4	5.93	0.52	0.61	1.34	4.62	0.00	0	0.22	0.02	0.00	0.53	1.00	1.23
5	4.46	0.27	0.36	1.41	4.11	0.16	0	0.08	0.21	0.00	0.28	1.00	1.53
6	5.94	0.37	0.07	0.94	2.69	0.31	0	0.12	0.47	0.04	0.03	1.00	0.75
7	5.47	0.10	0.15	0.78	1.64	0.77	0	0.20	0.46	0.05	0.25	1.00	0.75
8	10.76	0.50	1.40	1.80	4.82	0.06	0	0.17	0.19	0.01	0.60	1.00	0.62

Table D.36. Uranium Silicate Minerals for Comparison to Analytical Results

Name	Stoichiometry
Boltwoodite	$K(H_3O)(UO_2)(SiO_4)\ (H_2O)$
Na-Boltwoodite	$(Na,K)(UO_2)(SiO_3OH)(H_2O)_{1.5}$
Sklodowskite	$Mg(UO_2)_2(SiO_3OH)_2\ (H_2O)_5$
Soddyite	$(UO_2)_2(SiO_4)\ (H_2O)_2$
Uranophane	$Ca(H_3O)_2(UO_2)_2(SiO_4)_2\ (H_2O)_3$
Uranosilite	$(UO_2)Si_7O_{15}(H_2O)$
Weeksite	$K_{1-x}Na_x(UO_2)_2(Si_5O_{13})(H_2O)_4$

Inspection of multiple compositional maps (Figure D.53) for uranium, iron, and strontium (a proxy for carbonate minerals), along with the extent of x-ray absorption, could show the preferential association of uranium mineralization with particular elements or minerals. The absorption signal was dependent on local sample density, so it coarsely showed the distribution of mineral phases in the imaged sample. The distribution of uranium was heterogeneous within and between samples. It could occur in intragranular space (Figure D.53, 67AB ath), on grain surfaces (Figure D.48 and Figure D.53, 67AB pH 9.5), and as discrete grains (Figure D.53, 67AB pH 7.5). In the examples shown, the uranium abundance is apparently lower in leached samples (pH 7.5 and pH 9.5) than in the unleached sample (ath); this may be a result of uranium removal by leaching or an artifact of small sample size. Uranium mineralization did not appear to be preferential with respect to iron, strontium, or any specific mineral phase.

Figure D.53. Plots of Uranium, Iron, and Strontium Abundance, and of Overall X-Ray Absorption (4 pages)

Note that Uranium occurs in Disseminated and Concentrated Zones, but is not Apparently Associated Systematically With Minerals Rich in Iron or in Strontium (an Analogue to Calcium in Carbonate Minerals).

Sample 67AB ath

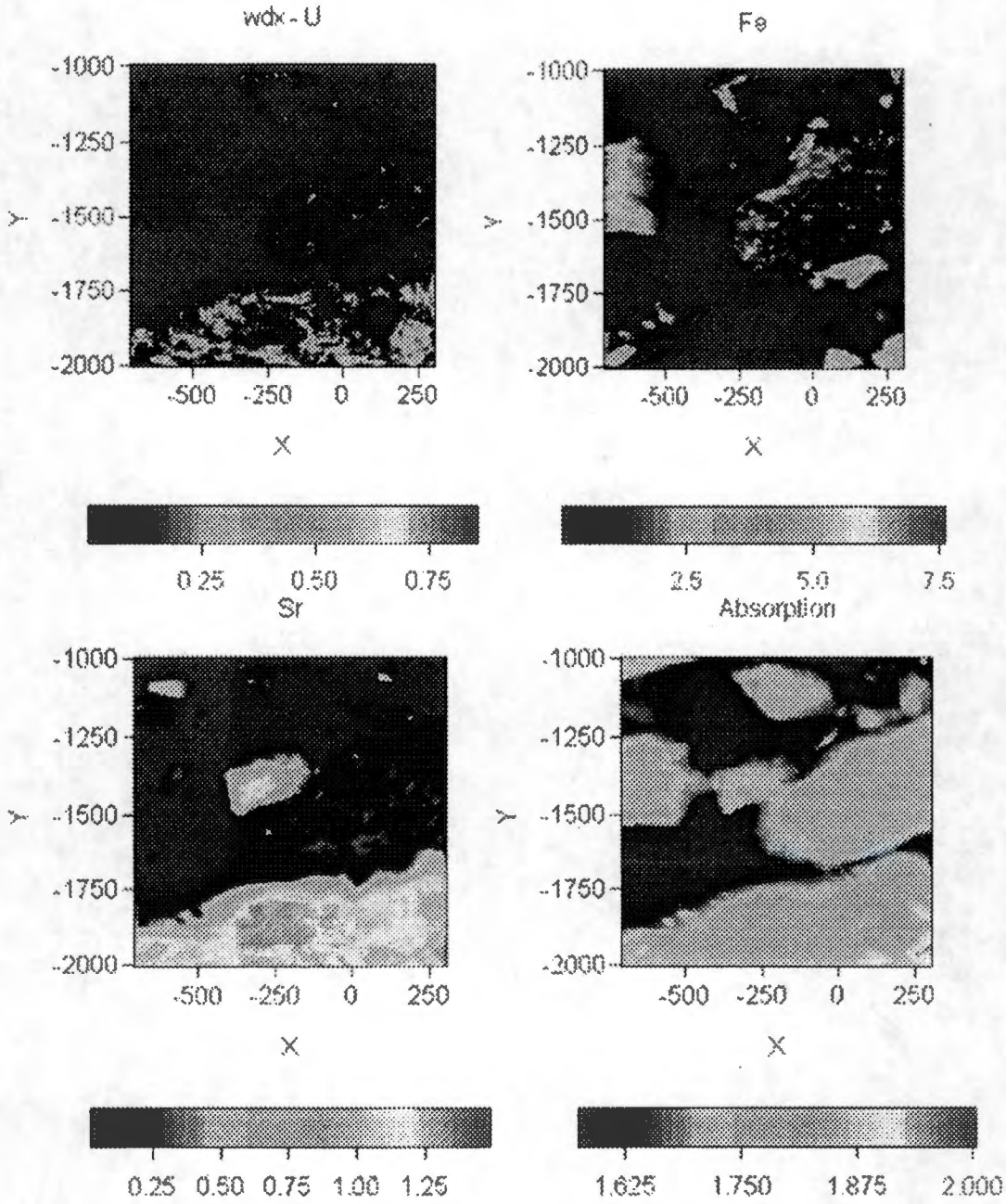

Figure D.51. Plots of Uranium, Iron, and Strontium Abundance, and of Overall X-Ray Absorption (4 pages)

Sample 67AB ath

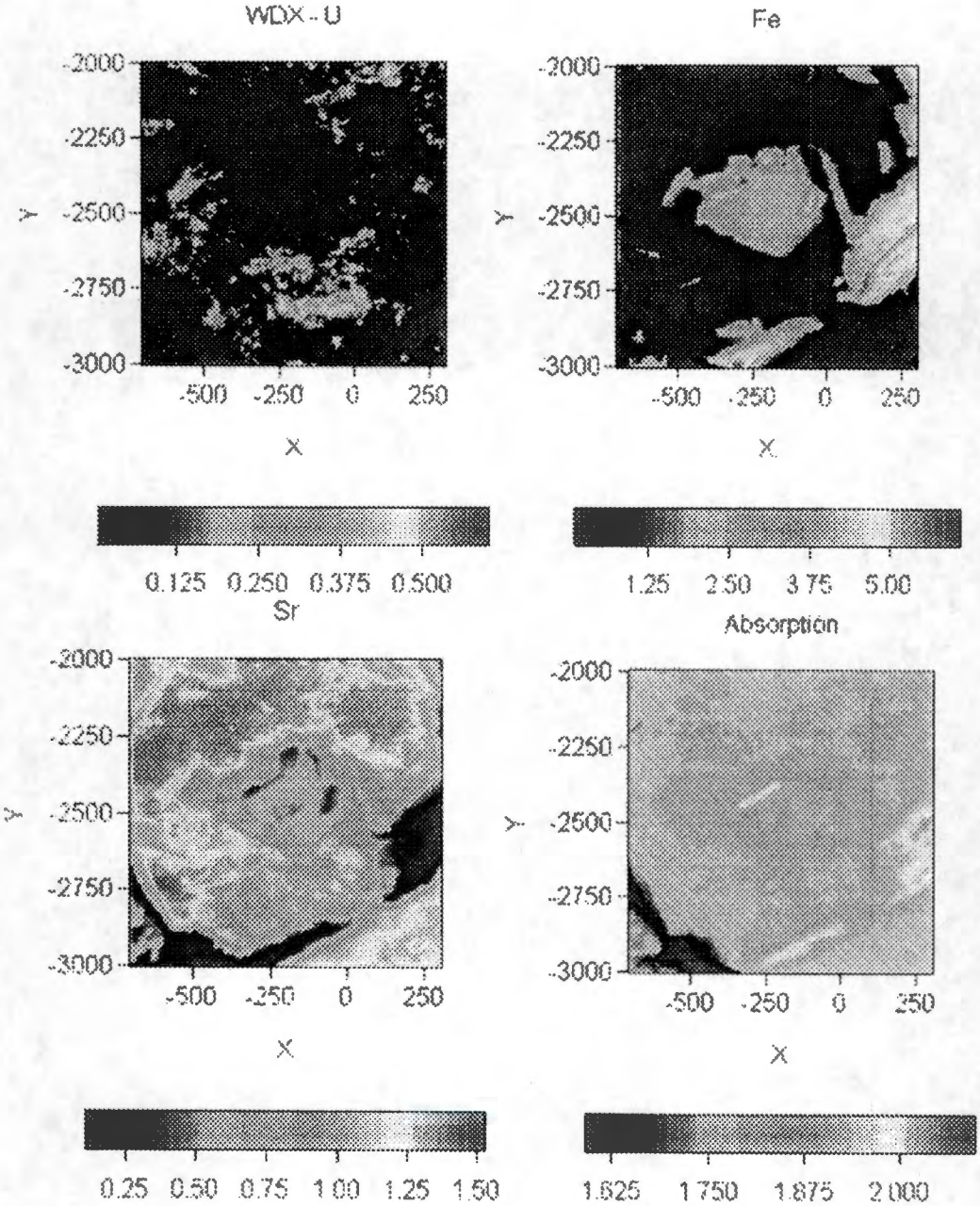

Figure D.51. Plots of Uranium, Iron, and Strontium Abundance, and of Overall X-Ray Absorption (4 pages)

Sample 67AB pH 7.5

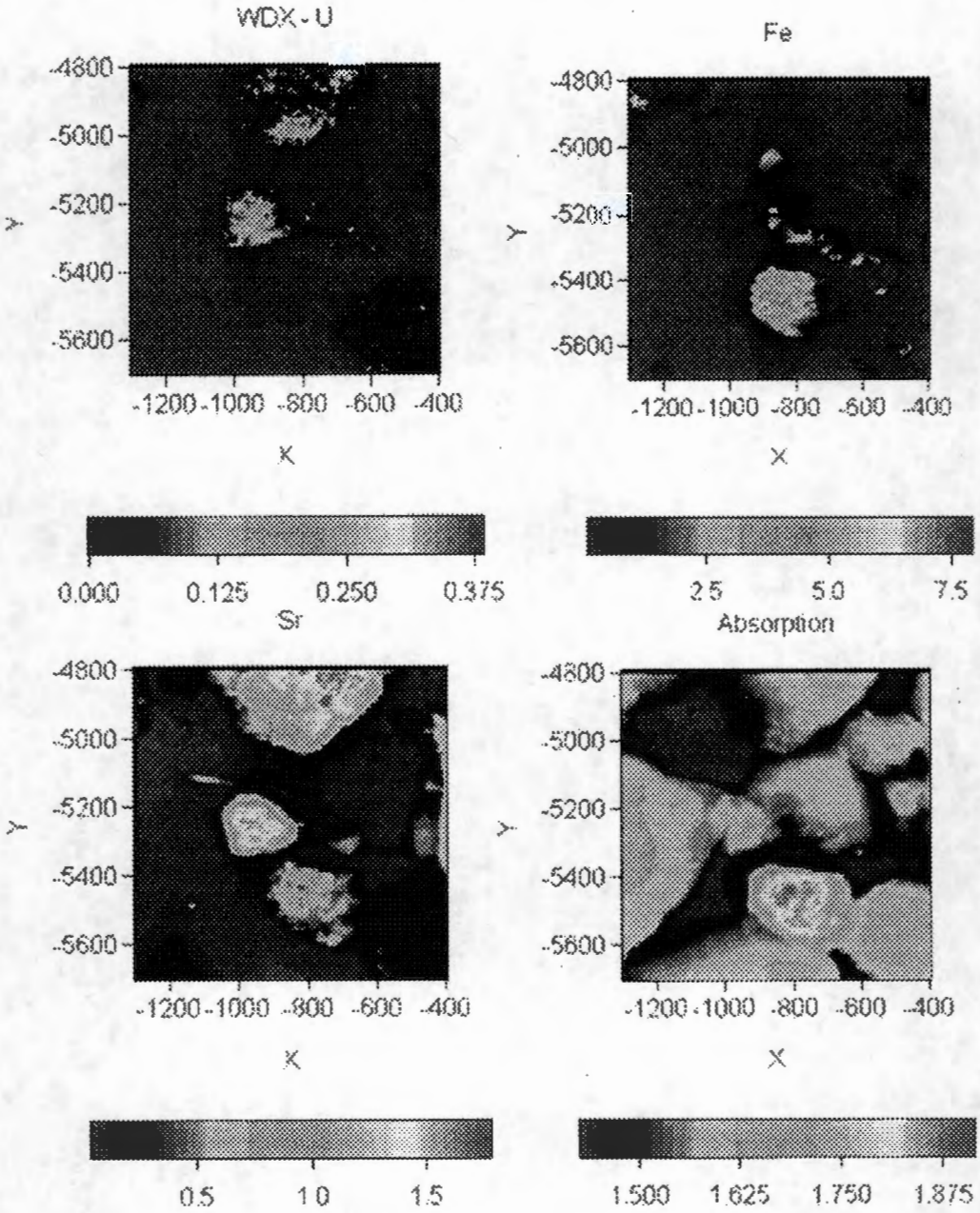

Figure D.51. Plots of Uranium, Iron, and Strontium Abundance, and of Overall X-Ray Absorption (4 pages)

Sample 67AB pH 9.5

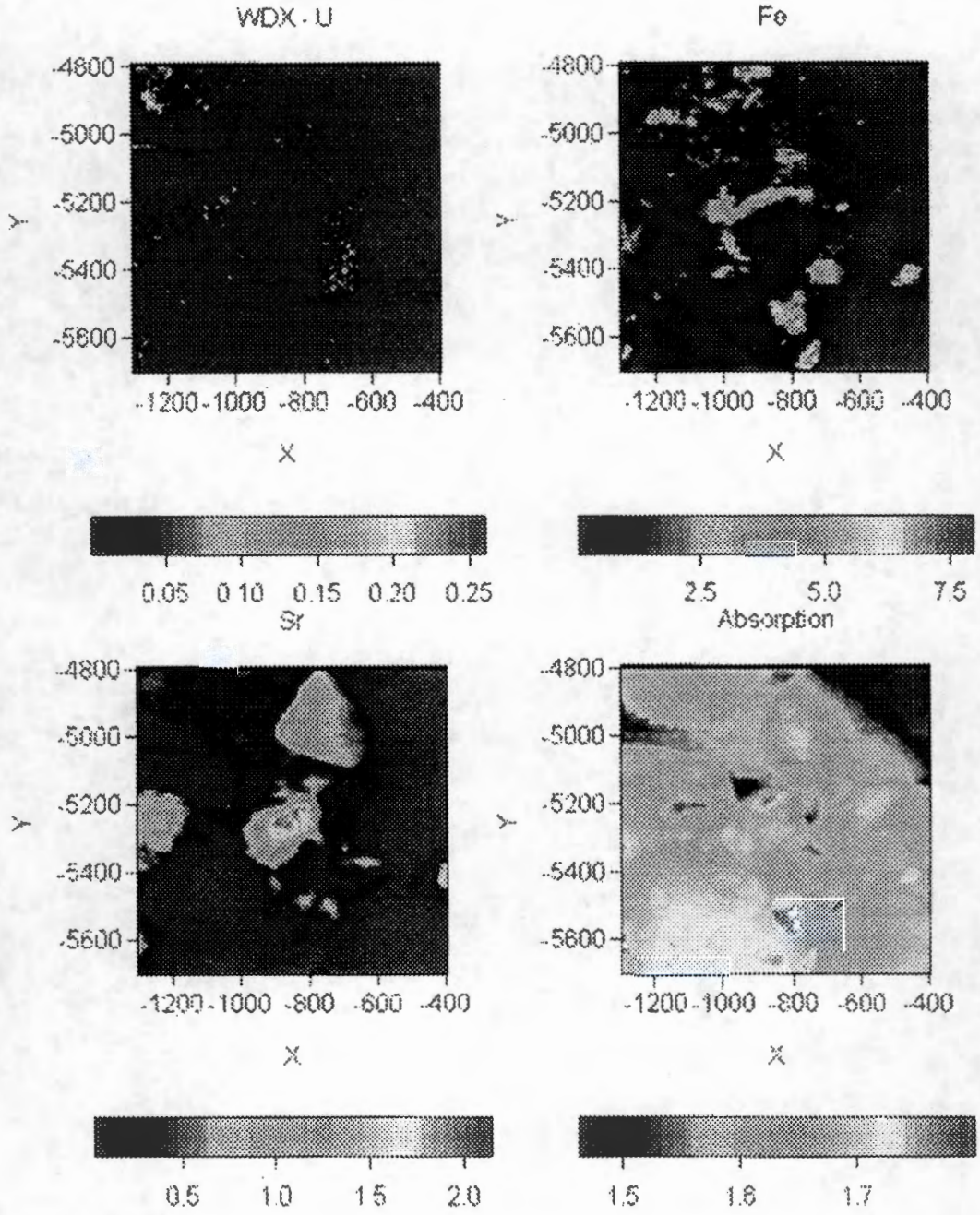

D.3.2.4 Conclusions

Sediment from core samples 57AB, 61AB, and 67Ab from borehole 299-E33-45 was examined to determine the spatial location mineral association, morphology, and composition of uranium-bearing solids. The following are primary conclusions from this work:

1. All of the uranium in these samples was hexavalent[U(VI)]. Bulk XANES and micro-XANES spectra were uniform and conformed to spectra from uranyl [$U(VI)O_2^{2+}$] containing minerals.

2. All of the observed uranium occurred as discrete grains, 1 to 3 μm across, occasionally as radiating clusters of acicular crystals.

3. Compositionally, the uranium solids consisted of uranium, silicon, oxygen, sodium, and potassium. Quantization of compositional data was poor due to grain-size constraints.

4. The limitation of candidate phases to potassium and sodium uranyl silicates could be helpful in determining the solid phase responsible for limiting aqueous uranyl concentrations; candidate reference minerals are boltwoodite [$K(H_3O)(U_2)(SiO_4)(H_2O)$], sodium-boltwoodite [$(Na,K)(UO_2)(SiO_3OH)(H_2O)_{1.5}$], weeksite [$K_{1-x}Na_x(UO_2)_2(Si_5O_{13})(H_2O)_4$], and uranophane [$Ca(UO_2)Si_2O7\text{-}6H_2O$].

5. The occurrence of minute uranium silicate minerals in microfractures indicates that waste solutions carried solute uranyl into this environment. The dissolution of silica in microfractures and at silicate grain boundaries could have caused the precipitation of uranyl silicates. Weeksite is a relatively high-silicon uranyl silicate mineral that precipitates in arid, evaporative environments.

6. The occurrence of uranyl silicates in micofractures suggests that the uranium in these solids will not be readily mobilized by leaching or in situ contact with an aqueous phase. Dissolution would be slowed by limitations on advection, the approach to uranyl mineral saturation in the microfracture environment, and solute diffusion from the microfracture.

7. The absence of a uniform sediment mineral phase association for the silicates indicates that there was not a mineral catalyst for their precipitation. Uranyl silicates apparently precipitated on available nucleation sites as thermodynamic saturation with respect to the precipitated solid was reached.

8. The precipitated solids may be heterogeneous in phase or composition, because the solution chemistry from which the minerals precipitated might not have been uniform at the microscopic scale of precipitation.

D.3.2.5 References

Chernov, D. C., 2000, *Electron Flight Simulator,* Small World LLC, Vienna, Virginia.

Eng, P. J., M. Newville, M. L. Rivers, and S. R. Sutton, 1998, Proc. SPIE 3449, 145.

Finch, R., and T. Murakami, 1999, "Systematics and Paragenesis of Uranium Minerals," In *Uranium: Mineralogy, Geochemistry, and the Environment*, P.C. Burns and R. Finch, eds., pp. 91-179.

Goldstein, J. I., D. E. Newberry, P. Echlin, D. C. Joy, A. D. Romig, Jr., C. E. Lyman, C. Fiori, and E. Lifshin, 1992, *Scanning Electron Microscopy and X-ray Microanalysis, Second Edition*, Plenum Press, New York, pp. 820.

Heald, S. M., D. L. Brewe, E. A. Stern, K. H. Kim, F. C. Brown, D. T. Jiang, E. D. Crozier, and R. A. Gordon, 1999, "XAFS and Micro-XAFS at the PNC-CAT Beamlines", *Journal of Synchrotron Radiation,* Vol. 6:347-349.

Zhong, Z., D. Chapman, B. A. Bunker, G. B. Bunker, R. Fischetti, and C. U. Segre, 1999, "A bent Laue analyzer for fluorescence EXAFS detection," *Journal of Synchrotron Radiation*, 6:212-216.

D.3.3 X-RAY SPECTROSCOPIC INVESTIGATION OF THE DISTRIBUTION AND SPECIATION OF URANIUM IN SAMPLES FROM THE BX-102 BOREHOLE

Jeffrey G. Catalano[1], John M. Zachara[2], and Gordon E. Brown, Jr.[1]

[1]Stanford University, Stanford, California 94305
[2]Pacific Northwest National Laboratory, Richland, Washington 99352

D.3.3.1 Introduction

In order to apply predictive reactive transport models to the Hanford Site, detailed knowledge of the chemical forms or speciation of contaminants is required. In the case of uranium, the important speciation parameters are:

1. oxidation state
2. types, number, and geometric arrangement of atoms in the first and second coordination spheres around uranium
3. the type and binding of uranium sorption complex (if adsorbed)
4. the type(s) of phase within which uranium is structurally incorporated [if present in a three-dimensional precipitate(s) or uranium-containing phase(s)]
5. the phase association of uranium
6. its microscopic distribution within the uranium-contaminated sediments beneath the Hanford tank farms.

The oxidation state of uranium has a strong effect on its mobility, as uranium(IV) is much less soluble, and thus less mobile than uranium(VI). Knowledge of the type(s) of adsorption complex or solid phase incorporating uranium is quite important for accurate transport modeling as uranium in an adsorbed form should be much more mobile than that incorporated into a crystalline or amorphous precipitate, depending upon its solubility, the presence of complexing ligands such as carbonate or phosphate, and pH. This is especially true for uranium(VI). Finally, understanding the phase association and spatial distribution of uranium on the microscale is essential to understanding how available it might be to reaction with porewaters, and thus the factors affecting the kinetics of desorption/dissolution of the uranium phase(s). Advanced X-ray absorption spectroscopic techniques, including both XAFS spectroscopy and X-ray fluorescence microprobe methods, can provide unique information on the speciation and spatial distribution of uranium in Hanford core samples with minimal sample preparation.

X-ray absorption fine structure (XAFS) spectroscopy has become a valuable technique for in situ studies of the molecular level speciation of heavy metals and metalloids in complex environmental samples, such as the core samples from beneath the Hanford tank farms (Zachara et al. 2002a, b) as well as samples from mine tailings (e.g., Cotter-Howells et al. 1994; Foster et al. 1997, 1998; Brown et al. 1999) and contaminated soils and sediments

(e.g., Bertsch et al. 1994; Pickering et al. 1995; Manceau et al. 1996, 2000; Hesterberg et al. 1997; O'Day et al. 1998, 2000; O'Day 1999; Allard et al. 1999; Morin et al. 1999, 2001; Kim et al. 2000; Isaure et al. 2002; Juillot et al. 2002). Analysis of the pre-edge and edge regions (the X-ray absorption near edge structure or XANES) of the XAFS spectrum of an element (usually covering the energy range from ~ 20 eV below the edge to 80-100 eV above the edge) provides information on the valence state and coordination environment of the element. The uranium L_{III}-edge XANES spectra of uranium(VI) versus uranium(IV) species, as well as for different crystalline forms containing uranium, show significant differences in energy position and structure.

Analysis of the extended X-ray absorption fine structure, or EXAFS, spectrum which extends from ~ 50 eV above the edge to ~ 800 eV above the edge, provides quantitative information on the number, distance, and identity of first-, second-, and, in favorable cases, more distant neighbors around an absorbing element. EXAFS analysis now provides structural information on first- and second-neighbor shells around an absorber comparable to that obtained in single-crystal x-ray diffraction analysis even in complex solids (O'Day et al. 1995). For absorbers in silicate glasses and in sorption complexes at mineral-water interfaces, EXAFS spectroscopy is unrivaled in the structural information it can provide for a wide range of elements, including paramagnetic and ferromagnetic species, at concentrations ranging from major levels (> 1.0 wt.%) to trace levels (< 100 ppm) in phases of all types (e.g., crystalline solids, amorphous solids, melts at high temperature, aqueous solutions, gases) without significant sample preparation or pre-treatment (Brown et al. 1988, 2001). EXAFS spectroscopy has been used to determine the molecular level speciation of uranium in crystalline model compounds (Thompson et al. 1995; Allen et al. 1996; Hudson et al. 1996), model sorption systems (Chisholm-Brause et al. 1992a, b; Dent et al. 1992; Manceau et al. 1992; Chisholm-Brause et al. 1994; Waite et al. 1994; Thompson et al. 1997, 1998; Reich et al. 1998; Hudson et al. 1999; Bargar et al. 1999, 2000; Moyes et al. 2000; Sylwester et al. 2000a, b; Redden et al. 2001; Reeder et al. 2001; Fuller et al. 2002), silicate glasses and melts (Farges et al. 1992; Farges and Brown 1997), synthetic and natural analogs of radioactive waste forms (Farges et al. 1993, 2001), contaminated sediments (Allen et al. 1994; Morris et al. 1996; Duff et al. 1997, 2000; Allard et al. 1999; Bostick et al. 2002), and highly alkaline solutions and brines (Clark et al. 1999; Wahlgren et al. 1999; Francis et al. 2000).

These EXAFS studies have been able to distinguish between the axial and equatorial oxygens around uranium(VI) and to detect second neighbors around uranium(VI) even in complex sorption systems with water present (e.g., Thompson et al. 1998). Detection and identification of second-neighbor cations is essential for determining if an inner-sphere complex versus an outer-sphere complex has formed or if a three-dimensional uranium-containing phase has precipitated. When precipitate phases or a mixture of precipitate phases and adsorbed uranium are present, linear combination least-squares fitting may be used in which the EXAFS spectra of appropriate uranium-containing model compounds are fit to the unknown spectra in order to determine which species of uranium are present in the unknown. This method has been used (e.g., Pickering et al. 1995; Foster et al. 1998; Ostergren et al. 1999; Manceau et al. 1999) in XAFS studies of other elements such as selenium, arsenic, and lead in contaminated soils and mining wastes to determine the proportions of different types of species of a given element present in a sample. The typical errors associated with this method are of the order of ± 10% of a phase.

X-ray fluorescence microprobe analysis may be used to study the distribution of different elements and of different species of each element in a thin section or bulk sample (Bertsch and Hunter 2001). A 5 μm x 5μm x-ray beam is typically used for such measurements and can be produced by a Kirkpatrick-Baez (K-B) focusing mirror assembly or by a tapered metal capillary. Element maps are made by collecting the x-ray fluorescence from the sample while rastering the sample under the beam. Areas of high concentration of an element (e.g., uranium) can then be moved to and XAFS spectra collected on the hot spot. This technique has been used successfully to study uranium in soils from Fernald, Ohio and sediments from the Savannah River Site (Bertsch et al. 1994), and evaporation pond sediments from the San Joaquin Valley, California (Duff et al. 1997, 2000).

In the present study, XAFS spectroscopy and x-ray fluorescence microprobe analyses were used to investigate the speciation and spatial distribution of uranium in samples collected from the BX-102 borehole.

D.3.3.2 Methods

Four samples from the BX-102 borehole were analyzed using XAFS spectroscopy (Table D.37). The sediment samples were packed in Teflon® sample holders sealed with 10 mil Kapton® tape, and then heat-sealed in polyethylene bags. They were shipped from PNNL to the Stanford Synchrotron Radiation Laboratory (SSRL) for XAFS spectroscopic analysis. Uranium L_{III}-edge XAFS spectra were measured at room temperature on the Molecular Environmental Sciences Beamline 11-2 (Bargar et al. 2002) at SSRL using a cryogenically cooled Si (220), $\phi = 90°$, double-crystal monochromator with the SPEAR ring operating at 60 to 100 mA electron current and 3 GeV energy. Data were collected in fluorescence-yield mode using a high-throughput 30-element, solid-state germanium detector equipped with a 6 μx strontium filter to minimize x-ray scatter. The vertical slit before the sample was adjusted to a height of 1 mm to enhance energy resolution. A collimating mirror before the monochromator was used for harmonic rejection, with a cutoff of 22 keV. Between 15 and 30 scans were collected for each sample. A yttrium metal foil was mounted between two ionization chambers downstream of the sample for energy calibration, which was monitored continuously during each EXAFS scan and was found to vary by not more than ±0.25 eV. All such variations were corrected for in the final spectra so that all spectra are referenced to the same energy scale. The first inflection point in the yttrium K-edge was set to 17038 eV.

Table D.37. Description of the Four BX-102 Borehole Samples Analyzed by XAFS Spectroscopy

Sample	Depth (ft bgs)	Uranium Concentration (ppm)
33A	73.14-73.64	173
53A	118.79-119.29	246
61A	130.70-131.20	356
67A	141.00-141.50	289

X-ray fluorescence mapping was performed on one sample, 61A, using a focused x-ray beam on SSRL beamline 11-2. Focusing of the x-ray beam for the x-ray fluorescence microprobe work was accomplished using a tapered metal microcapillary. This provided roughly 1.3×10^9 photons/s in a spot with a 14 μm full-width half-maximum (FWHM). The same monochromator settings and synchrotron ring conditions were used as described above. The sample was prepared for analysis by impregnating it in epoxy, followed by thin sectioning to ~80 μm thickness using standard petrographic techniques (Section D.3.2). The thin sections were covered with a 10 mil Kapton® tape at PNNL in order to protect against contamination of the experimental hutch at SSRL, and shipped to SSRL. The thin section was mounted on a motorized stage and brought up to within 50 μm of the end of the capillary. Uranium elemental mapping was accomplished by rastering the sample in the vertical and horizontal directions perpendicular to the beam. The incident and exit beam intensities were measured using gas-filled ion chambers, and the uranium L_α fluorescence was measured with a single-element, solid-state germanium detector. The incident beam was monochromatized to 17180 eV for mapping. Maps of the uranium fluorescence intensity, normalized to the incident beam intensity, provide a 2-dimensional distribution of relative uranium concentrations. Absolute concentrations were not determined because of the difficulty of correcting for matrix effects using known uranium standards. X-ray transmission maps of the same areas provide 2-dimensional density maps, as more electron-dense materials absorb more of the transmitted beam. As the epoxy filling the pore spaces is much less dense, and absorbs much less of the x-ray beam than the sediment material, the transmission maps are analogous to optical images of the thin sections. Each map is scaled independently, and different maps are not directly comparable in terms of relative uranium concentration. Uranium L_{III}-XAFS spectra were collected on areas of high uranium concentration using the single-element germanium detector.

Uranium L_{III}-XAFS data were processed using EXAFSPAK (George and Pickering 2000). XANES data were background-subtracted and normalized to an edge-step of 1. After background-subtraction, the EXAFS data ($\chi[k]$) were extracted and k^3-weighted. Phase-shift and backscattering amplitude functions for quantitative EXAFS fitting to a structural model were generated from the crystal structure of soddyite [$(UO_2)_2SiO_4 \cdot 2H_2O$] (Demartin et al. 1993) using the multiple scattering computer code FEFF 7 (Ankudinov and Rehr 1997; Rehr and Albers 2000). Accuracies on first- and second-neighbor bond distances were estimated to be ± 0.01 Å and ± 0.03 Å, respectively, based on comparison to fit results of EXAFS from compounds (soddyite and uranophane). As all samples contained a uranium backscatterer (Section D.3.2), suggestive of crystalline precipitates, linear combination fitting of the EXAFS was conducted to identify the potential crystalline phases present. An extensive model compound library was examined (Figure D.54), and linear combination least squares fitting was performed in EXAFSPAK. In the linear combination least squares fitting, the residual, $R = (k^3\chi_{exp} - k^3\chi_{model})/k^3\chi_{exp}$, was minimized. Principal component analysis (PCA) of the spectra was attempted in WinXAS (Ressler 1997), although this analysis failed to identify more than one component as discussed below.

Figure D.54. Model Compound Uranium L_{III}-EXAFS Library Used in Linear Combination Fitting of Sample EXAFS Data

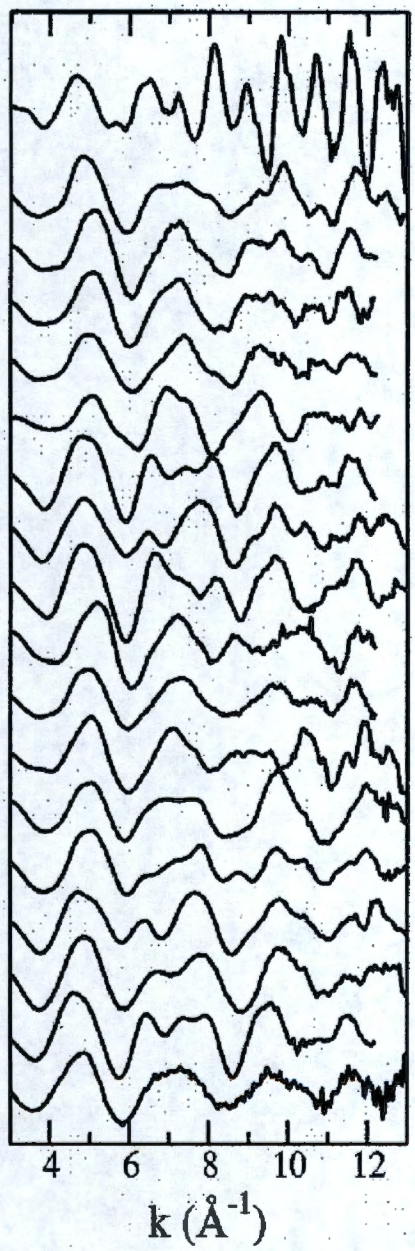

Name	Chemical Formula
Uraninite	UO_2
Soddyite, syn	$(UO_2)_2SiO_4 \cdot 2H_2O$
Uranophane	$Ca(UO_2)_2(SiO_3OH)_2 \cdot 5H_2O$
Kasolite	$PbUO_2SiO_4 \cdot H_2O$
Schoepite, syn	$(UO_2)_8O_2(OH)_{12} \cdot (H_2O)_{12}$
Clarkeite, syn	$Na_2U_2O_7 \cdot xH_2O$
Liebigite	$Ca_2(UO_2)(CO_3)_3 \cdot 11(H_2O)$
Rutherfordine	UO_2CO_3
Sodium uranyl carbonate	$Na_4(UO_2)(CO_3)_3 \cdot x(H_2O)$
Saleeite	$Mg(UO_2)_2(PO_4)_2 \cdot 8H_2O$
Phosphuranylite	$KCa(H_3O)_3(UO_2)_7(PO_4)_4O_4 \cdot 8(H_2O)$
Metaautunite	$Ca(UO_2)_2(PO_4)_2 \cdot 6H_2O$
Uranyl hydrogenphosphate	$UO_2HPO_4 \cdot 2H_2O$
Uranyl orthophosphate	$(UO_2)_3(PO_4)_2 \cdot 4H_2O$
Uranyl nitrate	$UO_2(NO_3)_2 \cdot 6H_2O$
Uranyl, aqueous	$UO_2^{2+}{}_{(aq)}$
Uranyl-carbonato, aqueous	$UO_2(CO_3)_3^{4-}{}_{(aq)}$
Uranyl adsorbed on smectite, pH = 7	$X\text{-}UO_2^{2+}$

D.3.3.3 Results

D.3.3.3.1 X-ray Microprobe Study of the Distribution of Uranium in Sample 61A. The distribution of uranium in one BX-102 sample, 61A, was investigated using x-ray fluorescence microprobe mapping. Uranium appears to be distributed heterogeneously throughout sample 61A, as shown in Figure D.55. More detailed maps of the areas around many of the uranium hotspots (Figure D.56 and Figure D.57) show that uranium appears to occur as discrete

~ 40 to 100 μm particles on the surface of and between larger sediments grains. However, the actual size of these particles may be much smaller, as the particle sizes interpreted from the maps are actually a convolution of the real particle sizes with the x-ray beam size on the sample. Additionally, what appears as individual particles in these images may actually be areas containing multiple smaller particles. These results suggest that uranium primarily occurs as a discrete solid phase or phases, and that no significant fraction of uranium occurs adsorbed onto mineral surfaces.

Figure D.55. Uranium L_α Fluorescence (top) and X-ray Transmission (bottom) Maps of a Thin Section from Sample 61AB

The Maps are 2 mm by 2 mm, with 20 μm Pixels. Also Shown are the Location of Four of the Five Uranium hotspots Analyzed by XANES Spectroscopy; Spot 5 is Located in an Area to the Right of the Map.

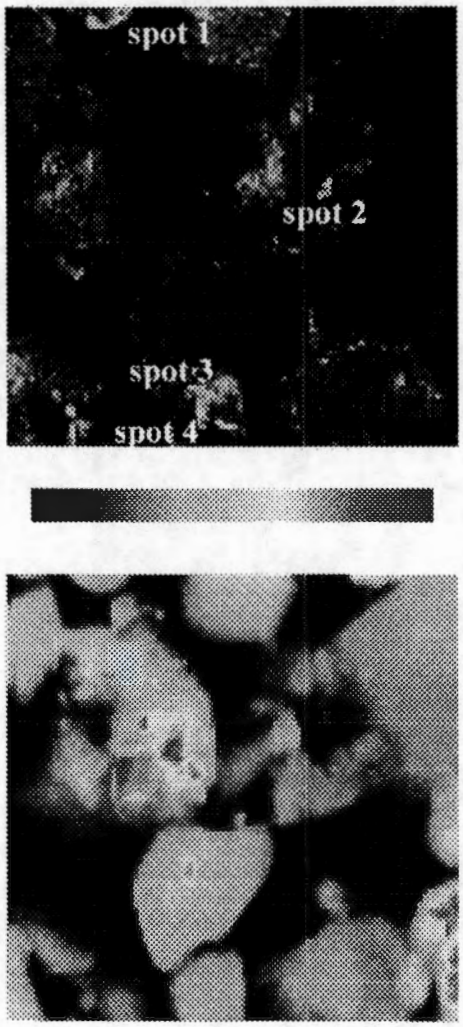

Figure D.56. Uranium L_α Fluorescence (left) and X-ray Transmission (right) Maps of the Areas Around (a) Hotspot 1, (b) Hotspot 2, (c) Hotspot 3, and (d) Hotspot The Maps are 100 μm by 100 μm, with 5 μm Pixels.

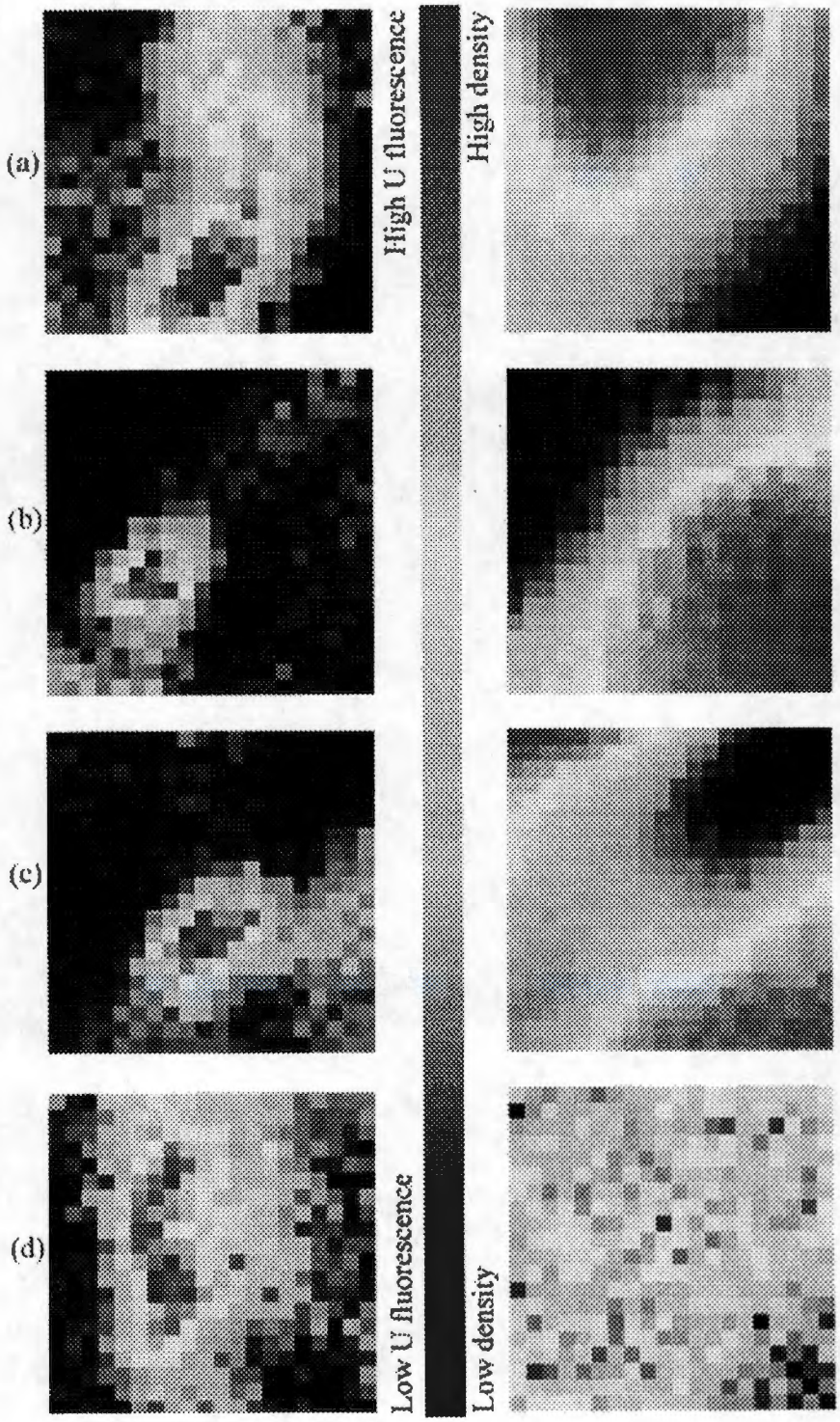

Figure D.57. Uranium Lα Fluorescence (top) and X-ray Transmission (bottom) Maps of the Area Around Hotspot 5
The Maps are 200 μm by 200 μm, with 5 μm Pixels. XAFS Spectroscopic Studies of the Speciation of BX-102 Samples.

Low U fluorescence High U fluorescence

Low density High density

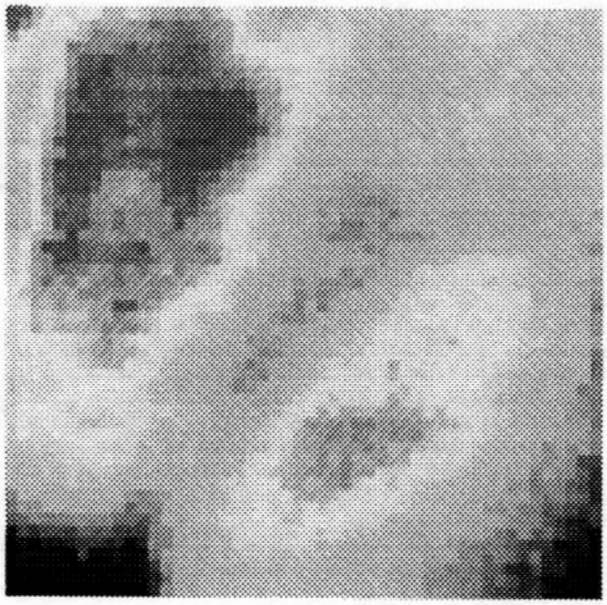

D.3.3.3.2 Oxidation State of Uranium in the BX-102 Core Samples. The oxidation state of uranium in the four BX-102 samples was investigated using XANES spectroscopy. All samples had nearly identical XANES spectra (Figure D.58). The edge energies of the XANES spectra for all of these samples are consistent with that of uranium(VI). Additionally, the shoulder occurring in the spectrum at ~ 17190 eV indicates that uranium(VI) occurs in the form of uranyl, UO_2^{2+} (Farges et al. 1992; Hudson et al. 1995). The oxidation state of the hotspots identified in the x-ray fluorescence microprobe analyses above was also investigated, using micro-XANES spectroscopy. All five hotspots analyzed consisted of uranium(VI), in the form of uranyl (Figure D.59). These results suggest that little or no reduction of uranium has occurred in the Hanford subsurface to date, and that there is little possibility for natural attenuation of a uranium plume at Hanford through reductive immobilization.

Figure D.58. XANES Spectra of the Four BX-102 Borehole Sample, as Well as Those of Schoepite, a Uranium(VI) Standard, and Uraninite, a Uranium(IV) Standard

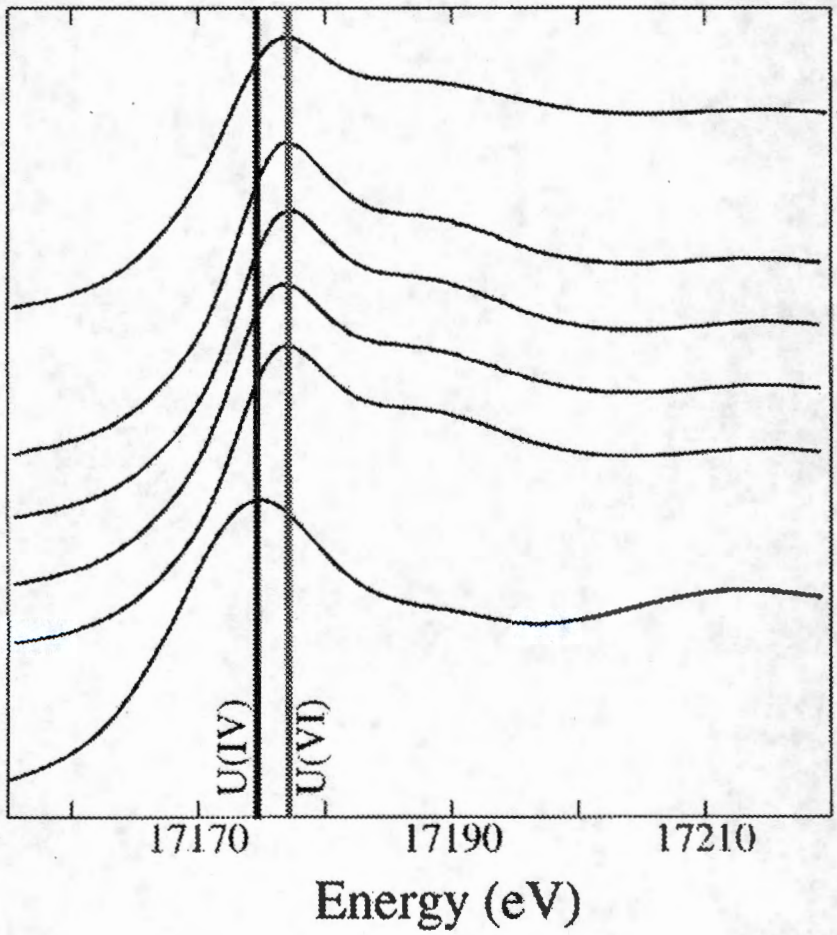

Figure D.59. Uranium L_{III} μ-XANES Spectra of Five Hotpots from the Sample 61A Thin Section

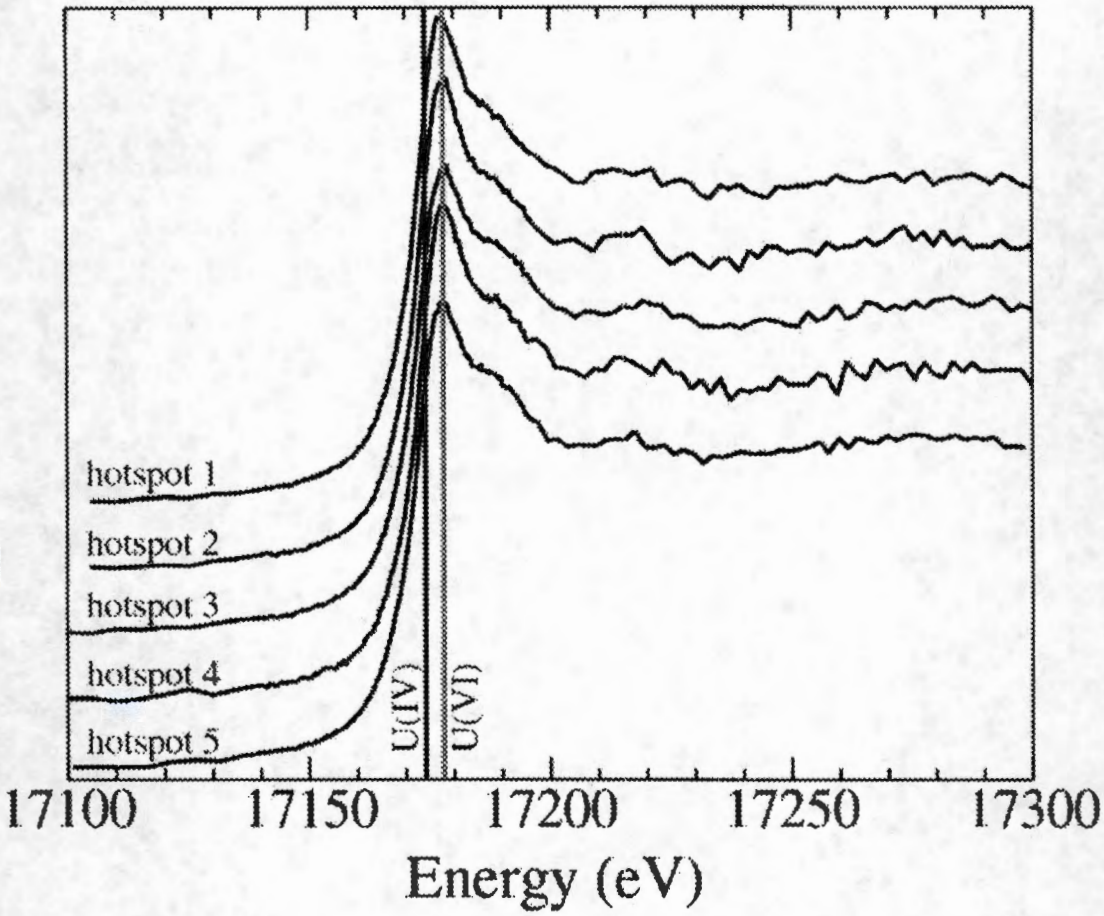

D.3.3.3.3 Speciation of Uranium(VI) in the BX-102 Core Samples. The speciation of uranium(VI) in the BX-102 samples was analyzed using EXAFS spectroscopy. After the initial background subtraction, the raw uranium L_{III}-EXAFS spectra were fit to a structural model using the phase-shift and backscattering amplitude functions described above (Figure D.60). Fits to the first oxygen shell were in good agreement with the local structure of uranyl observed in natural samples (Burns 1999a): two oxygen atoms at a distance of about 1.8 Å ($U{=}O_{ax}$), and four to six oxygen atoms in the range of 2.2 to 2.5 Å ($U\text{-}O_{eq1}$, $U\text{-}O_{eq2}$) (Table D.38). These data agree with the XANES results discussed above, confirming that uranium occurs predominantly in the 6+, uranyl form.

Further fitting of structural parameters to the uranium L_{III}-EXAFS data were limited to that of a uranium shell at distances > 3.8 Å. As the composition of the uranium-bearing phase(s) is unknown, fitting backscattering atoms in the intermediate range of 2.5 to 3.8 Å is not justified, as any number of potential structural ligands may occur at these distances, including carbonate, nitrate, phosphate, silicate, and sulfate. The scattering intensity from such groups is relatively weak, and thus fitting them without any a priori knowledge of the possible identity of these ligands or without subtracting the spectral contributions of uranyl ions (e.g., Fuller et al. 2002) is

unwise. However, fitting uranium backscatterers at distances > 3.8 Å is quite reasonable due to their large scattering amplitude. Uranium backscatterers were fit for all four samples (Table D.38). All samples had nearly identical fits of one to two uranium atoms at 3.92 ± 0.01 Å. Comparison of this uranium-uranium distance to that of known uranium mineral structures with uranium-uranium distances close to this value (Figure D.61) suggests that uranium occurs in the BX-102 samples as an uranophane group mineral, all of which have similar basic structures.

The uranophane group consists of the minerals uranophane (α and β), boltwoodite, sklodowskite, cuprosklodowskite, and kasolite. While the latter two have different uranium L_{III}-EXAFS spectra due to the presence of highly backscattering atoms (copper and lead), the uranium L_{III}-EXAFS spectra for the rest of these phases are nearly identical due to the weakly backscattering alkaline or alkaline earth cations in these structures (calcium in uranophane, sodium and potassium in boltwoodite, and magnesium in sklodowskite). Comparison of the crystallographic bond lengths for these minerals with the EXAFS-derived bond lengths in the BX-102 samples demonstrates that one or more of the uranophane group minerals make up most (> 95%) of the uranium in the sample.

While the fit results appear closest to the uranophane structure, any of the alkaline uranophane group minerals may be present as their structural parameters are all within the estimated errors for the EXAFS-derived parameters.

Table D.38. Uranium L_{III}-EXAFS Fitting Result for the Four BX-102 Core Samples Compared to the XRD-Derived Values for Uranophane, a Potential Phase Occurring in the Hanford Subsurface

The Estimated Standard Deviations (1σ) of the First- and Second-Neighbor Interatomic Distances and Coordination Numbers Derived from Fitting the EXAFS Data to a Structural Model are ±0.005 Å, ± 0.02 Å, and ± 0.3 Atoms, Respectively.

Sample		$U=O_{ax}$	$U-O_{eq1}$	$U-O_{eq2}$	U-U
33A	N R(Å)	2* 1.81	3.3 2.29	2.5 2.44	1.1 3.91
53A	N R(Å)	2* 1.81	3.9 2.28	2.1 2.45	1.8 3.93
61A	N R(Å)	2* 1.81	2.8 2.28	2.2 2.44	1.7 3.92
67A	N R(Å)	2* 1.82	3.2 2.28	1.8 2.46	1.5 3.93
α-Uranophane (Ginderow 1988)	N R(Å)	2 1.81	3 2.28	2 2.46	2 3.92
β-Uranophane (Viswanathan 1986)	N R(Å)	2 1.82	3 2.30	2 2.48	2 3.92
Sklodowskite (Ryan and Rosenzweig 1977)	N R(Å)	2 1.81	3 2.29	2 2.44	2 3.945
Boltwoodite (Burns 1998)	N R(Å)	2 1.81	3 2.30	2 2.45	3 3.95

* Value fixed during fitting

Figure D.60. Uranium L_{III}-EXAFS (right) and Corresponding Fourier Transforms (left) Data (black) and Structural Model Fits (red dashed) for the Four BX-102 Core Samples

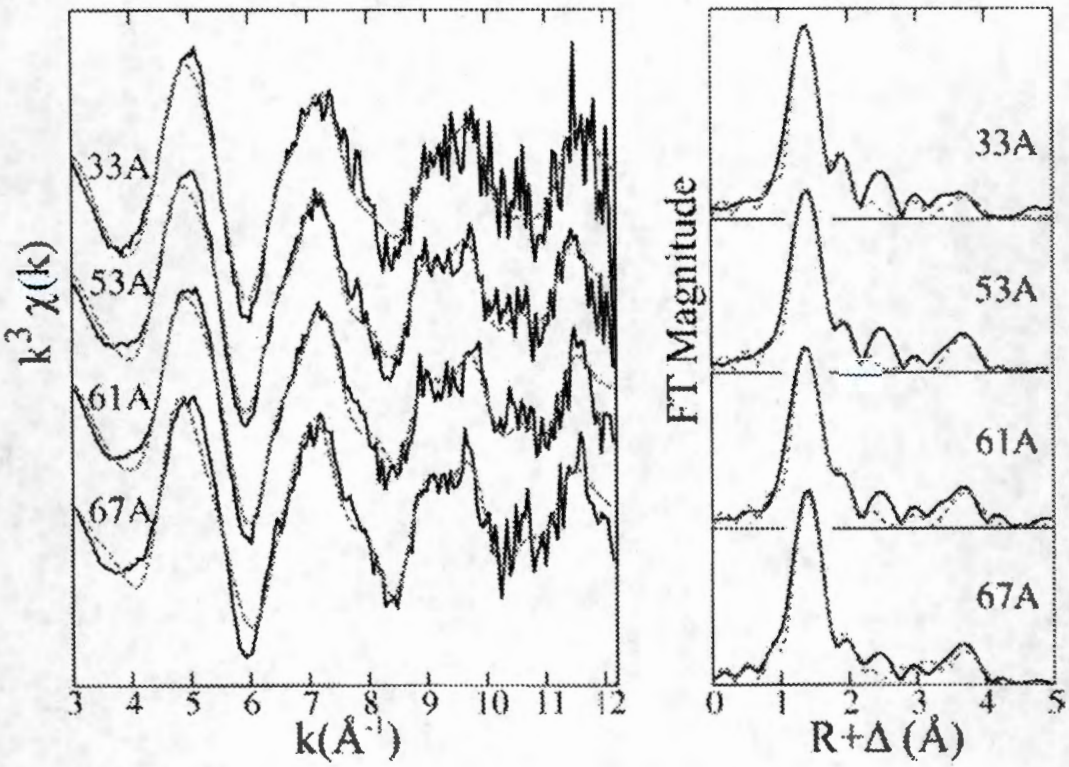

Uranophane, boltwoodite, and sklodowskite all may potentially be present in the subsurface beneath BX-102, as they only differ in the charge balancing alkaline or alkaline earth cations in their structures. Recent studies of synthetic samples of these phases suggest that these cations may exchange with other cations in solution (Burns 1999b), and that a limited solid solution of cations may also be possible (Burns 1998). These results suggest, in turn, that alkali or alkaline earth cations in the uranophane phases may have exchanged with those in the surrounding porewater extractions and suggest that sodium and calcium are the dominant cations present in these sediments, suggesting that uranophane and boltwoodite are the most likely phases present.

To further explore the potential uranium-containing phases present in the BX-102 samples, principal component analysis (PCA) was conducted. This analysis failed, suggesting that only one component is sufficient to fit the uranium L_{III}-EXAFS data and that multiple uranium-containing phases are not present. PCA only works properly when two or more phases are present. After this analysis, one-component linear combination least squares fitting was performed to investigate which phase from the uranium L_{III}-EXAFS model compound library (Figure D.54) fit the data best. For all four BX-102 samples, uranophane provided the smallest residual, and provided the best fit visually (Figure D.62). The fitting results indicate that uranophane comprises 98 to 102 % of the samples (i.e., effectively 100% considering the noise levels in the data).

Figure D.61. Comparison of Uranium-Uranium Distances Derived from the Fits to the Uranium L_{III}-EXAFS Spectra of the Four BX-102 Samples to Crystallographic Distances in Uranium Minerals

Only Minerals with Uranium-Uranium Distances in the Range of 3.8 – 4.35 Å Are Shown.

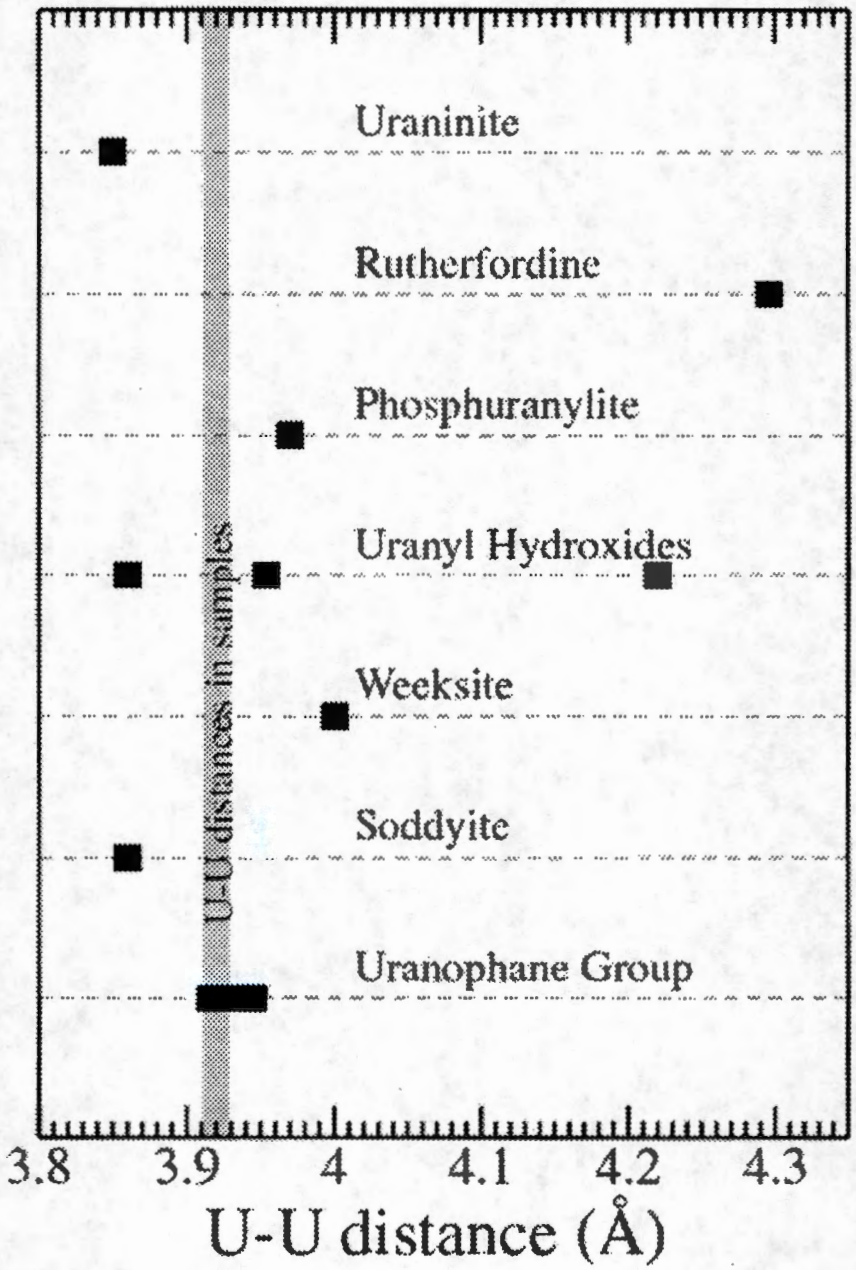

Figure D.62. Linear Combination Least Squares Fit of the Uranium L_{III}-EXAFS Spectra of Borehole BX-102 Samples Using One Component (Uranophane). Fit Percentages Have Not Been Normalized to 100%.

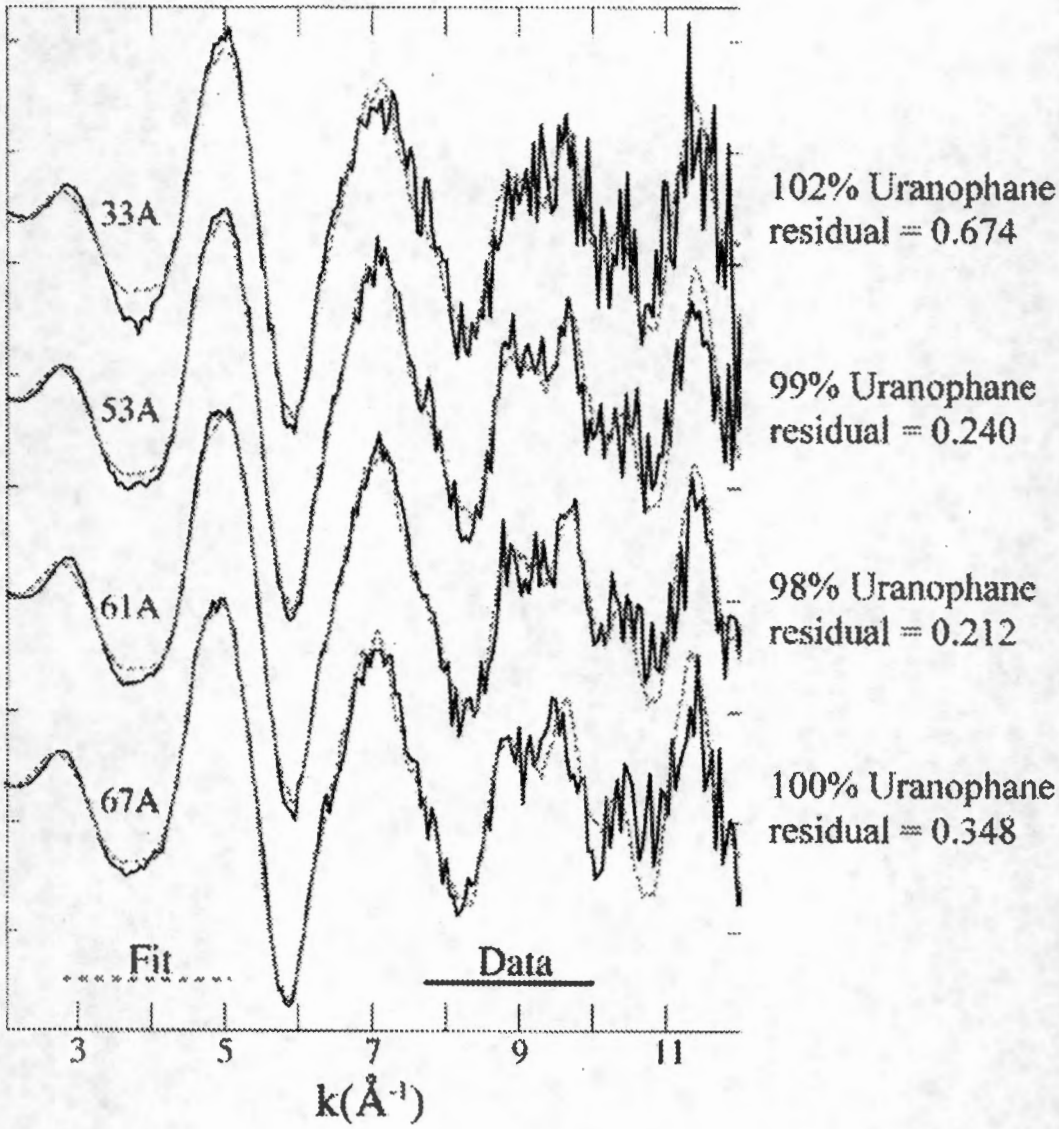

D.3.3.4 Conclusions

1. Uranium occurs under the BX tank farm as small particles or particle aggregates.

2. The primary oxidation state of uranium occurring in the subsurface under tank BX-102 is the (VI) form. Uranium containing sediment samples from borehole 299-E33-45 (i.e., 33A, 53A, 61A, and 62A) were studied by x-ray adsorption spectroscopy at the Stanford Synchotron Radiation Laboratory. The objectives of the measurements were to a) identify the spatial location and chemical association of uranium and b) to provide spectroscopic identification of the present uranium phase or phases.

3. The dominant form of uranium in the BX-102 sediments is a mineral or minerals from the uranophane group. Potential candidates consistent with the uranium L_{III}-EXAFS data and porewater chemistry are uranophane [$Ca(UO_2)_2(SiO_3OH)_2 \cdot 5H_2O$] or boltwoodite [$(K,Na)UO_2SiO_3OH \cdot 2.5H_2O$], or a mixture or solid solution of these two.

4. Additional transport of uranium under the BX-102 tank will likely be controlled by the solubility of uranophane and boltwoodite.

5. Future planned work, including more detailed x-ray fluorescence microprobe studies as well as micro-X-ray diffraction, should confirm the identity of these uranium-containing phases.

D.3.3.5 References

Allard, T., P. Ildefonse, K. Beaucaire, and G. Calas, 1999, "Structural Chemistry of Uranium Associated with Si, Al, Fe Gels in a Granitic Uranium Mine," *Chemical Geology*, Vol. 158:81-103.

Allen, P. G., J. M. Berg, C. J. Chisholm-Brause, S. D. Conradson, R. J. Donohoe, D. E. Morris, J. A. Musgrave, and C. D. Tait, 1994, "Determining Uranium Speciation in Contaminated Soils by Molecular Spectroscopic Methods: Examples from the Uranium in Soils Integrated Demonstration Technology Programs," *Radioactive Waste Management and Environmental Restoration*, Vol. 3:2063-2068.

Allen, P. G., D. K. Shuh, J. J. Bucher, N. M. Edelstein, C. E. A. Palmer, R. J. Silva, S. N. Nguyen, L. N. Marquez, and E. A. Hudson, 1996, "Determinations of Uranium Structures of EXAFS: Schoepite and Other U(VI) Oxide Precipitates," *Radiochimica Acta*, Vol. 75:47-53.

Ankudinov, A. L., and J. J. Rehr, 1997, "Relativistic Calculations of Spin-Dependent X-Ray-Absorption Spectra," *Physical Review B: Condensed Matter and Materials Physics*, Vol. 56(4):R1712-R1715.

Bargar, J. R., G. E. Brown, Jr., I. Evans, T. Rabedeau, M. Rowen, and J. Rogers, 2002, "A New Hard X-Ray XAFS Spectroscopy Facility for Environmental Samples, Including Actinides, at The Stanford Synchrotron Radiation Laboratory." In *Proceedings of the Euroconference and NEA Workshop on Speciation, Techniques, and Facilities for Radioactive Materials at Synchrotron Light Sources*, Grenoble, France, Sept. 10-12, 2000, Nuclear Energy Agency, Organization for Economic Cooperation and Development, Paris, pp. 57-68.

Bargar, J. R., R. Reitmeyer, and J. A. Davis, 1999, "Spectroscopic Confirmation of Uranium(VI)-Carbonato Adsorption Complexes on Hematite," *Environmental Science & Technology*, Vol. 33:2481-2484.

Bargar, J. R., R. Reitmeyer, J. J. Lenhart, and J. A. Davis, 2000, "Characterization of U(VI)-Carbonato Ternary Complexes on Hematite: EXAFS and Electrophoretic Mobility Measurements," *Geochimica et Cosmochimica Acta*, Vol. 64:2737-2749.

Bargar, J. R., R. Reitmeyer, and J. A. Davis, 1999, "Spectroscopic Confirmation of Uranium (VI)–Carbonato Adsorption Complexes on Hematite," *Environmental Science & Technology,* Vol. 33:2481-2484.

Bertsch, P. M., and D. B. Hunter, 2001, "Applications of Synchrotron-Based X-Ray Microprobes," *Chemical Reviews,* Vol. 101:1809-1842.

Bertsch P. M., D. B. Hunter, S. R. Sutton, S. Bajt, and M. L. Rivers, 1994, "In Situ Chemical Speciation of Uranium in Soils and Sediments by Micro X-Ray Absorption Spectroscopy," *Environmental Science & Technology,* Vol. 28:980-984.

Bostick, B. C., S. Fendorf, M. O. Barnett, P. M. Jardine, and S. C. Brooks, 2002, "Uranyl Surface Complexes Formed on Subsurface Media from DOE Facilities," *Soil Science Society of America Journal,* Vol. 66:99-108.

Brown, G. E., Jr., G. Calas, G. A. Waychunas, and J. Petiau, 1988, "X-Ray Absorption Spectroscopy and Its Applications in Mineralogy and Geochemistry," In *Spectroscopic Methods in Mineralogy and Geology – Reviews in Mineralogy*, Vol. 18, F. Hawthorne, ed., Mineralogical Society of America, Washington, D. C., pp. 431-512.

Brown, G. E., Jr., F. Farges, J. R. Bargar, and H. T. Berbeco, 2001, "Actinides in Silicate Glasses and Melts and on Mineral Surfaces: Information on Local Coordination Environments from XAFS Spectroscopy and Bond Valence Theory," In *Proceedings of the Euroconference and NEA Workshop on Speciation, Techniques, and Facilities for Radioactive Materials at Synchrotron Light Sources,* Grenoble, France, Sept. 10-12, 2000, Nuclear Energy Agency, Organization for Economic Cooperation and Development, Paris, pp. 141-148.

Brown, G. E., Jr., G. A. Parks, J. R. Bargar, and S. N. Towle, 1999, "Use of X-Ray Absorption Spectroscopy to Study Reaction Mechanisms at Metal Oxide-Water Interfaces," In *Kinetics and Mechanisms of Reactions at the Mineral/Water Interface – American Chemical Society Symposium Series 715,* D. L. Sparks and T. Grundl, eds., American Chemical Society, Columbus, Ohio.

Burns, P. C., 1998, "The Structure of Boltwoodite and Implications of Solid Solution Toward Sodium Boltwoodite," *Canadian Mineralogist,* Vol. 36(pt.4):1069-1075.

Burns, P. C., 1999a, "The Crystal Chemistry of Uranium," In *Uranium: Mineralogy, Geochemistry and the Environment*, P. C. Burns and R. Finch, eds., Mineralogical Society of America, Washington, D. C., Vol. 38, pp. 23-90.

Burns, P. C., 1999b, "Cs Boltwoodite Obtained by Ion Exchange from Single Crystals: Implications for Radionuclide Release in a Nuclear Repository," *Journal of Nuclear Materials*, Vol. 265(1-2):218-223.

Chisholm-Brause, C. J., S. D. Conradson, C. T. Buscher, P. G. Eller, and D. E. Morris, 1994, "Speciation of Uranyl Sorbed at Multiple Binding Sites on Montmorillonite," *Geochimica et Cosmochimica Acta,* Vol. 58:3625-3631.

Chisholm-Brause, C. J., S. D. Conradson, P. G. Eller, and D. E. Morris, 1992a, "Changes in Uranium(VI) Speciation upon Sorption onto Montmorillonite from Aqueous and Organic Solutions," In *Scientific Basis for Nuclear Waste Management XV – Materials Research Society Symposium Proceedings,* Materials Research Society, Warrendale, Pennsylvania, Vol. 257:315-322.

Chisholm-Brause, C. J., D. E. Morris, and R. E. Richard, 1992b, "Speciation of Uranium(VI) Sorption Complexes on Montmorillonite," In *Water-Rock Interaction, Proceedings of the 7th International Symposium,* Y. K. Kharaka and A. S. Maest, eds., Balkema, Rotterdam, pp. 137-140.

Clark, D. L., S. D. Conradson, R. J. Donohoe, D. W. Keogh, D. E. Morris, P. D. Palmer, R. D. Rogers, and C. D. Tait, 1999, "Chemical Speciation of the Uranyl Ion Under Highly Alkaline Conditions. Synthesis, Structures, and Oxo Ligand Exchange Dynamics," *Inorganic Chemistry,* Vol. 38:1456-1466.

Cotter-Howells, J. D., P. E. Champness, J. M. Charnock, and R. A. D. Pattrick, 1994, "Identification of Pyromorphite in Mine-Waste Contaminated Soils by ATEM and EXAFS," *Journal of Soil Science*, Vol. 45:393-402.

Demartin, F., C. M. Gramaccioli, and T. Pilati, 1993, "The Importance of Accurate Crystal Structure Determination of Uranium Minerals. II. Soddyite $(UO_2)_2SiO_4 \cdot 2H_2O$," *Acta Crystallographica,* Vol. C48:1-4.

Dent, A. J., J. D. F. Ramsay, and S. W. Swanton, 1992, "An EXAFS Study of Uranyl Ions in Solutions and Sorbed onto Silica and Montmorillonite Clay Colloids," *Journal of Colloid and Interface Science,* Vol. 150:45-60.

Duff, M. C., C. Amrhein, P. M. Bertsch, and D. B. Hunter, 1997, "The Chemistry of Uranium in Evaporation Pond Sediment in the San Joaquin Valley, California, U.S.A. Using X-Ray Fluorescence and XANES Techniques," *Geochimica et Cosmochimica Acta,* Vol. 61:73-81.

Duff, M. C., D. E. Morris, D. B. Hunter, and P. M. Bertsch, 2000, "Spectroscopic Characterization of Uranium in Evaporation Basin Sediments," *Geochimica et Cosmochimica Acta,* Vol. 64:1535-1550.

Farges, F., M. Harfouche, P. E. Petit, and G. E. Brown, Jr., 2001, "Actinides in Earth Materials: The Importance of Natural Analogs," In *Proceedings of the Euroconference and NEA Workshop on Speciation, Techniques, and Facilities for Radioactive Materials at Synchrotron Light Sources,* Grenoble, France, Sept. 10-12, 2000, Nuclear Energy Agency, Organization for Economic Cooperation and Development, Paris, pp. 13-29.

Farges, F., and G. E. Brown, Jr., 1997, "Coordination of Actinides in Silicate Melts," *Journal de Physique IV, Colloque,* Vol. C2:1009-1010.

Farges, F., R. C. Ewing, and G. E. Brown, Jr., 1993, "The Structure of Aperiodic, Metamict, (Ca, Th)$ZrTi_2O_7$: An EXAFS Study of the Zr, Th and U Sites," *Journal of Materials Research,* Vol. 8:1983-1995.

Farges, F., C. W. Ponader, G. Calas, and G. E. Brown, Jr., 1992, "Structural Environments of Incompatible Elements in Silicate Glass/Melt Systems: II. $U^{(IV)}$, $U^{(V)}$, and $U^{(VI)}$," *Geochimica et Cosmochimica Acta,* Vol. 56:4205-4220.

Foster, A. L., G. E. Brown, Jr., T. N. Tingle, and G. A. Parks, 1998, "Quantitative Arsenic Speciation in Mine Tailings Using X-Ray Absorption Spectroscopy," *American Mineralogist,* Vol. 83:553-568.

Foster, A. L., G. E. Brown, Jr., G. A. Parks, T. N. Tingle, D. Voigt, and S. L. Brantley, 1997, "XAFS Determination of As(V) Associated with Fe(III) Oxyhydroxides in Weathered Mine Tailings and Contaminated Soil from California, USA," *Journal de Physique IV, Colloque,* Vol. C2:815-816.

Francis, A. J., C. J. Dodge, J. B. Gillow, and H. W. Papenguth, 2000, "Biotransformation of Uranium Compounds in High Ionic Strength Brine by Halophilic Bacterium Under Denitrfying Conditions," *Environmental Science & Technology,* Vol. 34:2311-2317.

Fuller, C. C., J. R. Bargar, J. A. Davis, and M. J. Piana, 2002, "Mechanisms of Uranium Interactions with Hydroxyapatite: Implications for Groundwater Remediation," *Environmental Science & Technology,* Vol. 36:158-165.

George, G. N., and I. F. Pickering, 2000, "EXAFSPAK. Stanford Synchrotron Radiation Laboratory," http://www-ssrl.slac.stanford.edu/exafspak.html (accessed July 31, 2002).

Ginderow, D., 1988, "Structure de l'Uranophane Alpha, $Ca(UO_2)_2(SiO_3OH)_2 \cdot 5H_2O$," *Acta Crystallographica,* Vol. C44:421-424.

Hesterberg, D., D. E. Sayers, W. Zhou, G. M. Plummer, and W. P. Robarge, 1997, "X-Ray Absorption Spectroscopy of Lead and Zinc Speciation in a Contaminated Groundwater Aquifer," *Environmental Science & Technology,* Vol. 31:2840-2846.

Hudson, E. A., L. J. Terminello, B. E. Viani, M. Denecke, T. Reich, P. G. Allen, J. J. Bucher, D. K. Shuh, and N. M. Edelstein, 1999, "The structure of U^{6+} Sorption Complexes on Vermiculite and Hydrobiotite," *Clays and Clay Minerals,* Vol. 47:439-457.

Hudson, E. A., P. G. Allen, L. J. Terminello, M. A. Denecke, and T. Reich, 1996, "Polarized X-Ray-Absorption Spectroscopy of the Uranyl Ion: Comparison of Experiment and Theory," *Physical Review B: Condensed Matter and Materials Physics,* Vol. 54:156-165.

Isaure, M. P., A. Laboudigue, A. Manceau, G. Sarret, C. Tiffreau, P. Trocellier, G. Lamble, J. L. Hazemann, and D. Chateigner, 2002, "Quantitative Zn Speciation in a Contaminated Dredged Sediment by μ-PIXE, μ-SXRF, EXAFS Spectroscopy and Principal Component Analysis," *Geochimica et Cosmochimica Acta,* Vol. 66:1549-1567.

Juillot, F., G. Morin, P. Ildefonse, T. P. Trainor, M. Benedetti, L. Galoisy, G. Calas, and G. E. Brown, Jr., 2002, "Assessment of Zinc Speciation in Smelter-Impacted Soils by a Combination of XAFS Spectroscopy and Selective Chemical Extractions," *American Mineralogist*, submitted.

Kim, C. S., G. E. Brown, Jr., and J. J. Rytuba, 2000, "Characterization and Speciation of Mercury-Bearing Mine Wastes Using X-Ray Absorption Spectroscopy (XAS)," *Science of the Total Environment*, Vol. 261:157-168.

Manceau, A., M. C. Boisset, G. Sarret, J. L. Hazemann, M. Mench, P. Cambier, and R. Prost, 1996, "Direct Determination of Lead Speciation in Contaminated Soils by EXAFS Spectroscopy," *Environmental Science & Technology*, Vol. 30:1540-1552.

Manceau, A., L. Charlet, M. C. Boisset, B. Didier, and L. Spadini, 1992, "Sorption and Speciation of Heavy Metals on Hydrous Fe and Mn Oxides: From Microscopic to Macroscopic," *Applied Clay Science*, Vol. 7:201-223.

Manceau, A., B. Lanson, M. L. Schlegel, J. C. Harge, M. Musso, L. Eybert-Berard, J. L. Hazemann, D. Chateigner, and G. M. Lamble, 2000, "Quantitative Zn Speciation in Smelter-Contaminated Soils by EXAFS Spectroscopy," *American Journal of Science*, Vol. 300:289-343.

Morin, G., F. Juillot, P. H. Ildefonse, G. Calas, J. C. Samama, P. Chevallier, and G. E. Brown, Jr., 2001, "Mineralogy of Lead in a Soil Developed on a Pb-Mineralized Sandstone (Largentiére, France)," *American Mineralogist*, Vol. 86:92-104.

Morin, G., J. D. Ostergren, F. Juillot, P. H. Ildefonse, G. Calas, and G. E. Brown, Jr., 1999, "XAFS Determination of the Chemical Form of Lead in Smelter-Contaminated Soils and Mine Tailings: Importance of Sorption Processes," *American Mineralogist*, Vol. 84:420-434.

Morris, D. E., P. G. Allen, J. M. Berg, C. J. Chisholm-Brause, S. D. Conradson, R. J. Donohoe, N. J. Hess, J. A. Musgrave, and C. D. Tait, 1996, "Speciation of Uranium in Fernald Soils by Molecular Spectroscopic Methods: Characterization of Untreated Soils," *Environmental Science & Technology*, Vol. 30:2322-2331.

Moyes, L. N., R. H. Parkman, J. M. Charnock, D. J. Vaughan, F. R. Livens, C. R. Hughes, and A. Braithwaite, 2000, "Uranium Uptake from Aqueous Solution by Interaction with Goethite, Lepidocrocite, Muscovite, and Mackinawaite: An X-Ray Absorption Spectroscopy Study," *Environmental Science & Technology*, Vol. 34:1062-1068.

O'Day, P. A., J. J. Rehr, S. I. Zabinsky, and G. E. Brown, Jr., 1994, "Extended X-ray Absorption Fine Structure (EXAFS) Analysis of Disorder and Multiple-Scattering in Complex Crystalline Solids." *Journal of the American Chemical Society*, Vol. 116:2938-2949.

O'Day, P. A., 1999, "Molecular Environmental Geochemistry," *Reviews of Geophysics*, Vol. 37:249-274.

O'Day, P. A., S. A. Carroll, and G. A. Waychunas, 1998, "Rock-Water Interactions Controlling Zinc, Cadmium, and Lead Concentrations in Surface Waters and Sediments, U.S. Tri-State Mining District. I. Molecular Identification Using X-Ray Absorption Spectroscopy," *Environmental Science & Technology*, Vol. 32:943-955.

O'Day, P. A., S. A. Carroll, A. Randall, R. E. Martinelli, S. L. Anderson, J. Jelinski, and J. P. Knezovich, 2000, "Metal Speciation and Bioavailability in Contaminated Estuary Sediments, Alameda Naval Air Station, California," *Environmental Science & Technology*, Vol. 34:3665-3673.

Ostergren, J. D., G. E. Brown, Jr., G. A. Parks, and T. N. Tingle, 1999, "Quantitative Speciation of Lead in Selected Mine Tailings from Leadville, CO," *Environmental Science & Technology*, Vol. 33:1627-1636.

Pickering, I. J., G. E. Brown, Jr., and T. K. Tokunaga, 1995, "X-ray Absorption Spectroscopy of Selenium Transformations in Kesterson Reservoir Soils," *Environmental Science & Technology*, Vol. 29:2456-2459.

Redden, G., J. R. Bargar, and R. Bencheikh-Latmani, 2001, "Citrate-Enhanced Uranyl Adsorption on Goethite: An EXAFS Analysis," *Journal of Colloid and Interface Science*, Vol. 244:211-219.

Reeder, R. J., M. Nugent, C. D. Tait, D. E. Morris, S. M. Heald, K. M. Beck, W. P. Hess, and A. Lanzirotti, 2001, "Coprecipitation of Uranium(VI) with Calcite: XAFS, Micro-XAS, and Luminescence Characterization," *Geochimica et Cosmochimica Acta*, Vol. 65:3491-3503.

Rehr, J. J., and R. C. Albers, 2000, "Theoretical Approaches to X-Ray Absorption Fine Structure," *Reviews of Modern Physics*, Vol. 72:621-654.

Reich, T., H. Moll, T. Arnold, M. A. Denecke, C. Hennig, G. Geipel, G. Bernhard, H. Nitsche, P. G. Allen, J. J. Bucher, N. M. Edelstein, and D. K. Shuh, 1998, "An EXAFS Study of Uranium(VI) Sorption onto Silica Gel and Ferrihydrite," *Journal of Electron Spectroscopy and Related Phenomena*, Vol. 96:237-243.

Ressler, T., 1997, "WinXAS: A New Software Package Not Only for the Analysis of Energy-Dispersive XAS Data," *Journal de Physique IV*, Vol. 7(C2/pt.1):269-270.

Ryan, R. R., and A. Rosenzweig, 1977, "Sklodowskite MgO (UO3)2 (SiO2)2 (H2O)7," *Crystal Structure Communications*, Vol. 6(3):611-15.

Sylwester, E. R., E. A. Hudson, and P. G. Allen, 2000a, "Surface Interactions of Actinide Ions with Geologic Materials Studied by XAFS," In Application of Synchrotron Radiation Techniques to Materials Science, *Materials Research Society Symposium Proceedings*, S. R. Stock, S. M. Mini, and D. L. Perry, eds., Materials Research Society, Warrendale, Pennsylvania, Vol. 590:9-16.

Sylwester E. R., E. A. Hudson, and P. G. Allen, 2000b, "The Structure of Uranium (VI) Sorption Complexes on Silica, Alumina, and Montmorillonite," *Geochimica et Cosmochimica Acta*, Vol. 64:2431-2438.

Thompson, H. A., G. E. Brown, Jr., and G. A. Parks, 1995, "Low and Ambient Temperature XAFS Study of U(VI) in Solids and Aqueous Solutions," *Physica B*, Vols. 208 and 209:167-168.

Thompson, H. A., G. A. Parks, and G. E. Brown, Jr., 1998, "Structure and Composition of Uranium(VI) Sorption Complexes at the Kaolinite-Water Interface," In *Adsorption of Metals by Geomedia, Variables, Mechanisms, and Model Applications*, E. A. Jenne, ed., Academic Press, New York, pp. 349-370.

Thompson, H. A., G. E. Brown, Jr., and G. A. Parks, 1997, "XAFS Spectroscopic Study of Uranyl Coordination in Solids and Aqueous Solution," *American Mineralogist*, Vol. 82:483-496.

Viswanathan, K., and O. Harneit, 1986, "Refined Crystal-Structure of Beta-Uranophane; Ca(Uo2)2(Sio3oh)2.5h2o," *American Mineralogist*, Vol. 71(11-1):1489-1493.

Wahlgren, U., H. Moll, I. Grenthe, B. Schimmelpfennig, L. Maron, V. Vallet, and O. Gropen, 1999, "Structure of Uranium(VI) in Strong Alkaline Solutions. A Combined Theoretical and Experimental Investigation," *Journal of Physical Chemistry A*, Vol. 103:8257-8264.

Waite, T. D., J. A. Davis, T. E. Payne, G. A. Waychunas, and N. Xu, 1994, "Uranium (VI) Adsorption to Ferrihydrite: Application of a Surface Complexation Model," *Geochimica et Cosmochimica Acta*, Vol. 58(24):5465-5478.

Zachara, J. M., S. C. Smith, C. Liu, J. P. McKinley, R. J. Serne, and P. L. Gassman, 2002, "Sorption of Cs^+ to Micaceous Subsurface Sediments from the Hanford Site, USA," *Geochimica et Cosmochimica Acta*, Vol. 66:193-211.

Zachara, J. M., C. C. Ainsworth, G. E. Brown, Jr., J. G. Catalano, J. P. McKinley, O. Qafoku, S. C. Smith, J. E. Szecsody, S. J. Traina, and J. A. Warner, 2002, "Chromium Speciation and Mobility in a High Level Nuclear Waste Vadose Zone Plume," *Geochimica et Cosmochimica Acta*, submitted.

D.3.4 FLUORESCENCE SPECTROSCOPIC STUDIES OF URANIUM-BEARING VADOSE ZONE SEDIMENTS

Zheming Wang[1], John M. Zachara[1], Paul L. Gassman[1], Chongxuan Liu[1], and Jeff Catalano[2]

[1]Pacific Northwest National Laboratory, Richland, Washington 99352
[2]Stanford University, Stanford, California 94305

D.3.4.1 Introduction

The uranyl cation (UO_2^{2+}) and its various hydrolysis and carbonate complexes are the dominant forms of soluble uranium(VI) in Hanford sediment. The UO_2^{2+} cation is adsorbed by ion exchange to fixed charge sites on phyllosilicates (e.g., smectite, vermiculite) (McKinley et al. 1995; Turner et al. 1996) and by surface complexation to amphoteric hydroxyl sites on the edges of phyllosilicates (Borovec 1981; Davis 1991; McKinley et al. 1995; Pabalan and Turner 1996; Turner et al. 1996; Thompson et al. 1998) and on surfaces of aluminum (III), iron (III), and silica(VI) oxides (e.g., Waite et al. 1994; Hudson et al. 1999; Sylvester et al. 2000). All of these phases are present in Hanford sediments, albeit at highly variable concentrations. The sorption of uranyl is not limited to mononuclear species only. Simulations with surface complexation models suggest that under certain pH conditions, the uranyl cation can adsorb as a multinuclear species [e.g., $(UO_2)_3(OH)_5^+$] or as an oligomer (Dent et al. 1992; McKinley et al. 1995; Hudson et al. 1999). Uranyl-carbonate and phosphate aqueous complexes can adsorb as intact entities on oxide surfaces through the formation of ternary surface complexes (Bargar et al. 1999, 2000; Barnett et al. 2002; Bostick et al. 2002).

The uranyl cation exhibits complex crystal chemistry and may precipitate in sediment in various different forms (e.g., oxides, hydroxides, silicates, phosphates) depending on in situ or waste chemical conditions. Spectroscopic measurements have identified precipitated mineral phases, in addition to other adsorbed uranium species, in contaminated sediments from the U.S. Department of Energy (DOE) Fernald site in Ohio and Savannah River site in South Carolina (Morris et al. 1996; Hunter and Bertsch 1998). Fluorescence and Raman spectroscopic measurements identified meta-autunite $\{Ca[(UO_2)(PO_4)]_2(H_2O)_6\}$, phosphuranylite $\{Ca(UO_2)[(UO_2)_3(OH)_2(PO_4)_2]_2(H_2O)_{12}\}$, and uranyl hydroxide [schoepite, $(UO_2)_8O_2(OH)_{12}(H_2O)_{12}$] as the primary uranium(VI) precipitates in Fernald soil (Morris et al. 1996). Amorphous uranyl hydroxide particles appeared as the most common precipitated uranium(VI) phase using micro-x-ray absorption and micro-fluorescence spectroscopies in the sediment at the Savannah River site (Hunter and Bertsch 1998). Similar phases are believed to exist in Hanford waste sites (Swanson et al. 1999), but no documentation of their presence exists.

Uranyl shows green-yellow fluorescence emission spectra with unique vibronic features (Denning 1992; Bernard et al. 1996; Meinrath 1997). The intensity, bandwidth, and spacing of the vibronic bands of uranyl fluorescence spectra, along with its fluorescence lifetime, are highly sensitive to the bonding, symmetry, and local chemical environment of the uranyl ion. As such, they provide useful tools for the study of uranyl speciation (Denning 1992; Moulin et al. 1995; Meinrath 1997). Laser-induced fluorescence spectroscopy (LIFS) has been used to study the speciation of both adsorbed and precipitated uranium(VI) forms in clay mineral suspensions and subsurface sediment (Chisholm Brause et al. 1994; Duff et al. 2000).

In initial attempts to apply LIFS to contaminated Hanford sediment, it was observed that the uranyl fluorescence spectrum at room temperature was insufficiently resolved to identify the uranyl species present. The poor spectral resolution resulted from inhomogeneous line broadening, phonon bands, and fluorescence quenching by other metal ions and organic compounds in the sample (Thorne et al. 1987). In this scientific and technical research, however, it was found that the intensity and resolution of the fluorescence spectra of uranyl in the Hanford sediments could be improved significantly by lowering the sample measurement temperature to liquid helium values (~ 5° K). The resulting improved spectral resolution allowed identification of uranyl species by direct comparison of uranyl fluorescence spectra in the sediment with those of standard uranyl minerals and/or those of known uranyl species in solution.

D.3.4.2 Experimental Procedures

D.3.4.2.1 Sample Selection and Preparation of Mineral and Solution Standards. Twenty uranium mineral standards were obtained from either the American Museum of Natural History (AMNH) or the Smithsonian Institution (SI) (Table D.39). The mineral samples consisted of fine-grained crystallites ranging in size from tens of microns to more than one millimeter. These minerals represent those that may form in the pristine or waste-impacted Hanford subsurface in terms of formation conditions and chemical composition. X-ray diffraction (XRD) analysis was performed on a small portion of each of the mineral samples to ensure positive identification. Most of the mineral standards had high purity and crystallinity and were consistent with the identification provided by the sources (Table D.40). Only a few turned out to be misidentified: the received "andersonite" was actually liebigite with associate quartz and calcite. The "curite" was a mixture of curite and soddyite. The "soddyite" was a 50/50 mixture of soddyite and curite. The "phosphuranylite" was a 50/50 mixture of phosphuranylite and meta-autunite. Billietite was actually uranophane; and several minerals contained a small amount of the amorphous mineral background.

A set of standard uranium(VI)-carbonate solutions was synthesized at different pH values to assist in the identification of aqueous uranium(VI) species. Specific pH conditions were selected for those standards for which only one or two aqueous species were expected to dominate. Such conditions were identified by equilibrium speciation calculations (Figure D.63) using the MINTEQA2 software and the best and most current thermodynamic stability constant data of uranyl complexes (Grenthe 1992; Kalmykov and Choppin 2000).

Table D.39. List of Natural Standard Minerals and Corresponding Formulas

Uranyl Oxyhydroxides		
Becquerelite	$Ca(UO_2)_6O_4(OH)_6\ (H2O)_8$	
Billietite	$Ba(UO_2)_6O_4(OH)_6\ (H2O)_8$	eight interlayer waters
Clarkeite	$(Na,Ca)(UO_2)(O, OH)(H_2O)_n$	(n = 0 to 1)
Curite	$Pb_{1.5+x}(UO_2)_6O_{4+2x}(OH)_{3-2x}(H_2O)$	$(0 < x < 0.15)$
Schoepite	$(UO_2)_8O_2(OH)_{12}(H_2O)_{12}$	
Compreignacite	$K_2(UO_2)_6O_4(OH)(H_2O)_7$	sheet structure similar to becquerelite
Uranyl Carbonates		
Andersonite	$Na_2Ca(UO_2)(CO_3)_3(H_2O)_6$	
Liebigite	$Ca_2(UO_2)(CO_3)_3(H_2O)_{11}$	
Rutherfordine	UO_2CO_3	
Zellerite	$Ca(UO_2)(CO_3)_2(H_2O)_5$	
Uranyl Silicates		
Boltwoodite	$K(H_3O)(UO_2)(SiO_4)\ (H_2O)$	boltwoodite readily exchanges interlayer cation, i.e., cesium for sodium
Cuprosklodowskite	$Cu(UO_2)_2(SiO_3OH)_2\ (H_2O)_6$	
Kasolite	$Pb(UO_2)(SiO_4)(H_2O)$	
Sklodowskite	$Mg(UO_2)_2(SiO_3OH)_2\ (H_2O)_5$	
Soddyite	$(UO_2)_2(SiO_4)\ (H_2O)_2$	
Uranophane	$Ca(H_3O)_2(UO_2)_2(SiO_4)_2\ (H_2O)_3$	
Uranyl Phosphates		
Meta autunite	$Ca[(UO_2)(PO_4)]_2(H_2O)_6$	
Metatorbernite	$Cu[(UO_2)(PO_4)]_2(H_2O)_6$	
Phosphuranylite	$Ca(UO_2)[(UO_2)_3(OH)_2(PO_4)_2]_2(H_2O)_{12}$	
Saleeite	$Mg[(UO_2)(PO_4)]_2(H_2O)_{10}$	

Table D.40. Summary of X-Ray-Diffraction Analysis of the Natural Minerals

Uranyl Oxyhydroxides	
Becquerelite	The XRD pattern agreed well with that from JCPDF file 13-405.
Billietite	Sample is completely uranophane; there is no billietite present. Samples are not metamict at all; this is a high quality uranophane sample.
Clarkeite	This material appears to be highly metamict clarkeite.
Curite	Mixture of curite and soddyite, with soddyite dominating.
Schoepite	The XRD pattern generally matched up with the JCPDF pattern.
Compreignacite	Good match to synthetic compreignacite pattern.
Uranyl Carbonates	
Andersonite	XRD pattern is that of liebigite.
Liebigite	XRD pattern is that of liebigite.
Rutherfordine	—
Zellerite	Perfect match to database.
Uranyl Silicates	
Boltwoodite	Generally good peak agreement, especially with card 13-218. Slight amorphous background, i.e., sample is slightly metamict.
Cuprosklodowskite	Perfect match to card 8-290.
Kasolite	Good match to database, cards 12-210 and 29-788.
Sklodowskite	Highly crystalline sample, great match to database.
Soddyite	Appears to be a 50/50 mixture of soddyite and curite.
Uranophane	XRD pattern matched well with database, but a big amorphous background, suggesting a significant portion of the sample is metamict. Peak intensities are relatively weak.
Uranyl Phosphates	
Meta autunite	Perfect match to JCPDF card.
Metatorbernite	Perfect match.
Phosphuranylite	Looks like a 50/50 mixture with meta autunite. Can be separated by hand under UV light; meta autunite fluoresces, phosphuranylite does notfluoresce.
Saleeite	XRD pattern matches that of saleeite well, card 29-874.

Figure D.63. Aqueous Speciation of Uranium(VI) (Partial Pressure of $CO_2 = 10^{-3.5}$ atm; Total Uranium(VI) = 1 x 10^{-6} M; I = 0.1 M $NaClO_4$)

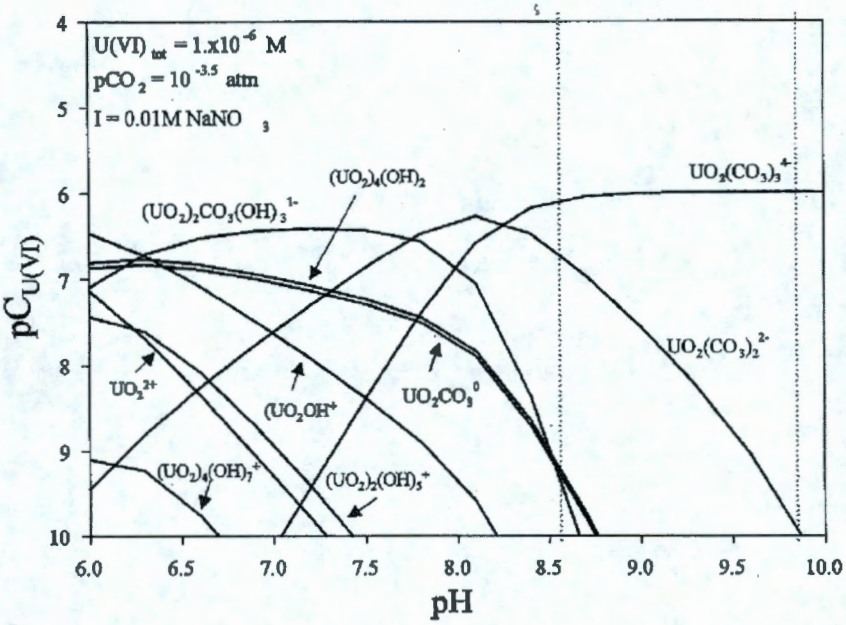

D.3.4.2.2 Hanford Samples. Three different types of Hanford samples were studied by LIFS. The first were vadose samples 53A, 61A, 61AB, and 67AB from the BX-102 core (borehole 299-E33-45). The second were sediment samples 61AB and 67AB that were contacted with one of four different electrolyte solutions:

1. Sodium bicarbonate (0.194 mM)-sodium nitrate (0.0498 M) solution with I = 0.05, pH 7.27, contact time: 4 weeks

2. Sodium bicarbonate (15.59 mM)-sodium carbonate (4.93 mM)-sodium nitrate (0.0245 M) with I = 0.05, pH 9.25, contact time: 4 weeks

3. Calcium carbonate-saturated calcium perchlorate (0.0219 M)-sodium perchlorate (0.0666 M) with I = 0.05, pH 7.57, contact time: 2 weeks

4. Calcium carbonate-saturated sodium perchlorate (0.0416 M)-sodium bicarbonate (4.44 mM)-sodium carbonate (4.44 mM)- perchloric acid (1.425 mM) with I = 0.05, pH 8.96, contact time: 2 weeks.

These solutions are abbreviated as sodium-1, sodium-2, calcium-1 and calcium-2 in the text. This experiment and other data from it are described in detail in Section D.3.5 of this Appendix. After reaching the desired contact time, an aliquot of the sediment suspension was withdrawn from the electrolyte, and the sediment and the solution were separated by filtration (pre-washed Centriplus YM-30 centrifugal device filters). Both the leached solids and the supernatant were analyzed by LIFS. The third sample type comprised porewaters (S01014-55 UFA and S01014-64 UFA) obtained by high-speed centrifugation of the high moisture content samples from the BX-102 core.

Table D.41. Chemical Composition (mmol/L) of Porewater from BX-102 Core Samples[a]

Component	BX-102 53A	BX-102 61A	BX-102 67A
UO_2^{2+}	0.769	2.483	1.633
K^+	1.640	1.302	1.506
Na^+	103.591	217.772	175.208
Ca^{2+}	1.477	0.666	1.592
Mg^{2+}	0.636	0.107	0.560
Cl^-	0.620	0.826	1.564
NO_3^-	17.132	17.977	38.539
SO_4^{2-}	4.890	8.866	18.514
PO_4^{3-}	0.165	4.119	0.203
H_4SiO_4	15.221	11.500	14.642
$CO_{2(tot)}$	atm_eq	Atm_eq	atm_eq
PH	8.88	9.50	9.00

[a]calculated from data reported in Serne et al. (2002)

D.3.4.2.3 Cryogenic Uranium(VI) Fluorescence Measurements. Fluorescence spectroscopic and lifetime measurements were performed in cryostat at liquid helium temperature. Individual solid samples were mounted in custom-built sealed copper sample holders fitted with sapphire optical windows. Solution samples (~ 100 μL) were transferred into a 3-mm x 3-mm quartz spectroscopic cell fitted with silicone stoppers. Atmospheric control was maintained throughout the sample-handling procedure except during the spectral acquisition. The samples were attached to the cold finger of a Cryo Industries RC-152 cryogenic workstation in which the sample cell was directly exposed to the vapor flow of liquid helium. The sample temperature was controlled by tuning both the liquid helium flow rate and the electric current applied to the internal heater of the cryostat through a Lakeshore 330 auto-tuning temperature controller. The normal fluorescence emission spectra of the sample was obtained by excitation at 415 nm, the spectral maximum of the first electronic absorption band, by the frequency doubled output of a Spectra-Physics Nd:YAG laser pumped MOPO-730 laser. The resulting fluorescence was collected at 75° to the excitation beam by a 2–inch diameter f/3 fused silica lens and focused by a 2–in. f/4 fused silica lens into the entrance slit of a 0.3-m focal length Acton SpectroPro 300i double monochromator spectrograph. For highly scattering samples, an Omega 493LP cutoff filter with a cutoff wavelength of 493 nm was placed in front of the entrance slit of the spectrograph to reject scattered laser light.

Time-resolved emission spectra were recorded using a thermoelectrically cooled Princeton Instruments PIMAX time-gated intensified CCD camera that was triggered by the delayed output of the laser pulse and controlled by the WinSpec™ data acquisition software. The same sample volume and geometry were maintained during analysis to allow semiquantitative analysis of the species distribution. Data analysis was performed using commercial software such as IGOR™.

Fluorescence decay analysis was checked further with the Globals program developed at the University of Illinois at Urbana-Champaign (Beechem et al. 1991).

D.3.4.3 Results

D.3.4.3.1 Cryogenic Fluorescence Spectroscopy. Lowering the sample temperature increases the fluorescence intensity and lifetimes of elements such as uranium(VI) by minimizing de-excitation pathways between the fluorophore and molecules of the solvent, quenchers, or other ground state molecules. A decrease in temperature sharpens the spectral profile and improves spectral resolution (Lakowicz 1991). The quenching of uranyl fluorescence by long-range proton transfer reactions in the solvent became negligible at liquid nitrogen temperature (i.e., 77 K) (Stepanov et al. 1984). The resolution of uranyl fluorescence measurements in soils was improved at lower temperatures because the quenching effects of various cations, anions, and organic molecules were reduced (Duff et al. 2000).

In this work, fluorescence spectroscopic measurements were performed on uranium(VI)-contaminated sediments and uranyl carbonate solutions at both liquid helium and liquid nitrogen temperature to ascertain the optimal conditions for characterizing uranium(VI) speciation in the field samples. Lowering the sample temperature greatly increased the fluorescence intensity (up to two orders of magnitude) and enhanced the spectral resolution for both solid and aqueous samples (Figure D.64). For uranium(VI)-carbonate solutions at pH 11 (Figure D.64, panel b) where higher-order carbonate complexes dominate, no fluorescence signal was observed at room temperature. However, cryogenic measurements showed a discernable fluorescence spectrum at liquid nitrogen temperature that increased in resolution at liquid helium temperature (6 K). Liquid helium was allowed to evaporate in the cryostat to cool the sample, yielding a measurement temperature that was slightly above 4.2 K.

D.3.4.3.2 Fluorescence Characteristics of Natural Uranium Minerals. All of the natural uranium-mineral standards showed bright green-yellow fluorescence when excited by laser light at 415 nm (Figure D.65 and Figure D.66). However, the relative fluorescence intensity varied by more than three orders of magnitude, with coffinite and metatorbernite being the least fluorescent. Uranophane and rutherfordine exhibited fluorescence intensity 10 times greater than coffinite and metatorbernite, while the others were from 100 to 1000 times more fluorescent. The wavelengths of the major vibronic bands on the fluorescence spectra are listed in Table D.42.

Figure D.64. Uranyl Fluorescence Emission Spectra at Different Temperature A) Hanford Sediment 53A with Uranium(VI)$_{Total}$ = 142 ppm; B) Aqueous Uranium(VI) in the Presence of 0.008 M Na_2CO_3 at pH 11. $[UO_2^{2+}] = 2 \times 10^{-5}$ M. λ_{ex} = 415 nm.

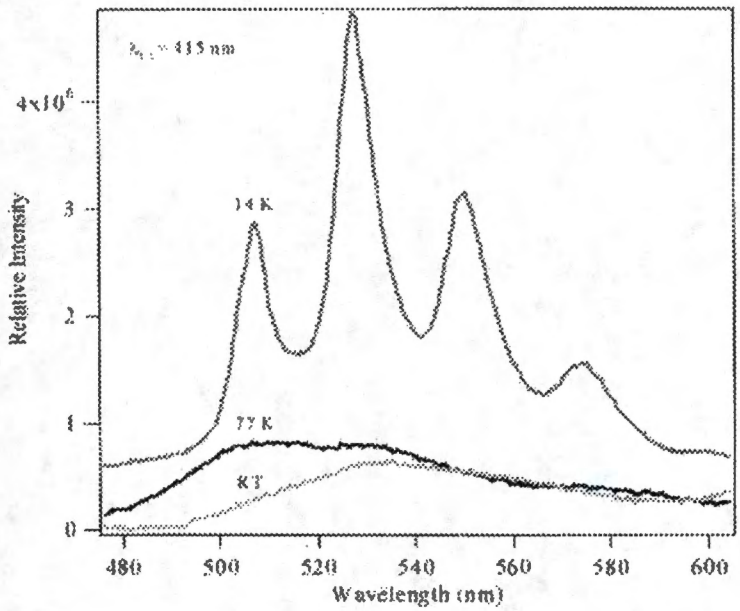

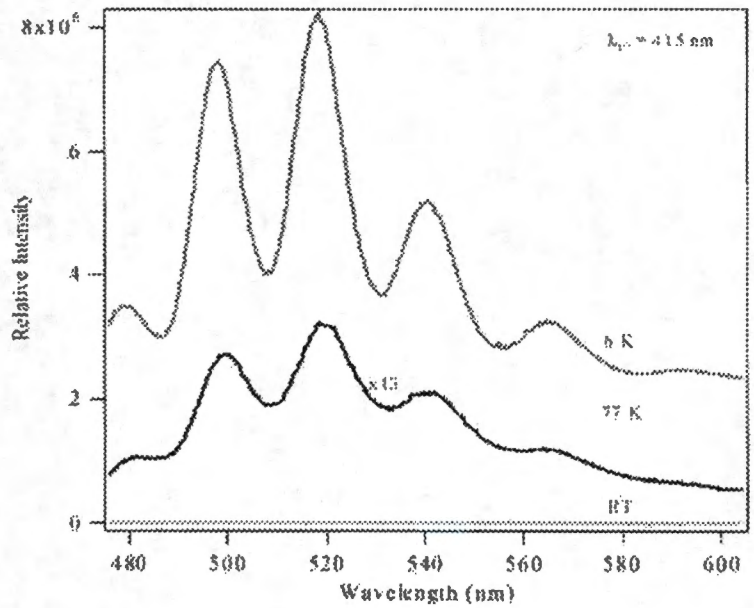

Figure D.65. Fluorescence Spectra of Standard Uranyl Minerals. λ_{ex} = 415 nm.

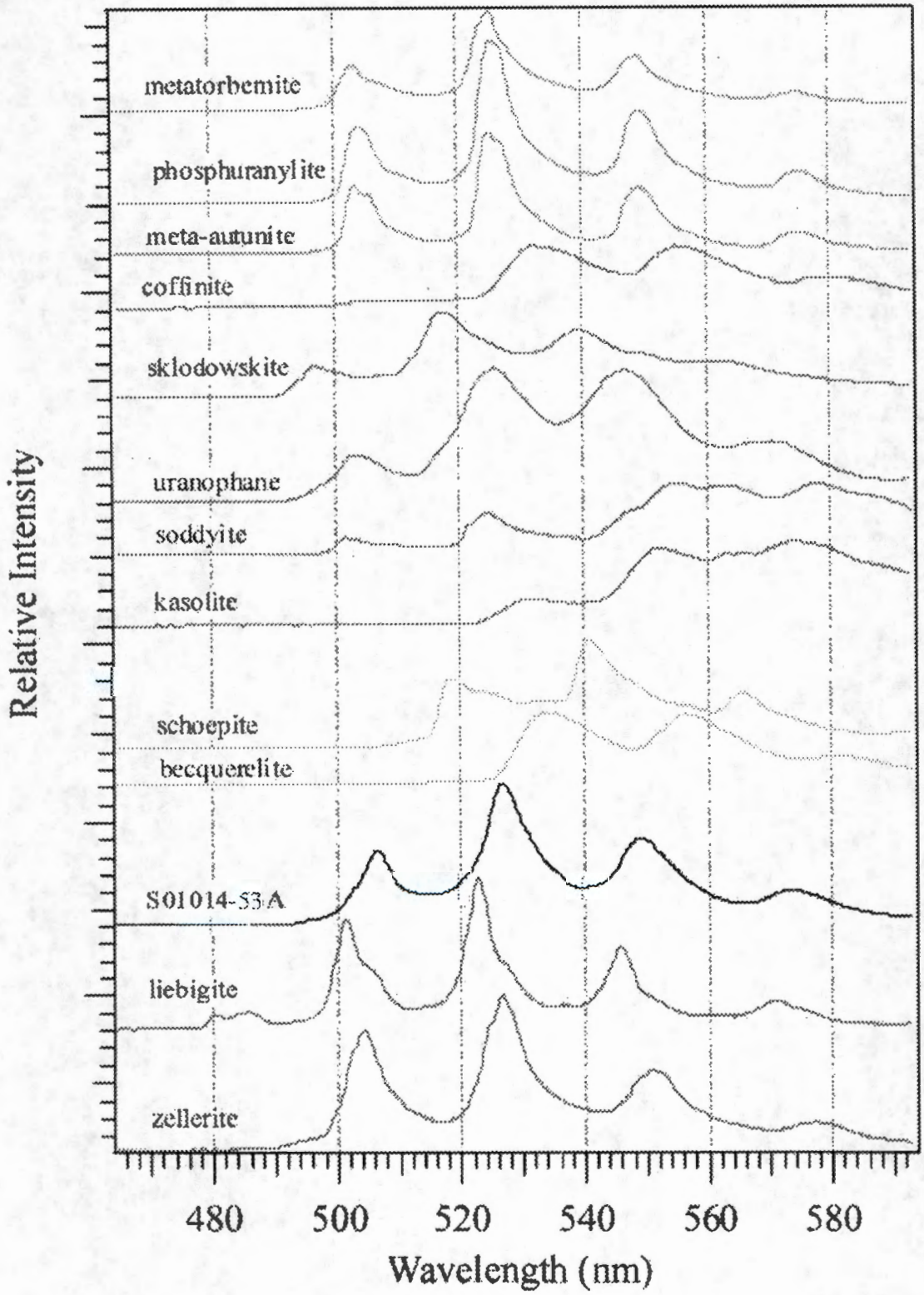

Figure D.66. Fluorescence Spectra of Standard Uranyl Minerals (Continued). λ_{ex} = 415 nm.

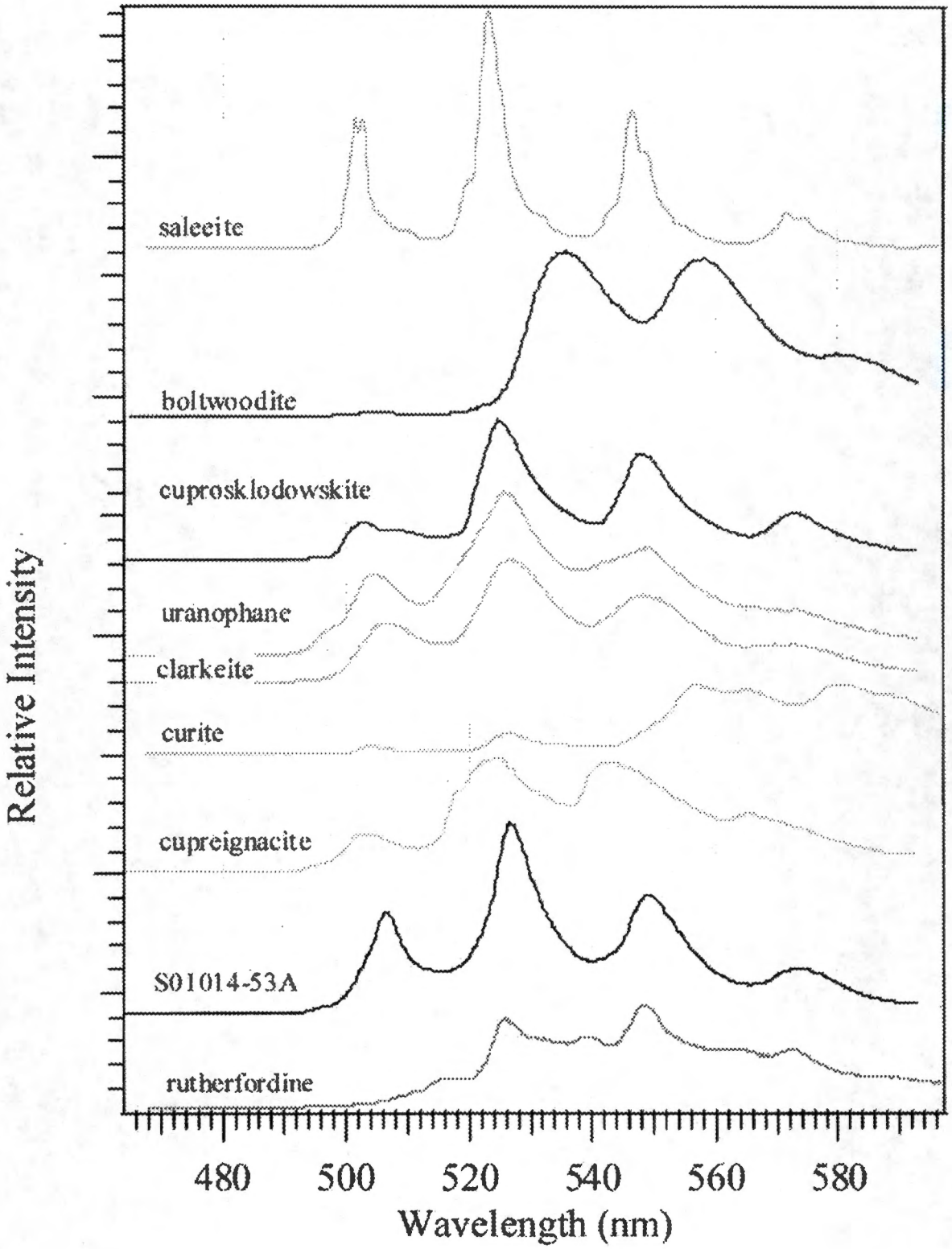

Table D.42. Fluorescence Spectral Characteristics of Standard Natural Minerals. λ_{ex} = 415 nm

Mineral	Spectral maxima (nm)
Uranyl Oxyhydroxides	
Becquerelite	-*, 534.2, 556.0, 580.4
Billietite**	504.4, 525.7, 549.0, 572.2
Clarkeite	506.1, 526.5, 548.0, 572.2
Curite	-*, 526.6, 557.0, 580.2
Schoepite	-*, 517.9, 540.5, 565.0
Compreignacite	504.1, 524.7, 542.7, 565.2
Uranyl Carbonates	
Liebigite	501.4, 522.7, 545.7, 570.8
Rutherfordine	-*, 525.6, 548.2, 572.5
Zellerite	504.4, 526.7, 551.0, 577.4
Uranyl Silicates	
Boltwoodite	505.4, 535.2, 558.0, 579.4[a]
Cuprosklodowskite	502.9, 524.7, 547.5, 573.5
Kasolite	-*, 531.2, 552.2, 574.2
Sklodowskite	496.6, 516.7, 538.7, 561.5
Soddyite	504.5, 527.4, 551.0, 576.3, 602.4
Uranophane	503.1, 525.5, 507.0, 570.5
Uranyl Phosphates	
Meta autunite	502.9, 524.7, 549.0, 574.9
Metatorbernite	503.1, 525.2, 549.3, 574.5
Phosphuranylite	503.4, 525.5, 548.7, 574.7
Saleeite	502.0, 523.1, 546.5, 571.7

* The peak intensity is too weak to identify.
** XRD pattern indicates that this mineral is actually uranophane.
[a] The reported data are inconsistent with literature (Vochten et al. 1997).

The closely spaced vibronic peaks on the emission spectra indicated that all of the uranium(VI) in the mineral phases was present as the uranyl entity. Among the 20 minerals studied, only coffinite contains uranium predominantly in the (IV+) oxidation state. It is well known that uranium (IV+) is not fluorescent. The noted fluorescence of coffinite suggests the likely presence of uranium(VI) impurities in the mineral specimen. The XRD analysis of this specimen indicated the presence of a mixed oxidation phase such as uraninite (U_3O_7). The fluorescence spectral profile of the coffinite (Figure D.65) was similar to the becquerelite, a uranyl oxyhydroxide with its fluorescence spectral bands shifted toward longer wavelengths.

The fluorescence spectra of the other mineral specimens were also in agreement with their XRD analyses, confirming the presence of mineral mixtures in some cases and single mineral phases in others. For example, XRD analyses indicated that the curite and soddyite samples were mixtures of both curite and soddyite. Time-resolved fluorescence measurements of these mineral mixtures (Figure D.67) documented the ability to discriminate between different species in mixtures. The time-resolved measurements showed that soddyite had a longer fluorescence lifetime than curite and that the two could be discriminated by measurements performed at distinctly different delay times (e.g., 1 μs and 800 μs). The fluorescence of curite decayed away after ~ 500 μs, leaving the emission spectra of soddyite alone (Figure D.67). In contrast, mineral specimens containing a single mineral phase such as saleeite (e.g., Figure D.66) exhibited identical fluorescence spectra regardless of time delay.

General trends were noted in the fluorescence emission spectra of the major mineral groupings of oxyhydroxides, silicates, carbonates, and phosphates. The phosphate minerals were the most fluorescent, and all showed distinctively sharp spectral profiles. Strong, highly resolved fluorescence spectra were obtained even at room temperature (not shown). Among the oxyhydroxides studied, the fluorescence spectra of all but the clarkeite were red-shifted toward longer wavelengths. Both the position and profiles of the fluorescence spectra for carbonate and silicate minerals varied as functions of the stoichiometry and crystal structure. At this time, neither a theoretical basis nor predictive relationships exist to define the dependence of the fluorescence spectrum of a uranyl compound on its chemical or crystal structure. Empirically, however, it is expected that direct comparison between the spectral signatures of the standard minerals and those of the sediment acquired under the same wavelength and environmental conditions will offer clues as to which uranium species exist in the Hanford sediments.

Figure D.67. Time-Resolved Fluorescence Emission Spectra of a Mixture of Soddyite and Curite; λ_{ex} = 415 nm.

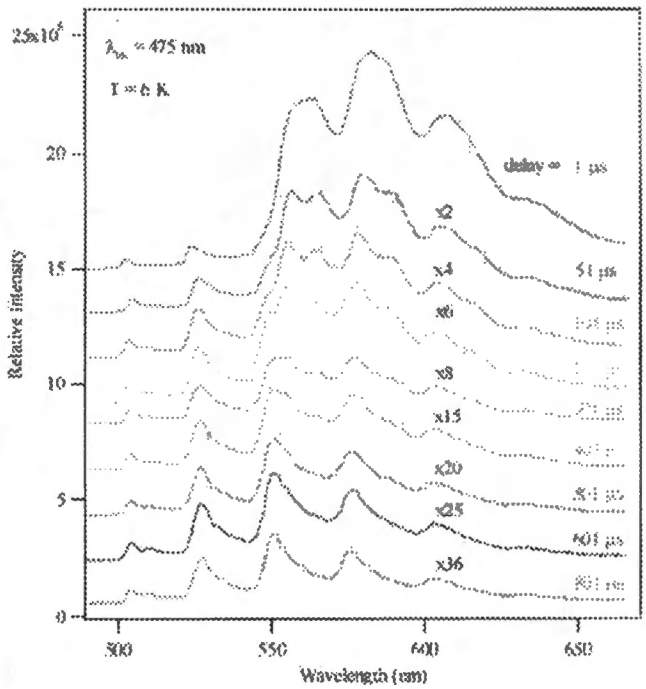

Figure D.68. Time-Resolved Fluorescence Emission Spectra of Saleeite ($Mg[(UO_2)(PO_4)]_2(H_2O)_{10}$). λ_{ex} = 415 nm.

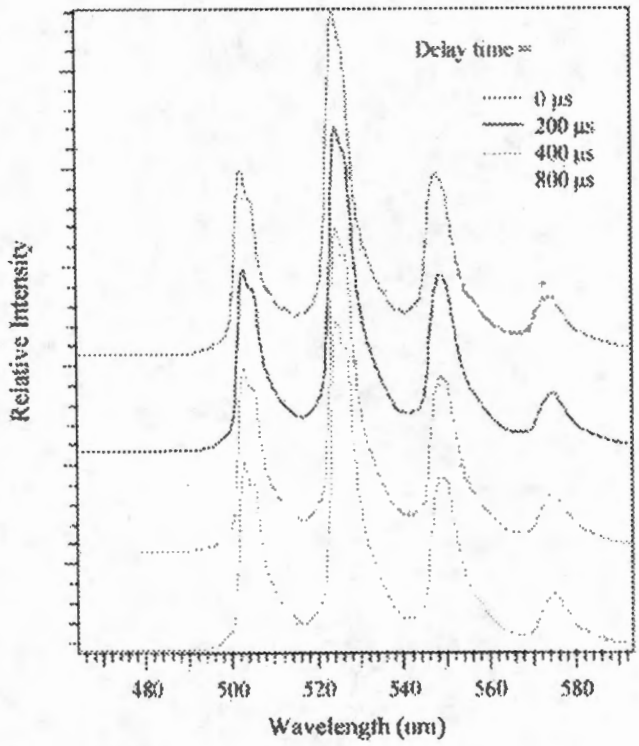

Differences were observed in the emission spectra of the natural and synthetic uranium minerals. For example, the fluorescence spectra of one synthetic clarkeite sample (not shown) deviated from the spectra of the natural clarkeite (Figure D.66). The synthetic clarkeite exhibited spectral positions consistent with the other uranyl oxyhydroxides (e.g., becquerelite) (Figure D.65), while the emission spectra of the natural clarkeite was similar to those of uranophane, a uranium(VI) silicate (Figure D.65 and Figure D.66). Similarly, the fluorescence spectra of the natural boltwoodite (Figure D.66) differed from those of a synthetic specimen reported by Vochten et al. (1997). Possible causes for such a difference are variation in hydration degree, or the presence of minor impurity phases.

D.3.4.3.3 Spectral Analysis of the BX-102 Sediment Samples. The four uranium-contaminated vadose zone sediment samples, although acquired at different depths beneath tank BX-102, exhibited nearly identical spectral profiles (Figure D.69). The spectra of all four sediments consisted of sharp, well-resolved spectral peaks characteristic of uranyl compounds emanating from a weak, broad fluorescence background. The fluorescence measurements implied the presence of a dominant, single uranyl species or a limited number of uranyl species with similar fluorescence behavior. The high background implied the presence of coexisting minor species such as adsorbed surface complexes or an amorphous uranyl compound. The peak spacings of ~ 766 cm^{-1} that are indicative of the strength of the symmetrical uranyl vibration energy were low compared to those for the aqueous uranyl ion at 872 cm^{-1} (Morris et al. 1994). The presence of a precipitate with strong interaction between the equatorial anions and

uranium(VI) was implied. A comparison of the sediment spectra with those of the mineral specimens indicated that, within the error of the fluorescence measurement, the uranium species in the sediment were most similar to: 1) meta-autunite and phosphuranylite [uranium(VI)-phosphates], and 2) soddyite and uranophane [uranium(VI)-silicates]. The sediment spectra were also very similar to the 77 K spectrum of synthetic boltwoodite reported by Vochten et al. (1997) at 77 K. Experiments are currently being conducted with synthetic sodium- and potassium-boltwoodite to confirm this observation.

The time-resolved fluorescence spectra of all four samples also were quite similar and showed only a small shift at different time delays (Figure D.70). The small spectral shift with time delay indicated that there was one dominant uranium(VI) species in the samples and one or more minor species in low concentration. The dominant and minor uranium(VI) species have different fluorescence lifetimes. It is also possible that there was a range of varying chemical/structural environments around one uranium(VI) species, leading to different fluorescence quenching efficiencies and thus different uranium(VI) fluorescence lifetimes.

Figure D.69. Fluorescence Emission Spectra of Hanford Vadose Sediments Under Tank BX-102 at 5.5 K. λ_{ex} = 415 nm.

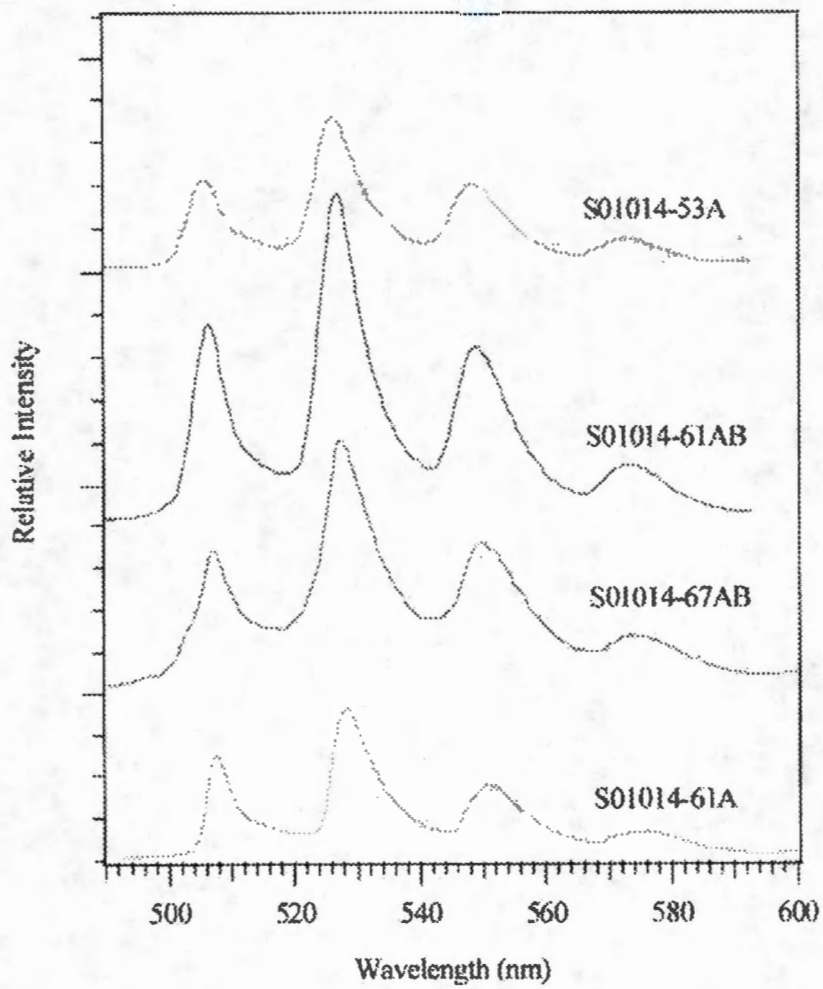

Figure D.70. Time-Resolved Fluorescence Emission Spectra of Hanford Vadose Zone Sediments S01014-61AB (upper panel) and S01014-67AB (lower panel) Under Tank BX-102 at 5.5 K. λ_{ex} = 415 nm.

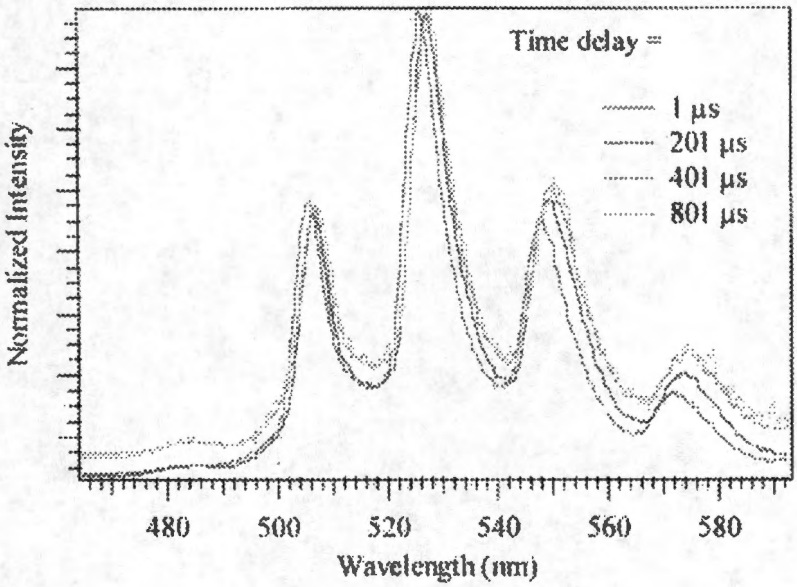

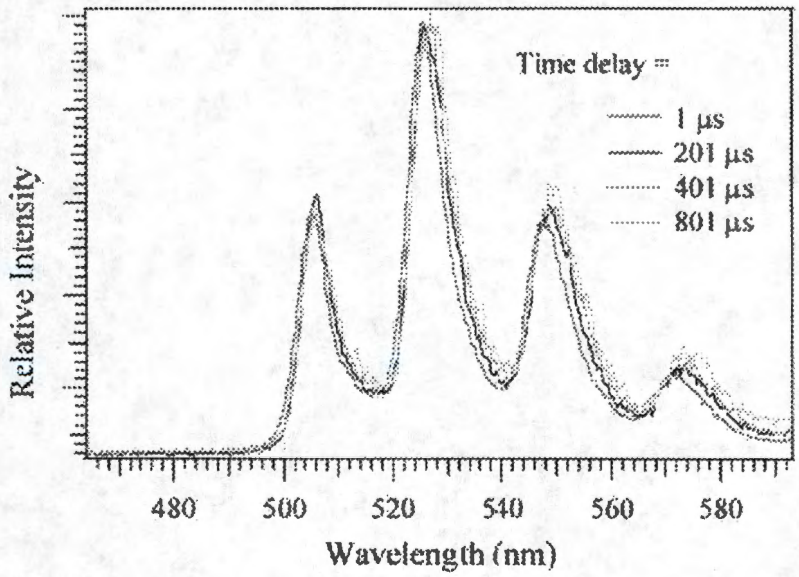

Table D.43. Fluorescence Spectral Characteristics of Hanford Vadose Zone Sediments. λ_{ex} = 415 nm

Sediment sample	Spectral maxima (nm)
-53A	506.4, 526.7, 549.5, 574.0
-61A	507.6, 528.3, 550.8, 547.5
-61AB	506.4, 527.0, 549.2, 573.2
-67AB	506.8, 527.1, 549.7, 573.7
After leaching with electrolyte solution Na-1	
-61AB	505.9, 527.0, 548.7, 573.5
-67AB	504.9, 525.7, 547.5, 571.5
After leaching with electrolyte solution Na-2	
-61AB	507.4, 527.7, 549.7, 574.7
-67AB	506.1, 526.5, 548.5, 573.5
After leaching with Ca^{2+}-saturated electrolyte solution Ca-1	
-61AB	503.6, 523.9, 546.7, 570.5
-67AB	504.1, 524.5, 547.2, 572.2
After leaching with Ca^{2+}-saturated electrolyte solution Ca-2	
-61AB	504.6, 525.2, 547.7, 572.0
-67AB	504.9, 525.5, 547.7, 571.7
U(VI) dissolved in electrolyte solution Na-1	
-61AB	481.0, 500.9, 520.7, 543.2, 568.2
-67AB	481.3, 500.1, 520.7, 542.7, 567.2
U(VI) dissolved in electrolyte solution Na-2	
-61AB	481.5, 501.4, 520.7, 540.3, 564.5
-67AB	481.3, 500.9, 520.7, 543.0, 568.2
U(VI) dissolved in Ca^{2+}-saturated electrolyte solution Ca-2	
-61AB	479.9, 499.8, 520.4, 542.4, 567.7
-67AB	480.2, 499.3, 521.4, 544.0, 567.7

D.3.4.3.4 Spectral Analysis of Uranium-Contaminated Sediments Equilibrated in Bicarbonate Electrolyte. The fluorescence spectra of the uranium(VI)-contaminated sediments that were equilibrated in sodium and calcium electrolytes were measured to ascertain whether the uranium(VI) spectral signature changed after leaching/solubilizing a portion of the precipitated uranium(VI) pool. A comparison of the spectra of the original and equilibrated sediment samples indicated that electrolyte contact and partial solubilization did not markedly change the spectral characteristics of the residual uranium(VI) species (Figure D.71 and Figure D.72; Table D.43). The fluorescence intensity of the sediment did change (e.g., decreased) with electrolyte contact in direct proportion to the quantity of uranium(VI) solubilized. This was a mass loss effect. Solubilization increased with the increasing pH and carbonate content of the electrolyte solution.

Figure D.71. Fluorescence Emission Spectra at 5.2K of Hanford Vadose Sediments -61AB (upper panel) and -67AB (lower panel) Under Tank BX-102 Before and After Leaching with Electrolyte Solutions Na-1 and Na-2.

The Compositions of the Electrolyte Solutions are: Na-1: $NaHCO_3$ (0.194 mM)-$NaNO_3$ (0.0498 M) Solution with I = 0.05, pH 7.2 7, contact time: 4 weeks; Na-2: $NaHCO_3$ (15.59 mM)-Na_2CO_3 (4.93 mM)-$NaNO_3$ (0.0245 M) with I = 0.05, pH 9.25, contact time: 4 weeks; λ_{ex} = 415 nm.

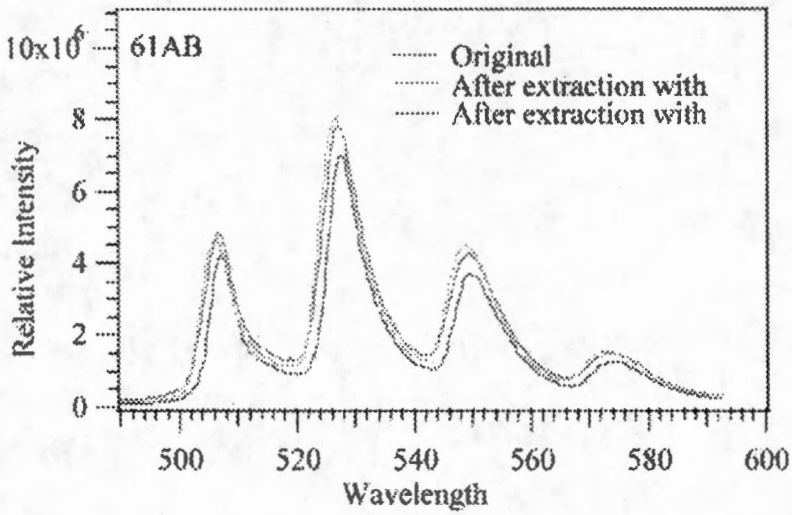

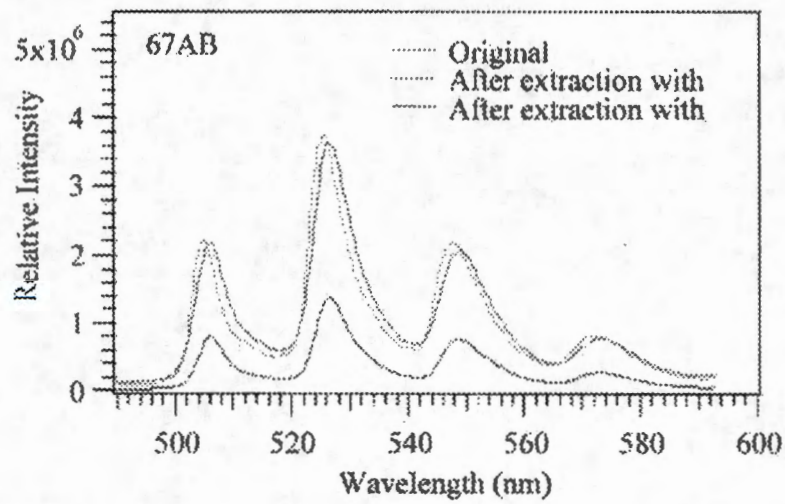

Figure D.72. Fluorescence Emission Spectra at 5.2 K of Hanford Vadose Sediments -61AB (upper panel) and -67AB (lower panel) Under Tank BX-102 Before and After Leaching with Ca^{2+}-Saturated Electrolyte Solutions, Ca-1 and Ca-2.

The Compositions of the Electrolyte Solutions are: Ca-1: $CaCO_3$-saturated $Ca(ClO_4)_2$ (0.0219 M)-$NaClO_4$(0.0666 M) with I = 0.05, pH 7.57, contact time: 2 weeks; Ca-2: $CaCO_3$-saturated $NaClO_4$(0.0416 M)-$NaHCO_3$ (4.44 mM)-Na_2CO_3 (4.44 mM)-$HClO_4$(1.425 mM) with I = 0.05, pH 8.96, contact time: 2 weeks. λ_{ex} = 415 nm.

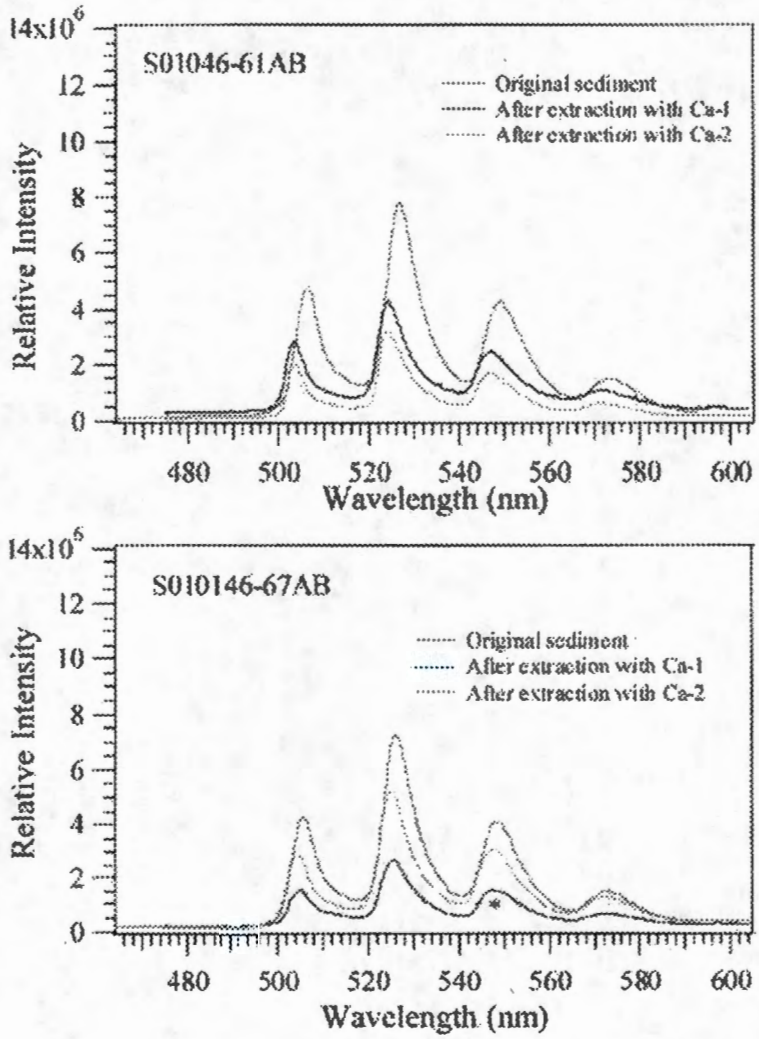

The fluorescence spectra of the uranium leached into the electrolyte solutions were completely different from the spectral signature of uranium in the sediments (Figure D.73 and Figure D.74, Table D.43). All of the vibronic peaks were blue-shifted to shorter wavelength as compared to the solid sediments. The relative spectral intensities were higher in both sodium and calcium electrolytes at higher pH (e.g., sodium-2 and calcium-2) because of increased solubility of sediment uranium(VI) in the higher pH filtrate (see percent uranium dissolved in Figure D.73 and Figure D.74, and Section D.3.5.)

Figure D.73. Fluorescence Emission Spectra of Uranyl from Hanford Vadose Sediments - 61AB (upper panel) and -67AB (lower panel) Leached into the Electrolyte Solutions Na-1 and Na-2.

The Compositions of the Electrolyte Solutions are: Na-1: $NaHCO_3$ (0.194 mM)-$NaNO_3$ (0.0498 M) solution with I = 0.05, pH 7.2 7, contact time: 4 weeks; Na-2: $NaHCO_3$ (15.59 mM)-Na_2CO_3 (4.93 mM)-$NaNO_3$ (0.0245 M) with I = 0.05, pH 9.25, contact time: 4 weeks λ_{ex} = 415 nm.

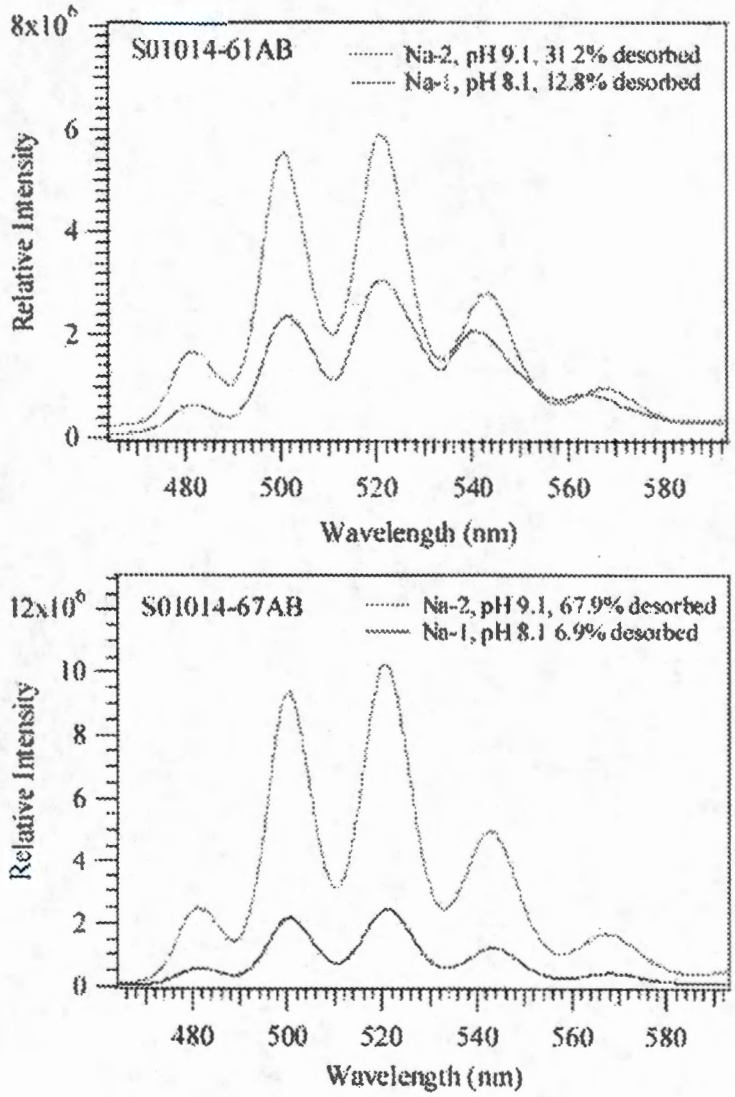

Figure D.74. Fluorescence Emission Spectra at 5.2 K of Uranyl from the Sediment -61AB (upper panel) and -67AB (lower panel) Leached into the Ca^{2+}-Saturated Electrolyte Solutions, Ca-1 and Ca-2.

The Compositions of the Electrolyte Solutions are: Ca-1: $CaCO_3$-saturated $Ca(ClO_4)_2$ (0.0219 M)-$NaClO_4$(0.0666 M) with I = 0.05, pH 7.57, contact time: 2 weeks; Ca-2: $CaCO_3$-saturated $NaClO_4$(0.0416 M)-$NaHCO_3$ (4.44 mM)-Na_2CO_3 (4.44 mM)-$HClO_4$(1.425 mM) with I = 0.05, pH 8.96, contact time: 2 weeks. λ_{ex} = 415 nm.

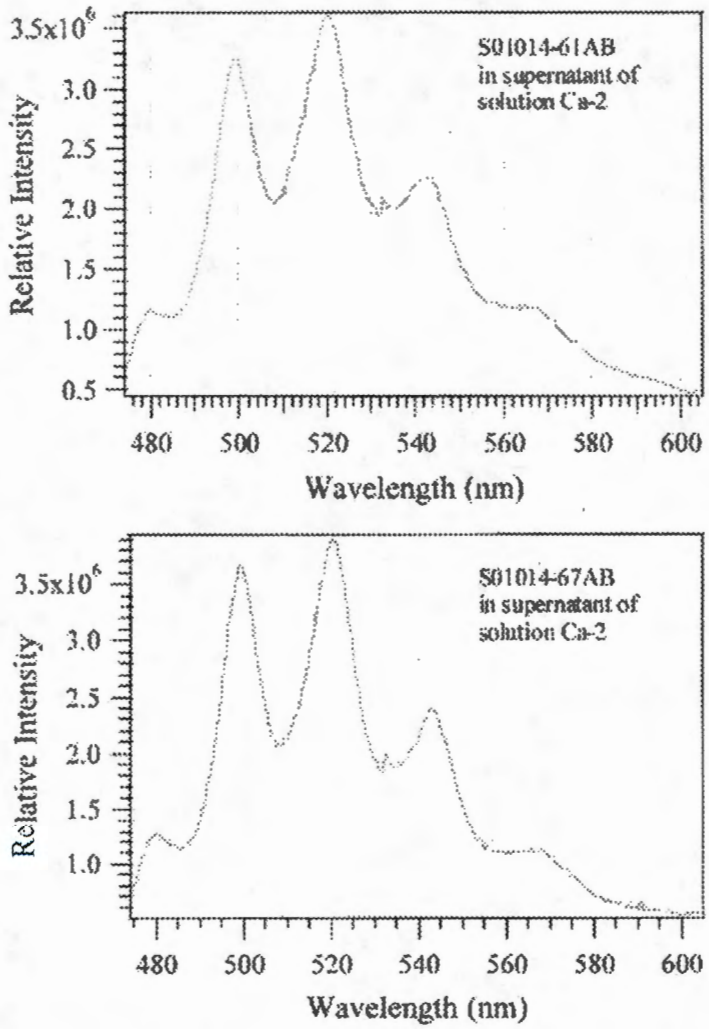

D.3.4.3.5 Spectral Analysis of Aqueous Species and Porewaters. A series of uranyl-carbonate solutions was carefully prepared at selected pH values (pH 1 to 11) to function as aqueous "standards" for LIFS analyses. These solutions all were prepared in sodium electrolyte, with the exception of one sample at pH 8.0 prepared in calcium electrolyte (Table D.44). Thermodynamic calculations indicated that the uranyl bis- $[UO_2(CO_3)_2^{2-}]$ and tris-carbonate complexes $[UO_2(CO_3)_3^{4-}]$ dominated uranyl speciation between pH 7.5 to pH 11, while the dicalcium-urano-tris-carbonate complex, $Ca_2UO_2(CO_3)_3$, was dominant in calcium

electrolyte at pH 8. Between pH 6.5 to pH 8.0, the mixed ligand carbonate hydroxyl complex $[(UO_2)_2(OH)_3(CO_3)^-]$ was present with the highest concentration. At even lower pH (6.0 to 6.5), the major uranium(VI) species are the hydroxyl complexes $[UO_2OH^+, UO_2(OH)_2]$.

Table D.44. Fluorescence Spectral Characteristics of U(VI) in Sodium Carbonated Solutions at Different pH I = 0.1 M Sodium Perchlorate. λ_{ex} = 415 nm.

Solution pH	Spectral maxima (nm)
1.2	487.6, 509.6, 532.7, 558.7, 585.7
4.0	487.8, 509.5, 532.7, 559.0, 586.3
6.0	478.5, 497.9, 518.1, 540.4, 565.5
6.8	479.0, 498.4, 518.3, 540.4, 565.5
8.0	480.3, 499.2, 519.4, 541.4, 565.5
11.0	479.2, 498.4, 518.6, 540.7, 565.0
8.0 with 0.02 M Ca^{2+}	482.0, 501.7, 522.6, 545.5, 570.7

The obtained spectral signatures varied with pH (i.e., uranium-speciation) (Figure D.75). The largest spectral shifts of the samples occurred between pH 4 and 6, corresponding to the hydrolysis of uranyl ion, UO_2^{2+} (beyond the pH range of Figure D.63). Discernable changes in the spectral position and/or the half-width were apparent for samples between pH 6 and pH 11 as well as with the addition of Ca^{2+}. Clearly, both hydrolysis and complexation by the carbonate anion causes a red shift of the fluorescence spectra toward the longer wavelength. This is consistent with the observations by Meinrath (1997) and Bernhard et al. (1996) at room temperature. It was noticed that in solutions in which the bis- and tris-carbonate complexes were dominant, the fluorescence intensity was inversely proportional to the sample temperature. At room temperature, the fluorescence was completely quenched. This is likely an indication that the carbonate anion is a strong fluorescence quencher for uranyl fluorescence, although the detailed quenching mechanism is yet to be understood. Analysis and interpretation of the LIF spectra of these aqueous samples at liquid helium temperatures has only recently begun. The current interpretations are therefore preliminary, and additional spectral measurements of these solutions under different conditions are ongoing.

A comparison of the fluorescence spectra of the uranium(VI) solubilized from the contaminated sediments (Figure D.73 and Figure D.74) and those of the aqueous uranyl carbonate solutions (Figure D.75) confirmed that the desorbed uranium(VI) existed as aqueous uranyl carbonate complexes such as the bis- and tris-carbonate complexes, $UO_2(CO_3)_2^{2-}$, $UO_2(CO_3)_3^{4-}$. The fluorescence spectra of desorbed uranium(VI) in the calcium carbonate-saturated carbonate electrolyte solutions (calcium-1 and calcium-2) (Figure D.74) did not show any substantial difference from those in the Na^+-based carbonate electrolyte solutions (sodium-1 and sodium-2) (Figure D.73). These, in turn, were all consistent with the fluorescence spectra for uranyl carbonate solutions in sodium electrolyte at similar pH where Ca^{2+} was absent. It was concluded that the concentration of Ca^{2+} was too low (< 0.02 M) in the calcium carbonate electrolyte solutions (calcium-1 and calcium-2) to drive the formation of the dicalcium-urano-tris-carbonate complex, $Ca_2UO_2(CO_3)_3$.

Figure D.75. Fluorescence Emission Spectra of Uranyl Carbonate Solutions at Different pH at 5.5 K. I = 0.1 M; $[Na_2CO_3] = 8 \times 10^{-3}$ M; $[UO_2^{2+}] = 2 \times 10^{-5}$ M; $\lambda_{ex} = 415$ nm.

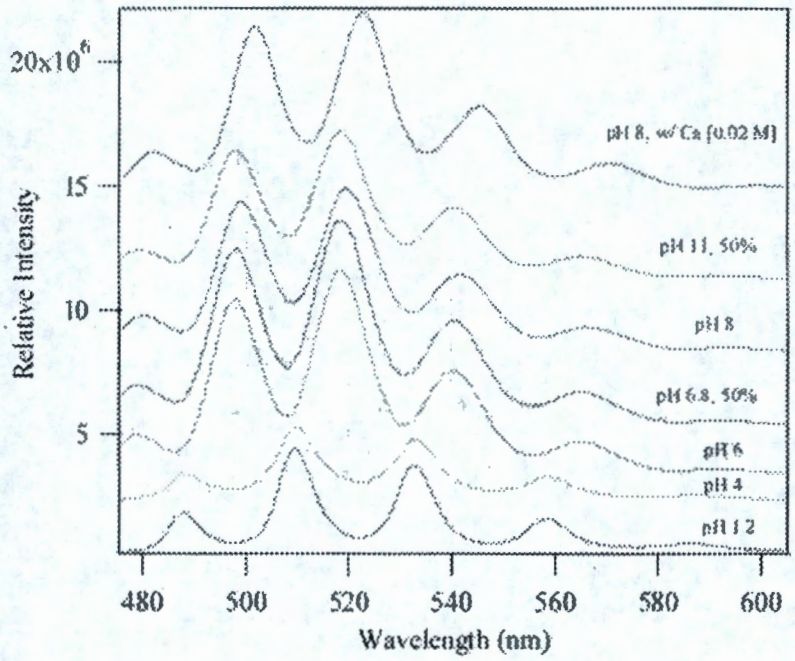

Dominant species are their relative concentrations are:

pH 8, with 0.02 M Ca2+:	Ca2UO2(CO3)3	> 99%
pH 11:	UO2(CO3)34-	> 99%
pH 8:	UO2(CO3)2 2-	> 52%
	UO2(CO3)34-	~ 10%
	(UO2)2(OH)3CO3-	~ 48%
pH 6.8:	(UO2)2(OH)3CO3-	> 72%
	UO2(OH)2	> 11%
	UO2CO30	> 11%
pH 6.0:	UO2(OH)+	34.6%
	UO2(OH)2	> 15%
	UO2CO30	> 15%
pH 4:	UO22+	> 90%
pH 1.2:	UO22+	> 99%

Table D.45. Fluorescence Spectral Characteristics of U(VI) in Porewaters of Hanford Sediments. $\lambda_{ex} = 415$ nm.

Sediment Sample	Spectral maxima (nm)
-55 UFA	479.7, 499.0, 520.4, 542.4, 567.7
-64 UFA	479.7, 498.8, 519.9, 542.7, 567.5

D.3.4.3.6 Fluorescence Characteristics of Porewater Samples. Sediment porewaters offer a critical link between the leaked tank waste streams and the current chemical state of uranium(VI) in the sediment. The porewater concentrations and speciation reflect the energetics of different uranium(VI) phases and phase associations and the impact of other waste-derived and endogenous chemical components. The porewater uranium(VI) species include those that are mobile and currently migrating. The uranium(VI) concentrations in the porewaters of the two samples were high enough to record a well-resolved fluorescence spectrum (Figure D.76), in spite of their relatively low total uranium(VI) contents compared to samples 53, 61, and 67. The fluorescence spectra of the two extracted porewaters (Figure D.76) were quite similar to those of the uranyl carbonate solutions at pH 8, in which the uranyl bis- and tris-carbonate complexes, $UO_2(CO_3)_2^{2-}$, $UO_2(CO_3)_3^{4-}$, are the major species (Figure D.63 for the speciation and Figure D.75 for spectra). Hence, these results suggest that uranyl bis- and tris-carbonate complexes also were the dominant in situ solution species in the contaminated sediments. Such conclusions are generally consistent with the results of the speciation modeling of the porewaters of samples 53, 61, and 67 (Table D.46). The results of the speciation modeling for porewaters suggest the presence of between 0.3 % to 26.0% dicalcium-uranyl-tris(carbonate) complex, $Ca_2UO_2(CO_3)_3$, in solutions of samples 53, 61, and 67 (Table D.46). However, more detailed analysis of the fluorescence spectra (Figure D.76) and the concentration of calcium in porewaters of sample 55 and 64, as well as additional speciation modeling, are needed for any positive identification of their presence in the porewaters of samples 55 and 64. Even though the reference "aqueous species" standards did not contain examples of phosphate or silicate complexes, reference spectra for these complexes have been published, and the LIFS spectra (Figure D.76) of the porewaters showed no evidence of their presence.

Figure D.76. Fluorescence Emission Spectra at 5.2 K of Hanford Vadose Zone Porewaters Under Tank BX-102. λ_{ex} = 415 nm.

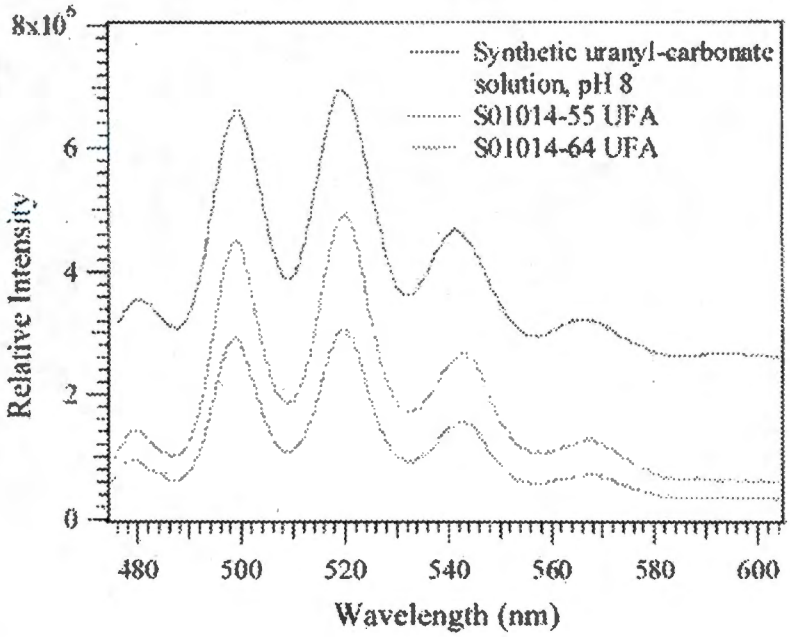

Table D.46. Uranyl Speciation (mol/L) of Porewater Extracted from Selected BX-102 (Borehole 299-E33-45) Core Samples

Species	BX-102 53A	BX-102 61A	BX-102 67A
UO_2^{2+}	$3.85x10^{-15}$	$1.57x10^{-18}$	$1.06x10^{-15}$
$UOOH^+$	$8.86x10^{-12}$	$1.26x10^{-14}$	$2.78x10^{-12}$
$UO_2(OH)_2(aq)$	$2.58x10^{-9}$	$1.40x10^{-11}$	$9.96x10^{-10}$
$UO_2(OH)_3^-$	$8.04x10^{-9}$	$1.97x10^{-10}$	$4.36x10^{-9}$
$UO_2(OH)_4^{2-}$	$1.26x10^{-12}$	$1.54x10^{-13}$	$1.05x10^{-12}$
$(UO_2)_3(OH)_7^-$	$5.57x10^{-14}$	$4.22x10^{-20}$	$4.67x10^{-15}$
$UO_2CO_3(aq)$	$2.25x10^{-9}$	$1.22x10^{-11}$	$8.71x10^{-10}$
$UO_2(CO_3)_2^{2-}$	**$6.10x10^{-6}$ (0.8%)**	**$7.50x10^{-7}$ (0.0%)**	**$5.07x10^{-6}$ (0.3%)**
$UO_2(CO_3)_3^{4-}$	**$5.63x10^{-4}$ (73.2%)**	**$2.48x10^{-3}$ (99.7%)**	**$1.46x10^{-3}$ (89.6%)**
$(UO_2)_3(CO_3)_6^{6-}$	$7.70x10^{-11}$	$6.08x10^{-13}$	$1.44x10^{-10}$
$(UO_2)_2CO_3(OH)_3^-$	$2.03x10^{-8}$	$2.77x10^{-12}$	$4.33x10^{-9}$
$Ca_2UO_2(CO_3)_3(aq)$	**$2.00x10^{-4}$ (26.0%)**	**$7.42x10^{-6}$ (0.3%)**	**$1.65x10^{-4}$ (10.1%)**
$UO_2PO_4^-$	$4.48x10^{-10}$	$1.51x10^{-11}$	$1.49x10^{-10}$
$UO_2HPO_4(aq)$	$1.04x10^{-12}$	$7.73x10^{-15}$	$2.45x10^{-13}$
$UO_2H_3SiO_4^+$	$6.01x10^{-11}$	$1.48x10^{-14}$	$1.34x10^{-11}$
Total	$7.69x10^{-4}$	$2.48x10^{-3}$	$1.63x10^{-3}$

Number in parentheses is the species percentage of total uranyl concentration in the sample. No solid phase is allowed to precipitate. The major uranyl species are in **bold** font.

D.3.4.4 Conclusions and Implications

1. This work demonstrated that cryogenic uranyl fluorescence measurement at liquid helium temperature significantly enhances both the fluorescence signal level and spectral resolution of uranyl by effectively reducing the inhomogeneous line-broadening effect, suppressing the phonon bands, and minimizing fluorescence quenching by impurities. The cryogenic method offers improved possibilities for identifying uranyl species in complex environmental samples. Strong fluorescence signals were obtained in all Hanford sediment and water samples contaminated with uranium(VI).

2. The fluorescence emission spectra of U(VI) were recorded from four BX-102 sediment samples that contained from 142 to 415 ug/g of total uranium. The emission spectrum of each of the four samples was quite similar, indicating the presence of a common uranium(VI) phase or phases. Time-resolved measurements showed little shift with delay, indicating that most of the uranium(VI) was associated with a single type of uranium(VI) precipitate. The lack of change in the emission spectrum with the leaching of up to 60% of the precipitated uranium(VI) pool further supports the conclusion that only one dominant uranium(VI) phase exists.

3. The well-resolved vibronic peaks in the fluorescence spectra of the four sediment samples suggested that the major fluorescence species was a crystalline uranyl mineral phase. Such conclusion was consistent with the x-ray microprobe analyses reported in Section D.3.2. A comparison of the uranium(VI) fluorescence spectra in the sediments with those of known uranium (VI) the mineral specimens indicated that the uranyl

mineral in the sediments was most probably a uranyl phosphate (phosphuranylite or meta-autunite, specifically) or a uranyl silicate (soddyite, uranophane, or boltwoodite). Additional reference samples of the uranyl phosphate and silicate mineral phases are being sought for LIFS measurement to refine the spectral library for these important Hanford phases. Other spectroscopic (e.g., Raman) and solubility analyses are currently underway to more definitively identify the chemical and structural properties of the uranium(VI) precipitate.

4. The porewaters from both 299-E33-45 sediments -55 and -64 showed fluorescence spectra that were almost identical to those of uranyl bis- and tris-carbonate complexes at pH 8, $UO_2(CO_3)_2^{2-}$ and $UO_2(CO_3)_3^{4-}$. Although identification continues of different uranyl hydroxyl and carbonate complexes in detail from their LIF characteristics through ongoing work, it seems to be safe to say that uranium(VI) bis- and tris-carbonate complexes are the dominant aqueous species in the porewaters. Therefore, they are the most prominent candidates for species responsible for the subsurface migration of uranium(VI).These uranium species are apparently migrating through the Hanford vadose zone. There was no evidence for the presence of phosphate or other types of complexes in spite of the tentative presence of silicate, phosphate, and other potential precipitates in porewater.

D.3.4.5 References

Bargar, J. R., R. Reitmeyer, and J. A. Davis, 1999, "Spectroscopic Confirmation of Uranium(VI)-Carbonato Adsorption Complexes on Hematite," *Environmental Science and Technology,* Vol. 33:2481-2484.

Bargar, J. R., R. Reitmeyer, J. J. Lenhart, and J. A. Davis, 2000, "Characterization of U(VI)-Carbonato Ternary Complexes on Hematite: EXAFS and Electrophoretic Mobility Measurements," *Geochimica et Cosmochimica Acta*, Vol. 64:2737-2749.

Barnett, M. O., P. M. Jardine, and S. C. Brooks, 2002, "Uranium(VI) Adsorption to Heterogeneous Subsurface Media: Application of a Surface Complexation Model," *Environmental Science and Technology,* Vol. 36:937-942.

Beechem, J. M., E. Gratton, M. Ameloot, J. R. Knutson, and L. Brand, 1991, "The Global Analysis of Fluorescence Intensity and Anisotropy Decay Data: Second-Generation Theory and Programs," In *Topics in Fluorescence Spectroscopy, Vol. 2. Principles,* J. R. Lakowicz, ed., Plenum Press, New York, pp. 241-306.

Bernhard, G., G. Geipel, V. Brendler, and H. Nitsche, 1996, "Speciation of Uranium in Seepage Waters of a Mine Trailing Pile Studied by Time-Resolved Laser-Induced Fluorescence Spectroscopy (TRLFS)," *Radiochimica Acta,* Vol. 74:87-91.

Borovec, Z., 1981, "The Adsorption of Uranyl Species by Fine Clay," *Chemical Geology,* Vol. 32:45-58.

Bostick, B. C., S. Fendorf, M. O. Barnett, P. M. Jardine, and S. C. Brooks, 2002, "Uranyl Surface Complexes Formed on Subsurface Media from DOE Facilities," *Soil Science Society of America Journal,* Vol. 66:99-108.

Chisholm-Brause, C. J., S. D. Conradson, C. T. Buscher, P. G. Eller, and D. E. Morris, 1994, "Speciation of Uranyl Sorbed at Multiple Binding Sites on Montmorillonite," *Geochimica et Cosmochimica Acta,* Vol. 58:3625-3631.

Davis, J. A., 2001, *Surface Complexation Modeling of Uranium (VI) Adsorption on Natural Mineral Assemblages,* NUREG/CR-6708, Office of Nuclear Regulatory Research, U.S. Nuclear Regulatory Commission, Washington, D. C., pp. 214.

Denning, R. G., 1992, "Electronic Structure and Bonding in Actinyl Ions," *Structure and Bonding,* Vol. 79:215-276.

Dent, A. J., J. D. F. Ramsay, and S. W. Swanton, 1992, "An EXAFS Study of Uranyl Ions in Solutions and Sorbed onto Silica and Montmorillonite Clay Colloids," *Journal of Colloid Interface Science,* Vol. 150:45-60.

Duff, M. C., D. E. Morris, D. B. Hunter, and P. M. Bertsch, 2000, "Spectroscopic Characterization of Uranium in Evaporation Basin Sediments," *Geochimica et Cosmochimica Acta,* Vol. 64(9):1535-1550.

Hudson, E. A., L. J. Terminello, B. E. Viani, M. Denecke, T. Reich, P. G. Allen, J. J. Bucher, D. K. Shuh, and N. M. Edelstein, 1999, "The Structure of U^{6+} Sorption Complexes on Vermiculite and Hydrobiotite," *Clays and Clay Minerals,* Vol. 47:439-457.

Hunter, D. B., and P. M. Bertsch, 1998, "In Situ Examination of Uranium Contaminated Soil Particles by Micro-X-ray Absorption and Micro-Fluorescence Spectroscopies," *Journal of Radioanalytical and Nuclear Chemistry,* Vol. 234:237-242.

Grenthe, I., 1992, *Chemical Thermodynamics of Uranium,* North Holland, New York.

Kalmykov, S. N., and G. R. Choppin, 2000, "Mixed $Ca^{2+}/UO_2^{2+}/CO_3^{2-}$ Complex Formation at Different Ionic Strengths," *Radiochimica Acta,* Vol. 88:603-606.

Kaplan, D. I., T. L. Gervais, and K. M. Krupka, 1998, "Uranium(VI) Sorption to Sediments Under High pH and Ionic Strength Conditions," *Radiochimica Acta,* Vol. 80:201-211.

Lackowicz, J. R., 1991, *Topics in Fluorescence Spectroscopy,* Plenum Press, New York.

Meinrath, G. R., 1997, "Uranium (VI) Speciation by Spectroscopy," *Journal of Radioanalytical and Nuclear Chemistry,* Vol. 224:119-126.

McKinley, J. P., J. M. Zachara, S. C. Smith, and G. D. Turner, 1995, "The Influence of Uranyl Hydrolysis and Multiple Site-Binding Reactions on Adsorption of U(VI) to Montmorillonite," *Clays and Clay Minerals,* Vol. 43:586-598.

Morris, D. E., P. G. Allen, J. M. Berg, C. J. Chisholm-Brause, S. D. Conradson, R. J. Donohoe, N. J. Hess, J. A. Musgrave, and C. D. Tait, 1996, "Speciation of Uranium in Fernald Soils by Molecular Spectroscopic Methods: Characterization of Untreated Soils," *Environmental Science and Technology,* Vol. 30:2322-2331.

Morris, D. E., C. J. Chisholm-Brause, M. Barr, S. D. Conradson, and P. G. Eller, 1994, Optical Spectroscopic Studies of the Sorption of UO_2^{2+} Species on a Reference Smectite," *Geochimica,* Vol. 58:3613-3623.

Moulin, C., P. Decambox, V. Moulin, and J. G. Decaillon, 1995, "Uranium Speciation in Solution by Time-Resolved Laser-Induced Fluorescence," *Analytical Chemistry,* Vol. 67:348-353.

Pabalan, R. T., and D. T. Turner, 1996, "Uranium (6+) Sorption on Montmorillonite: Experimental and Surface Complexation Modeling Study," *Aquatic Geochemistry,* Vol. 2:203-226.

Stepanov, A.V., E. B. Preobrazhenskaya, and S. A. Nikitina, 1984, "Influence of Temperature on the Fluorescence of Uranyl in Frozen Solutions of Phosphoric and Sulfuric Acids in the Presence of Quenchers," *Radiochimica,* Vol. 26:798-803.

Swanson, L. C., V. J. Rohay, and J. M. Faurote, 1999, *Hydrogeologic Conceptual Model for the Carbon Tetrachloride and Uranium/Technetium Plumes in the 200 West Area: 1994 through 1999 Update*, BHI-01311, Rev. 0, CH2M HILL Hanford Group, Inc., Richland, Washington.

Sylvester, E. R., E. A. Hudson, and P. G. Allen, 2000, "Surface Interactions of Actinide Ions with Geologic Materials Studied by XAFS," *Material Research Society Symposium Proceedings,* Vol. 590:9-16.

Thompson, H. A., G. A. Parks, and G. E. Brown, Jr., 1998, "Structure and Composition of Uranium(VI) Sorption Complexes at the Kaolinite-Water Interface," In *Adsorption of Metals by Geomedia, Variables, Mechanisms, and Model Applications,* E.A. Jenne, ed., Academic Press, New York, pp. 349-370.

Thorne, J. R. G., A. Harrison, I. D. Morrison, and R. G. Denning, 1987, "Fluorescence Line Narrowing in Uranyl Glasses," *Journal of Luminescence,* Vol. 38:156-158.

Turner, G. D., J. M. Zachara, J. P. McKinley, and S. C. Smith, 1996, "Surface-Charge Properties and UO_2^{2+} Adsorption of a Subsurface Smectite," *Geochimica et Cosmochimica Acta,* Vol. 60:3399-3414.

Vochten, R., N. Blaton, O. Peeters, K. van Springel, and L. van Haverbeke, 1997, "A New Method of Synthesis of Boltwoodite and of Formation of Sodium Boltwoodite, Uranophane, Sklodowskite and Kasolite from Boltwoodite," *The Canadian Mineralogist,* Vol. 35:735-741.

Waite, T. D., J. A. Davis, T. E. Payne, G. A. Waychunas, and N. Xu., 1994, Uranium(VI) Adsorption to Ferrihydrite: Application of a Surface Complexation Model," *Geochimica et Cosmochimica Acta,* Vol. 58(24):5465-5478.

D.3.5 THERMODYNAMICS AND DISSOLUTION KINETICS OF URANYL MINERALS IN HANFORD BX-102 SEDIMENTS

Chongxuan Liu[1], John M. Zachara[1], and Odeta Qafoku[1], and Steve Heald[1,2]

[1]Pacific Northwest National Laboratory, Richland, Washington 99352
[2]Argonne National Laboratory, Argonne, Illinois 60439

D.3.5.1 Introduction

Research described in Sections D.3.2 through D.3.4 of this appendix has shown that sorbed uranium in samples from borehole 299-E33-45 exists primarily in precipitated state, most probably as a hydrated uranyl silicate. These precipates were observed in grain cavities, grain fractures, and as discontinuous grain coatings. In this study, the rate and extent of uranyl desorption/dissolution from three high-uranium samples from 299-E33-45 were measured to provide insights on the future migration of the in-ground uranium pool and its potential to impact groundwater. The research strived to determine the dissolution behavior of the precipitated uranyl phase over a range of pH and electrolyte concentrations representative of subsurface geochemical environment in WMA B-BX-BY. Various experiments were performed to assess whether the phase exhibited a characteristic equilibrium solubility value, and the time required to reach the equilibrium state. Rate studies evaluated chemical kinetic and mass transfer controls on dissolution. Changes to the chemical composition and spatial distribution of the uranyl phase during dissolution were monitored by CLIFS and x-ray microprobe (XRM). The thermodynamics of potential uranyl phases in the sediments (in addition to silicates), aqueous uranyl speciation in sediment porewater, and the extent and rates of dissolution were analyzed using linear free energy, chemical equilibrium, and kinetic models. The results are also manipulated to show the complex effects of the dissolution process on the desorption K_d of uranium.

D.3.5.2 Background

Uranyl minerals precipitate under various geochemical conditions. Uranium(VI) mineral assemblages can be quite complex in natural (Finch and Murakami 1999) and contaminated (Buck et al. 1996; Morris et al. 1996) environments. Phase differentiation depends on the geochemical conditions of the uranium(VI)-carrying fluid and its interaction with the surrounding soil matrix. Finch and Murakami (1999) provide an overview of the geochemical conditions leading to the formation of different uranyl mineral groups including: sulfates, carbonates, oxyhydroxides, silicates, arsenates, phosphates, and vanadates. Vanadates are the most insoluble among the uranyl minerals. In the presence of vanadium, carnotite has been discovered as a primary mineral associated with calcretes and gypcretes in arid regions of the United States, western Australia, and southwestern Africa (Langmuir 1978). The uranyl arsenates and sulfates are uncommon. The most commonly observed uranyl minerals include carbonates, oxyhydroxides, silicates, and phosphates. These mineral groups are typical oxidation products of primary uranium(VI) ore minerals (Frondel 1956; Korzeb et al. 1997), corrosion products of spent nuclear fuel (Finch and Ewing 1992; Finch and Murakami 1999), and in-ground precipitates at uranium(VI)-contaminated sites (Buck et al. 1996; Morris et al. 1996).

The sequence of uranyl mineral formation depends on the thermodynamic and kinetic properties of the different uranium(VI) mineral phases and the paragenetic geochemical conditions. Oxyhydroxides were observed to be the first to precipitate in natural environments surrounding uranium ore (Pearcy et al. 1994; Foord et al. 1997; Korzeb et al. 1997) or the first phase to form during the corrosion of uraninite under oxidizing conditions (Finch and Ewing 1992; Finch and Murakami 1999), even in silica-saturated waters (Frondel 1956; Smith 1984; Wronkiewicz et al. 1992, 1996; Pearcy et al. 1994). Oxyhydroxides are more stable than uranyl carbonates and their precipitation kinetics are more favorable than silicates and phosphates, which are thermodynamically more stable in most natural environments. The minimal structural rearrangement required from uraninite may account for the kinetic favorability of oxyhydroxides over other phases (Evans 1963). In natural environments, the most common natural oxyhydroxide is gummite, a mixture of dehydrated schoepite and related compounds with chemical formulas of $[(UO_2)(OH)_2](H_2O)_{0.5}$ and $(UO_2)(OH)_2$ (Foord et al. 1997). Schoepite and becquerelite are common corrosion products of spent fuel in either silica-saturated (Wronkiewicz et al. 1992, 1996) or silica-deficient waters (Finch and Ewing 1992; Pearcy et al. 1994).

The oxyhydroxides, which precipitate rapidly, transform to more stable phases (i.e., silicates or phosphates) in environments containing silicate or phosphate. A suite of natural silicates has been identified, including soddyite, sklodowskite, boltwoodite, uranophane, weeksite, uranosilite, and others (Isobe et al. 1992; Pearcy et al. 1994; Elton and Hooper 1995; Korzeb et al. 1997). Among phosphates, autunites are the most common secondary form (Langmuir 1978). Phosphuranylite also was found in association with autunites (Korzeb et al. 1997). The uranyl carbonates typically form in environments with high carbon dioxide pressures or high evaporation or low concentrations of silicate or phosphate (Langmuir 1978).

Kinetic investigations of uranyl mineral dissolution are limited in the literature. One laboratory study indicated that the dissolution process was most influenced by the identity and complexation strength of ligands in the associated aqueous solution (Sowder et al. 2001). The dissolution rates of metashoepite and becquerelite were faster than those for autunites and chernikovite in solutions of acetic acid and EDTA complexing ligands, but slower in bicarbonate solutions (Sowder et al. 2001). A higher concentration of complexant leads to a higher dissolution rate. The literature base is insufficient to predict the dissolution rate of a given uranium(VI) mineral phase under specified geochemical conditions.

In a broader sense, the dissolution of uranyl from sediments typically includes both mineral dissolution and desorption. A field study at the Koongarra uranium deposit indicated that uranium(VI) in sediments was present in adsorbed and precipitated pools (Payne et al. 2001). The adsorbed pool was in equilibrium with aqueous phase, and the desorption process could be described by a surface complexation model. The rate and extent of dissolution of the precipitated phases were not studied, however.

Other limited desorption/dissolution studies indicate that the release of uranium(VI) from laboratory-spiked pristine materials (Fuhrmann et al. 1997; Giammar and Hering 2001) and uranium-contaminated sediments (Braithwaite et al. 1997; Mason et al. 1997) exhibits kinetic behavior. The rate of desorption/dissolution was found to decrease with increasing exposure time to uranium contamination. Equilibrium desorption of uranium(VI) from goethite was observed with less than 1 month aging, but strong kinetic behavior developed with 6 months

aging (Giammar and Hering 2001). A desorption/dissolution half-life of more than 10 years was reported for sediments subjected to long-term uranium contamination (Braithwaite et al. 1997).

In this study, the rate and extent of uranyl desorption/dissolution from sediments contaminated by metal waste in the BX tank farm was investigated. Three high-uranium samples from borehole 299-E33-45 were leached in sodium and sodium-calcium-bicarbonate electrolyte solutions for time periods exceeding 140 days. The changes in the uranyl phase after dissolution were identified using X-ray microprobe (XRM) and laser-induced florescence spectroscopy (LIFS). The thermodynamics of potential uranyl phases in sediments, aqueous uranyl speciation in the sediment-associated porewaters, and the extent and rates of dissolution were analyzed using linear free energy, chemical equilibrium, and kinetic models.

D.3.5.3 Thermodynamic Properties of Potential Relevant Uranium(VI) Phases

Free energy data for potential uranyl phases in Hanford sediment were collected from the literature or calculated. The mineral phases included oxyhydroxides, carbonates, silicates, and phosphates. Although oxyhydroxides and carbonates do not appear to be important in the BX-102 sediments based on preliminary spectroscopic analyses (Sections D.3.2 to D.3.5), these minerals are found at other contaminated sites of comparable geochemistry (Buck et al. 1996; Morris et al. 1996) and merit consideration as relevant environmental phases.

A regression method developed by Chen et al. (1999) was used to calculate the free energies of those uranyl minerals for which the literature reported either no, or inconsistent, values. For comparison and completeness, the regression method was used also to calculate the free energies of other uranyl minerals for which measured or estimated values already are available. The minerals and their respective free energies are listed in Table D.47.

The regression method assumes that each uranyl mineral is composed of a few basic structural components. The number and type of components for a specific mineral are determined from the chemical composition of the mineral and structural information obtained through X-ray diffraction. The free energy of a mineral was assumed to be the linear combination of free energies of these basic constituent structural components.

Table D.47. Thermodynamic Properties of Potential Relevant Uranyl Minerals that May Form in Hanford Sediment

Solid phase	Formula	ΔG_0^f (kJ/mol)		Source
		M/E[a]	Calculated[b]	
Oxyhydroxides				
Metaschoepite	$[(UO_2)_8O_2(OH)_{12}](H_2O)_{10}$	-13092.0(M)	-13127.0	1
Schoepite	$[(UO_2)_8O_2(OH)_{12}](H_2O)_{12}$		-13609.2	
Becquerelite	$Ca[(UO_2)_6O_4(OH)_6](H_2O)_8$	-10305.8(E)	-10324.7	2
Clarkeite	$Na_2(UO_2)_2O_3$	-3011.5(E)	-3008.6	5
Carbonates				
Rutherfordine	UO_2CO_3	-1563.0(M)	-1561.7	3
Liebigite	$Ca_2[UO_2(CO_3)_3](H_2O)_{11}$	-6468.6(E)	-6446.5	2
Zellerite	$Ca[UO_2(CO_3)_2](H_2O)_5$		-3883.5	
Silicates				
Boltwoodite	$K[UO_2(SiO_3OH)](H_2O)_{1.5}$		-2814.4	
Na-Boltwoodite	$Na[UO_2(SiO_3OH)](H_2O)_{1.5}$	-2844.8(E)	-2838.9	4
Uranophane	$Ca[UO_2(SiO_3OH)]_2(H_2O)_5$	-6192.3(E)	-6189.2	4
Soddyite	$(UO_2)_2(SiO_4)(H_2O)_2$	-3655.7(E)	-3658.2	4
Uranosilite	$UO_2(Si_7O_{15})$		-7138.8	
Na-Weeksite	$Na_2(UO_2)_2(Si_5O_{13})(H_2O)_3$	-7993.9(E)	-8001.8	4
Weeksite	$K_2(UO_2)_2(Si_5O_{13})(H_2O)_3$		-7952.7	
Phosphates				
Metaautunite	$Ca[(UO_2)_2(PO_4)_2](H_2O)_6$		-6122.7	
Chernikovite	$(UO_2HPO_4)(H_2O)_4$	-3064.7(M)	-3063.5	5
Phosphuranylite	$KCa(H_3O)_5(UO_2)[(UO_2)_3(PO_4)_2O_2]_2(H_2O)_8$		-15437.9	
Na-Autunite	$Na_2[(UO_2)_2(PO_4)_2]$	-4736.3 (E)	-4646.9	6
K-Autunite	$K_2[(UO_2)_2(PO_4)_2]$	-4782.3 (E)	-4597.8	6

[a]Using regression method (Chen et al. 1999)
[b]Only measured/estimated from experiment is listed; M/E indicated measured or estimated from experiment.
1. (O'Hare et al. 1988); 2. (Finch 1997); 3. (Sergeyeva et al. 1972); 4. (Chen et al. 1999) calculated from experimental results by (Nguyen et al. 1992); 5. (Grenthe et al. 1992); 6. (Langmuir 1978) calculated from experimental results by (Muto et al. 1968).

A component is a cation coordination polyhedron expressed in a form of oxide or hydroxide that represents a fundamental structural or chemical fragment of a uranium(VI) mineral. Because the cations in crystal structures are commonly coordinated directly to oxygen atoms, hydrogen ions sharing oxygen with other cations are also considered to be part of the structural water, so that all structural components are expressed as *cation oxides* in this method. The structural water was assumed to be a different component from hydration water. A uranyl polyhedron could have coordination numbers of 4, 5, and 6 (Burns et al. 1997). These uranyl polyhedra are assumed as different structural components.

With these treatments and assumptions, the formation energies of the different structural components (fragments, Table D.48) were estimated using the multiple linear regression approach of Chen et al. (1999) from minerals with known thermodynamic properties. The free energies of these structural components were then used to calculate the free energies of other

uranyl minerals. The free energies of uranyl minerals calculated with this method are listed in the column headed *Calculated* in Table D.47.

Table D.48. Molar Contribution of Structural Components to ΔG_0^f of Uranyl Minerals.[a]

Component	UO_3	Na_2O	K_2O	CaO	SiO_2	CO_2	P_2O_5	$H_2O_{(s)}$	$H_2O_{(H)}$
$-\Delta G_0^f$ (kJ/mol)	1161.05	686.54	637.45	715.77	853.96	400.61	1638.25	237.94	241.10

[a]data from (Chen et al. 1999). $H_2O_{(s)}$ and $H_2O_{(H)}$ indicate structural and hydration water respectively.

The method worked well for the minerals with known thermodynamic properties. This was expected, because the free energies of the structural components were estimated from those thermodynamic properties. The method is statistically empirical, and its reliability depends strongly on the number of uranyl minerals used in the regression analysis (Chen et al. 1999). Unfortunately, uranyl minerals with credible thermodynamic properties are limited (Grenthe et al. 1992; Hemingway 1982). Consequently, the outcomes obtained with the method may be biased by the small number of uranyl minerals with known properties. Nevertheless, this method was used as an approximation technique in calculating the free energies of potential uranyl phases at the Hanford Site with unknown free energy.

Using the free energies of the uranyl minerals (the measured, estimated, or calculated values listed in Table D.47) and auxiliary components (Table D.49) from Grenthe et al. (1992), stability constants for Hanford relevant uranyl minerals except for becquerilite and liegibite (Table D.50) were calculated. Some arguments remain regarding the estimated free energies of these latter two minerals (Chen et al. 1999; Finch and Murakami 1999). Two reported solubility products exist for becquerelite that differed by more than 10 log units (Vochten and Van Haverbeke 1990; Casa et al. 1997). The estimated value for becquerelite in (Table D.47) was taken from Finch (1997). Finch and Murakami (1999) later suggested that the free energy value calculated from the regression method of Chen et al. (1999) and also shown in (Table D.47) was the most reliable value available. This calculated value lies between those estimated from solubility products by Casa et al. (1997) and Vochten and Van Haverbeke (1990). The calculated free energy was, therefore, used for calculating the becquerelite stability constant. The calculated free energy was also used for determining the stability constant of liegibite because the calculated value was between those reported by Finch (1997) and Chen (1999) based on the solubility data in Alwan and Williams (1980).

Table D.49. Free Energy of Auxiliary Components for Calculating Stability Constant of Uranyl Minerals[a]

Component	ΔG_0^f (kJ/mol)
UO_2^{2+}	-952.55
$H_2O_{(l)}$	-237.14
CO_3^{2-}	-527.90
PO_4^{3-}	-1025.49
H_4SiO_4	-1307.74
Ca^{2+}	-552.81
Na^+	-261.95
K^+	-282.51

[a]data from Grenthe et al. (1992)

D.3.5.4 Thermodynamic Analysis of Porewater

The estimated porewater composition of samples 53A, 61A, and 67A that were based on the water extraction data and moisture content measurements of Serne et al. (2002) (Table D.51) were analyzed with a thermodynamic model to assess the nature of aqueous species and uranyl solids in equilibrium with the fluid phase.

The geochemical equilibrium speciation model MINTEQA2 was used in conjunction with a thermodynamic database compiled by the authors that included the stability constants listed in Table D.50 for uranyl minerals. Three aqueous uranyl species: (listed in order of decreasing significance) $UO_2(CO_3)_3^{4-} > Ca_2UO_2(CO_3)_3 > UO_2(CO_3)_2^{2-}$ were found to dominate the aqueous uranyl composition (Table D.52). The percentage of species $UO_2(CO_3)_3^{4-}$ was greater than 90% when pH >= 9.0 because of the higher CO_3^{2-} concentration and relatively low Ca^{2+} concentration in porewater. The percentage of $Ca_2UO_2(CO_3)_3$ increased with decreasing pH, and represented approximately 25% of the total uranium at pH 8.8. The Complexed uranyl species with silicate, phosphate, and hydroxide were computed to be negligible.

A unique uranium(VI) solid phase was not computed to be in equilibrium with porewater. Sodium-boltwoodite, uranophane, sodium-weeksite, soddyite, becquerelite, clarkeite, zellerite, and sodium-autunite (Table D.53) were all calculated to be slightly undersaturated or over saturated in one or more of the porewaters [e.g., $\log(IQ/K_{sp})$ - -2.5 to +2.5]. Sodium-boltwoodite was saturated in all three porewaters, while both uranophane and sodium-weeksite were saturated in samples 53A and 67A but not in sample 61A. The saturation indexes of the three minerals were the lowest at pH 9.5 (61A) because of the low concentration of UO_2^{2+} as a species. The high carbonate concentration decreased the UO_2^{2+} activity through the formation of aqueous uranyl carbonate complexes (Table D.52).

Both boltwoodite and weeksite did not achieve saturation because of the low aqueous K^+ concentrations in porewater. However, natural boltwoodite and weeksite typically contain a mixture of K^+ and Na^+ (Baturin and Sidorenko 1985; Burns 1998), especially in environments with a high Na^+, such as Hanford sediment. The formation energy of these mixed minerals is unknown and may range between the two end products, assuming no excessive energy of mixing. The mixed sodium and potassium boltwoodite and weeksite also could be saturated or be near saturation because of the high sodium concentration in porewater. The uranyl minerals that computed to be in near equilibrium (e.g., saturation) with the porewater were subjected to further solubility analysis in this study.

Table D.50. Stability Constants for Potentially Relevant Minerals at Hanford Site

Minerals	Reaction	log K
Oxyhydroxides		
Metaschoepite	$8UO_2^{2+} + 24H_2O = [(UO_2)_8O_2(OH)_{12}](H_2O)_{10} + 16H^+$	-38.50
Schoepite	$8UO_2^{2+} + 26H_2O = [(UO_2)_8O_2(OH)_{12}](H_2O)_{12} + 16H^+$	-30.98
Becquerelite	$6UO_2^{2+} + Ca^{2+} + 18H_2O = Ca[(UO_2)_6O_4(OH)_6](H_2O)_8 + 14H^+$	-37.13
Clarkeite	$2Na^+ + 2UO_2^{2+} + 3H_2O = Na_2(UO_2)_2O_3 + 6H^+$	-22.59
Carbonates		
Rutherfordine	$UO_2^{2+} + CO_3^{2-} = UO_2CO_3$	14.46
Liebigite	$UO_2^{2+} + 2Ca^{2+} + 3CO_3^{2-} + 11H_2O = Ca_2[UO_2(CO_3)_3](H_2O)_{11}$	34.36
Zellerite	$UO_2^{2+} + Ca^{2+} + 2CO_3^{2-} + 5H_2O = Ca[UO_2(CO_3)_2](H_2O)_5$	23.94
Silicates		
Boltwoodite	$UO_2^{2+} + K^+ + H_4SiO_4 + 1.5H_2O = K[UO_2(SiO_3OH)](H_2O)_{1.5} + 3H^+$	-14.74
Na-Boltwoodite	$UO_2^{2+} + Na^+ + H_4SiO_4 + 1.5H_2O = Na[UO_2(SiO_3OH)](H_2O)_{1.5} + 3H^+$	-5.81
Uranophane	$2UO_2^{2+} + Ca^{2+} + 2H_4SiO_4 + 5H_2O = Ca[UO_2(SiO_3OH)]_2(H_2O)_5 + 6H^+$	-11.70
Soddyite	$2UO_2^{2+} + H_4SiO_4 + 2H_2O = (UO_2)_2(SiO_4)(H_2O)_2 + 4H^+$	-5.04
Uranosilite	$UO_2^{2+} + 7H_4SiO_4 = UO_2(Si_7O_{15}) + 2H^+ + 13H_2O$	20.13
Na-Weeksite	$2UO_2^{2+} + 2Na^+ + 5H_4SiO_4 = Na_2(UO_2)_2(Si_5O_{13})(H_2O)_3 + 6H^+ + 4H_2O$	-4.42
Weeksite	$2UO_2^{2+} + 2K^+ + 5H_4SiO_4 = K_2(UO_2)_2(Si_5O_{13})(H_2O)_3 + 6H^+ + 4H_2O$	-18.84
Phosphates		
Metaautunite	$2UO_2^{2+} + Ca^{2+} + 2PO_4^{3-} + 6H_2O = Ca[(UO_2)_2(PO_4)_2](H_2O)_6$	33.46
Chernikovite	$UO_2^{2+} + PO_4^{3-} + H^+ + 4H_2O = (UO_2HPO_4)(H_2O)_4$	24.19
Phosphuranylite	$7UO_2^{2+} + Ca^{2+} + K^+ + 4PO_4^{3-} + 15H_2O$ $= KCa(H_3O)_3(UO_2)[(UO_2)_3(PO_4)_2O_2]_2(H_2O)_8 + 5H^+$	48.29
Na-Autunite	$2UO_2^{2+} + 2Na^+ + 2PO_4^{3-} = Na_2[(UO_2)_2(PO_4)_2]$	44.90
K-Autunite	$2UO_2^{2+} + 2K^+ + 2PO_4^{3-} = K_2[(UO_2)_2(PO_4)_2]$	45.76

Table D.51. Chemical Composition (mmol/L) of Porewater from BX-102

Component	BX-102 53A	BX-102 61A	BX-102 67A
UO_2^{2+}	0.769	2.483	1.633
K^+	1.640	1.302	1.506
Na^+	103.591	217.772	175.208
Ca^{2+}	1.477	0.666	1.592
Mg^{2+}	0.636	0.107	0.560
Cl^-	0.620	0.826	1.564
NO_3^-	17.132	17.977	38.539
SO_4^{2-}	4.890	8.866	18.514
PO_4^{3-}	0.165	4.119	0.203
H_4SiO_4	15.221	11.500	14.642
$CO_{2(tot)}$	atm_eq	atm_eq	atm_eq
PH	8.88	9.50	9.00

Table D.52. Uranyl Speciation (mol/L) of Porewater from BX-102

Species	BX-102 53A	BX-102 61A	BX-102 67A
UO_2^{2+}	3.85×10^{-15}	1.57×10^{-18}	1.06×10^{-15}
$UOOH^+$	8.86×10^{-12}	1.26×10^{-14}	2.78×10^{-12}
$UO_2(OH)_2(aq)$	2.58×10^{-9}	1.40×10^{-11}	9.96×10^{-10}
$UO_2(OH)_3^-$	8.04×10^{-9}	1.97×10^{-10}	4.36×10^{-9}
$UO_2(OH)_4^{2-}$	1.26×10^{-12}	1.54×10^{-13}	1.05×10^{-12}
$(UO_2)_3(OH)_7^-$	5.57×10^{-14}	4.22×10^{-20}	4.67×10^{-15}
$UO_2CO_3(aq)$	2.25×10^{-9}	1.22×10^{-11}	8.71×10^{-10}
$UO_2(CO_3)_2^{2-}$	**6.10×10^{-6} (0.8%)**	**7.50×10^{-7} (0.0%)**	**5.07×10^{-6} (0.3%)**
$UO_2(CO_3)_3^{4-}$	**5.63×10^{-4} (73.2%)**	**2.48×10^{-3} (99.7%)**	**1.46×10^{-3} (89.6%)**
$(UO_2)_3(CO_3)_6^{6-}$	7.70×10^{-11}	6.08×10^{-13}	1.44×10^{-10}
$(UO_2)_2CO_3(OH)_3^-$	2.03×10^{-8}	2.77×10^{-12}	4.33×10^{-9}
$Ca_2UO_2(CO_3)_3(aq)$	**2.00×10^{-4} (26.0%)**	**7.42×10^{-6} (0.3%)**	**1.65×10^{-4} (10.1%)**
$UO_2PO_4^-$	4.48×10^{-10}	1.51×10^{-11}	1.49×10^{-10}
$UO_2HPO_4(aq)$	1.04×10^{-12}	7.73×10^{-15}	2.45×10^{-13}
$UO_2H_3SiO_4^+$	6.01×10^{-11}	1.48×10^{-14}	1.34×10^{-11}
Total	**7.69×10^{-4}**	**2.48×10^{-3}**	**1.63×10^{-3}**

Number in parentheses is the species percentage of total uranyl concentration in the sample. No solid phase is allowed to precipitate. The major uranyl species are in **bold** font.

Table D.53. Saturation Index of Porewater in BX-102 Sediments with Respect to Potential Relevant U (VI) Minerals

Minerals	Log (IQ/K_{sp})		
	BX-102 53A	BX-102 61A	BX-102 67A
Oxyhydroxides			
Metaschoepite	-15.14	-33.18	-18.38
Schoepite	-7.62	-25.66	-10.86
Becquerelite	0.83	-12.28	-1.44
Clarkeite	-1.18	-3.89	-1.35
Carbonates			
Rutherfordine	-4.28	-6.53	-4.68
Liebigite	-8.99	-10.41	-9.07
Zellerite	-1.62	-3.45	-1.86
Silicates			
Boltwoodite	-8.60	-11.13	-9.10
Na-Boltwoodite	2.13	0.01	1.89
Uranophane	2.89	-2.72	1.95
Soddyite	-1.96	-7.23	-2.92
Uranosilite	-31.22	-38.81	-32.68
Weeksite	-14.87	-22.20	-16.31
Na-Weeksite	3.15	-3.37	2.24
Phosphates			
Metaautunite	-15.38	-19.20	-16.46
Chernikovite	-7.38	-9.50	-8.00
Phosphuranylite	-45.64	-59.97	-49.12
Na-autunite	-2.66	-5.10	-3.26
K-autunite	-5.40	-8.65	-6.53

D.3.5.5 Dissolution Experiments

D.3.5.5.1 Experimental Procedures. Uranium-contaminated sediments from the BX-102 borehole 299-E33-45 [53AB (119 ft bgs), 61AB (131 ft bgs), and 67AB (141.25 ftbgs)] were obtained from the RPP sample repository. The pH of the sediments was measured in deionized H_2O (2 g field moist sediment in 10mL H_2O) using a combination pH microelectrode calibrated at pH 7.0 and 10.0. Triplicate subsamples of each sediment were air dried for 3 days and the moisture content calculated on an air-dry basis. The total concentrations of U(VI) and other metals in the air-dry sediments were determined by X-ray fluorescence (XRF) (Table D.54).

Table D.54. Sediment Characterization

Sediment ID	Al	Si	K	Ca	Fe	U	Sr	Mn	Water pH	Moisture content on air-dry basis
	%					ug g^{-1}				%
53 AB	6.51	32.7	2.11	2.9	3.54	112	383	668		2.43
61 AB	6.59	32.9	2.07	2.9	3.64	404	397	684	9.36	2.14
67 AB	6.52	32.7	2.04	2.86	3.23	327	399	540	9.14	2.25

MINTEQA2 3.1 (Allison 1991) was used to calculate Na-NO_3 electrolyte compositions at constant ionic strength (0.05 M), constant CO_2 pressure ($p_{CO2}=10^{-3.5}$ atm), and different pH values (from 7.0 to 9.5 every 0.5 pH unit). These electrolyte solutions were synthesized by appropriate additions of $NaNO_3$, $NaHCO_3$, Na_2CO_3, NaOH, or HNO_3. The electrolytes were sparged with air for at least one weak to attain carbon dioxide equilibria with slight pH adjustments made to attain the desired values. Electrolyte pH was stable. A similar set of electrolyte solutions ranging from pH 7.0 to pH 9.0 were made to be in equilibrium with calcite ($CaCO_3$). These were composed of $Ca(ClO_4)_2$, $NaHCO_3$, Na_2CO_3, NaOH, or $HClO_4$, and $CaCO_{3(s)}$. These solutions were open to the atmosphere and were allowed to equilibrate with $CaCO_{3(s)}$ for months before use. The calcite-equilibrated solutions were filtered through 0.22um-GV Millipore filters to remove solid-phase calcite before use, in the desorption/dissolution experiments. All electrolyte solutions had stable pH before their use in the uranium desorption experiments. The compositions and pH of these solutions are presented in Table D.55.

Table D.55. Electrolyte pH and Composition

Solution ID	Na^+	ClO_4^-	Ca^{+2}	HCO_3^-	CO_3^{2-}	pH
	M		mM			
Na-1	0.05			0.0678		6.95
Na-2	0.05			0.1940		7.27
Na-3	0.05			0.5973		7.61
Na-4	0.05			1.7980	0.0580	8.16
Na-5	0.05			5.3470	0.5800	8.67
Na-6	0.05			15.5900	4.9300	9.25
Ca-1		0.1406	71.1			7.02
Ca-2	0.0666	0.1104	21.9			7.57+/-0.02
Ca-3	0.0966	0.0988	1.75			8.05
Ca-4	0.0996	0.0975	0.314	0.7000	0.7	8.35
Ca-5	0.0986	0.0963	0.0821	0.9200	0.92	8.37
Ca-6	0.0965	0.0846	0.0121	4.4400	4.44	8.96+/-0.02

The time-dependent desorption of uranium (VI) was studied at initial pH values of 7.5 and 9.5 in sodium and calcium electrolyte. The calcium electrolyte was used to asses whether the formation of $Ca_2UO_2(CO_3)_3^0$ complexes (a predominant aqueous species in field samples) influenced desorption rate. Replicate samples of field-moist sediments were mixed with the sodium and calcium electrolytes at concentration of 200g L^{-1}, in acid-washed Teflon centrifuge tubes. The sediments were not air-dried prior to experimentation to avoid any changes to uranium (VI) speciation (e.g., precipitation) that drying might induce. The sediment suspensions were agitated in a rotating shaker (50 rpm) at room temperature with atmospheric gas pressure.

After desired reaction times ranging from hours to several months, the suspensions were removed from the shaker, and were centrifuged at 5100 rpm for 20 min. A 0.2 mL aliquot of supernatant was removed and acidified with 0.1 M HNO_3. The experiment was designed so that

repeated sample removal would have little or no change on the solid-to-solution ratio, which was desired to be kept constant. In practice, this ratio changed by 6% over the entire course of the experiment. Extensive pretesting with a variety of filters and centrifuguation speeds documented that the phase separation scheme used above provided aqueous samples free of uranium-containing colloids. This filter pretesting, however, showed that several filter types exhibited high sorptivity for trace uranium (VI). Consequently the use of these and other filters were avoided whenever possible. The acidified centrifugate samples were diluted and analyzed for uranium (VI) with a Kinetic Phosphorescence Analyzer (KPA) (Chemchek Instrument Inc., Richland, Washington). The detection limit of uranium (VI) with KPA was 4.9 ng L^{-1}. All standards, and samples were prepared in 0.1 M HNO_3 to provide a consistent sample matrix (Sowder 1998).

Aqueous samples with known uranium(VI) concentrations [500 and 1000 μg L^{-1} U(VI)] were used as control samples for each pH and electrolyte to evaluate the potential adsorption of uranium to the walls of the acid-washed Teflon centrifuge tubes used for sediment equilibrations. No such adsorption was observed in any electrolyte during the course of the experiment.

The suspensions were filtered through prewashed (30mL electrolyte +2mL sample) centriplus YM-30 centrifugal device filters for phase separation at the end of the desorption experiment. The aqueous phase was analysed for uranium(VI) before and after filtration. There was no indication of the presence of suspended uranium-containing colloids in the aqueous phase. The pH of supernatant was immediately measured on a 1mL aliquot. The filtrate and the moist sediments (retained by the filter) were analysed by Time-Resolved Laser-Induced Fluorescence Spectroscopy (TRLFS). Corresponding sediment duplicates were washed free of soluble uranium(VI) with 2mL of deionized water, centrifuged, and air dried for thin section preparations.

D.3.5.5.2 Experimental Results. Uranyl solubility of BX-102 samples ranged from 2 to 55 mg/L in batch electrolytes of sodium and sodium-calcium after 65 and 149 days of equilibration (Figure D.77). The uranyl solubility showed two regions in each sample: a region where U(VI) concentrations were constant with pH (i.e., pH < 8.2) and a region where U(VI) concentration increased with increasing pH (i.e., pH > 8.2). The uranyl solubility varied significantly between different samples, but less so with electrolyte composition (e.g., $NaHCO_3$ as compared to $NaHCO_3$-$CaCO_3$). The solubility at pH < 8.2 showed a trend of 61AB > 67AB > 53 AB. The rate of solubility increase with pH was largest in sample 67AB. Near pH 9.0, the solubility trend was 67AB > 61AB > 53AB.

Figure D.77. Uranyl Solubility in Sodium or Sodium-Calcium Electrolyte Suspensions

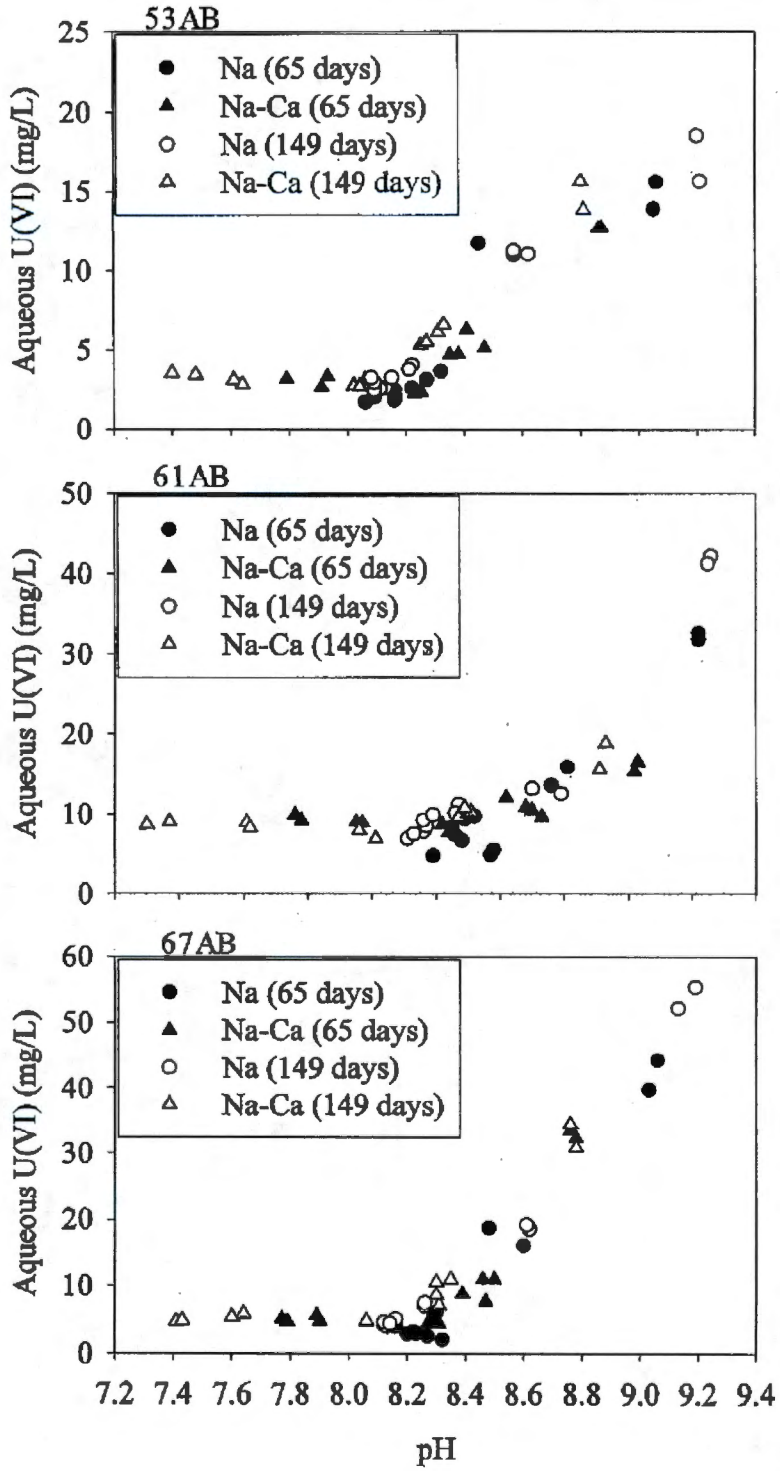

Figure D.78. Uranium(VI) Time-Dependent Dissolution from BX-102 Sediments in Sodium-Nitrate Electrolye

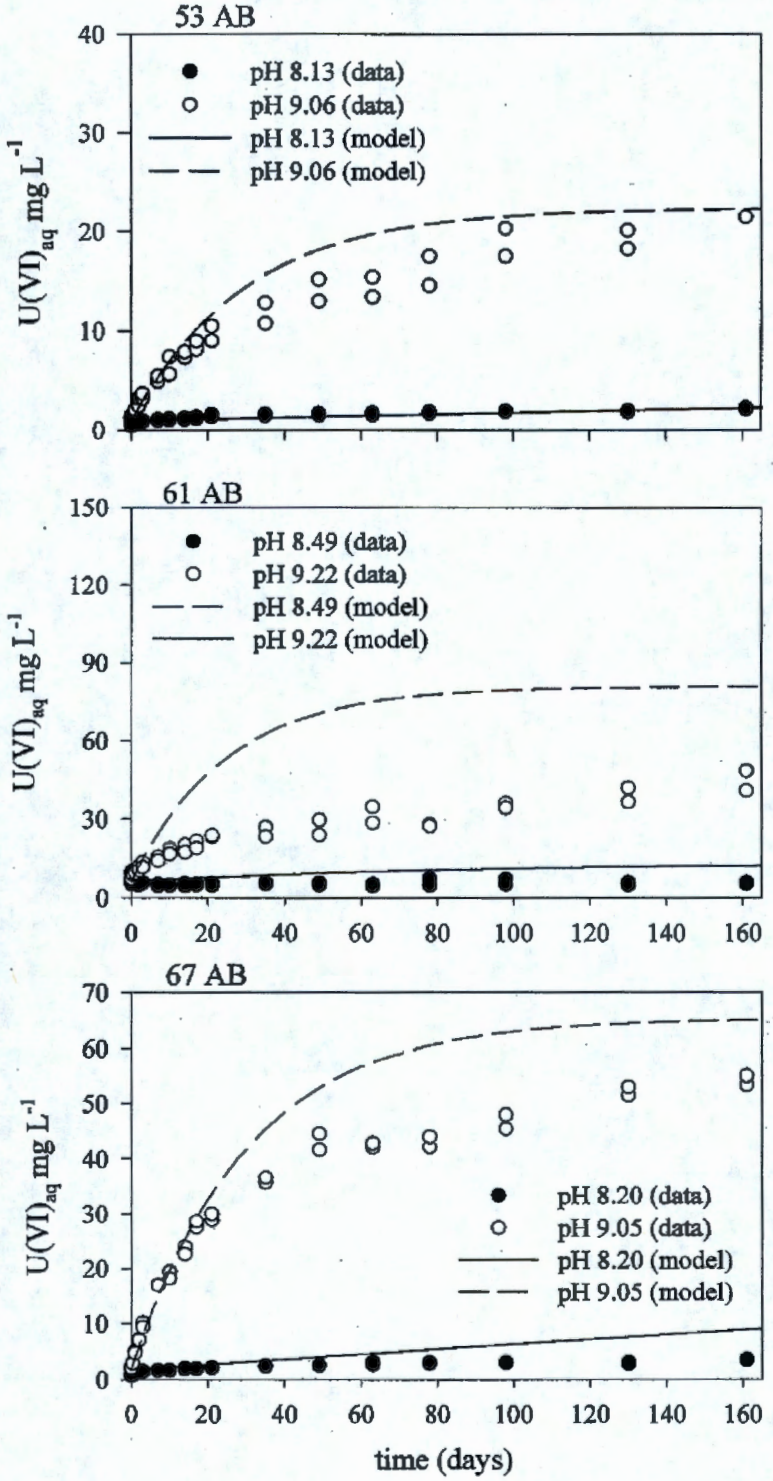

Figure D.79. Uranium(VI) Time-Dependent Dissolution from BX-102 Sediments in Sodium-Calcium Electrolyte

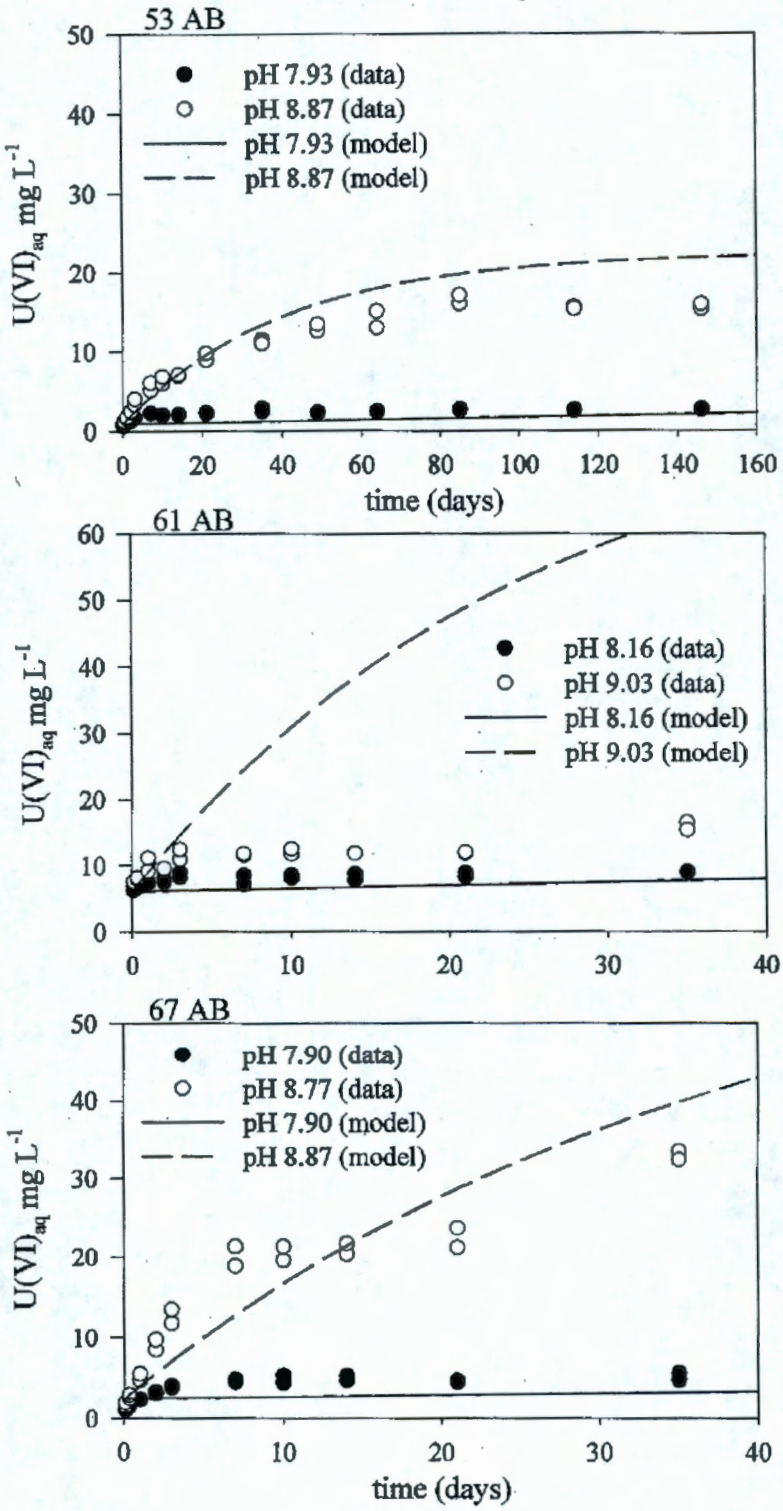

Uranyl release from the BX-102 samples showed kinetic behavior (Figure D.78 and Figure D.79). In both electrolytes with low pH, uranyl concentration increased slightly with time and reached steady-state after about 100 hours. The steady-state concentrations were consistent with those observed in the solubility experiments (Figure D.77). In both electrolytes with high pH (i.e., ~ 9.0), uranium(VI) was continuously released/dissolved from the sediment samples. The rate of uranyl release decreased after 3 days of equilibration in sample 61AB, and after 20 days in samples 53AB and 67AB. For samples 53A, 61AB, and 67AB, respectively, the leached uranium was 76%, 34%, and 66 % of the total uranium (Table D.54) in sodium electrolyte (pH 9.0) after 80 days of equilibration, and 63%, 20%, and 50% in the sodium-calcium electrolyte after 35 days of equilibration. The percentage of leached uranium(VI) increased to 96%, 52%, and 86% for 53A, 61AB, and 67AB, respectively after 161 days in sodium electrolyte.

All samples showed an instantaneous release of uranium(VI) in both electrolytes (Figure D.78 and Figure D.79). The amount of this release in samples 53AB and 67AB was approximately equaled to the total concentration of uranium(VI) estimated to be in porewater. The diluted uranium(VI) concentration was estimated to be 0.87 mg/L and 1.7 mg/L (Table D.56) in samples 53A and 67A, respectively, based on the water extractable U(VI) (Table D.51), the sediment moisture content (Table D.54), and the solids density in the electrolyte suspension. The initial release of uranium(VI) from sample 61A, however, was more than double that expected from the porewater concentration (2.5 mg/L), suggesting the desorption of weakly sorbed uranyl by the bicarbonate/carbonate enriched electrolyte.

Table D.56. Calculated Solutes (μmol/L) in the Solid Suspensions Contributing from Sediment Porewater

Component	Calculated[a]		
	53A	61A	67A
UO_2^{2+}	3.65	10.41	7.19
K^+	7.78	5.46	6.63
Na^+	491.51	912.54	771.09
Ca^{2+}	7.01	2.79	7.01
Mg^{2+}	3.02	0.45	2.47
Cl^-	2.94	3.46	6.88
$4NO_3^-$	81.29	75.33	169.61
SO_4^{2-}	23.20	37.15	81.48
PO_4^{3-}	0.78	17.26	0.89
H_4SiO_4	72.22	48.19	64.44
$CO_{2(tot)}$	atm_eq	atm_eq	atm_eq

[a]Calculated from porewater data (Table D.51), moisture content (Table D.54), and solid density of 200g/L in suspension.

D.3.5.6 Physical Model of Uranyl Leaching

X-ray microprobe analyses of sediments 61 and 67 showed that uranium(VI) existed in the sediments as a precipitated phase that partially coated specific mineral grains and filled internal channels and fractures (Figure D.80 and Figure D.81). After contact with pH 9.0 electrolyte that induced uranium(VI) dissolution, the thickness and intensity of uranium(VI) grain coatings was much reduced (e.g., 61AB, Figure D.80f). The uranium(VI) remaining after dissolution resided primarily in intraparticle regions at lower concentration (showing intensity) compared with that before leaching. In sample 67AB, uranium concentration (intensity) decreased after leaching, both on the grain surface and within intraparticle regions (Figure D.81d). The ratio of uranium within intraparticle regions to that on the grain surface appeared to increase after dissolution. The leaching process did not significantly change the apparent uranyl mineral composition in the sediment, as suggested by the LIFS spectra of the sediments showing only minor changes (Section D.3.4). These results suggested that: 1) the precipitated uranyl phases on the sediment surface and in intraparticle regions were similar, 2) leaching did not result in significant differential dissolution of uranyl minerals if there were more than two uranyl phases in the sediments, and 3) the dissolution process appeared to involve the preferential leaching of uranyl phases on the solid surface and mass transfer limited removal from intraparticle regions, with stronger mass transfer effects noted on sample 61AB than on 67AB.

A physical model of uranyl dissolution (described below) was conceptualized by coupling the results of the batch and kinetic experiments with XRM images and LIFS analysis.

- *Mixing/equilibrium exchange* – Weakly-sorbed and porewater uranium(VI) was immediately released and diluted by leaching electrolytes.

- *Dissolution* – Uranium(VI) mineral dissolution was driven under saturated conditions in the aqueous phase.

- *Release to solution* – Uranyl is released directly to aqueous phase by the dissolution of grain coatings on mineral surfaces or through diffusion from intraparticle regions.

Figure D.80. X-ray Microscopic Image of BX-102 Sample 61

Density Maps on Left Define the Distribution of Mineral Grains in Sample. Purple and Blue Define Pore Space, and Green to Red Define Mineral Grains. Uranium Distribution on Right is Defined by Green, Yellow, and Red, with Yellow-Red Being the Highest Concentration. Total Image Size is 1mm x 1mm.

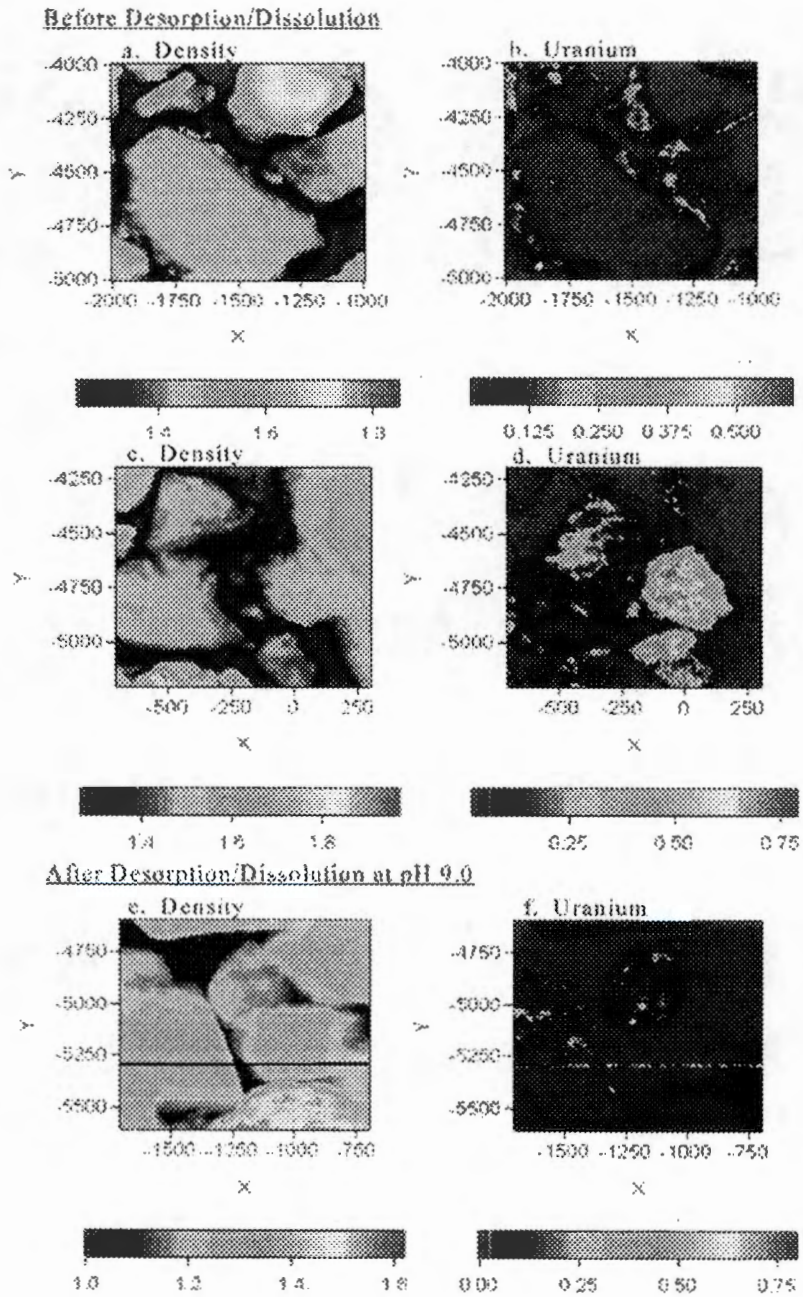

Figure D.81. X-ray Microscopic Image of BX-102 Sample 67

Density Maps on Left Define the Distribution of Mineral Grains in Sample. Purple and Blue Define Pore Space, and Green to Red Define Mineral Grains. Uranium Distribution on Right is Defined by Green, Yellow, and Red, with Yellow-Red Being the Highest Concentration. Total Image Size is 1mm x 1mm.

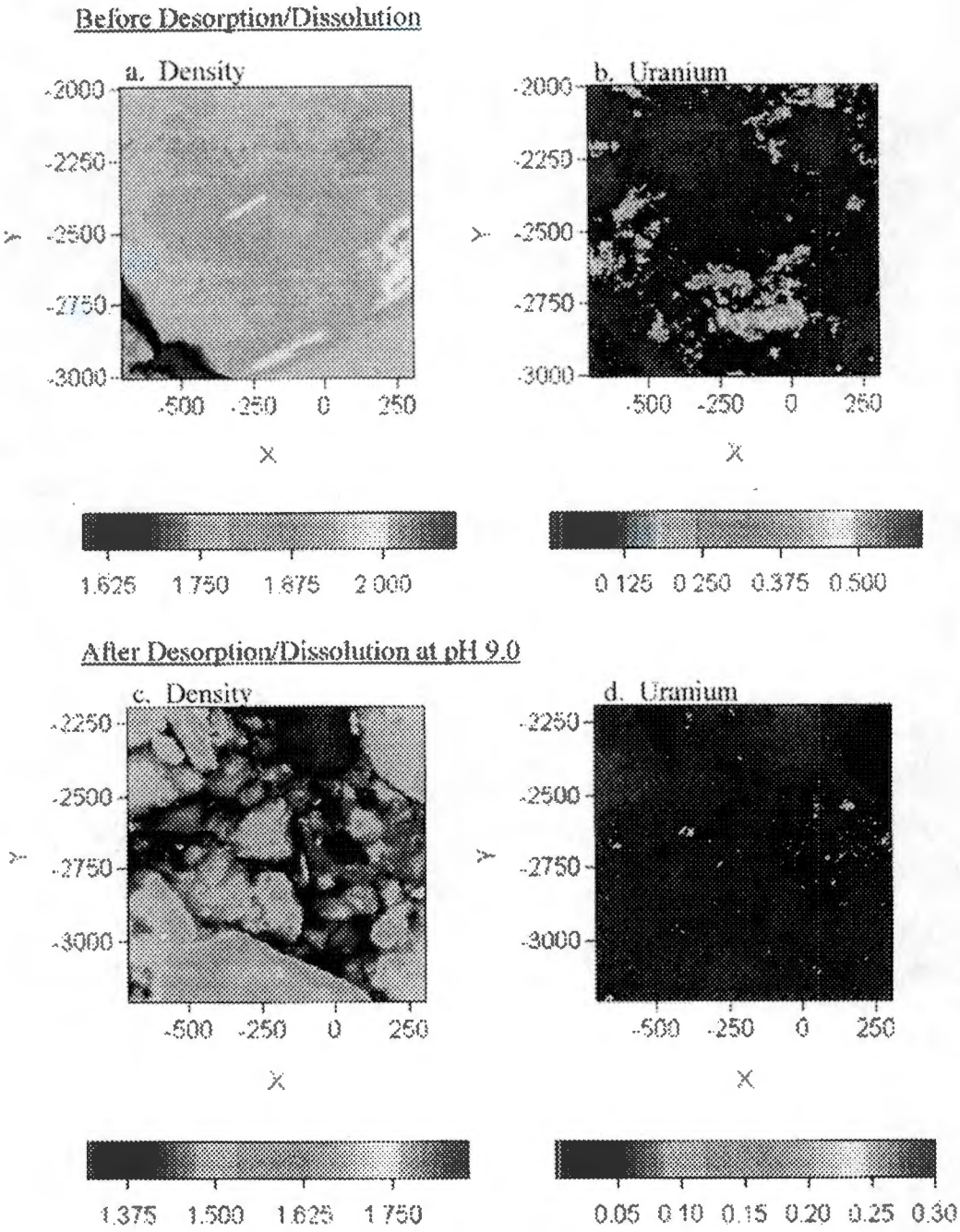

D.3.5.7 Thermodynamic and Kinetic Analysis of Uranyl Dissolution

The concentrations of uranium, silicate, sodium, and calcium in the aqueous phase of the dissolution experiments (Table D.57 and Table D.58) were much higher than could be attributed to the dilution of porewater alone (Table D.56), indicating the dissolution of these solutes from sediment. Uranyl solubility was calculated with respect to selected uranyl minerals using MINTEQA2 (Figure D.82 and Figure D.83), and the measured silicate, phosphate, sodium, and calcium concentrations in leaching solutions. The uranyl minerals considered in the calculation were those that computed close to equilibrium in the porewaters (Table D.53), including uranophane, sodium-boltwoodite, soddyite, sodium-weeksite, sodium-autunite, zellerite, clarkeite, and becquerelite. In the calculation, total uranium (VI) in suspension was fixed to the measured value for each sample (Table D.54). The total uranium (VI) was distributed between aqueous and solid phases in the input file. The aqueous concentration was set to equal the measured uranium (VI) in the suspension (Table D.57 and Table D.58), and the solid-phase concentration was the difference between total and aqueous uranium (VI) after adjusting for the stoichiometric relationship of a specific uranyl mineral. The solution was allowed to equilibrate with only one uranyl mineral through the dissolution/precipitation. The uranyl concentration calculated to be in equilibrium with that specific phase was assumed to be the solubility of that mineral in the solution. The carbonate concentration in the suspensions was assumed to be in equilibrium with the atmosphere.

Figure D.82. Measured and Calculated Uranyl Solubility of Samples 61AB and 67AB in $NaNO_3$ (0.05M) Electrolyte

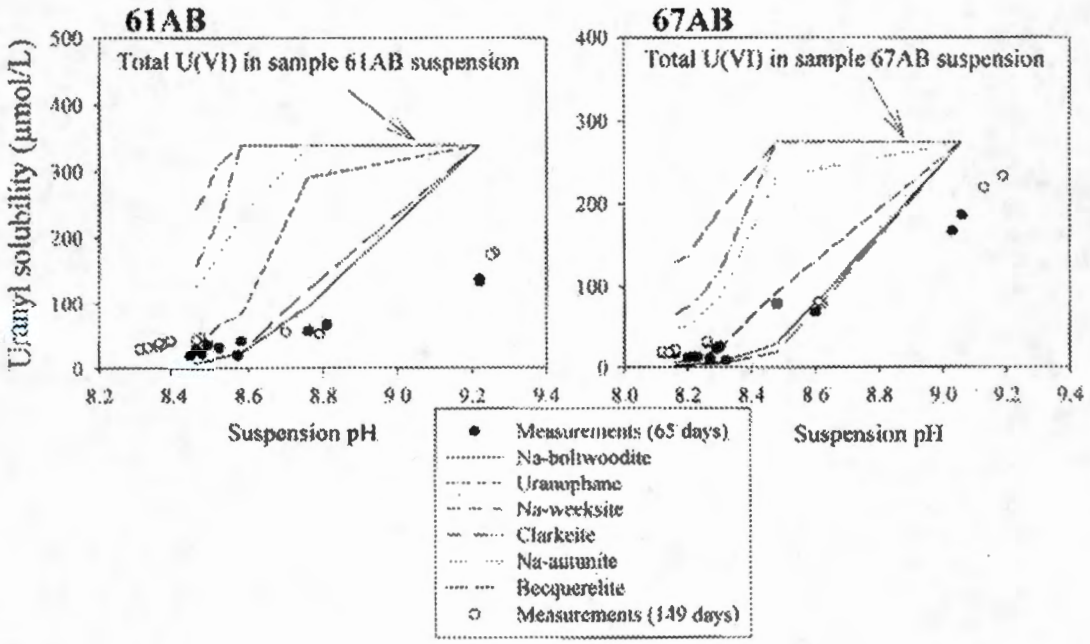

Figure D.83. Measured and Calculated Uranyl Solubility of Samples 61AB and 67AB in Sodium-Calcium (0.05M) Electrolyte

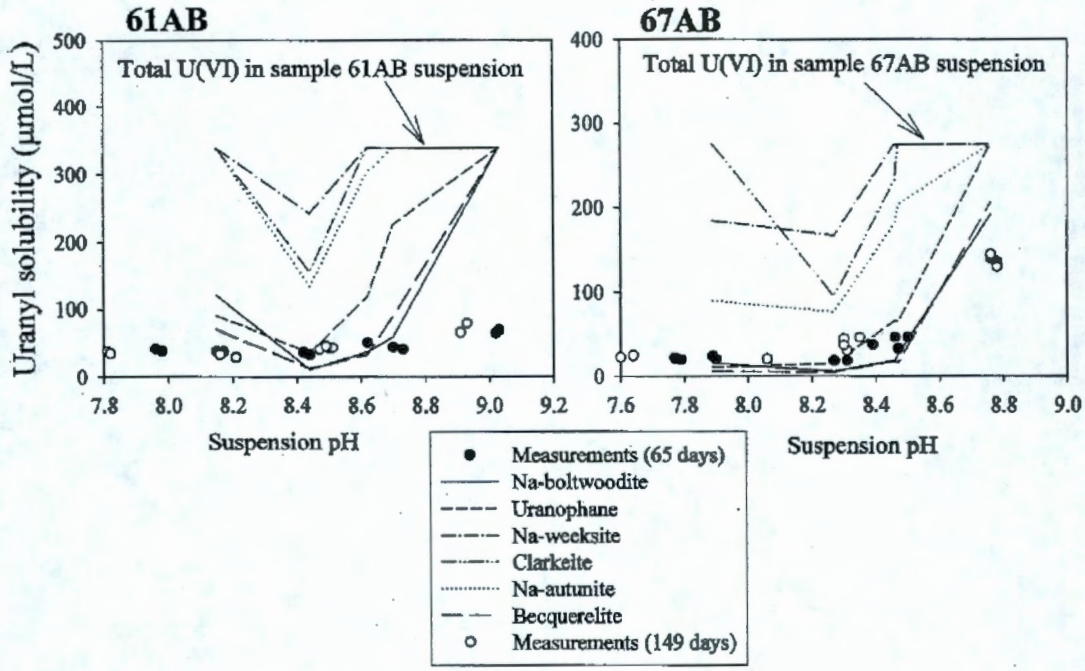

The calculated solubility of uranyl minerals (Table D.59 and Table D.60) is low at neutral or slight alkaline pH and rapidly increases with pH in both sodium and sodium-calcium electrolytes except for soddyite, sodium-weeksite, and zellerite, which generally reached the maximum solubility (e.g., all the sediment uranium was dissolved). The maximum calculated solubility is the total uranium concentration in the sediment suspension (e.g., 100% dissolution). Among the calculated minerals, the solubility of uranophane, Na-boltwoodite, and becquerelite matched well with the measured in both electrolytes when pH < 8.5 (Figure D.82 and Figure D.83). At high pH (i.e., pH > 8.5), the calculated solubility of these minerals is consistent with the trend of the measurement, which showed an increase with pH. The calculated solubility values were, however, higher than the measured values. These results were expected because uranium dissolution reached a steady state value after about 200 hours at low pH (pH 8.0), but dissolved continuously for 161 days at high pH (i.e., >9.0), as shown in the kinetic leaching results (Figure D.78 and Figure D.79). The measured solubility of samples 53AB and 67AB (only 67AB is shown in Figure D.82 and Figure D.83) was closer in concentration to the computed values than were those from sample 61AB in the high pH region (pH >8.5). The result is also expected from the XRM images. XRM measurement (Figure D.80and Figure D.81
Figure D.81) showed that a larger fraction of uranium remained in the intraparticle region of 61AB than that of 67AB after 65 days of equilibration, possibly implying that the mass transfer kinetics of uranium from intraparticle domains of 61AB were slower than for 67AB. The kinetic results (Figure D.78 and Figure D.79) also showed a slower dissolution rate in sample 61AB than in samples 53AB and 67AB.

Table D.57. Selected Solutes Measured in the Aqueous Phase of the Sodium-Electrolyte Solubility Experiment (Figure D.77)

Sediment	Electrolyte pH	Suspension pH	UO_2^{2+} (μmol/L)	H_4SiO_4 (μmol/L)	PO_4^{3-} (mmol/L)	Na^+ (mmol/L)	Ca^{2+} (μmol/L)
BX-102 53AB	6.95	8.16	7.72	233.39	bd	45.32	0.80
	6.95	8.06	7.16	217.27	bd		0.79
	7.27	8.09	8.45	209.78	bd	45.15	0.79
	7.27	8.16	10.35	222.12	bd		0.78
	7.61	8.16	9.10	216.74	bd	43.36	0.67
	7.61	8.22	10.88	194.00	bd		0.66
	8.16	8.27	13.06	224.67	bd	46.32	0.49
	8.16	8.32	15.22	199.96	bd		0.46
	8.67	8.57	46.25	229.81	bd	44.72	0.24
	8.67	8.45	49.36	240.30	bd		0.33
	9.25	9.06	65.53	251.64	bd	42.83	0.06
	9.25	9.05	58.28	244.53	bd		0.05
BX-102 61AB	6.95	8.48	27.98	220.66	4.76	46.85	0.21
	6.95	8.57	20.44	220.96	4.94		0.20
	7.27	8.58	22.99	227.67	4.85	47.59	0.18
	7.27	8.39	19.75	245.42	5.88		0.13
	7.61	8.46	30.76	231.71	5.86	48.28	0.21
	7.61	8.45	35.29	217.03	5.95		0.24
	8.16	8.52	40.89	210.03	5.17	48.98	0.17
	8.16	8.49	39.53	218.72	5.91		0.18
	8.67	8.76	57.35	214.61	6.85	46.46	0.06
	8.67	8.81	66.55	240.74	7.87		0.07
	9.25	9.22	133.61	258.76	8.11	46.37	0.04
	9.25	9.22	137.18	265.89	7.83		0.05
BX-102 67AB	6.95	8.20	12.22	189.32	bd	46.02	0.68
	6.95	8.32	8.65	180.71	bd		0.62
	7.27	8.16	16.93	182.22	bd	45.24	0.70
	7.27	8.23	12.76	191.33	bd		0.72
	7.61	8.22	13.38	172.77	bd	45.67	0.61
	7.61	8.27	10.85	190.79	bd		0.57
	8.16	8.30	25.71	179.24	bd	46.06	0.44
	8.16	8.29	22.94	180.36	bd		0.47
	8.67	8.48	78.72	204.67	bd	45.15	0.26
	8.67	8.60	67.62	205.12	bd		0.20
	9.25	9.06	186.19	262.83	bd	42.83	0.05
	9.25	9.06	167.33	279.68	bd		0.06

Table D.58. Selected Solutes Measured in the Aqueous Phase of the Sodium-Calcium-Electrolyte Solubility Experiment (Figure D.78)

Sediment	Electrolyte pH	Suspension pH	UO_2^{2+} (μmol/L)	H_4SiO_4 (μmol/L)	PO_4^{3-} (μmol/L)	Na^+ (mmol/L)	Ca^{2+} (mmol/L)
BX-102 53AB	7.02	8.06	13.06	175.84	bd	3.52	63.48
	7.02	7.79	13.26	257.43	bd		68.71
	7.57	7.91	11.08	163.85	bd	53.42	18.44
	7.57	7.93	13.84	225.83	bd		19.63
	8.05	8.25	9.90	206.88	bd	74.64	1.85
	8.05	8.23	9.44	211.29	bd		1.91
	8.35	8.47	21.57	210.16	bd	77.64	0.83
	8.35	8.41	26.46	234.74	bd		0.98
	8.37	8.38	19.87	220.91	bd	42.08	0.60
	8.37	8.35	19.64	229.62	bd		0.61
	8.96	8.86	53.41	220.10	bd	45.98	0.14
	8.96	8.87	53.50	233.18	bd		0.15
BX-102 61AB	7.02	7.96	41.67	184.41	bd	7.53	63.26
	7.02	7.98	38.61	267.67	bd		
	7.57	8.15	37.80	127.01	bd	59.68	17.49
	7.57	8.17	37.41	251.65	bd		
	8.05	8.44	32.41	210.41	4.17	82.86	0.95
	8.05	8.42	36.66	218.96	4.29		0.98
	8.35	8.70	44.09	192.98	5.54	84.86	0.27
	8.35	8.68	45.70	195.53	5.28		0.29
	8.37	8.62	50.56	212.50	5.96	45.89	0.17
	8.37	8.73	40.69	217.89	6.13		0.16
	8.96	9.03	69.36	215.73	6.99	49.20	0.05
	8.96	9.02	64.47	224.28	7.18		0.06
BX-102 67AB	7.02	7.79	19.77	145.01	bd	4.31	63.65
	7.02	7.77	21.65	214.80	bd		65.27
	7.57	7.89	23.79	145.06	bd	56.29	18.70
	7.57	7.90	20.12	200.18	bd		19.47
	8.05	8.27	18.38	174.57	bd	77.77	1.81
	8.05	8.31	18.45	210.95	bd		1.89
	8.35	8.46	46.35	183.29	bd	79.30	0.86
	8.35	8.50	46.31	215.85	bd		0.94
	8.37	8.47	32.59	178.74	bd	43.67	0.54
	8.37	8.39	37.15	232.51	bd		0.61
	8.96	8.76	140.53	215.03	bd	45.85	0.20
	8.96	8.78	136.01	243.41	bd		0.20

The close match between the measured uranium concentrations and the computed solubility of uranophane, sodium-boltwoodite, and becquerelite confirmed that these phases might be present in the sediment samples. The comparable solubility of these phases under the geochemical conditions present in the sediment samples, however, prevented unequivocal identification from solubility measurement alone. These minerals were also computed to be saturated in the porewaters of at least one sediment sample (Table D.53). The implied existence of these phases from solubility measurement is reliant upon the accuracy and completeness of the thermodynamic solubility data of the uranyl minerals considered and the assumption that the uranium leaching was controlled by mineral solubility alone. Although both the batch and kinetic results were consistent with a dissolution reaction, other processes (with less probability) may also have influenced the uranium(VI) release rate and extent, such as kinetic desorption, mass transfer-limited desorption, and intraparticle diffusion coupled with uranyl occlusion or sequestration within intraparticle regions.

The increase in uranium solubility with increasing pH was caused by carbonate complexation. Three uranyl carbonate complexes were dominant in porewater (Table D.52 and Section D.3.4). In the leaching suspensions, calculations showed that four carbonate species [$UO_2(CO_3)_3^{4-}$, $Ca_2UO_2(CO_3)_3$, $UO_2(CO_3)_2^{2-}$, and $(UO_2)_2CO_3(OH)_3^-$] represented 100% of the aqueous uranium(VI). The concentration of the aqueous UO_2^{2+} species was calculated to be less than 10^{-11} mol/L at pH 8.0 and decreased to less than 10^{-15} mol/L at pH 9.0 because of increasing carbonate concentration. The decrease of aqueous UO_2^{2+} through carbonate complexation induced the dissolution of the uranyl solid phase.

The increase in CO_3^{2-} concentration with increasing pH could also enhance the rate of uranyl mineral dissolution. Ligand- (carbonate)-promoted dissolution is believed to control the kinetics of uraninite solubility in carbonate solutions (Nicol and Needes 1977; Hiskey 1979, 1980; Shoesmith et al. 1989, 1996a, 1996b, 1998; Sharma et al. 1996; Sunder et al. 1997; De Pablo et al. 1999). These studies showed that electron transfer, coordination of carbonate species on the surface, and detachment of uranium-carbonate species from the surface were three steps controlling uraninite dissolution. Given these previous studies and the current experimental observation that uranyl dissolution rates from BX-102 sediment increased with the pH (or carbonate concentration), the following reaction scheme was proposed for uranyl dissolution from Hanford sediments:

A. coordination of carbonate species on the uranium(VI) mineral surface and further complexation in the aqueous phase:

$$\equiv U(VI) + CO_3^{2-} \underset{k_{-1}}{\overset{k_1}{\Leftrightarrow}} \equiv U(VI) - CO_3^{2-} \tag{1}$$

B. detachment of complexed uranyl species from the mineral surface:

$$\equiv U(VI) - CO_3^{2-} \overset{k_2}{\Rightarrow} \left[U(VI) - (CO_3)_n^{2-2n}\right]_{(aq)} \tag{2}$$

Assuming that the detachment (B) is a rate-limiting step, a kinetic rate expression from reactions (1) and (2) can be expressed as

$$\frac{dU(VI)aq}{dt} = k_2 K_1 \{\equiv U(VI)\}\{CO_3^{2-}\} \tag{3}$$

where K_1 is the equilibrium constant for reaction (1). The rate scheme described by A and B considers only dissolution kinetics far away from equilibrium. Using transitional state theory for mineral dissolution (e.g., Aagaard and Helgeson 1982), a rate expression can be expressed for "near equilibrium conditions" by limiting Equation (3) with the solubility relationship:

$$\frac{dU(VI)aq}{dt} = k_2 K_1 \{\equiv U(VI)\}\{CO_3^{2-}\}\left(1 - IQ/K_{sp}\right) \quad (4)$$

where K_{sp} is the solubility product and IQ is the ion activity quotient.

The rate expression (4) requires information on the concentration of surface sites on the uranyl precipitates that are available for the coordination with CO_3^{2-}. Such information is difficult to obtain because it requires surface characterization of microscopic uranyl minerals in the sediment matrix. Here it was assumed that the uranyl mineral surface site concentration was proportional to the total uranyl concentration remaining in the sediment. With this assumption,

$$\frac{dU(VI)_{aq}}{dt} = k[U(VI)_{tot} - U(VI)_{aq}]\{CO_3^{2-}\}\left(1 - IQ/K_{sp}\right) \quad (5)$$

was obtained where k is a lumped parameter, IQ is the ion activity quotient, and IQ/K_{sp} is a measure of distance from equilibrium.

Equation (5) was solved by coupling aqueous speciation reactions of uranium(VI) and the measured concentrations of Na^+ and Ca^{2+}, H_4SiO_4, PO_4^{3-}, and pH in suspensions (Table D.57 and Table D.58). All aqueous uranium(VI) species listed in Table D.52 were considered in updating the ion activity quotient (IQ) at each time step. The activity coefficients of aqueous species were calculated using the Davies equation. The K_{sp} is the inverse of the stability constants shown in Table D.50. Only results using uranophane as a model solid phase were reported (see model results in Figure D.78 and Figure D.79) because its solubility matched well with the measured value (Figure D.82 and Figure D.83) and spectroscopic measurements (Sections D.3.3 and D.3.4) implied its presence. The results using sodium-boltwoodite or becquerelite were similar because of the comparable solubility of these phases under the experimental conditions used. A multiple phase assemblage could be added into the model if present. Total carbonate concentration in the suspension was assumed to be in equilibrium with atmospheric carbon dioxide ($10^{-3.5}$ atm). The measured uranium concentration at time zero in the suspension was used as an initial condition for Equation (5). The k in Equation (5) was treated as an only fitting parameter, and it was determined by fitting Equation (5) to all dissolution profiles (Figure D.78 and Figure D.79).

The model in Equation (5) described the dissolution results well for the entire duration in suspensions with low pH and the short duration release at higher pH (Figure D.78 and Figure D.79) with a fitted rate parameter, k, of 105 $M^{-1}day^{-1}$. In suspensions with high pH, the model predicted greater amounts of uranium dissolution than the experimental results after approximately 3 days for sample 61AB, and 20 days for samples 53AB and 67AB. Because the model in Equation (5) considered only the dissolution reaction, the over-prediction of the experimental results suggested that mass transfer limited the release of uranium(VI) at higher pH. The possible importance of mass transfer was supported by the XRM measurements that showed that the residual uranium after leaching was located primarily intraparticle regions. Furthermore, SEM observations in Section D.3.2 (Figure D.51 and Figure D.52) showed that U(VI) precipitates existed in small inter-particle fractures with limited accessibility or contact

with the fluid phase. For as yet unknown reasons, mass transfer had a greater impact on uranium release from 61AB than on the other two samples.

D.3.5.8 Implications of Solubility Behavior to Kd

The distribution coefficient (K_d) is used in performance assessment calculations to describe retardation extent through the retardation factor. Some adsorption processes exhibit a linear isotherm with unit slope at low concentration, and, for these, a single value of K_d can be used to describe the solid-liquid partitioning process as it controls retardation. Here, the K_d for uranium in the desorption/dissolution experiments was found to vary greatly with pH, carbonate concentration, and contact time for all three sediments (Figure D.84). Values of K_d ranged from high value (e.g., > 400 ml/g) where uranium would be virtually immobile, to lower values (e.g., < 3.2 ml/g) where retarded mobility would occur. The K_d would also vary significantly with rock:water ratio if this variable had been changed in the experiments, because the total amount of uranium that will dissolve from a solid phase is dependent on the volume of water in contact with it. These large variations in K_d result from the fact that uranium solid-liquid distribution is controlled by a kinetic solubility process.

The large noted variation in K_d with less than one pH unit of change in BX-102 sediment (Figure D.84) indicates that a single value of K_d will not be an accurate predictor of uranium retardation in the BX-102 uranium plume. The measured pH values in the BX-102 core samples vary by over one unit; proximate samples can exhibit significantly different pH values (Serne et al., 2002). Moreover, the variations in K_d noted between the three sediments show that K_d is a complex and dynamic function of uranyl mineral type and distribution on and within sediment grains, dissolution kinetics, and mass transfer rates from intraparticle regions and grain coatings to aqueous solution. These complex dependencies argue strongly against the use of K_d to forecast the future redistribution of the BX-102 plume unless a bounding calculation is desired. More sophisticated geochemical simulators that explicitly deal with the solubility process, as well as its kinetics and mass transfer rates are needed.

Figure D.84. Distribution Coefficients (K_d) for Uranium in Kinetic Desorption/Dissolution Experiments in Sodium-Electrolyte

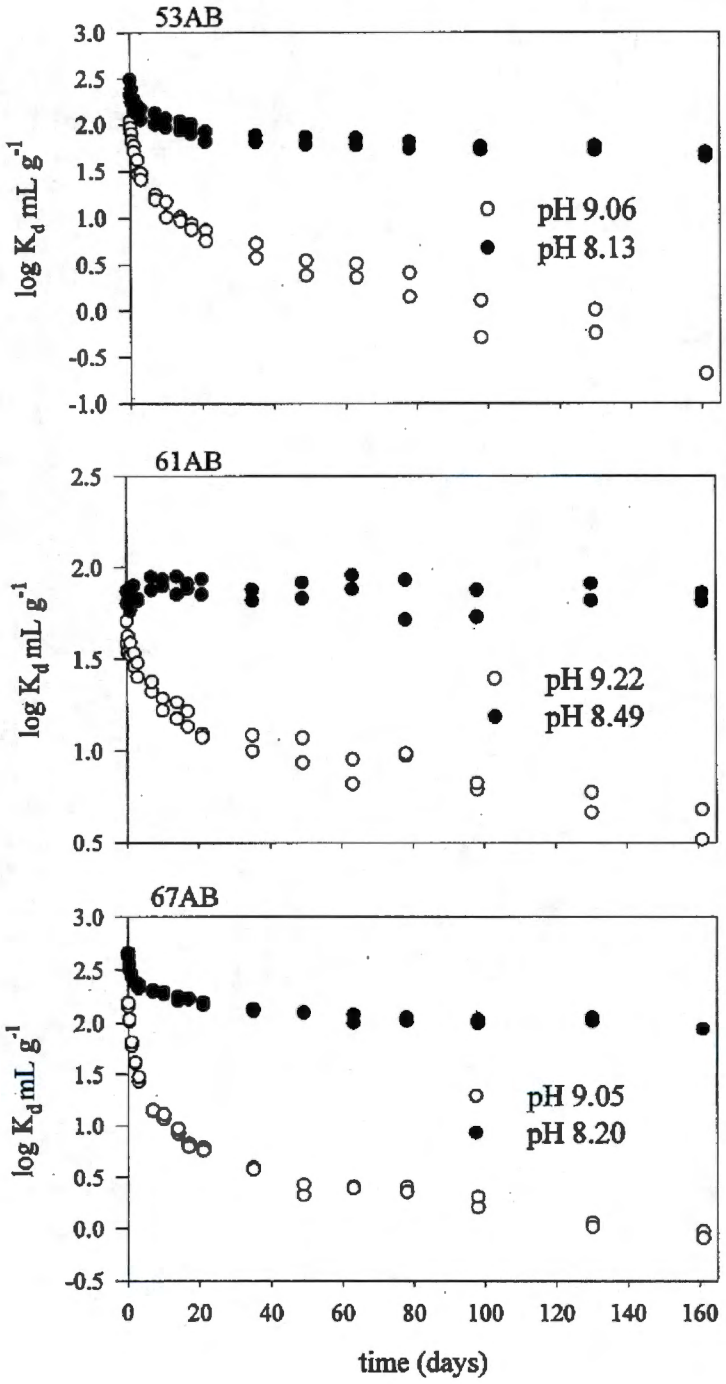

D.3.5.9 Conclusions

The solubility and dissolution rates of uranium precipitates in BX-102 samples 53AB, 61AB, and 67AB were measured as a function of pH to provide insights on the future mobility of the sediment-associated uranium pool. Potential changes to the sediment uranium pool were measured over the course of the dissolution experiments by X-ray microscopy and laser-induced fluorescence spectroscopy. The resulting experimental data, when combined with thermodynamic and kinetic analyses allowed the following conclusions to be reached:

1. The solubility of the sediment uranium phase increased with increasing pH and carbonate concentration of the contacting electrolyte. The absolute concentrations of dissolved uranium released by the sediment ranged between 20 and 55 mg/L (8×10^{-5} mol/L and 2.3×10^{-4} mol/L) at pH 9. The solubility behavior of the in situ uranium precipitate exhibited thermodynamic properties like that of uranophane, boltwoodite, or becquerelite. The solubility behavior of these three phases is quite similar under the geochemical conditions found in Hanford sediment, and the presence of one phase over the other cannot be readily discriminated from solubility measurement.

2. The uranium precipitate in the BX-102 tank farm sediments dissolved rapidly to equilibrium at pH 7.5, where the overall solubility of the phase was small. Time periods well in excess of 100 days were required for uranium dissolution at pH > 9.0 where uranium solubility is high because of carbonate complexation. Slow dissolution kinetics at higher pH are thought to result from the intraparticle residence of much of the precipitated uranium pool (Figure D.51). X-ray and electron microscopy showed that a significant fraction of the precipitated uranium was present in the interiors of mm-sized grains exhibiting significant diffusion path-length. A kinetic model that did not incorporate uranium mass transfer/diffusion from particle interiors did not simulate well the release rate and extent at extended time periods.

3. Because of the kinetic solubility behavior of the precipitated uranium phase, K_d is not constant and varies in complex fashion with aqueous chemical composition and pH, water:rock ratio (e.g., water content), and contact time.

4. Close to 90% or more of the sediment uranium exists in precipitated state, and is not mobile at the current pH (8.5 to 9.0) and water content (< 5% by mass) of the vadose zone sediment. The low water content of the sediment and limited solubility of the precipitated phase prevent significant mass transfer from the mineral phase to porewater.

5. Precipitated uranium will function as a long-term source to porewater. An increase in water content over current values will allow more of the uranium precipitate to dissolve into porewater. Accordingly, limiting the infiltration flux of meteoric water at the ground surface is the best strategy to reduce the total amount of uranium that is solubilized into porewater.

Table D.59. Calculated Solubility of Uranyl Minerals in the Solid Suspensions of Sodium-Electrolyte

Sediment	Suspension pH	Na- boltwoodite	Soddyite	Uranophane	Na-Weeksite	Clarkite	Becquerelite	Na-Zellerite	Autunite
BX-102 53AB	8.16	1.35	44.31	2.93	94.11	51.96	1.10	94.11	36.81
	8.09	0.93	29.24	2.06	90.60	42.35	0.66	94.11	29.24
	8.16	1.36	42.66	3.10	94.11	50.61	1.00	94.11	37.21
	8.27	2.42	84.05	6.81	94.11	65.74	2.08	94.11	54.98
	8.57	23.82	94.11	75.22	94.11	94.11	20.81	94.11	94.11
	9.06	94.11	94.11	94.11	94.11	94.11	94.11	94.11	94.11
BX-102 61AB	8.48	10.99	339.45	42.01	262.60	181.00	10.31	339.45	139.30
	8.58	22.35	339.45	82.42	339.45	339.45	23.75	339.45	229.60
	8.46	8.92	339.45	36.13	242.90	157.00	8.92	339.45	126.60
	8.52	16.22	339.45	65.16	310.90	225.80	14.87	339.45	174.80
	8.76	95.41	339.45	290.60	339.45	339.45	121.40	339.45	339.45
	9.22	339.45	339.45	339.45	339.45	339.45	339.45	339.45	339.45
BX-102 67AB	8.20	2.85	75.80	8.15	136.40	74.68	1.91	274.76	52.25
	8.16	2.33	58.55	6.54	129.70	64.97	1.42	274.76	48.23
	8.22	3.61	90.21	10.70	149.00	81.20	2.22	274.76	57.02
	8.30	6.52	158.20	21.77	191.20	117.20	4.21	274.76	86.30
	8.48	28.79	274.76	93.41	274.76	274.76	18.89	274.76	232.00
	9.06	274.76	274.76	274.76	274.76	274.76	274.76	274.76	274.76

Table D.60. Calculated Solubility of Uranyl Minerals in the Solid Suspensions of Sodium-Calcium-Electrolyte.

Sediment	Suspension pH	Na- boltwoodite	Soddyite	Uranophane	Na-Weeksite	Clarkeit	Becquerelite	Na-Zellerite	autunite
BX-102 53AB	7.79	26.09	94.11	15.36	94.11	94.11	10.46	94.11	94.11
	8.25	4.61	94.11	10.69	94.11	94.11	4.73	94.11	68.94
	8.47	12.21	94.11	40.20	94.11	94.11	14.57	94.11	94.11
	8.38	6.86	94.11	15.35	94.11	94.11	5.02	94.11	94.11
	8.86	94.11	94.11	94.11	94.11	94.11	94.11	94.11	94.11
BX-102 61AB	8.15	121.00	339.45	90.95	339.45	339.45	70.00	339.45	339.45
	8.44	10.68	339.45	35.30	241.70	155.90	12.49	339.45	134.40
	8.70	59.19	339.45	225.60	339.45	339.45	89.90	339.45	339.45
	8.62	36.54	339.45	119.10	339.45	339.45	32.71	339.45	302.22
	9.03	339.45	339.45	339.45	339.45	339.45	339.45	339.45	339.45
BX-102 67AB	7.89	15.86	182.10	10.74	274.76	5.12	274.76	89.09	274.76
	8.27	5.43	189.40	15.21	94.68	4.65	274.76	76.16	94.68
	8.46	19.11	274.76	65.30	232.10	17.88	274.76	181.30	232.10
	8.47	25.60	274.76	64.37	274.76	15.94	274.76	202.80	274.76
	8.76	191.30	274.76	274.76	274.76	274.76	205.30	274.76	274.76

D.3.5.10 References

Aagaard, P., and H. C. Helgeson, 1982, "Thermodynamic and Kinetic Constraints on Reaction Rates Among Minerals and Aqueous Solutions, 1. Theoretical Considerations," *American Journal of Science,* Vol. 282:237-285.

Allison, J. D., D. S. Brown, and K. J. Novo-Gradac, 1991, *MINTEQA2/PRODEFA2, A Geochemical Assesment Model for Environmental Systems: Version 3.0 User's Manual,* U.S. Environmental Protection Agency, Athens, Georgia.

Alwan, A. K., and P. A. Williams, 1980, "The Aqueous Chemistry of Uranyl Minerals. Part 2. Minerals of Liebigite Group," *Mineralogical Magazine*, Vol. 43:665-667.

Baturin, S. V., and G. A. Sidorenko, 1985, "Crystal Structure of Weeksite (K.62Na.38)(UO2)2(Si5O13)(H2O)3," *Doklady Akademii Nauk SSSR,* Vol. 282:1132-1136.

Braithwaite, A., F. R. Livens, S. Richardson, and M. T. Howe, 1997, "Kinetically Controlled Release of Uranium from Soils," *European Journal of Soil Chemistry*, Vol. 48:661-673.

Buck, E. C., N. R. Brown, and N. L. Dietz, 1996, "Contaminant Uranium Phases and Leaching at the Fernald Site in Ohio," *Environmental Science & Technology,* Vol. 30(1):81-88.

Burns, P. C., 1998, "The Structure of Boltwoodite and Implications of Solid Solution Toward Sodium Boltwoodite," *Canadian Mineralogist,* Vol. 36(pt.4):1069-1075.

Burns, P. C., R. C. Ewing, and F. C. Hawthorne, 1997, "The Crystal Chemistry of Hexavalent Uranium: Polyhedral Geometries, Bond-Valence Parameters and Polymerization of Polyhedral," *Canadian Mineralogist*, Vol. 35:1551-1570.

Casa, I., J. Vruno, E. Cera, R. J. Finch, and R. C. Ewing, 1997, "Characterization and Dissolution Behavior of a Becquerelite from Shinkolobwe, Zaire," *Geochimica et Cosmochimica Acta*, Vol. 61:3879-3884.

Chen, F., R. C. Ewing, and S. B. Clark, 1999, "The Gibbs Free Energies and Enthalpies of Formation of U6+ Phases: An Empirical Method of Prediction," *American Mineralogist,* Vol. 84:650-664.

De Pablo, J., I. Casas, J. Gimenez, M. Molera, M. Rovira, L. Duro, and J. Bruno, 1999, "The Oxidative Dissolution Mechanism of Uranium Dioxide. I. The Effect of Temperature in Hydrogen Carbonate Medium," *Geochimica et Cosmochimica Acta,* Vol 63(19/20):3097-3103.

Elton, N. J., and J. J. Hooper, 1995, "Supergene U-Pb-Cu Mineralization at Loe Warren, St Just, Cornwall, England," *Journal of the Russell Society,* Vol. 6:17-26.

Evans, H. T. J., 1963, "Uranyl Ion Coordination," *Science*, Vol. 141:154-158.

Finch, R., and T. Murakami, 1999, "Systematics and Paragenesis of Uranium Minerals," In *Uranium: Mineralogy, Geochemistry and the Environment*, P. C. Burns and R. J. Finch, eds., Mineralogical Society of America, Washington, D. C., Vol. 38, pp. 91-179.

Finch, R. J., 1997, "Thermodynamic Stabilities of U(VI) Minerals: Estimated and Observed Relationships," In *Scientific Basis for Nuclear Waste Management XX – Materials Research Society Symposium Proceedings,* W. J. Gray and I. R. Triay, eds., Materials Research Society, Warrendale, Pennsylvania, Vol. 465, pp. 1185-1192.

Finch, R. J., and R. C. Ewing, 1992, "The Corrosion of Uraninite under Oxidizing Conditions," *Journal of Nuclear Materials*, Vol. 190:133-156.

Foord, E. E., S. L. Korzeb, F. E. Lichte, and J. J. Fitzpatrick, 1997, "Additional Studies on Mixed Uranyl Oxide-Hydroxide Hydrate Alteration Products of Uraninite from Palermo and Ruggles Granitic Pegmatities, Grafton County, New Hampshire," *Canadian Mineralogist*, Vol. 35:145-151.

Frondel, C., 1956, "The Mineralogical Composition of Gummite," *American Mineralogist*, Vol. 41:539-568.

Fuhrmann, M., H. Zhou, J. Neiheisel, M. A. A. Schoonen, and R. Dyer, 1997, "Sorption/Desorption of Radioactive Contaminates by Sediment from the Kara Sea," *The Science of the Total Environment*, Vol. 202:5-24.

Giammar, D. E., and J. G. Hering, 2001, "Time Scales for Sorption – Desorption and Surface Precipitation of Uranyl on Goethite," *Environmental Science & Technology*, Vol. 35:3332-3337.

Grenthe, I., J. Fuger, R. J. M. Konings, R. J. Lemire, A. B. Muller, C. Nguyen-Trung, and H. Wanner, 1992, *Chemical Thermodynamics Series, Vol. 1: Chemical Thermodynamics of Uranium*, Elsevier Science, Oxford, United Kingdom.

Hemingway, B. S., 1982, "Thermodynamic Properties of Selected Uranium Compounds and Aqueous Species at 298.15K and 1 bar and at Higher Temperatures – Preliminary Model for the Origin of Coffinite Deposits," pp. 90. *U.S. Geological Survey Open Report 82-619*.

Hiskey, J. B., 1979, "Kinetics of Uranium Dioxide Dissolution in Ammonium Carbonate," *Institution of Mining and Metallurgy, Transactions, Section C,* Vol. 88:c145-c152.

Hiskey, J. B., 1980, "Hydrogen Peroxide Leaching of Uranium in Carbonate Solutions," *Institution of Mining and Metallurgy, Transactions, Section C,* Vol. 89:c145-c152.

Isobe, H., T. Murakami, and R. C. Ewing, 1992, "Alteration of Uranium Minerals in the Koongarra Deposit, Australia: Unweathered Zone," *Journal of Nuclear Materials*, Vol. 190:174-187.

Korzeb, S. L., E. E. Foord, and F. E. Lichte, 1997, "The Chemical Evolution and Paragenesis of Uranium Minerals from the Ruggles and Palermo Granitic Pegmatites, New Hampshire," *Canadian Mineralogist,* Vol. 35:135-144.

Langmuir, D., 1978, "Uranium Solution-Mineral Equilibria at Low Temperatures with Applications to Sedimentatory Ore Deposits," *Geochimica et Cosmochimica Acta,* Vol. 42:47-569.

Mason, C. F., W. R. Turney, B. M. Thomson, N. Lu, P. A. Longmire, and C. J. Chisholm-Brause, 1997, "Carbonate Leaching of Uranium from Contaminated Soils," *Environmental Science & Technology,* Vol. 31(10):2707-2711.

Morris, D. E., P. G. Allen, J. M. Berg, C. J. Chisholm-Brause, S. D. Conradson, R. J. Donohoe, N. J. Hess, J. A. Musgrave, and C. D. Tait, 1996, "Speciation of Uranium in Fernald Soils by Molecular Spectroscopic Methods: Characterization of Untreated Soils," *Environmental Science & Technology,* Vol. 30(7):2322-2331.

Muto, T., S. Hirono, and H. Kurata, 1968, "Some Aspects of Fixation of Uranium from Natural Waters", Japan Atomic Energy Research Institute Report NSJ Transl. No. 91, *Mining Geology* (Japan), Vol. 15:287-298.

Nguyen, S. N., R. J. Silva, H. C. Weed, and J. E. J. Andrews, 1992, "Standard Gibbs Free Energies of Formation at the Temperature 303.15 K of Four Uranyl Silicates: Soddyite, Uranophane, Sodium Boltwoodite and Sodium Weeksite," *Journal of Chemical Thermodynamics,* Vol. 24:359-376.

Nicol, M. J., and C. R. S. Needes, 1977, "The Anodic Dissolution of Uranium Dioxide-II in Carbonate Solution," *Electrochimica Acta,* Vol. 22:1381-1384.

O'Hare, P. A. G., B. M. Lewis, and S. N. Nguyen, 1988, "Thermochemistry of Uranium Compounds XVII. Standard Molar Enthalpy of Formation at 298.15K of Dehydrated Schepite UO3.0.9H2O. Thermodynamics of (Schoepite + Dehydrated Schoepite + Water)," *Journal of Chemical Thermodynamics*, Vol. 20:1287-1296.

Payne, T. E., R. Edis, B. R. Fenton, and T. D. Waite, 2001, "Comparison of Laboratory Uranium Sorption Data with 'in situ Distribution Coefficient' at the Koongarra Uranium Deposit, Northern Australia," *Journal of Environmental Radioactivity*, Vol. 57:35-55.

Pearcy, E. C., J. D. Prinkryl, W. M. Murphy, and B. W. Leslie, 1994, "Alteration of Uraninite from the Nopal I Deposit, Pena Blanca District, Chihuahua, Mexico, Compared to Degradaton of Spent Nuclear Fuel in the Proposed US High-Level Nuclear Waste Repository at Yucca Mountain, Nevada," *Applied Geochemistry*, Vol. 9:713-732.

Sergeyeva, E. I., A. A. Nikitin, I. L. Khodakovkiy, and G. B. Naumov, 1972, "Experimental Investigation of Equilibria in the System UO_3-CO_2-H_2O in 25-200 °C Temperature Interval," *Geochemistry International*, Vol. 9:900-910.

Sharma, J. N., K. Bhattacharya, R. G. Swami, S. K. Tangri, and T. K. Mukherjee, 1996, "Studies of the Kinetics of UO_2 Dissolution in Carbonate-Bicarbonate Medium Using Sodium Hypochlorite as Oxidant," *Journal of Radioanalytical and Nuclear Chemistry Letters*, Vol. 214(3):223-233.

Shoesmith, D. W., J. S. Betteridge, and W. H. Hocking, 1996a, "The Cathodic Reduction of Oxygen on n-type UO_2 in Dilute Alkaline Aqueous Solution," *Journal of Electroanalytical Chemistry*, Vol. 406:69-81.

Shoesmith, D. W., S. Sunder, M. G. Bailey, and N. H. Miller, 1996b, "The Corrosion of Used Nuclear Fuel in Aqueous Perchlorate and Carbonate Solutions," *Journal of Nuclear Materials*, Vol. 227:287-299.

Shoesmith, D. W., S. Sunder, M. G. Bailey, and G. J. Wallace, 1989, "The Corrosion of Nuclear Fuel (UO_2) in Oxygenated Solution," *Corrosion Science*, Vol. 29(9):1115-1128.

Shoesmith, D. W., S. Sunder, and J. C. Tait, 1998, "Validation of an Electrochemical Model for the Oxidative Dissolution of Used CANDU Fuel," *Journal of Nuclear Materials*, Vol. 257:89-98.

Smith, D. K., 1984, "Uranium Mineralogy," In *Uranium Geochemistry, Mineralogy, Geology, Exploration and Resources*, B. de Viro, G. Capaldi, and P. R. Simpson, eds., Institution of Mining and Metallurgy, Doncaster, United Kingdom, pp. 43-71.

Sowder, A. G., S. B. Clark, and R. A. Fjeld, 1998, "The Effect of Sample Matrix Quenching on the Measurement of Trace Uranium Concentrations in Aqueous Solutions Using Kinetic Phosphorimetry," *Journal of Radioanalytical and Nuclear Chemistry*, Vol. 234(1-2):257-260.

Sowder, A. G., S. B. Clark, and R. A. Fjeld, 2001, "The Impact of Mineralogy in the U(VI)-Ca-PO_4 System on the Environmental Availability of Uranium," *Journal of Radioanalytical and Nuclear Chemistry*, Vol. 248(3):517-524.

Sunder, S., D. W. Shoesmith, M. Kolar, and D. M. Leneveu, 1997, "Calculations of Used Nuclear Fuel Dissolution Rates Under Anticipated Canadian Waste Vault Conditions," *Journal of Nuclear Materials*, Vol. 250:118-130.

Vochten, R., and L. Van Haverbeke, 1990, "Transformation of Schoepite into the Uranyl Oxide Hydrates: Becquerelite, Billietite, and Wolsendorfite," *Contributions to Mineralology and Petrology*, Vol. 43:65-72.

Wronkiewicz, D. J., J. K. Bates, T. J. Gerding, E. Veleckis, and B. S. Tani, 1992, "Uranium Release and Secondary Phase Formation During Unsaturated Testing of UO_2 at 90 °C," *Journal of Nuclear Materials*, Vol. 190:107-127.

Wronkiewicz, D. J., J. K. Bates, S. F. Wolf, and E. C. Buck, 1996, "Ten-Year Results from Unsaturated Drip Tests with UO_2 at 90 °C: Implications for the Corrosion of Spent Nuclear Fuel," *Journal of Nuclear Materials*, Vol. 238:78-95.

D.4.0 FLUID MIGRATION AND TRANSPORT

Introduction

Decisions on the management of wastes in the B, BX, and BY tank tarms will be based on predictions of contaminant transport in the Hanford Site vadose zone. This section describes the status of ongoing efforts to build a quantitatively mechanistic understanding of field-scale, subsurface fluid migration and transport processes at the B, BX, and BY tank farms that will lead to scientifically defensible predictions of contaminant behavior.

At the B, BX, and BY tank tarms, the key waste management issues involve the in-ground inventory of contaminants and their predicted arrival at compliance points. To address these issues, knowledge of source terms, hydrogeologic processes and properties, as well as geochemical processes and properties is needed. This information comes from several ongoing activities: characterization performed by the Tank Farms Vadose Zone (TFVZ) core project, laboratory and field experiments performed by the Science and Technology Project organization, and process-specific research performed by Environmental Management Science Program projects. These data have been or are being developed for a variety of purposes and, in most cases, have not been systematically examined in a comprehensive, field-scale, modeling framework for consistency. An important role of the current modeling effort, therefore, is to identify inconsistencies between the observations and the process-level understanding, and prioritize areas that merit additional investigation. One difficulty with the retrospective reconstruction of historical tank waste release events is the very limited availability of data to characterize source terms and compare with modeling results. In this respect, the laboratory and field studies provide invaluable, comprehensive data sets on the dynamics of liquid migration and contaminant mobility that would otherwise not be available.

Field measurements of contaminant distribution in WMA B-BX-BY have shown at least several cases of enhanced lateral fluid migration. This phenomenon is most evident in the area immediately east of tanks BX-101 and BX-102 where overlapping plumes of metal waste and isotope recovery waste exist (Section 3.2.1). These plumes, which originated from different sources at different times, have defined a common flow path through the vadose zone. In both of these plumes, the extent of lateral migration (e.g., 30 m) was quite remarkable and was equal to or greater than the depth of vertical penetration. Lateral migration to the northeast also has been observed in the strontium-90 plume believed to result from a transfer line leak near tank B-110 (Section 3.2.2), and lateral migration is speculated to have transported water and contaminants from past-practices sites (e.g., cribs) adjacent to WMA B-BX-BY to the vadose zone below the tank farms (Section 3.2.3). These observations truly define a new conceptual model for water and waste migration in the Hanford vadose zone that has major implications to future projections of contaminant fluxes to groundwater and the need and strategies for corrective action.

Over the past two years, there has been growing awareness that significant lateral migration may occur under certain circumstances in the Hanford vadose zone. Lateral migration in the S-SX tank farm was implied by relative distributions of cesium-137 and technetium-99 beneath tanks SX-108 and SX-115 and by isotope geochemical measurements of perched moisture on the top of the Plio-Pleistocene unit (Knepp et al. 2001). Lateral migration and the causes for it were documented in a series of vadose zone field injection experiments performed at the Groundwater

Protection Program's Vadose Zone Field Test Facility near PUREX in the 200 West Area (Gee et al. 2002).

In this section, results are summarized from the injection experiments performed at the Vadose Zone Test Facility with the objective of defining the extent of lateral migration that may occur in the Hanford vadose zone and the potential geohydrologic causes (Section D.4.1). Such information is provided with the belief that similar phenomena with similar causes have occurred in WMA B-BX-BY. Second, modeling studies are presented and discussed on liquid and solute migration through the sedimentary geologic system proximate to tank BX-102 (Section D.4.2) with emphasis on the uranium plume. Sensitivity studies were performed on a number of critical hydrogeologic parameters believed to influence lateral migration with the objective of identifying those most important in the B, BX, and BY tank farms. The results provide important insights on the impact of small (i.e., subgrid scale), discontinuous sediment layers and their properties necessary to recreate the degree of lateral water and uranium migration noted in the field. Third, a one-dimensional reactive transport modeling assessment (Section D.4.3) was performed for cesium-137 resulting from the tank BX-102 overfill event. The calculation objective was to evaluate whether deeply distributed cesium-137 in borehole 21-02-04 near BX-102 could have resulted from transport through the sediment column, as opposed to an alternative mechanism, such as migration along the borehole casing.

D.4.1 HYDROLOGIC TESTS OF LATERAL FLOW AND TRANSPORT IN THE HANFORD VADOSE ZONE

Anderson L. Ward[1], Glendon W. Gee[1], and Zhuanfang L. Zhang[1]

[1]Pacific Northwest National Laboratory, Richland, Washington 99352

D.4.1.1 Introduction

Extensive lateral flow appears to dominate every transport experiments, planned and unplanned, in the Hanford Site vadose zone over the past 40 years. Contaminant plumes typically show extensive lateral spreading, with splitting along flow paths and multiple zones of high contaminant concentrations, even in sediments that appear homogeneous and isotropic at the regional scale. Infiltration tests conducted in the early 1960s demonstrated preferential lateral migration of fluids. For example, Figure D.85 shows the wetting pattern in a typical outcrop of the Hanford formation following the infiltration of water from a surface source demarcated by the white rectangular box on the surface.

Figure D.85. Lateral Spreading of Water in Hanford Formation Sediments White Box Delineates Infiltration Area. Dark Zones are Wetted Sediment. Lateral Spreading is Greater than 10:1 in these Heterogeneous Layers.

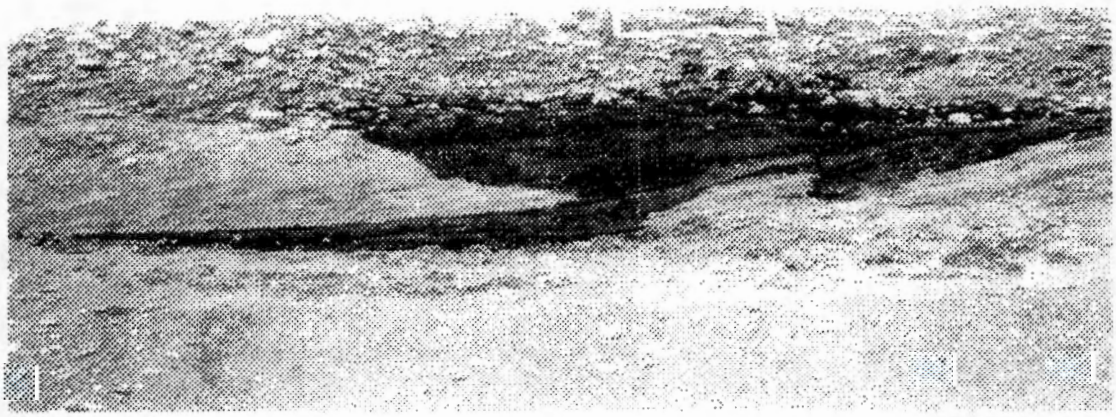

While fluid quantities were not reported, the pictorial representation of lateral spreading is clear. Water was applied over an area that was about 0.5 m diameter. The extent of the wetting front is around 5 m, or roughly 10 times the diameter of the application zone. The wetting front appears to be strongly influenced by the location of contacts between the coarse-grained and fine-grained facies. At this site, the pattern of wetting appears to result from wicking within a layer that is texturally finer than the adjacent sediments.

This layer, which is comprised of cross-laminated facies, has been observed at other sites. Although the laminates are typically only a few centimeters in thickness and may extend from a few centimeters to tens of centimeters laterally, they exert significant control on water and solute distribution patterns. Figure D.86 shows moisture and dye distributions at the Army Loop Road Clastic Dike Site at Hanford following an infiltration experiment conducted in the summer of 2001 to study of the effects of clastic dikes on subsurface transport (Murray et al. 2001). This

site is the location of the current Vadose Zone Transport Field Study aimed at investigating later flow processes. In this study, water was applied as a steady flux at a rate of about one tenth of mean K_S. Under the experimental conditions, water and a dye tracer, which was used as a surrogate for a sorbing contaminant, bypassed significant portions of the pore domain. Close examination showed dark thin typically sloping bands of higher moisture and dye concentrations commingled with bands of lower moisture. These facies initially showed no discernible differences in texture from the main sand matrix. However, particle size analysis showed these facies were typically 1 cm or less in thickness and of a slightly finer texture than the surrounding medium. It appears that at low saturations, heterogeneity causes water to flow in increasingly tortuous paths and regions of low conductivity are bypassed. Transport occurs mainly in the finer textures, and contaminants can bypass regions occupied by coarser textures that are perhaps low-K regions at this flux.

Figure D.86. Moisture and Dye Distributions at the Army Loop Road Clastic Dike Site at the Hanford Site

(a) The Effect of Thin Cross-Laminated Facies on Local Scale Transport and (b) Manifestation of the Effect of Anisotropy on Local- and Macro-Scale Transport.

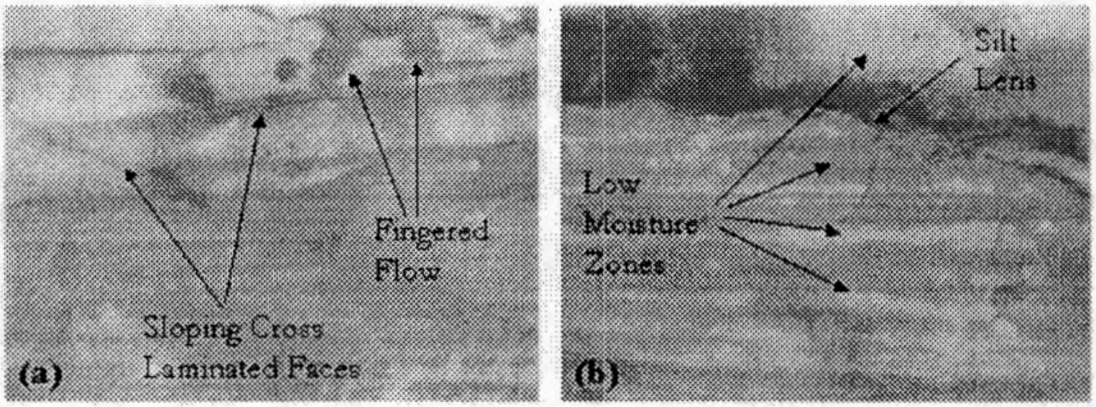

Such observations of lateral migration from surface infiltration tests illustrates the impact of heterogeneity on transport in the subsurface and confirms the importance of sedimentary architecture as a control of variability in permeabilities and ultimate the distribution of water and contaminants. They also suggest a relationship between saturation and the expression of heterogeneity, which may be due to contrasts in hydraulic conductivity. Similar observations of anomalously high lateral solute velocities have also been observed in the Hanford tank farms. This phenomenon will undoubtedly affect the fate and transport, particularly of reactive contaminants, as pore by pass could lead to an underestimation of concentrations at compliance boundaries

Geology is neither uniform, homogeneous, nor isotropic in space. The processes that create near surface geology leave behind patterns with variations in space (heterogeneity), orientation (anisotropy), and scale (particle sizes and their distribution). In the vadose zone, the lateral flow phenomenon is often attributed to anisotropy in the hydraulic conductivity tensor. It is clear from Figure D.85 and Figure D.86 that Hanford formation sediments are anisotropic. Anisotropic sediments are defined as materials that have dimensionally dependent hydraulic

properties. Typically for stratified soils, the effective horizontal hydraulic conductivity, K_H, is considerably greater than the vertical hydraulic conductivity, K_V. Literature values of K_H typically exceed K_V by factors of 2 to 10. Recent measurements conducted under the vadose zone transport field studies at the Army Loop Road Clastic Dike Site show K_H:K_V ratios exceeding 60:1 near saturation. These ratios could easily exceed 100:1 at lower saturations. A detailed discussion of anisotropy can be found in standard hydrology texts and in recent review articles on the subject (Bear 1972; Bear et al. 1987; Gelhar et al. 1979; Zaslavsky and Sinai 1981; Yeh et al. 1985a, b, c; McCord et al. 1991, 1997). For the vadose zone, Stephens and Heermann (1988) conducted laboratory studies that clearly illustrate lateral spreading of moisture in unsaturated, layered sands similar to that observed in Figure D.85 and Figure D.86. McCord et al. (1991) conducted tracer experiments in the field and also demonstrated moisture dependency of anisotropy. The simple concept is that as soil wets up, it becomes more conductive, so that wetter zones persisting in the vadose zone are typically more conductive than dry zones with comparable textures. Slightly sloping subsurface layers, not subject to evaporation or water loss from plant root uptake, can contribute to significant lateral drainage (McCord et al. 1991).

Based on observations in layered Hanford sediments, as typified in Figure D.85 and Figure D.86, attempts were made to account for so called feathering or lateral spreading of fluids in the vadose zone, particularly in relation to tank leak estimation techniques (Jansen et al. 1973). Because numerical computer models for subsurface transport were largely unavailable at the time, simple analytical methods were used which approximated the contaminant spread from a given leak point. A worst case was assumed to be transport from below the midpoint of the tank bottom to a dry well a short distance from the edge of the tank. A conical flow path was assumed and angles between 30 and 60 degrees (from vertical) were used to compute the possible depths at which the leak would intercept the dry well. As an example, Jansen et al. (1973) computed that sediment with 50% saturation could sustain a leak up to 200,000 gal for a 30-degree angle and 68,000 gal for a 60-degree angle, before detection. In these cases, detection would occur in the dry wells at 24 m (78 feet) and 8.5 m (28 feet) below the tank bottom, respectively. If there were an impermeable layer located 4.6 m (15 feet) below the tank bottom, Jansen et al. (1973) computed that the detectable leak volume would be reduced but could still range from 1,500 gal to 12, 000 gal. The true effects of layering of the strata could only be approximated, but it is clear that huge uncertainties in leak detection occur as a result of unknowns in how and when lateral spreading occur in sediments beneath waste tanks.

Isaacson (1982) provided an analysis for establishing dry well monitoring frequency that considered many of the features of the Jansen et al. (1973) analysis. Included was a geometric factor that incorporated hydrologic anisotropy in a qualitative manner. For example, if the probable diameter of the wetted zone was estimated to be 50 feet and the leak was thought to be confined to a relatively thin lens of 10 feet, the geometry factor was computed to be 10/50 or 0.2. It appears that such a geometric estimate of anisotropy is at best highly subjective and qualitative. Unfortunately, no guidelines were provided for ensuring that accurate geometric estimates could be made in the Hanford vadose zone.

Standard practices for predicting transport under unsaturated conditions do not account for the random heterogeneity and strong anisotropy that can be expected under the extremes of nonlinear flow behavior typical of the Hanford vadose zone. More importantly, even though

lateral flow due to variable anisotropy has dominated every field experiment (both planned and unplanned) performed at the Hanford Site, it is unaccounted for in all but a few models. During 2001, a series of experiments conducted under the Vadose Zone Transport Field Study have focused on understanding the phenomenon of lateral spreading and quantifying anisotropy in hydraulic conductivity in the heterogeneous vadose zone at Hanford. The general goal of these studies is to develop predictive capabilities that can be used in tank farms and elsewhere to determine the fate of contaminant plumes, their rates of movement, and spatial distributions.

D.4.1.2 The Vadose Zone Transport Field Study Site

During May and June of 2000, a mock tank leak test field experiment was carried out at the 299-E24-111 Experimental Test Well Site (also know as the Sisson and Lu site) in the 200 East Area. The Sisson and Lu site was the location of a series of earlier tracer tests using nitrate, chloride, barium, rubidium, calcium, and the short-lived radionuclides cesium-134 and strontium-85 conducted during the early 1980s (Sisson and Lu 1984). Figure D.87 is a schematic map of the site showing the locations of a set of steel-cased wells that were installed for those tracer studies. Also shown on this figure are the locations of the injection well and the sampling boreholes used for this project.

The primary purpose of the current test was to identify mechanisms controlling transport processes in the Hanford sediments (Ward and Gee 2000). In 2000, over a 4-week period, 5 aliquots of approximately 4,000 liters of water each were leaked into the subsurface at the Sisson and Lu site. The water was gravity-fed into the sediments at a depth of 4.5 m through a 15 cm inner diameter cased borehole. A variety of different geophysical methods (e.g., neutron logging, electrical resistance tomography, crosshole seismic tomography) were used to track the movement of the leak fluids in the subsurface. In addition, a tracer cocktail containing 2 Kg of D_2O, 3 g $NaH^{13}CO_3$, 25 mg ^{87}Sr, 1 mg ^{145}Nd, 1 mg ^{179}Hf, 3 mg ^{207}Pb, and 1000 ppm of bromide was added to a third aliquot of leak fluids. The spread of tracers over time was monitored by measuring the isotope ratios and bromide concentrations in samples of the porewater extracted from a series of boreholes. In 2001, an additional suite of tracers and fluid were applied to the test site. A hypersaline fluid (36% by wt. sodium thiosulfate) was injected to the ground. 19,000 L were injected over the course of 5 weeks. This was followed by 11,400 L of salt-free river water. Monitoring of the site using neutron logging was continued for two months after the final water injection.

The geology of the Sisson and Lu site consists of coarse- to fine-grained sands and silts from the upper part of the Hanford formation. Last and Caldwell (2001) and Last et al. (2001) identified six distinctive units in the upper 17 m of the sediments (the sequence where the tracer tests were conducted) that could be correlated between boreholes. The stratigraphic column in Figure D.88 summarizes this classification scheme.

Figure D.87. Schematic of Well Placement at the Sisson and Lu Experimental Site

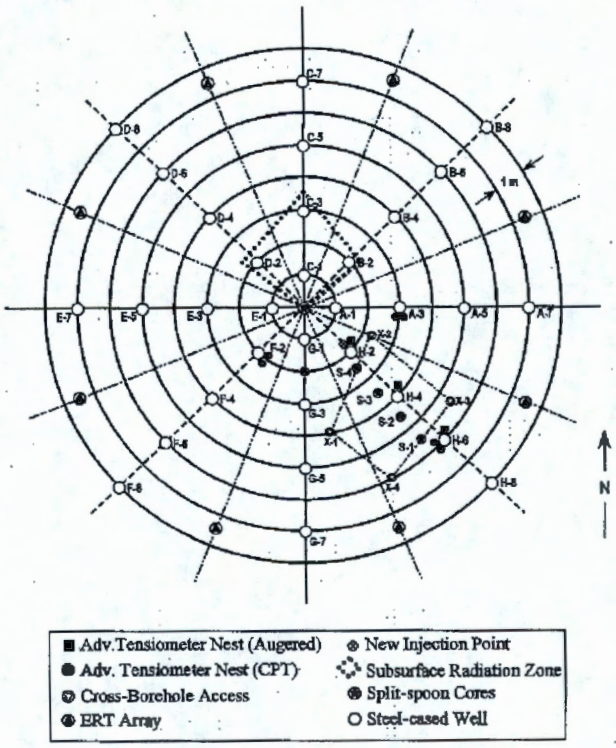

Figure D.88. Stratigraphic Column at the Sisson and Pre-Injection Moisture Contents Profile Measured for Samples from the S1 Core Lu Experimental Site

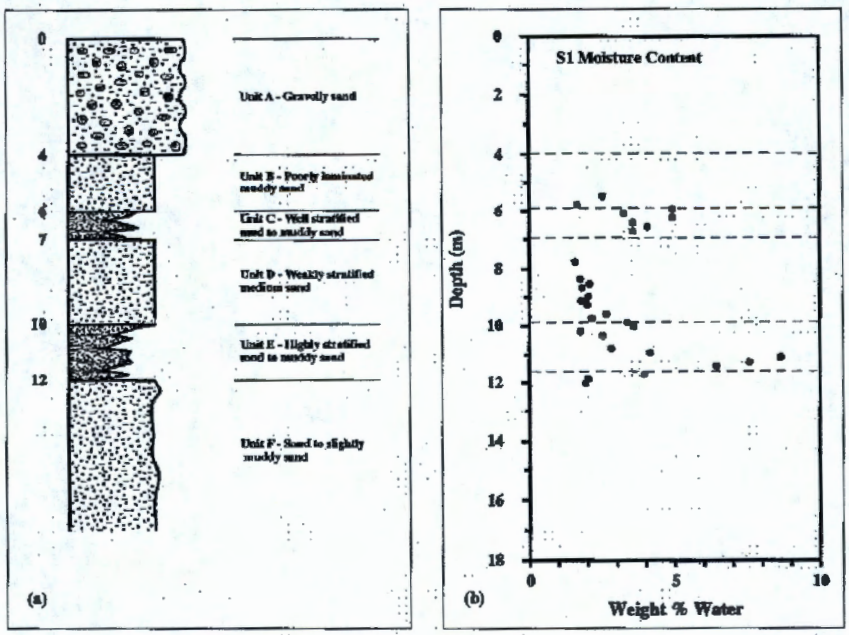

The key features of the sediments are the two highly stratified units at depths of 6 to 7-8 m (unit C) and 10 to 12 m (unit E). These stratified layer sequences are not texturally dissimilar from the surrounding sediments. Percent fines or material passing the 270-mesh screen (< 53 μm) vary at the site from 9 to 29% while the average of 15 to 20% is typical of medium to coarse textured sands at the Hanford Site. The finer layers that exist frequently at the 6 and 10 m depths do not appear to be continuous (Last et al. 2001).

Also plotted on Figure D.88 are the moisture contents of the sediments measured for samples from a borehole drilled before the leak test was conducted (Last and Caldwell 2001). In the coarser, poorly laminated units, the water contents were generally low (~2 wt.% water). In the two stratified units (Figure D.88 C and E), the moisture contents of the sediments were higher (to >8 wt% water), especially in the bottom meter of the lower stratified layer.

Thus far, field-measured distributions of soil water content have been analyzed using three-dimensional spatial-moment analysis (Gee and Ward 2001). Results clearly show that the subsurface distributions of both dilute and hypersaline fluids are controlled by an interaction between small-scale horizontal stratification and fluid properties. The centers of mass for the two plumes were similar in the lateral and transverse directions, but were significantly different in the longitudinal plane. The cumulative travel depth of the center of mass for both the dilute and hypersaline water plumes showed a nonlinear increase with time and injected volume, indicative of the highly nonlinear transport process. After 20,000 L (5,283 gal), the hypersaline plume had traveled 2.6 times deeper than the dilute plume. Most of the difference occurred during the initial stages of the experiment with the vertical center of mass of the hypersaline plume being twice as deep as that of the dilute plume. Over time, the hypersaline plume also remained more compact when compared to the dilute plume. The test site shows evidence of macroscopic anisotropy, comparing the ratio of fluxes in the principal directions for the dilute plume. Mean velocities were $\bar{v}_x = 0.0067$ m (0.022 ft) d^{-1}; $\bar{v}_y = 0.0062$ m (0.02 ft) d^{-1}; and $\bar{v}_z = 0.0052$ m (0.017 ft) d^{-1}. The average v_x/v_y ratio was 1.079 while the average v_x/v_z ratio was 0.128.

Ionic tracer distributions were analyzed using one-dimensional spatial moments. Distributions of resident concentration profiles were generally asymmetric with a large mass occurring at 5 to 7 m (16 to 23 ft), and a smaller mass at 10 to 12 m (33 to 39 ft) with a preferred flow path to the southeast. At the test site, there are two relatively fine-textured layers, one at about a 6-m (20-ft) depth and one at about the 12-m (39-ft) depth. The locations of multiple peaks were coincident with the general location of finer-textured lenses derived from lithologic logs. The fine sandy sediments in these layers controlled the migration of the water in both tests and caused a substantial increase in transverse solute advection, while confining the moisture plume to a depth of 13 m (43 ft) in the fiscal year 2000 test. During the fiscal year 2001 tests, elevated water content and tracer concentrations were observed at depths of 16 m (52.5 ft) at two monitoring locations in the southeast quadrant of the monitoring site, suggesting that the plume had penetrated below the lower (12-m [39-ft] depth) confining layer. The exact cause of the observed preferential transport has not been determined at this point, but it could be due to fingering induced by the fluid properties, or simply to rapid flow along an improperly grouted sampling point or access tube. The location of the peak tracer concentrations was almost identical for F^-, Cl^-, Br^-, NO_3^-, $S_2O_3^-$, and PO_4^{2-} but somewhat larger for SO_4^{2-} in the fiscal year

2001 tests. The distribution of SO_4^{2-} also appeared very sensitive to textural changes. The location of centers of mass for the different tracers was somewhat different and increased from about 5.7 m (18.7 ft) to 8.4 m (27.6 ft) in the order $PO_4^{2-} < Br < F^- < S_2O_3^- < NO_3^- < Cl^- SO_4^{2-}$. The deeper penetration of Cl^- relative to NO_3^- and $S_2O_3^-$ may be indicative of preferential transport due to anion exclusion, a mechanism that would be of great significance to the transport of technetium-99.

These observations illustrate the importance of sedimentary architecture as a control of spatial variability in hydraulic conductivity and emphasize the need to consider local-scale textural discontinuities in conceptual models of field-scale transport at the Hanford Site. Lateral spreading of contaminant plumes has been observed in the vadose zone at Hanford tank farms and other waste sites. Preliminary modeling of the distribution of the fiscal year 2000 test was performed using the Pacific Northwest National Laboratory (PNNL) Subsurface Transport Over Multiple Phases (STOMP) simulator. The site was modeled as a heterogeneous system conditioned on initial water-content distributions and parameterized with constitutive properties of over 20,000 soil types. To date, these simulations have come closest to reproducing field observations of any of the simulations of experiments performed at this site. Although the general features of the predicted water-content distributions are similar to those observed in the field, the current conceptual and numerical model does not yet adequately describe the extensive lateral spreading observed in the field.

Moisture-dependent anisotropy, an extreme of nonlinear flow behavior, can both subdue and enhance predicted migration rates depending on local stratigraphy and lead to the costly over-engineering of remediation and risk management strategies. Yet, standard practices for predicting transport under unsaturated conditions do not account for the random heterogeneity and strong anisotropy that can be expected under conditions typical of the Hanford vadose zone. In fact, this phenomenon is unaccounted for in all but a few models. Those models considering this phenomenon are formulated on the presumption that flow can be linearized and treated as a small perturbation to the unsaturated flow dynamics and are in contradiction of prevailing knowledge of field manifestations. In addition to the incomplete conceptual model, model parameterization for field-scale simulations continues to be a major limitation. Work is ongoing to evaluate the processes that can cause accelerated transport of hypersaline plumes and to develop techniques to facilitate upscaling and parameterization of field-scale models.

Work in fiscal year 2001 has led to the development of a parameter scaling method that can be coupled with inverse-flow modeling to estimate constitutive parameters for heterogeneous soils at the field-scale. The method is based on first assigning unique scaling factors to similar soil textures in the field after which field-scale reference hydraulic parameter values are then estimated through inverse modeling of the field experiments. The parameters for individual layers are subsequently obtained through inverse scaling of the fitted reference values using the a priori relationships between the reference parameter values and the specific value for each layer. STOMP was combined with the universal inverse modeling code (UCODE) to estimate the unsaturated hydraulic parameters. Three cases of heterogeneity, i.e., homogeneous soil, layered soil, and heterogeneous soil, were used to test the new technique. Predictive modeling of drainage from a well-characterized lysimeter site at Hanford that has both laboratory and field-measured soil hydraulic properties, resulted in an overestimation of soil water content, θ, and an underestimation of pressure heads, ψ. However, using field-scale parameter values

derived from inverse-flow modeling with the new scaling technique resulted in significantly better model fits for both θ and ψ (Figure D.89 and Figure D.90).

Figure D.89. Comparison of the (a) Observed and (b) Predicted Soil Water Contents at the H-Section of the Injection Experiment using Parameters Derived from a Combination of Parameter Scaling and Inverse Modeling

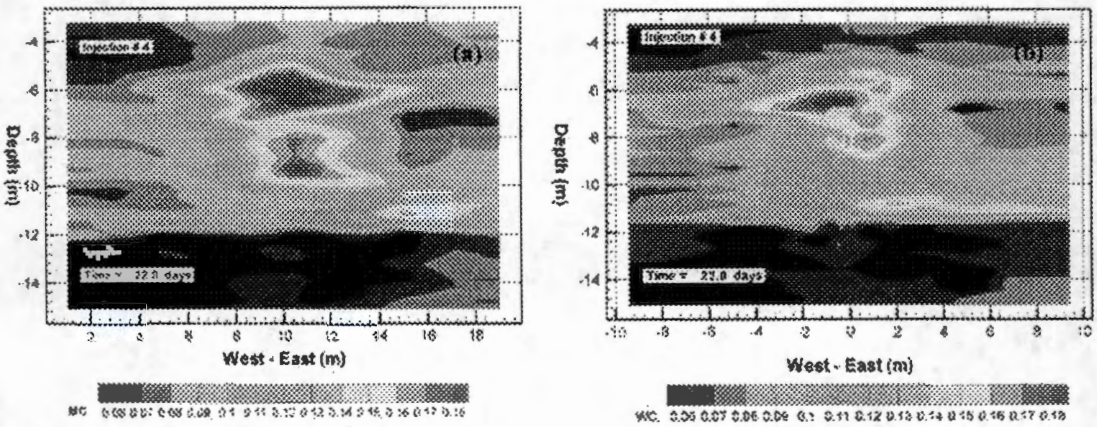

Figure D.90. Comparison of the Predicted and Observed Soil Water Contents at the H Section of the Injection Experiment Described in Sisson and Lu (1984) Parameterizations: (a) lab-scale parameter values, (b) field-scale parameter values after the recursive inversion. Dashed lines: the 1:1 line. Solid lines: linear regression line.

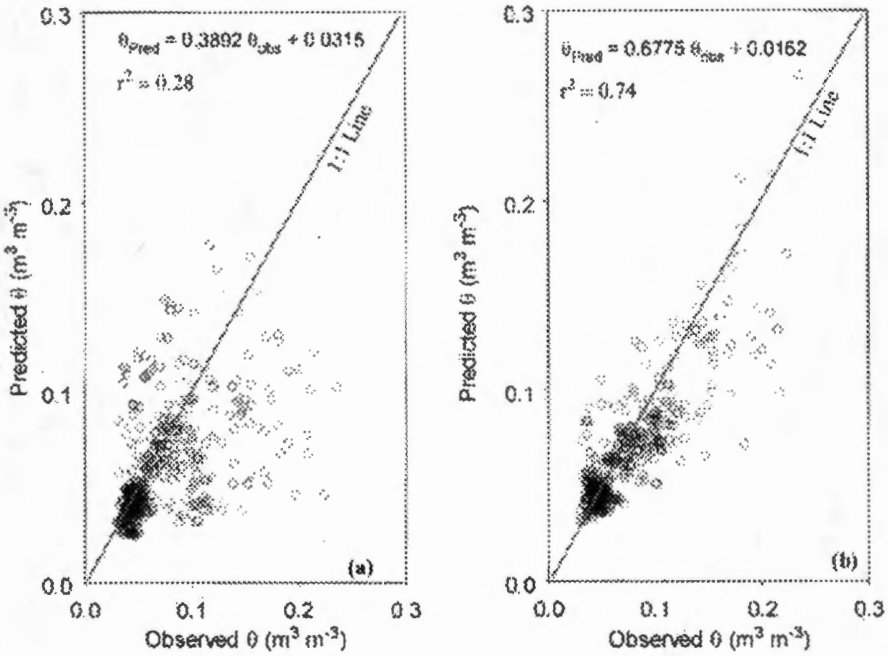

The simulation of drainage from a layered soil at a well-instrumented field site near the 300 Area at Hanford also resulted in an overestimation of θ and ψ when the local-scale parameter values were used. Again, using field-scale parameter estimates, obtained from the inverse scaling method, resulted in smaller prediction errors with regression coefficients of 0.956 to 0.997 between the observed and predicted values of θ and ψ, respectively. Application of this technique to the estimation of hydraulic parameters from the Vadose Zone Transport Field Study experiments has commenced with a two-dimensional simulation. The prediction of water-content distributions using laboratory-measured parameter values resulted in very poor model fits ($r^2 = 0.28$). However, using inverse scaling improved the goodness of fit with r^2 increasing to 0.74. Parameters derived from these studies will be compared with those derived from core measurements with the goal of developing an upscaling methodology. Such techniques are critical to the development of long-term, field-scale transport predictions. This type of inverse analysis will be an ongoing effort in fiscal year 2002 and fiscal year 2003.

The advanced characterization methods (i.e., ERT [electrical resistance tomography], HRR [high resolution resistivity], and XBR [cross borehole radar]) for the vadose zone all have significant promise as diagnostic tools for defining the depth and extent of vadose-zone plumes at Hanford, particularly where monitoring wells can be adapted for use by these instruments. XBR requires polyvinyl chloride (PVC) casing, but HRR and ERT can be adapted for use with steel-cased wells, the typical infrastructure that currently exists at the Hanford tank farms. HRR appears to be particularly useful in being capable of diagnosing the lateral extent of the plume. Evaluation of the characterization methods will continue during future field experiments.

D.4.1.3 Implications of Studies at the Vadose Zone Transport Field Study Site for the BX Tank Farm

Injection experiments at the S&T Vadose Zone Transport Field Study Site have demonstrated that lateral migration is important in evaluating transport and suggests mechanisms that may have occurred in the BX tank farm. The S&T field experiments documented cases of lateral unsaturated fluid migration promoted by discontinuous, low permeability laminations/lenses in the H2 (Hanford formation) that occurred at the 6 and 10-meter depths at the field test site. These observations support a conceptual model of moisture-dependent anisotropy, whereby metal wastes migrate horizontally along a conductive fine-textured lamination until it terminates, or its air entry potential is sufficiently low such as to allow breakthrough. The waste fluid migrates vertically after breakthrough, until encountering another wetter, conductive lamination that, again, promotes lateral migration. Lateral migration of tens of meters from the point of origin is possible with anisotropic media similar to the Hanford formation sedimentary deposits. It appears that the mechanism of anisotropic flow could have contributed to the lateral migration of uranium in a northeasterly direction from tank BX-101 to the west of tank BX-102. The distance of migration of several tens of meters seems plausible for liquid migration at this site, particularly with the known volumes that were largely discharged.

Because current conceptualizations of state-dependent anisotropy have failed to describe field observations, this phenomenon will be a major component of studies conducted under the Science and Technology Project of the Groundwater Protection Program and the EMSP programs in fiscal year 2003. In addition, field studies of subsurface uranium transport are planned for fiscal year 2003.

D.4.1.4 References

Bear, J., 1972, *Dynamics of Fluids in Porous Media*, Elsevier, New York.

Bear, J, C. Braester, and P. Menier, 1987, "Effective and Relative Permeabilities of Anisotropic Porous Media," *Transport Porous Media*, Vol. 2:310-316.

Gee, G. W., and A. L. Ward, 2001, *Vadose Zone Transport Field Study, Status Report*, PNNL-13679, Pacific Northwest National Laboratory, Richland, Washington.

Gelhar, L. W., A. L. Gutjahr, and R. L. Naff, 1979, "Stochastic Analysis of Macrodispersion in Aquifers," *Water Resources Research*, Vol. 19(1):161-180.

Isaacson, R. E., 1982, *Supporting Information for the Scientific Basis for Establishing Dry Well Monitoring Frequencies*, RHO-RE-EV-4 P, Rockwell Hanford Operations, Richland, Washington.

Jansen, G., D. P. Granquist, R. D Dierks, J. N. Hartley, O. H. Koski, J. A. Merrill, and C. A. Ratliff, 1973, *Review of ARCHO Waste Tank Leak and Level Monitoring Systems and Material Balance Techniques*, BNWL-B-308, Battelle, Pacific Northwest Laboratories, Richland, Washington.

Last, G. V., and T. G. Caldwell, 2001, *Core Sampling in Support of the Vadose Zone Transport Field Study*, PNNL-13454, Pacific Northwest National Laboratory, Richland, Washington.

Last, G. V., T. G. Caldwell, and A. T. Owen, 2001, *Sampling of Boreholes WL-3A through -12 in Support of the Vadose Zone Transport Field Study*, PNNL-13631, Pacific Northwest National Laboratory, Richland, Washington.

McCord, J. T., D. B. Stephens, and J. L. Wilson, 1991, "The Importance of Hysteresis and State-Dependent Anisotropy in Modeling Variably Unsaturated Flow," *Water Resources Research*, Vol. 27:1501-1517.

McCord, J. T., C. A. Gotway, and S. H. Conrad, 1997, "Impact of Geologic Heterogeneity on Recharge Using Environmental Tracers: Numerical Modeling Investigation," *Water Resources Research*, Vol. 33:1229-1240.

Ward, A. L., and G. W. Gee, 2000, *Detailed Test Plan for Simulated Leak Tests*, PNNL-13263, Pacific Northwest National Laboratory, Richland, Washington.

Yeh, T.-C., L. W. Gelhar, and A. L. Gutjahr, 1985a, "Stochastic Analysis of Unsaturated Flow in Heterogeneous Soils. 1. Statistically Isotropic Media," *Water Resources Research*, Vol. 21:447-456.

Yeh, T.-C., L. W. Gelhar, and A. L. Gutjahr, 1985b, "Stochastic Analysis of Unsaturated Flow in Heterogeneous Soils. 2. Statistically Anisotropic Media with Variable," *Water Resources Research*, Vol. 21:457-464.

Yeh, T.-C., L. W. Gelhar, and A. L. Gutjahr, 1985c, "Stochastic Analysis of Unsaturated Flow in Heterogeneous Soils. 3. Observations and Applications," *Water Resources Research*, Vol. 21:465-471.

Zaslavsky, D., and G. Sinai, 1981, "Surface Hydrology. I. Explanation of Phenomena," *Journal of Hydraulic Division America Society Civil Engineering*, Vol. 107(HY1): 53-64.

D.4.2 MODELING STUDIES OF FLUID FLOW AND SOLUTE TRANSPORT AT TANK BX-102 IN THE HANFORD VADOSE ZONE

Karsten Pruess[1] and Steve Yabusaki[2]

[1]Lawrence Berkeley National Laboratory, Berkeley, California 94750
[2]Pacific Northwest National Laboratory, Richland, Washington 99352

D.4.2.1 Introduction

A key issue at the Hanford Site is the possible impact of uncontrolled releases of tank wastes on future groundwater quality. At the B, BX, and BY tank farms, modeling of fluid flow, solute transport, and chemical reactions is being performed to better understand past tank waste release events in the context of historical and contemporary field measurements. At issue is the quantity of contaminants of concern released to the subsurface, the behavior of these contaminants in the subsurface, and future risks posed by these contaminants. New knowledge from these analyses will support longer-term predictions of contaminant fate needed for WMA B-BX-BY waste management decisions.

D.4.2.1.1 Contaminated Sediments Near Tank BX-102. Tanks BX-101, BX-102, and BX-103 are a set of 530,000-gallon (2006.3 m^3), single-shelled tanks linked together by transfer lines in a gravity-fed "cascade" from BX-101 to BX-102 to BX-103. The 30 ft (9.144 m) high, 75 ft (22.86 m) diameter tanks were constructed in 1946. In October 1969, gamma probe readings in a dry well (now known as 21-27-11) approximately 72 ft (21.95 m) from BX-102 rapidly rose above the maximum detection level of the probe (Womack and Larkin 1971). In response to this suspected leak from BX-102, nineteen dry wells were installed to characterize the extent of vadose zone contamination. Gross gamma logs of these wells identified a large plume of undifferentiated gamma-emitting radionuclides to the east and northeast of BX-102. Twenty-seven years later, spectral gamma logging (DOE-GJO 1997, 1998) of these dry boreholes was able to identify a uranium-238 plume extending at least 150 ft (45.72 m) to the northeast and 75 ft (22.86 m) to the southeast. Uranium-238 observed in RCRA well E33-41 (in 1991) at a depth of 137 ft (41.76 m), is consistent with the uranium-238 plume identified by the data from the nearby dry wells and probably represents the farthest (northeast) known extent of the plume, which is approximately 160 ft (48.77 m) northeast of tank BX-102. From the spatial distribution of radionuclides observed in the spectral gamma logging, it was inferred that the plume source was near borehole 21-02-04 on the southeast edge of tank BX-102. Shallowest uranium-238 measurements were found to the east and southeast of the source, but the principal plume tracks to the north-northeast as indicated by the highest concentrations and deepest measurements.

Prior to the spectral gamma logging of the BX tank farm dry wells in 1997, it was widely believed that the vadose zone plume identified in 1970 had resulted from a BX-102 leak of cesium-137 recovery waste in 1969. Conversely, the uranium-238 discovered in sediments during the construction of well 299-E33-41 in 1991 was thought to have come from cribs in the B tank farm since there were no known uranium-bearing metals waste releases from the B, BX, and BY tank farms at the time. The identification of significant concentrations of uranium-235/238 by spectral gamma logging in 1997, however, was not consistent with the

cesium-137 recovery waste that was being processed through BX-102 in 1969. Uranium-235/238 was a significant component of metals waste that was transferred through the BX-101/BX-102/BX-103 series of cascaded tanks when the tanks were first put into service in 1948.

The only documented release of metals waste in this area was found in a recently (1992) declassified *Hanford Works Monthly Report* dated February 1951 that describes an overfill event at tank BX-102 that resulted in the release of 91,600 gallons (346.7 m^3) of metals waste (General Electric Company 1951). At the beginning of February 1951, metals waste containing depleted uranium from B Plant extractions was run through the BX-101/BX-102/BX-103 cascade series. On February 9, 1951, it was found that the waste was not reaching the terminal tank in the cascade (BX-103). Subsequent measurements showed the liquid level in BX-102 had risen above the overflow point of 16 ft (7.803 m), indicating a plug in the effluent line to BX-103. On February 20, the liquid level in BX-102 was allowed to rise to 17 ft (5.182 m) to increase the head in an attempt to break the plug. A few days later, the liquid level in BX-102 was observed to be dropping slowly while the liquid levels in the succeeding tanks remained unchanged. A day later, radiation determinations in the BX-102 dry well (assumed to be 21-27-11) were positive. By this time, the liquid levels in BX-102 had decreased 6 inches (152.4 mm). The released radioactive wastes included an estimated 4 to 10 metric tons of uranium.

While it seems reasonable that the uranium plume emanating from the southeast side of tank BX-102 is the result of the 91,600-gal metals waste release in 1951, the description of the release event and the present position of the plume have raised several important questions about the conceptual model of flow and transport in the Hanford vadose zone:

- How did metals waste from the 1951 overfill event travel over 120 ft (36.58 m) from the apparent source on the southeast side of BX-102 to well 21-27-11 in three weeks or less?
- How did metals waste from the 1951 overfill event travel over 170 ft (51.82 m) laterally and 137 ft (41.76 m) vertically from the apparent source on the southeast side of BX-102 to well 299-E33-41?
- How fast are the various components of the metals waste traveling through the vadose zone?

For the most part, the postulated transport has taken place within a single geologic layer, H2, described in Lindsey et al. (2001) as a coarse to medium sand. The rapid and large lateral transport in the absence of identifiable intervening geologic layers challenges commonly held notions of solute transport in the Hanford vadose zone. Improved understanding of the conditions responsible for these behaviors will have significant implications for the interpretation of historical waste release events and, more importantly, for the prediction of future migration of radioactive waste components of concern.

The goal of this work is to develop a predictive understanding of processes controlling contaminant migration at the B, BX, and BY tank farms. The initial objective is to understand the events that have resulted in the current distribution of radionuclides near tank BX-102. The documentation of a significantly large (91,600 gal) release of metals waste at BX-102 in 1951 and the identification of a vadose zone uranium-238 plume near BX-102 provide a unique

opportunity to investigate flow and transport processes responsible for the timing and extent of migrating tank waste. New knowledge from these investigations will also lead to improved estimates and predictions of the spatial and temporal distributions of important non-gamma emitting radionuclides (e.g., technetium-99).

Numerical subsurface flow and transport simulators will be used to test alternative vadose zone conceptual models that can plausibly link the 1951 overfill event with the lateral transport exhibited by the contemporary uranium-238 distribution. In particular, the investigation will focus on the effect of sloping sediments in the context of: 1) discrete continuous layers within the H2 lithologic unit, 2) local anisotropy, and 3) bulk or apparent anisotropy.

D.4.2.1.2 Geology. The overfill event and subsequent waste migration occurred in two gross hydrostratigraphic units: the backfill and the H2 unit (Khaleel et al. 2001). The base of the BX tank farm was excavated in the Hanford formation to a depth of approximately 37 ft (11.28 m) bgs with a one percent slope down to the north to accommodate the sequence of gravity-fed, cascading tanks. Although the base of the tank farm was undoubtedly compacted by heavy machinery operating around the tanks, there is no evidence of uranium accumulation on the tank farm base or transport along the engineered 1% downslope to the north. In fact, the shallowest uranium-238 concentrations are found at 43 ft (13.11 m) bgs, approximately 6 ft (1.83 m) deeper than the tank base at the bottom of the backfill in the H2. Thus, the focus of this study is on the H2 layer.

The gross geological interpretation of the H2 unit did not identify any distinct, continuous intervening layers, but there is evidence of thin (1 to 10 cm) silty, fine sand layers with varying degrees of continuity within WMA B-BX-BY. A re-examination of drillers logs, lithologic logs and, where available, geophysical logs from eight boreholes/wells (not including the dry boreholes) within and surrounding the WMA identified three silty fine sand intervals subdividing the upper Hanford formation H2 unit sand at approximately 75 ft (22.86 m), 100 ft (30.48 m) and 120 ft (36.58 m) depths in well 299-E33-45. Reasonable correlations could be made for the 75 ft (22.86 m) and 120 ft (36.58 m) intervals in the majority of the surrounding wells, whereas the 100 ft (30.48 m) interval appeared to be a less distinct, localized feature. With this data set, the average dip was calculated to be approximately 3% (1.5 to 2 degrees) to the north-northeast. The structural attitude of the two subsurface intervals (i.e., 75 ft [22.86 m] and 120 ft [36.58 m]) is the same as at the land surface (surface topography) which dips approximately 1.5 to 2 degrees to the north-northeast. This consistency in bedding structure suggests that the underlying shallow zone deposition may be related to the same depositional forces and features that created the larger scale remnant surface topography (in this local region there is dip toward the north into a paleochannel), i.e., the ancestral cataclysmic flood/paleo Columbia River channels.

The lack of explicit stratigraphic features controlling lateral transport within the H2 lithologic unit is consistent with observations of lateral solute migration resulting from discontinuous small scale laminations and lenses in field experiments in Hanford sands (including the Sisson and Lu site, which is also in the 200 East Area; Gee and Ward 2001). These small-scale features are not discernible in continuous cores or with standard characterization techniques. Aqueous fluids have been observed to move downdip along these thin (< 1 cm) laminations until the lamination ends or a weakness is encountered. At that point, the liquid moves downward until another lamination is encountered and the process is repeated. Local anisotropy within the background

sands and within the fine silty sand laminations is very weak, <1.5. From a modeling perspective, the laminations are subgrid features that can only be accommodated through an upscaled or bulk anisotropy.

Net infiltration through the undisturbed land surface is estimated at 0.01 to 5 mm/yr depending on vegetation type, and at 5 tp 10 cm/yr through land surface disturbed by tank farm construction (Fayer et al 1996). Large discharges of aqueous fluids from cribs and trenches have also occurred in the WMA B-BX-BY area. These could have produced substantial alteration to natural moisture regimes, and thereby affected the behavior of the BX-102 spill. Elevated concentrations of uranium in the vadose zone near BX-102 persist to this day, and are sometimes correlated with distinct silt layers with elevated moisture content (cf. logs of borehole 299-E33-45).

D.4.2.1.3 Issues for Flow and Transport Modeling. The purpose of the present study is to determine the mechanisms and conditions that gave rise to such pronounced lateral flow effects observed near tank BX-102 and other locations in WMA B-BX-BY. Two basic issues need to be addressed: 1) what causes lateral diversion on such large scales, > 20 m, and 2) what causes the solutes to persist throughout the sedimentary profile, and especially at certain distinct layers, and prevents them from simply being flushed away by continuous seepage from ambient infiltration. Answers to these questions could help understand the present distribution and likely future behavior of contaminants.

While the spatial pattern of uranium-238 indicates a source at the southeast edge of BX-102, the highest uranium-238 concentrations were measured at deeper locations in boreholes that were not adjacent to BX-102. This implies that the uranium-238 was mobile during the initial migration away from BX-102. This behavior can be contrasted with strongly sorbing contaminants such as cesium-137, which are typically found close to the source with concentrations diminishing with distance from the source. After approximately 50 years of residence, the stability of uranium-238 at relatively shallow depths (Myers 1999) would seem to indicate that it has been immobilized in or on the solid phases. At an ambient moisture content of approximately $\theta = 5\%$ that was observed in the subsurface near BX-102 down to approximately the 64 m depth, estimated net infiltration of $u_{in} = 5 - 10$ cm/yr translates into a pore velocity for solute travel of $v = u_{in}/\theta = 1 - 2$ m/yr. This suggests that non-reactive solutes introduced in 1951 should no longer be found at shallow horizons.

The observation of substantial lateral migration of solutes raises a number of questions:

- How much of this effect is due to a broadening of the plume as it descends, from effects such as capillarity, dispersion, and molecular diffusion?
- How much of the lateral migration is due to advective displacement, i.e., due to flow and transport that is offset from the vertical direction?
- What is the nature of plume displacement and broadening?
- Do these effects occur throughout the sediments, or are they primarily caused by flow processes that are associated with specific discrete layers?

Pronounced lateral flow effects have frequently been seen at Hanford in fluids leaked from tanks, and have also been observed in controlled and carefully instrumented injection experiments (Sisson and Lu 1984; Rockhold et al. 1999; Gee and Ward 2001). Figure D.91 shows field observations following the Sisson and Lu (1984) injection experiment. Increases in moisture content are seen to propagate away from the injection point in discrete layers, but this does not necessarily imply that lateral moisture migration preferentially occurs in those layers. It is also possible that moisture migrates through a larger more dispersed volume, and that larger moisture contents in certain layers simply arise from accumulation of descending moisture. These two alternative conceptual models are sketched in Figure D.92.

Figure D.92 is highly simplified and schematic, and ignores other important hydrogeologic features. For example, layers in the Hanford sediments may be dipping, and lateral migration could be enhanced in the downslope direction. In addition to discrete layers that are sufficiently thick to be visible in borehole logging, there are fine layers and laminations down to cm and mm-scale. Small-scale layering can cause strong anisotropy, giving rise to large hydraulic conductivity in the direction parallel to bedding, and small conductivity perpendicular to bedding. The anisotropy is expressed as the ratio of (sub-)horizontal to (sub-)vertical hydraulic conductivity, $a = K_h/K_v$, and may be a function of moisture tension.

Figure D.91. Observed Water Content Distribution Following the Sisson and Lu Injection Experiment along a North-South Transect (from Rockhold et al. 1999)

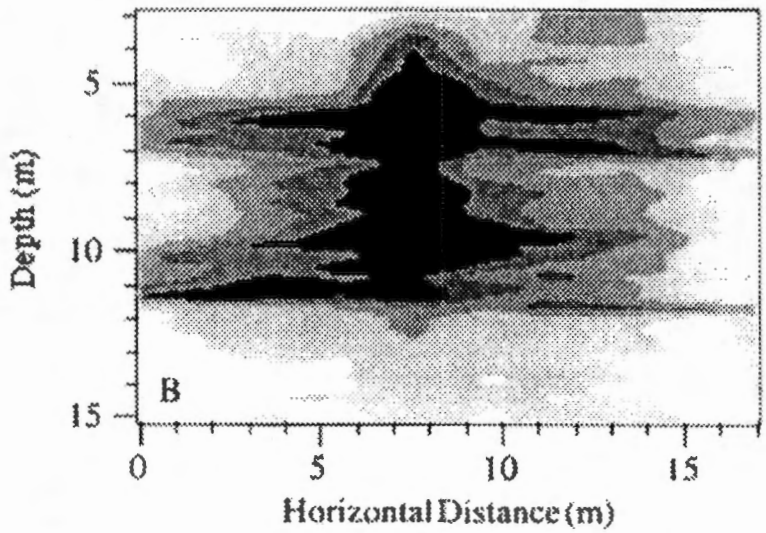

Figure D.92. Alternative Conceptual Models for Lateral Moisture Migration in a Layered Medium

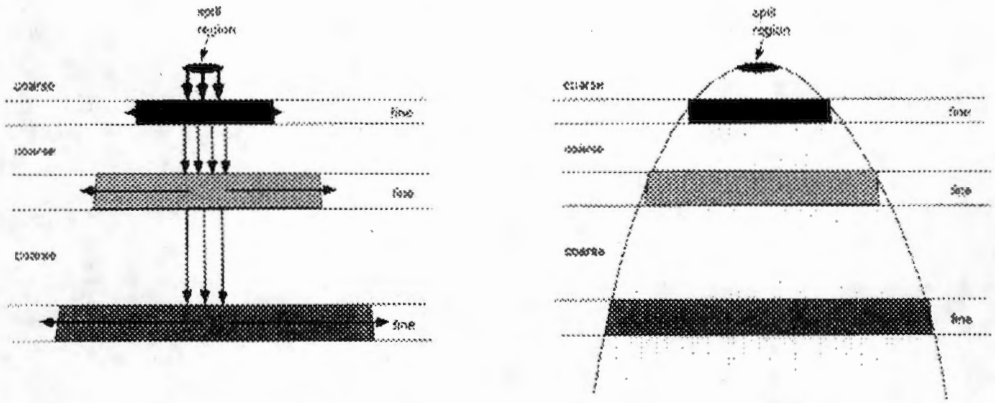

(a) (b)

Figure D.92 (a) shows a combination of downward migration in coarse layers, combined with lateral flow in fine layers. Different shading is intended to indicate different moisture contents. Figure D.92 (b) shows a situation where moisture R migration occurs in a more volume-averaged manner, but moisture accumulation is concentrated in fine layers.

The objective is to develop mathematical models that use existing information for hydrogeologic conditions and parameters to reproduce observed flow and transport behavior in the field. The main parameters determining unsaturated flow behavior are the relationships between moisture content, hydraulic conductivity, and capillary pressure. No measurements of soil moisture characteristics are available for the sediments in the B, BX, and BY tank farms. However, there are data sets for samples from the vicinity of these tank farms that can be used as surrogates (Khaleel and Freeman 1995; Khaleel et al. 2001). Recent data from the nearby Sisson and Lu injection site Vadose Zone Transport field study were also made available and have been used for this study. One fundamental limitation is that moisture tension and hydraulic conductivity characteristics are typically measured on laboratory specimens of small size (e.g., a few inches). Applicability of such measurements to the field scale is questionable. The models are built on the basis of laboratory-measured data, but the possibility of making scale-dependent modifications is left open if laboratory-scale parameters are unable to explain field observations leaving open the issue of scaling parameters to field-scale applications.

D.4.2.2 Definition of Test Case

Tank BX-102 has a capacity of 530,000 gal (2,006.3 m^3, Jones et al. 2001). Lateral migration of solutes spilled from BX-102 has occurred near the 22.9 m (75 ft) depth below ground surface (bgs), at an elevation where a strong spike of elevated moisture was seen in borehole 299-E33-45, drilled to the southeast of tank BX-102 (Section 3.0). The horizon in question occurs within the H2 unit, which is a thick unit described as coarse to medium sand. The large-scale hydrogeologic description does not include any differentiation at this depth, but the drilling log for well 299-E33-45 indicates a "muddy very fine to fine sand unit" at 22.9 m depth bgs (Section 2.6.2.1.2). This unit has an approximately 3% slope towards the northeast, corresponding to an angle of 1.718°. Initial 2-dimensional work carried out in this study used a slope angle of 3° (Section D.4.2.5); new information made available during the course of the study suggested that the slope was close to 3%, and that value was used in the 3-dimensional

modeling work (Section D.4.2.7). Some of the units near tank BX-102 have larger slopes of from 10° to 20° or more. Data on stratigraphy near BX-102 are given in Table D.61.

Laboratory measurements of moisture contents on samples obtained during drilling of borehole 299-E33-45 provide important constraints for hydrogeologic properties and conditions. Moisture contents down to the 64 m depth are generally close to 5%, with larger values of 14 to 25% reported at specific silty horizons. Hydrogeologic data from the nearby Sisson and Lu site also provide useful constraints.

The data package for B, BX, and BY tank farms modeling described in Section 4.0 (Khaleel et al. 2001) includes an east-west geologic section that passes just north of tank BX-102. This section shows the H1 unit having a thickness of about 7 m and extending to 20 m bgs west of BX-102. The contact with the underlying H2 sand slopes upward going east, and H1 pinches out about 20 m east of BX-102. This section shows no indication of the muddy very fine sand associated with the observed moisture spike at 22.9 m bgs, and also shows no features at depths of 120 ft and 170 ft where additional moisture spikes were seen in borehole 299-E33-45. Elevated moisture content beneath 220 ft bgs correlates with the Plio-Pleistocene unit there.

Table D.61. Stratigraphic Sequence at B, BX, and BY Tank Farms

Unit	thickness (m)		to depth (m)	
	(a)		(a)	(b)
backfill	12.7	11.5	12.7	11.5
gravelly sand H1	6.3	0	19.	11.5
coarse to medium sand H2	58.7	40.3	77.7	51.8
slightly pebbly to very coarse sand H3	7.6	14.6	85.3	66.4
silty sand (ppu)	6.1	6.4	91.4	72.5
Ringold gravel/sandy gravel (ppl)	6.4	6.7	97.8	79.2

(a) section at X = 573648, Y = 137348

(b) from 299-E33-45 borehole log (Appendix B)

Very large uranium concentrations were measured in borehole 299-E33-45 at 75 ft bgs, and also deeper at 120 ft bgs (Appendix B).

Important issues for unsaturated flow and transport modeling relate to scale. Thin layers and laminations down to the cm-mm scale are capable of causing considerable enhancement of lateral flow as compared to downward flow. An analysis of layering anisotropy for the formations at the BX tank farm was performed (Gee and Ward 2001). Figure D.93 shows hydraulic conductivity functions for laboratory samples from sediments near the B, BX, and BY tank farms that were presented by Khaleel et al. (2001). These data were analyzed using the composite medium approximation (COMA) (Pruess 2002) to obtain insight into the possible magnitude of anisotropy. The COMA method is based on interpreting each of the samples in the hydraulic conductivity data set as representing a distinct layer, which gives an upper limit for the strength of such anisotropy. As seen in Figure D.93 and Table D.62, the data provided by Khaleel et al. (2001) yield rather weak anisotropy at ambient flow conditions (corresponding to a

hydraulic conductivity of 0.1 m/yr or 3.17×10^{-9} m/s), typically considerably less than one order of magnitude. These results may be due to the limited coverage of small-scale layering in the data set. The drilling report for 299-E33-45 (Section 3.0 and Appendix B) suggests that there are many thin layers, which were evidently not captured by the limited number of samples included in Khaleel et al. (2001). The analysis of solute transport in the sediments near BX-102 suggests that anisotropy may be considerably stronger than estimated from the data of Khaleel et al. (Section D.4.2.5.3).

Table D.62. Anisotropy at a Conductivity of 0.1 m/yr (3.17×10^{-9} m/s), Calculated with a COMA Model from Data Provided by Khaleel et al. (2001) for Different Stratigraphic Units

Formation	Anisotropy	P_{suc} (Pa)
Ringold	6.22	1.387e4
H1	3.04	2.439e4
H2	2.74	1.955e4
H3	2.45	2.306e4
silty sand	1.14	4.380e4

Another data set relevant for flow and transport at tank BX-102 provides laboratory measurements of characteristic curves for samples from the nearby Sisson and Lu injection site (Gee and Ward 2001). Figure D.94 shows hydraulic conductivity characteristics of these samples. For a base case model, data of sample 2-2225 was adopted for the sand units, while sample 2-2230 data were used to represent the silt layer near 23 m depth (Table D.63 and Figure D.95). A composite medium (COMA) representation for the sands was also explored, in which a certain fraction of vertical thickness was assumed to consist of (thin) silt layers. For most COMA calculations, it was assumed that 90% of vertical thickness had sand properties, while 10% correspondsed to tighter silt layers with properties of sample 3-0589 given in the WMA B-BX-BY data package (Table D.63; Khaleel et al. 2001). The resulting composite hydraulic conductivity functions are shown in Figure D.95. Anisotropy is seen to be rather weak at the hydraulic conductivities corresponding to ambient moisture conditions. Specifically, for K = 10 cm/yr we have an anisotropy a = 2.42 ($P_{suc} = 1.147 \times 10^4$ Pa), while for K = 1 cm/yr this increases to a = 10.2 ($P_{suc} = 1.514 \times 10^4$ Pa). Accordingly, the predicted lateral flow diversion under these conditions turns out to be weak also (Section D.4.2.5.1).

Figure D.93. Hydraulic Conductivity Functions for Different Stratigraphic Units from the WMA B-BX-BY Data Package (Khaleel et al. 2001)
The lines show correlations obtained for different laboratory samples. Horizontal and vertical hydraulic conductivities derived for a strictly layered COMA model are shown as symbols.

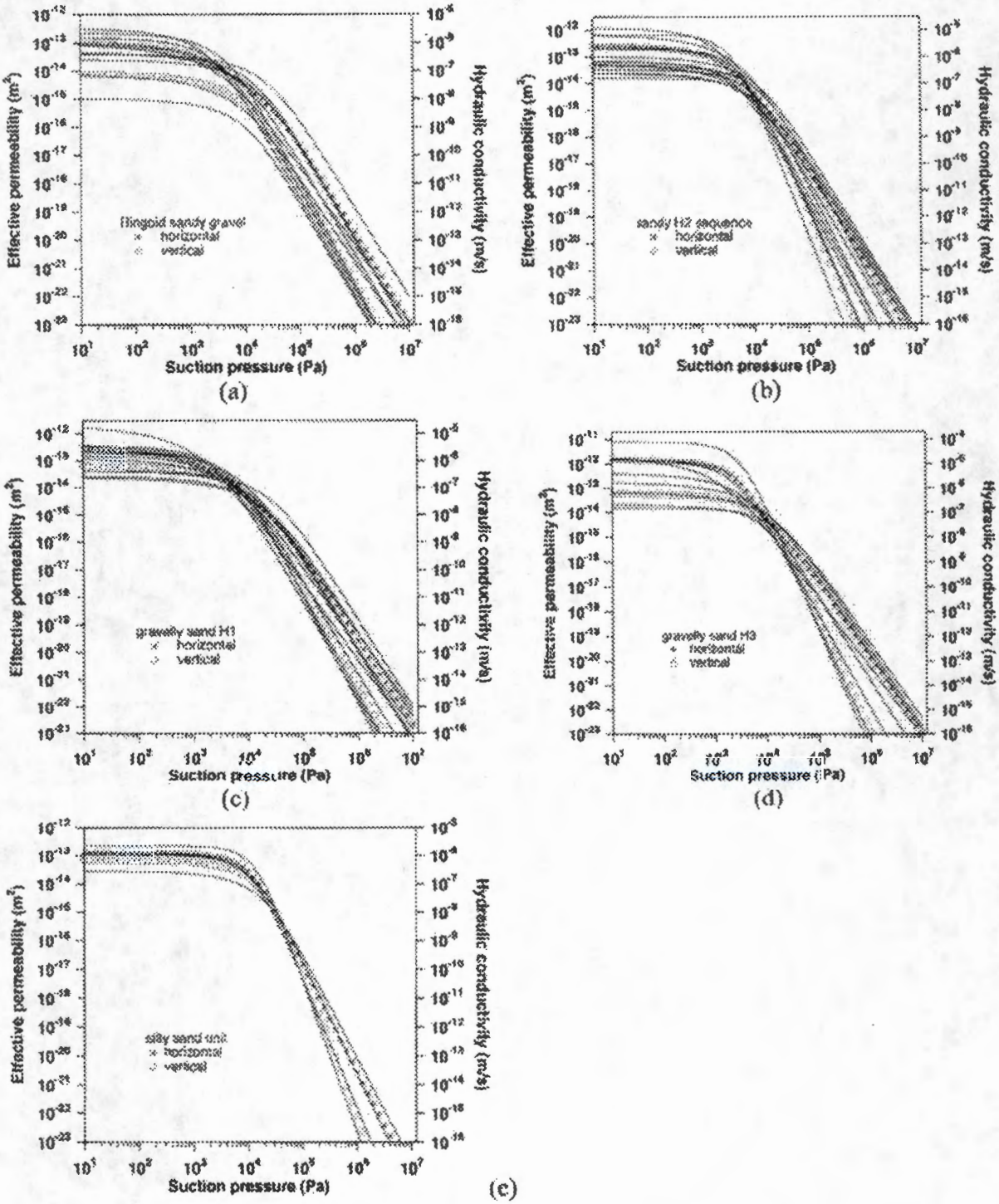

Figure D.94. Hydraulic Conductivities for 15 Samples from the Sisson and Lu Site

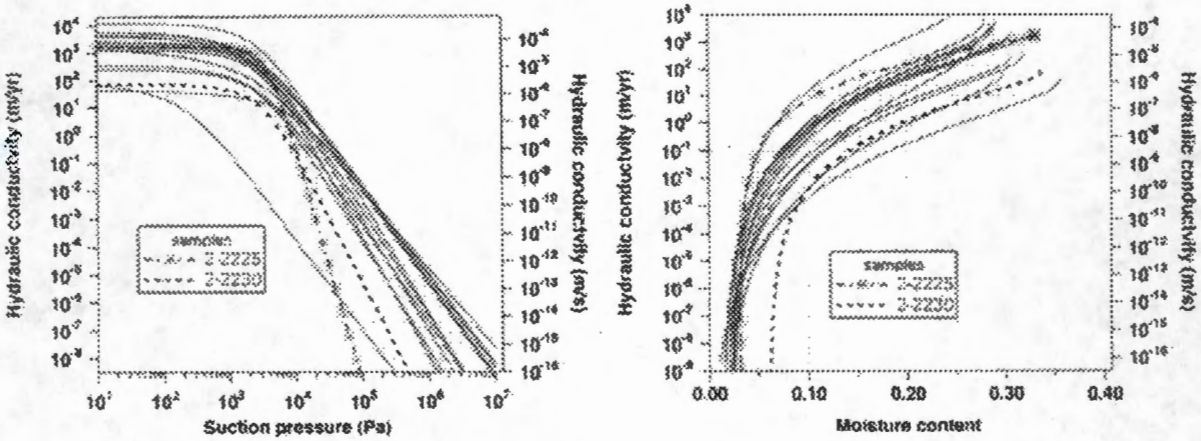

Table D.63. Formation Parameters for R-Z Model[a]

Parameter Facies	Absolute Permeability (m^2)	Porosity	Liquid Rel. Perm.		Cap. Pressure $\rho g/\alpha$ (Pa)
			m	S_{lr}	
sand (2-2225)	5.50e-12	0.3317	0.719	0.0953	3.922e3
silt (2-2230)	4.73e-14	0.4290	0.418	0.0625	1.720e4
sample 3-0589	2.20e-13	0.3366	0.515	0.1800	1.307e4

[a] m and α are the customary van Genuchten (1980) parameters; $S_{lr} = \theta_r/\theta_s$ is irreducible saturation.

Figure D.95. Hydraulic Conductivity Functions Selected for Base Case The COMA Curves Correspond to a Medium Composed of Sand 2-2225 and Silt 2-2230

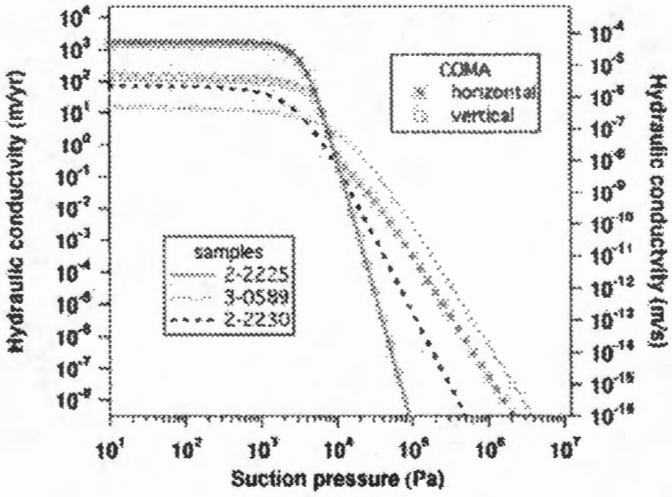

Attempts at detailed definition of layering heterogeneity and identification of hydrogeologic parameters for the units near tank BX-102 are ongoing. Given the current limitations of geometric and hydrogeologic data, fluid spills are studied in hypothetical model systems, which are specified to capture important features at the site of the BX-102 fluid spill. The purpose of this kind of analysis is to determine whether or not observations of fluid spill behavior near tank BX-102 are consistent with plausible subsurface features, and known mechanisms of flow. The fundamental variables to investigate are: 1) hydrogeologic properties of the layers, 2) the slope of the contact between layers of high and low effective hydraulic conductivity, and 3) rates and duration of fluid spills.

D.4.2.3 Modeling Approach

The fluid spill at tank BX-102 poses a 3-dimensional flow problem. Numerical simulations would be simplified greatly, and finer discretization with better accuracy could be employed, if the problem could be reduced to 2-dimensions. In order to model a 2-dimensional vertical section, it would be necessary to allocate a certain fraction of total spill rate to that section. However, such an allocation would be arbitrary, and would prejudice the interplay of vertical flow and lateral flow in different directions. As an alternative 2-dimensional approximation, a radially symmetric model may be considered. An advantage of such a model is that it actually represents a 3-dimensional volume, and no arbitrary assumptions about allocating a fraction of total spill rate to the model need to be made. Unfortunately, however, important features of the flow system at tank BX-102 do not possess radial symmetry. This is obvious for the neighborhood of the spill point itself, which is believed to be near the perimeter of tank BX-102. Another feature that violates radial symmetry is the excavation and subsequent placement of backfill at the BX tank farm, which provides a steeply dipping linear feature, along which hydrogeologic properties change from those of backfill to those of undisturbed sediments. The aforementioned violations of radial symmetry occur at shallow depths. For an analysis that is focused on the fate of the spilled fluid and the solutes carried with it, there may still be merit in ignoring those violations of radial symmetry at shallow depths. A more serious limitation arises from the fact that the generally quite permeable sediments at the site contain numerous thin (i.e., decimeters to centimeters and less) textural layers, which are non-horizontal, inducing a downdip migration that cannot be captured in a radial model. The sloping contact between sands of higher and silts of lower absolute permeability is believed to play a significant role in causing lateral diversion of spilled fluid in the downslope direction. Depending on prevailing moisture tension, downward migrating fluid may enter a layer of small-saturated hydraulic conductivity only at small rates, or may remain largely confined to finer-grained layers and advance into the coarser material below only with considerable delay and at small rates due to capillary barrier effects.

In spite of these features, which violate radial symmetry, it is believed that important insights into flow behavior at tank BX-102 can be gained from a radial flow model. A 2-dimensional radial (R-Z) model is a convenient and computationally efficient setup within which to explore flow mechanisms, and examine the suitability of proposed hydrogeologic parametrizations to produce lateral flow diversion (Section D.4.2.4). Effects of sloping layers are studied in 2-dimensional vertical section models. From the surface downward, the first extensive silt layer that has been recognized and may be implicated in lateral flow diversion occurs at a depth interval from approximately 22.7 to 23.0 m bgs in well 299-E33-45.

There are several processes that could amplify lateral flow, including salinity-driven redistribution of moisture towards the plume, moisture migration towards the plume due to gradients in surface tension, and moisture migration due to osmotic effects. Salinity of the aqueous phase in tank BX-102 was considerable; waste fluids contained 0.5 lb/gal uranium and were approximately 2.5 molar carbonate. (Table D.4.2.4 of RPP-7389 lists carbonate much lower, as 0.6 mol/l). The former translates into approximately 60 g/L and the latter 150 g/L. Other solutes were present as well, so that salinity appears to have been significant, with fluid density and viscosity quite different from water. However, a considerable fraction of solids may have precipitated (Jones et al. 2001), so that the salinity of the leaked fluid may have been less.

The simulations reported below were carried out with the TOUGH2 code, using the EOS9 fluid properties package (Pruess et al. 1999). Salinity effects were neglected and fluids were modeled with density and viscosity properties as for pure water ($\rho = 999.2$ kg/m^3 and $\mu = 1.136 \times 10^{-3}$ Pa-s at assumed conditions of T = 15 °C, P = 1.013 bar). The gas phase is considered a passive bystander at constant pressure, i.e., a Richards' equation approximation is used. Non-isothermal effects are ignored. All calculations done so far assume that the spill occurred at a constant rate over a 3-week period.

Molecular diffusivity of aqueous solutes is of order 10^{-9} m^2/s (de Marsily 1986), and in partially saturated porous media is smaller due to saturation-dependent tortuosity effects. At the rather dry conditions prevailing in the Hanford vadose zone, effective diffusivity in the aqueous phase is expected to be below 10^{-10} m^2/s. The length scale of diffusive penetration over time t can be estimated as $y = \sqrt{2Dt}$, which for t = 50 yr and D = 10^{-10} m^2/s gives y ~ 0.56 m. This indicates that broadening of solute plumes from molecular diffusion will be insignificant in single-porosity media. Diffusive effects may become significant in multiple-porosity (multi-region) media, where they can contribute to solute exchange between regions with mobile and immobile water, causing potentially large dispersion of solute plumes (Gwo et al. 1996). All simulations reported here used a single-porosity description, and molecular diffusion was neglected.

D.4.2.4 Two-Dimensional R-Z Model

A first 2-dimensional R-Z model was specified to extend from the ground surface to a depth of 40 m. Vertical grid resolution was 1 m down to 7 m bgs, followed by increased spacing of up to 3 m, then finer grid spacing of 0.3 m was used in the vicinity of the silt layer that extends from 22.7 to 23 m bgs. Beneath the silt layer, the grid resolution is gradually coarsened, and the grid ends at 40 m bgs with a layer thickness of 5 m. Free drainage conditions are employed at the bottom boundary of the model. Radially, the model also extends to 40 m, using 40 increments of 1 m each. The model was run in two variations: 1) assuming the sand to be homogeneous, and 2) accounting for the presence of sub-grid scale layering in the sand by means of a composite medium approximation (COMA) (Pruess 2002). For the COMA model, it was assumed that 90% of vertical thickness of the sand has properties as shown in Table D.63 for sample 2-2225, while 10% of vertical thickness is made up of tighter silt layers. For the latter, properties were assumed as given for sample 3-0589 (Table D.63), leading to COMA characteristic curves as shown in Figure D.95.

Initial conditions prior to the fluid spill were obtained by running the model to gravity-capillary equilibrium for an applied net infiltration rate of 10 cm/yr at the land surface. Simulated

moisture contents are virtually identical for both models (Table D.64), and agree very well with moisture contents measured on samples obtained during drilling of well 299-E33-45.

Table D.64. Simulated Moisture Content for 10 cm/yr Net Infiltration

Facies Model	Sand	Silt
1) homogeneous	5.1 %	24.5 %
2) COMA	5.1 %	24.6 %

The fluid spill was modeled by discharging 346.7 m^3 (91,600 gal) of water at a constant rate over a period of three weeks. The source of the spill was placed at a depth of 4.5 m, in the center of the radially symmetric model. A conservative tracer was added to the spilled fluid to be able to track it. Net infiltration occurs at 10 cm/yr at the ground surface. After three weeks, the spill is terminated, and the flow system is simulated for a period of 50 years, so that final conditions correspond to the year 2001. Results are given in Figure D.96 through Figure D.98.

Figure D.96 shows total rates of fluid flow across three different horizons for the model with homogeneous properties for the sand. The topmost horizon is at 5 m bgs, immediately beneath the spill point, while the horizons at 22 and 24 m bgs are just above and below the silt layer. It is seen that response from the spill at the 22 m horizon occurs with a time delay of approximately 4×10^5 s, and a slightly larger delay at the 24 m horizon. Response to terminating the spill is almost instantaneous. The behavior of the COMA model is significantly different, (Figure D.97). There is a noticeable delay of water flow even at the 5 m horizon, and the delay at the 22 m horizon is approximately 1.3×10^6 s, much larger than for the homogeneous model. The response to cessation of the spill after three weeks (1.8144×10^6 s) is also delayed, as flow rates continue to increase at the 22 and 24 m levels. Peak flow rates occur after 2.7×10^6 s at 22 m depth and after 2.9×10^6 s at 24 m depth. Peak flow rates are considerably reduced in magnitude and amount to only slightly more than half of the peak flow rate at 5 m depth. This behavior is consistent with what is expected from stronger lateral flow effects in the COMA model, which would delay and dampen peak flow rates.

Flow rates of spilled fluid for both models are shown in (Figure D.98) at the 22 and 24 m horizons. It is seen that the arrival of spilled fluid is delayed in the COMA model, and that its peak flow rate is somewhat reduced also. It was expected that the reduction of total flow rates in the COMA model (Figure D.97) would enhance capillary barrier effects at the silt layer, and would produce an additional retardation effect between the 22 and 24 m horizons. The results as shown in Figure D.98 indicate that the COMA model indeed gives rise to more retardation in absolute terms (larger Δt between the breakthrough curves at 22 and 24 m), but the effects are not large, and the ratios of breakthrough times at 24 and 22 m are similar for both models. The peak flow rate of spilled fluid in the COMA model occurs after 2.85×10^6 s (32.9 days) at 22 m depth, while at 24 m depth it occurs after 3.05×10^6 s (35.3 days). This modest delay is due primarily to increased fluid storage in the silt layer under wetter conditions. Capillary barrier effects (lateral flow diversion) at the silt layer are weak, due to the weak contrast in hydraulic conductivities at the relevant suction pressures of order 10^4 Pa.

Figure D.96. Simulated Water Flow Rates Across Different Horizons for the Model with Homogeneous Properties for the Sand

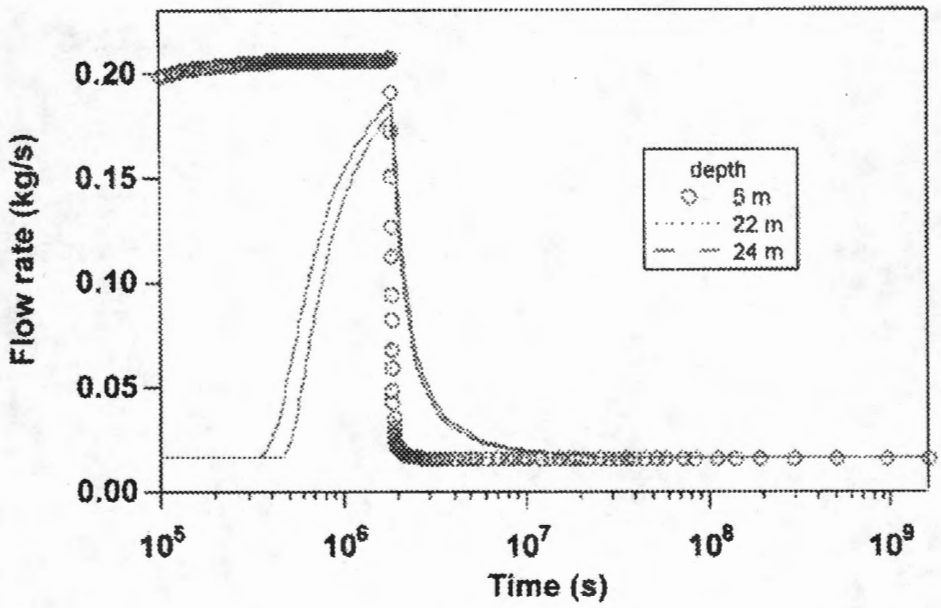

Figure D.97. Simulated Water Flow Rates Across Different Horizons for the COMA Model that Includes Silt Layers Amounting to 10% of Vertical Thickness in the Sand

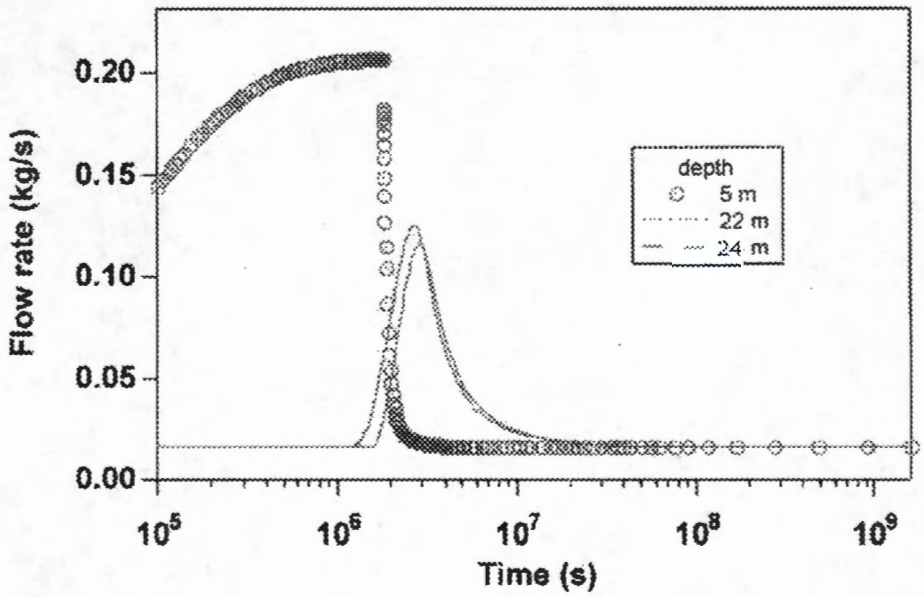

Figure D.98. Simulated Flow Rates of Spilled Fluid Across Different Horizons for the Model with a Homogeneous Sand and for the COMA Model

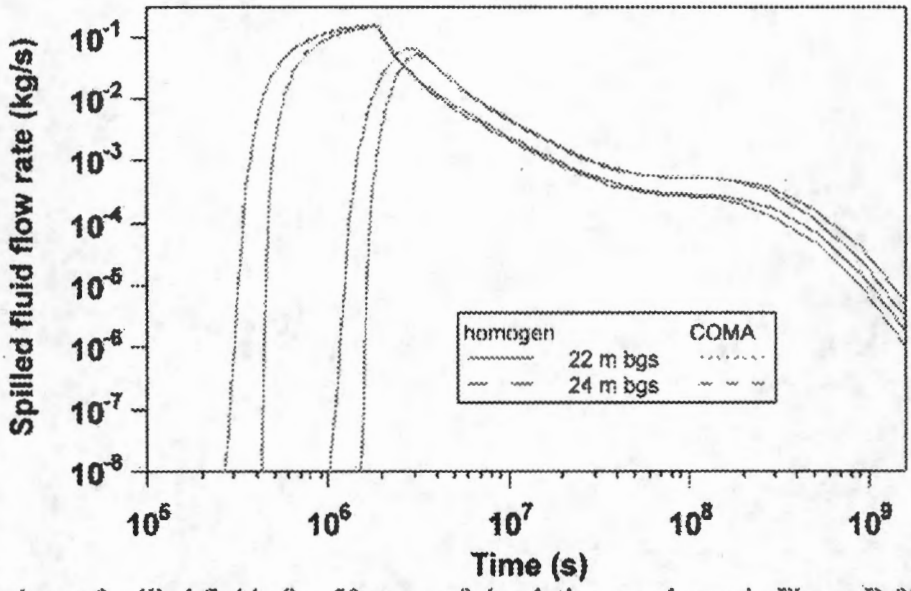

Mass fractions of spilled fluid after 50 years of simulation are shown in Figure D.99. At this time, all moisture contents have returned to their original (pre-spill) values, but considerable amounts of spilled fluids remain in the system. The COMA calculation (Figure D.99b) shows more lateral spreading and a somewhat slower downward progression of the plume. The break provided by the silt layer is insignificant in either case.

Figure D.99. Mass Fractions of Spilled Fluid after 50 Years for the Model with a Homogeneous Sand (a) and for the COMA Model (b)

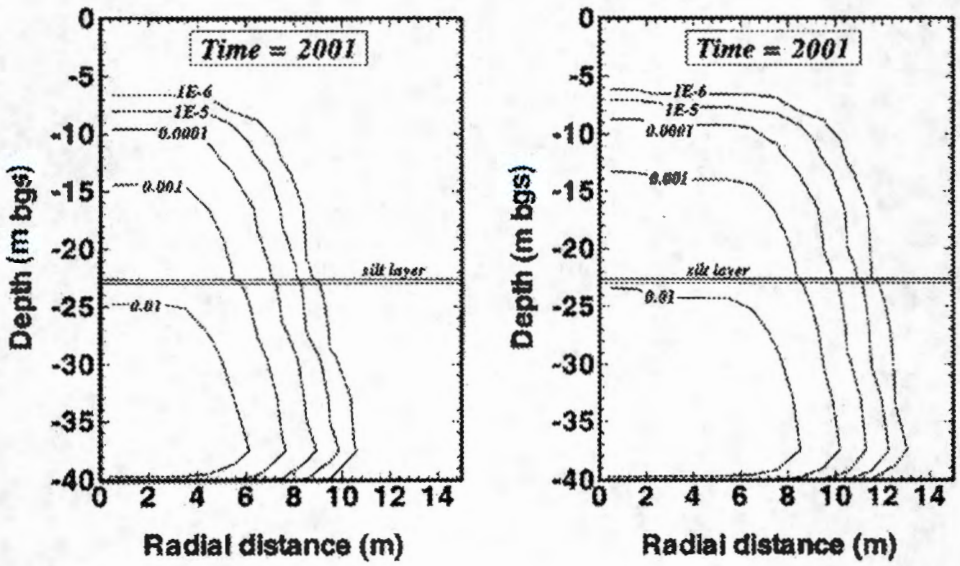

As was discussed above, the calculation presented here ignores the slope of the silt layer at 22.7 to 23.0 m depth, and therefore will underestimate the effect of that barrier. However, if the slope of that layer indeed is as small as the most recent estimate of 3°, then that layer may not have a significant impact. It does not seem possible that retardation and liquid holdup at that layer could be greatly enhanced. It appears that a much greater contrast in hydrogeologic properties between the sand and silt layers and/or considerably larger slope would be needed to generate substantially stronger lateral diversion.

D.4.2.5 Two-Dimensional Vertical Section

A 2-dimensional vertical section model was set up to study the possibility of lateral displacement of the moisture plume in the downslope direction upon descent. A 100 m (horizontal) by 60 m (vertical) section of 1 m thickness was modeled and subdivided with 1 m grid spacing, except that finer gridding of 0.3 m was used near the explicitly modeled silt layer in the depth interval from 22.7 to 23.0 m (Figure D.100). The entire section was tilted against the horizontal direction; two angles of $\alpha = 3°$ and 10° were explored (Figure D.101). The section is oriented from southwest to northeast, perpendicular to the observed steepest slope of the silt layer near the 23 m depth. Boundary conditions were net infiltration of 10 cm/yr at the top, free drainage at the bottom, and saturation profiles corresponding to steady flux of 10 cm/yr maintained at the left and right boundaries. Cases where net infiltration was reduced to 1 cm/yr over part of the section, corresponding to net infiltration in undisturbed sediments beyond the tank farm excavations, were also explored. These did not produce significantly different solute migration and are not further discussed in this report.

It is not possible to properly replicate the behavior of a fluid spill, which is intrinsically 3-dimensional, in a 2-dimensional section model, because the relationship between volume and surface area of the moisture plume will be different. Applying the same spill rate in a 2-dimensional as in a 3-dimensional model will give rise to larger moisture contents and water fluxes. The fluid spill was modeled in the 2-dimensional section by injecting water with a conservative tracer at 4.5 m depth over a 3-week period at a rate that produced a similar moisture regime as the 91,600 gal spill did in the R-Z model.

Figure D.100. Gridding used for 2-Dimensional Tilted Section

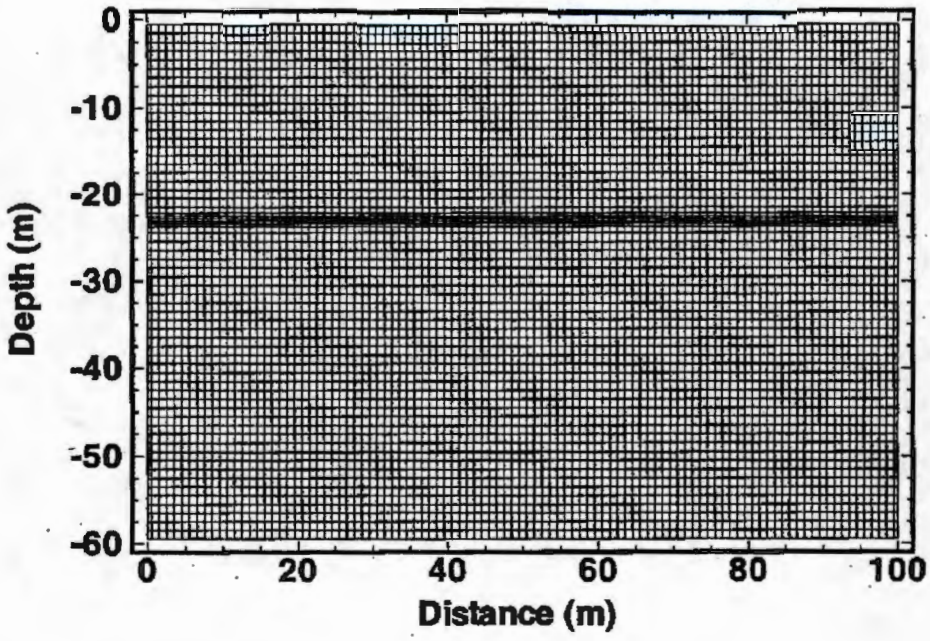

Figure D.101. Schematic of 2-Dimensional Section, Tilted by an Angle α Against the Horizontal Direction

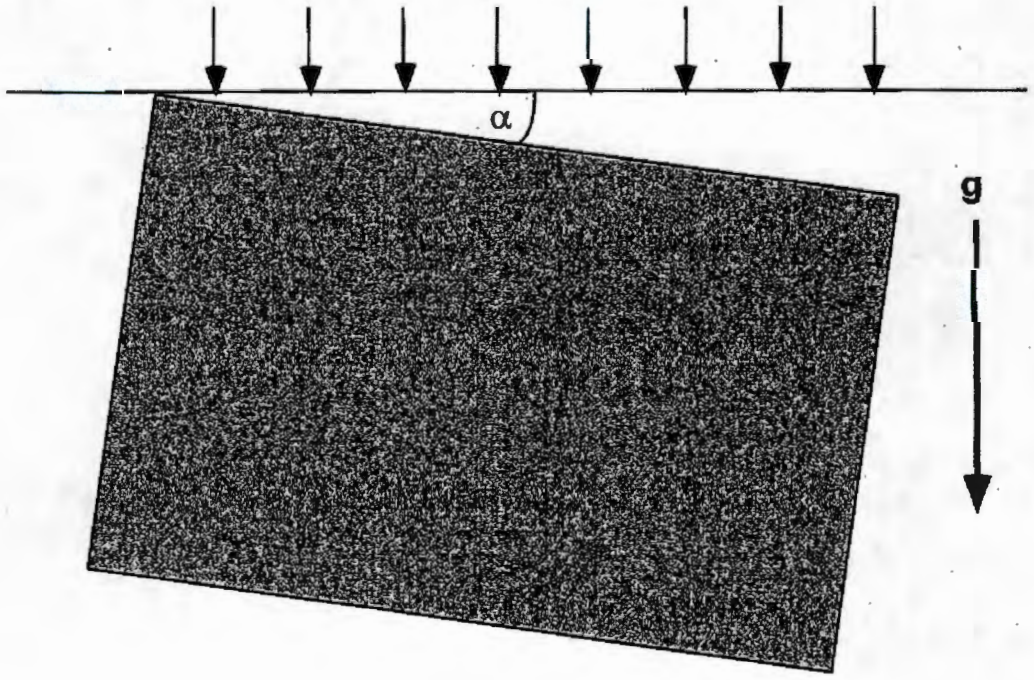

D.4.2.5.1 Exploratory Calculations. Initial exploratory calculations used a smaller section of 80 m length and 40 m depth. The composite medium description of the medium and the hydrogeologic properties of the explicitly modeled silt layer were the same as in the R-Z model. Results for moisture contents and mass fractions of spilled fluid at different times and tilt angles of 3° and 10°, respectively, are given in Figure D.102 through Figure D.105, where injection was made at 4.5 m depth and 40 m lateral distance. It is seen that increased slope angle results in more plume spreading and more downdip migration. The moisture plumes show that the explicitly modeled silt layer provides very little lateral diversion. Also note that the moisture plume dissipates very quickly, in a matter of weeks. At later time, water flows return to the pattern from ambient infiltration, and conservative solute is passively carried along in the ambient flow field. Taking the contour for a mass fraction of 0.001 as the extent of the solute plume, lateral extent of the plume after 50 yr at the depth of the silt layer is estimated as 19 m for 3° slope and 23 m for 10° slope. Downdip migration as measured by the leading edge of the 0.001 mass fraction contour is 15 m for 3° slope and 28 m for 10° slope. The 10° numbers are approaching the range seen in field observations near tank BX-102, but the 3° values are too small. By visually identifying the centroids of the solute plumes, the deviation of the plume trajectory from the sub-vertical coordinate axis can be estimated as 11.3° and 34.4° for tilt angles of 3° and 10°, respectively, corresponding to angles of 8.3° and 24.4° against the true vertical.

The overall conclusions from the simulations discussed above are that: 1) lateral diversion and broadening of moisture and solute plumes are weaker than observed in the field, and 2) for the hydrogeologic conditions and parameters used here, the explicitly modeled silt layer provides very little lateral diversion. Instead, lateral flow occurs primarily from an overall anisotropy that is due to sub-grid scale layering. How can substantially stronger lateral flow be obtained? The simulations provide little support for the idea that lateral flow would primarily occur in specific recognizable layers. A more plausible hypothesis is that (sub-)horizontal-to-vertical anisotropy may be considerably stronger than assumed in the above models. Stronger anisotropy is discussed in Section D.4.1.

Figure D.102. Simulated Moisture Content in a Model with Layers Sloping at an Angle of 3° Slope

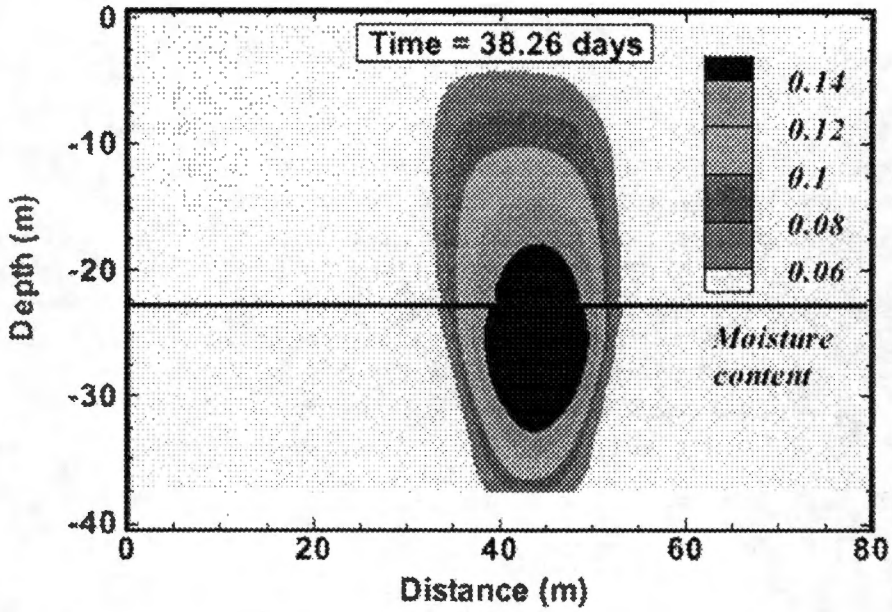

Figure D.103. Simulated Mass Fractions of Spilled Fluid after 50 years in the Model with 3° Slope

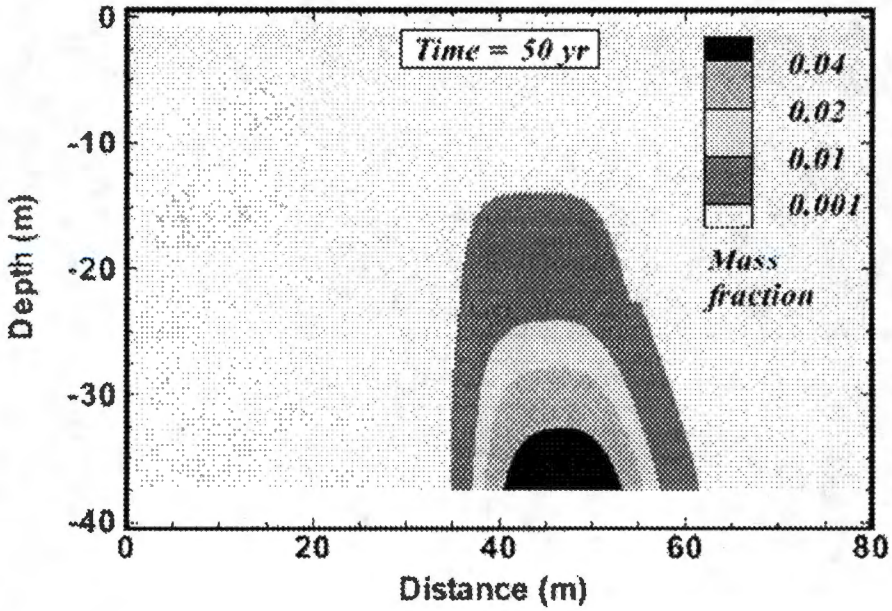

Figure D.104. Simulated Moisture Content in a Model with Layers Sloping at an Angle of 10°Slope

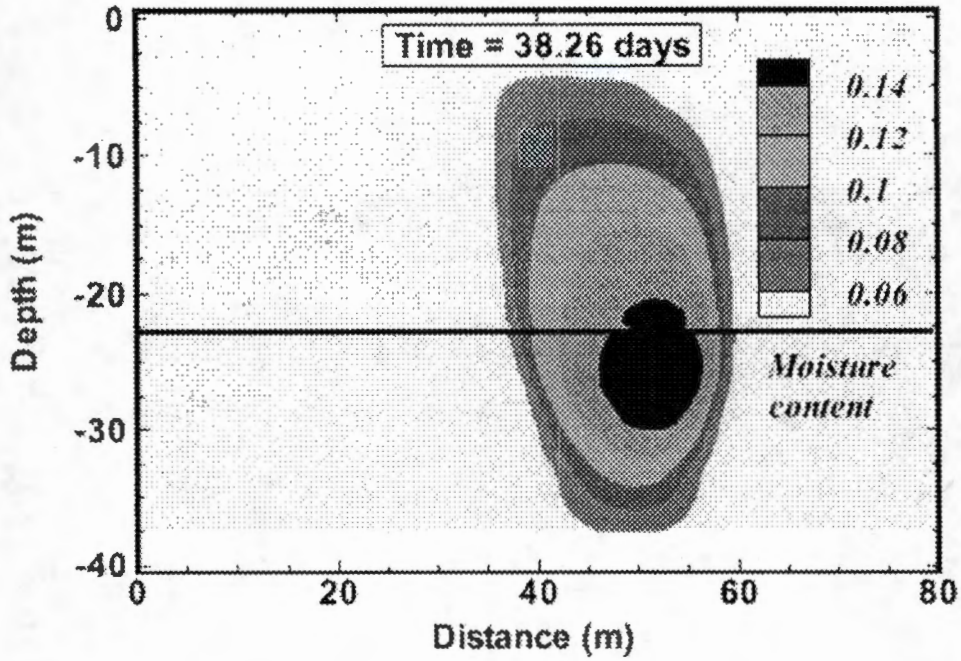

Figure D.105. Simulated Mass Fractions of Spilled Fluid after 50 years in the Model with 10° Slope

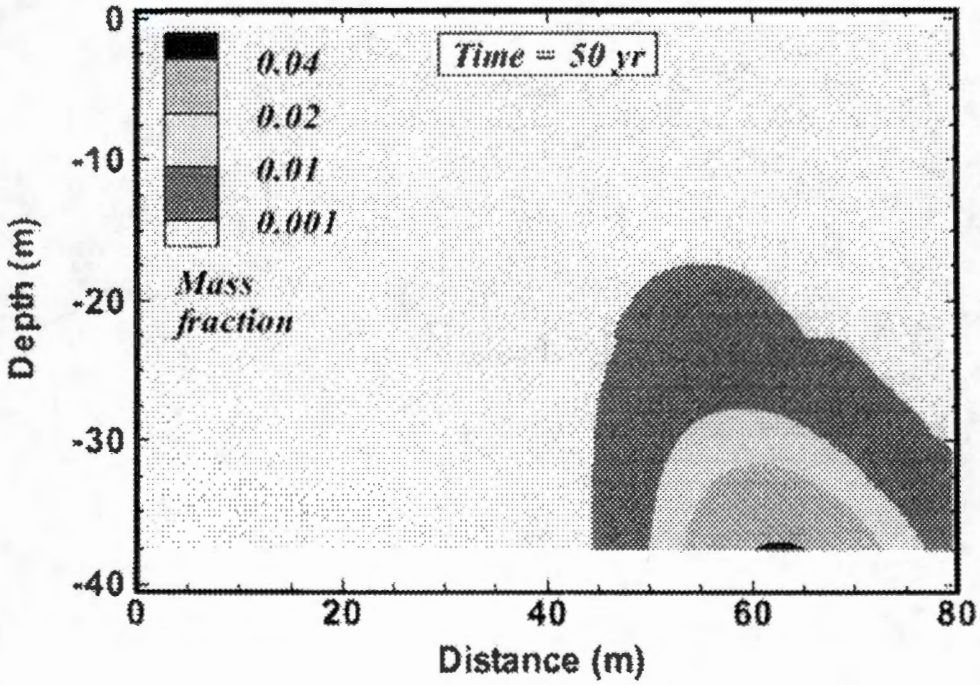

D.4.2.5.2 Model with Strong Lateral Anisotropy. The strength of anisotropy needed to obtain lateral diversion commensurate with observations can be easily estimated, as follows. Assuming that the hydraulic conductivity tensor is aligned with bedding, volumetric fluxes parallel and perpendicular to bedding are given by

$$u_h = K_h \sin\alpha \quad (5.1)$$

$$u_v = K_v \cos\alpha \quad (5.2)$$

where α is the tilt angle. As a rough estimate, it is considered that moisture migration should occur at a 45° angle with respect to the vertical, i.e., descending moisture plumes should be displaced sideways by as much as their downward migration. This requires that (sub-)horizontal and (sub-)vertical fluxes be equal, so that

$$a = K_h/K_v = \cot\alpha \quad (5.3)$$

This function is plotted in Figure D.106. Specifically, for a slope of 3°, an anisotropy of a = 19.1 is required. For a slope of 3%, corresponding to an angle of 1.72°, an anisotropy of a = 33.3 would be required. A possible approach would be to build a COMA model from individual hydraulic conductivity functions available in Hanford data sets in such a way as to obtain the desired anisotropy at a hydraulic conductivity corresponding to ambient infiltration flux, while also enforcing the constraint that vertical hydraulic conductivity corresponding to that flux should occur at a moisture content of 5%. Here, the simplest model that can be made consistent with field observations is pursued. The characteristic curves for sample 2-2225 continue to be used, and an anisotropy of 20 independent of moisture content is imposed. In order to achieve this anisotropy, either K_h can be increased or K_v can be decreased or a combination of the two. These revisions may be made by appropriate changes in $K_{s,h}$ and $K_{s,v}$, the saturated hydraulic conductivities in sub-horizontal and sub-vertical directions, respectively.

It was noted above that the $K(\theta)$ curve selected for the sands provides a hydraulic conductivity of 10 cm/yr, corresponding to the presumed ambient infiltration, at a moisture content of approximately 5%, in agreement with field observations. If K_v were reduced, a larger moisture content would be required to achieve a conductivity of 10 cm/yr. For example, reduction of K_v by a factor 20 would cause an increase to $\theta \sim 8$ %, which is ruled out by the field measurements. K_v is essentially fixed by the observed moisture content. To obtain an anisotropy of 20, K_h must therefore be increased by a factor of approximately 20, or slightly less if a small reduction in K_v, that would still be consistent with a moisture content near 5%, is considered. This requires $K_{s,h} \sim 110 \times 10^{-12}$ m^2 (~ 110 darcy) in the (sub-)horizontal direction, a value that seems unreasonably large. However, in the model, $K_{s,h}$ is merely a calibration parameter that is used to obtain the desired flow behavior and anisotropy for unsaturated conditions. Conditions remain unsaturated in the simulation so that $K_{s,h}$ is not actually engaged in the calculation, and no particular significance should be attached to its value. At ambient conditions of 10 cm/yr net infiltration, hydraulic conductivity in the vertical direction is 3.17×10^{-9} m/s, corresponding to an effective permeability of 0.317×10^{-15} m^2, or 0.317 millidarcy. For an anisotropy factor of 20, horizontal effective permeability is then 6.34×10^{-15} m^2, a value that does not seem unreasonably large.

Figure D.106. Horizontal-to-Vertical Conductivity Anisotropy Required for Moisture Migration to Occur at a 45° Angle with Respect to the Vertical, as a Function of Layer Slope

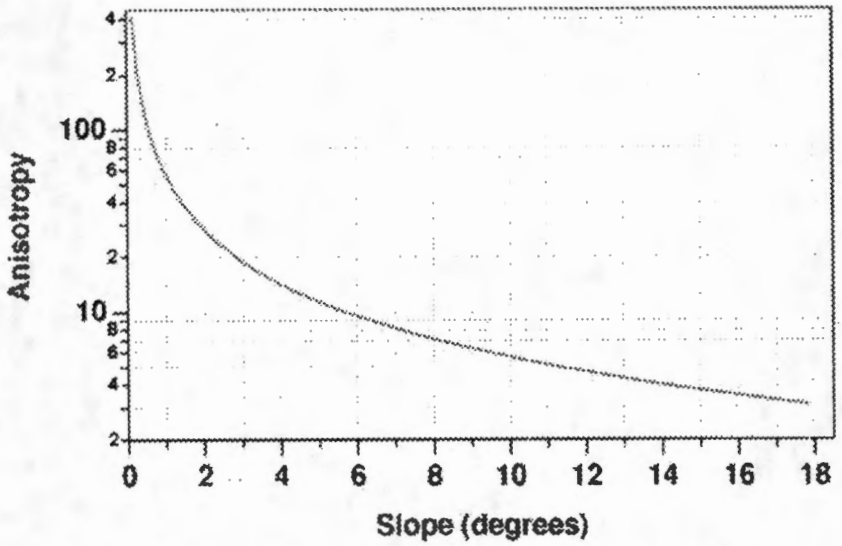

In practical applications, the K_S-parameter in van Genuchten's formulation (1980) is often interpreted as a fit parameter for describing unsaturated flow, and it may be considerably different from the true saturated hydraulic conductivity. Khaleel et al. (1995) examined the application of van Genuchten-Mualem relationships to unsaturated hydraulic conductivity at low water contents. Their analysis showed that, when K_S is adjusted to match unsaturated conductivities in the dry regime, saturated hydraulic conductivity may be overestimated by as much as two orders of magnitude.

Results for the case with anisotropy a = 20 independent of moisture tension are given in Figure D.107 through Figure D.111. The injection point was located at 4.5 m depth and at a distance of 21 m from the left boundary. It is seen that moisture and solute plumes now move along a trajectory that is approximately 45° away from the vertical, as expected. In addition, the plume spreading is enhanced relative to the earlier cases of weaker anisotropy, so that moisture contents decrease more rapidly (compare Figure D.107 with Figure D.102 and Figure D.104). Figure D.108 shows that substantial concentrations of spilled fluid migrate over lateral distances of 30 m in a matter of a few weeks. Figure D.109 was included to show that after some years, the moisture plume is completely obliterated, indicating that over most of the time period since 1951, solute transport occurred in essentially unaltered ambient flow fields. Mass fractions of spilled fluid after 8.65 years show a broad distribution that covers the region where strong signals from uranium in the spilled fluid were detected (Figure D.110). The explicitly modeled silt layer (22.7 to 23.0 m depth) provides an insignificant increment of lateral diversion, even with the enhanced horizontal conductivity. After 50 yr, corresponding to the year 2001, most of the spilled fluid has migrated to greater depth, due to the flushing action of infiltration at the land surface at a rate of 10 cm/yr (Figure D.111). Of course, if net infiltration were smaller less downward migration would occur.

The model with anisotropy a = 20 may be considered calibrated to field observations of moisture contents and solute travel. Simulated moisture contents for natural infiltration conditions remain unchanged when (sub-)horizontal conductivities are increased, and agree with observed values of approximately 5% throughout most of the section, and approximately 24% at the silt layer. Solute transport behavior is in general agreement with field observations, which suggests that solute moves comparable distance in lateral and downward directions. This calibration was achieved for a realistic value of 3° for layer slope, and using laboratory-measured characteristic curves (sample 2-2225), the sole adjustment being the introduction of an anisotropy ratio of 20.

One aspect of field observations not reproduced by the model is the persistence of solutes throughout the profile. Several possible effects may be considered to explain this. The model is anisotropic but essentially homogeneous, except for the single explicitly represented silt layer, so that all solute travels with volume-averaged velocities. In reality, there may be multi-region behavior, with water fluxes much smaller in some places than in others (e.g., at the base of the tank farm excavation were soil was compacted and concrete spilled), so that some of the solutes are subject to much less flushing action than others. Another possible hydrogeologic effect could be that net infiltration decreases towards the ambient value of 0.5 to 1 cm/yr away from the region with construction-disturbed land surface, slowing the downward flushing action. Persistence of solutes at shallower horizons may also involve chemical effects, such as precipitation, complexation, and sorption that could reduce the mobility of radionuclide species.

Figure D.107. Moisture Plume for Anisotropy a = 20 at 38.26 Days after Start of Injection The Injection Point was Located at 4.5 m Depth and at a Distance of 21 m from the Left Boundary.

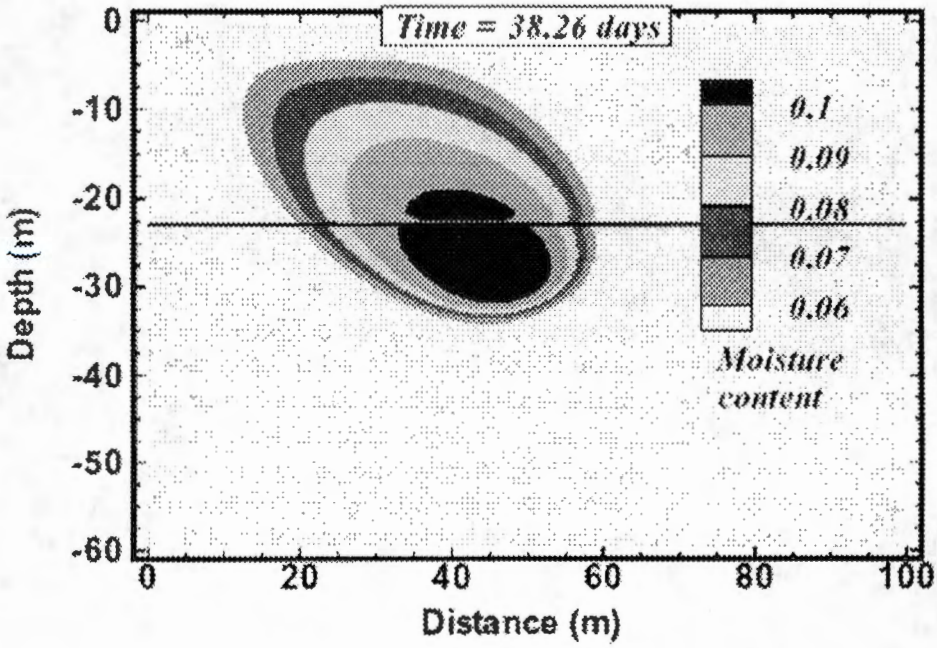

Figure D.108. Simulated Mass Fractions of Spilled Fluid after 38.3 Days for Anistotropy a = 20

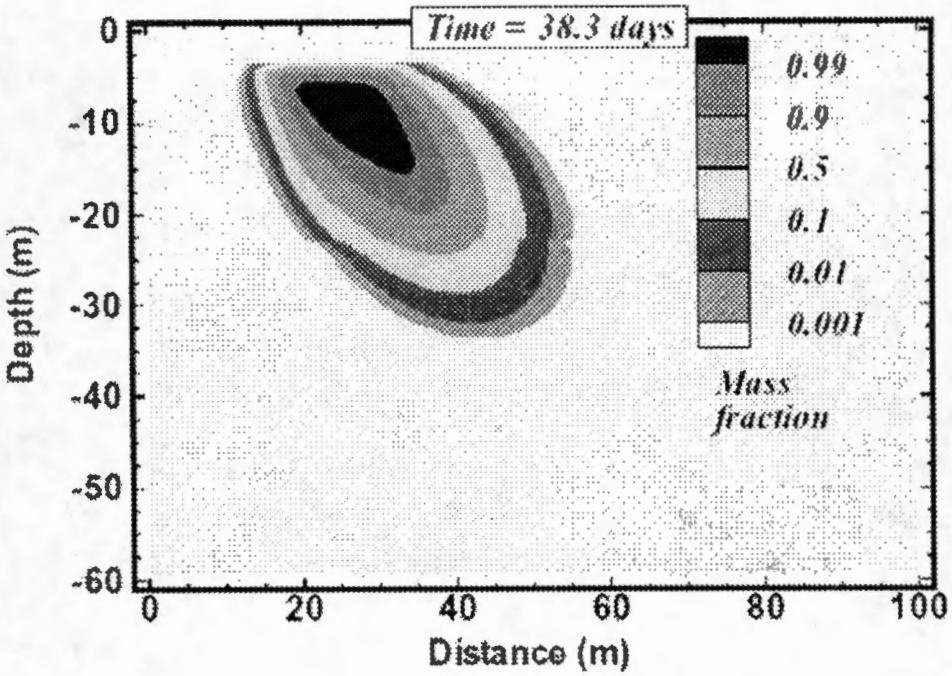

Figure D.109. Moisture Plume for Anisotropy a = 20 at 8.65 yr after Start of Injection

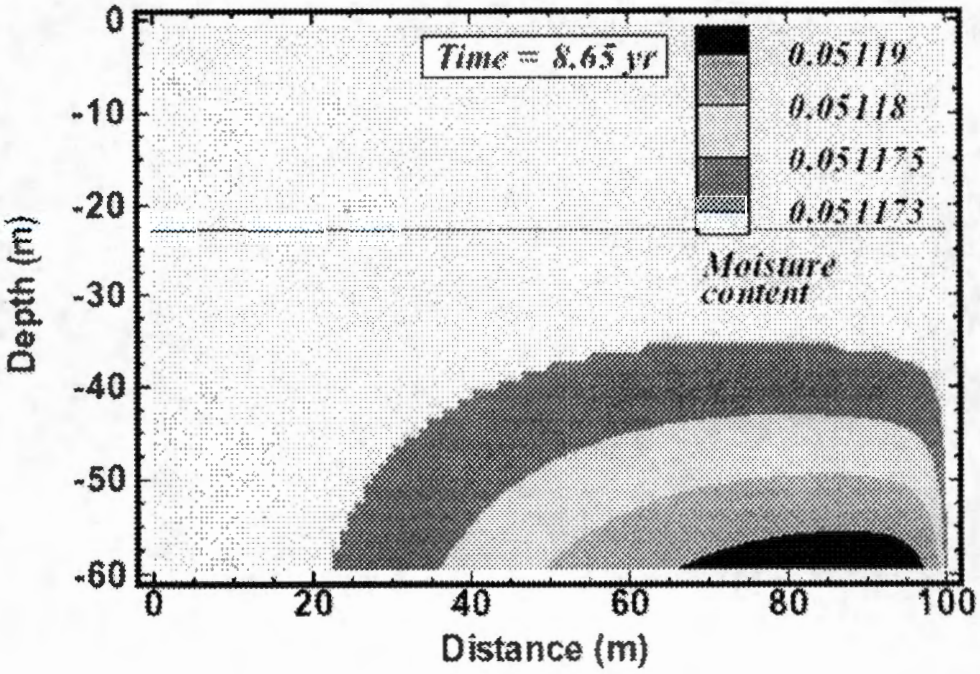

Figure D.110. Simulated Mass Fractions of Spilled Fluid after 8.65 yr for Anistotropy a = 20

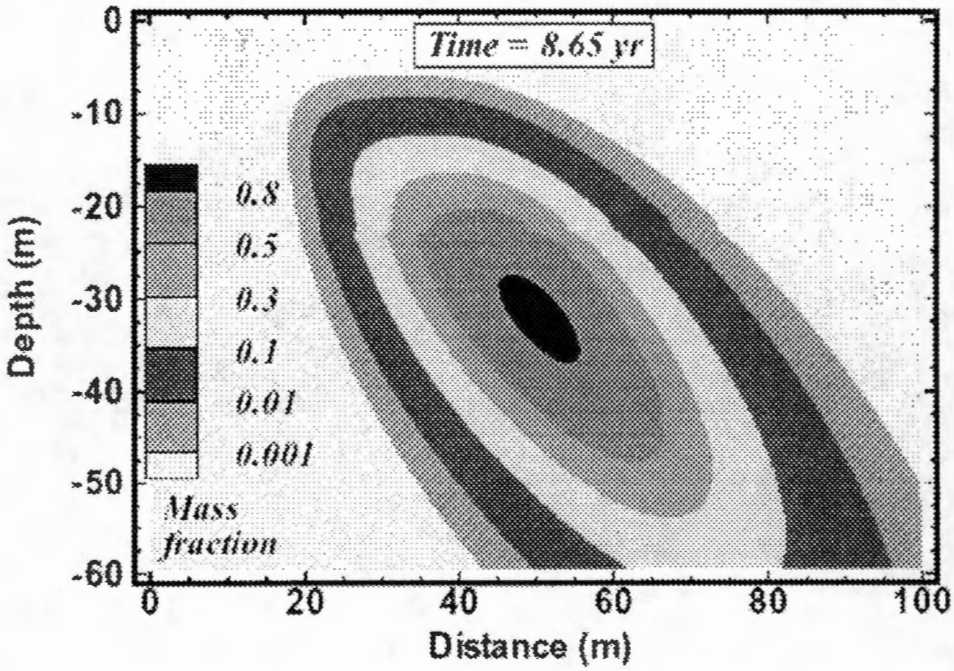

Figure D.111. Simulated Mass Fractions of Spilled Fluid after 50 yr for Anistotropy a = 20

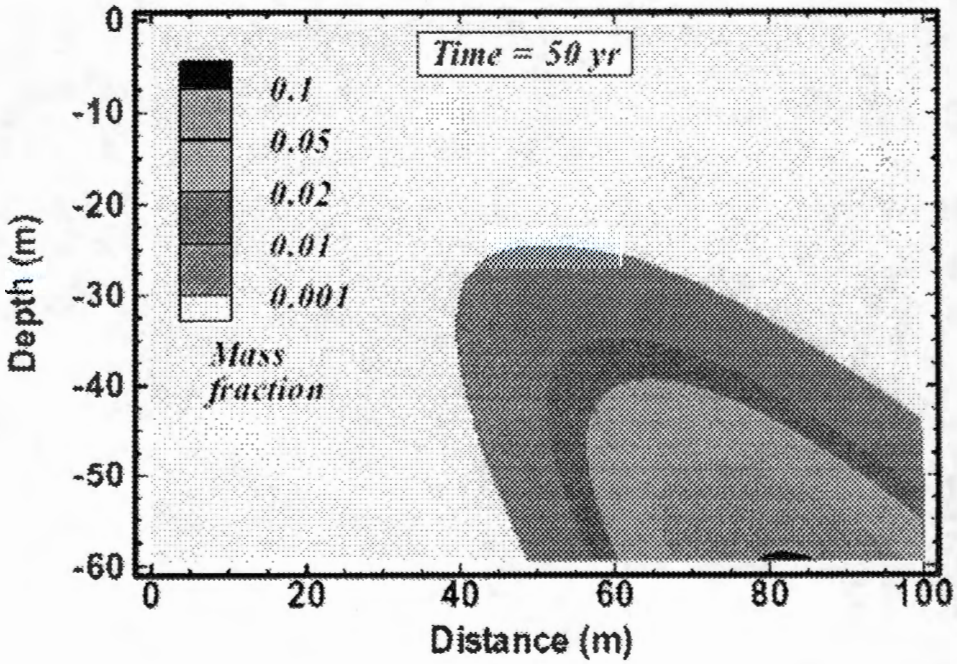

D.4.2.5.3 Model with Horizontal Layering and Strong Lateral Anisotropy. The strong anisotropy invoked in the preceding section in conjunction with sloping layers leads to trajectories of the moisture and solute plumes that are considerably offset from the vertical. The enhanced (sub-)horizontal hydraulic conductivity will also accelerate lateral plume spreading from capillary effects, and it is of interest to examine how much lateral migration can be induced by capillary effects alone, without an overall advective displacement from sloping layers. Accordingly, a 2-dimensional vertical section model identical to the one presented in Section D.4.2.5.2 was studied, but assuming that all layers are strictly horizontal. For the case with horizontal layering, injection was made into the center of the model, at a distance of 50 m.

Results for simulated mass fractions of spilled fluid are given in Figure D.112 and Figure D.113. It is seen that lateral broadening of the plume as measured by the 0.001 mass fraction contour amounts to approximately 13 m, which is considerably smaller than lateral solute migration observed in the field. There is very little, if any, transverse plume broadening between 8.65 yr and 50 yr, which is explained from the absence of any driving force for lateral flow after moisture contents have returned to ambient levels.

Figure D.112. Simulated Mass Fractions of Spilled Fluid after 8.65 yr for a System with Horizontal Layers and an Anistotropy a = 20

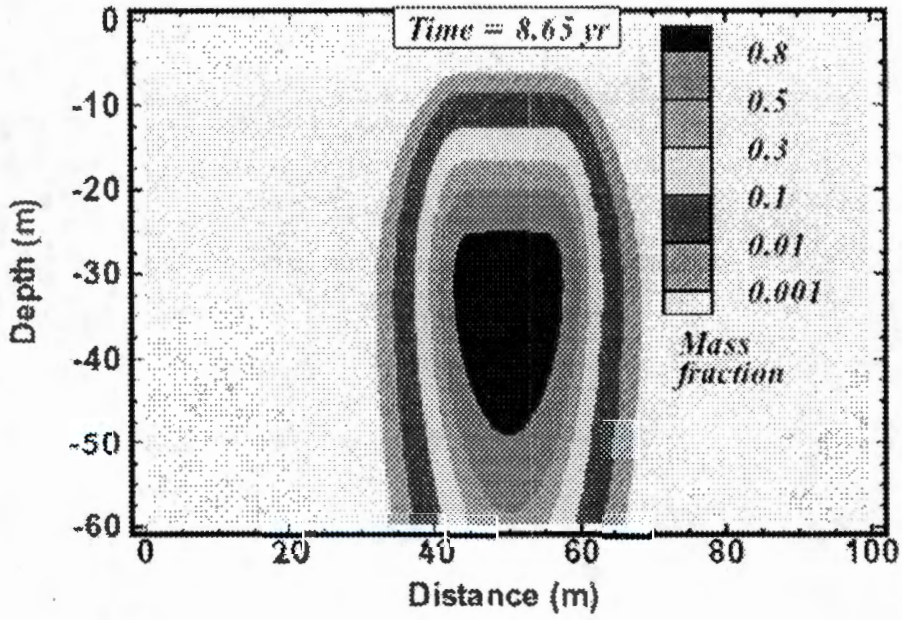

Figure D.113. Simulated Mass Fractions of Spilled Fluid after 50 yr for a System with Horizontal Layers and an Anistotropy a = 20

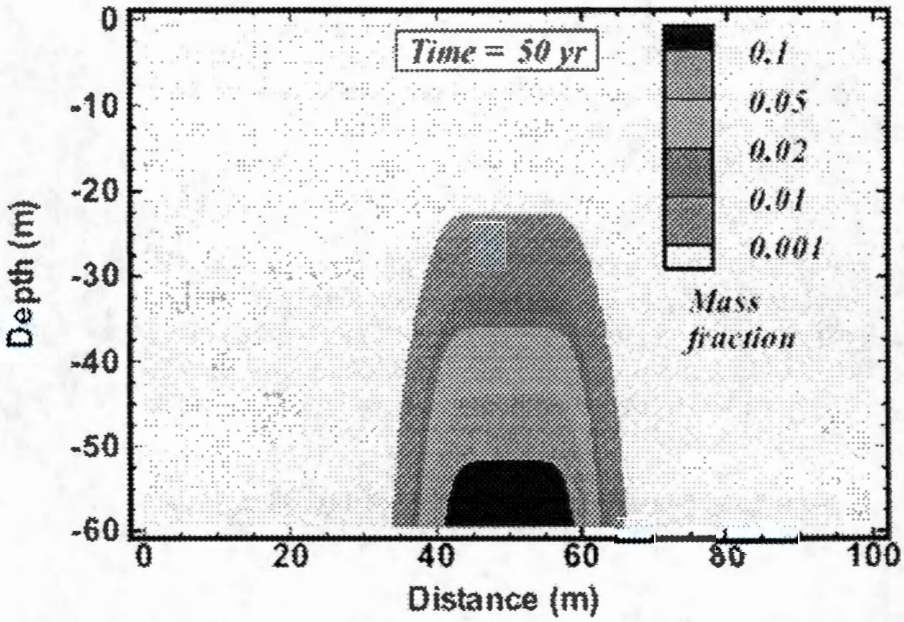

The case with horizontal layering was also run in the R-Z model (Figure D.114). Transverse plume broadening is consistent with results from the vertical section model. There is stronger lateral migration than in the cases with no or weak moisture-tension dependent anisotropy; compare Figure D.91.

From these results, it is concluded that capillary-driven plume broadening is an important process, but is insufficient to explain lateral migration of solutes over distances of 20 m or more that were observed in the field.

There is much less transverse plume broadening for the system with horizontal layers than was observed for sloping layers with strong anisotropy (Figure D.110). These differences are due to numerical dispersion; see Section D.4.2.6 below.

Figure D.114. Mass Fractions of Spilled Fluid for a System with Horizontal Layers and an Anistotropy a = 20

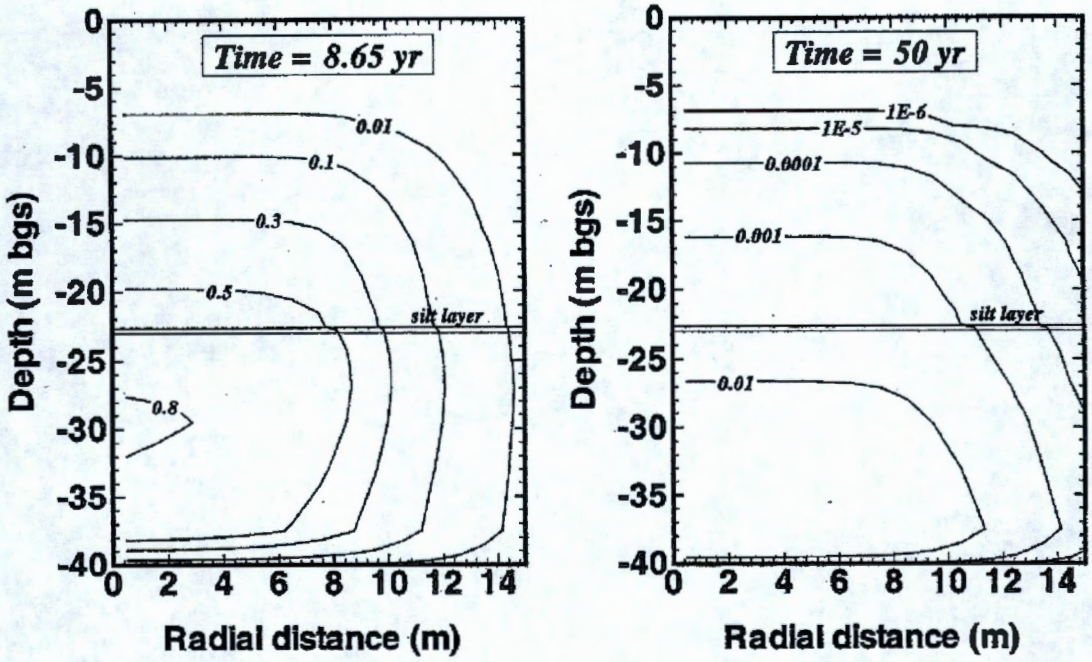

D.4.2.6 Space Discretization Issues

Propagation of moisture and solute plumes in finite difference grids is subject to space discretization errors, which introduce artificial numerical dispersion into solutions to flow and transport problems. Here, a brief analysis of such errors is presented to shed light on the strong plume broadening observed for the case with strong anisotropy (Section D.4.2.5.2).

Using a multiphase notation, Richards' equation for unsaturated flow in an anisotropic medium with permeability tensor $\hat{\mathbf{k}}$ can be written

$$\frac{\partial}{\partial t}\phi S = \frac{1}{\mu}\mathrm{div}\left(k_r\,\hat{\mathbf{k}}(\nabla P_{cap} - \rho \mathbf{g})\right) \tag{6.1}$$

Here, ϕ is porosity, S is liquid saturation, μ is viscosity, k_r is relative permeability, P_{cap} is capillary pressure, ρ is fluid density, and $\mathbf{g}$ is acceleration of gravity. In writing Equation (6.1), it is assumed that fluid density and viscosity are constants throughout the flow domain. From Equation (6.1), a mass balance equation for solute transport is given by

$$\frac{\partial}{\partial t}\phi S X = \frac{1}{\mu}\mathrm{div}\left(X k_r\,\hat{\mathbf{k}}(\nabla P_{cap} - \rho \mathbf{g})\right) \tag{6.2}$$

where X is the mass fraction of solute in the aqueous phase. Equation (6.2) includes only advective transport. A more complete formulation should consider molecular diffusion and hydrodynamic dispersion as well, but here, effects of finite difference space discretization on the advective term are of interest. The special case of advective transport in a homogeneous but

anisotropic unsaturated medium at constant saturation throughout, as is appropriate for steady infiltration, is now considered. Then k_r and P_{cap} will also be constants, and Equation (6.2) simplifies to

$$\frac{\partial}{\partial t}X = -\frac{k_r \rho}{\phi S \mu}\,\mathrm{div}\left(X\,\hat{\mathbf{k}}\mathbf{g}\right) \tag{6.3}$$

The analysis is specialized further to two dimensions and considers a permeability tensor whose principal axes are aligned in the directions parallel and perpendicular to bedding. This results in

$$\hat{\mathbf{k}}\mathbf{g} = \mathbf{e}_p\, k_p\, g \sin\alpha + \mathbf{e}_q\, k_q\, g \cos\alpha \tag{6.4}$$

where $\mathbf{e}_p$ and $\mathbf{e}_q$ are unit vectors parallel and perpendicular to bedding, k_p and k_q are the principal components of the permeability tensor, and α is the slope angle. Equation (6.3) becomes

$$\frac{\partial}{\partial t}X = -\frac{k_r \rho g}{\phi S \mu}\left(k_p \sin\alpha \frac{\partial X}{\partial p} + k_q \cos\alpha \frac{\partial X}{\partial q}\right) \tag{6.5}$$

This is a first-order hyperbolic equation, which describes mass transport with components of pore velocity in p and q-directions given by

$$v_p = k_r k_p \rho g \sin\alpha / \phi S \mu \tag{6.6a}$$

$$v_q = k_r k_q \rho g \cos\alpha / \phi S \mu \tag{6.6b}$$

Substituting finite difference approximations for the first-order space derivatives in Equation (6.5) is tantamount to adding higher-order space derivatives. For a grid system aligned with the principal axes of the permeability tensor, the second-order term appearing on the r.h.s. of the space-discretized version of Equation (6.5) is found to be (Pruess 1991)

$$\frac{h}{2}\left(v_p \frac{\partial^2 X}{\partial p^2} + v_q \frac{\partial^2 X}{\partial q^2}\right) \tag{6.7}$$

where h is the grid spacing. Space discretization is thus seen to introduce anisotropic diffusion with diffusivities of $v_p h/2$ and $v_q h/2$ in p and q-directions, respectively. The corresponding dispersivities are equal to half the grid spacing.

In a grid system where nodal lines are aligned with horizontal and vertical directions ($\alpha = 0$), numerical dispersion in the horizontal direction is seen to be exactly zero, so there will be no artificial transverse plume broadening in this case. For the model with strong anisotropy presented in Section D.4.2.5.2, pore velocities are approximately 2 m/yr in both p and q-directions, which, for the h = 1 m grid spacing used, gives rise to numerical dispersion with a diffusivity of $D = 1\ m^2/yr = 3.17 \times 10^{-8}\ m^2/s$. This is more than an order of magnitude larger than typical solute diffusivities in free (bulk) water, and more than two orders of magnitude larger than effective aqueous phase diffusivities under the rather dry conditions in the Hanford sediments. Lateral plume broadening from this numerical diffusivity can be estimated as $y = \sqrt{2Dt}$, which corresponds to y = 4.16 m after 8.65 yr, and y = 10.0 m after 50 yr. This numerical artifact explains why the solute plumes in the tilted grid system used for the case with strong anisotropy are significantly broader (Figure D.110 and Figure D.111) than those for the system with horizontal layers in which the grid is aligned with horizontal and vertical directions

(Figure D.112 and Figure D.113). The trajectory of the solute plume, especially the large lateral diversion for strong anisotropy, is not affected by numerical dispersion.

Although the origin of the solute plume dispersion in the simulations is numerical, the effect is not entirely artificial. Indeed, heterogeneities of the medium will introduce a physical (hydrodynamic) dispersion due to spatially and temporally variable flow velocities. The numerical dispersivity of 0.5 m that is present in the calculations may well have the right order of magnitude for approximating physical dispersion on the length scale analyzed in the simulations.

D.4.2.7 Three-Dimensional Model

In order to avoid artificial effects encountered in 2-dimensional vertical section models, a fully 3-dimensional model was set up with specifications that closely correspond to the 2-dimensional section with strong lateral anisotropy presented in Section D.4.2.5.2. As shown in Figure D.115, the model domain is a parallelepiped with Y'-Z' dimensions identical to those in the 2-dimensional section model (Figure D.100), while a thickness of 50 m was used in the X-direction. The Y' and Z' coordinate axes in Figure D.115 are denoted with primes to indicate that these axes are attached to the parallelepiped ("body-fixed" coordinates), which as a whole is rotated around the X-axis to represent the sloping of sedimentary layers at the site. The Y' axis points in northeasterly direction and in the 2-dimensional section had been rotated downward by 3°. During the course of this study, updated estimates for the slope of sedimentary deposition in the vicinity of BX-102 became available. Analysis of geologic markers corresponding to thin, semi-continuous silty fine sand layers in the H2 Hanford formation unit identified a slope of $\alpha = 1.5 - 2.0$ degrees [$\tan(\alpha) = 0.03$] dipping to the north-northeast. Accordingly, this was the slope used in the 3-dimensional model. In order to preserve the feature of the 2-dimensional model with strong anisotropy that (sub)horizontal and (sub-) vertical volumetric fluxes should be approximately equal, anisotropy was specified as $a = \cot(\alpha) = 1/.03 = 33.3$ (Equation 5.3). This will cause flow to proceed at an angle of 45° with respect to the vertical. All other hydrogeologic parameters were identical to those used in the 2-dimensional section model. Grid spacing was generally 2.5 m in X and Y'-directions, 2 m in Z'-direction, with smaller increments used in the Z'-direction at and near the explicitly modeled silt layer at 22.7 - 23.0 m depth. The calculational grid has a total of 15,543 blocks. Boundary conditions were the same as in the 2-dimensional section, namely, net infiltration of 10 cm/yr at the top, free drainage at the bottom, and saturation profiles corresponding to steady flux of 10 cm/yr maintained at the left (Y' = 0) and right (Y' = 100 m) boundaries. The fluid spill was modeled by injecting water with a conservative tracer into a grid block with $2.5 \times 2.5 = 6.25$ m^2 footprint area and 12.5 m^3 volume located at Z' = -5 m depth, at a distance of Y' = 21.25 m from the left boundary. A total of 91,600 gal (346.7 m^3) was injected at constant rate over a 3-week period. Because of symmetry, only a 25-m thick section extending from X = 0 to X = 25 m needs to be modeled; the X = 0 and X = 25 m planes were modeled as no flow boundaries.

Figure D.115. Definition Domain of the Three-Dimensional Model

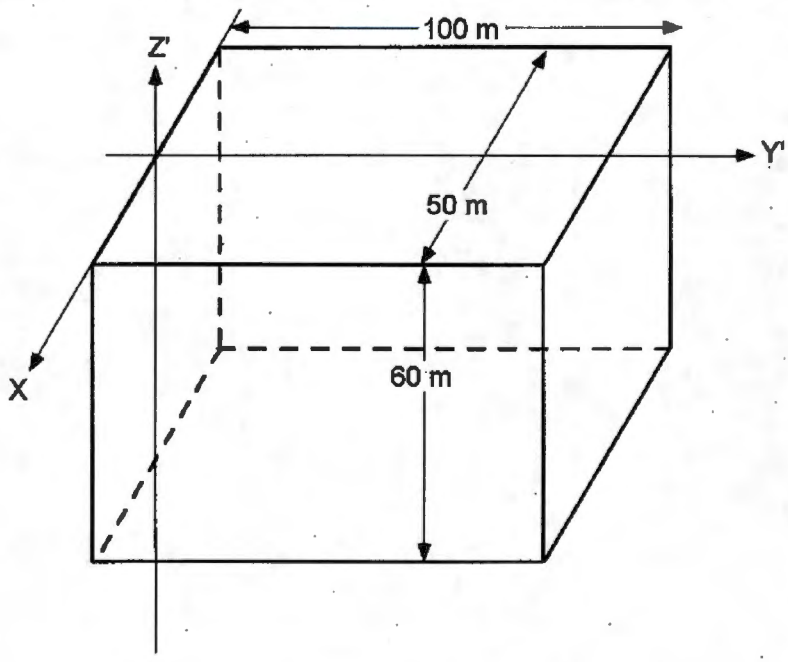

Results for the 3-dimensional model are given in Figure D.116 through Figure D.118, and Figure D.120 through Figure D.125. Figure D.116 shows total water flow rate across three horizons at different depths. For ambient infiltration at a rate of 10 cm/yr, the volume infiltrated into the modeled domain in one year is V = 25x100xcos(1.7184°)x0.1 = 248.89 m^3. The total background mass flow rate is then

$$q = \frac{V\rho}{t} = \frac{25 \times 100 \times \cos(1.7184°) \times 0.1 \times 999.213}{365.25 \times 24 \times 3600} = 7.912 \times 10^{-3}\, kg/s \qquad (7.1)$$

The water density of ρ = 999.213 kg/m3 corresponds to conditions of (T, P) = (15 °C, 1.013 x 105 Pa). In response to the fluid spill, flow rate across the Z' = -6 m horizon increases until injection ceases after 3 weeks (1.8144 x 106 s), and then quickly returns to the ambient rate. At deeper horizons, the fluid pulse arrives with much reduced amplitude, reflecting the weakening of the moisture spike as the plume broadens from capillary and dispersive effects (the latter being due to numerical dispersion (Section D.4.2.6). Figure D.117 and Figure D.118 show that the moisture plume weakens rapidly with time. After one year, maximum increases in moisture content are 0.6% above the background value of 5.1%. Accordingly, the disturbance of the ambient flow field due to the fluid spill is rather short-lived; moisture contents are essentially back to ambient values after 1 year, and solute movement subsequent to this time occurs in an essentially unaltered ambient infiltration field. The silt layer is visible in Figure D.117 and Figure D.118 as a linear feature with elevated moisture content.

Figure D.116. Water Flow Rate Across Three Horizons at 6, 22, and 50 m depth, respectively, shown on logarithmic time scale (top) and linear time scale (bottom)

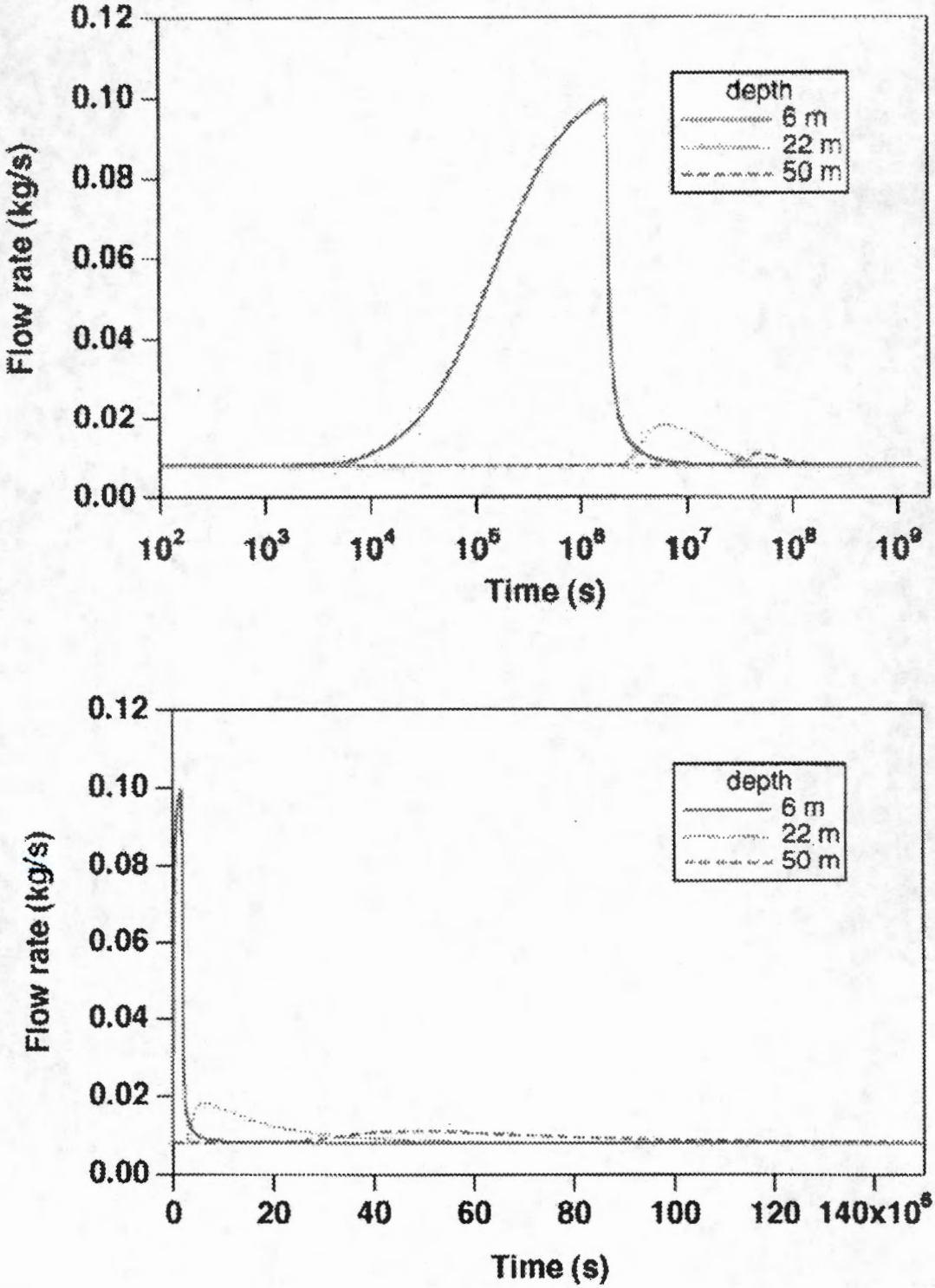

Figure D.117. Moisture Distribution in the Vertical Plane X = 1.25 m after 38.26 days

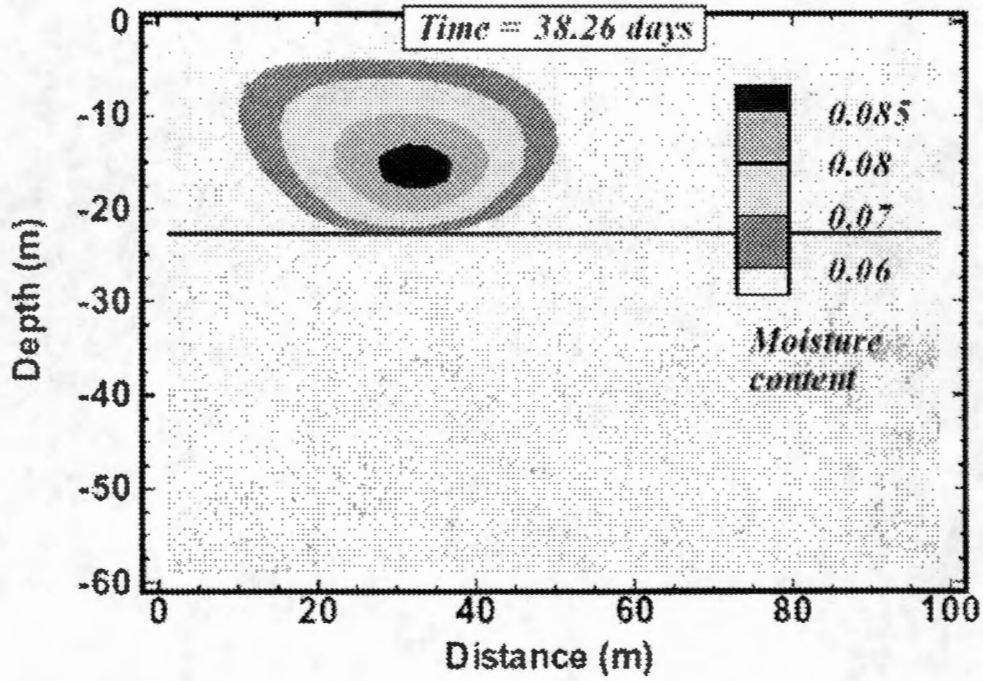

Figure D.118. Moisture Distribution in the Vertical Plane X = 1.25 m after 1 year

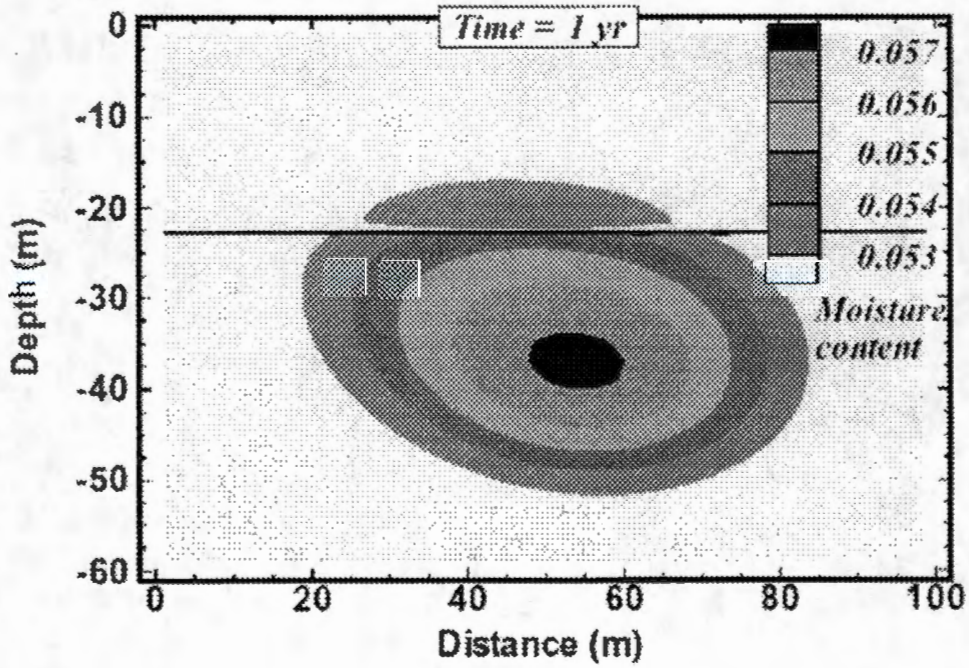

Solute migration is considerably retarded relative to the propagation velocity of a moisture disturbance. In a partially saturated medium with moisture content $\theta = \phi S$, where ϕ is porosity and S liquid saturation, migration of a conservative tracer in a flow field with Darcy velocity (volumetric flux) u occurs with a velocity

$$v_t = \frac{u}{\theta} \tag{7.2}$$

Equation (7.2) is valid for a single-porosity medium, in which solute is distributed locally uniformly throughout the porewater. Under ambient conditions, $\theta \approx 0.05$, so that for an applied volumetric flux of $u = 0.1$ m/yr, tracer propagation velocity is $v_t = 0.1/0.05 = 2$ m/yr. Some complications arise for anisotropic media. Consider a situation as depicted in Figure D.119, where gravity-driven seepage proceeds in a domain 1 at a velocity v_1, then encounters an interface below which there is an anisotropic medium. Suppose that the principal axes of anisotropy are rotated against the horizontal and vertical directions in such a way that flow in the anisotropic domain 2 proceeds with velocity v_2 at an angle β against the horizontal direction. The cross-sectional area for flow is then reduced by a factor $\sin(\beta)$, and conservation of volume demands that $v_2 \sin\beta = v_1$, so that $v_2 = v_1/\sin\beta$. For $v_1 = 2$ m/yr and $\beta = 45°$, $v_2 = 2.828$ m/yr. The rate of downward advancement in domain 2 is $v_2 \sin\beta = v_1$, unaltered from that in domain 1.

Figure D.119. Gravity-Driven Seepage in an Anisotropic Medium

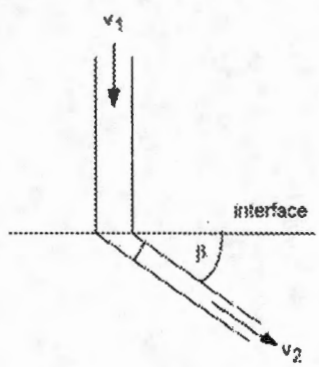

The migration velocity of saturation (moisture) disturbances in gravity-driven flow is given by (Pruess 1991)

$$v_S = \frac{k\rho g}{\phi\mu}\frac{dk_{rl}}{dS} = \frac{u}{\phi}\frac{dk_{rl}/dS}{k_{rl}} \tag{7.3}$$

where k is absolute permeability, ρ and μ are liquid density and viscosity, respectively, g is acceleration of gravity, and k_{rl} is relative permeability. The ratio of tracer velocity relative to that of moisture disturbances is

$$\frac{v_t}{v_S} = \frac{k_{rl}/S}{dk_{rl}/dS} \tag{7.4}$$

Because relative permeability functions are concave upward (positive curvature), this ratio is always less than 1 and will attain small values where the slope of the relative permeability function $k_{rl}(S)$ is large. These notions are borne out by contour diagrams of solute plumes at different times shown in Figure D.120, Figure D.121, Figure D.123, and Figure D.125. 38.26 days after the beginning of the spill, conservative solute is just arriving at the silt layer at 23 m depth. The movement of the center-of-mass of the solute plume in 1 year is comparable to that of the moisture plume in 38.26 days; compare Figure D.121 with Figure D.117. After 8.65 yr, the center of the solute plume has just passed the silt layer. Lateral broadening of the solute plume in the X-direction (Figure D.115) occurs only as long as elevated moisture contents give rise to capillary-driven sideways flow. Comparing Figure D.122 and Figure D.124, it is seen that despite considerable longitudinal elongation, there is no further lateral broadening of the solute plume after the moisture plume has dissipated. After 50 years, only small solute concentrations remain at the silt layer, and most of the solute has migrated below the bottom boundary of the model domain (Figure D.125). From the velocity estimate made from Equation (7.2), it is expected the center of the solute plume near - 100 m depth at that time. Note that these estimates were made for a single-porosity medium; if poorly accessible pore regions are present into which solute may diffuse, then larger concentrations could persist at shallower levels for longer times.

Tracer breakthrough curves (BTCs) at different depth horizons are shown in Figure D.126. These data represent flowing concentrations averaged over planes at different depths Z', and were computed as X = {flow rate of spilled water}/{total rate of water flow}. At the 22 m horizon, there is a double-hump structure, which arises from the interplay of larger solute concentrations being propagated more rapidly near the center of the plume, and the later arrival of the bulk of the solute inventory in the more diffuse fringe (Pruess 2002). Increasing dilution effects are evident from the lower amplitude and broader peaks in the BTC at deeper horizons.

Figure D.120. Solute Distribution in the Vertical Plane X = 1.25 m after 38.26 days

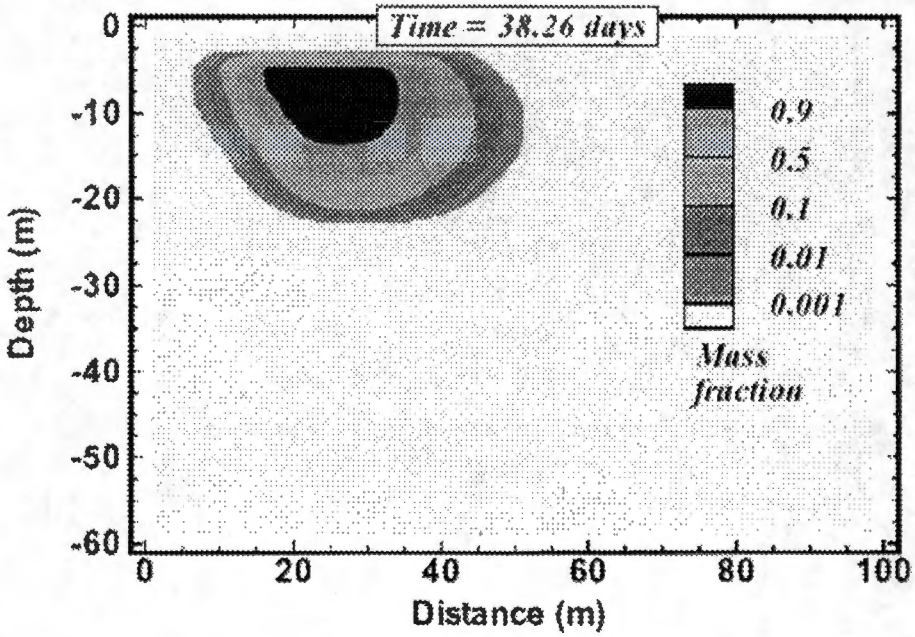

Figure D.121. Solute Distribution in the Vertical Plane X = 1.25 m after 1 year

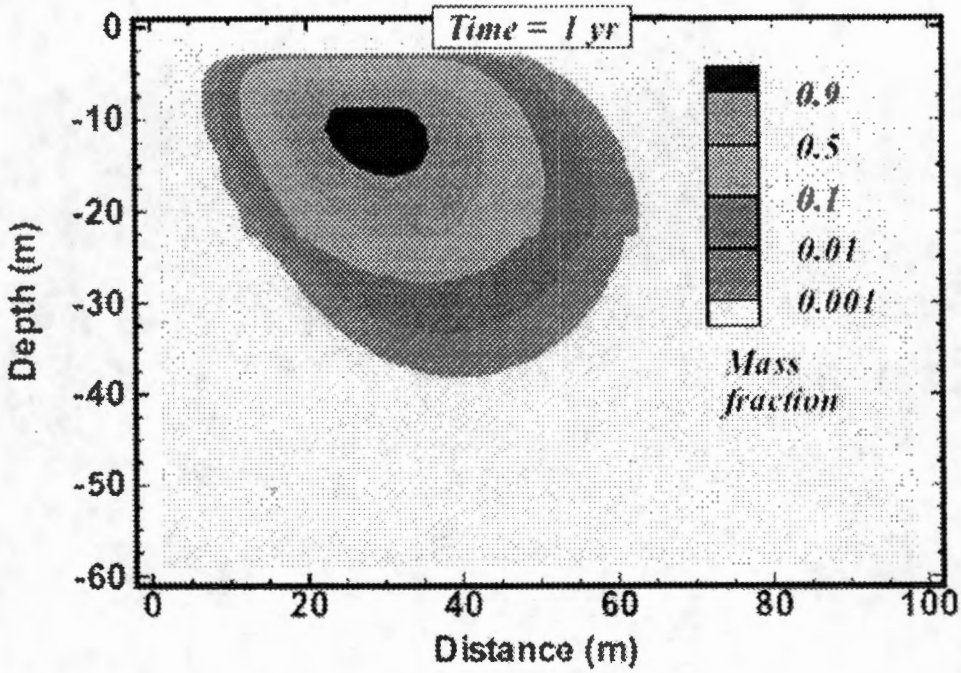

Figure D.122. Solute Ddistribution in the (sub-)horizontal Plane Z' = -13.0 m after 1 year

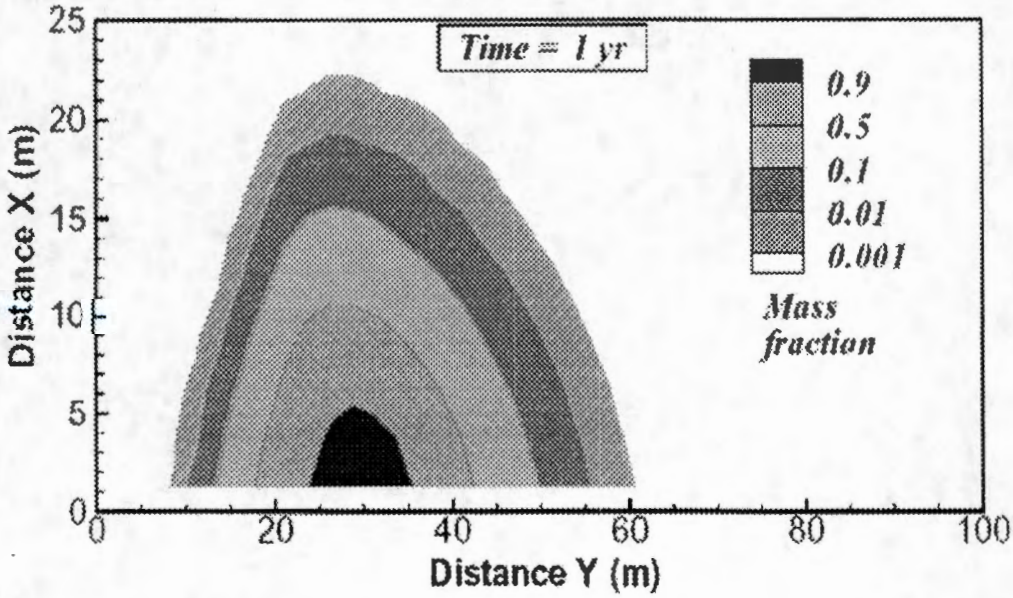

Figure D.123. Solute Distribution in the Vertical Plane X = 1.25 m after 8.65 years

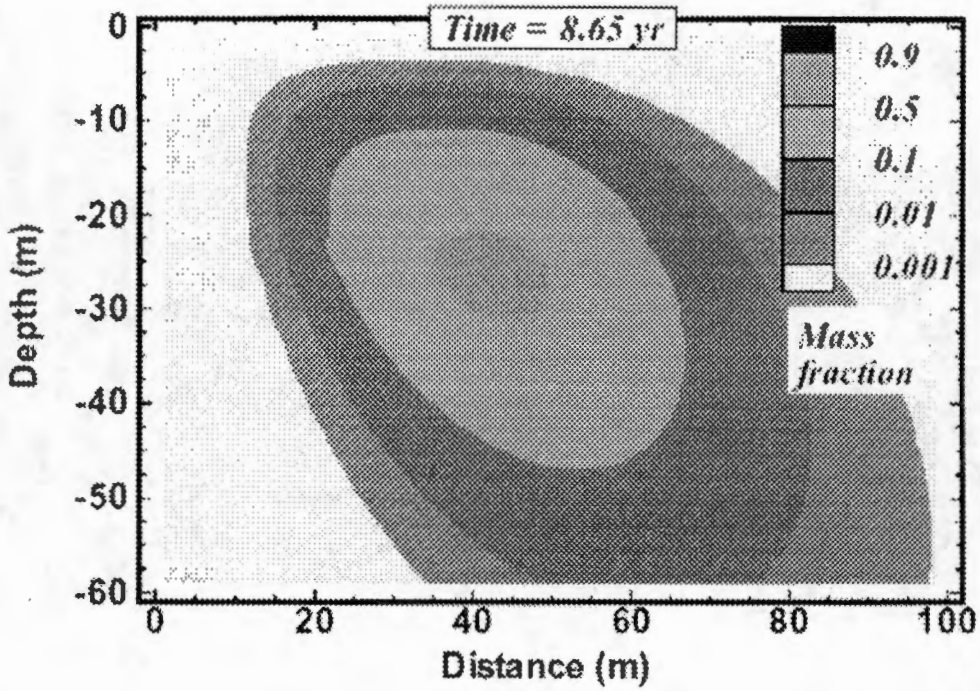

Figure D.124. Solute Distribution in the (sub-)horizontal Plane Z' = -27.0 m after 8.65 years

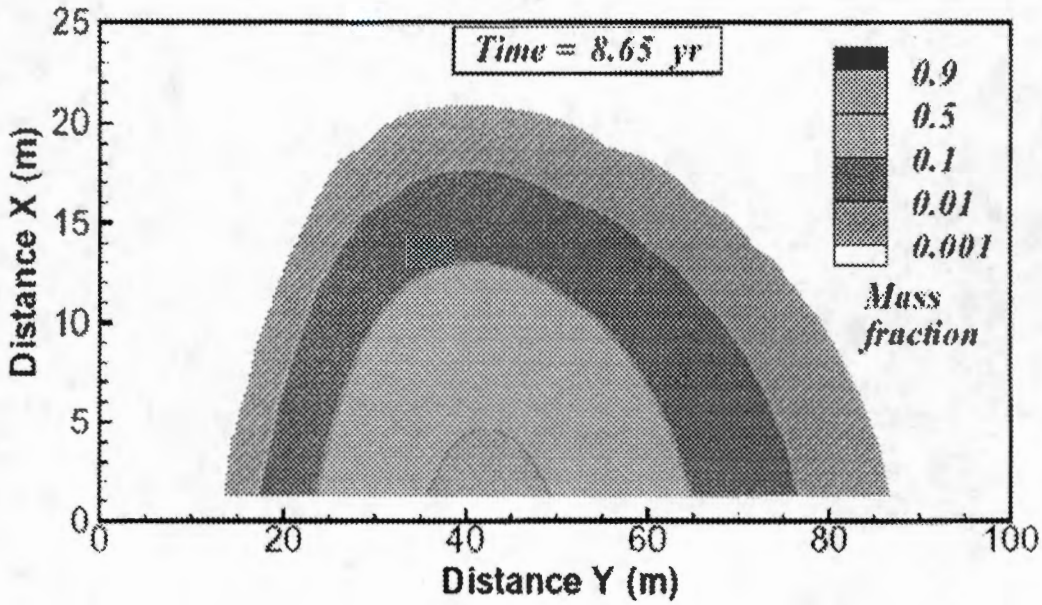

Figure D.125. Solute Distribution in the Vertical Plane X = 1.25 m after 50 years

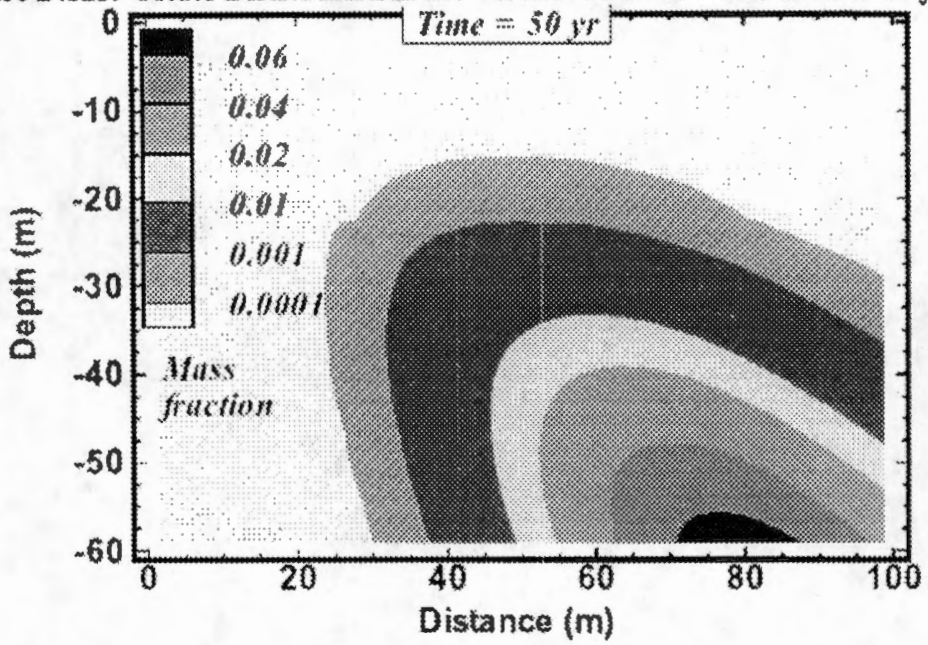

Figure D.126. Tracer Breakthrough Curves at Different Depths, on Logarithmic Time Scale (top) and Linear Time Scale (bottom)

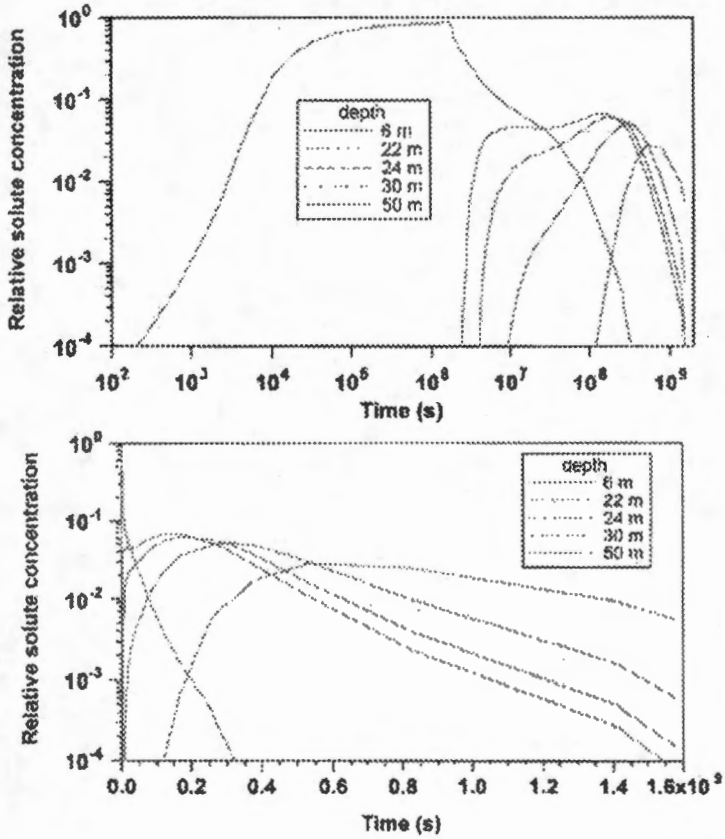

D.4.2.8 Conclusions

The key to substantial lateral flow effects is the strong anisotropy found in the layered sediments of the Hanford vadose zone. In a layered system, hydraulic conductivity parallel to bedding may be much larger than in the perpendicular (downward) direction. This will enhance lateral flow, and in systems with sloping layers, migration of moisture as well as solutes may be offset from the vertical by large angles. Enhanced (sub-) horizontal conductivity also accelerates plume broadening and lateral spreading from capillary forces.

This study has investigated mathematical models for moisture and solute migration at tank BX-102 that are constrained by field observations and laboratory measurements on samples. The models are capable of reproducing observed moisture contents and flow and transport behavior, and provide useful insight into flow and transport mechanisms affecting fluid spills. A key finding is that enhanced lateral flow cannot be attributed to strong flow diversion at a few major layers, but is caused by strong anisotropy throughout, due to pervasive multi-scale layering of the sediments.

An as yet unresolved problem is the observed persistence at relatively shallow depths of solutes that presumably have limited reactivity with the sediments. Volume-averaged models of unsaturated seepage suggest that these solutes should have been flushed downward by ambient infiltration. A possible hypothesis is that their persistence may be caused by local variability in infiltration fluxes and exchanges between regions with different moisture mobility. Alternatively, they may become immobilized chemically due to sorption, complexation, or precipitation.

The main findings of this study can be summarized as follows:

- Uranium-238 transport has occurred in a single stratigraphic unit, H2, which extends from depths of 35 ft to 170 ft (10.67 to 51.82 m), and was described by Lindsey et al. (2001) as a coarse to medium sand. Despite the "homogeneous" lithologic classification, large-scale lateral migration of uranium-238 has been observed.

- Lateral migration of uranium-238 from the BX tank farm extends beyond the dry wells to at least 299-E33-41, a RCRA well an additional 100 ft (30.48 m) to the northeast of the contemporary BX-102 borehole (i.e., 299-E33-45), indicating lateral migration of at least 170 ft (51.82 m) at a vertical depth of 137 ft (41.76 m).

- Cores from the contemporary boreholes 299-E33-45, 299-E33-46, and 299-E33-338, examination of logs from nearby RCRA wells (i.e., 299-E33-41, 299-E33-339, 299-E33-42), and neutron moisture logging of dry boreholes 21-27-02, 21-27-09, 21-27-10, and 21-27-11 indicate the presence of continuous, thin (1 to 10 cm), silty fine sand layers at depths of 75 ft (22.86 m), 100 ft (30.48 m), and 120 ft (36.58 m) within the H2. These layers exhibit a 3% slope that dips to the northeast, which is consistent with the ground surface slope outside of the disturbed areas of the tank farms and the predominant axis of the uranium-238 and antimony-125 distributions.

- Modeling results suggest that the few (2 or 3) semi-continuous silty fine sand layers that have been identified in the H2 unit cannot by themselves account for current moisture contents and radionuclide distributions to the east and northeast of BX-102.

- Capillary-driven plume broadening is an important process, but is insufficient to explain lateral migration of solutes over distances of 20 m or more that were observed in the field.

- Large permeability anisotropy ratios (20 or more) are necessary to simulate the lateral uranium-238 migration and distribution. In order to preserve the observed moisture contents, horizontal permeabilities were enhanced in our model, as opposed to decreasing the vertical permeabilities.

- The current interpretation, based on observations at the field experiments, is that there are numerous, discontinuous, low permeability laminations/lenses in the H2 unit oriented with 3% general slope towards the northeast. Liquid migrates sub-horizontally along a lamination until the lamination terminates or is weak enough to allow breakthrough, whereupon it migrates vertically until encountering another lamination.

- Simulations that approximate field observations of soil moisture and uranium extent are consistent with a very rapid transport (i.e., 4 weeks) from the 1951 tank BX-102 source to the present location. This agrees with historical accounts as well as gross gamma logs from 1975 to 1990, which indicate that uranium-238 and antimony-125 mass has remained stable at most depth intervals when corrected for radioactive decay.

- The depth and extent of the antimony-125 plume is consistent with a more recent (late 1960s and early 1970s) cesium-137 recovery waste released from the vicinity of BX-101. No specific release event has been identified as the source of this antimony-125 distribution, but the relatively short half-life of 2.758 years constrains the event timing to a PUREX supernate processed at B Plant in the identified time frame.

- The driving force for moisture redistribution of the 91,600-gal pulse in 1951 is significantly diminished within a few weeks of the end of the release, whereupon recharge becomes the principal driving force. For a 10 cm/year recharge with 5% moisture content, the nominal pore velocity and transport rate is 2 meters per year.

D.4.2.9 References

de Marsily, G., 1986, *Quantitative Hydrogeology*, Academic Press, Orlando, Florida.

DOE-GJO, 1997, *Vadose Zone Characterization Project at the Hanford Tank Farms: Tank Summary Data Report for Tank BX-102*, GJ-HAN-89, prepared by U.S. Department of Energy, Grand Junction Office, Grand Junction, Colorado, for U.S. Department of Energy, Richland Operations Office, Richland, Washington.

DOE-GJO, 1998, *Vadose Zone Characterization Project at the Hanford Tank Farms: Addendum to the BX Tank Farm Report*, GJO-98-40-TAR/GJO-HAN-19, prepared by U.S. Department of Energy, Grand Junction Office, Grand Junction, Colorado, for U.S. Department of Energy, Richland Operations Office, Richland, Washington.

Fayer, M. J., G. W. Gee, M. L. Rockhold, M. D. Freshley, and T. B. Walters, 1996, "Estimating Recharge Rates for a Groundwater Model Using a GIS", *Journal of Environmental Quality*, Vol. 25, No. 3, pp. 510-518.

Gee, G. W., and A. L. Ward, 2001, *Vadose Zone Transport Field Study: Status Report*, PNNL-13679, Pacific Northwest National Laboratory, Richland, Washington.

General Electric Company, 1951, *Hanford Works Monthly Report for February 1951*, HW 20438, prepared for the Atomic Energy Commission, Richland, Washington.

Gwo, J. P., P. M. Jardine, G. V. Wilson, and G. T. Yeh, 1996, "Using a Multiregion Model to Study the Effects of Advective and Diffusive Mass Transfer on Local Physical Nonequilibrium and Solute Mobility in a Structured Soil," *Water Resources Research*, Vol. 32(3):561-570.

Jones, T. E., B. C. Simpson, M. I. Wood, and R. A. Corbin, 2001, *Preliminary Inventory Estimates for Single-Shell Tank Leaks in B, BX, and BY Tank Farms*, RPP-7389, Rev. 0, CH2M HILL Hanford Group, Inc., Richland, Washington.

Khaleel, R., and E. J. Freeman, 1995, *Variability and Scaling of Hydraulic Properties for 200 Area Soils, Hanford Site*, WHC-EP-0883, Westinghouse Hanford Company, Richland, Washington.

Khaleel, R., J. F. Relyea, and J. L. Conca, 1995, "Evaluation of van Genuchten-Mualem Relationships to Estimate Unsaturated Hydraulic Conductivity at Low Water Contents," *Water Resources Research*, Vol. 31(11):2659-2668.

Khaleel, R., T. E. Jones, A. J. Knepp, F. M. Mann, D. A. Myers, and M. I. Wood, 2001, *Modeling Data Package for B-BX-BY Field Investigation Report (FIR)*, RPP-9223, Rev. 0, CH2M HILL Hanford Group, Inc., Richland, Washington.

Lindsey, K. A., S. E. Kos, and K. D. Reynolds, 2001, *Vadose Zone Geology of Boreholes 299-E33-45 and 299-E33-46 B-BX-BY Waste Management Area, Hanford Site, South-Central Washington*, RPP-8681, Rev. 0, prepared for the Office of River Protection, CH2M HILL Hanford Group, Inc., Richland, Washington.

Myers, D. A., 1999, *Analysis of Historical Gross Gamma Logging Data from BX Tank Farm*, HNF-3531, Rev. 0, Waste Management Northwest/Three Rivers Scientific, Richland, Washington.

Pruess, K., 1991, "Grid Orientation and Capillary Pressure Effects in the Simulation of Water Injection into Depleted Vapor Zones," *Geothermics*, 20(5/6):257-277.

Pruess, K., 2002, "A Composite Medium Approximation for Unsaturated Flow in Layered Sediments," *Water Resources Research*, (submitted).

Pruess, K., C. Oldenburg, and G. Moridis, 1999, *TOUGH2 User's Guide, Version 2.0*, LBNL-43134, Lawrence Berkeley National Laboratory, Berkeley, California.

Rockhold, M. L., 1999, "Conditional Simulation and Upscaling of Soil Hydraulic Properties," In *Characterization and Measurement of the Hydraulic Properties of Unsaturated Porous Media*, van Genuchten, Leij, and Wu (eds), U.S. Salinity Laboratory, Riverside, California, pp. 1391-1401.

Sisson, J. B., and A. H. Lu, 1984, *Field Calibration of Computer Models for Application to Buried Liquid Discharges: A Status Report*, RHO-ST-46P, Rockwell Hanford Operations, Richland, Washington.

Van Genuchten, M. Th., 1980, "A Closed-Form Equation for Predicting the Hydraulic Conductivity of Unsaturated Soils," *Soil Science Society of America Journal*, Vol. 44:892-898.

Womack, J. C. and D. J. Larkin, 1971, *Investigation and Evaluation of 102-BX Tank Leak*, Atlantic Richfield Hanford Company, ARH-2034, Richland, Washington.

D.4.3 CESIUM-137 REACTIVE TRANSPORT MODELING AT TANK BX-102

Steven B. Yabusaki[1], Steve C. Smith[1], and Carl I. Steefel[2]

[1]Pacific Northwest National Laboratory, Richland, Washington 99352
[2]Lawrence Livermore National Laboratory, Livermore, California 94550

D.4.3.1 Introduction

In the present study, a one-dimensional reactive transport simulator was used to model cesium-137 subsurface migration from the BX-102 overfill event in 1951. The reactive transport model was parameterized using a series of Cs-137 adsorption measurements in B tank farm sediments. The objective of the modeling was to determine if the deeply distributed Cs-137 observed in borehole 21-02-04 could be naturalized as resulting from transport through sediment, or whether an alternative pathway (e.g., migration down the borehole casing) need be evoked.

As part of a tank leak investigation at BX-102 in 1970, 19 boreholes were installed to determine the spatial extent of a suspected release of tank waste (Womack and Larkin 1971). The additional boreholes identified the origin of a gamma-emitting plume at tank BX-102 with a likely source at the tank footing 40 ft (12 m) bgs on the southeast side of the tank near borehole 21-02-04, where the highest gamma ray activity was detected. Borehole 21-02-04 was also the only borehole in the area drilled to groundwater. 51 kCi of cesium-137 were estimated to have leaked according to Fraser and Larkin (1974) and cesium-137 was detected in the groundwater at 21-02-04. Recent spectral gamma logging of borehole 21-02-04 in 1997 and 1999 identified cesium-137 concentrations sufficiently high to mask other gamma emitting radionuclides in this borehole. Figure D.127 is the Cs-137 concentration distribution with depth measured in 1999 with a special high-rate logging system (DOE-GJO 2000). Although cesium-137 below a depth of 83 ft (25 m) has been attributed to borehole effects at 21-02-04, there have been changes noted in the distribution of cesium-137 between 1970 and 1999 that have been interpreted as cesium migration (Randall and Price 1999).

It is likely that many of the radionuclides identified by the gross and spectral gamma logging predate the 1969 event that triggered the installation of the dry boreholes. Under this scenario, a large volume waste release would have been necessary to drive the uranium plume to its present position to the east and northeast of BX-102. The only documented large-scale release of waste at BX-102 was found in a recently (1992) declassified *Hanford Works Monthly Report* dated February 1951 (General Electric Company 1951) that described an overfill event at BX-102 that resulted in the release of 91,600 gallons (346.7 m^3) of metals waste over approximately three weeks. In addition to cesium-137, the metals waste contained depleted uranium and elevated concentrations of sodium and bicarbonate from B Plant extractions.

Figure D.127. Cesium-137 Concentrations in Borehole 21-02-04 Measured with High Rate Logging System (DOE-GJO 2000)

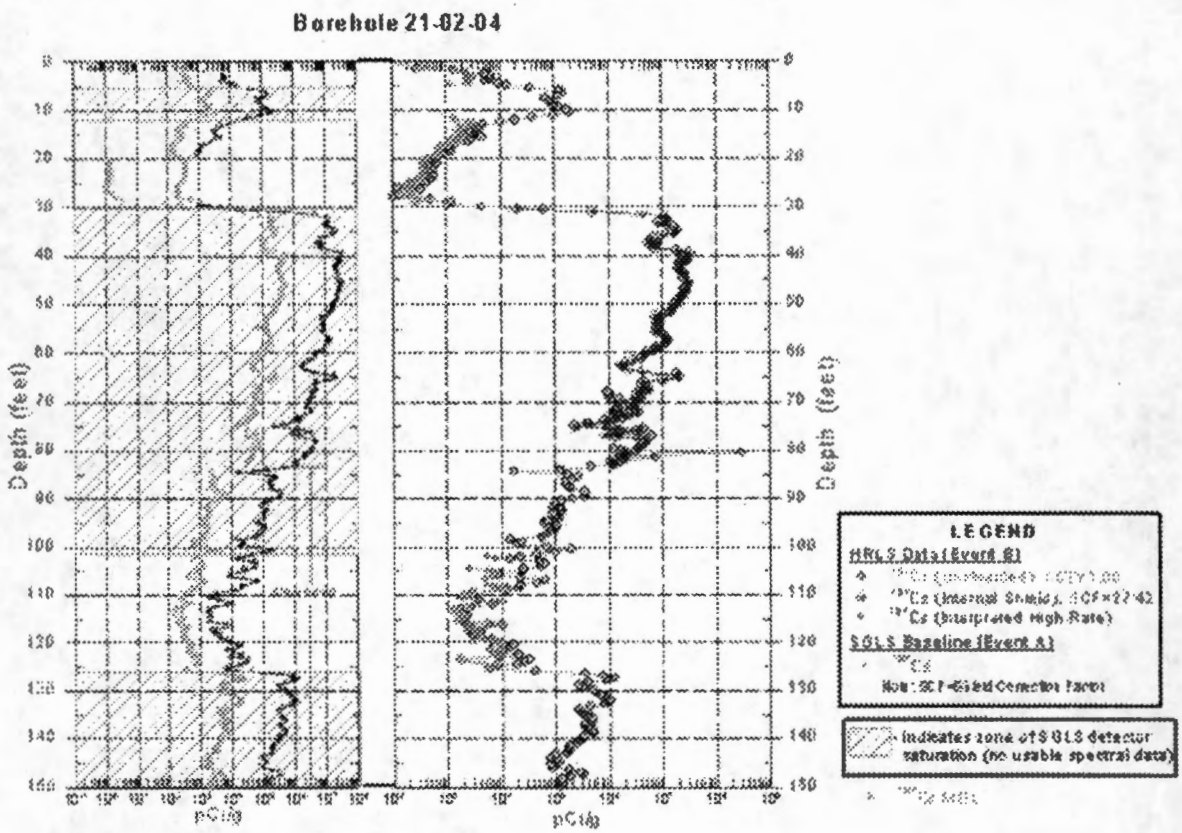

D.4.3.2 Experiment Descriptions

A series of cesium adsorption experiments were performed to identify and characterize ion exchange behavior in 1 M $NaNO_3$ and 1 M $NaHCO_3$ electrolyte solutions over a large range of cesium concentrations. Concentrations of the Na^+, NO_3^-, and HCO_3^- are of the same order as comparable components from the metals waste in tank BX-102 at the time of the 1951 overfill; cesium concentrations in the waste are bracketed by the large range of cesium that was tested. The matrix of 32 batch measurements is summarized in Table D.65. All experiments were performed in replicate.

Table D.65. Matrix of Adsorption Measurements

SEDIMENT	ELECTROLYTE SOLUTION	
	1 M $NaNO_3$	1 M $NaHCO_3$
Upper B Composite Sediment	Initial Cesium Concentration (M/L): 10^{-1}, 10^{-2}, 10^{-3}, 10^{-4}, 10^{-5}, 10^{-6}, 10^{-7}, 10^{-9}	Initial Cesium Concentration (M/L): 10^{-1}, 10^{-2}, 10^{-3}, 10^{-4}, 10^{-5}, 10^{-6}, 10^{-7}, 10^{-9}
Lower B Composite Sediment	Initial Cesium Concentration (M/L): 10^{-1}, 10^{-2}, 10^{-3}, 10^{-4}, 10^{-5}, 10^{-6}, 10^{-8}, 10^{-9}	Initial Cesium Concentration (M/L): 10^{-1}, 10^{-2}, 10^{-3}, 10^{-4}, 10^{-5}, 10^{-6}, 10^{-8}, 10^{-9}

D.4.3.2.1 Sediments. Two B tank farm < 2 mm composite sediments from RCRA monitoring well 299-E33-337 were used: an upper composite representing the depth interval 36 to 70 ft bgs, and a lower composite representing the depth interval 75 to 120 ft bgs. The preparation and characterization of these composite samples are described in detail in Zachara et al in Section D.2.1.

D.4.3.2.2 Cation Exchange Capacity. Cation exchange capacity was measured using a sequential extraction of the B tank farm upper and lower composite sediments (< 2 mm size fraction). The intent of the initial extraction with deionized water was to dissolve readily soluble salts and account for porewater cations. Following the deionized water extraction, the sediment was contacted with 1 mol/L ammonium chloride solution for 4 hours. The cations present in the second extract were assumed to be associated with the exchange sites of the sediments and were readily exchangeable by ammonium. The sum of the adsorbed cations represented the concentration of exchange sites per gram of soil. For the B tank farm upper composite sediment, the mean of three replications was 79.3 μeq/g net ammonium extractable. Similarly, the mean for the B tank farm lower composite sediment was 73.1μeq/g net ammonium extractable. These CECs were between the 120 μeq/g reported by Steefel et al. (2002) for an SX tank farm sediment and the Hanford fine sand composite CEC of 50.2 μeq/g reported by Zachara et al. in Section D.2.1.

D.4.3.2.3 Equilibration with Cesium-137 Spike Solutions. Stock 1 M $NaNO_3$ or 1 M $NaHCO_3$ electrolytes were prepared with cesium-137-labeled CsNO3 to produce the series of initial cesium concentrations in the experiment matrix. Each solution was allowed 20 hours to equilibrate at 25 °C with the sediments at a nominal solid solution ratio of 250 g/L.

D.4.3.3 Experimental Results

Results from the B tank farm cesium sorption experiments are summarized in Table D.66 and Table D.67 for the 1 M $NaNO_3$ electrolyte and Table D.68 and Table D.69 for the 1 M $NaHCO_3$ electrolyte. In general in all four of these cases, cesium sorption behavior (Figure D.128 and Figure D.129) exhibits the same general trend and variability with Cs^+ concentrations. On the log – log K_d graph, there appear to be at least two regimes of cesium sorption behavior: 1) high, nearly constant K_d (0.1 L/g) for Cs^+ concentrations below 10^{-8} moles/L, and 2) a variably decreasing K_d for Cs^+ concentrations greater than 10^{-8} moles/L that eventually goes to 0.001 L/g at a Cs^+ concentration of 0.1 moles/L. Differences between the cases are small but consistent: the lower composite sediment cesium K_d is always slightly smaller than the upper composite sediment K_d in both electrolyte solutions. Conversely, the cesium K_d is always slightly higher in the $NaHCO_3$ electrolyte than the $NaNO_3$ electrolyte for both sediments.

Table D.66. Distribution of Cesium on B Tank Farm Upper Composite Sediment in 1 M $NaNO_3$ Electrolyte

Initial [Cs] (mol/L	Solid density (g/L)	% Sorbed	pH	Kd (L/g)	Final [Cs]aq (mol/L)	Final [Cs]ads (mol/g)	Total Cs (mol/L)
1.0E-01	249	20.26	8.91	1.022E-03	6.656E-02	6.801E-05	8.348E-02
1.0E-01	250	20.95	8.93	1.062E-03	6.586E-02	6.992E-05	8.331E-02
1.0E-02	251	37.23	9.07	2.364E-03	6.187E-03	1.463E-05	9.857E-03
1.0E-02	251	35.79	9.07	2.223E-03	6.312E-03	1.403E-05	9.829E-03
1.0E-03	249	56.06	9.08	5.121E-03	4.710E-04	2.412E-06	1.072E-03
1.0E-03	250	56.91	9.11	5.279E-03	4.596E-04	2.426E-06	1.067E-03
1.0E-04	252	64.81	9.05	7.304E-03	3.748E-05	2.738E-07	1.065E-04
1.0E-04	249	64.44	9.10	7.279E-03	3.768E-05	2.743E-07	1.060E-04
1.0E-05	249	76.60	9.15	1.313E-02	2.485E-06	3.263E-08	1.062E-05
1.0E-05	250	79.98	9.10	1.596E-02	2.123E-06	3.388E-08	1.061E-05
1.0E-06	250	93.37	9.12	5.621E-02	7.041E-08	3.958E-09	1.061E-06
1.0E-06	251	92.35	9.12	4.822E-02	8.110E-08	3.911E-09	1.061E-06
1.0E-07	250	95.72	9.12	8.941E-02	4.586E-09	4.101E-10	1.072E-07
1.0E-07	251	95.86	9.10	9.217E-02	4.423E-09	4.077E-10	1.067E-07
1.0E-09	248	95.90	9.13	9.431E-02	8.107E-11	7.645E-12	1.976E-09
1.0E-09	252	96.15	9.15	9.907E-02	7.572E-11	7.501E-12	1.965E-09

Table D.67. Distribution of Cesium on B Tank Farm Lower Composite Sediment in 1 M $NaNO_3$ Electrolyte

Initial [Cs] (mol/L	Solid density (g/L)	% Sorbed	pH	Kd (L/g)	Final [Cs]aq (mol/L)	Final [Cs]ads (mol/g)	Total Cs (mol/L)
1.0E-01	248	18.53	9.11	9.153E-04	6.909E-02	6.324E-05	8.481E-02
1.0E-01	247	16.60	9.10	8.056E-04	7.071E-02	5.696E-05	8.478E-02
1.0E-02	248	27.14	9.21	1.500E-03	7.507E-03	1.126E-05	1.030E-02
1.0E-02	248	27.91	9.18	1.560E-03	7.459E-03	1.164E-05	1.035E-02
1.0E-03	249	51.58	9.21	4.275E-03	5.280E-04	2.257E-06	1.091E-03
1.0E-03	249	52.74	9.24	4.475E-03	5.142E-04	2.301E-06	1.088E-03
1.0E-04	250	56.72	9.23	5.235E-03	4.679E-05	2.449E-07	1.081E-04
1.0E-04	248	57.50	9.21	5.463E-03	4.589E-05	2.507E-07	1.080E-04
1.0E-05	248	69.97	9.22	9.392E-03	3.228E-06	3.031E-08	1.075E-05
1.0E-05	248	70.24	9.23	9.519E-03	3.208E-06	3.053E-08	1.078E-05
1.0E-06	247	90.91	9.19	4.050E-02	9.758E-08	3.952E-09	1.073E-06
1.0E-06	250	91.20	9.21	4.143E-02	9.506E-08	3.938E-09	1.080E-06
1.0E-08	249	95.55	9.21	8.625E-02	5.278E-10	4.553E-11	1.186E-08
1.0E-08	249	95.74	9.19	9.047E-02	5.047E-10	4.566E-11	1.185E-08
1.0E-09	250	95.79	9.19	9.111E-02	8.360E-11	7.616E-12	1.987E-09
1.0E-09	249	95.15	9.22	7.884E-02	9.649E-11	7.608E-12	1.990E-09

Table D.68. Distribution of Cesium on B Tank Farm Upper Composite Sediment in 1 M $NaHCO_3$ Electrolyte

Initial [Cs] (mol/L)	Solid density (g/L)	% Sorbed	pH	Kd (L/g)	Final [Cs]aq (mol/L)	Final [Cs]ads (mol/g)	Total Cs (mol/L)
1.0E-01	251	20.32	8.38	1.016E-03	6.727E-02	6.831E-05	8.442E-02
1.0E-01	250	18.36	8.37	9.002E-04	6.878E-02	6.192E-05	8.425E-02
1.0E-02	250	37.74	8.38	2.420E-03	6.229E-03	1.508E-05	1.000E-02
1.0E-02	250	39.22	8.37	2.582E-03	5.779E-03	1.492E-05	9.509E-03
1.0E-03	251	62.67	8.37	6.678E-03	4.041E-04	2.698E-06	1.083E-03
1.0E-03	250	62.95	8.37	6.790E-03	4.001E-04	2.717E-06	1.080E-03
1.0E-04	251	70.78	8.38	9.645E-03	3.156E-05	3.044E-07	1.080E-04
1.0E-04	251	69.25	8.37	8.958E-03	3.307E-05	2.963E-07	1.076E-04
1.0E-05	251	81.15	8.36	1.716E-02	2.025E-06	3.474E-08	1.074E-05
1.0E-05	249	83.01	8.37	1.960E-02	1.824E-06	3.575E-08	1.074E-05
1.0E-06	249	94.08	8.37	6.381E-02	6.356E-08	4.056E-09	1.074E-06
1.0E-06	250	94.58	8.35	6.968E-02	5.827E-08	4.060E-09	1.075E-06
1.0E-07	249	97.01	8.37	1.304E-01	3.233E-09	4.215E-10	1.083E-07
1.0E-07	252	96.90	8.43	1.240E-01	3.348E-09	4.150E-10	1.079E-07
1.0E-09	250	97.09	8.37	1.336E-01	5.796E-11	7.744E-12	1.994E-09
1.0E-09	251	97.55	8.39	1.592E-01	4.865E-11	7.746E-12	1.989E-09

Table D.69. Distribution of Cesium on B Tank Farm Lower Composite Sediment in 1 M $NaHCO_3$ Electrolyte

Initial [Cs] (mol/L)	Solid density (g/L)	% Sorbed	pH	Kd (L/g)	Final [Cs]aq (mol/L)	Final [Cs]ads (mol/g)	Total Cs (mol/L)
1.0E-01	249	16.65	8.48	8.019E-04	7.072E-02	5.671E-05	8.485E-02
1.0E-01	248	17.07	8.48	8.300E-04	7.045E-02	5.848E-05	8.495E-02
1.0E-02	250	30.61	8.50	1.766E-03	7.169E-03	1.266E-05	1.033E-02
1.0E-02	251	31.74	8.48	1.853E-03	7.059E-03	1.308E-05	1.034E-02
1.0E-03	249	58.20	8.48	5.584E-03	4.574E-04	2.554E-06	1.094E-03
1.0E-03	249	57.95	8.49	5.535E-03	4.590E-04	2.541E-06	1.091E-03
1.0E-04	249	65.19	8.48	7.524E-03	3.784E-05	2.847E-07	1.087E-04
1.0E-04	248	65.16	8.47	7.541E-03	3.749E-05	2.827E-07	1.076E-04
1.0E-05	250	74.63	8.49	1.175E-02	2.752E-06	3.235E-08	1.085E-05
1.0E-05	247	73.41	8.48	1.117E-02	2.869E-06	3.204E-08	1.079E-05
1.0E-06	249	93.25	8.52	5.551E-02	7.281E-08	4.041E-09	1.078E-06
1.0E-06	251	93.29	8.50	5.553E-02	7.245E-08	4.023E-09	1.081E-06
1.0E-07	251	96.81	8.47	1.208E-01	3.469E-09	4.191E-10	1.087E-07
1.0E-07	251	96.82	8.48	1.214E-01	3.449E-09	4.186E-10	1.085E-07
1.0E-09	251	97.36	8.50	1.468E-01	5.274E-11	7.743E-12	1.994E-09
1.0E-09	251	97.12	8.50	1.344E-01	5.752E-11	7.730E-12	2.000E-09

Figure D.128. Cesium Sorption on B Tank Farm Upper and Lower Composite Sediments in 1 M $NaNO_3$ Electrolyte (top) and 1 M $NaHCO_3$ (bottom)

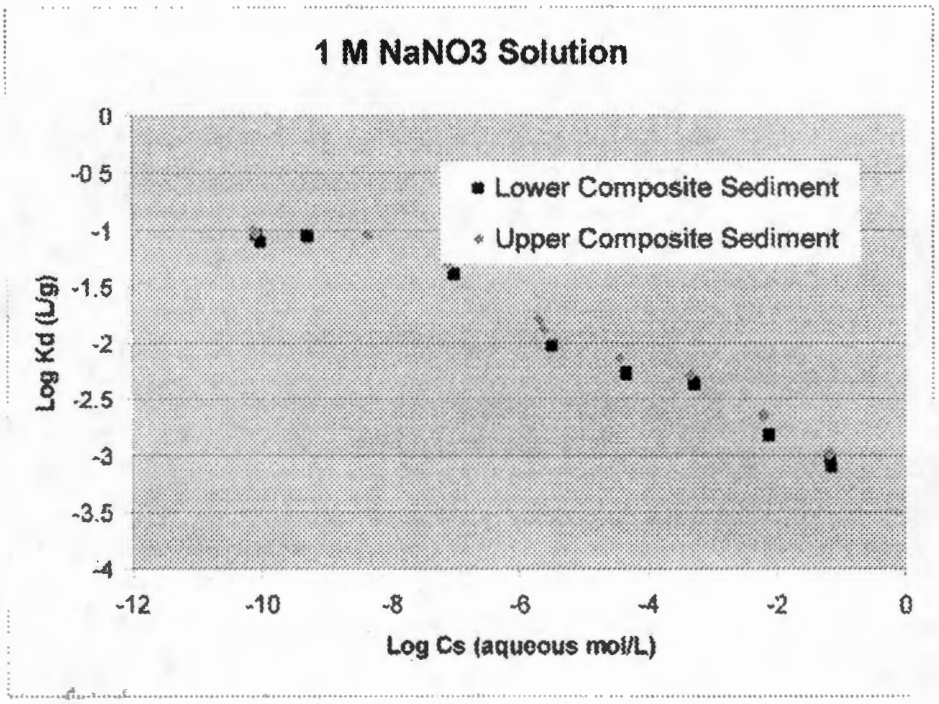

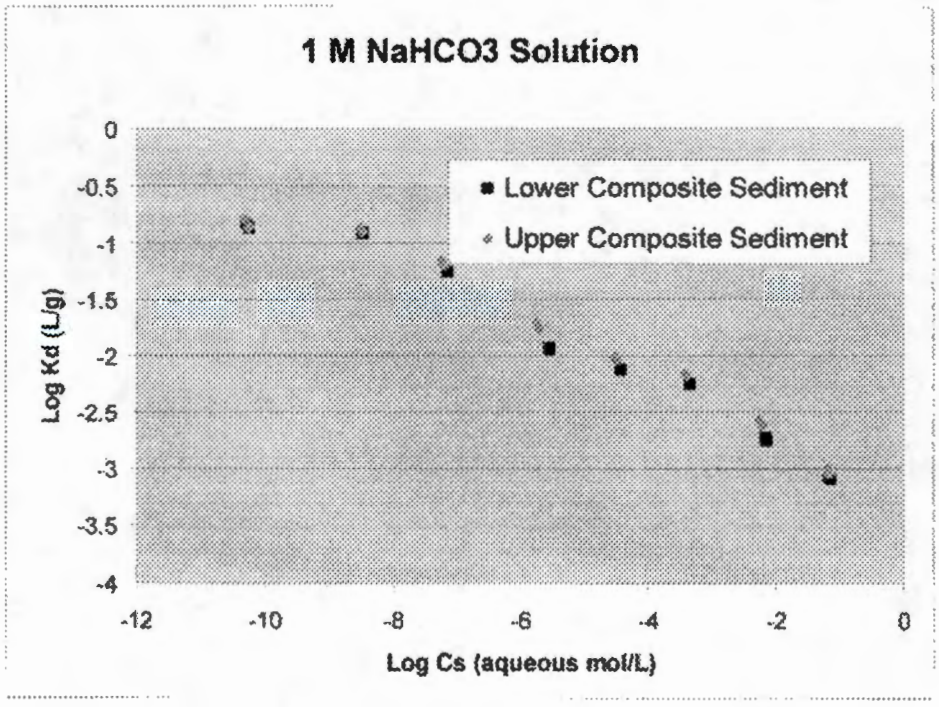

D.4.3.4 Modeling Cesium Adsorption Experiments

D.4.3.4.1 Multisite Ion Exchange Model. The experimental results were analyzed with a reactive transport simulator (Steefel and Yabusaki 1996; Steefel 2001) to test the applicability of a cesium multicomponent ion exchange model developed for SX tank farm sediments (Steefel et al. 2002) in the 200 West Area of the Hanford Site. This model used three exchange sites to account, in part, for a wide range of affinity for cesium: from frayed edges and intralamellar sites in micas at the high end, to surfaces of expansible layer silicates at the lower end (Zachara et al. 2002). The fitting of the high affinity site concentrations (exchange sites 1 and 2 in Table D.70) and a set of selectivity coefficients for each site (Table D.71) were based on a comprehensive array of batch and column experiments performed on a composite sediment representative of the SX tank farm vadose zone. The low affinity site concentration was set to the total CEC of 120 μeq/g, which was reasonable considering the two high affinity sites accounted for 0.02% and 0.22% of the total CEC. To accommodate hypersaline tank farm waste, the ion exchange model addressed high-ionic strength activity corrections within the framework of a Debye-Huckel activity model, supplemented by effective equilibrium constants for $CsNO_3$ and $NaNO_3$ ion pairs. The effective equilibrium constants for $CsNO_3$ and $NaNO_3$ were calibrated by fitting free ion activities to values predicted by the Pitzer-based speciation code GMIN (Felmy 1995).

Table D.70. Distribution of Exchange Sites for SX Tank Farm Sediments (Steefel et al. 2002)

Exchange Site	Concentration (μeq/g)
1	0.0228
2	0.262
3	120

Table D.71. Equilibrium Constants for SX Tank Farm Sediments (Steefel et al. 2002)

Reaction	Log K
$NaX1 + Cs^+ = Na^+ + CsX1$	7.25
$NaX2 + Cs^+ = Na^+ + CsX2$	4.93
$NaX3 + Cs^+ = Na^+ + CsX3$	1.99
$KX1 + Cs^+ = K^+ + CsX1$	4.99
$KX2 + Cs^+ = K^+ + CsX2$	1.83
$KX3 + Cs^+ = K^+ + CsX3$	0.74
$0.5CaX1_2 + Cs^+ = 0.5Ca^{2+} + CsX1$	15.27
$0.5CaX2_2 + Cs^+ = 0.5Ca^{2+} + CsX2$	10.89
$0.5CaX3_2 + Cs^+ = 0.5Ca^{2+} + CsX3$	3.2
$NaNO_3(aq) \rightarrow Na^+ + NO_3^-$	0.37
$CsNO_3(aq) \rightarrow Cs^+ + NO_3^-$	0.47
Debye-Huckel Bdot parameter (Cs-X)	-0.136

D.4.3.4.2 Modeling Cesium Sorption on B Tank Farm Sediments. The matrix of cesium adsorption measurements (Table D.65) on B tank farm sediments was modeled with the multicomponent ion exchange model developed for the SX tank farm sediments. For each batch experiment, three different CECs were tested: 1) the sum of exchangeable cations (in μeq/g) displaced from B tank farm sediment by ammonium chloride (79.3 μeq/g for the upper composite and 73.1 μeq/g for the lower composite sediments), 2) a value of 120 μeq/g determined for SX sediment by Na-22 isotopic exchange, and 3) the ammonium chloride extractable cations from Hanford fine sand composite (50.2 μeq/g, (Zachara et al. Section D.2.1). The relative CEC distribution over the three exchange site types was in the same proportions as the SX tank farm sediment calibration. All other reaction parameters calibrated for cesium ion exchange on SX tank farm sediments were used without modification.

The initial cesium concentration for each modeled experiment was based on the sum of the measured cesium in sorbed and aqueous form, not the nominal solution concentration added to the sediment. Solid solution ratios, pH, nitrate, and bicarbonate were the only other experiment-specific information used in the modeling analyses.

D.4.3.4.3 Modeling Results for the Batch Experiments. The three CECs tested within the existing cesium multisite, multicomponent ion exchange model were able to capture the general behavior for all the experiments (i.e., upper B composite sediment, lower B composite sediment, 1 M $NaNO_3$ solution, and 1 M $NHCO_3$ solution) over 10 orders of Cs^+ concentrations. The comparison of the model predictions of cesium sorption for the upper B composite sediment is in Figure D.129. Of the three CECs tested, the Hanford fine sand composite CEC of 50.2 μeq/g consistently provided the best match for all cases.

D.4.3.4.4 Modeling Discussion for Batch Experiments. Results from the modeling of the batch experiments demonstrated that the three-site multicomponent cesium ion exchange model developed for the SX tank farm sediments could be adapted for use on the B tank farm sediments with a CEC of 50.2 μeq/g. While the experimentally derived CECs (i.e., 79.3 μeq/g and 73.1 μeq/g for the upper and lower B composite sediments, respectively) in conjunction with the multisite ion exchange model provided reasonable predictions of cesium sorption, predictions with the Hanford fine sand composite CEC of 50.2 μeq/g were always better overall. While a refitting of the exchange site concentrations and selectivity coefficients for the B composite sediments could be performed to accommodate the experimentally-derived CECs, the predictive capability of the existing multisite cesium ion exchange model with only an adjustment of the total CEC was deemed sufficient for scoping calculations of cesium migration in the BX tank farm.

Figure D.129. Comparison of Model Predictions of Cesium Sorption for the Upper B Tank FarmComposite Sediment Batch Experiments

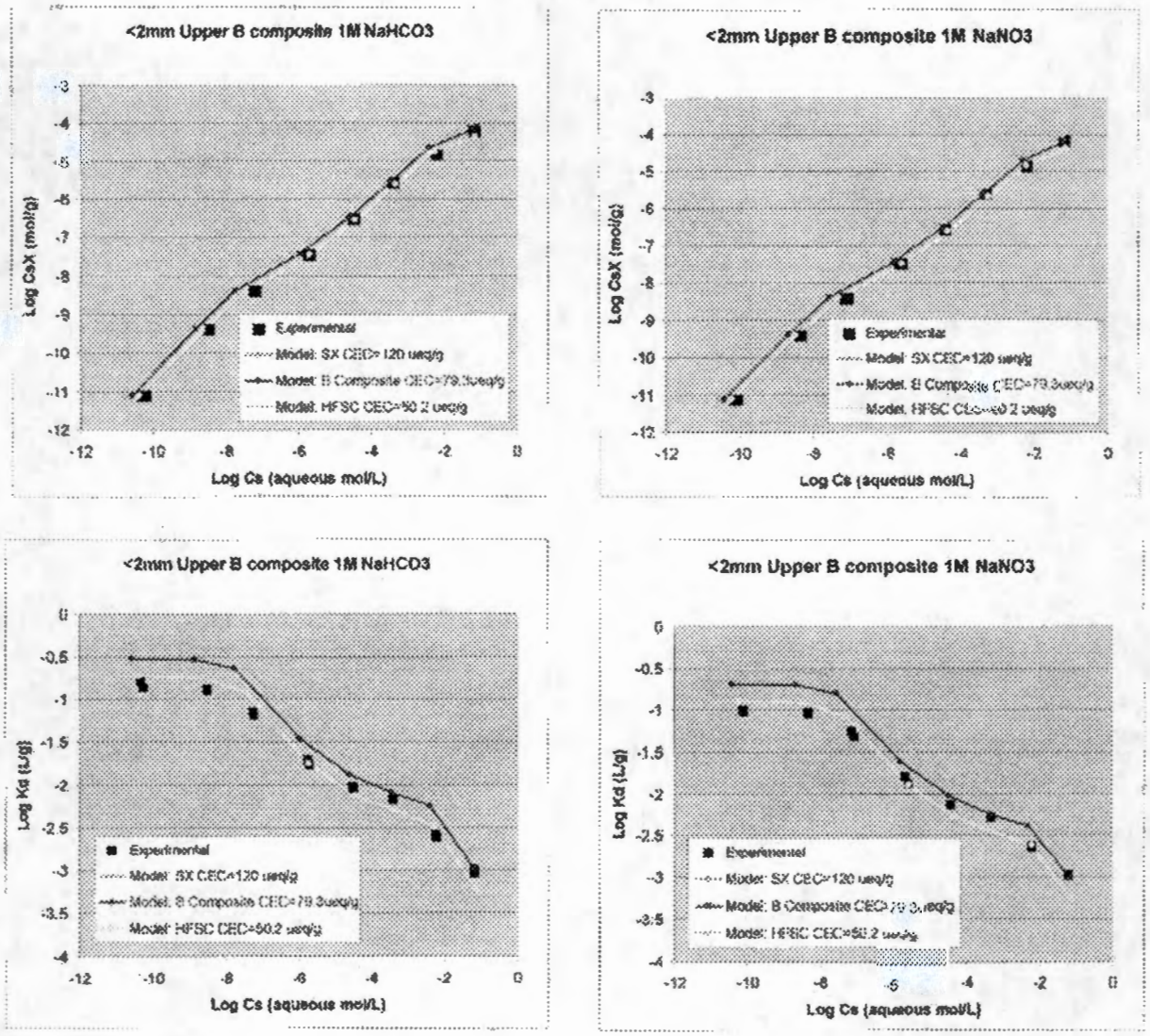

Figure D.130. Comparison of Model Predictions of Cesium Sorption for the Lower B Tank Farm Composite Sediment Batch Experiments

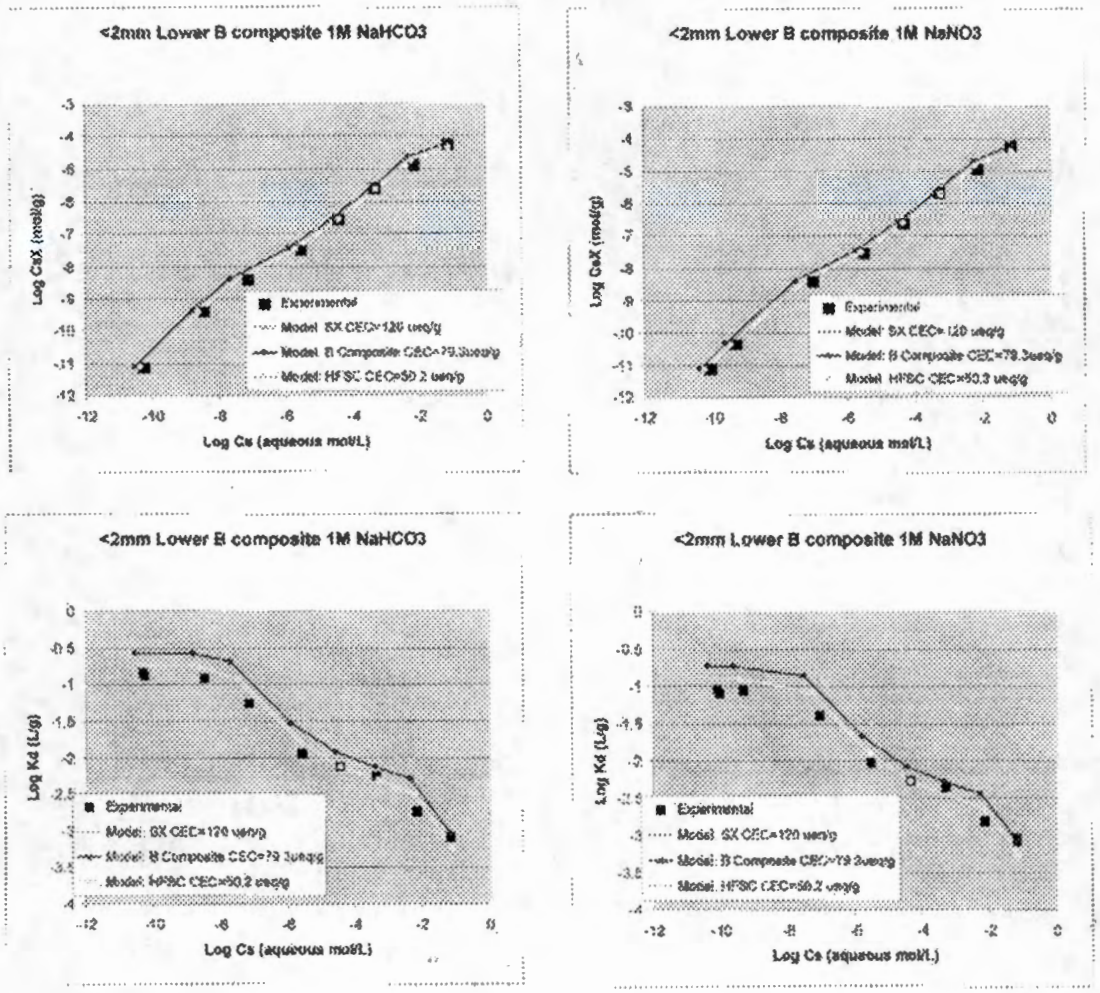

D.4.3.5 Application to Tank BX-102

D.4.3.5.1 Overfill Event. The updated multisite ion exchange model was applied to the prediction of cesium migration from tank BX-102. A one-dimensional scoping calculation was performed based on the February 1951 overfill event at tank BX-102 that released 91,600 gallons of tank waste over approximately 3 weeks (General Electric Company 1951). Flux rates and moisture contents from the three-dimensional vadose zone flow modeling study in Section D.4.2 were used to develop the hydrologic conditions for the one-dimensional scoping calculations.

D.4.3.5.2 Geology. The flow modeling in Section D.4.2 focused on the behavior of the H2 unit of the Hanford formation. The same emphasis was used and only the vertical section between the tank at approximately 40 ft (12 m) bgs and the bottom of the H2 at 170 ft (52 m) bgs was examined.

D.4.3.5.3 Flow Rate. The flow rates of interest at BX-102 are the 100 mm/year recharge, which amounts to 2.74×10^{-4} m/day and the overfill rate of 1.32 m/day based on a 21-day, 91,600-gallon release over an area of 12.5 m^2 (Section D.4.2). The highest moisture content (19.4%) predicted by the three-dimensional flow modeling performed in Section D.4.2 occurred during the overfill event. The lowest moisture content (5.12%) occurred with the background condition from the long-term recharge.

D.4.3.5.4 CEC for Bulk Sediment. Since the laboratory experiments on the B tank farm composite sediments were performed on the <2 mm size fraction, an estimate was needed of the CEC for the bulk sediment. Assuming that all the cation exchange capacity is associated with the <2 mm size fraction and extrapolating to the particle size distribution in the upper B composite sediment resulted in a bulk sediment CEC of 36.0 μeq/g.

D.4.3.5.5 Solid Solution Ratio. To calculate the solid solution ratio, a porosity of 0.416 (Rockhold 1999), a particle density of 2.80 g/cm^3 (Appendix B), and moisture contents from Section D.4.2 were used. Solid solution ratios ranged from 8426 g/L (corresponding to 19.4% moisture content) during the leak event to 31,930 g/L (corresponding to the 5.12% moisture content) under the 100 mm/year recharge.

D.4.3.5.6 Magnesium Selectivity Coefficients. Magnesium was not included in the cesium sorption experiments that were the basis of the multisite ion exchange model of the SX tank farm sediments. For the BX-102 field application, it was assumed that the Mg^{++} selectivity coefficients were the same as the other divalent cation, Ca^{++}.

D.4.3.5.7 Waste Composition. The initial concentrations of chemical components in the tank waste are based on a reconstructed BX-102 composition (Jones et al. 2001) at the time of the 1951 overfill. Although speciation of the reconstructed composition identified minerals that were thermodynamically favored to precipitate (e.g., calcite and apatite), the higher electrolyte concentrations were maintained as a conservative simplification that would increase the competition with cesium for exchange sites. Total concentrations of the major ions appear in Table D.72.

D.4.3.5.8 Total Cesium. Jones et al. (2001) reported cesium in terms of cesium-137 concentrations. Total cesium is considerably higher because cesium-133 and cesium-135 accompanied cesium-137 in the waste streams transferred to the tank farms. Measurements of the ratio of total cesium to cesium-137 in the slant borehole at tank SX-108 averaged 4.76 (Appendix A of Knepp 2002). This was approximately 37-year old waste. Since only the cesium-137 decays appreciably during this time period, the total cesium to cesium-137 ratio at the time of the waste generation can be calculated. "Undecaying" the cesium-137 fraction over 37 years results in a total cesium to cesium-137 ratio of 2.61 at the time of the original waste transfer. Assuming that the 1951 overfill event came from the transfer of waste that had not significantly aged, we applied this ratio to the Jones (2001) cesium-137 estimate of 8.61×10^{-7} M/L, which results in a total cesium concentration of 2.24×10^{-6} M/L.

D.4.3.5.9 Geochemical Conditions. The initial porewater chemistry is taken from sample C3391 in the H2 Hanford unit at 77.3 ft bgs from borehole 299-E33-338, an uncontaminated borehole south of the B tank farm (Appendix B). The exchange sites are equilibrated with these

concentrations prior to the start of the transport simulation. The initial condition including exchanged cation concentrations is summarized in Table D.72. At the conclusion of the tank waste loading flow regime, the initial condition was used as the aqueous boundary condition for the balance of the simulation.

Table D.72. Concentrations of Porewater and Waste Source

	INITIAL CONDITIONS		SOURCE
Component	**Aqueous Total Concentration (molality)**	**Exchange Site Concentration (equiv / g)**	**Aqueous Total Concentration (molality)**
Cs^+	0.0	0.0	2.24E-6
Na^+	5.85E-3	1.21E-06	2.92E+0
Ca^{++}	3.90E-3	1.92E-05	1.33E-2
Mg^{++}	1.74E-3	8.76E-06	0.0
K^+	1.77E-3	6.79E-06	2.73E-3
HCO_3^-	2.70E-2		6.43E-1
NO_3^-	4.37E-4		5.76E-1
Cl^-	5.94E-4		1.25E-2
SO_4^{--}	9.58E-4		2.30E-1
pH	7.14		10.5

D.4.3.6 Tank BX-102 Modeling

D.4.3.6.1 Modeling Approach. The goal of the modeling was to obtain an order of magnitude understanding of cesium migration beneath tank BX-102 based upon the characterization of cesium ion exchange in a laboratory setting. A one-dimensional model is used here for simplicity with the recognition that multidimensional modeling studies are under way but will not be available for publication in this document. A succession of two steady states based loosely on the three-dimensional flow modeling in Section D.4.2 is used to represent the 21-day waste release and subsequent migration under the background recharge rate of 100 mm/yr. The 130-ft (40-m), one-dimensional model domain was uniformly discretized into 0.5 m grid cells. Diffusion and dispersion were ignored in this calculation.

D.4.3.6.2 Modeling Results. After 21 days of constant loading of BX-102 waste into the vadose zone column, cesium is predicted to sorb strongly to the initial sediments it encounters. The predicted position of the cesium front after the first 21 days in the system is 5.25 meters into the formation (Figure D.131). This is significant in view of the 6.8 m/d pore velocity imposed in this one-dimensional model domain during this time period. The apparent retardation factor for these conditions is 31.7. Under the conditions modeled, this represents the lowest retardation that could occur as other conditions have much lower concentrations of competing cations, which are associated with higher cesium K_ds. Over 70% of the cesium is associated with the high affinity exchange site (i.e., site 1) with the balance divided nearly equally between the other two exchange sites.

After the overfill event, the background recharge rate of 100 mm/yr and moisture content of 0.0512 were imposed on the waste that had already entered the system. After 50 years of simulation under these conditions, there was essentially no additional migration of the cesium front (Figure D.131). Exchanged cesium concentrations did not change significantly although small changes from differential sorption and desorption were occurring in the first 1.5 meters with a net increase in the cesium concentration on the low affinity exchange site, and a commensurate decrease on the second higher affinity exchange site. These changes are relatively small when compared to the effect of radioactive decay on the cesium-137 fraction during this time period.

D.4.3.6.3 Discussion of Modeling Results. The modeling results indicate that the primary penetration of cesium into the formation occurs during the dynamics of the loading event, in this case, the BX-102 overfill in 1951. For the waste composition modeled, cesium transport during the loading event is highly retarded resulting in a localized distribution near the point of entry. Flow modeling in the vadose zone sediments near BX-102 described in Section D.4.2 demonstrated that elevated moisture contents from the 91,600-gallon liquid release rapidly return to near-background conditions in a few months. Once the waste loading stops and the system returns to the recharge driven flow regime in this short time period, the cesium is essentially immobilized. Under these conditions, radioactive decay of the cesium-137 fraction is the dominant transformation process.

While a more detailed three-dimensional modeling study with heterogeneous material properties and anisotropic permeability may predict a different depth for the cesium-137 exchange front, the one-dimensional model has identified a considerable retardation effect that severely limits cesium migration, even during a large volume release event. Based on these analyses, other mechanisms would have to be invoked to account for the deep cesium migration observed at tank BX-102. This is consistent with field observations and modeling analyses at tank SX-115 (Steefel and Yabusaki 2001), which identified very limited cesium migration despite cesium-137 and sodium concentrations (8.31×10^{-6} M and 3.593 M, respectively; Jones et al. 2000) that were considerably higher than concentrations at tank BX-102 (8.61×10^{-7} M and 2.92; Jones et al. 2001). One significant difference between the two cases is the CEC, 120 μeq/g, for the SX tank farm sediments and 50.2 μeq/g for the B tank farm sediments.

Figure D.131. Predicted Spatial Distribution of Total Cesium on Exchange Sites After 21 Days (left) and 50 Years (right)

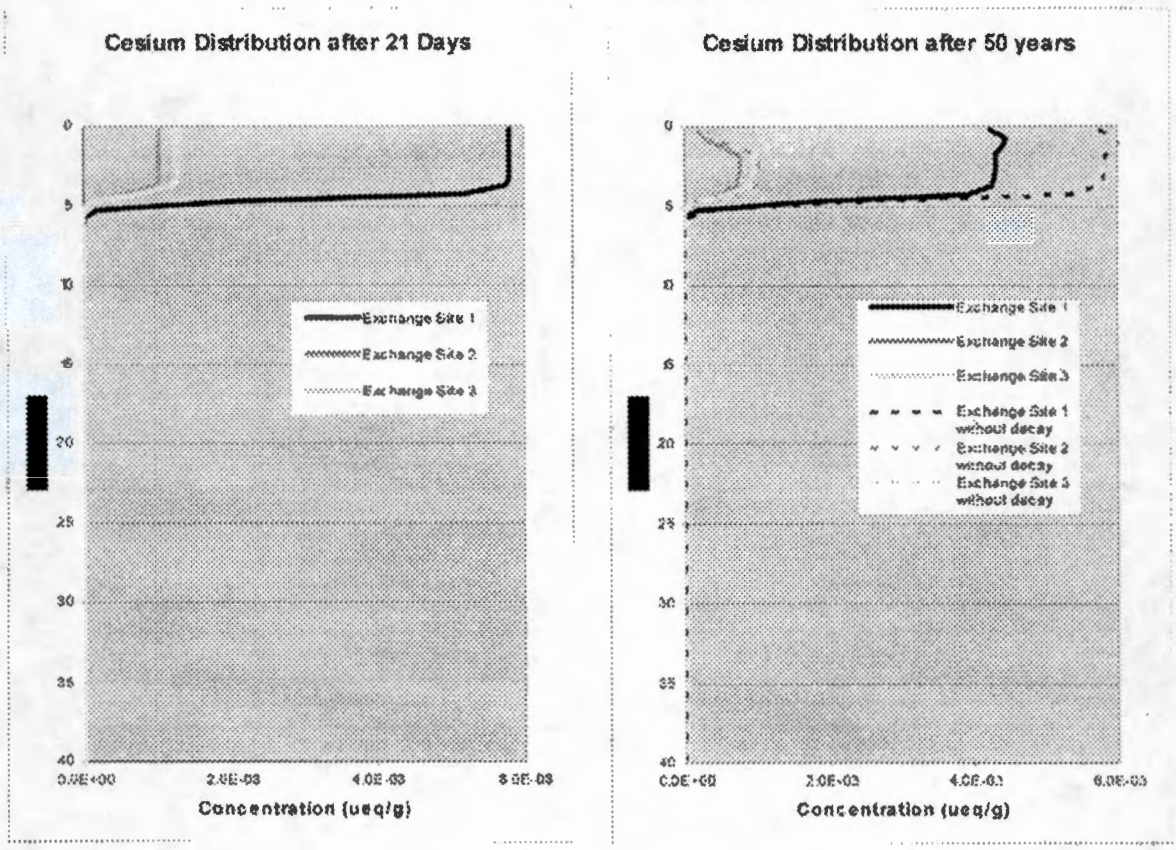

D.4.3.7 Conclusions

A matrix of cesium adsorption experiments was performed on two sediments (i.e., upper and lower B tank farm composites) from the 200 East Area of the Hanford Site using two electrolyte solutions (1 M $NaNO_3$ and 1 M $NaHCO_3$) with initial cesium concentrations ranging from 10^{-1} M to 10^{-9} M. The adsorption behavior of the two sediments was nearly identical. A multisite cesium multicomponent ion exchange model developed for SX tank farm sediments was adapted for use on the B tank farm composite sediments by testing three laboratory-derived cation exchange capacities. A CEC of 50.2 μeq/g was found to provide the best predictions of the cesium adsorption behavior in the B tank farm sediments. The resulting adsorption model was modified for field conditions during the 1951 tank BX-102 overfill event by adjusting the CEC based on particle size distribution and the solid solution ratio based on moisture content.

Specific findings from these analyses are:

1. For the experimental conditions that were investigated, the multisite, multicomponent cesium ion exchange model developed for SX tank farm sediments could be adapted for use on the B tank farm sediments by adjusting the cation exchange capacity and retaining the fitted selectivity coefficients.

2. Application of the modified ion exchange model to the 1951 BX-102 overfill event using a one-dimensional multicomponent reactive transport simulator suggests that the cesium exchange front should be highly retarded (retardation factor of 31.7) during the active waste release period. Essentially all the cesium migration is predicted to take place under this regime of high flow and high electrolyte loading.
3. After the overfill event, as moisture contents rapidly return to their recharge-driven values, the reintroduction of lower background electrolyte concentrations through the zone of exchanged cesium does not result in further mobilization.
4. Without subsequent flow and/or waste release events of similar magnitude, the dominant process controlling cesium concentrations is radioactive decay.

D.4.3.8 References

DOE-GJO, 2000, *Vadose Zone Characterization Project at the Hanford Tank Farms: Addendum to the BX Tank Farm Report*, GJO-98-40-TARA/GJO-HAN-19, Prepared by U.S. Department of Energy, Grand Junction Office, Grand Junction, Colorado for U.S. Department of Energy, Richland Operations Office, Richland, Washington.

Felmy, A. R., 1995, "GMIN, A Computerized Chemical Equilibrium Program Using a Constrained Minimization of the Gibbs Free Energy: Summary Report", In *Chemical Equilibrium and Reaction Models*, Soil Science Society of America, Madison, Wisconsin.

Fraser, M. C. and D. J. Larkin, 1974, Memorandum to H.P. Shaw, Subject: "Radionuclide Inventories in Leaks from Transfer Lines and Tanks," Atlantic Richfield Hanford Company, Richland, Washington.

General Electric Company, 1951, *Hanford Works Monthly Report for February 1951*, HW-20438, Operated for the Atomic Energy Commission, Richland, Washington.

Jones, T. E., R. A. Watrous, and G. T. Maclean, 2000, *Inventory Estimates for Single-Shell Tank Leaks in S and SX Tank Farms*, RPP-6285, Rev. 0, CH2M HILL Hanford Group, Inc., Richland, Washington.

Jones, T. E., B. C. Simpson, M. I. Wood, and R. A. Corbin, 2001, *Preliminary Inventory Estimates for Single-Shell Tank Leaks in B, BX, and BY Tank Farms*, RPP-7389, Rev. 0, CH2M HILL Hanford Group, Inc., Richland, Washington.

Knepp, A. J., 2002, *Field Investigation Report for Waste Management Area S-SX*, RPP-7884, Rev. 0, CH2M HILL Hanford Group, Inc., Richland, Washington.

Randall, R. R. and R. K. Price, 1999, *Analysis of Historical Gross Gamma Logging Data from BX Tank Farm*, HNF-3531, Rev.0, prepared by Waste Management Northwest and Three Rivers Scientific for Lockheed Martin Hanford Corporation, Richland, Washington.

Rockhold, M. L, 1999, "Conditional Simulation and Upscaling of Soil Hydraulic Properties," In *Characterization and Measurement of the Hydraulic Properties of Unsaturated Porous Media*, van Genuchten, Leij, and Wu (eds), pp. 1391-1401. U.S. Salinity Laboratory, Riverside, California.

Steefel, C. I., 2001, *GIMRT, Version 1.2: Software for Modeling Multicomponent Multidimensional Reactive Transport, Users's Guide*, UCRL-MA-143182, Lawrence Livermore National Laboratory, Livermore, California.

Steefel, C. I., S. Carroll, P. Zhao, S. Roberts, 2002, "Cesium Migration in Hanford Sediment: A Multi-Site Cation Exchange Model Based on Laboratory Transport Experiments," accepted for publication in the *Journal of Contaminant Hydrology*.

Steefel, C. I., and S. B. Yabusaki, 2001, *Evaluation of the Field Exchange Capacity of Hanford Sediments with Implications for ^{137}Cs Migration*, PNNL-2001-7, Pacific Northwest National Laboratory, Richland, Washington.

Womack, J. C. and D. J. Larkin, 1971, *Investigation and Evaluation of the 102-BX Tank Leak*, ARH-2035, Atlantic Richfield Hanford Company, Richland, Washington.

Zachara, J. M., S. C. Smith, C. Liu, J. P. McKinley, R. J. Serne, and P. L. Gassman, 2002, "Sorption of Cs^+ to Micaceaous Subsurface Sediments from the Hanford Site, USA," *Geochimica et Cosmochimica Acta*, Vol. 66:193-211.

D.5.0 ISOTOPE TRACKING OF THE FATE AND TRANSPORT OF RADIONUCLIDES IN B, BX, AND BY TANK FARMS SEDIMENTS

The isotopic compositions of a number of contaminants and associated compounds provide ideal tracers for following the movement of specific waste streams through the subsurface. Isotopic analyses are generally much more precise and reproducible than most chemical analyses, making it possible to use isotopic measurements to detect relatively small inputs from specific sources. This is critical for determining the origins of subsurface contaminants where multiple possible sources are present such as in the Hanford Site tank farms. Without this information, it can be difficult, if not impossible, to determine the potential impact of specific waste streams. In this section, preliminary results on the uranium isotopic compositions of vadose zone contamination are presented. Using distinct differences between the isotopic compositions of natural uranium and the multiple anthropogenic sources of uranium present at Hanford, it has been possible to narrow down the potential origins of this contamination, including being able to link the groundwater plume to its likely origin.

In addition to providing potential fingerprints for different contaminant sources, some isotopic measurements can be used to understand interaction between the waste fluids and the sediments. Through previous work on uncontaminated background samples, it has been possible to determine the natural shifts in stable strontium isotope ratios ($^{87}Sr/^{86}Sr$) that are produced by exchange between the infiltrating porewaters and the sediments. By comparison, high-pH waste streams (such as the one in the sediments in the vicinity of tank B-110) isotopically equilibrate with the sediments much more quickly, indicating that the waste fluids are causing rapid dissolution of silicate minerals in the sediments. This information can be used to quantify the impact of interaction between the fluids and the sediments on the chemistry of the waste fluids and assess the effect that interaction will have on contaminant transport through the vadose zone.

D.5.1 THE ISOTOPIC COMPOSITIONS OF WATER LABILE URANIUM FROM 299-E33-45 AND 299-E33-46 CORE SAMPLES: IMPLICATIONS FOR THE SOURCE AND HISTORY OF GROUNDWATER CONTAMINATION IN THE WMA B-BX-BY AREA

John N. Christensen[1], P. E. Dresel[2], Mark Conrad[1], Kate Maher[3], and Donald J. DePaolo[1,3]

[1]Lawrence Berkeley National Laboratory, Berkeley, California 94720
[2]Pacific Northwest National Laboratory, Richland, Washington 99352
[3]University of California, Berkeley, California 94720

D.5.1.1 Introduction

Natural sources of uranium have a uniform $^{238}U/^{235}U$ ratio (with the notable exception of the Oklo natural reactor), but can have variable $^{234}U/^{238}U$ depending on natural processes that can disturb the secular equilibrium of the ^{238}U decay chain. In contrast, anthropogenic U can have altered $^{238}U/^{235}U$ due to ^{235}U enrichment for nuclear applications or to changes due to the burn up of natural or enriched uranium in nuclear reactors. In addition, the consumption of uranium fuel rods in reactors produces ^{236}U (half-life = 23 million years), an isotope that does not occur naturally, through neutron capture by ^{235}U. These contrasts in uranium isotopic compositions of natural and anthropogenic uranium, as well as the wide variation in the isotopic composition of different anthropogenic uranium sources, promotes the measurement of uranium isotopic composition as a tracer of uranium contamination in the environment. Here is reported the isotopic compositions of uranium from vadose zone samples obtained from two contaminated cores in the B, BX, and BY tank farms. The isotopic analyses are discussed in relation to previous measurements of groundwater uranium isotopic composition in order to produce a link between vadose zone and groundwater contamination, identify contamination sources, and provide estimates of the relative proportions of anthropogenic uranium in the analyzed samples. In addition, the uranium isotopic compositions measured in the vadose zone and groundwater samples can be related to calculated estimates of the uranium isotopic compositions of different waste fluids to constrain the history of contamination events in the B, BX, and BY tank farms.

D.5.1.2 Analytical Methods

Sediment samples from two cores were analyzed, one core from near tank BX-102 (borehole 299-E33-45) and one near tank B-110 (borehole 299-E33-46). Depths of the analyzed samples are provided in Table D.73 and Table D.74. Analyses were conducted on de-ionized water rinses of sediment samples from the cores that remained after previous chemical and radiological analyses were completed. Concentrations of total uranium of the rinses were determined by ICP-MS at PNNL.

Table D.73. Uranium Isotopic Data Core 299-E33-45 (Near Tank BX-102)

Sample	Ave. depth, feet	PW [U] ppb	$^{234}U/^{238}U \times 10^6$	$\pm 2\sigma \times 10^6$	$^{238}U/^{235}U$	$\pm 2\sigma$	$^{236}U/^{238}U \times 10^6$	$\pm 2\sigma \times 10^6$	†% Anthr.
S01014-01A	10.64	44.1	59.84	0.06	138.142	0.067	0.712	0.012	0.90
S01014-06A	20.84	14.6	60.19	0.10	138.116	0.059	0.602	0.019	0.76
S01014-33A	73.39	29705.2	54.12	0.12	147.900	0.054	78.97	0.10	100
S01014-35A	78.19	22406.3	54.12	0.14	147.888	0.061	78.51	0.09	100
S01014-40A	88.65	9019.7	54.00	0.12	147.902	0.087	78.94	0.12	100
S01014-54A	120.99	661396.2	53.98	0.04	147.861	0.046	78.82	0.15	100
S01014-72A	151.55	92930.5	53.96	0.13	147.888	0.108	78.74	0.16	100
S01014-78A	160.85	70364.4	54.12	0.16	147.906	0.068	78.72	0.11	100
S01014-82A	168.65	5316.2	54.04	0.11	147.924	0.082	78.55	0.11	100
S01014-83A	171.05	4804.5	53.87	0.07	147.99	0.15	78.81	0.13	100
S01014-93A	190.65	47916.1	53.95	0.12	147.881	0.042	78.78	0.09	100
S01014-116A	231.45	16.9	57.48	0.11	138.950	0.040	8.22	0.04	10.4

Table D.74. Uranium Isotopic Data Core 299-E33-46 (Near Tank B-110)

Sample	Ave. depth, feet	PW [U] ppb	$^{234}U/^{238}U \times 10^6$	$\pm 2\sigma \times 10^6$	$^{238}U/^{235}U$	$\pm 2\sigma$	$^{236}U/^{238}U \times 10^6$	$\pm 2\sigma \times 10^6$	²% Anthr.
S01052-06A	21.12	24.1	62.45	0.12	138.051	0.071	0.789	0.011	1.47
S01052-21A	53.02	69.4	56.33	0.11	142.496	0.052	35.20	0.08	65.68
S01052-26A	60.72	560.2	54.44	0.06	144.368	0.036	52.15	0.07	97.31
S01052-36A	79.95	2161.2	54.35	0.04	144.470	0.120	53.64	0.07	100
S01052-38A	83.05	3425.0	54.34	0.04	144.510	0.110	53.46	0.12	100
S01052-42A	90.62	160.2	56.24	0.12	142.333	0.074	35.79	0.07	66.78
S01052-47A	98.62	580.3	55.96	0.05	142.974	0.044	39.46	0.04	73.63
S01052-53A	111.42	150.1	60.27	0.12	138.724	0.020	6.78	0.05	12.66
S01052-57A	119.92	141.4	60.81	0.06	137.881	0.051	0.437	0.004	0.82
S01052-82A	164.55	42.8	60.39	0.12	137.966	0.070	0.209	0.005	0.39
S01052-90A	179.85	27.2	59.87	0.08	137.901	0.041	0.303	0.005	0.57

Percent anthropogenic uranium in porewater based on $^{236}U/^{238}U$, see text.

For the isotopic analyses, the uranium was chemically separated from the allotted sample aliquots. The uranium isotopic compositions ($^{234}U/^{238}U$, $^{238}U/^{235}U$ and $^{236}U/^{238}U$) were measured on a multiple collector ICP source magnetic sector mass spectrometer (MC-ICPMS) at Lawrence Berkeley National Laboratory. This instrument is equipped with nine movable Faraday cups, 2 movable channeltron electron multipliers, and an axial Daly photo multiplier system with ion counting. The Daly system is situated behind a wide angle retardation potential lens providing an abundance sensitivity at mass 237 compared to mass 238 of ~80 ppb. Uranium isotopes 235 and 238 were measured on Faraday cups, while isotopes 234 and 236 were measured on the Daly system. Corrections for mass fractionation and Daly-Faraday inter-calibration were calculated from bracketed analyses of an in-house secular equilibrium natural uranium standard. Isotopic compositions were normalized to $^{238}U/^{235}U = 137.88$ of the standard solution. The measured concentrations and isotopic compositions are compiled for borehole 299-E33-45 in Table D.73 and for borehole 299-E33-46 in Table D.74.

D.5.1.3 Results

D.5.1.3.1 Borehole 299-E33-45. A total of 12 samples were measured from core 299-E33-45 near tank BX-102. The uranium concentrations of the de-ionized water rinses outline a distinct plume between 72 to 205 ft depth in the core, with a peak at about 120 to 130 ft depth (Table D.73). Nine of the samples analyzed come from this plume region, including the highest concentration sample. The U isotopic compositions of these nine samples are essentially homogenous in $^{234}U/^{238}U$, $^{238}U/^{235}U$, and $^{236}U/^{238}U$ across the uranium contamination plume. The weighted average ratios are $^{234}U/^{238}U = 5.3979 \times 10^{-5}$ (±0.097%, 95% confidence limits), weighted average $^{238}U/^{235}U = 147.889$ (±0.014%, 95% confid.), and weighted average $^{236}U/^{238}U = 7.875 \times 10^{-5}$ (±0.16%, 95% confid.). The extremely high U concentrations of the plume samples (from 4,800 ppb to 660,000 ppb calculated for porewater in the plume compared to background values of 15 to 150 ppb), and the consistency of their measured U isotopic compositions, indicate that this is the isotopic signature of the U contaminant. In contrast, a sample (S01014-116A) from within a perched water body at 231.45 ft depth has a distinct isotopic composition ($^{234}U/^{238}U = 5.748 \times 10^{-5}$ (±0.19% 2σ), $^{238}U/^{235}U = 138.950$ (±0.029% 2σ) and $^{236}U/^{238}U = 8.22 \times 10^{-6}$ (±0.2% 2σ)). Two samples (S01014-1A and S01014-6A) from near the top of the 299-E33-45 core from depths of 10.6 ft and 20.8 ft have near normal isotopic compositions ($^{238}U/^{235}U = 138.142$ and 138.116, respectively), but with small but measurable $^{236}U/^{238}U$ (7.1×10^{-7} and 6.0×10^{-7}, respectively).

The data for 299-E33-45 are presented on a plot of $^{238}U/^{235}U$ versus $^{236}U/^{238}U$ in Figure D.132. In addition, data for Hanford groundwater samples (Dresel et al. 2002) and estimates of the U isotopic compositions of the tank leaks in the WMA B-BX-BY areas (Jones et al. 2001) are plotted on this figure. On such a plot, natural U should plot on the x-axis ($^{236}U/^{238}U = 0$) at a value of $^{238}U/^{235}U = 137.88 \pm 0.04$. The U isotopic compositions representing the plume in 299-E33-45 form a tight cluster, while the perched water zone sample and the two shallow samples fall closer to the $^{238}U/^{235}U$ axis. A best-fit line through the plume data (nine points) and the data for S01014-116A from the perched water zone gives an intercept of 137.908±0.044 (±2σ, MSWD=1.3), within error of the $^{238}U/^{235}U$ of natural uranium. This suggests that the sample S01014-116A consists of a mixture of natural uranium and anthropogenic uranium. Assuming the weighted average $^{238}U/^{235}U$ (= 147.889±0.021) of the plume samples as the end member

contaminant, then 10.7±0.4% of the uranium in that sample is anthropogenic. A similar calculation based on $^{236}U/^{238}U$ gives an indistinguishable but better constrained result of 10.44±0.07%. Likewise, plotting $^{234}U/^{238}U$ against $^{236}U/^{238}U$ (Figure D.133) can give an estimate for the pre-contamination $^{234}U/^{238}U$ of sample 116A. At $^{236}U/^{238}U = 0$, the $^{234}U/^{238}U$ is $5.789 \pm 0.022 \times 10^{-5}$ (±95%, MSWD=2.8) which indicates an excess of ^{234}U relative to ^{238}U ($^{234}U/^{238}U$ activity ratio = 1.056±4) as is typical of natural groundwater samples. Similar calculations based on $^{236}U/^{238}U$ can be made for samples S01014-1A and S01014-6A, indicating <1% anthropogenic U in those shallow samples (0.90±0.02% and 0.76±0.03%, respectively). The $^{234}U/^{238}U$ of these two samples corrected for the anthropogenic component are for $1A = 5.989 \pm 0.007 \times 10^{-5}$ and for $6A = 6.024 \pm 0.011 \times 10^{-5}$. Therefore, both these samples exhibit similar excesses of ^{234}U ($^{234}U/^{238}U$ activity ratios of 1.092±0.001 and 1.099±0.002).

Figure D.132. $^{238}U/^{235}U$ versus $^{236}U/^{238}U$

Grey filled squares data for water extractions from samples from the borehole 299-E33-45 (near tank BX-102) contaminated core, black solid squares data for water extractions of samples from the borehole 299-E33-46 (near tank B-110) contaminated core. Open squares are estimates by Jones et al. (2001) of the uranium isotopic composition of tank leaks in the WMA B-BX-BY area. Filled black circles are uranium isotopic data for groundwater samples from Dresel et al. (2002).

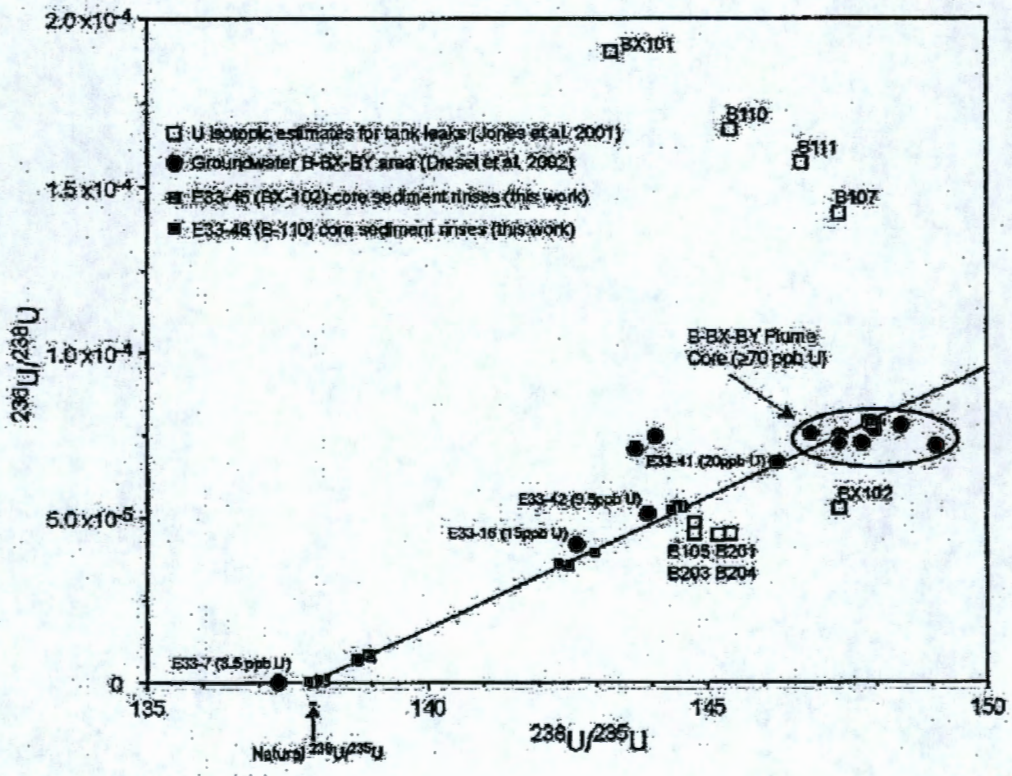

Figure D.133. $^{234}U/^{238}U$ versus $^{236}U/^{238}U$

Grey filled squares data for water extractions from samples from the borehole 299-E33-45 (near tank BX-102) contaminated core, black solid squares data for water extractions of samples from the borehole 299-E33-46 (near tank B-110) contaminated core. Filled black circles are uranium isotopic data for groundwater samples from Dresel et al. (2002).

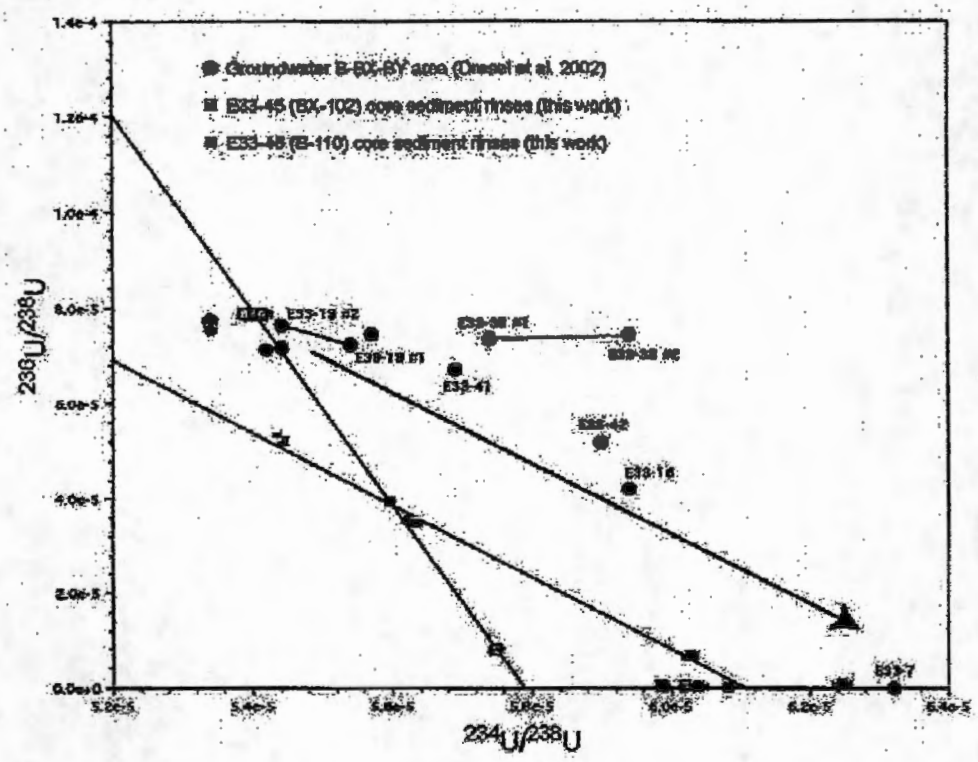

D.5.1.3.2 Borehole 299-E33-46. Eleven samples were analyzed from 299-borehole 299-E33-46 near tank B-110. The calculated porewater U concentrations in this core are much lower than in borehole 299-E33-46, with ~9,700 ppb being the highest concentration found. From the concentration data (Table D.74), the U contamination plume covers a depth range from approximately 50 ft to 125 ft, with a peak concentration at ~70 ft depth. Eight samples are from this zone, two from greater depth (samples S01052-82A from 164.5 ft and S01052-90A from 180 ft) and one sample (S01052-06A) from within the backfill at a depth of 21 ft. Unfortunately, the sample with the highest U concentration, S01052-31A was not available for U isotopic analysis, but the next highest concentration samples were analyzed.

The eight samples from the 299-E33-46 plume exhibit a significant range in isotopic composition compared to the 299-E33-45 plume (Table D.74). The two highest concentration samples (S01052-38A and S01052-36A) analyzed, though, have similar isotopic compositions and likely represent the composition of the contaminant uranium. The average isotopic compositions of those two samples are: $^{234}U/^{238}U = 5.434 \times 10^{-5}$ (±0.057%, 95% confidence), $^{238}U/^{235}U = 144.492$ (±0.056%, 95%), and $^{236}U/^{238}U = 5.359 \times 10^{-5}$ (±0.12%, 2σ internal). The

data for the 299-E33-46 samples are also plotted on Figure D.132. The best-fit line to the plume data has an intercept of 137.90±0.22, indistinguishable from the value for natural uranium. In a plot of $^{234}U/^{238}U$ versus $^{236}U/^{238}U$ (Figure D.133), the data for the 299-E33-46 plume forms a linear array with an intercept at $^{234}U/^{238}U = 6.091 \pm 0.028 \times 10^{-5}$ ($\pm 2\sigma$ MSWD=11). This value falls roughly at the mean of the measured $^{234}U/^{238}U$ of the three remaining samples (S01052-06A, S01052-82A, and S01052-90A) that have very low $^{236}U/^{238}U$ and $^{238}U/^{235}U$ that is very close (S01052-06A and S01052-82A) or indistinguishable (S01052-90A) from the natural ratio. From these relationships, it can be concluded that the samples from the plume zone likely vary from 100% anthropogenic to 0.8% anthropogenic. These values were calculated on the basis of the measured $^{236}U/^{238}U$ and with the assumption that samples S01052-38A and S01052-36A represents the composition (ave. $^{236}U/^{238}U = 5.39 \times 10^{-5}$) of the contaminant uranium (Table D.73). The percentage of anthropogenic uranium can be used to estimate the concentration of natural uranium in the samples. This is shown in Figure D.134, and compares the measured porewater uranium concentrations and the estimated natural uranium porewater concentrations. In general, the corrected uranium concentrations appear consistent with the stratigraphy.

Figure D.134. Depth versus ^{238}U Concentration (ppb) in Porewater for the Borehole 299-E33-46 core Near Tank B-110

Filled squares are samples analyzed for uranium isotopic composition for this report. Numbers in parentheses are porewater uranium concentrations corrected for the anthropogenic portion as calculated based on measured $^{236}U/^{238}U$. Inset to figure is a plot of $^{234}U/^{238}U$ versus $^{236}U/^{238}U$ for the samples from the borehole 299-E33-46 uranium contamination plume. Numbers to left of data points are porewater uranium concentrations, while number pairs to right of data points are uranium pore concentrations corrected for anthropogenic uranium and the depth in the core of the sample.

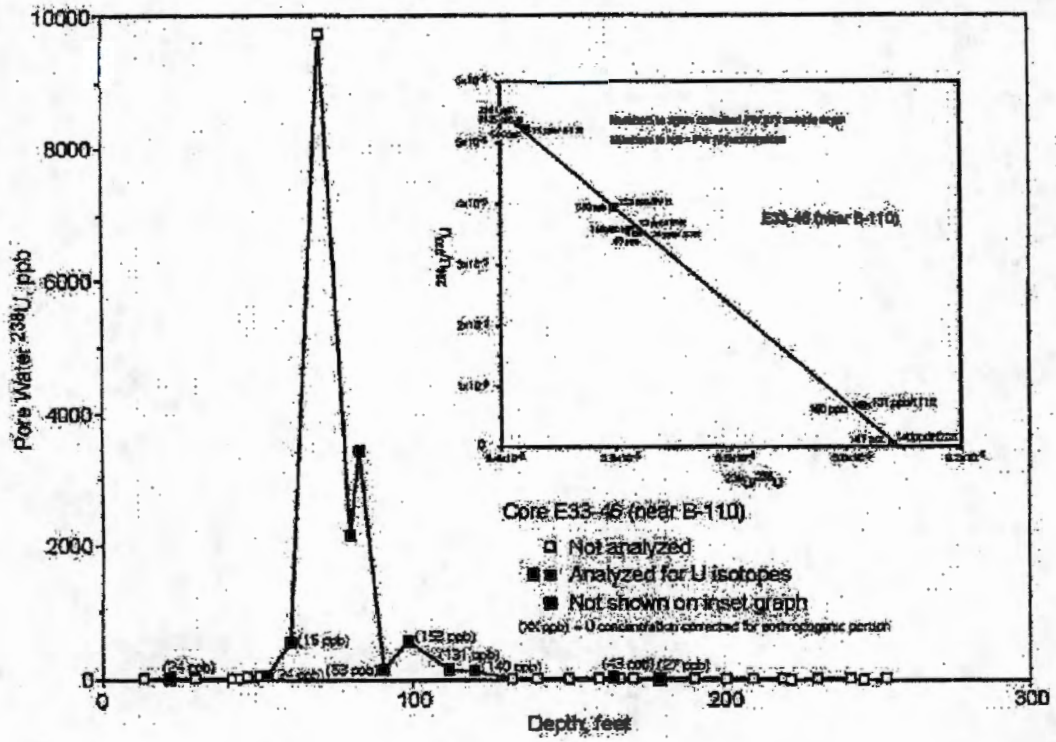

D.5.1.4 Discussion

D.5.1.4.1 Source of the WMA B-BX-BY Area Groundwater Uranium Plume. The results of the U isotopic analyses above can be compared to inventory estimates for the single-shell tanks (Jones et al. 2001) and to analyses of groundwater samples (Dresel et al. 2002). The cluster of data representing the plume in 299-E33-45 is a close match to the core of the WMA B-BX-BY groundwater U plume (data within oval on Figure D.132). This relationship implicates the 1951 overflow event from tank BX-102 as the primary source of the U contamination plume in the groundwater. This composition, however, is distinct from the inventory estimate for the BX-102 spill by Jones et al. (2001), which therefore may be incorrect. On the plot of $^{234}U/^{238}U$ versus $^{236}U/^{238}U$ (Figure D.133), the WMA B-BX-BY groundwater data fall along an array from the 299-E33-46 plume toward groundwater sample 299-E33-7, supporting the connection between the 299-E33-45 (tank BX-102) vadose zone contamination and groundwater contamination.

The isotopic composition of the WMA B-BX-BY groundwater U plume is consistent with the model estimates of production from the Al clad-0.71% ^{235}U (natural uranium) fuel type (Dresel et al. 2002). In addition, Dresel et al. (2002) provide a model history of the abundances of ^{234}U, ^{235}U, and ^{236}U of the fuel rods that were processed by the Hanford plants. The average abundances of ^{235}U, 6.72×10^{-3}, and ^{236}U abundance, 7.82×10^{-5}, for the 299-E33-45 plume are consistent with the composition of Al-0.71 fuel rods processed in approximately mid-1951. This supports the conclusion that the 1951 tank BX-102 event is the source of the vadose zone and groundwater contamination. The abundance of ^{234}U did not vary much for the Al 0.71% ^{235}U fuel, but the average ^{234}U abundance, 5.36×10^{-5}, for the 299-E33-45 plume is consistent with the A1-0.71% ^{235}U fuel and distinct from other fuel types processed later.

Assuming that the 299-E33-45 vadose zone U plume represents the source of U contamination in the groundwater samples (data from Dresel et al. 2002) from wells 299-E33-41 (20 ppb U), 299-E33-42 (9.5 ppb U), and 299-E33-16 (15 ppb U) (Figure D.132), the fraction of altered U in those samples and their pre-contamination U concentrations estimated. This indicates for 299-E33-41, 84% altered U and had a pre-contamination U concentration of 3.2 ppb, for 299-E33-42, 62% altered U and a pre-contamination U concentration of 3.6 ppb, and for 299-E33-16, 50% altered U and a pre-contamination U concentration of 7.3 ppb. These adjusted U concentration compare well to a sample from well 299-E33-7 with a U concentration of 3.5 ppb in which no ^{236}U was detected and therefore likely represents uncontaminated groundwater. The implication is that most, if not all, of the uranium in the groundwater samples from the WMA B-BX-BY area is consistent with contamination by the 1951 tank BX-102 event. This is supported by recent modeling of the supernatant chemical compositions for the B, BX, and BY tanks (Lichtner 2002, Section D.3.1) that indicates that the highest supernatant uranium concentration (by several orders of magnitude) was in tank BX-102. This, together with the large volume of that leak (347,000 liters of solution), suggests it as an important source of uranium contamination in the area.

D.5.1.4.2 Source of the Vadose Zone Uranium Plume in Borehole 299-E33-46. The isotopic composition of the 299-E33-46 U plume does not match the isotopic composition estimated by Jones et al. (2001) for the 1970 to 1971 leak from tank B-110. Even if this estimate is in error, the ^{236}U abundance (5.322×10^{-5}) and ^{235}U abundance (6.873×10^{-3}) would appear to be inconsistent with the composition of fuel processed in the late 1960s (see estimates by Dresel et al. 2002). Rather, such a composition would indicate A1-0.71 fuel from early (pre-1950) in the history of processing. Therefore, it is possible that the plume in the 299-E33-46 core is not related to the 1970 to 1971 leak from tank B-110, but related to an earlier unrecorded leak. In support, the modeled supernatant uranium concentration for tank B-110 is very small, on the order of 6×10^{-10} moles/L compared to 0.1 moles/L for tank BX-102 (Lichtner 2002, Section D.3.1). On that basis, the B-110 leak was probably not a significant source of uranium contamination.

Given the large volume of material spilled from tank BX-102, the possibility exists that the 299-E33-46 plume is a diluted mixture of tank BX-102 uranium and background uranium picked up during lateral spreading of the contaminant fluid. In a plot of $^{234}U/^{238}U$ versus $^{236}U/^{238}U$, the data for the 299-33-46 plume forms a linear array that represents mixing between anthropogenic uranium and background natural uranium (Figure D.133; see also inset to Figure D.134), as was also concluded from the plot of $^{238}U/^{234}U$ vsersu $^{236}U/^{238}U$. However, the 299-E33-45 plots off

the line defined by the 299-E33-46 plume samples. This suggests that there were probably separate sources for the 299-E33-45 and 299-E33-46 plumes.

This distinction can also be expressed in terms of the $^{236}U/^{234}U$ of the two vadose plumes. The $^{236}U/^{234}U$ for the 299-E33-45 plume is 1.489±0.003, which is distinct from the $^{236}U/^{234}U$ (0.986±0.001) of the 299-E33-46 plume (represented by samples S01052-36A and S01052-38A). In addition, as noted above, the WMA B-BX-BY groundwater samples follow a trend away from the 299-E33-45 (BX-102) plume toward background $^{234}U/^{238}U$ (represented by 299-E33-7) on Figure D.133. The data for the 299-E33-46 plume fall along a separate mixing line. This emphasizes the connection between the 299-E33-45 plume and the WMA B-BX-BY groundwater contamination, indicating that the groundwater plume is more closely related to that plume.

D.5.1.5 Conclusions

Multiple collector ICP-MS provides a very sensitive and precise technique for the measurement of U isotopic composition. It is able to provide $^{236}U/^{238}U$ (or ^{236}U abundance) measurements down to the 10^{-7} range with ~1% precision, and precision in $^{238}U/^{235}U$ down to ±0.035% at the 2σ level.

This technique was applied to water extractions of uranium from sediment samples from two contaminated cores, 299-E33-45 and 299-E33-46, taken near tanks BX-102 and B-110. From the uranium isotopic data, it can be concluded:

1. The vadose zone uranium contamination plume in borehole 299-E33-45 is the source of groundwater uranium contamination in the B-BX-BY area.
2. The source of the uranium contamination in borehole 299-E33-45 is most likely the 1951 tank BX-102 spill event of processed aluminum clad natural uranium fuel.
3. The vadose zone uranium contamination in borehole 299-E33-46 near tank B-110 is probably not related to the 1970 to 1971 leak from tank B-110. The uranium isotopic composition indicates early (pre-1950) processing of aluminum clad natural uranium fuel.
4. The uranium in the vadose plumes in cores 299-E33-45 and 299-E33-46 are derived from different sources.
5. Uranium isotopic measurements provide a sensitive means to tracing uranium contamination and defining the fraction of anthropogenic uranium in porewater and groundwater samples.

D.5.1.6 References

Dresel, P. E., J. C. Evans, and O. T. Farmer III, 2002, *Investigation of Isotopic Signatures for Sources of Groundwater Contamination at the Hanford Site*, PNNL-13763, Pacific Northwest National Laboratory, Richland, Washington.

Jones, T. E., B. C. Simpson, M. I. Wood, and R. A. Corbin, 2001, *Preliminary Inventory Estimates for Single-Shell Tank Leaks in B, BX, and BY Tank Farms,* RPP-7389, CH2M HILL Hanford Group, Inc., Richland, Washington.

D.5.2 STRONTIUM ISOTOPE EVIDENCE FOR INTERACTION BETWEEN WASTE FLUIDS AND SEDIMENTS IN THE WMA B-BX-BY VADOSE ZONE

Mark E. Conrad[1], John N. Christensen[1], Katharine Maher[2], and Donald J. DePaolo[1,2]

[1]Lawrence Berkeley National Laboratory, Berkeley, California 94720
[2]University of California, Berkeley, California 94720

D.5.2.1 Introduction

The concentration of strontium in vadose zone porewaters is relatively low relative to the concentration in the rocks (2 to 4 orders of magnitude). As a result, the strontium isotope ratios of the porewaters can be sensitive indicators of interaction between the fluids and the rock matrix. The degree and nature of interaction between pore fluids and the Hanford Site sediments is of special concern given the extreme chemical compositions of the waste fluids and the importance of processes such as sorption, mineral precipitation and dissolution on the transport of radionuclides (especially ^{90}Sr) in the waste fluids. To examine this interaction, the $^{87}Sr/^{86}Sr$ isotope ratios of de-ionized water rinses of sediment samples from the boreholes 299-E33-45 and 299-E33-46 have been measured.

D.5.2.2 Results

D.5.2.2.1 Borehole 299-E33-45. The $^{87}Sr/^{86}Sr$ ratios of de-ionized water rinses of 12 sediment samples from borehole 299-E33-45 have been measured and the results of these analyses are given in Table D.75. The upper 9 samples (from between 10 to 191 ft depth) had strontium isotope ratios ranging from 0.7138 to 0.7150. The lowest 3 samples (from between 200 and 254 ft depth) have significantly lower ratios (0.7106 to 0.7132).

The relatively homogenous values measured for the upper part of this core are in contrast with the results of an extensive set of de-ionized water rinses of sediment samples from borehole 299-W22-48, a background borehole drilled in the 200 West Area (Maher et al., in review). In the borehole 299-W22-48 samples, the $^{87}Sr/^{86}Sr$ ratios of the de-ionized water rinses ranged from 0.721 in the shallow subsurface down to 0.715 near the base of the Hanford formation. It is possible that this represents a difference between the two areas. Alternatively, the range of values measured in the upper part of the 299-E33-45 core matches the range values that have been measured for Columbia River water (the primary source of water that was used for Hanford operations) and it is also possible that this reflects addition of significant amounts of process water to the sediments (either from tank leaks or surface disposal of dilute fluids).

The deeper samples from borehole 299-E33-45 are from the bottom of the Hanford formation and into the Plio-Pleistocene formation. The lower $^{87}Sr/^{86}Sr$ ratios measured for these samples are similar to the values measured in borehole 299-W22-48.

Table D.75. Strontium Isotopic Data Core 299-E33-45 (Near Tank BX-102)

Sample	Ave. depth (ft)	PW [Sr] ppb	$^{87}Sr/^{86}Sr$	$\pm 2\sigma$
S01014-01A	10.6	376	0.714877	0.000010
S01014-06A	20.8	337	0.713920	0.000013
S01014-33A	73.4	2549	0.714212	0.000009
S01014-35A	78.2	547	0.714975	0.000011
S01014-72A	151.6	6757	0.714138	0.000010
S01014-78A	160.9	5048	0.714515	0.000009
S01014-82A	168.7	1790	0.713758	0.000010
S01014-83A	171.1	1876	0.713775	0.000011
S01014-93A	190.7	1936	0.714084	0.000010
S01014-99A	201.4	2646	0.713155	0.000010
S01014-116A	231.5	2132	0.710603	0.000009
S01014-129A	253.7	1963	0.711683	0.000010

D.5.2.2.2 Borehole 299-E33-46. The results of analyses of de-ionized water rinse samples from borehole 299-E33-46 are given in Table D.76. The limited number of analyses for this borehole (only 7 samples were successfully analyzed) are due to the extremely low porewater Sr concentrations in the sediments from the area of the contaminant plume (between 40 and 120 ft depth) coupled with the small volumes of liquid from the de-ionized water rinses of these samples that were available.

There is one major difference between the results of the analyses for the 299-E33-45 and the 299-E33-46 samples. Outside of the contaminant plume, the de-ionized water rinses from the 299-E33-46 samples have $^{87}Sr/^{86}Sr$ ratios in the same range as the upper samples from 299-E33-45 (all of the samples analyzed from 299-E33-46 are from the upper 180 ft of the core). Within the plume, however, the $^{87}Sr/^{86}Sr$ values of the de-ionized water rinses are lower, especially from the most contaminated sample that was able to be measured (S01052-38A), which had a ratio of 0.7118. This value is significantly lower than any de-ionized water rinse sample from the Hanford formation that has been measured to date.

Table D.76. Strontium Isotopic Data Core 299-E33-46 (Near Tank B-110)

Sample	Ave. depth (ft)	PW [Sr] ppb	$^{87}Sr/^{86}Sr$	$\pm 2\sigma$	^{90}Sr (ppt)[a]
S01052-06A	21.1	657	0.713759	0.000007	ND
S01052-38A	83.1	63	0.711785	0.000014	4.991
S01052-42A	90.6	297	0.713234	0.000010	0.032
S01052-47A	98.6	185	0.713442	0.000014	0.112
S01052-57A	119.9	184	0.714266	0.000016	0.003
S01052-82A	164.6	839	0.714205	0.000010	0.014
S01052-90A	179.9	619	0.713933	0.000009	0.019

[a] Concentration of ^{90}Sr extracted with 8 N HNO_3 (ppt of dry sediment).

D.5.2.3 Discussion

D.5.2.3.1 Strontium Isotopic Evidence for Enhanced Dissolution of Silicate Minerals by the Fluids in the 299-E33-46 Plume. The $^{87}Sr/^{86}Sr$ values measured for the de-ionized water rinse samples from borehole 299-E33-46 are plotted versus depth on Figure D.135 along with the total Sr concentrations in the rinse samples and the ^{90}Sr concentrations in concentrated nitric acid leaches of the samples. In the area of the plume, there is a clear decrease in the concentration of Sr in the de-ionized water rinses. As noted in Section D.2.4, interaction between the high-pH waste fluids and the sediments led to a combination of sorption of Sr in ion exchangeable states and precipitation in high magnesium calcite, causing the low porewater Sr concentrations.

The bulk sediments in the Hanford formation have $^{87}Sr/^{86}Sr$ ratios between 0.710 and 0.712 whereas the porewaters have much higher ratios (up to 0.721), especially in the upper part of the Hanford formation (Maher et al., in review). The cause of the high ratios in the porewaters is not clear, but is suspected to be due to rapid weathering of a mineral phase with high ratios (e.g., biotite or muscovite). As the fluids infiltrate, slow dissolution of the other minerals in the rock leads to a general decrease in the $^{87}Sr/^{86}Sr$ ratios of the vadose zone porewaters with depth in borehole 299-W22-48. In 299-E33-46, there is a similar decrease associated with the waste plume. Given the relatively recent introduction of the waste fluids (i.e., ~50 yrs ago), this implies that there has been significant dissolution and exchange of strontium between the waste fluids and the sediments. Furthermore, given that the waste fluids are precipitating carbonates, this exchange must be primarily with the silicate minerals in the sediments (e.g., feldspars).

The extent of Sr exchange between the waste fluids and the sediments is a function of the rate at which the fluid moves through the sediment and the degree of mineral dissolution. This information could potentially provide valuable information for estimating the kinetics of in situ reaction rates between the waste fluids and the sediments.

Figure D.135. Concentrations and $^{87}Sr/^{86}Sr$ Ratios of Sr in De-Ionized Water Leaches and Acid-Extractable 90Sr in the Sediments Plotted versus Depth in Borehole 299-E33-46

Also shown is the range of $^{87}Sr/^{86}Sr$ ratios in sediments from the Hanford formation.

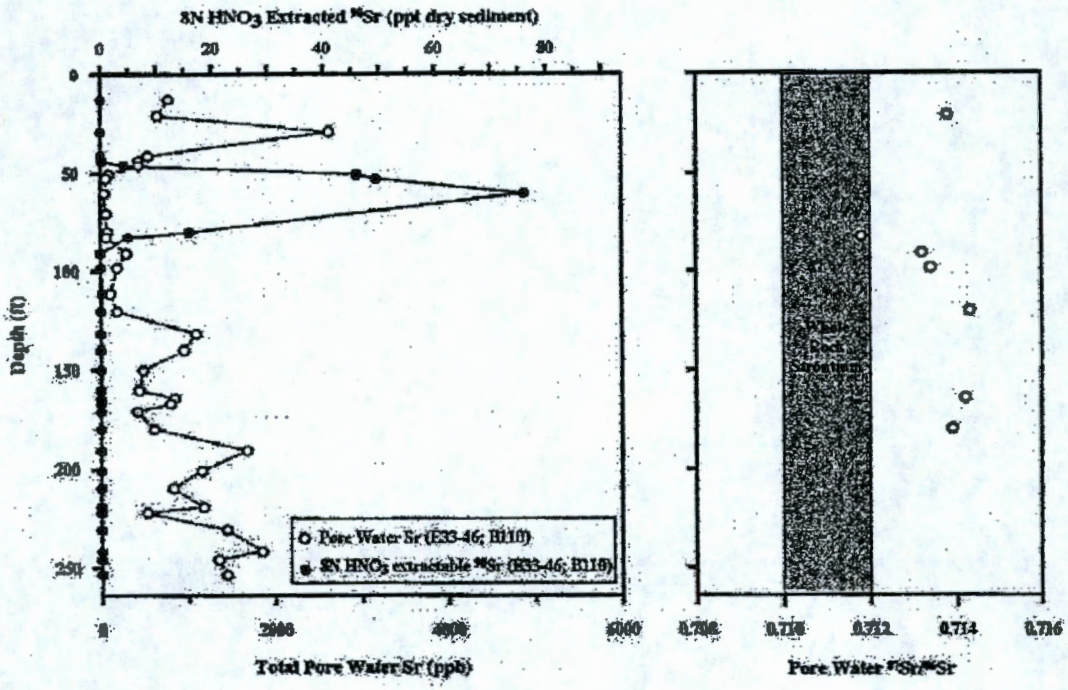

D.5.2.4 Conclusions

1. The de-ionized water rinses of the borehole 299-E33-45 and 299-E33-46 core samples suggest that the vadose zone in WMA B-BX-BY has undergone extensive interaction with fluids derived from Columbia River water (e.g., process waters).
2. There is a strong shift in the $^{87}Sr/^{86}Sr$ ratios in the de-ionized water rinses from the contaminant plume in borehole 299-E33-46, indicating that the high-pH waste fluids in this plume have resulted in rapid dissolution of silicate minerals in the sediments.

D.5.2.5 Reference

Maher, K., D. J. DePaolo, M. E. Conrad, and J. R. Serne, in review, "Vadose Zone Infiltration Rate at Hanford, Washington, inferred from Sr isotope measurements," *Water Resources Res.*

This page intentionally left blank.